

# **MORE EFFICIENT COLD-FORMED STEEL ELEMENTS AND BOLTED CONNECTIONS**



A thesis submitted for the degree of  
Doctor of Philosophy  
In the Faculty of Engineering of  
The University of Sheffield

by

JUN YE

Department of Civil and Structural Engineering  
The University of Sheffield

August, 2016

This page is intentionally left in blank

# ABSTRACT

Modern society is challenged by economic and environmental issues, requiring engineers to develop more efficient structures. Using cold-formed steel (CFS) frame in construction industry can lead to more sustainable design, since it requires less material to carry the same load compared with other materials. However, the application of CFS structural systems is limited to low story buildings due to the inherent weaknesses of premature buckling behaviour of members and the low ductility of connections. Consequently, current design guidelines of CFS systems are very conservative especially in the case of seismic design. Furthermore, there is no generic optimisation framework for the CFS elements, capable of taking into account both manufacturing/construction constraints and post-buckling behaviour.

This study aims to better understand, to predict, and to optimise CFS elements based on their strength and post-buckling behaviour. The optimised elements can be then included in full-structure modelling to develop more efficient CFS structural connections with high ductility and energy dissipation capacity, suitable for multi-story buildings in seismic regions.

The geometrical dimensions of manufacturable CFS cross-sections were optimised regarding their maximum compressive and bending strength. All the sections were considered to have a fix coil width and thickness while the optimisation was performed based on effective width method suggested in EC3. The optimised solutions were achieved using Particle Swarm Optimisation (PSO) algorithm. The accuracy of the optimisation procedure was assessed using experimentally validated nonlinear Finite Element (FE) analyses accounting for the effect of imperfections. To allow for the development of a new 'folded-flange' beam cross-section, the effective width method in EC3 was extended to deal with the presence of multiple distortional buckling modes. Improved strength were achieved for CFS elements by using the proposed optimisation framework.

A non-linear shape optimisation method was presented for the optimum design of CFS beam sections based on their post-buckling behaviour. A developed PSO algorithm was linked to the ABAQUS finite element programme for inelastic post-buckling analysis and optimisation. The results also demonstrate that the optimised sections develop larger plastic area, which is particularly important in seismic design of moment-resisting frames.

An experimental programme was carried out at the University of Sheffield to investigate the design and optimisation, considering interactive buckling in cold-formed steel channels under compression and bending. Both standard and optimised sections were tested. The specimen imperfections were measured using a specially designed set-up with laser displacement. Material tests were also carried out to determine the tensile properties of the flat plate and of the cold-worked corners. A total of 36 columns with three lengths and 6 back-to-back beams were completed. The column specimens were tested under a concentrically applied load and with pin-ended boundary conditions while the beams were tested in a four-point bending configuration. Based on the tests, numerical models were proposed and calibrated and the proposed optimisation framework was verified.

A numerical study on the structural behaviour of CFS bolted beam-to-column connections under cyclic loading was presented. An innovative two node element which can take into account the slippage-bearing effects was proposed and implemented using an ABAQUS user defined subroutine. The connection performance in terms of strength, ductility, energy dissipation capacity and damping coefficient were investigated. The effects of bolt configuration, cross-sectional shapes and thicknesses on the connection performance were therefore examined. It is indicated that the proposed numerical model is robust and computationally efficient to simulate the failure modes and moment-rotation response of CFS bolted moment resisting connections.

# PUBLICATIONS

## Peer-reviewed journal papers (published):

Ma WX, Becque J, Hajirasouliha I, and Ye J. (2015). Cross-sectional optimization of cold-formed steel channels to Eurocode 3. *Engineering Structures*, 101: 641-651.

Ye J, Hajirasouliha I, Becque J, and Pilakoutas K. (2016). Development of more efficient cold-formed steel channel sections in bending. *Thin-Walled Structures*, 101: 1-13.

Ye, J, Hajirasouliha I, Becque J, and Eslami A. (2016). Optimum design of cold-formed steel beams using Particle Swarm Optimisation method. *Journal of Constructional Steel Research*, 122: 80-93.

## Peer-reviewed journal papers (under submission):

Ye J, Hajirasouliha I, Becque J, Lim J B P. Development of optimum cold-formed steel sections for maximum energy dissipation in seismic applications. *Computers and Structures*.

Ye J, Hajirasouliha I, Becque J, and Pilakoutas K. Experimental investigations on CFS channel columns subjected to local-flexural interactive buckling. *Thin-Walled Structures*.

Ye J, Hajirasouliha I, Becque J, and Pilakoutas K. A numerical investigation of local-flexural interactive buckling of CFS plain and lipped channel columns. *Thin-Walled Structures*.

Ye J, Mojtabaei S, Hajirasouliha I, Becque J, and Pilakoutas K. Local and distortional buckling behaviour of CFS back-to-back channels: an analytical investigation. *Journal of Constructional Steel Research*

Ye J, Mojtabaei S, Hajirasouliha I, Becque J, and Pilakoutas K. Seismic behaviour of cold-formed steel bolted moment connections: an analytical study. *Engineering Structures*.

## Peer-reviewed conference papers:

Ye J, Hajirasouliha I, Becque J & Pilakoutas K (2016). Experimental investigation of local-flexural interactive buckling of CFS channel columns. *The 7th International Conference on Coupled Instabilities in Metal Structures*. Baltimore, Maryland, USA, 7 November-8 November 2016

Ye J, Meza FJ, Hajirasouliha I, Becque J & Pilakoutas K (2016). Experimental investigation of the bending capacity of cfs back-to-back channel sections. *The 8th International Conference on Steel and Aluminium Structures*. Hong Kong, China, 7 December 2016 – 9 December 2016.

Ye J, Hajirasouliha I, Becque J & Lim J (2016). Optimisation of cold-formed steel sections for maximum energy dissipation capacity and strength. *The International Colloquium on Stability and Ductility of Steel Structures*. Timisoara, Romania, 30 May 2016 - 1 June 2016.

Ye J, Hajirasouliha I & Becque J (2015). Cold-formed steel channel beams: From optimal design to development of a novel section. *The Annual Postgraduate Research Student Conference* (pp 1-7). Sheffield, UK, 15 April 2015 - 15 April 2015.



## ACKNOWLEDGMENTS

I don't like departure, however, I have to because I have a dream. I have been familiar with the Engineering Mappin Building which is in a classical style with red bricks. I studied here with my colleagues and exchange my ideas with my friends from different cultures and backgrounds.

This work would not have been possible without the financial support of the departmental scholarship at the University of Sheffield and this is also gratefully acknowledged.

I would like to express my deepest gratitude to my supervisors Dr Iman Hajirasouliha and Prof. Kypros Pilakoutas, and my nice research advisers Dr Jurgen Becque and Dr Maurizio Guadagnini. Your guidance, inspiration and continuous encouragement made this thesis possible. I am really thankful to Dr James Lim at the University of Auckland for his invaluable advice and co-supervision on my work.

Thank you to all my colleagues in rooms E110a and D120, particularly to Reyes Garcia Lopez and Seyed Mohammad Mojtabaei. It was a pleasure to work with you guys. You were helping me not only on my research but also on my daily life.

The experimental programme on the cold-formed steel specimens at the University of Sheffield was completed thanks to the assistance and technical expertise of the Heavy Structures Laboratory staff. Special thanks go to Shaun Waters and Don Jenkins for their continuous help and support. Thank you also to Kieran Nash and Chris Todd, who were involved at different stages of the programme. My appreciation also goes to Hao Wen and Francisco Meza Ortiz, who helped during the final part of the beam tests.

Thanks to my previous supervisors Prof. Boqing Gao and Prof. Xudong Fu in Zhejiang University and Wuhan University. You are supporting me from a different place and giving me guidance all the time on my life and research.

To my family: thank you for your support and encouragement.

I would like to express my gratefulness to my lover: Guan Quan in the Fire Group at the University of Sheffield. We have been sharing happiness, enjoying life and helping with each other for 6 years by now. Hope we will get married and have children and continue to make our life and research rich and fruitful. Thank you very much for your support all the time.

# TABLE OF CONTENTS

<b>ABSTRACT</b>	<b>I</b>
<b>PUBLICATIONS</b>	<b>II</b>
<b>ACKNOWLEDGMENTS</b>	<b>III</b>
<b>TABLE OF CONTENTS</b>	<b>IV</b>
<b>LIST OF FIGURES</b>	<b>IX</b>
<b>LIST OF TABLES</b>	<b>XIV</b>
<b>LIST OF SYMBOLS</b>	<b>XVI</b>
<b>CHAPTER 1. INTRODUCTION</b>	<b>1</b>
1.1 BACKGROUND	1
1.2 NECESSITY OF RESEARCH	3
1.2.1 <i>Optimisation of CFS elements for maximum strength</i>	3
1.2.2 <i>Optimisation of CFS elements for improved post-buckling behaviour</i>	4
1.2.3 <i>Optimisation of CFS elements and experimental validation</i>	4
1.2.4 <i>Performance of CFS moment resisting connections</i>	5
1.3 AIMS AND DETAILED OBJECTIVES	6
1.4 THESIS LAYOUT	7
<b>CHAPTER 2. LITERATURE REVIEW</b>	<b>11</b>
2.1 CFS SECTIONS	11
2.2 DESIGN OF CFS MEMBERS	18
2.2.1 <i>EC3</i>	19
2.2.2 <i>Direct Strength Method</i>	20
2.3 SEISMIC BEHAVIOUR OF CFS MEMBERS	22
2.4 COLD-FORMED STEEL CONNECTIONS	23
2.5 OPTIMISATION OF CFS ELEMENTS	26
2.6 CFS STRUCTURAL SYSTEM	28
2.7 SUMMARY	31
<b>CHAPTER 3. OPTIMISATION OF CFS COLUMNS USING PARTICLE SWARM OPTIMISATION METHOD</b>	<b>33</b>
3.1 INTRODUCTION	34
3.2 DESIGN OF CFS COLUMNS BASED ON EC3	34
3.2.1 <i>Design for local buckling</i>	34
3.2.2 <i>Design for distortional buckling</i>	35
3.2.3 <i>Design for global buckling</i>	36
3.2.4 <i>The shift of the effective centroid</i>	36
3.3 PARTICLE SWARM OPTIMISATION METHOD	37
3.4 OPTIMISATION PROCEDURE	38
3.4.1 <i>Problem definition</i>	38
3.4.2 <i>Optimised results and comparison</i>	41
3.5 NONLINEAR FE ANALYSIS OF THE OPTIMISED COLUMNS	44
3.6 DESCRIPTION AND COMPARISON OF THE RESULTS	47
3.7 SUMMARY AND CONCLUSIONS	50
<b>CHAPTER 4. OPTIMUM DESIGN OF CFS BEAMS USING PARTICLE SWARM OPTIMISATION METHOD</b>	<b>51</b>

## Table of contents

---

4.1	INTRODUCTION	51
4.2	DESIGN OF CFS BEAMS BASED ON EC3	53
4.2.1	<i>Design for local buckling</i>	53
4.2.2	<i>Design for distortional buckling</i>	55
4.2.3	<i>Design for global buckling</i>	56
4.3	DEFINITION OF OPTIMISATION PROBLEM	56
4.4	OPTIMISATION OF CFS BEAMS	60
4.4.1	<i>Laterally braced beams</i>	60
4.4.2	<i>Laterally unbraced beams</i>	62
4.5	NONLINEAR FE ANALYSIS CONSIDERING INITIAL GEOMETRIC IMPERFECTIONS	66
4.5.1	<i>FE modelling</i>	67
4.5.2	<i>Experimental verification of the FE model</i>	67
4.6	FE SIMULATIONS OF THE OPTIMISED CHANNEL SECTIONS	73
4.6.1	<i>Laterally braced beams</i>	73
4.6.2	<i>Laterally unbraced beams</i>	75
4.7	EVALUATION OF THE EC3 BASED APPROACH	77
4.8	SUMMARY AND CONCLUSIONS	79
<b>CHAPTER 5. DEVELOPMENT OF A MORE EFFICIENT CFS CHANNEL SECTION IN BENDING</b>		<b>81</b>
5.1	INTRODUCTION	82
5.2	DESIGN OF CFS MEMBERS BASED ON EC3	82
5.2.1	<i>Local buckling</i>	82
5.2.2	<i>Distortional buckling</i>	83
5.3	OPTIMISATION PROCEDURE	86
5.3.1	<i>Problem definition</i>	86
5.3.2	<i>Optimisation solutions</i>	89
5.4	FE ANALYSIS	92
5.4.1	<i>FE modelling and parameters</i>	92
5.4.2	<i>FE analysis of folded-flange sections with varying dimensions</i>	94
5.4.3	<i>FE results of optimised cross-sections</i>	97
5.5	COMPARISON OF THE RESULTS AND DISCUSSION	99
5.6	SUMMARY AND CONCLUSIONS	100
<b>CHAPTER 6. DEVELOPMENT OF OPTIMUM CFS SECTIONS FOR MAXIMUM ENERGY DISSIPATION IN SEISMIC APPLICATIONS</b>		<b>103</b>
6.1	INTRODUCTION	104
6.2	DEVELOPMENT OF OPTIMUM CFS SECTIONS FOR SEISMIC APPLICATIONS	105
6.3	FE ANALYSES OF CFS BEAM SECTIONS	106
6.3.1	<i>FE models</i>	107
6.3.2	<i>Flexural strength and post-buckling behaviour of sections</i>	107
6.3.3	<i>Ductility capacity of sections</i>	110
6.3.4	<i>Energy dissipation capacity of sections</i>	112
6.4	FORMULATION OF OPTIMISATION PROBLEM AND OPTIMISATION METHOD	114
6.4.1	<i>Problem formulation</i>	114
6.4.2	<i>Optimisation technique</i>	117
6.5	OPTIMISATION RESULTS AND DISCUSSIONS	119
6.6	CONCLUSIONS	123
<b>CHAPTER 7. EXPERIMENTAL INVESTIGATIONS ON CFS CHANNEL COLUMNS CONSIDERING INTERACTIVE BUCKLING</b>		<b>125</b>
7.1	INTRODUCTION	126
7.2	SPECIMEN GEOMETRY	127

## Table of contents

---

7.3	MATERIAL PROPERTIES	130
7.4	IMPERFECTION MEASUREMENTS	131
7.5	COLUMN TESTS	133
7.6	TEST RESULTS	135
7.7	CONCLUSIONS	140
<b>CHAPTER 8. A NUMERICAL INVESTIGATION OF LOCAL-FLEXURAL INTERACTIVE BUCKLING OF STANDARD AND OPTIMISED COLUMNS</b>		<b>143</b>
8.1	INTRODUCTION	144
8.2	DIRECT STRENGTH METHOD FOR CFS COLUMN DESIGN	145
8.3	OPTIMISATION OF CFS BEAM-COLUMNS	146
8.4	NUMERICAL MODELLING	147
8.4.1	<i>Material model</i>	147
8.4.2	<i>Boundary conditions</i>	148
8.4.3	<i>Element type and mesh size</i>	150
8.4.4	<i>Imperfections</i>	150
8.4.5	<i>Numerical results</i>	152
8.5	EVALUATION OF EC3 AND DSM DESIGN METHODS	155
8.6	EVALUATION OF THE OPTIMISATION PROCESS	156
8.7	CONCLUSIONS	158
<b>CHAPTER 9. EXPERIMENTAL INVESTIGATION OF THE BENDING CAPACITY OF CFS BACK-TO-BACK STANDARD AND OPTIMISED BEAMS</b>		<b>159</b>
9.1	INTRODUCTION	160
9.2	SECTION GEOMETRY AND LABELLING	160
9.3	MATERIAL PROPERTIES	162
9.4	IMPERFECTION MEASUREMENTS	163
9.5	TEST SET-UP	165
9.6	TEST RESULTS	165
9.6.1	<i>Deformed shape</i>	165
9.6.2	<i>Ultimate capacity</i>	168
9.7	CONCLUSIONS	169
<b>CHAPTER 10. LOCAL AND DISTORTIONAL BUCKLING OF STANDARD AND OPTIMISED CFS BACK-TO-BACK CHANNELS: A NUMERICAL STUDY</b>		<b>171</b>
10.1	INTRODUCTION	172
10.2	DIRECT STRENGTH METHOD (DSM)	173
10.3	OPTIMISATION OF CFS BEAMS	174
10.4	NUMERICAL MODELLING	176
10.4.1	<i>Material model</i>	176
10.4.2	<i>Boundary conditions</i>	177
10.4.3	<i>Element type and mesh</i>	179
10.4.4	<i>Bolt modelling</i>	179
10.4.5	<i>Imperfections</i>	182
10.4.6	<i>Numerical results</i>	184
10.5	EVALUATION OF CURRENT DESIGN METHODS OF EC3 AND DSM	189
10.6	EVALUATION OF THE OPTIMISATION PROCESS	189
10.7	CONCLUSIONS	190
<b>CHAPTER 11. BEHAVIOUR OF CFS BOLTED CONNECTIONS: A NUMERICAL PARAMETRIC STUDY</b>		<b>193</b>
11.1	INTRODUCTION	194
11.2	FINITE ELEMENT MODEL	196

## Table of contents

11.2.1	<i>Bolt modelling</i>	196
11.2.2	<i>Geometry, boundary conditions and element types</i>	199
11.2.3	<i>Material model</i>	200
11.2.4	<i>Imperfections</i>	201
11.2.5	<i>Solution technique and load regime</i>	202
11.2.6	<i>Validation of FE modelling</i>	203
11.3	CONNECTION CONFIGURATIONS FOR PARAMETRIC STUDY	208
11.4	CROSS-SECTIONS CLASSIFICATION	209
11.4.1	<i>Eurocode concept</i>	209
11.4.2	<i>Finite strip method</i>	213
11.5	PARAMETRIC FINITE ELEMENT ANALYSIS RESULTS	214
11.5.1	<i>AISC requirements for the connection</i>	217
11.5.2	<i>Moment capacity of the connections</i>	218
11.5.3	<i>Ductility ratio</i>	219
11.5.4	<i>Energy dissipation</i>	220
11.5.5	<i>Damping coefficient</i>	221
11.5.6	<i>Effect of the thickness of gusset plate</i>	224
11.6	DSM DESIGN FOR COLD-FORMED SECTIONS	225
11.6.1	<i>Local buckling strength</i>	225
11.6.2	<i>Distortional buckling strength</i>	226
11.6.3	<i>Comparison between FE results of CFS bolted-moment connections and DSM design rules for pure bending</i>	226
11.7	CONNECTIONS WITH SLIPPAGE	227
11.7.1	<i>Effect of slip resistance</i>	227
11.7.2	<i>Effect of bolt arrangement and channel thickness</i>	229
11.7.3	<i>Maximum moment capacity</i>	229
11.7.4	<i>Energy dissipation</i>	230
11.7.5	<i>Damping coefficient</i>	231
11.7.6	<i>AISC requirements for the connection with slippage</i>	233
11.8	DEVELOPMENT OF A TWO NODE ELEMENT TO MODEL THE SLIP BEARING BEHAVIOUR OF BOLTS	235
11.9	SUMMARY AND CONCLUSIONS	238
<b>CHAPTER 12.</b>	<b>SUMMARY AND CONCLUSIONS, AND RECOMMENDATIONS FOR FUTURE WORK</b>	<b>241</b>
12.1	SUMMARY AND CONCLUSIONS	241
12.1.1	<i>Optimisation of CFS columns</i>	242
12.1.2	<i>Optimisation of CFS beams</i>	242
12.1.3	<i>Development of more efficient CFS beam sections</i>	243
12.1.4	<i>Optimisation of CFS beams based on their post-buckling behaviour</i>	244
12.1.5	<i>Experimental work on standard and optimised CFS columns</i>	245
12.1.6	<i>Experimental work on standard and optimised CFS beams</i>	245
12.1.7	<i>Numerical study on optimised CFS columns</i>	246
12.1.8	<i>Numerical study on optimised CFS beams</i>	247
12.1.9	<i>Behaviour of CFS bolted connections</i>	248
12.2	RECOMMENDATIONS FOR FUTURE WORK	250
<b>REFERENCES</b>		<b>253</b>
<b>APPENDIX COMPUTER PROGRAMMES</b>		<b>270</b>

This page is intentionally left in blank

# LIST OF FIGURES

Figure 1.1. A multi-storey hot-rolled steel frame in Sheffield.....	1
Figure 1.2. Cold-formed steel (a) portal frame and (b) framing residential building .....	2
Figure 1.3. CFS beams with (a) curved flanges and (b) folded flanges.....	5
Figure 2.1. Manufacturing process for cold-formed steel members using roller or press-braking process (Amouzegar et al. 2016).....	12
Figure 2.2. (a) Different cross-sectional shapes (Yu and LaBoube 2010) (b) Variety of cross-sections made from dimpled steel sheets (Hadley Industries plc) (c) Dimpled steel sheets produced by the UltraSTEEL® process in Hadley Industries plc (Hadley Industries plc).....	12
Figure 2.3. Evolution of cold-formed Zed and Channel purlin sections (Davies 2000). .....	13
Figure 2.4. Different shapes of cross sections of cold-formed channel beams with (a) Triangular hollow flanges (Avery, Mahendran and Nasir 2000) (b) LiteSteel beam with rectangular hollow flanges (Anapayan, Mahendran and Mahaarachchi 2011) (c) Delta hollow flanges (Mohebkhah and Azandariani 2015) (d) rectangular hollow flanges (Tondini and Morbioli 2015) (e) stiffened rectangular hollow flanges (Tondini and Morbioli 2015) (f) open drop flanges (Magnucki, Paczos and Kasprzak 2010) (g) closed drop flanges (Magnucki, Paczos and Kasprzak 2010) and (h) double box flanges (Magnucka-Blandzi and Magnucki 2011) .....	14
Figure 2.5. Columns with complex intermediate and edge stiffeners (Chen et al. 2010, Yan and Young 2002) .....	15
Figure 2.6. Section geometries of the innovative steel columns (Narayanan and Mahendran 2003) .....	15
Figure 2.7. Cold-formed steel built-up sections (Wang and Young 2016a, Wang and Young 2016b) .....	16
Figure 2.8. Cold-formed and concrete composite beam (Hanaor 2000). .....	17
Figure 2.9. Cold-formed steel composite elements with (a) bamboo (Li et al. 2015, Li et al. 2012) and (b) wood (Kyvelou et al. 2015).....	18
Figure 2.10. Buckling modes of a lipped channel in compression using CUFSM (Schafer 2006).....	19
Figure 2.11. Effective width of plane element restrained along both edges (Davies 2000).....	20
Figure 2.12. Distortional buckling model : (a) flange with edge stiffener (b) flexural buckling of edge stiffener as a strut on elastic foundation and (c) flexural buckling curve for edge stiffener (CEN 2005b) .	20
Figure 2.13. Responses of bolted CFS beam–column moment-resisting connections: (a) energy dissipation through slippage and bearing failure ;(b) through beam section (Sabbagh et al. 2012a).....	23
Figure 2.14. (a) Beam-column connection with stiffeners (Sabbagh et al. 2013) and (b) CFS truss bolted connection (Zaharia and Dubina 2006).....	24
Figure 2.15. (a) Sleeve and overlapped connections (Yang and Liu 2012, Zhang and Tong 2008) and (b) Details of apex joint (Lim and Nethercot 2003).....	24
Figure 2.16. (a) connection presented by Uang et al. (Uang et al. 2010) and (b) by Sabbagh et al. (Sabbagh et al. 2012b).....	26
Figure 2.17. Optimal cross sections found by using GA and DSM (Leng et al. 2011) .....	27
Figure 2.18. Evolution of CFS cross-sections by adding bents (Sabbagh et al. 2012a).....	28
Figure 2.19. Moment-rotation behaviour of the CFS cross-sections (Sabbagh et al. 2012a).....	28
Figure 3.1. Effective area of (a) a plain C channel; and (b) a lipped channel with stiffener.....	35
Figure 3.2. Flange and web models of a lipped channel section for distortional buckling calculations. ....	35
Figure 3.3. Standard CFS column section (BW C17515) with the total coil length of 341mm.....	40
Figure 3.4. Stress-strain behaviour of CFS plate used in the FE modelling.....	45
Figure 3.5. Schematic illustration of the FE model of the columns with pin-ended boundary conditions..	46
Figure 3.6. Comparison of the axial capacity of the standard and optimised columns with 1 m length ...	49
Figure 3.7. Comparison of the axial capacity of the standard and optimised columns with 2 m length ...	49
Figure 3.8. Comparison of the axial capacity of the standard and optimised columns with 3 m length ...	50
Figure 4.1. Effective width of (a) lipped channel; (b) internal compression element; and (c) outstand compression element .....	54
Figure 4.2. Simplified models for distortional buckling calculations .....	55

List of figures

Figure 4.3. Standard CFS beam cross-section (TATA-A3709).....	56
Figure 4.4. Optimal cross-sections for laterally restrained beams using different prototypes .....	61
Figure 4.5. Comparison of the flexural strength of standard and optimised cross-sections for laterally braced beams .....	62
Figure 4.6. Optimised results for member capacity of lipped channel beams .....	63
Figure 4.7. Comparison of the flexural strength of the optimised and standard cross-sections for laterally unbraced beams .....	64
Figure 4.8. Comparison of the flexural strength of the optimised and standard cross-sections for laterally braced beams obtained using the DSM and EC3 .....	65
Figure 4.9. Comparison of the flexural strength of the optimised and standard cross-sections for laterally unbraced beams obtained using the DSM .....	65
Figure 4.10. Schematic illustration of Yu and Schafer’s (Yu and Schafer 2006, Yu and Schafer 2007) distortional buckling test set-up and cross-sectional geometry .....	67
Figure 4.11. FE model and boundary conditions.....	69
Figure 4.12. Distortional imperfections in the FE model.....	69
Figure 4.13. Comparison between experimental results (Yu and Schafer 2006, Yu and Schafer 2007) and results of FE analyses for laterally braced specimen D11.5Z092-3 for 3 mesh sizes (mesh sensitivity analysis) .....	71
Figure 4.14. CFS beam with negative lateral-torsional imperfection .....	72
Figure 4.15. FE model and boundary conditions for laterally unbraced beams.....	72
Figure 4.16. Typical failure mode of laterally unbraced beams (specimen 10L17e0 at ultimate load) .....	72
Figure 4.17. Comparison between experimental results and FE analysis for laterally unbraced specimen 10L17e0 (Put et al. 1999).....	73
Figure 4.18. Boundary conditions in the FE models of channel sections.....	74
Figure 4.19. Comparison of FE predicted strengths of optimised and standard cross-sections for laterally braced beams .....	75
Figure 4.20. FE model for laterally unbraced standard and optimised beams .....	75
Figure 4.21. Moment-lateral deflection curves at mid-span of the optimised unbraced beams.....	76
Figure 4.22. Comparison of FE predicted flexural strengths of optimised and standard cross-sections for laterally unbraced beams .....	76
Figure 4.23. Flexural strength ratio of the optimised sections to the standard section for (a) laterally braced beams and (b) for laterally unbraced beams using the same amount of material.....	79
Figure 5.1. Local buckling mode of a folded-flange cross-section: (a) buckled shape, (b) effective area of the cross-section for local buckling, (c, d) web under stress gradient .....	83
Figure 5.2. Distortional buckling mode of a channel section with intermediate and edge stiffeners (a) distortional buckled shape and (b) equivalent struts .....	84
Figure 5.3. (a) Actual system, and (b) simplified model to analyse distortional buckling of type 1.....	85
Figure 5.4. (a) Actual system, and (b) simplified model to analyse distortional buckling of type 2.....	86
Figure 5.5. Selected commercial CFS beam cross-section .....	87
Figure 5.6. Iteration history of the maximum bending capacity of prototype ⑩.....	90
Figure 5.7. FE model of the folded-flange beam subjected to local/distortional buckling .....	93
Figure 5.8. Geometric imperfections: (a) local buckling, and (b) distortional buckling .....	93
Figure 5.9. Moment-rotation curve of the folded-flange sections.....	96
Figure 5.10. Schematic view of the behaviour of axially compressed panels (adapted from (Jones 2006)) .....	97
Figure 5.11. Buckling shapes at peak load of the optimised and standard sections (Stress: MPa) .....	98
Figure 5.12. Comparison of the moment capacities of different prototypes .....	99
Figure 6.1. Development of CFS sections towards curved flanges to increase cross-sectional ductility (Sabbagh et al. 2012a).....	105
Figure 6.2. Reduction of the width-to-thickness ratio by using intermediate stiffeners and folding the flanges .....	106



## List of figures

Figure 6.3. Boundary conditions and loading points for the cantilever beam.....	108
Figure 6.4. Various cross-sectional shapes for back-to-back channel beams and their failure modes at a drift angle of 0.04rad (SMF limit) .....	109
Figure 6.5. Moment-rotation curves of the beams with the dimensions in Figure 6.5.....	110
Figure 6.6. Equivalent energy elastic-plastic (EEEE) bi-linear models of the load-deformation curve(ASM 2009) .....	111
Figure 6.7. Ductility of the 6 selected CFS beams with the same amount of material .....	112
Figure 6.8. Comparison of (a): maximum equivalent plastic strain; (b): Energy dissipation capacity.....	113
Figure 6.9. A cantilever beam model for optimisation process .....	114
Figure 6.10. Flowchart of optimisation for maximum dissipated energy.....	118
Figure 6.11. Iteration history of the objective of dissipated energy for folded flange channel section....	119
Figure 6.12. Energy dissipation capacity of optimum sections versus maximum plastic strain limit.....	121
Figure 6.13. Maximum energy dissipated of prototypes subjected to various maximum plastic strain constraints at 4% drift ratio .....	121
Figure 6.14. Distribution of von Mises stress of standard and optimal beams subjected to $\bar{\epsilon}_p \leq 0.2$ at drift ratio of 4% .....	123
Figure 7.1. Buckling modes of a lipped channel: (a) local, (b) distortional, (c) global and (d) interactive modes.....	126
Figure 7.2. Symbol definitions and nominal cross-sectional dimensions.....	128
Figure 7.3. Tensile material tests for: (a) flat coupons (b) corner coupons .....	130
Figure 7.4. Imperfection measurement set-up .....	132
Figure 7.5. Location of the imperfection measurement .....	132
Figure 7.6. Specimen boundary conditions.....	134
Figure 7.7. Test set-up .....	135
Figure 7.8. Positions of strain gauges and LVDTs at mid-height of columns.....	135
Figure 7.9. Failure modes of 1000 mm long columns with section type B .....	136
Figure 7.10. Failure modes of 1000 mm long columns with section type C .....	136
Figure 7.11. Axial load versus end shortening curves for tested specimens.....	137
Figure 8.1. Symbol definitions and nominal cross-sectional dimensions.....	147
Figure 8.2. Stress–strain curves resulted from (a) flat and (b) corner coupon tests.....	148
Figure 8.3. Boundary conditions of FE model against test .....	149
Figure 8.4. Axial load vs shortening of A1000-a specimen with various friction factors defined in the contact properties of FE analyses.....	150
Figure 8.5. (a) The measured imperfection profiles; (b) Incorporating measured imperfections into FE models.....	151
Figure 8.6. Imperfection inclusion .....	151
Figure 8.7. Axial load-axial shortening relationship resulting from FE against Test .....	153
Figure 8.8. Deformation of FE model vs actual specimen (A1000-a) at points a, b and c.....	153
Figure 8.9. Compressive strength of the standard section to the optimised sections using the same amount of material .....	157
Figure 9.1. Symbol definitions and nominal cross-sectional dimensions.....	161
Figure 9.2. Tensile material tests for: (a) flat coupons (b) corner coupons .....	162
Figure 9.3. The set-up for imperfection measurement.....	164
Figure 9.4. Schematic view of: (a) experimental set-up (b) lateral support system .....	165
Figure 9.5. Failure progression and Moment vs Mid-span deflection in beam C180-2.....	167
Figure 9.6. Failure progression and Moment vs Mid-span deflection in beam A230-2.....	167
Figure 9.7. Failure progression and Moment vs Mid-span deflection in beam B270-2.....	168
Figure 9.8. Moment vs mid-span deflection for all beams .....	169
Figure 10.1. Symbol definitions and nominal cross-sectional dimensions.....	175
Figure 10.2. Stress–strain curves resulted from (a) flat and (b) corner coupon tests.....	177
Figure 10.3. Typical experimental setup of four-point bending tests of back-to-back beam sections .....	178

## List of figures

---

Figure 10.4. Boundary conditions of FE model against test.....	179
Figure 10.5. Load-deformation relationship of a bolt slipping and bearing against a steel plate .....	181
Figure 10.6. Single bolt modelling in ABAQUS: (a) components defined in a connector; (b) reducing the bearing behaviour by coupling the node at bolt position to a number of nodes around .....	182
Figure 10.7. Measured imperfection in B270-1a (a) profile; (b) included in the FE model (magnified 50 times).....	183
Figure 10.8. Measured imperfection profile and its Fourier representation.....	183
Figure 10.9. Imperfection inclusion.....	184
Figure 10.10. Moment versus mid-span deflection relationship resulting from FE against Test.....	185
Figure 10.11. Deformed shapes from the test of beam C180-2 and stress distributions (MPa) from the FE analysis, recorded at three stages of loading (see Figure 10.10) .....	186
Figure 10.12. Deformed shapes from the test of beam A230-2 and stress distributions (MPa) from the FE analysis, recorded at three stages of loading (see Figure 10.10) .....	187
Figure 10.13. Deformed shapes from the test of beam B270-2 and stress distributions (MPa) from the FE analysis, recorded at three stages of loading (see Figure 10.10) .....	188
Figure 10.14. Flexural strength of the optimised sections to the standard section using the same amount of material .....	190
Figure 11.1. Configuration of CFS moment resisting connections with (a) curved flange beam (Sabbagh et al. 2012a) and (b) folded flange beam (Ye et al. 2016b) .....	195
Figure 11.2. Relationship between a single bolts bearing against steel plate to full CFS connection.....	197
Figure 11.3. Single bolt modelling in ABAQUS: (a) definition of fastener; (b) components defined in a connector section and (c) slip-bearing relationship defined in a connector section .....	198
Figure 11.4. Boundary conditions of the FE model for beam-column connection .....	200
Figure 11.5. FE model of the beam-column connection with fastener definition .....	200
Figure 11.6. Stress-strain curve from the coupon test was used in the FE model(Sabbagh et al. 2012b).	201
Figure 11.7. Deformation at first buckling mode shape: (a) in the case of monotonic load (b) in the case of cyclic load (Sabbagh et al. 2012b) (mm).....	202
Figure 11.8. Cyclic loading regime for the test (Sabbagh et al. 2012b) and numerical study.....	203
Figure 11.9. Comparison between tested (Sabbagh et al. 2011) and analysed moment-rotation curves of connection A1: (a) monotonic load and (b) cyclic load .....	204
Figure 11.10. Comparison between tested and analysed buckled shape of the profiles of connection A1: (a) Failure shape from the test (Sabbagh et al. 2011); (b) monotonic load (MPa) and (c) cyclic load (MPa) at $\vartheta=0.07$ rad (Point E in Figure 11.9).....	205
Figure 11.11. Comparison between tested (Sabbagh et al. 2011) and analysed moment-rotation curves of connection B2: (a) monotonic load and (b) cyclic load .....	206
Figure 11.12. Comparison between tested and analysed buckled shape of connection B2: (a) Failure shape from the test (Sabbagh et al. 2011); (b) monotonic load (MPa) and (c) cyclic load (MPa) at rotation of $\vartheta=0.09$ rad (Point F in Figure 11.11) .....	207
Figure 11.13. Details of the back-to-back beam sectional dimensions with L=2000 mm .....	208
Figure 11.14. Different bolt distribution patterns.....	209
Figure 11.15. Cross-sectional classification based on moment-rotation curves.....	210
Figure 11.16. Typical boundary conditions, constrains and loading points of cantilever channels .....	211
Figure 11.17. Normalised moment–rotation responses for cross-section classification: (a) $t=1$ and 2 mm and (b) $t=4$ and 6 mm .....	212
Figure 11.18. Moment-rotation cyclic relationship and backbone curve of the connections with flat flange beam section and circular bolt distribution configuration.....	215
Figure 11.19. Strength to slenderness relationship of different sectional shapes .....	219
Figure 11.20. Ductility to slenderness relationship of different sectional shapes.....	220
Figure 11.21. Energy dissipation to slenderness relationship of different sectional shapes.....	221
Figure 11.22. Definition of the damping coefficient .....	222
Figure 11.23. Damping coefficient at maximum moment .....	223
Figure 11.24. Damping coefficient at ultimate (near failure) .....	223

## List of figures

---

Figure 11.25. Effect of gusset plate thickness on the bending capacity of the connections .....	224
Figure 11.26. Comparison between FE cyclic results of bolted moment connections and DSM for design of CFS sections under pure bending.....	227
Figure 11.27. The behaviour of connection with cross section class 1 using different bolt pretensions and configurations: (a) Circle; (b) Diamond; (c) Square .....	228
Figure 11.28. Moment-rotation cyclic relationship and backbone curve of the connections with flat flange beam section and circular bolt distribution configuration (with slippage) .....	229
Figure 11.29. Comparison of moment capacities of connections with and without slippage .....	230
Figure 11.30. Comparison of energy dissipation capacities of connections with and without slippage ..	231
Figure 11.31. Damping coefficient up to maximum moment.....	232
Figure 11.32. Damping coefficient at ultimate (near failure).....	233
Figure 11.33. Moment-rotation curves of connection B2 with slippage-bearing action defined in ABAQUS (2007) .....	235
Figure 11.34. Hysteresis rule for a bolt slipping and bearing against a steel sheet .....	236
Figure 11.35. Relationship between the UEL and ABAQUS .....	237
Figure 11.36. Cyclic response of a single bolt during cyclic loading .....	237
Figure 11.37. Comparison between tested and analysed moment-rotation curves of connection B2 with 1mm slippage defined .....	238

# LIST OF TABLES

Table 3.1. Optimisation prototypes, variables and constraints .....	39
Table 3.2. Comparison of the geometrical dimensions and axial capacity of the optimised sections with the standard section .....	42
Table 3.3. Effective cross-sections of optimised sections under compression and flexural moment .....	43
Table 4.1. Selected prototypes, design variables and constraints .....	59
Table 4.2. Dimensions of optimal solutions for laterally restrained beams .....	61
Table 4.3. Local and distortional ultimate strengths for laterally braced beams obtained using the DSM65	
Table 4.4. Local, distortional, and global ultimate strengths for laterally unbraced beams obtained using the DSM .....	66
Table 4.5. Cross-sectional dimensions .....	68
Table 4.6. Comparison of the bending resistances obtained from FE analysis and experiment with different imperfection values in negative direction .....	70
Table 4.7. Comparison of the bending resistances obtained from FE analysis and experiment with different imperfection values in positive direction .....	70
Table 4.8. Comparison of ultimate capacities obtained from FE analysis and experiment for laterally unbraced braced beams (lipped channels) .....	73
Table 4.9. The critical buckling modes and the buckling half-wave length for laterally restrained beams	74
Table 4.10. Comparison of predicted strengths with FE results for laterally braced beams .....	77
Table 4.11. Comparison of predicted strengths with FE results for laterally unbraced beams .....	77
Table 5.1. Selected prototypes, design variables and constraints .....	88
Table 5.2. Geometrical details and bending capacities of the optimised sections .....	90
Table 5.3. Effective cross-sections of the optimised beams, presented at the same scale .....	92
Table 5.4. Dimensions of the folded-flange cross-sections and bending capacity obtained from EC3 and FEM .....	95
Table 5.5. Effective cross-sections and buckled shapes of the folded-flange beams (presented at a consistent scale) .....	96
Table 5.6. Comparison of the bending moment capacities of the optimised and standard sections obtained from EC3 and FE analysis .....	98
Table 6.1. Selected prototypes, design variables and constraints .....	116
Table 6.2. Dimensions and energy dissipation capacity of optimum design CFS cross-sections using different prototypes .....	120
Table 7.1. Measured dimensions of specimens with cross-section A (mm) .....	128
Table 7.2. Measured dimensions of specimens with cross-section B (mm) .....	128
Table 7.3. Measured dimensions of specimens with cross-section C (mm) .....	129
Table 7.4. Measured dimensions of specimens with cross-section D (mm) .....	129
Table 7.5. Critical buckling stress and buckle half-wave length for nominal cross-sections A-D .....	129
Table 7.6. Tensile properties of the flat and corner regions .....	131
Table 7.7. Maximum amplitudes of local, distortional and overall imperfections in tested columns .....	133
Table 7.8. Ultimate capacities of specimens with cross-section A .....	138
Table 7.9. Ultimate capacities of specimens with cross-section B .....	138
Table 7.10. Ultimate capacities of specimens with cross-section C .....	139
Table 7.11. Ultimate capacities of specimens with cross-section D .....	139
Table 8.1. Comparison of FE results with tested compressive strength .....	154
Table 8.2. Evaluation of the EC3 and DSM design methods against experimental results .....	155
Table 9.1. Measured dimensions of specimens with cross-section A .....	161
Table 9.2. Measured dimensions of specimens with cross-section B .....	161
Table 9.3. Measured dimensions of specimens with cross-section C .....	161
Table 9.4. Tensile properties of flat and corner coupons .....	163

## List of tables

---

<i>Table 9.5. Maximum amplitudes of local, distortional imperfections in single channel before assembling</i>	164
<i>Table 9.6. Maximum amplitudes of local, distortional imperfections in single channel after assembling</i>	164
<i>Table 9.7. Ultimate capacities of the test specimens</i>	169
<i>Table 10.1. Comparison of FE results with tested flexural strength</i>	189
<i>Table 10.2. Evaluation of the design methods of DSM and EC3</i>	189
<i>Table 11.1. Basic properties of the gusset plates (Sabbagh, Petkovski, Pilakoutas and Mirghaderi 2012b)</i>	201
<i>Table 11.2. Cross-sectional classification of the CFS cross-sections</i>	213
<i>Table 11.3. Characteristic parameters of the EEEP model for all the cyclic modelling</i>	216
<i>Table 11.4. AISC requirements for the CFS bolted connection with slippage</i>	234

# LIST OF SYMBOLS

$A_{eff}$	effective area of cross-section
$A_s$	the edge stiffener area
$b$	flange dimension
$b_e$	the effective width of the plate
$c$	lip dimension
$c_1$	cognitive parameter to indicate the degree of confidence in the solution $P_{best,i}$
$c_2$	constant parameter to reflect the confidence level that the swarm as a whole has reached a favourable position.
$D$	bending rigidity of a plate
DSM	Direct Strength Method
$d$	dimension of returned lip
$d_0$	nominal bolt diameter
$E$	elastic modulus
EC3	Eurocode 3
$E(\mathbf{X})$	dissipated energy
$EI_y$	flexural rigidity about the minor axis of cross-sections
$EI_w$	warping rigidity of cross-sections
$e_N$	shift of the effective centroid
$e$	distance between the centroid of the edge stiffener and the pivot point
$f_y$	yield stress
GA	Genetic Algorithm

## List of symbols

---

$GJ$	the torsional rigidity cross-sections
$G_{best}^k$	position of the best particle in the swarm in iteration $k$
$h$	cross-sectional height
$I_s$	second moment of area of the stiffener assembly about an axis through its centroid parallel to the plate
$I_x$	second moment of inertia around $x$ axis of the CFS section
$K$	spring stiffness per unit length applied in the edge stiffeners
$K_0$	torque coefficient
$L$	span length of the unbraced CFS beam
$L_e$	effective length of tested columns
$l$	total coil width of CFS sheet
$M_{b,Rd}$	member bending moment resistance
$M_{crd}$	elastic distortional critical buckling moments of CFS members
$M_{cre}$	elastic global critical buckling moments of CFS members
$M_{crl}$	elastic local critical buckling moments of CFS members
$M_n$	flexural strength of a CFS beam using direct strength method
$M_{nd}$	nominal flexural strength of a CFS beam designed for distortional buckling
$M_{ne}$	nominal flexural strength of a CFS beam designed for global buckling
$M_{nl}$	nominal flexural strength of a CFS beam designed for local buckling and considering local–global interaction
$n_b$	number of slip planes
$N_{b,Rd}$	compressive capacity of a member according to the flexural- torsional or torsional-flexural buckling depending on the relative slenderness

## List of symbols

---

$N_{cr}$	minimum of the elastic flexural/torsional/ flexural-torsional buckling capacity
$N_{c,Rd}$	compressive capacity of cross-sections
$N_s$	axial capacity in a column without any external bending moment
$P_b$	preloading force
$P_{crl}$	elastic local buckling load
$P_{crd}$	elastic distortional buckling load
$P_{cre}$	elastic global buckling load
$P_{nl}$	nominal axial strength of a column designed corresponding to local buckling and considering local–global interaction
$P_{nd}$	nominal axial strength of a column designed corresponding to distortional buckling
$P_{ne}$	nominal axial strength of a column designed corresponding to global buckling
$P_n$	axial strength of the column using direct strength method
PSO	Particle Swam Optimisation Method
$P_{best,i}^k$	best position of the $i^{th}$ particle over its history up to iteration $k$
$R$	distance ratio of the position of intermediate stiffeners
$R_0$	plastic rotation capacity
$R_B$	bolt bearing force
$R_{ult}$	ultimate bearing strength of a bolt against a steel sheet
$r_1$	a random number uniformly distributed between 0 and 1
$r_2$	a random number uniformly distributed between 0 and 1
$s$	dimension of intermediate stiffeners



## List of symbols

---

$T$	input tightening torque applied to the fastener head or nut
$t$	thickness of the CFS sections
$u_{\min}$	the lower bounds of design variables
$u_{\max}$	the upper bounds of design variables
$V_i$	velocity vectors of $i^{\text{th}}$ particle
$w$	inertial weight factor in the particle swarm optimisation method
$x_i$	design variables of cross-sectional dimensions in the optimisation process
$y_1$	distances from the centroid of the section to the extreme fibers in compression
$y_2$	distances from the centroid of the section to the extreme fibers in tension
$\gamma_{M_0}$	partial factor in ultimate limit state
$\Delta_{slip}$	slippage deformation in a bolt
$\Delta t$	time increment
$\delta_{br}$	bearing deformation of a bolt against a steel sheet
$\varepsilon_{0.2}$	total strain at 0.2% proof stress
$\varepsilon_1$	average reading from strain gauges at compression side of the CFS section
$\varepsilon_2$	average reading from strain gauges at the tension side of the CFS section
$\varepsilon_{ij}^p(\tau)$	is the plastic strain tensor
$\bar{\varepsilon}_p$	maximum allowable equivalent plastic strain
$\varepsilon_p(t)$	equivalent plastic strain
$\varepsilon_{true}$	true strain from the stress-strain curve of coupon test
$\eta$	penalty factor

## List of symbols

---

$\theta_1$	angle of inclined lip
$\theta_2$	angle of intermediate stiffeners
$\theta_u$	rotation corresponding to the 80% of the peak bending moment in the post buckling range
$\theta_y$	yield displacement based on the equivalent bi-linear curve
$\lambda$	regression coefficients
$\lambda_c$	global slenderness for column
$\lambda_d$	slenderness for distortional buckling
$\lambda_{LT}$	slenderness ratio for lateral torsional buckling
$\lambda_l$	slenderness ratio for local buckling
$\lambda_{l,red}$	refined slenderness ratio for local buckling considering interactive effect of distortional buckling
$\mu$	ductility of the CFS sections
$\mu_0$	friction coefficient of the contact surfaces in CFS sheets
$\mu_1$	regression coefficient in the bolt modelling
$\nu$	Poisson's ratio
$\rho$	reduction factor on the plate width
$\rho_i$	position vectors of $i^{\text{th}}$ particle
$\sigma_{0.2}$	0.2% proof stress
$\sigma_{cr}$	elastic local buckling stress of the plate
$\sigma_{cr,s}$	elastic buckling stress of the plate-stiffener assembly
$\sigma_{ij}$	the stress tensor

## List of symbols

---

$\sigma_{true}$	true stress from the stress-strain curve of coupon test
$\sigma_u$	tensile strength of steel coupons
$\chi_{LT}$	reduction factor for lateral torsional buckling in EC3
$\psi$	the ratio of the end stresses in a plate

This page is intentionally left in blank

# CHAPTER 1. Introduction

---

## 1.1 Background

Sustainable construction aims at reducing the environmental impact of buildings on human health and natural environment by efficiently using energy and resources as well as reducing waste and pollution. Steel is popular in multi-storey construction due to its high strength-to-weight ratio and ductility. Hot-rolled steel sections have been successfully used for the construction of multi-storey buildings (Figure 1.1) for more than 150 years. However, hot-rolled sections are often available in a limited number of standard sectional profiles and lengths leading to up to 30% redundant material during the design process (Yu and Laboube 2010).



**Figure 1.1. A multi-storey hot-rolled steel frame in Sheffield**

Cold-formed steel (CFS) sections are more flexible in terms of cross-sectional profiles (made through cold-rolling and press braking) and, therefore, can lead to more efficient design solutions with less redundant material and waste during manufacturing (Lawson et al. 2005). Therefore, from an environmental and sustainable viewpoint, CFS structural systems are appropriate options for modular and multi-storey structures in residential and industrial construction (Figure 1.2).



**Figure 1.2. Cold-formed steel (a) portal frame and (b) framing residential building**

The advantages of constructing CFS framing systems (Figure 1.2) using CFS sections instead of conventional hot-rolled sections include high strength to weight ratio, off-site manufacturing, smaller foundations, pre-galvanised members with good durability, ease of fabrication that allows fast and large-volume production, and easy transportation. With relatively higher yielding strength and thinner plates, CFS elements are also easy to stack and erect with less labour.

Optimisation of CFS portal frames (Phan et al. 2012) has shown that up to 20% material has been saved through the change of cross-sectional dimensions of members and frame topology. There is currently no generic framework for the optimum design of complex CFS structural systems capable of considering the manufacturing and construction constraints. However, before the development of a general framework for the optimisation of CFS structural systems, the following limitations need to be addressed:

(1) Owing to their large flat width-to-thickness ratios, CFS elements are susceptible to local/distortional and global buckling, which can result in low buckling resistance and consequently low capacity and ductility (Sabbagh et al. 2012a). This shortcoming limits the performance of CFS systems in multi-storey buildings and makes them vulnerable to collapse under extreme load events (e.g. earthquake).

(2) The flexibility of the manufacturing process allows the fabrication of cross-sections with various shapes. However, these are not always developed to comply with all of the criteria included in current proposed design specifications. In addition, existing CFS elements are not usually optimised to improve the non-linear inelastic performance of elements and connections based on a detailed analysis.

(3) Thinner plates can cause premature local buckling failure along the connection-lengths, leading to a semi-rigid behaviour of the joints (Wrzesien et al. 2012) which has to be taken into account in the design. This may also cause excessive deflection under serviceability limit state

and the development of energy dissipation mechanisms of bolt slippage under extreme loading that are difficult to model and quantify.

## 1.2 Necessity of Research

The use of CFS sections as main structural components is generally restricted to stud-wall frames (Figure 1.2(b)) with relatively low deformability/ductility (Fulop and Dubina 2004). Compared with hot-rolled steel structures, the weaknesses of CFS structures are typically a result of premature local buckling in sections (due to large width/thickness ratios) and lack of strength and stiffness in connections (Sato and Uang 2010). As a result, CFS moment-resisting frames with bolted connections are usually limited to single-storey dwellings (Sato and Uang 2009, Sato and Uang 2010). To use CFS moment-resisting frames for multi-storey buildings, there is a need to prevent premature local buckling of the CFS elements so as to allow the development of more plastic deformation. In addition, while the general view is that thin-walled CFS elements are not suitable for moment-resisting frames (Calderoni et al. 2009), recent studies at the University of Sheffield (Sabbagh et al. 2012a, Sabbagh et al. 2012b) and by Serror et al. (Serror et al. 2016) showed that, by using appropriate detailing, CFS beam-column moment resisting connections can be developed to meet the requirements of rigid and full strength joints with high ductility.

### 1.2.1 Optimisation of CFS elements for maximum strength

CFS members can be produced in a wide variety of section profiles and, typical characteristics such as intermediate stiffeners, inclined lips, folded plates, returned lips are easy to be rolled. Therefore, identifying optimised cross section geometries is of great interest to manufacturers and structural designers. However, this is a complex optimisation problem, since the strength of CFS members is controlled by local/distortional and global buckling and their interaction. Previous studies on the optimisation of CFS elements are mainly limited to varying dimensions of standard cross-sections (lipped channel beam (Lee et al. 2005b); channel columns with and without lips (Lee et al. 2006b); and hat, I and Z cross section CFS beams (Adeli and Karim 1997)), which are not necessarily optimal sections. The Direct Strength Method (DSM), a newer design method of CFS specimens, has recently been used to obtain the optimum shape for open CFS cross section columns (Leng et al. 2011). However, these studies did not consider manufacturing and construction constraints and, proposed the use of highly complex shapes that are not suitable for practical applications due to high manufacturing costs and difficulty in connecting to other elements. In addition, the proposed sections did not necessarily comply with current design specifications in terms of shapes and cross-sectional plate width-to-thickness ratios.

### **1.2.2 Optimisation of CFS elements for improved post-buckling behaviour**

Optimisation of CFS elements on their maximum strength under bending and compression has led to significant reduction of material saving in the design process (Leng et al. 2014, Liu et al. 2004, Ma et al. 2015, Tian and Lu 2004b). However, optimisation of CFS elements only based on their buckling strength does not always optimise their ultimate performance (i.e. post-buckling behaviour and ductility). Optimisation of the flange shape for hot-rolled H beams has been shown to lead to an increased energy dissipation under monotonic and cyclic loads by combining an optimisation algorithm with detailed nonlinear Finite Element analysis (Pan et al. 2007). In other research, the positions and thicknesses of the stiffeners of link members, working as passive control devices in hot-rolled eccentrically braced frames, was optimised for maximum energy dissipation (Deng et al. 2015). The flexibility of CFS members with respect to the manufacturing and construction processes offers great scope and potential to develop cross-sections with high ductility and energy dissipation.

However, no research has previously been carried out on the optimisation of CFS members to improve their post-buckling behaviour, ductility and energy dissipation capacity.

### **1.2.3 Optimisation of CFS elements and experimental validation**

Experimental investigation on the ultimate strength has been conducted on CFS single beam section with simple and complex edge stiffeners (Wang and Zhang 2009, Yu and Schafer 2006, Yu and Schafer 2003), design equations and recommendations on single CFS beam sections were proposed based on these tests. CFS back-to-back sections, which are made from connecting two channel sections, are able to provide larger torsional rigidity. In order to study the flexural behaviour of cold-formed steel channel beams, an experimental research was conducted by Hsu and Chi (Hsu and Chi 2003) on the back-to-back CFS beams under the monotonic and cyclic load. An experimental and numerical study on the behaviour CFS built-up beam members was conducted by Laín et al. (Laín et al. 2013). It is found by researchers (Laín et al. 2013) that the behaviour of those beams was significantly affected by the screw distribution and the interaction of local/distortional and lateral-torsional buckling. It was also observed that in some of the specimens without load transfer plates, web crippling happened due to load concentration, as is the failure phenomena indicated by some researchers (Chen et al. 2015). Manikandan et al. (Manikandan et al. 2014) studied the bending behaviour of innovative CFS back-to-back channel sections with folded flange and complex edge stiffeners experimentally and numerically. It is shown in their study that the sections with complex edge stiffener and folded flange possessed the maximum bending strength. More recently, Wang and Young (Wang and Young 2016a) experimentally investigated the behaviour of simply supported built-up section beams with different web intermediate stiffeners under four-point bending and three-point bending. The behaviour and design rule for built-up section beam were



## Chapter 1. Introduction

presented with extended numerical study (Wang and Young 2016b). All of these tests were designed for the development of design guidelines on CFS specimens while no comparison between standard and optimised sections were presented.

Therefore, newly proposed cross-sectional shapes and dimensions are not usually optimised on the basis of detailed numerical analyses and experimental validation and calibration.

CFS elements have been optimised based on design codes such as AISI (AISI 2007), AS/NZS (AS/NZS 1996) and EC3 (CEN 2005a, CEN 2005b). The buckling strength of the CFS elements in these studies were determined by using the “effective width” concept (Von Karman et al. 1932), which for non-conventional cross sections is cumbersome since a number of iterations are included due to the change of neutral axis and the interaction between different buckling modes.

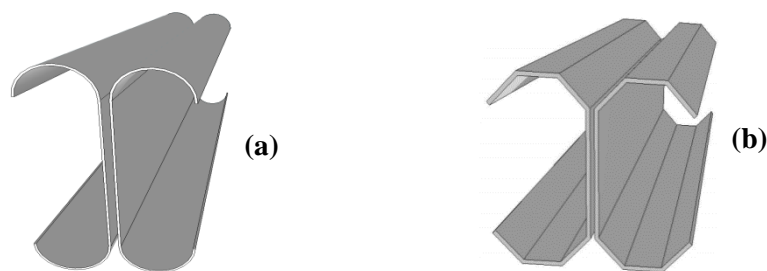
Free form optimisation of CFS elements based on DSM (Leng et al. 2011) may lead to non-compliant shapes and plate width-to-thickness ratios.

Failure to take into account all of these factors (e.g. ignores inter-element equilibrium and compatibility) may lead to insufficiently accurate results.

### 1.2.4 Performance of CFS moment resisting connections

Analytical and experimental investigations on the monotonic and cyclic behaviour of bolted moment resisting connections in CFS construction are still limited. Recent experimental and analytical studies have demonstrated that the buckling strength of CFS elements can be significantly improved by using new section shapes (Sabbagh et al. 2011, Sabbagh et al. 2012b, Serror et al. 2016). Premature buckling mode of typical CFS elements (local buckling of the flange) can be delayed by using curved flange sections, as shown in Figure 1.3(a). Feedback from industry, however, highlighted that curved sections are difficult to manufacture and connect to.

More practical shapes need to be developed by taking into account both manufacturing and construction constraints (see for example Figure 1.3(b)).



**Figure 1.3. CFS beams with (a) curved flanges and (b) folded flanges**

## Chapter 1. Introduction

Although numerical studies have been already carried out to study the rotational capacity of beams subjected to cyclic load (Serror et al. 2016), a reliable way of modelling the bearing and slippage behaviour of bolted connections has not yet been proposed.

Further research is required in this field so as to develop more accurate predictive models for the optimum design of CFS bolted connections.

### 1.3 Aims and detailed objectives

The main aim of this research is to understand, predict, and optimise the strength of CFS elements. A framework to optimise CFS elements with energy dissipation capacity (ductility) for seismic applications will be also proposed. The optimised elements can be then included in full-structure modelling to develop more efficient CFS structural sub-frames with high ductility and energy dissipation capacity, suitable for multi-story buildings in seismic regions. The detailed objectives are as follows:

(1) To develop a software for the calculation of gross and effective properties of CFS cross-sections based on the “effective width” concept. Typical characteristics of intermediate stiffeners, inclined lips, returned lips should be taken into account. The software should be able to design columns, beams and beam-column connections.

(2) To develop a framework to obtain optimised CFS standard elements by considering the local/distortional and global buckling and their interaction, as well as manufacturing and constructional constraints. All plate width-to-thickness ratios in EC3 will be considered as constraints and the load carrying capacity of the members will be set as the optimisation target.

(3) To develop a new analytical model to predict the capacity of an innovative folded-flange CFS cross-section. Models to calculate the local, distortional buckling strength will be proposed and used to obtain optimum shapes.

(4) To investigate experimentally and analytically the effectiveness of the proposed optimisation framework at improving the performance of CFS elements. The developed numerical models will be validated on the basis of the experimental results.

(5) To optimise the energy dissipation capacity of CFS elements based on their post-buckling behaviour for seismic applications. The maximum plastic strain is used as a measure for rotational ductility, which is used as one of the constraints for optimisation.

(6) To develop efficient CFS moment-resisting connections with higher stiffness and ductility by introducing innovative CFS sections along the connection-lengths. The performance of the connections will be assessed through detailed Finite Element (FE) models in ABAQUS.

## Chapter 1. Introduction

(7) To evaluate the performance of the developed CFS moment-resisting connections under cyclic loads using FE models. The FE models will be calibrated/validated based on existing experimental data. The failure modes and response of CFS bolted connections will be studied to determine their strength, ductility and energy dissipation capacity.

(8) To develop a reliable model for the analysis of CFS single lap connections subjected to cyclic loading.

### 1.4 Thesis layout

This thesis is divided into twelve chapters. The thesis combines three chapters written following the “traditional” thesis format (chapters 1, 2 and 12), and chapters consisting of “stand-alone” journal papers (chapters 3 to 11). A brief overview of each chapter is given in the following:

Chapter 2 presents a literature review. The first section reviews research on different CFS sections, representative design guidelines, behaviour of CFS members, CFS connections, optimisation of CFS elements and CFS structural systems. The advantages and limitations of currently available optimisation techniques for CFS elements and CFS connections are discussed.

Chapter 3 is based on Ma et al. (Ma et al. 2015) and discusses an optimisation strategy for the geometrical dimensions of all manufacturable C-shape cross-sections (i.e. with and without lip and middle stiffeners). For the optimisation, all of the sections were considered to have a fixed coil width and thickness while the optimisation was performed based on the load capacity obtained following the provisions of effective width method suggested in EC3 (2005). The optimised solutions were found using a Genetic algorithm.

Chapter 4 is based on Ye et al. (Ye et al. 2016a) and develops a methodology for the optimisation of the flexural strength of CFS beams considering local, distortional and lateral torsional buckling. Six different CFS channel section prototypes are selected and then optimised with respect to their flexural strength, determined according to the effective width based provisions of Eurocode 3 (EC3) part 1-3. The accuracy of the optimisation procedure is assessed using experimentally validated nonlinear Finite Element (FE) analyses accounting for the effect of imperfections.

Chapter 5 is based on Ye et al. (Ye et al. 2016b) and introduces a methodology for the development of optimised CFS beam sections with maximum flexural strength for practical applications. The optimised sections are designed to comply with Eurocode 3 (EC3) geometrical requirements as well as with a number of manufacturing and practical constraints. To allow for the development of a new ‘folded-flange’ cross-section, the effective width method in EC3 is extended to deal with the possible occurrence of multiple distortional buckling modes.

## Chapter 1. Introduction

Chapter 6 discusses the seismic performance of CFS elements and introduces a methodology for optimising their post-buckling behaviour in the nonlinear inelastic range. A non-linear shape optimisation method is presented for the optimum design of CFS beam sections. The relative dimensions of the cross-section, the location and number of intermediate stiffeners and the inclined lip angle are considered as main design variables. All plate slenderness limit values and limits on the relative dimensions of the cross-sectional components, set by the EC 3, are taken into account as constraints on the optimisation problem. An additional constraint is considered where maximum equivalent plastic strain is restricted to ensure a sufficient level of ductility. Global optimal solutions are obtained through the Particle Swarm Optimisation (PSO) algorithm. The developed PSO algorithm is linked to the ABAQUS finite element programme for inelastic post-buckling analysis and optimisation.

Chapter 7 describes an experimental programme carried out at the University of Sheffield to investigate the interaction of local and overall flexural buckling in cold-formed steel channels under axial compression. The results of a total of 36 column tests, including three different lengths and four different types of cross-section, are discussed and commented upon and comparisons with EC3 are made.

Chapter 8 develops a reliable numerical model to investigate the interaction of local and global buckling modes in pin-ended CFS columns. The validated FE model is then used to assess the adequacy of the “effective width method” in EC3 and Direct Strength Method (DSM) in estimating the design capacity of a wide range of conventional and optimum design CFS channel column sections.

Chapter 9 describes an experimental programme carried out at the University of Sheffield to investigate the local and distortional buckling behaviour of CFS beams. The beam specimens were assembled using channels, with a nominal thickness of 1.5 mm and depths ranging from 180 mm to 270 mm, in a back-to-back configuration. The results of a total of six tests on back-to-back beams, including three different cross-sectional geometries, are discussed and the behaviour of the specimens is compared to the predictions of EC3.

Chapter 10 discusses the development of a reliable numerical model to investigate the flexural strength and failure modes of CFS back-to-back channels beams. The developed FE models are verified against experimental results and are then used to assess the adequacy of the effective width method in EC3 and Direct Strength Method (DSM) in estimating the design capacity of conventional and optimum design CFS channel beam sections.

Chapter 11 presents an extensive parametric study on the structural behaviour of CFS bolted beam-to-column connections under cyclic loading. The performance of the connection is assessed in terms of strength, ductility, energy dissipation capacity and damping coefficient.

## Chapter 1. Introduction

Furthermore, the effects of bolt distribution configuration, cross-sectional shapes, gusset plate and cross-sectional thicknesses on the connection performance are also examined. A two node element is also developed that can take into account the bolt slippage, bearing deformation and the bolt hole elongation.

Finally, Chapter 12 summarises the research work, draws general conclusions and gives recommendations for future work.

This page is intentionally left in blank

## **CHAPTER 2. Literature review**

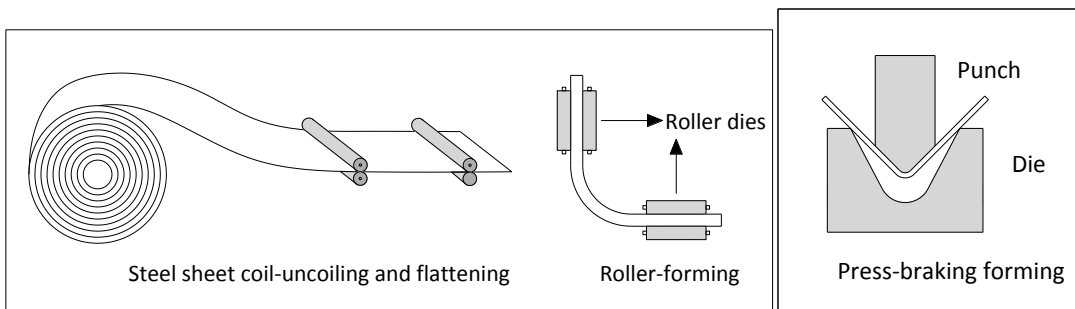
---

This chapter reviews available research on structural performance of different CFS sections, CFS connections and CFS structural systems. The first part presents research on the different shapes of CFS sections and addresses issues of their structural behaviour. This is followed by a critical discussion on the main international design guidelines for CFS. The research of seismic behaviour of CFS elements and connections is then reviewed, followed by an analysis of previous research on the optimisation of CFS elements. A discussion on CFS structural systems is included at the end of this chapter.

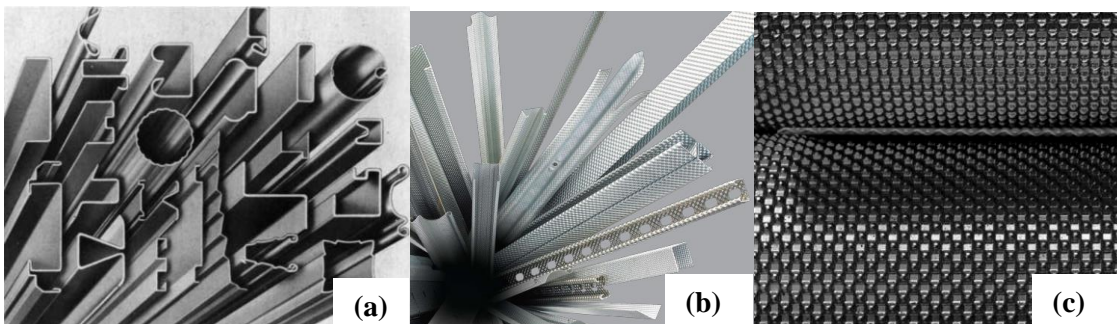
### **2.1 CFS sections**

CFS sections are generally produced by using a number of manufacturing processes i.e. coiling, uncoiling, flattening and cold-forming or press-braking process (Figure 2.1). This flexibility of the manufacturing process allows a number of commercially available cross-sections with

various shapes to be made (Figure 2.2(a)), and consequently favourable strength-to-weight ratios can be obtained. The manufacturing process is also applicable to cross-sections made from plain steel sheets and other forms. For example, CFS dimpling sections (Figure 2.2(b)) are produced by employing the dimpled steel sheets, which have been made from plain steel sheets using the UltraSTEEL® process in Hadley Industries plc (Hadley Industries plc). The process uses a pair of rolls which is designed with rows of uniquely shaped teeth that stretch the plain surface and form the dimples from both sides of the steel sheet. The dimpled sheet (Figure 2.2(c)) can then be progressively formed into the required products by using either the rolling or the press-braking machine, as shown in Figure 2.1.



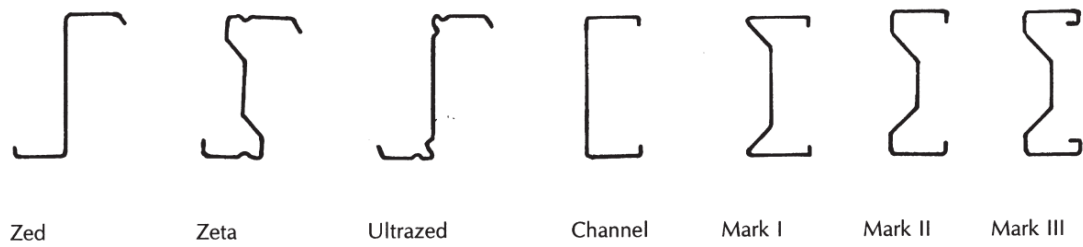
**Figure 2.1. Manufacturing process for cold-formed steel members using roller or press-braking process (Amouzegar et al. 2016).**



**Figure 2.2. (a) Different cross-sectional shapes (Yu and LaBoube 2010) (b) Variety of cross-sections made from dimpled steel sheets (Hadley Industries plc) (c) Dimpled steel sheets produced by the UltraSTEEL® process in Hadley Industries plc (Hadley Industries plc)**

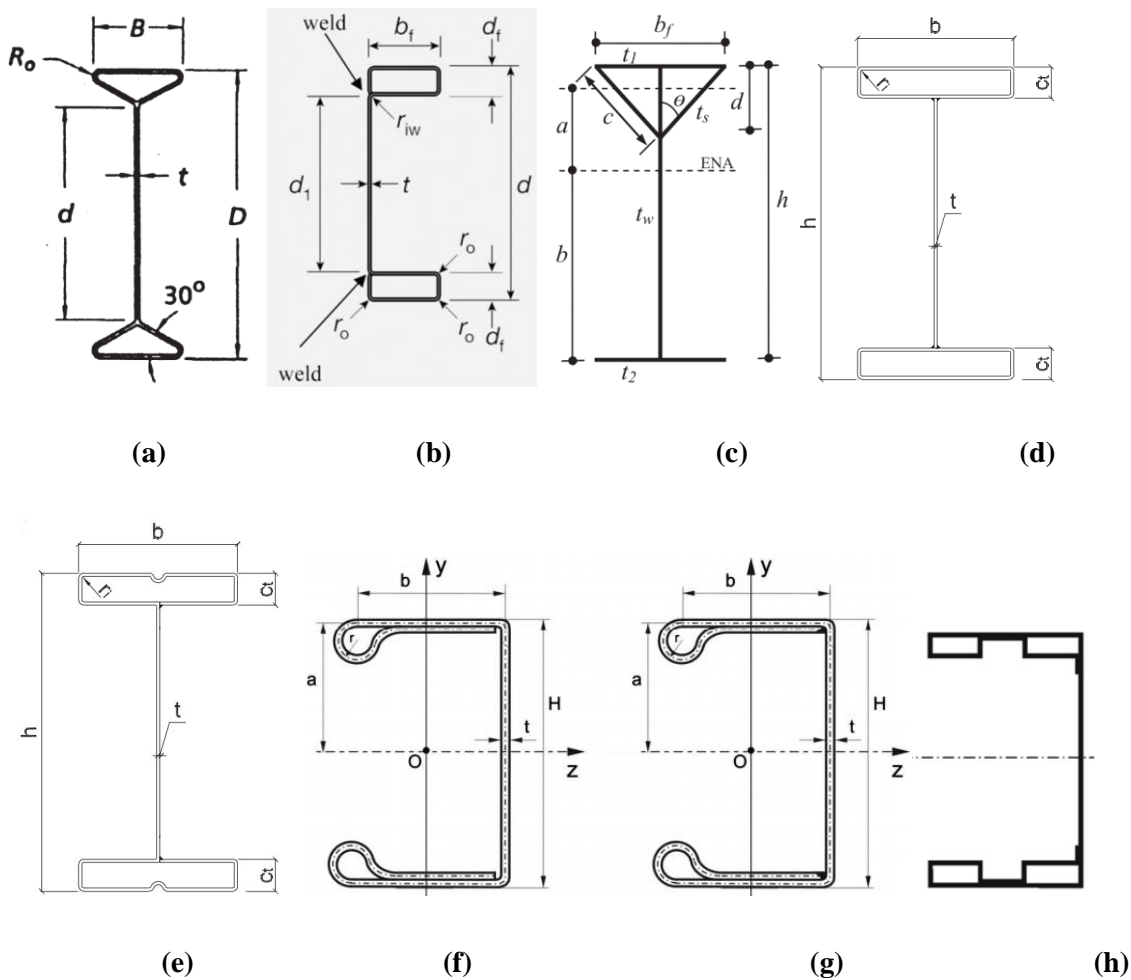
As a result of the use of higher strength steels, CFS profiles are generally characterised by a thin wall thickness, which is inevitably accompanied by a reduced resistance to local/distortional buckling. The inherently low resistance to buckling is addressed by manufacturing highly stiffened sections with more folds and stiffeners (Davies 2000). This trend can be appropriately illustrated by the various modifications made to purlin sections. Starting from the conventional lipped channels and Zed sections, purlins have evolved into a number of more complex sections with stiffened webs and flanges, returned and inclined lips, as shown in Figure 2.3.





**Figure 2.3. Evolution of cold-formed Zed and Channel purlin sections (Davies 2000).**

Due to their flexibility in terms of cross-sectional shapes, CFS members are shaped for both structural and non-structural applications such as purlin & side rail systems, steel framing systems, window or door reinforcements, mezzanine floors, strut systems and industrial cladding systems, storage racks. By using these new and more complex shapes, CFS sections can be designed to have higher resistance to local-distortional buckling. To improve the buckling strength of CFS beams, a wide range of sections with different types of flange shapes have been developed, as shown in Figure 2.4. These include symmetrical I-beam with triangular hollow flanges (Avery et al. 2000), LiteSteel beam with rectangular hollow flanges (Anapayan et al. 2011), delta hollow flange beams (Mohebkah and Azandariani 2015), unstiffened and stiffened rectangular hollow flange beams (Tondini and Morbioli 2015), open and closed drop Flanges (Magnucki et al. 2010) and also double box flanges (Magnucka-Blandzi and Magnucki 2011). Experimental studies and analytical and numerical models were used to investigate cross-sectional local/distortional buckling, shear buckling, as well as member lateral torsional buckling. These studies have proven that those innovative sections possess better performance in terms of load bearing capacity and stiffness (Anapayan et al. 2011, Avery et al. 2000, Magnucka-Blandzi and Magnucki 2011, Magnucki et al. 2010, Mohebkah and Azandariani 2015, Tondini and Morbioli 2015, Uzzaman et al. 2016), and that they can meet the requirement of longer span in practical applications.



**Figure 2.4. Different shapes of cross sections of cold-formed channel beams with (a) Triangular hollow flanges (Avery et al. 2000) (b) LiteSteel beam with rectangular hollow flanges (Anapayan et al. 2011) (c) Delta hollow flanges (Mohebkhah and Azandariani 2015) (d) rectangular hollow flanges (Tondini and Morbioli 2015) (e) stiffened rectangular hollow flanges (Tondini and Morbioli 2015) (f) open drop flanges (Magnucki et al. 2010) (g) closed drop flanges (Magnucki et al. 2010) and (h) double box flanges (Magnucka-Blandzi and Magnucki 2011)**

Since the elastic compressive stress in a column is generally more uniform than in beams, it is shown that column strengths can be more easily enhanced with more flexible cross-sections. This is due to the fact that (a) intermediate stiffeners are able to increase the local buckling strength of single plate among the cross-sections; (b) edge stiffeners contribute to the distortional buckling strength of compressive stiffeners and (c) cross-sectional dimensions are easier to be adjusted to change the gross cross-sectional properties which contribute to the global stability. Therefore, the design of columns with complex edge stiffeners, intermediate stiffeners, stiffeners with inclined angle have been investigated by many researchers (Chen et al. 2010, Manikandan and Arun 2016, Yan and Young 2002, Young 2008b, Zhang et al. 2007a), as shown in Figure 2.5.

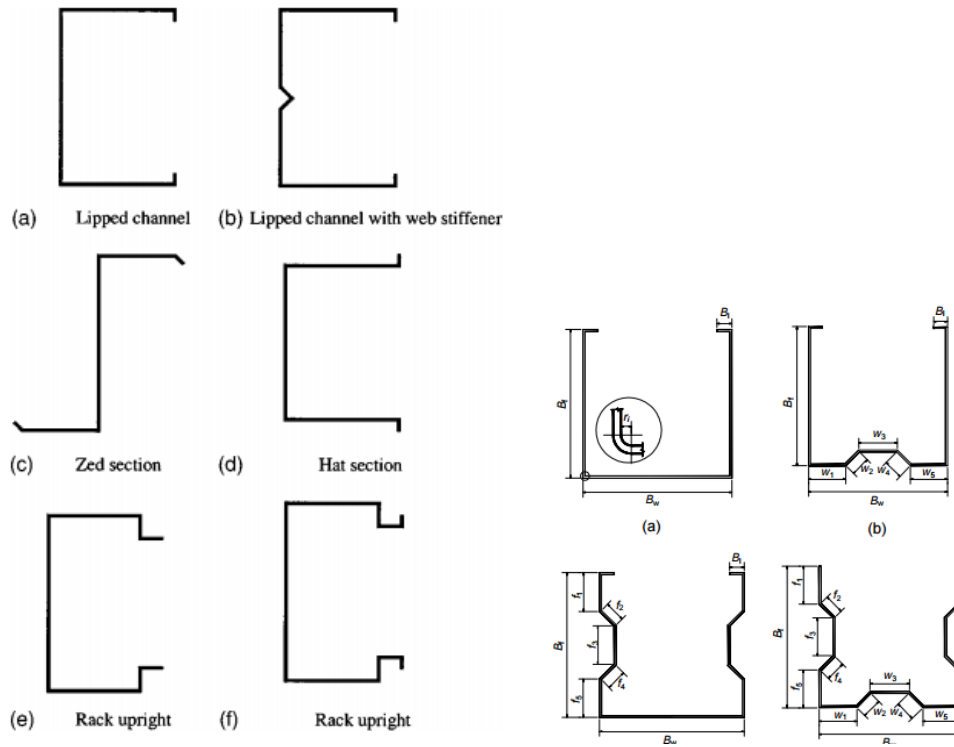


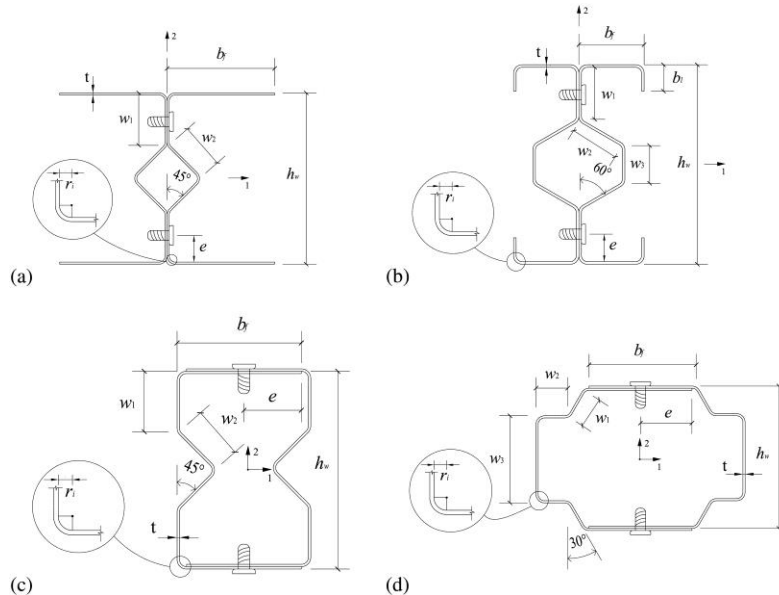
Figure 2.5. Columns with complex intermediate and edge stiffeners (Chen et al. 2010, Yan and Young 2002)

Column 1	Column 2	Column 3	Column 4
Column 5	Column 6	Column 7	Column 8
Column 9	Column 10	Column 11	Column 12
Column 13	Column 14	Column 15	Column 16

Figure 2.6. Section geometries of the innovative steel columns (Narayanan and Mahendran 2003)

In order to further improve the buckling strength of columns, Narayanan and Mahendran (Narayanan and Mahendran 2003) conducted experimental and numerical studies on CFS columns with innovative cross-sectional shapes. All of the sections failed by distortional buckling and the local buckling was successfully delayed by using smaller flat plates in the sections, as shown in Figure 2.6.

All of the sections above are generally manufactured by using the same steel coil and are either cold rolled or brake pressed into structural shapes, as the process shown in Figure 2.1. As a result, cold-formed steel sections are usually manufactured to be singly-, point-, or non-symmetric open shapes. Open sections have relatively poor torsional properties and are weak in twisting compared to closed sections. Therefore, open sections would fail most probably by local/distortional buckling possibly coupled with global twisting/bending depending on the dimension of the cross-sectional shapes and the lengths of the members. Built-up sections, which are assembled from a number of single channel sections with connectors, have the potential to provide improved strength and stiffness when applied in longer spans. However, there are currently no mature guidelines for the design of cold-formed steel built-up sections. For example, Eurocode 3 (CEN 2005b) simply adds up the strength of individual CFS channels while the North American Specification standard (AISI 2007) adopted a modified slenderness ratio for built-up column design.

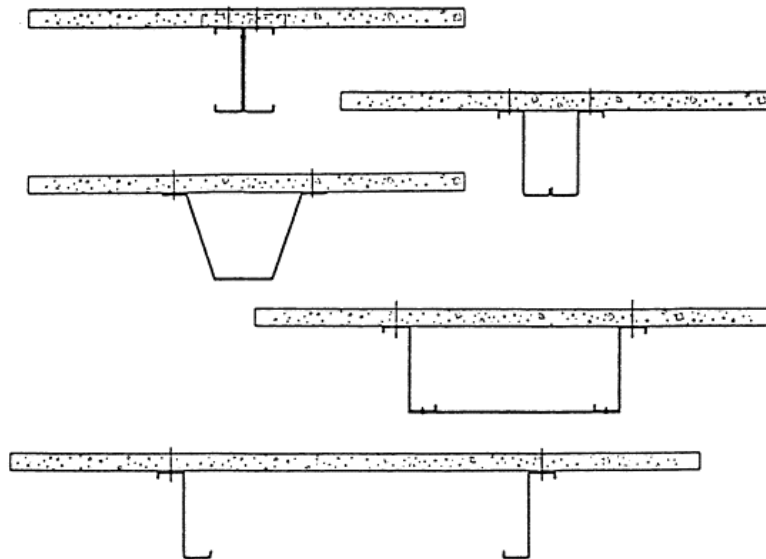


**Figure 2.7. Cold-formed steel built-up sections (Wang and Young 2016a, Wang and Young 2016b)**

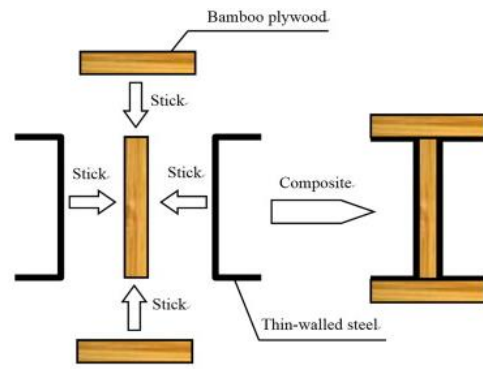
The use of CFS built-up sections has attracted the attention of several researchers, For example, Piyawat et al. (Piyawat et al. 2012) studied the axial load carrying capacity of doubly symmetric built-up cold-formed sections with simple I and box shape. Zhang and Young (Zhang and Young 2015) investigated the design of cold-formed steel built-up open section columns with longitudinal stiffeners and more recently, Wang and Young (Wang and Young 2016a, Wang

and Young 2016b) conducted numerical and experimental studies on the performance of CFS built-up sections with intermediate stiffeners under bending (Figure 2.7) and developed DSM equations for design.

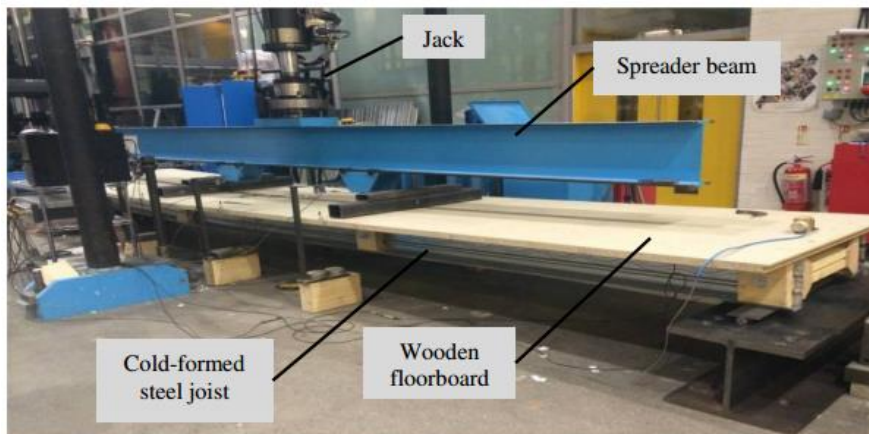
The widespread use of CFS as construction material is also attracting more research on its use in composite structures. Hanaor (Hanaor 2000) conducted experimental research on the use of cold-formed sections as composite beams in concrete slab systems. Different CFS cross-sectional shapes were tested with concrete slabs and extensive push-out tests of numerous types of connectors were conducted. A review on the cold-formed steel and concrete composite system can be found in research (Lawan et al. 2015). Other Cold-formed steel composite structures include bamboo–steel composite beams (Figure 2.9(a)) (Li et al. 2015, Li et al. 2012) and Cold-Formed Steel and wood floors (Figure 2.9(b)) (Kyvelou et al. 2015).



**Figure 2.8. Cold-formed and concrete composite beam (Hanaor 2000).**



(a)

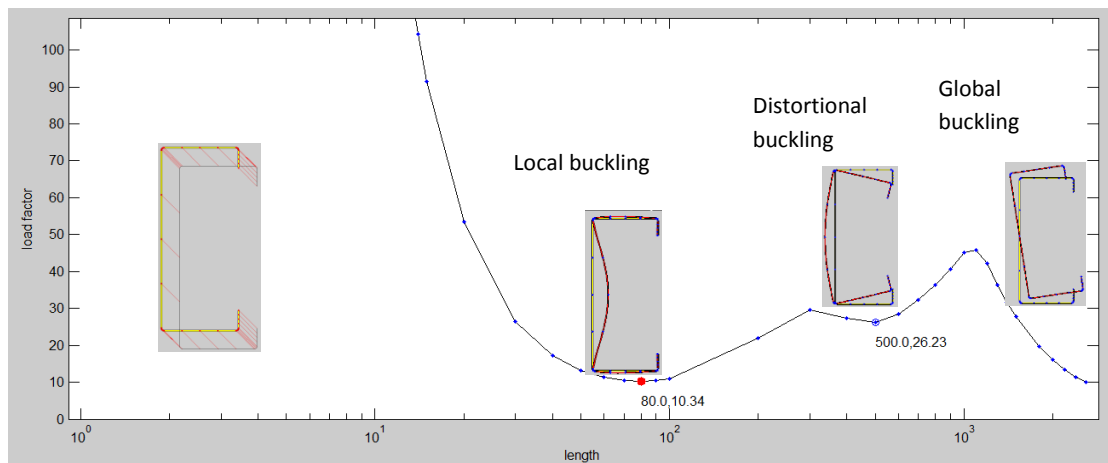


(b)

**Figure 2.9. Cold-formed steel composite elements with (a) bamboo (Li et al. 2015, Li et al. 2012) and (b) wood (Kyvelou et al. 2015)**

## 2.2 Design of CFS members

Three basic modes of buckling of CFS members can be identified (see for example Figure 2.10) (Schafer 2006). As defined in EC3, part 1-3 (CEN 2005b), local buckling is a mode involving flexural deformation in each individual plate without transverse deformation of the lines of intersection of adjacent plates. Distortional buckling is a mode of buckling characterised by the change in cross-sectional shapes excluding local buckling. Global buckling (torsional-flexural buckling, lateral-torsional buckling) is a mode in which compression members can bend and twist simultaneously without change of cross-sectional shapes.



**Figure 2.10. Buckling modes of a lipped channel in compression using CUFSM (Schafer 2006)**

The development and introduction of different design specifications for cold-formed thin-walled structures have been represented by a number of design codes such as AISI (AISI 2007), ANZ (AS/NZS 1996) and EC3 specifications (CEN 2005b). The European design code EC3 (CEN 2005b) and the AISI, Appendix 1 (AISI 2007), include two representative design concepts for cold-formed steel members, however, they are fundamentally different.

### 2.2.1 EC3

The European standard EC3 for CFS structures design is based on the well-known effective width concept, first proposed by Von Karman (Von Karman et al. 1932). This recognizes the fact that local buckling of the sectional plates has the effect of shifting the load-bearing stresses towards the corner zones, and reduces the efficiency of the central parts in carrying compressive loads. In addition, EC3 is consistent with the traditional design philosophy of steel structures, where a number of design curves for local/distortional and global buckling are used.

The basic idea for the design of a CFS section according to EC3 (CEN 2005b) is to represent the reduction in the effectiveness of a locally and distortional buckled plate with a non-uniform stress distribution by using an effective plate under a simplified linear stress distribution, as shown in Figure 2.11. The effective widths of plate with different boundary conditions and stress gradients can be calculated according to EC3 (CEN 2005a).

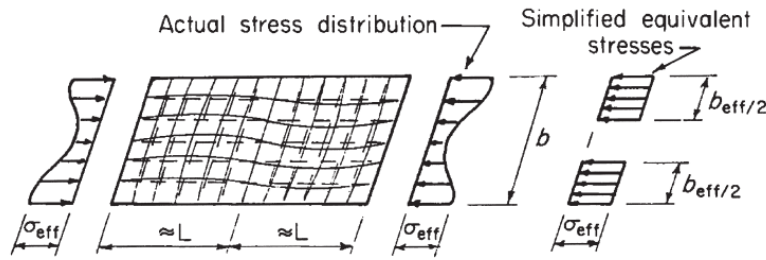


Figure 2.11. Effective width of plane element restrained along both edges (Davies 2000)

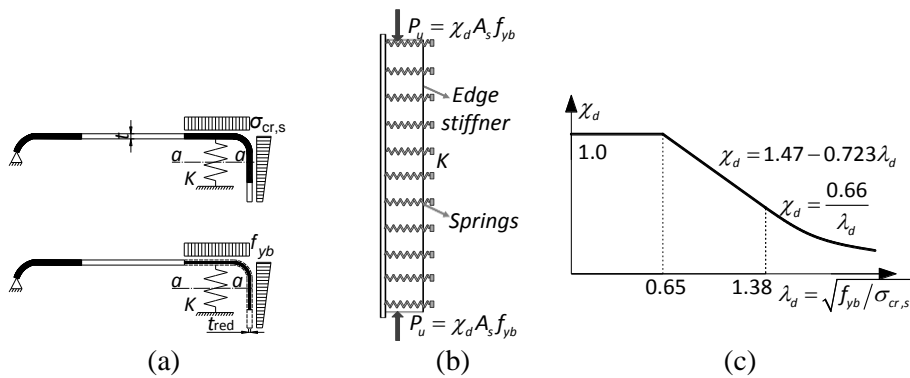


Figure 2.12. Distortional buckling model: (a) flange with edge stiffener (b) flexural buckling of edge stiffener as a strut on elastic foundation and (c) flexural buckling curve for edge stiffener (CEN 2005b)

EC3 (CEN 2005b) bases the design for distortional buckling on the assumption that the effective parts of edge stiffener behave as a strut (Figure 2.12) continuously supported by elastic springs of stiffness  $K$  along its centroid axis. The buckling of edge stiffener is then taken into account by using a reduced thickness in the effective edge stiffener. EC3 (CEN 2005b) also use this model to calculate the reduced thickness of intermediate stiffeners.

Instead of the gross cross-sectional properties, EC3 (CEN 2005b) subsequently uses the effective cross-section to design CFS members for global buckling. The method of effective width concept for design of CFS members according to EC3 is complex and requires the use of an iterative procedure; however, it is consistent with the design guidelines for class 1-class 3 sections (CEN 2005c). Recent research on the improvement of the effective width method has been conducted by other researchers (Batista 2009, Bernuzzi 2015, Bernuzzi and Maxenti 2015, Bernuzzi and Simoncelli 2015, Dubina and Ungureanu 2014, He and Zhou 2014, Hui et al. 2016, Ungermann et al. 2014, Yu and Yan 2011).

### 2.2.2 Direct Strength Method

The Direct Strength Method (DSM) proposed in Appendix 1 of the AISI specifications (AISI 2007) is an alternative to the traditional effective width method to predict the load carrying capacity of CFS members. This method integrates a computational stability analysis into the design process. In a first step, the elastic local, distortional and global buckling loads are



determined. Using these elastic buckling loads and the load that causes first yield, the strength is then directly predicted based on a series of simple empirical equations (AISI 2007). While calculation of the effective properties can be tedious for complex CFS cross-sections, only gross section properties are needed in the DSM. The elastic buckling loads of CFS members can be calculated using software such as CUFSM (Schafer 2006). A comprehensive review of the DSM has been presented by Schafer (Schafer 2008).

Currently, the DSM has been proven to be efficient and effective for the design of typical and prequalified CFS sections (AISI 2007). However, plain channel and angle sections cannot be designed according to DSM. Initially, DSM was limited to a number of prequalified cross-sections, was unable to design beam-columns, neglected the shift of effective centroid and could not account for interactive buckling (Ungermann et al. 2012).

The DSM has been further developed to include the analysis of flexural beams, compression members, combined compression and bending, members deficient in shear and the interactive buckling of members. See for example design recommendations by researchers (Ajeesh and Jayachandran 2016, Kumar and Kalyanaraman 2014, Kwon et al. 2009, Landesmann and Camotim 2013, Landesmann et al. 2016) for the design of columns, by researchers (Anbarasu 2016, Nandini and Kalyanaraman 2010, Pham et al. 2014a, Pham and Hancock 2013, Ren et al. 2016, Wang and Young 2014) for beam and purlins, guidelines proposed by researchers (Degtyareva and Degtyarev 2016, Mahendran and Keerthan 2013, Pham et al. 2015, Pham et al. 2014a, Pham et al. 2014b) for shear design and design recommendations (Kumar and Jayachandran 2016, Torabian et al. 2016, Torabian et al. 2015) for beam-columns and for interactive buckling (Cava et al. 2016, Dinis et al. 2012, Dinis and Camotim 2015, Martins et al. 2016).

With the development of DSM, the design procedure relies heavily on the buckling signature curve concept and this has led to a significant increase of research into the different methods for elastic buckling analysis of thin-walled steel sections. The conventional finite element method can be used whereas CFS sections are susceptible to local/distortional, global buckling and their interaction. Therefore, it is essential to isolate the individual buckling modes i.e. the pure local, distortional, global and shear buckling modes for computational efficiency in terms of design. The majority of the research in elastic buckling has concentrated on: a) the constrained finite strip method (cFSM) from Professor Schafer at the Johns Hopkins University and Professor Adany at Budapest University of Technology and Economics (Adany and Schafer 2006a, Adany and Schafer 2006b); b) the finite strip method (FSM) for shear buckling developed by Pham and Hancock at the University of Sydney (Hancock and Pham 2013); c) the general beam theory (GBT) mainly from Professor Camotim at the Universidade de Lisbon (Goncalves et al. 2010) and d) an alternative modal decomposition method based on polarisation developed by Dr

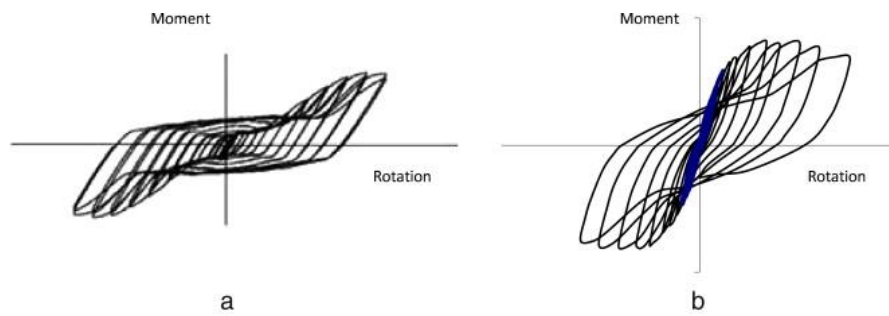
Becque at the University of Sheffield (Becque 2015). Other researchers' work on elastic buckling and modal decomposition can also be found in the literature (Camotim and Basaglia 2013, Li and Becque 2016, Li et al. 2014, Naderian and Ronagh 2015, Silvestre 2007).

Recent developments on the elastic buckling and modal decomposition can be mainly found in the field of shear and localised buckling analysis (Hancock and Pham 2015, Hancock and Pham 2013), elastic buckling of perforated members (Nedelcu 2014, Smith and Moen 2014), and shell or finite element based analysis (Ád ány 2016, Nedelcu 2014, Nedelcu 2012).

### **2.3 Seismic behaviour of CFS members**

The CFS sections have been widely used as envelope structures such as secondary cladding, purlins and wall panels in moment-resisting frame systems. However, the application of CFS elements as primary structural components is generally restricted to one-storey portal frames and low-rise stud-wall frames with low ductility in non-seismic areas (Dubina et al. 2012). Compared with conventional hot-rolled steel structures, the CFS structures are susceptible to premature local/distortional buckling in sections with large width-to-thickness ratio. Also conventional CFS connections usually cannot provide high strength and ductility. This implies that the conventionally developed strong-column weak-beam, and strong-connection weak-components seismic design philosophies adopted in seismic design codes (AISI 2005) cannot be directly used in CFS structures due to lack of ductility in CFS elements and connections. This restricts the application of multi-storey moment-resisting CFS framing systems in seismic regions (Dubina et al. 2012).

Recent studies on CFS bolted systems showed that both beams and columns can be designed in accordance with the capacity design principles to remain elastic during a strong seismic event (Sato and Uang 2013, Sato and Uang 2010, Uang et al. 2010). In their proposed design methodology the seismic energy has been dissipated mainly through the slippage and bearing failure caused by bolt-sheeting connection, as shown in Figure 2.13(a). Another design philosophy was developed by Bagheri-Sabagh et al. (Sabbagh et al. 2012a, Sabbagh et al. 2011) by using appropriate detailing such as longitudinal and transverse stiffeners to prevent premature buckling in the vicinity of connections and new CFS cross-sections with added bent corners to increase the capacity of the CFS cross-sections. The seismic energy is thus dissipated through a mechanism by bolt slip and cross-section buckling similar to the plastic hinges behaviour in hot-rolled steel elements, as shown in Figure 2.13(b). This implies that with the development of more efficient CFS elements, high performance moment-resisting CFS framing systems can be achieved.



**Figure 2.13. Responses of bolted CFS beam-column moment-resisting connections: (a) energy dissipation through slippage and bearing failure ;(b) through beam section (Sabbagh et al. 2012a)**

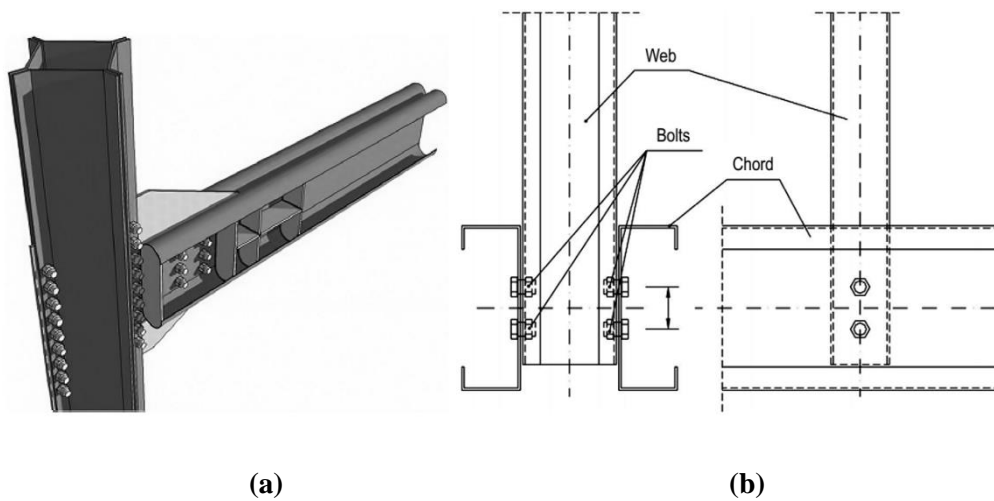
In order to fully understand the behaviour of CFS systems subjected to an earthquake scenario, there is a need to first expand current knowledge on CFS at member level. Existing research on cyclic behaviour of cold-formed steel members is still limited. An early investigation on the cyclic behaviour and energy dissipation associated with local buckling deformations in CFS beams subjected to cyclic bending (Calderoni et al. 2009) indicated that strength degrades rapidly in the initial cycles and remains almost the same in subsequent cycles. This was the result of localized inelastic buckling deformations (and fracture in the cross-section) gradually spreading through the cross-section as the number of cycles increased. The observed strength can be beneficial in the context of collapse analysis and design of CFS systems. An experimental program was conducted by Padilla-Llano et al. (Padilla-Llano et al. 2016) to investigate the cyclic bending behaviour and energy dissipation of CFS channel members experiencing local, distortional or overall buckling. CFS axial members were also tested under cyclic load by Padilla-Llano et al. (Padilla-Llano et al. 2014). The members were designed to fail by local, distortional or global buckling modes, and it was found that the total energy dissipated within a small length and decreased with increasing cross-sectional slenderness. More recently, tests were carried out on CFS lipped channel and curved channel beams in a moment-resisting frame subjected to cyclic bending (Serror et al. 2016). The effect of configurations with and without out-of-plane stiffeners on the energy dissipation, the moment strength and the ductility was investigated. Beams with curved section were proven to possess higher ductility and dissipate more energy.

## 2.4 Cold-formed steel connections

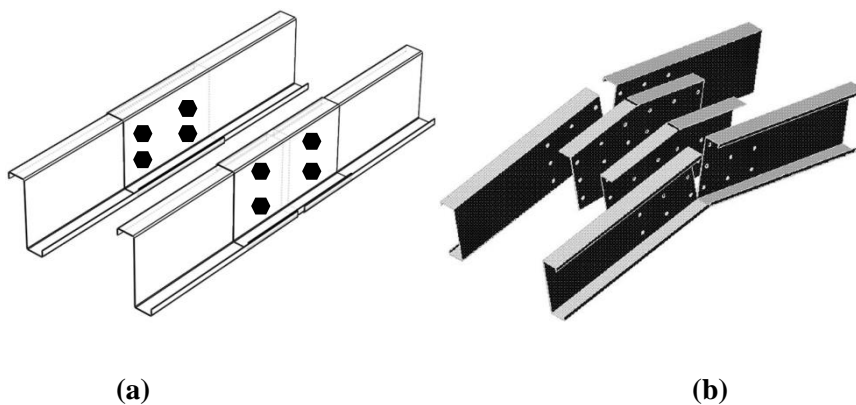
Unlike the design of hot-rolled steel structures, the design guidelines for CFS connections are still limited (CEN 2005d). Detailed design procedures for CFS connections are not always available in design codes due to the wide variety of joints used in the construction industry (Yu and LaBoube 2010) such as bolts or self-tapping screws (Lennon et al. 1999). The performance of single-lap bolted connections was examined (Bolandim et al. 2013, Chung and Ip 2001, Chung and Ip 2000, Kim et al. 2015, Kim et al. 2008, Teh and Gilbert 2014, Teh and Yazici 2013, Yu and Panyanouvong 2013). Screwed connections were studied by a number of

researchers (Fiorino et al. 2007, Peterman et al. 2014, Rahmanishamsi et al. 2016, Ye et al. 2016c, Zhao et al. 2014) and sheet or sheathing splitting, bearing failure and net section tension rupture were the most common failure modes observed in these single fastener studies.

Bolted connections are frequently used on site due to their efficient assembly. The most commonly used CFS bolted connections consist of: 1) beam-to-column joints with gusset plate or apex joints used in portal frames and low-storey buildings (Figure 2.14(a)); 2) bolted connections used in truss elements (Figure 2.14(b)), and 3) sleeve or overlapped connections for beam-to-beam or purlins (Figure 2.15).



**Figure 2.14. (a) Beam-column connection with stiffeners (Sabbagh et al. 2013) and (b) CFS truss bolted connection (Zaharia and Dubina 2006)**



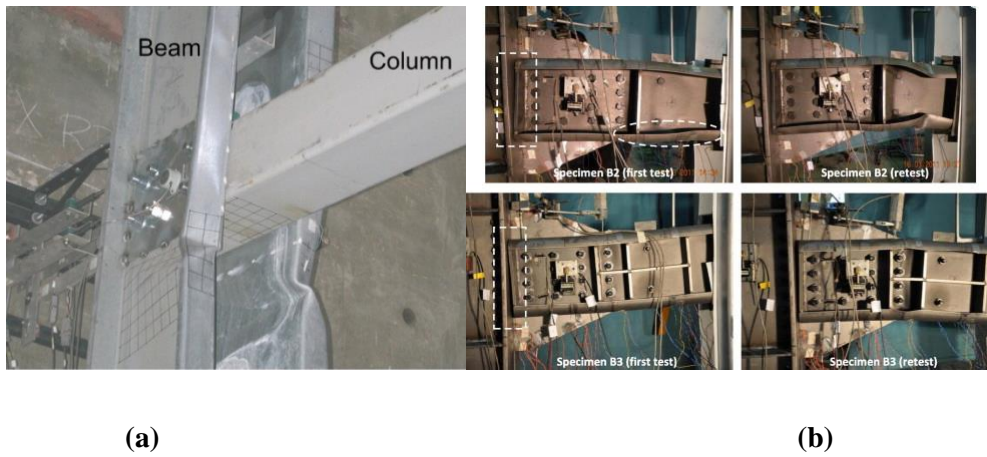
**Figure 2.15. (a) Sleeve and overlapped connections (Yang and Liu 2012, Zhang and Tong 2008) and (b) Details of apex joint (Lim and Nethercot 2003)**

Design guidelines for CFS connections are limited to their fundamental strength prediction of bolted fastenings (CEN 2005d, AISI 2007). These design rules for individual fastenings have been typically developed from test data with limited ranges of material properties and geometrical dimensions (Bryan 1993, Fisher 1964, Rogers and Hancock 1998, Teh and Yazici 2013) and therefore, should be carefully used in design and construction. While it is important

to assess the load carrying capacity of connections, it is also crucial to examine the stiffness and deformation characteristics of CFS connections. The local carrying capacity and deformation characteristics of CFS sleeve joints or overlapped connections (Gutierrez et al. 2011, Ho and Chung 2006, Liu et al. 2015a, Liu et al. 2015b, Yang and Liu 2012), CFS apex joints (Elkersh 2010, Lim and Nethercot 2004a, Lim and Nethercot 2004b, Lim and Nethercot 2003, Ozturk and Pul 2015) and bolted moment resisting connections have been investigated through experiments. Analytical formulas have also been proposed to predict the load-displacement curve and rotational stiffness (Bučmys and Daniūnas 2015, Bučmys and Šaučiuvėnas 2013). The behaviours of connectors in CFS storage racks were examined experimentally and numerically by researchers (Baldassino and Bernuzzi 2000, Bernuzzi and Castiglioni 2001, Gilbert and Rasmussen 2010, Markazi et al. 1997, Shah et al. 2016, Yin et al. 2016).

Nevertheless, analytical and experimental investigations on the monotonic and cyclic behaviour of bolted moment resisting connections in CFS construction are still limited. Uang et al (Uang et al. 2010) presented an experimental study on joints, where double channel beams were connected to HSS columns. The beams were directly connected to the column only with bolts but without any other components as shown in Figure 2.16(a). A ductile yielding mechanism was achieved through the inelastic action of bolt slippage and bearing in the sheets. A model to simulate the cyclic behaviour of the connection was proposed. However, the width-to-thickness ratios were limited strictly to prevent the local buckling in the vicinity of connections. Although a relatively high ductility was achieved, this was at the expense of a reduction in rotational stiffness.

Sabbagh et al. (Sabbagh et al. 2013, Sabbagh et al. 2012b) demonstrated that both high rotational stiffness and ductility could be achieved by using cross-sections with curved flanges (also see Figure 2.14). This was also studied and proved by other researchers (Serror et al. 2016). Also, vertical and horizontal stiffeners were used to prevent pre-mature buckling along the connection as shown in Figure 2.16(b) and moment-rotation behaviour with and without slippage were observed. The main disadvantage of the sections examined by Sabbagh et al. is that the curved-flange cross-sections are hard to manufacture and the additional welding work of the stiffeners creates a problem for fast and large-volume production of CFS products.



**Figure 2.16.** (a) connection presented by Uang et al. (Uang et al. 2010) and (b) by Sabbagh et al. (Sabbagh et al. 2012b)

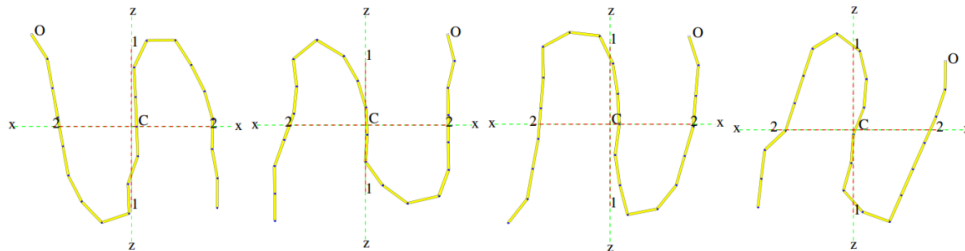
## 2.5 Optimisation of CFS elements

CFS sections can be manufactured in a wide range of cross-sections and, therefore, identifying the optimised cross-sectional shapes for CFS elements is of great interest to both manufactures and designers. Optimisation of CFS profiles is a complex process since the strength of CFS members composed of thinner plates are determined by local, distortional, and global buckling modes and their interactions.

Early research on the optimisation of cold-formed steel sections started by Seaburg and Salmon (Seaburg and Salmon 1971) with the minimum weight design. In their research, cold-formed hat-shaped sections were optimised according to the steepest descent method. Later, Adeli and Karim (Adeli and Karim 1997) optimised hat, I- and Z-shapes cross-sections using the neutral network method. Lee et al. (Lee et al. 2005b, Lee, Kim and Park 2006b) investigated the optimum design of channel beams and columns by using the micro genetic algorithms. Tian and Lu (Tian and Lu 2004a) investigated the minimum weight of the cold-formed C-channel sections with and without lips with a fix coil width subjected to a prescribed axial compressive load. Toward this, they have developed a simple optimisation procedure that assumes the simultaneous occurrence of all failure modes in a minimum weight structure. Different failure modes including yielding, flexural buckling, torsional-flexural buckling, and local buckling were considered, while the failure criterion was based only on the compressive strength. The accuracy of the developed analytical procedure was confirmed through experimental tests on the optimised C-sections with and without lips. In another study and using micro genetic algorithm (MGA), Lee et al. (Lee et al. 2006a) found the optimum design of CFS channel cross-sections with and without lips under axial compression. The optimum design formulation of CFS columns is derived based on the AISI specification (AISI 2001). The optimum results of different parameters were presented in the form of the design curves for different axial loads and column lengths.

Nevertheless, these research studies focused on the optimisation of the geometrical dimensions of conventional cross-sections and the solution space of other prototypes has not been considered. Thus, optimal solutions may not have been necessarily achieved.

In past studies, the strength capacities of selected prototypes were either determined using the conventional “effective width method” ((CEN 2005b, AISI 2007, Von Karman et al. 1932) or the more recently developed “direct strength method” (DSM) (AISI 2007) (e.g. by using finite strip method (FSM)) (Li and Schafer 2010b, Schafer 2006). Leng et al. (Leng et al. 2011) combined the DSM with the gradient-based steepest descent method as well as genetic and simulated annealing algorithms to obtain CFS sections with maximum capacity and their work resulted in the free-form sections shown in Figure 2.17. Gilbert et al. (Gilbert et al. 2012), and Moharrami et al. (Moharrami et al. 2014) conducted similar research while modified their optimisation algorithms to search for the minimum of the local, distortional and global buckling stress. The resulting shapes, although exhibiting significant improvement in strength, require very high manufacturing costs. Leng et al. (Leng et al. 2014) extended their previous works by incorporating constraints on the number of bent rollers, which resulted in reduced manufacturing costs. Additional work on the combination of DSM (Direct Strength Method) and GA (Genetic Algorithm) can be found in other references (Kumar and Sahoo 2016, Madeira et al. 2015, Wang et al. 2016a, Wang et al. 2016b).



**Figure 2.17. Optimal cross sections found by using GA and DSM (Leng et al. 2011)**

Sabbagh et al. (Sabbagh et al. 2012a) investigated the efficiency of six different shapes of CFS beams cross-sections (Figure 2.18) analytically. The results demonstrated that the strength and ductility of the CFS sections can be significantly improved through the introduction of bent rollers (from section 1 to section 6 in Figure 2.18). For example, Figure 2.19 shows that the premature buckling behaviour can be delayed by using the curved cross-sections. Nevertheless, curved cross-sections are difficult to manufacture and connect to other structural and non-structural elements such as floor systems and more practical shapes should be developed.

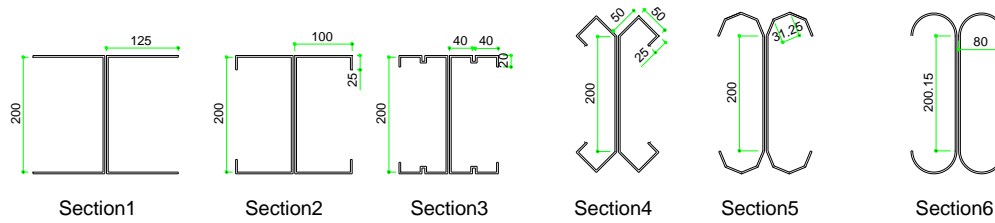


Figure 2.18. Evolution of CFS cross-sections by adding bents (Sabbagh et al. 2012a)

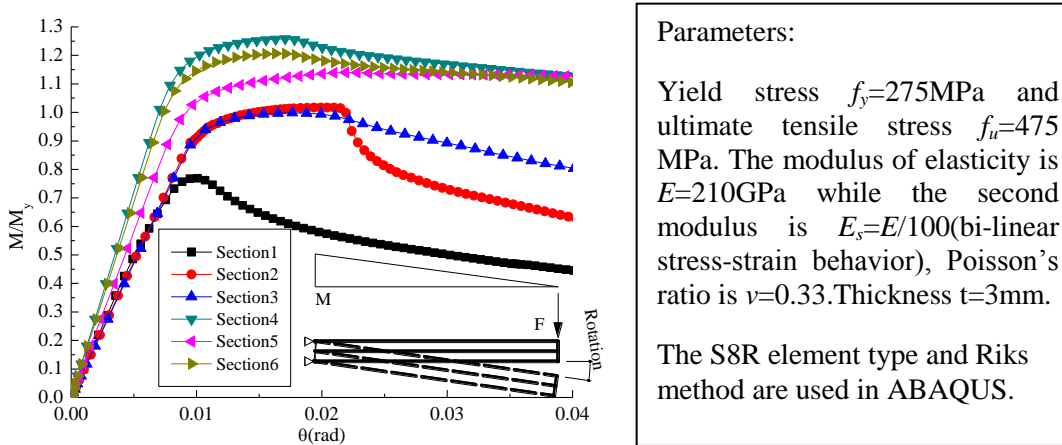


Figure 2.19. Moment-rotation behaviour of the CFS cross-sections (Sabbagh et al. 2012a)

Optimising the dimensions of cross-sectional shapes of the CFS elements can increase their ultimate strength. However, the limitation is that the known DSM strength equations were originally developed for pre-qualified beams or column sections, and were not validated (numerically or experimentally) for the design of more complex profiles. Therefore, for practical optimisation of non-predefined (or general) sections there is a need to develop suitable methods by considering manufacturing and construction constraints. Moreover, the optimisation of CFS cross-sectional shapes based on the buckling strength may not always optimise their energy dissipation capacity and ductility, which are especially important for seismic design applications.

## 2.6 CFS structural system

There are a number of structural systems available in the CFS construction, such as CFS truss roofs, CFS shear/stud wall system, CFS portal frame, CFS moment-resisting system and some other innovative structural forms (Dao and van de Lindt 2013).

The shear/stud wall structures have been widely used in residential buildings and frames composed of shear/stud walls can be used for multi-story buildings. A great number of experimental studies have been conducted to investigate their shear performances under lateral loading scheme. Fülöp and Dubina (Fulop and Dubina 2004) conducted a full-scale shear test on a CFS stud wall system with various configurations like diagonal strap braces, door openings, sheathing with corrugated sheet or Oriented Strand Board (OSB). The tested results show that the hysteretic behaviour is characterised by significant pinching and reduced energy dissipation.



Similar research on the behaviour of sheathed stud wall was carried out in other research as well (Lin et al. 2014, Miller and Pekoz 1994, Pan and Shan 2011, Serrette et al. 1997). In more recent studies by Ye et al. (Ye et al. 2015, Ye, Wang and Zhao 2016c), the effects of sheathing material, stud dimensions, stud spacing and fastener spacing were investigated extensively. The behaviour of CFS shear walls comprising single and double-sided steel sheathing was examined experimentally by Mohebbi et al. (Mohebbi et al. 2015). In this research study, the failure modes of sheathing-to-frame connection failure and stud buckling were observed in detail. It was also found that the sheathing screw failure with a bearing type led to higher energy dissipation. Mohebbi et al. (Mohebbi et al. 2016) also conducted experiments on the seismic behaviour of steel sheathed CFS stud walls cladded by gypsum and fibre cement boards. Different types of cladding boards were combined with steel sheathing and it was observed that the use of cladding can lead to a safer and more efficient design and to an increased energy dissipation capacity.

The dynamic behaviour of single and double story steel-sheathed CFS framed shear walls was examined experimentally by Shamim et al. (Shamim et al. 2013). Wang and Ye (Wang and Ye 2016) conducted cyclic tests on two and three story CFS shear-walls with reinforced end studs and reported a very good performance in terms of shear strength and energy dissipation capacity. Dao and Lindt (Dao and van de Lindt 2014, Dao and van de Lindt 2013) used an experimentally validated numerical model to study the seismic performance of CFS V-braced buildings and found that the buildings performed very well compared with the required performance criteria at the global level.

Schafer et al. (Nakata et al. 2012, Schafer et al. 2016) conducted a full-scale shake table test on CFS framed buildings. The experimental work was accompanied by an extensive numerical study and addressed various research issues, including: stud wall testing, characterisation, and modelling; cyclic beams and columns testing, characterization, and modelling; CFS screw connection testing, characterisation and modelling and whole building shake table testing, and modelling. Their research shows that it is essential to use more detailed numerical models to simulate the behaviour of full-scale CFS building system subjected to seismic load.

As discussed above, the use of CFS stud wall systems to develop a higher shear resistance is common practise. However, stud wall system restricts the architectural flexibility, reduces open spaces and limits future planning modification. An alternative to CFS shear walls is the use of CFS portal frames that solely composed of fully CFS beams, columns and moment-resisting connections. CFS portal frames are being used more frequently and therefore, research on their structural performance is increasingly being undertaken. The ultimate strength of CFS sub-frames was investigated by Lim and Nethercot (Lim and Nethercot 2004a, Lim and Nethercot 2003), and Yu et al (Yu et al. 2005). Dundu (Dundu 2011) investigated the design approach for

CFS portal frames. The design of beams, columns and beam-columns were discussed by using the effective width method while recommendations were made for the design of CFS bolted moment-resisting connections. The limit of deflection of the frames was also discussed. Phan et al. (Phan et al. 2011) optimised the topology of CFS portal frames using Genetic Algorithm. The effect of wind action was investigated whereas serviceability limit state was not taken into consideration. Kim et al. (Rasmussen et al. 2016) and Zhang et al. (Zhang et al. 2015) developed a beam finite element method that enables the consideration and effect of local/distortional buckling deformations. It was realized that the development of local/distortional buckling reduces the stiffness of CFS members. The results were verified through the use of a shell based finite element method. Following the development of the element, second-order effects in locally and/or distortionally buckled frames were investigated by Zhang et al. (Zhang et al. 2016a) to more accurately capture the true deformations and internal forces and moments of the portal frames. Subsequently, an experimental program was conducted (Zhang et al. 2016b) to investigate the structural behaviour of CFS portal frames subjected to the occurrence of local/distortional buckling prior to global sway buckling. A critical evaluation was made on the accuracy of existing design guidelines to predict the ultimate strength of the frames tested.

The stressed skin diaphragm action in CFS portal frame was investigated by Wrzesien et al. (Wrzesien et al. 2015) using experimental tests. Two types of joints with and without roof sheeting were used in the CFS frames. It was shown that due to the stressed skin action developed in the CFS frame, the internal portal frame with roof sheeting resisted about three times more lateral load than the bare frame and the deflection of the internal frame was reduced by 90% when compare to the bare frame in terms of serviceability limit state. Optimisation of CFS portal frame taking into account of the stressed skin diaphragm action was conducted by Phan et al. (Phan et al. 2015), who concluded that the material cost of a frame can be reduced by up to 53% when considering the stressed-skin action.

The behaviour of CFS moment-resisting frame with concrete filled CFS column and CFS back-to-back beams was investigated under cyclic load (Sabbagh et al. 2010). The tested CFS moment-resisting frames showed satisfactory seismic performance subjected to lateral cyclic load. In another study by Johnston et al. (Johnston et al. 2015a, Johnston et al. 2015b) , the collapse behaviour of CFS portal frames subjected to elevated temperatures was investigated. The test and numerical results showed the importance of connection rigidity in the modelling of CFS frame under fire.

CFS trusses are commonly used structural forms for constructing light-weight floors and roofs of portal frame structures. The optimisation of CFS space structures was conducted firstly by Tashakori and Adeli (Tashakori and Adeli 2002), who considered strength, stability and

serviceability limits in their design approach. A flat-panel double layer grid structure and a spherical double layer space truss were optimised by the authors using the devised methodology. A neural dynamics model has been used as the optimisation algorithm for the minimum weight design. An experimental study on a truss assemblage and its composed pin-joints were tested by Mathieson et al. (Mathieson et al. 2016) and a good agreement was achieved between the experimental results and the finite element modelling in terms of stiffness.

## 2.7 Summary

From the review of the literature discussed above, the following research needs were identified and will be addressed in more detail in the following chapters:

- It is apparent that the flexibility in the manufacturing of CFS sections allows the development of innovative shapes with improved resistance to local and distortional buckling. CFS sections can be stiffened by using intermediate stiffeners, edge stiffeners and increasing the folds among cross-sections. In addition, exploiting the composite action between CFS elements and other materials such as wood, bamboo and concrete can assist in developing a more economic design of CFS sections. However, the manufacturing and constructional restraints should be taken into account when innovative cross-sections are developed.
- Understanding and studying the main aspects of structural behaviour, advantages and deficiencies of CFS sections is a first step to improve their performance and efficiency. Therefore, prior to the optimisation of different cross-sectional shapes of CFS sections, it is essential to develop a procedure that can be used for the design of CFS sections. Both the effective width concept and the DSM can be used for the optimisation of CFS members. However, the sections should be predefined for the design procedure.
- The results of several studies indicated that optimising the profiles of CFS cross-sections based on their inelastic post-buckling behaviour can offer a great potential to improve the seismic performance of CFS framing sub-structures and full-scale systems.
- More practical cross sectional shapes should be developed to allow easier on-site connections by taking the manufacturing and construction factors into consideration. In addition, advanced numerical models should be developed to simulate the inelastic and cyclic behaviour of bolted connections with and without slippage so as to more accurately capture the behaviour of CFS connections.
- The optimisation of CFS cross-sectional shapes based on the buckling strength may not always optimise their energy dissipation capacity and ductility, which are especially important for seismic design applications.

- The research on seismic behaviour of CFS truss and frame system is still limited. At the same time, CFS buildings with longer span and more flexible layouts are in demand for people's requirements. Therefore, more research should be conducted on CFS bare frame and frame system considering the effect of cladding and stressed skin diaphragm action.

## **CHAPTER 3. Optimisation of CFS columns Using Particle Swarm Optimisation Method**

---

This chapter reports on the results of an investigation pertaining on the optimal design of cold-formed steel (CFS) columns with respect to their maximum compressive strength. A total of 10 channel cross-section were considered and their geometrical dimensions were optimised in pin-ended columns with three different length; 1m, 2m, and 3m. In the optimisation procedure, the thickness and total coil width were retained to be constant. In order to comply with the manufacturing and constructional restraints, the selected prototypes and optimisation process satisfy the requirements of Eurocode 3 (EC3). The cross-sectional properties and flexural strength of the sections was determined based on the effective width method suggested in EC3, while the optimisation process was performed using particle swarm optimisation method. The flexural strength of the optimised sections were also obtained using the nonlinear finite element (FE) analysis and the results were compared with those of effective width method suggested in EC3.

### 3.1 Introduction

There have also been a few studies on optimisation of cross-section of CFS columns. Literature review on the optimisation of CFS columns can be found in Section 2.5. As pointed out in Section 2.7. despite some research on size optimisation of CFS column with C-sections, no single research included the domain of all channel cross-sections commonly manufactured and used in construction industry. As a result, this study was aimed at optimising the geometrical dimensions of all manufacturable C-shape cross-sections (i.e. with and without lip and intermediate stiffeners). For the optimisation, all the sections were considered to have a fix coil width and thickness while the optimisation was performed based on the load capacity obtained following the provisions of effective width method suggested in EC3 (CEN 2005b). The optimised solutions were arrived using particle swarm optimisation (PSO) method while the results was also validated using the nonlinear FE analysis. To facilitate the procedure, both the optimisation and strength calculation were performed using a program developed in Matlab (Mathworks 2011, Appendix A.1).

### 3.2 Design of CFS columns based on EC3

It is clear according to EC3 that calculation of the effective properties requires an iterative procedure and the round corner effects are essential for consideration. In the optimisation process, the axial capacities of the sections were calculated according to the effective width method provisions of EC3. To provide a better illustration of the method, a summary of the requirements of this guideline in order to design CFS structural members under critical buckling conditions is provided in the following.

#### 3.2.1 Design for local buckling

The local buckling design of CFS members are addressed in EC3 using the effective width concept, first proposed by Von Karman (Von Karman et al. 1932). It recognizes the fact that local buckling of the plates constituting the cross-section has the effect of shifting the load-bearing stresses towards the corner zones, while the central parts of the plates become less effective in carrying load. The cross-section is consequently idealized with the “effective cross-section” as shown in solid black line in Figure 3.1. This effective area is assumed to carry the full compressive load applied to the section.

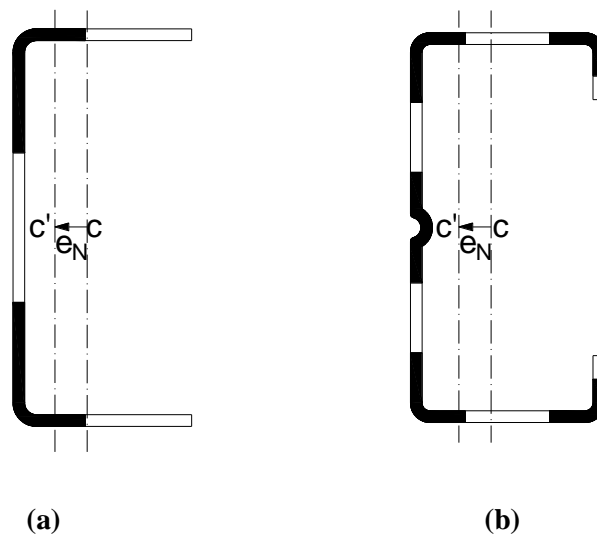


Figure 3.1. Effective area of (a) a plain C channel; and (b) a lipped channel with stiffener

### 3.2.2 Design for distortional buckling

Distortional buckling is considered as flexural-torsional buckling of plate subassemblies and therefore requires in-plane movement as well as out-of-plane movement of one or more plates. This is naturally accompanied by the intersecting lines of certain plates undergoing displacements out of their original positions, unlike what happens in local buckling. While EC3 accounts for local buckling by a reduction of the effective width of the constituent plates, distortional buckling is taken into account by reducing the effective plate thickness. The elastic distortional buckling stress, necessary for the calculation of a distortional slenderness, is thereby obtained from a simplified model where the restraining effect of the adjacent plates is simulated by elastic springs as illustrated in Figure 3.2.

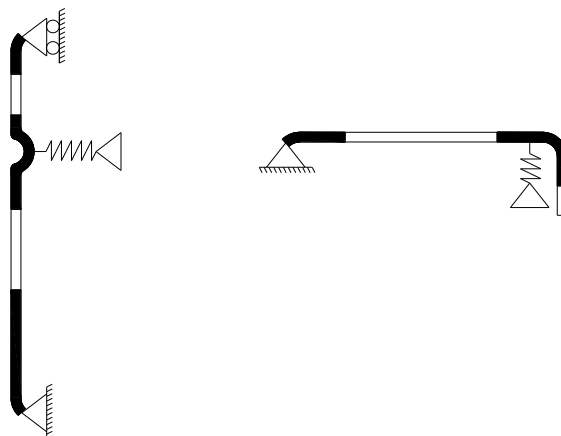


Figure 3.2. Flange and web models of a lipped channel section for distortional buckling calculations.

### 3.2.3 Design for global buckling

The design a CFS column for global buckling in EC3 requires the determination of the global slenderness,  $\lambda_c$  which is defined as

$$\lambda_c = \sqrt{\frac{A_{eff} f_y}{N_{cr}}} \quad (3.1)$$

where  $N_{cr}$  is the minimum of the elastic flexural, torsional or flexural-torsional buckling loads based on the gross cross-section. It should be noted that the slenderness is calculated using the effective area of cross-section,  $A_{eff}$  to account for local-global interaction buckling (i.e. the fact that local/distortional buckling erodes the global buckling stiffness).

### 3.2.4 The shift of the effective centroid

For a section lacking double symmetry, the centroid of the gross section and that of the effective section generally would not match, as depicted in Figure 3.1. A pin-ended column with a load applied at the centroid of the gross section will therefore sustain an additional bending due to the shift of the effective centroid once the local/distortional buckling takes place. EC3 accounts for this through an interaction equation for an axial force  $N$  combined with a moment of  $M = N e_N$ , where  $e_N$  is the shift of the effective centroid. However, this phenomenon is not observed in a fixed-ended column as the shift in the line of action of internal force is balanced by a shift in the line of action of external force (Young and Rasmussen 1999). Hence, local buckling in a fix-ended column would not produce any extra bending. According to EC3, the axial force,  $N_s$  in a column without any external bending moment is defined by

$$N_s = \left( \frac{1}{\left( \frac{1}{N_{b,Rd}} \right)^{0.8} + \left( \frac{e_N}{M_{b,Rd}} \right)^{0.8}} \right)^{1.25} \quad (3.2)$$

where  $N_{b,Rd}$  is the buckling resistance of a compression member according to the flexural-torsional or torsional-flexural buckling depending on the relative slenderness and  $M_{b,Rd}$  represents the design cross-section and member bending moment resistance of the weak axis and based on the effective bending properties. Also,  $e_N$  is the shift of the centroidal axes as shown in Figure 3.1.



### 3.3 Particle Swarm Optimisation method

The objective of the optimization was to maximize the bending capacity of CFS beams according to EC3, subjected to the design constraints and practical limitations listed in Table 1. Due to the high nonlinearity of the problem, a Particle Swarm Optimisation (PSO) method was adopted. PSO is a population-based algorithm, which is inspired by the swarming behaviour of biological populations such as flocks of birds or schools of fish. The mechanism has some parallels with evolutionary computational techniques, such as Genetic Algorithms (GA). An initial population of solutions is randomly selected, but unlike GA, solutions are optimised by updating generations without any evolution operators such as crossover or mutation. The potential solutions in PSO, called particles, move in the problem space by following the current optimum particles. This usually leads to a better efficiency in terms of computational time and cost and, therefore, a faster convergence rate compared to GA (Hassan et al. 2005, Jeong et al. 2009). Also, the required parameters in the PSO is less than those in the GA (Beghi et al. 2012).

PSO is inspired by the swarming behaviour of biological populations such as flocks of birds or schools of fish. An initial population of solutions is randomly selected and the solutions are optimised by updating generations without any evolution operators such as crossover or mutation (unlike GA). The potential solutions in PSO, called particles, move in the problem space by following the current optimum particles to search for the global optimal solution. A swarm is comprised of  $N$  particles moving around a  $D$ -dimensional search space, in which each particle represents a potential solution to the optimisation problem. The position and velocity vectors of  $i^{\text{th}}$  particle are  $\rho_i = \{\rho_{i1}, \rho_{i2}, \dots, \rho_{ij}, \dots, \rho_{iD}\}$  and  $V_i = \{v_{i1}, v_{i2}, \dots, v_{ij}, \dots, v_{iD}\}$ , respectively, where  $i = 1, 2, 3, \dots, N$ . In each iteration step, the  $i^{\text{th}}$  particle updates its position and velocity based on a combination of its personal best position over its history, and the position of the particle within the swarm with the best position in the previous iteration. This can mathematically described as:

$$V_i^{k+1} = w \cdot V_i^k + c_1 \cdot r_1 \cdot (P_{best,i}^k - \rho_i^k) / \Delta t + c_2 \cdot r_2 \cdot (G_{best}^k - \rho_i^k) / \Delta t \quad (3.3)$$

$$\rho_i^{k+1} = \rho_i^k + V_i^{k+1} \cdot \Delta t \quad (3.4)$$

where the subscripts  $i$  and  $k$  denote the particle and the iteration number, respectively.  $\Delta t$  is the time increment.  $P_{best,i} = \{p_{i1}, p_{i2}, \dots, p_{ij}, \dots, p_{iD}\}$  represents the best position of the  $i^{\text{th}}$  particle over its history up to iteration  $k$ , while  $G_{best} = \{g_1, g_2, \dots, g_j, \dots, g_D\}$  shows the position of the best particle in the swarm in iteration  $k$ . The cognitive parameter  $c_1$  indicates the degree of confidence in the solution  $P_{best,i}$  obtained from each individual particle. The constant parameter  $c_2$  is a social parameter to reflect the confidence level that the swarm as a whole has reached a

favourable position. In addition,  $r_1$  and  $r_2$  factors are two independent random numbers uniformly distributed between 0 and 1, adding a random searching aspect within the feasible region. Finally  $w$  is the inertial weight factor used to preserve part of the previous velocity of the particles to improve the convergence of the optimisation process.

### 3.4 Optimisation procedure

#### 3.4.1 Problem definition

This study was aimed at optimising the CFS columns with different length. A total of 10 cross-sections were considered as the prototypes, as illustrated in Table 3.1. This table also summarizes the optimisation variables and constraints corresponding to each prototype. These shapes were selected considering the manufacturing and construction restraints. Each cross-section was optimised individually with respect to its axial capacity determined according to EC3. All the limitations prescribed by EC3 on the slenderness values and the relative dimensions of the plate components in the cross-section were thereby taken into account as constraints on the optimisation problem in addition to a constant thickness of  $t = 1.5 \text{ mm}$  and a total coil width of  $l = 341 \text{ mm}$  for all prototypes. The optimised prototype with the maximum capacity then represented the overall optimum solution. The results of optimisation were also compared to a standard CFS cross-section (BW C17515) with the same total coil width and thickness as shown in Figure 3.3. The radius of all round corners, elastic modulus and Poisson's ratio were assumed as  $3 \text{ mm}$ ,  $210 \text{ GPa}$  and  $0.3$ , respectively. The steel yield strength was considered to be  $f_y = 450 \text{ MPa}$ . the optimisation problem can be formulated as a minimisation problem, defined by

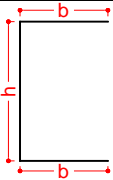
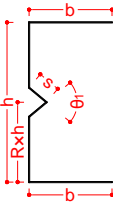
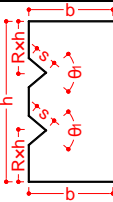
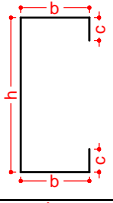

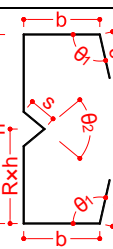
$$\min f(x) = -\min \{N_s, N_{b,Rd}, N_{c,Rd}\} / \gamma_{M0} \quad (3.5)$$

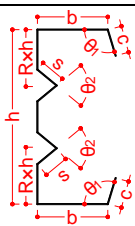
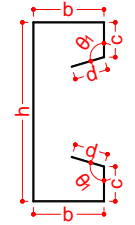
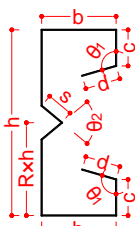
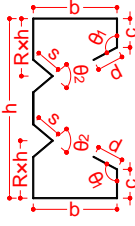
$$u_{\min} \leq x_i \leq u_{\max} \quad \text{for } i = 1, \dots, N$$

where  $f(x)$  is the design moment resistance of a column.  $N_s$  is the axial member resistance considering shift of centroid as described in Sections 3.2.4,  $N_{b,Rd}$  and  $N_{c,Rd}$  are the resistance of member and cross-section, respectively. Also,  $\gamma_{M0}$  is the partial factor in ultimate limit state. It is worth mentioning that the inelastic reserve capacity is always taken into account according to EC3 when calculating the bending resistance. For each variable,  $x_i$ , the lower and upper bounds,  $u_{\min}$  and  $u_{\max}$  respectively, are considered according to EC3 as summarised in Table 3.1.

The sections were optimised for three different lengths (1, 2, and 3m). The effective lengths for bending and torsion were assumed to be identical. The optimisation was carried out for a pin-ended column with warping allowed at the ends. This boundary condition considers the effect of the shift in effective centroid by using a beam-column interaction equation as described in Section 3.2.

**Table 3.1. Optimisation prototypes, variables and constraints**

Prototype	Prototype section	Design variables	Constraints based on EC3	$u_{\min}$	$u_{\max}$	Comments
①		$x = b/L$	$b/t \leq 50$ $b/t \leq 500$	0	0.220	EN1993-1-3 Clause 5.2
②		$x_1 = b/L$ $x_2 = R$ $x_3 = \theta_1$ $x_4 = s$	$b/t \leq 50$ $b/t \leq 500$ $0.1 \leq R \leq 0.9$ $\pi/6 \leq \theta_1 \leq \pi/2$ $10 \leq s \leq 20$	0 0.1 $\pi/6$ 10	0.220 0.9 $\pi/2$ 20	EN1993-1-3 Clause 5.2
③		$x_1 = b/L$ $x_2 = R$ $x_3 = \theta_1$ $x_4 = s$	$b/t \leq 50$ $b/t \leq 500$ $0.1 \leq R \leq 0.4$ $\pi/6 \leq \theta_1 \leq \pi/2$ $10 \leq s \leq 20$	0 0.1 $\pi/6$ 10	0.220 0.4 $\pi/2$ 20	EN1993-1-3 Clause 5.2
④		$x_1 = c/b$ $x_2 = b/L$	$0.2 \leq c/b \leq 0.6$ $b/t \leq 60$ $c/t \leq 50$ $b/t \leq 500$	0.2 0	0.6 0.264	EN1993-1-3 Clause 5.2
⑤		$x_1 = c/b$ $x_2 = b/L$ $x_3 = \theta_1$	$0.2 \leq c/b \leq 0.6$ $b/t \leq 60$ $c/t \leq 50$ $b/t \leq 500$ $\pi/4 \leq \theta_1 \leq 3/4\pi$	0.2 0 $\pi/4$	0.6 0.264 $3/4\pi$	EN1993-1-3 Clause 5.2
⑥		$x_1 = c/b$ $x_2 = b/L$ $x_3 = R$ $x_4 = \theta_1$ $x_5 = \theta_2$ $x_6 = s$	$0.2 \leq c/b \leq 0.6$ $b/t \leq 60, c/t \leq 50$ $b/t \leq 500$ $\pi/4 \leq \theta_1 \leq 3/4\pi$ $\pi/6 \leq \theta_2 \leq \pi/2$ $0.1 \leq R \leq 0.9$ $10 \leq s \leq 20$	0.2 0 0.1 $\pi/4$ $\pi/6$ 10	0.6 0.264 0.9 $3/4\pi$ $\pi/2$ 20	EN1993-1-3 Clause 5.2

Prototype	Prototype section	Design variables	Constraints based on EC3	$u_{\min}$	$u_{\max}$	Comments
⑦		$x_1=c/b$ $x_2=b/L$ $x_3=R$ $x_4=\theta_1$ $x_5=\theta_2$ $x_6=s$	$0.2 \leq c/b \leq 0.6, b/t \leq 60$ $c/t \leq 50, b/t \leq 500$ $\pi/4 \leq \theta_1 \leq 3/4\pi$ $\pi/6 \leq \theta_2 \leq \pi/2$ $0.1 \leq R \leq 0.4, 10 \leq s \leq 20$	0.2 0 0.1 $\pi/4$ $\pi/6$ 10	0.6 0.264 0.4 $3/4\pi$ $\pi/2$ 20	EN1993-1-3 Clause 5.2
⑧		$x_1=c/b$ $x_2=d/b$ $x_3=b/L$ $x_4=\theta_1$	$0.2 \leq c/b \leq 0.6, 0.1 \leq d/b \leq 0.3$ $b/t \leq 90, c/t \leq 60$ $d/t \leq 50, b/t \leq 500$ $\pi/4 \leq \theta_1 \leq 3/4\pi$	0.2 0.1 0 $\pi/4$	0.6 0.3 0.264 $3/4\pi$	EN1993-1-3 Clause 5.2
⑨		$x_1=c/b$ $x_2=d/b$ $x_3=b/L$ $x_4=R$ $x_5=\theta_1, x_6=\theta_2$ $x_7=s$	$0.2 \leq c/b \leq 0.6, 0.1 \leq d/b \leq 0.3$ $b/t \leq 90, c/t \leq 60$ $d/t \leq 50, b/t \leq 500$ $\pi/4 \leq \theta_1 \leq 3/4\pi$ $\pi/6 \leq \theta_2 \leq \pi/2$ $0.1 \leq R \leq 0.9$ $10 \leq s \leq 20$	0.2 0.1 0 0.1 $\pi/4$ $\pi/6$ 10	0.6 0.3 0.264 0.9 $3/4\pi$ $\pi/2$ 20	EN1993-1-3 Clause 5.2
⑩		$x_1=c/b$ $x_2=d/b$ $x_3=b/L$ $x_4=R$ $x_5=\theta_1, x_6=\theta_2$ $x_7=s$	$0.2 \leq c/b \leq 0.6, 0.1 \leq d/b \leq 0.3$ $b/t \leq 90, c/t \leq 60$ $d/t \leq 50, b/t \leq 500$ $\pi/4 \leq \theta_1 \leq 3/4\pi$ $\pi/6 \leq \theta_2 \leq \pi/2$ $0.1 \leq R \leq 0.4$ $10 \leq s \leq 20$	0.2 0.1 0 0.1 $\pi/4$ $\pi/6$ 10	0.6 0.3 0.264 0.4 $3/4\pi$ $\pi/2$ 20	EN1993-1-3 Clause 5.2

In the optimisation process, the starting point was set to be the commercially available C channel section, as shown in Figure 3.3. However, it also allowed for the more complex double edge folds, inclined edge folds and intermediate stiffeners. In addition, the effects of intersection angle and side length of intermediate stiffeners (ranged from  $\pi/6$  to  $\pi/2$  and 10 to 20 mm, respectively) were taken into account as constraints in the optimisation. Other constraints include the limits on the ratios of the plate width to thickness, relative dimension ratios, and internal angle of edge stiffeners

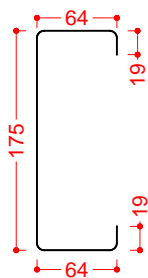


Figure 3.3. Standard CFS column section (BW C17515) with the total coil length of 341mm

### 3.4.2 Optimised results and comparison

To facilitate the optimisation procedure, both optimisation algorithm and strength calculation were performed using a program developed in Matlab (Mathworks 2011, Appendix A.1). In the optimisation process, the population of particle swarm was taken as 100, and the same number was also used for iterations except for prototypes ⑨ and ⑩ where the program ran for 160 iterations to obtain the optimum value. The maximum and minimum inertia weight factors in the PSO were 0.95 and 0.4, respectively. For optimisation, each of the pre-defined prototypes was run three times and the results with maximum compression capacity were chosen as the optimal cross-section. The selected prototypes were aimed at investigating the effect of geometrical details and positions of edge and intermediate stiffeners.

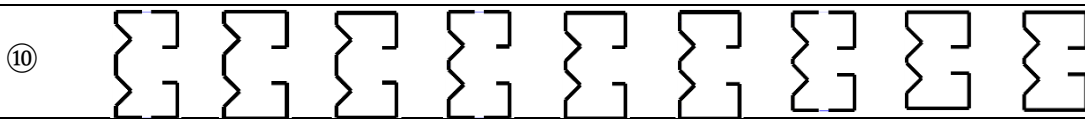
Table 3.2 compares the axial capacities and geometric properties of the optimised cross-section are compared with those of the standard cross-section. Also, a schematic illustration of the optimised cross-sections for columns with three different lengths is provided in Table 3.3 where thick black lines represent the fully effective parts and lines with intermediate thickness indicate those have been reduced to consider for the distortional buckling of edge and intermediate stiffeners. The thin blue lines signify the ineffective portions of the cross-section. EC3 determines the effective cross-sections under the axial load and the moment resulted from the shift of the centroid separately. Under a pure axial load, the effective areas of the optimal cross-sections are listed under the column with symbol “A” in Table 3.3. The shift  $e_N$  has significant effect on the resistance of the members. According to EC3, the effect of the shift in the centroid should be considered by controlling the worse scenarios of shifting on both direction (i.e. towards the web or edges). These two cases were determined in column B<sub>1</sub> and B<sub>2</sub> of for the edge stiffeners and the web part under compression, respectively.

**Table 3.2. Comparison of the geometrical dimensions and axial capacity of the optimised sections with the standard section**

Prototypes	Length (m)	h (mm)	b (mm)	c (mm)	d (mm)	s (mm)	$\theta_1$ (deg)	$\theta_2$ (deg)	Corner radius	Optimal strength (kN)
Standard	1	175	64	19	-	-	-	-	-	71.4
	2	175	64	19	-	-	-	-	-	52.1
	3	175	64	19	-	-	-	-	-	33.2
①	1	210	65	-	-	-	-	-	-	55.3
	2	191	75	-	-	-	-	-	-	40.3
	3	191	75	-	-	-	-	-	-	26.1
②	1	176	75	-	-	10	30	-	0.5	65.6
	2	176	75	-	-	10	30	-	0.5	51.5
	3	176	75	-	-	10	30	-	0.5	35.7
③	1	159	75	-	-	15	55	-	0.302	86.5
	2	172	75	-	-	15	90	-	0.297	57.4
	3	172	75	-	-	15	90	-	0.297	35
④	1	132	65	39	-	-	90	-	-	102.1
	2	132	65	39	-	-	90	-	-	71.1
	3	132	65	39	-	-	90	-	-	42.6
⑤	1	140	63	38	-	-	105	-	-	102
	2	145	61	37	-	-	110	-	-	73.9
	3	150	60	36	-	-	120	-	-	46.3
⑥	1	154	51	30	-	20	100	45	0.5	113.7
	2	159	54	33	-	14	110	90	0.5	79.1
	3	154	55	33	-	20	120	90	0.5	47.6
⑦	1	136	50	30	-	20	115	55	0.287	135.2
	2	147	54	32	-	20	120	90	0.3	81.5
	3	145	54	33	-	20	120	90	0.297	49.5
⑧	1	113	60	36	18	-	90	-	-	118.2
	2	128	59	35	13	-	90	-	-	73.9
	3	135	59	35	9	-	90	-	-	42.8
⑨	1	94	60	36	18	20	90	70	0.5	148.7
	2	110	58	35	16	20	90	90	0.5	90.5
	3	104	59	36	18	20	90	90	0.5	47.7
⑩	1	102	58	35	15	20	90	90	0.267	140.6
	2	103	58	35	14	20	90	90	0.32	76.1
	3	94	59	35	18	20	90	90	0.32	39.3

**Table 3.3. Effective cross-sections of optimised sections under compression and flexural moment**

Prototype	L=1m			L=2m			L=3m		
	A	B1	B2	A	B1	B2	A	B1	B2
①									
②									
③									
④									
⑤									
⑥									
⑦									
⑧									
⑨									



For the plain channel of prototype ①, the effective portions of both web and flange are quite small signifying the weakness of this cross-section under local buckling. As a result, a significant shift of centroid was observed in this section. Iteration procedures of the centroidal axes in order to calculate the effective properties of the plated assemblies are important in this prototype since it is sensitive to the shift value of centroid,  $e_N$ . Adding intermediate stiffener to this plain channel section can increase the axial capacity by up to 56% as observed in prototypes ② and ③. However, this increment was not so significant for the  $3m$  long columns. This can be attributed to the fact that adding intermediate stiffeners can increase the effective portions of the plates, improving local buckling strength for short columns whereas, the increased effective portions in web exacerbated the shift of centroid, which may decrease the axial compressive resistance of long columns.

As indicated by the effective cross-sections of prototypes ④ and ⑤, the length of lips tends to be around 60% of the flange width which is identical to the allowed value in EC3. This can increase the moment of inertia of the edge stiffeners, providing more spring stiffness to prevent distortional buckling. In addition, changing the inclined angle of the edge stiffeners can result in keeping the centroid in its initial position and increasing the second moment of area to achieve high elastic critical buckling resistance for longer columns as observed from prototype ⑤ in which the inclined angle increased with the column length. However, angle of lips has just little effects on the ultimate resistance of columns. Introducing the web stiffeners in prototypes ⑥ and ⑦ resulted in reducing the flange width in these prototypes compared with prototype ⑤. Since the axial capacity of the columns is calculated based on the effective cross-sectional area and a reduction factor related to the relative slenderness ratio, it is governed by the interaction of the local and global buckling according to EC3. The stiffeners in the web can significantly improve the local buckling strength of the web plates. However, this will cause the shift of centroid and changes the gross cross-sectional properties which relates to the global buckling behaviour.

With introducing the web stiffeners, the cross-sections of prototypes ⑨ and ⑩ showed to arrange themselves to a more stocky effective property. The flanges of these two cross-sections could be fully effective with narrower plates (smaller relative slenderness). However, the flanges adjusted to be wider to provide more effective portions toward the side of lips, preventing the centroidal axis of the effective cross-sections to shift toward web side. The interaction behaviour of the local/distortional and global buckling for columns in prototypes ⑨



and ⑩ were less significant compared to the effective cross-section of prototype ⑧ which can be due to the higher local buckling resistance of these two prototypes achieved by the use of intermediate stiffeners.

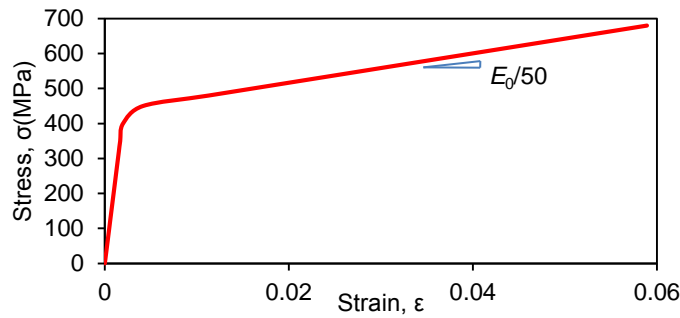
### 3.5 Nonlinear FE analysis of the optimised columns

In order to evaluate the reliability of the optimisation procedure, the axial capacity of columns with the optimised and standard sections were also determined using the detailed nonlinear FE models considering the geometrical imperfections. The FE modelling and analyses were performed in ABAQUS (ABAQUS 2011).

The three-dimensional (3D) FE model of the columns with optimised and standard sections were developed in the commonly used ABAQUS software. To model the characteristics of the CFS plate the general purpose S4R element, a 4-node quadrilateral shell element with reduced integration was employed. Through the sensitivity analysis the maximum mesh size has been selected to be equal to  $5\text{mm}$  with at least four elements in the corners. To simulate the material behaviour of CFS plate, the constitutive stress-strain model suggested by Haidarali and Nethercot (Haidarali and Nethercot 2011) as shown in Figure 3.4, was used. This model is comprised of the basic Ramberg-Osgood stress-strain relationship up to 0.2% proof stress followed by a straight line up to ultimate point. The slope of the linear part is equal to  $E/50$  where  $E$  stands for the initial elastic modulus. The stress-strain behaviour of the CFS material in this model is defined by

$$\begin{aligned} \varepsilon &= \frac{\sigma}{E} + 0.002 \left( \frac{\sigma}{\sigma_{0.2}} \right)^n & \text{for } \sigma \leq \sigma_{0.2} \\ \varepsilon &= \varepsilon_{0.2} + \frac{50(\sigma - \sigma_{0.2})}{E} & \text{for } \sigma \geq \sigma_{0.2} \end{aligned} \quad (3.6)$$

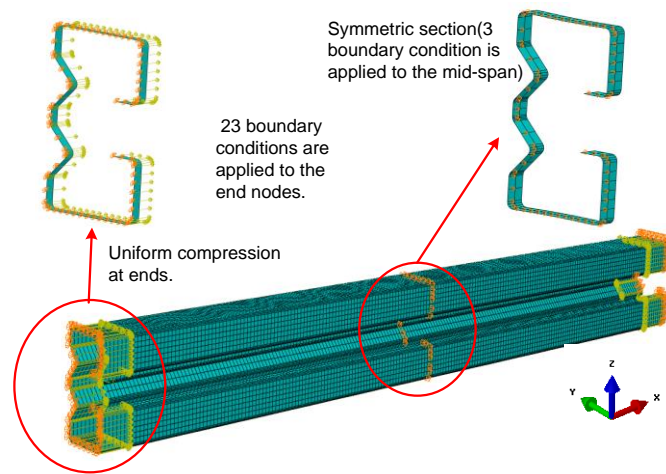
where  $\sigma$  and  $\varepsilon$  are stress and strain, respectively. Also,  $\sigma_{0.2} = 450\text{N/mm}^2$  is the 0.2% proof stress,  $\varepsilon_{0.2}$  is the total strain at  $\sigma_{0.2}$ ,  $n$  stands for the shape parameter recommended by Gardner and Ashraf (Gardner and Ashraf 2006) to be taken as 28 for high strength steel (with  $f_y = 350\text{--}450\text{N/mm}^2$ ), and  $E$  is the elastic modulus which is taken equal to  $210\text{GPa}$ .



**Figure 3.4. Stress-strain behaviour of CFS plate used in the FE modelling**

In the FE simulation, the effects of geometrical imperfections were also considered by scaling the critical buckling modes to specific amplitudes and superposing them into the initial perfect geometry. The shapes of the geometrical imperfections are generated using CUFSM (Li and Schafer 2010b), a finite strip software. Only the imperfection of the critical one of the local and distortional buckling modes observed in the signature curve obtained from CUFSM, was chosen to superpose as the localized imperfection while global imperfection magnitude was considered as  $L/1000$  where  $L$  is the total length of the column. For prototypes ④ to ⑩ and the standard section (BW C17515) which were with edge stiffeners, the magnitudes of the local and distortional geometrical imperfections were considered based on the cumulative distribution function (CDF) values proposed by Schafer and Peköz (Schafer and Pekoz 1998). In such cases, the type 1 and type 2 imperfections with a CDF value of 50% which have 34% and 94% of the original thickness, respectively, were adopted in the FE modelling. However, the plain channel sections (i.e. prototypes ① to ③) don't have a distortional buckling mode and the FE modelling with the imperfections of 50% CDF value showed a great deviation. To overcome this problem, the effect of imperfection for these three prototypes were considered as 25% of the cross-sectional thickness based on the study performed by Young and Yan (Young and Yan 2002).

Originally, Schafer et al. (Schafer et al. 2010) recommended boundary conditions on CFS collapse modelling, where they employed kinematic constraints at ends to force the member to bend and twist about known reference point to reflect the global behaviour of columns. Their suggested boundary condition prevents the warping of cross-sections. However, for pin-ended columns, EC3 typically allows the free warping at both ends of the members. Thus, the boundary conditions of the FE models were modified to simulate a pin-ended column, as shown in Figure 3.5. The longitudinal movement of the columns was precluded through restraining the nodal displacement of the mid-length cross-section while the horizontal displacement of the column was restricted by restraining the nodes at the end cross-sections. Consequently, the longitudinal displacements at both ends were intentionally retained free to allow the warping of the end cross-sections. Also, the axial forces were applied to the nodes of the end cross-sections.



**Figure 3.5. Schematic illustration of the FE model of the columns with pin-ended boundary conditions**

To build the geometrical modelling of the optimised cross-sections, the coordinates of the cross-sections were determined using a program developed in Matlab (Mathworks 2011, Appendix A2 and A4). The information was then imported to CUFSM (Li and Schafer 2010b) to obtain the critical half-wavelengths and mode shapes using the classical elastic buckling analysis. For the local, distortional and global buckling modes, the magnitudes and directions for the deformations of the cross-sectional nodes can be determined from in the array “shapes” of CUFSM. Therefore, the shape of the initial imperfections was obtained from the array while the sinusoidal functions were used for the distribution of initial imperfections along the columns. The mesh density and material properties used in the FE modelling in ABAQUS were identical to those used in the finite strip method performed with CUFSM.

To avoid the convergence problem during the nonlinear analysis, the load was applied with the displacement control method. The solution was arrived using the Riks method considering the effect of the large deformations to track the post-buckling behaviour. The maximum step sizes were modified to assure reliable results with at least 20 iterations before arriving at the peak bending moment (Schafer et al. 2010).

The FE models were developed for the optimised columns with three different lengths ( $1m$ ,  $2m$  and  $3m$ ). The geometrical dimensions, thickness, and material properties such as elastic modulus and yield stress were assumed to be identical to those used in the optimisation procedure. It is worth noting that the round corners of the cross-sections were also modelled in all the FE analyses.

### 3.6 Description and comparison of the results

The axial capacities of the optimised and standard cross-sections obtained from the FE analyses are compared with those calculated according to EC3 in Figure 3.6, Figure 3.7 and Figure 3.8

for columns with 1m, 2m, and 3m in length. Despite some differences, a good agreement was observed between results obtained from FE analysis with those calculated based on EC3.

For 1 m long columns, compressive capacities are more likely to be governed by the interaction of local/distortional and global buckling. For this type of columns, comparison of the results obtained from FE analysis and EC3 showed that, except for the standard BW columns, EC3 slightly overestimates the capacities of columns. As observed in Figure 3.6, the compressive capacities of the plain channel columns without or with only one web stiffener are even lower than the standard BW cross-section which can be due to the more vulnerable behaviour to the interactive buckling. For prototypes ④ and ⑤, the FE results of 1 m channel column showed that the change of inclined angle of lips may lead to decrease of the compressive capacity, though the results from EC3 shows little effect. Even by just optimising the dimensions of the standard BW cross-section, the bending capacity can be enhanced by 43% and 23.6 % according to EC3 and FE results, respectively. However, the best prototype for 1m long column is prototype ⑨ in terms of compressive capacity where 108.3% and 77.1% increase can be achieved according to EC3 and FE modelling compared to the standard section. The results also indicated that despite prototype ⑩ occupies the biggest number of stiffeners; its compressive strength could not be necessarily the highest. Because of the intermediate and edge stiffeners in this prototype, the local buckling is unlikely to happen (see the effective cross-section shapes of prototype ⑩ in Table 3.3) and the stiffeners take up some of the material which could be better used for the development of gross sectional properties (the second moment of area about weak axis to prevent the shift of centroid). A similar trend was also observed from the results of 2m and 3m columns with the same prototype.

For the column with 2m and 3m in length, there were some discrepancies between the FE and EC3 results in different cross-sections. It should be mentioned that for longer columns, the effect of local/distortional buckling behaviour is less important compared with 1m long columns. However, EC3 still considers the shift of centroidal axis by calculating the effective cross-sectional properties based on the yield stress. Regarding the axial capacity, the best performance in columns with 3m length was observed in prototype 6 from both the FE results and EC3 while the axial capacity of prototype ⑨ calculated according to EC3 indicated highest strength for 2m long columns. The effect of edge stiffeners on the compressive capacity of 3m column is negligible since long columns fails under global buckling mode before the happening of local/distortional buckling mode. However, with the prototype ⑨, the compressive strength of columns with 2m in length can be increased by 73.7% and 59.2% according to EC3 and FE results, respectively compared to the standard cross-sections. For the columns with 3m in length, prototype ⑥ achieves 43.4% and 42.9% more than the standard BW cross-sections, accordingly.

Taking the manufacture cost into consideration, prototype ⑤ and ⑥ offered numerous advantages compared to other cross-sections since they need only 4 and 7 rollers to shape the cross-sections while possess relatively high compressive capacities. Prototypes ①-③ are not good choices for application since their compressive capacities are relatively low though they are easy to manufacture.

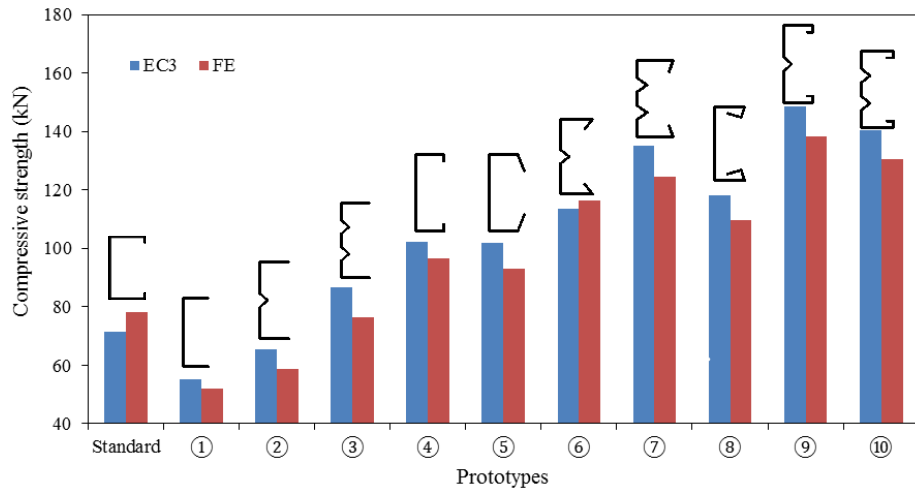


Figure 3.6. Comparison of the axial capacity of the standard and optimised columns with 1 m length

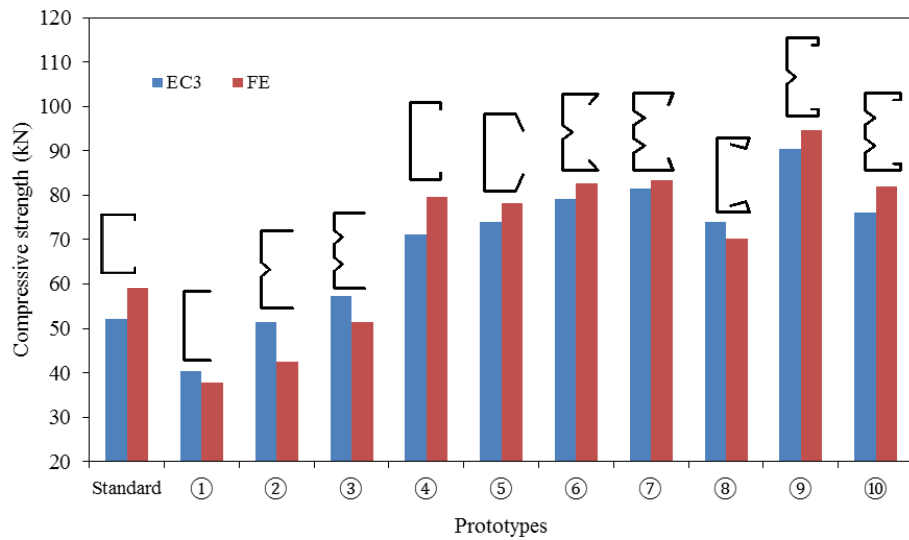
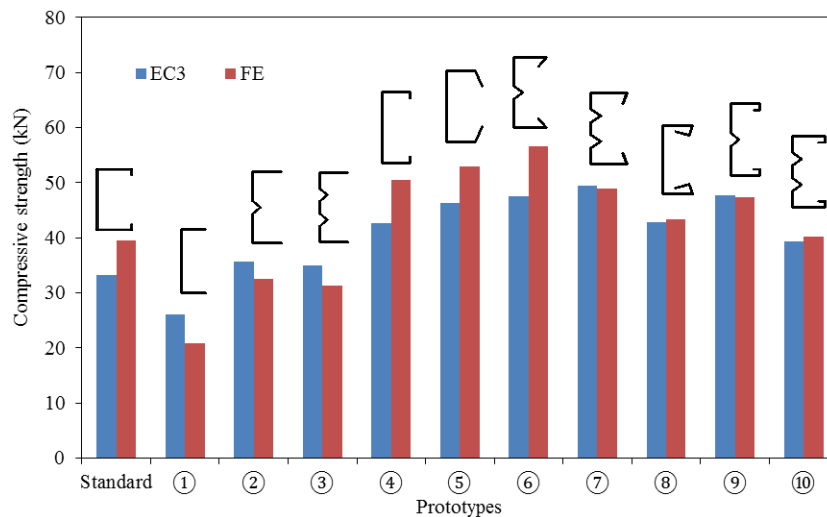


Figure 3.7. Comparison of the axial capacity of the standard and optimised columns with 2 m length



**Figure 3.8. Comparison of the axial capacity of the standard and optimised columns with 3 m length**

### 3.7 Summary and conclusions

This chapter presents a framework for the optimisation of CFS columns to achieve the optimal compressive capacity with various cross-sections. As the prototypes, 10 channel cross-sections were selected and the geometrical dimensions of each individual prototype were optimised with respect to its axial capacity. The thickness and coil length of the prototypes were kept constant during the optimisation process. The selected prototypes were comprised of the plain channels, channels with single inclined lips, channels with double folded lips with one or two intermediate stiffeners incorporated into the web. All relative geometrical proportions recommended in EC3 were taken into account as optimisation constraints. The optimisation procedure was performed using a program developed in Matlab.

For comparison purposes, a commercially available standard cross-section with the same total coil width and thickness was selected and its axial capacity was compared with those of optimised cross-section in columns with 3 different lengths:  $1m$ ,  $2m$  and  $3m$ . The axial capacities of the optimised cross-sections determined based on EC3 were also verified against detailed nonlinear FE analysis considering the effect of geometrical imperfection. The compressive capacity has been found to be highly dependent on the shift of centroid and the effective cross-section of the prototypes. It was concluded that the axial capacity of the standard cross-section can be enhanced up to 108.3%, 73.7% and 43.4% according to EC3 but 77.1%, 59.2% and 42.9% with regard to the FE modelling, in columns with  $1m$ ,  $2m$  and  $3m$  length, respectively. The largest axial capacity for columns with  $1m$  and  $2m$  in length was observed in prototype 9 (channel with double-fold lips and one web stiffener) while for  $3m$  long column, prototype 6 (channel with single lip and one web stiffener) offered the highest axial capacity

# **CHAPTER 4. Optimum design of CFS beams using Particle Swarm Optimisation Method**

---

Optimisation on CFS columns was presented in Chapter 3, in this chapter, a detailed investigation was conducted on the practical optimisation of CFS beams using a Particle Swarm Optimisation (PSO) method. Six different CFS channel section prototypes were selected and then optimised with respect to their flexural strength, determined according to the effective width based provisions of Eurocode 3 (EC3) part 1-3 (CEN 2005b). Comparing the capacities of the optimised sections to those of the original channel sections with the same amount of structural material, significant improvements were obtained. The accuracy of the optimisation procedure was assessed using experimentally validated nonlinear Finite Element (FE) analyses accounting for the effect of imperfections. The results indicated that, using the same amount of material, the optimum sections offered up to 25% and 75% more flexural strength for laterally braced and unbraced CFS beams, respectively, while they also satisfied predefined manufacturing and design constraints..

## **4.1 Introduction**

Cold-formed steel (CFS) structural elements and systems are widely used in the construction industry, for instance in trusses, modular building panels, stud walls, purlins, side rails, cladding

and even as the primary load-bearing structure in low- to mid-rise buildings. Compared to their hot-rolled counterparts, CFS members are often found to be more economical and efficient, due to inherent advantages such as a light weight, an ease and speed of erection and a greater flexibility in manufacturing cross-sectional profiles and sizes. Many cold-rolling companies have the ability to custom roll sections on demand, adapted to certain particular applications. It is this versatility on the manufacturing side which makes the problem of finding optimal cross-sectional shapes of great interest to structural engineers. In general, cross-sectional optimisation methods of CFS members can be classified into two categories. One can either aim to determine an optimal cross-sectional shape without any initial restrictions on its form (shape optimisation), or optimise the relative dimensions of a cross-section with a predefined shape (size optimisation).

As an example of shape optimisation, Liu et al. (Liu et al. 2004) introduced a knowledge-based approach for optimisation of CFS column sections. Initial knowledge about what constitutes a ‘good’ design is thereby established by training a Bayesian classification tree learning algorithm. This knowledge is subsequently used to reduce the global design space to a lower dimensional expert-based feature space. The results showed that optimised cross-sectional shapes can demonstrate a much higher capacity (by up to 300%) compared to conventional cross-sections. Moharrami et al. (Moharrami et al. 2014) found the optimal shapes of open CFS cross-sections in compression, using a fixed coil width and plate thickness. The compressive strength of a given section was thereby evaluated using a combination of the Finite Strip Method (FSM) and the Direct Strength Method (DSM). However, their study did not consider manufacturing and construction constraints and, therefore, highly complex shapes were identified that are not suitable for practical applications due to their high manufacturing costs and the difficulty in connecting to other elements. The resulting shapes also did not classify as pre-qualified sections under the DSM rules, thus questioning the optimisation approach. Leng et al. (Leng et al. 2014b) later improved this method by incorporating end-user constraints and limiting the numbers of rollers in the manufacturing process. CFS columns with different lengths were optimised and more practical shapes were obtained, which however still did not meet the DSM pre-qualification conditions.

Several research projects have previously been carried out aimed at optimising the relative dimensions of predefined conventional CFS cross-sections such as  $C$ -,  $Z$ -, or  $\Sigma$ -shapes. Adeli and Karim (Adeli and Karim 1997) developed a Neural Network methodology for the optimum cross-sectional design of CFS beams, considering conventional hat,  $I$ -, and  $Z$ -cross-sections. Using Micro Genetic Algorithms, Lee et al. (Lee et al. 2005a, Lee et al. 2006a) optimised the geometry of CFS channel beams and columns under a uniformly distributed load and a compressive axial load, respectively. Their numerical results were presented in the form of optimum design curves for various load levels. Tran and Li (Tran and Li 2006) presented a



theoretical study on the optimisation of lipped channel beams subjected to uniformly distributed transverse loading. The failure modes of local, distortional and global buckling, as well as yielding, in combination with deflection limits, were considered and the optimisation process aimed to minimize the coil width. The shape optimisation of CFS channel beams with ‘drop’ flanges (rounded return lips shaped like a water drop) was described by Magnucki et al. (Magnucki and Paczos 2009). They found that channel beams with closed drop flanges can offer better performance compared to beams with open drop flanges or standard lips. More recently, Ma et al. (Ma et al. 2015a) optimised CFS compression and bending members according to EC3 (CEN 2005b) by using the genetic algorithm toolbox in Matlab. They investigated the influence of the column length and the shift of the effective centroid, induced by local/distortional buckling, on the optimum design solutions. The practicality of their solutions was guaranteed by constraining the overall shape of the cross-section to a channel, but no additional manufacturing or construction constraints were taken into account in the study.

The research presented in this chapter aimed to develop a new practical framework to optimise CFS channel beam sections while considering both manufacturing and design constraints. The Particle Swarm Optimisation (PSO) method was thereby adopted to achieve optimum design solutions according to the European design guidelines for CFS structural members (CEN 2005a, CEN 2005b, CEN 2005c). The complexity of the non-linear optimisation problem was managed by using the Eurocode design regulations as a ‘black-box’ tool in the optimisation procedure. The adequacy of Eurocode 3 in predicting increasing/decreasing trends in capacity as a result of changing geometric parameters and adding features like stiffeners and return lips was then evaluated by modelling the optimal sections using detailed FE models accounting for material and geometric non-linearity, as well as imperfections. The developed FE models were first validated against existing experimental results.

## **4.2 Design of CFS beams based on EC3**

In this study, the flexural strength of CFS sections was calculated based on the Effective Width Method, following the provisions of EN1993-1-3 (CEN 2005b) and EN1993-1-5 (CEN 2005a). The adopted design procedure is described briefly in the following sections.

### **4.2.1 Design for local buckling**

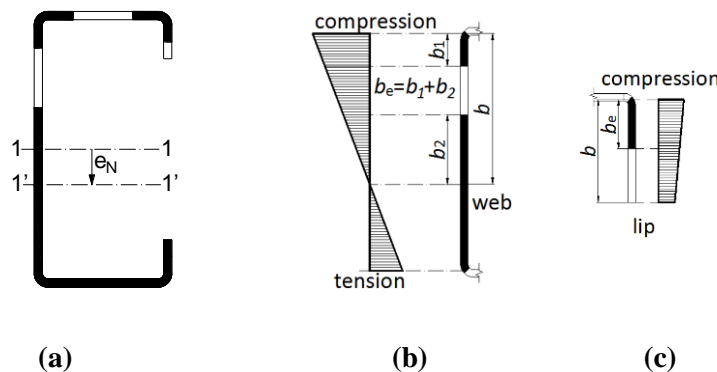
In Eurocode 3, the effect of local buckling is considered through the effective width concept. It is based on the observation that local buckling causes a loss of compressive stiffness in the centre of a plate supported along both longitudinal edges (labelled an ‘internal’ plate element in EC3), or along the free edge of a plate supported along one longitudinal edge (an ‘outstand’ element) as a result of non-linear effects. The corner zones of the cross-section consequently become the main load-bearing areas and are idealized in the effective width concept as carrying

the totality of the load. The effective area of a sample cross-section is indicated in solid black line in Figure 4.1. It is thereby noted that local buckling causes the centroid of the effective cross-section to shift over a distance  $e_N$  relative to the original centroid of the gross cross-section. According to EN1993-1-5 (CEN 2005a), the effective widths of internal and outstand compression elements are given by (see Figure 4.1):

$$\rho = \frac{b_e}{b} = \begin{cases} \frac{1}{\lambda_1} \left( 1 - \frac{0.055(3+\psi)}{\lambda_1} \right) & \text{for internal compression element} \\ \frac{1}{\lambda_1} \left( 1 - \frac{0.188}{\lambda_1} \right) & \text{for outstand compression element} \end{cases} \quad (4.1)$$

$$\text{with } \lambda_1 = \sqrt{\frac{f_y}{\sigma_{cr}}} \quad (4.2)$$

In Equation (4.1),  $\rho$  is the reduction factor on the plate width and  $b$  and  $b_e$  are the total and the effective width of the plate, respectively. The slenderness ratio  $\lambda_1$  relates the material yield stress  $f_y$  to the elastic local buckling stress of the plate  $\sigma_{cr}$  and  $\psi$  is the ratio of the end stresses in the plate. It is worth mentioning that, in principle, Eurocode 3 calculates the effective cross-section  $A_{eff}$  using the yield stress  $f_y$  in Equation (4.2), while some design standards (in particular the North-American (AISI 2007) and Australian/New Zealand (AS/NZS 1996) specifications) use the global buckling stress of the beam. It should also be noted that the calculation of the effective cross-section in bending is an iterative process, since the neutral axis of the effective cross-section shifts over a distance which depends on the loss of effective section in the flange and the upper portion of the web and this, in turn, affects the stress distribution. Although not required by EC3 guidelines, full iterations to convergence were carried out in this study.



**Figure 4.1. Effective width of (a) lipped channel; (b) internal compression element; and (c) outstand compression element**

### 4.2.2 Design for distortional buckling

Distortional buckling of a CFS section is a process which requires in-plane as well as out-of-plane displacements of some of the constituent plates. Specifically related to lipped channels, it can be seen as lateral-torsional buckling of the flange-lip subassembly, but distortional buckling can also occur in the web when intermediate stiffeners are included.

While EC3 accounts for local buckling through a reduction of the effective width of the constituent plates, distortional buckling is instead taken into account by reducing the effective plate thickness. The elastic distortional buckling stress, required for the calculation of the distortional slenderness  $\lambda_d = \sqrt{f_y / \sigma_{cr,s}}$ , is obtained through a simplified model where the restraining effect of the adjacent plates is simulated by elastic springs, as illustrated in Figure 4.2. The elastic buckling stress of the plate-stiffener assembly  $\sigma_{cr,s}$  is then given by:

$$\sigma_{cr,s} = \frac{2\sqrt{KEI_s}}{A_s} \quad (4.3)$$

where  $E$  is the modulus of elasticity,  $I_s$  is the second moment of area of the stiffener about an axis through its centroid parallel to the plate,  $K$  is the spring stiffness per unit length and  $A_s$  is the stiffener area. The spring stiffness  $K$  is determined by applying a unit load  $f = 1$  (per unit length) to the full cross-section at the centroid of the stiffener assembly and by calculating the corresponding displacement.

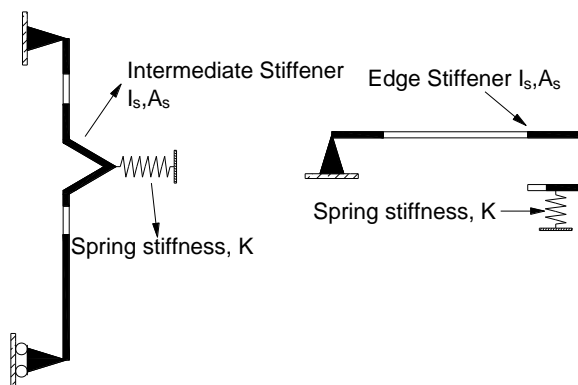


Figure 4.2. Simplified models for distortional buckling calculations

EC3 provides the option to refine the local slenderness ratio  $\lambda_l$  of the plates using an iterative process based on the following equation:

$$\lambda_{l,red} = \lambda_l \sqrt{\chi_d} \quad (4.4)$$

where  $\chi_d$  is a prescribed function of the distortional buckling slenderness  $\lambda_d$ . When calculating  $\lambda_d$  in each iteration,  $f_y$  should be replaced by  $\sigma_{com} = \chi_d \cdot f_y$ . This option provided by EC3 was implemented in the study and the iterations continued until  $\chi_{d,n} \approx \chi_{d,(n-1)}$ .

### 4.2.3 Design for global buckling

According to EC3, the design of CFS members for global buckling requires the calculation of a global slenderness. For CFS beam elements, the slenderness for lateral-torsional buckling is defined as:

$$\lambda_{LT} = \sqrt{\frac{W_{eff} f_y}{M_{cr}}} \quad (4.5)$$

where  $M_{cr}$  is the elastic lateral-torsional buckling moment based on the gross cross-section, and  $W_{eff}$  is the effective section modulus.

## 4.3 Definition of optimisation problem

The optimisation procedure aimed to optimise CFS cross-sections with regard to their bending capacity, determined according to EC3. The starting point of the optimisation was the commercially available channel section shown in Figure 4.3. The thickness of  $t = 1.2 \text{ mm}$  and the total coil width of  $l = 333 \text{ mm}$  were kept constant in the optimisation process, so that the total material use was also kept identical for all cross-sections. The radius of the rounded corners (measured along the heart line of the section), the elastic modulus and the Poisson's ratio were taken as  $2.5 \text{ mm}$ ,  $210 \text{ GPa}$  and  $0.3$ , respectively. The yield strength of the steel was assumed to be  $f_y = 350 \text{ MPa}$ .

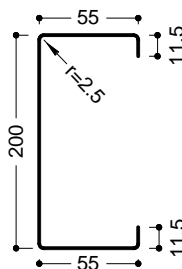


Figure 4.3. Standard CFS beam cross-section (TATA-A3709)

To ensure that the optimisation process resulted in practically useful cross-sections, the following measures were taken:

1. The basic overall shape of the cross-section was restricted to a channel. In current construction practice, channels (and Z-sections) are the most commonly used CFS beam sections. The succession of flat plate elements within the cross-section permits a straightforward manufacturing process and allows for easy connections with trapezoidal steel deck or other roof/floor systems, as well as bridging, cleat plates, etc. This stands in contrast with the often complex and curved shapes typically encountered as the result of unrestricted shape optimisation procedures. This objective was achieved by considering six different prototypes, listed in Table 4.1. All prototypes are based on a channel shape, but they allow the inclusion of a single web stiffener, double web stiffeners, inclined lips and double-fold (return) lips. These additions are typically within the capability of commercial cold-rolling enterprises. Each prototype was optimised individually, after which the overall optimum among the six optimised prototypes was identified.
2. In practical situations, additional constraints typically come into play. These constraints may be quite case-dependent and may, for instance, be related to the ability to connect the beam to other elements, or be imposed by the manufacturing process itself. In this particular case the following constraints were imposed:
  - a. The width of the flanges was required to be at least 30mm in order to connect trapezoidal decking or plywood boards to the beam by means of screws. This width was determined after consultation with the industrial partner on the project.
  - b. The lip needs to be of a sufficient length. A lip of, for instance, 1mm or 2mm length cannot be rolled or brake-pressed. The industrial partner on the project suggested a minimum length of 5-10mm. Therefore, as indicated in Table 4.1,  $c \geq 10\text{mm}$  was imposed for a single lip and combined with  $d \geq 5\text{mm}$  for a return lip.
  - c. The height of the web was specified to be at least 100mm in order to allow a connection to be made (e.g. to a cleat plate) with at least two bolts and/or for bridging to be connected.

One of the major advantages of the PSO algorithm is that these constraints can easily be altered and others added. The constraints merely result in a restriction of the search space of the particle swarm.

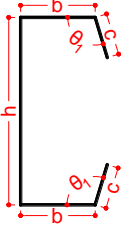

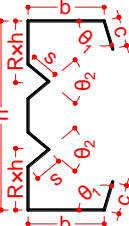
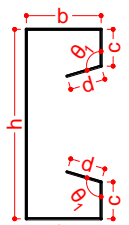
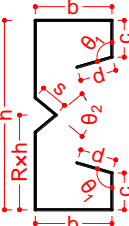
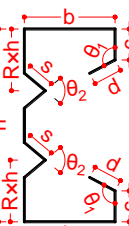
In addition to the practical constraints mentioned above, the EC3 design rules also impose certain limits on the plate width-to-thickness ratios, the relative dimensions of the cross-section and the angle of the edge stiffeners. These constraints were also taken into account in the optimisation procedure and are listed in Table 1 under the heading ‘Constraints based on EC3’.

Finally, the opening angle  $\theta_2$  and the length  $s$  of the intermediate stiffeners was limited within the ranges of  $\pi/6$  to  $\pi/4$  and 5 mm to 10 mm, respectively. The optimisation was conducted separately for laterally braced and un-braced beams, as discussed in the following sections.

It is clear that both the choice of the prototypes and the addition of practical constraints significantly restrict the solution space. An unconstrained ‘free-form’ optimisation would most likely result in a cross-section with a higher ultimate capacity, with this ‘overall optimum’ solution not being contained within the current restricted search space. However, the aim of the research was to produce cross-sections with practical relevance and the prototypes in Table 4.1 were decided on after consultation with the industry partner.

It is also noted that, while the chosen constraints are quite specific, the proposed optimisation framework is generally applicable and can be used in combination with different prototypes and different constraints.

Table 4.1. Selected prototypes, design variables and constraints

Prototype	Prototype section	Design variables	Constraints based on EC3	$u_{\min}$	$u_{\max}$	Comments	Manufacturing & practical limitations (mm)
①		$x_1=c/b$ $x_2=b/l$ $x_3=\theta_1$	$0.2 \leq c/b \leq 0.6$ $b/t \leq 60$ $c/t \leq 50$ $b/t \leq 500$ $\pi/4 \leq \theta_1 \leq 3/4\pi$	0.2 0.09 $\pi/4$	0.6 0.216 $3/4\pi$	EN1993-1-3 Table 5.1 and Equation (5.2a), Clause 5.5.3.2(1)	$b \geq 100$ $b \geq 30$ $c \geq 10$
②		$x_1=c/b$ $x_2=b/l$ $x_3=R$ $x_4=\theta_1$ $x_5=\theta_2$	$0.2 \leq c/b \leq 0.6$ $b/t \leq 60$ $c/t \leq 50$ $b/t \leq 500$ $\pi/4 \leq \theta_1 \leq 3/4\pi$ $\pi/6 \leq \theta_2 \leq \pi/2$	0.2 0.09 0.1 $\pi/4$ $\pi/6$	0.6 0.216 0.9 $3/4\pi$ $\pi/2$	EN1993-1-3 Table 5.1 and Equation (5.2a), Clause 5.5.3.2(1)	$b \geq 100$ $b \geq 30$ $c \geq 10$ $0.1 \leq R \leq 0.9$
③		$x_1=c/b$ $x_2=b/l$ $x_3=R$ $x_4=\theta_1$ $x_5=\theta_2$	$0.2 \leq c/b \leq 0.6$ $b/t \leq 60$ $c/t \leq 50$ $b/t \leq 500$ $\pi/4 \leq \theta_1 \leq 3/4\pi$ $\pi/6 \leq \theta_2 \leq \pi/2$	0.2 0.09 0.1 $\pi/4$ $\pi/6$	0.6 0.216 0.4 $3/4\pi$ $\pi/2$	EN1993-1-3 Table 5.1 and Equation (5.2a), Clause 5.5.3.2(1)	$b \geq 100$ $b \geq 30$ $c \geq 10$ $0.1 \leq R \leq 0.4$
④		$x_1=c/b$ $x_2=d/b$ $x_3=b/l$ $x_4=\theta_1$	$0.2 \leq c/b \leq 0.6$ $0.1 \leq d/b \leq 0.3$ $b/t \leq 90$ $c/t \leq 60$ $d/t \leq 50$ $b/t \leq 500$ $\pi/4 \leq \theta_1 \leq 3/4\pi$	0.2 0.1 0.09 $\pi/4$	0.6 0.3 0.216 $3/4\pi$	EN1993-1-3 Table 5.1 and Equation (5.2a,b), Clause 5.5.3.2(1)	$b \geq 100$ $b \geq 30$ $c \geq 10$ $d \geq 5$
⑤		$x_1=c/b$ $x_2=d/b$ $x_3=b/l$ $x_4=R$ $x_5=\theta_1$ $x_6=\theta_2$	$0.2 \leq c/b \leq 0.6$ $0.1 \leq d/b \leq 0.3$ $b/t \leq 90$ $c/t \leq 60$ $d/t \leq 50$ $b/t \leq 500$ $\pi/4 \leq \theta_1 \leq 3/4\pi$ $\pi/6 \leq \theta_2 \leq \pi/2$	0.2 0.1 0.09 0.1 $\pi/4$ $\pi/6$	0.6 0.3 0.216 0.9 $3/4\pi$ $\pi/2$	EN1993-1-3 Table 5.1 and Equation (5.2a,b), Clause 5.5.3.2(1)	$b \geq 100$ $b \geq 30$ $c \geq 10$ $d \geq 5$ $0.1 \leq R \leq 0.9$
⑥		$x_1=c/b$ $x_2=d/b$ $x_3=b/l$ $x_4=R$ $x_5=\theta_1$ $x_6=\theta_2$	$0.2 \leq c/b \leq 0.6$ $0.1 \leq d/b \leq 0.3$ $b/t \leq 90$ $c/t \leq 60$ $d/t \leq 50$ $b/t \leq 500$ $\pi/4 \leq \theta_1 \leq 3/4\pi$ $\pi/6 \leq \theta_2 \leq \pi/2$	0.2 0.1 0.09 0.1 $\pi/4$ $\pi/6$	0.6 0.3 0.216 0.4 $3/4\pi$ $\pi/2$	EN1993-1-3 Table 5.1 and Equation (5.2a,b), Clause 5.5.3.2(1)	$b \geq 100$ $b \geq 30$ $c \geq 10$ $d \geq 5$ $0.1 \leq R \leq 0.4$

## 4.4 Optimisation of CFS beams

In practical applications, the boundary conditions of laterally braced and laterally unbraced beams represent two distinct situations. The laterally braced beams are representative, for instance, of floor beams connected to a steel deck with concrete topping, where the compression flange is continuously supported. On the other hand, roof purlins subject to wind uplift where the rotational stiffness of the roof diaphragm is insufficient to provide full restraint should be designed as laterally unbraced beams with a representative effective length, and the effects of lateral-torsional buckling should be taken into account. Therefore, in this study, laterally braced and unbraced beams are optimised independently.

### 4.4.1 Laterally braced beams

In many practical applications the CFS beams are laterally restrained, for instance by the presence of a floor system. In that case the optimisation problem can be formulated as a maximisation problem, defined by:

$$\max f(x) = W_{eff} f_y / \gamma_{M0} \quad u_{min} \leq x_i \leq u_{max} \quad \text{for } i = 1, \dots, N \quad (4.6)$$



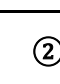



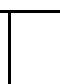
where  $f(x)$  is the design moment resistance of a cross-section about the major axis and  $W_{eff}$  is the effective section modulus, as introduced in Section 4.2. Also,  $\gamma_{M0}$  is the partial safety factor prescribed by EC3 for the ultimate limit state, which is equal to 1.0. For each design variable  $x_i$ , the lower and upper bounds  $u_{min}$  and  $u_{max}$  are determined by the EC3 design constraints as well as the manufacturing limitations summarised in Table 4.1.

The selected prototypes in this study were aimed at investigating the effects of changing the relative geometric dimensions of the cross-section and the configurations of the edge and intermediate stiffeners (see Table 4.1). The optimisation framework required the development of two distinct pieces of software, developed in Matlab (Mathworks 2011): a programme implementing the EC3 design rules and further used as a ‘black box’, and a programme carrying out the PSO. The population of the particle swarm was taken as 100 for all prototype sections. To obtain good convergence, the number of iterations was set to 100 for prototypes ① to ④, while this was increased to 160 for prototypes ⑤ and ⑥ to accommodate the larger number of design parameters. The maximum and minimum inertial weight factors were chosen as 0.95 and 0.4, respectively. Each of the prototypes was optimised three times to ensure consistent results were obtained. The maximum difference in ultimate capacity encountered between the three runs was less than 10%. Out of the three resulting cross-sections, the one with the highest capacity was selected.



**Table 4.2. Dimensions of optimal solutions for laterally restrained beams**

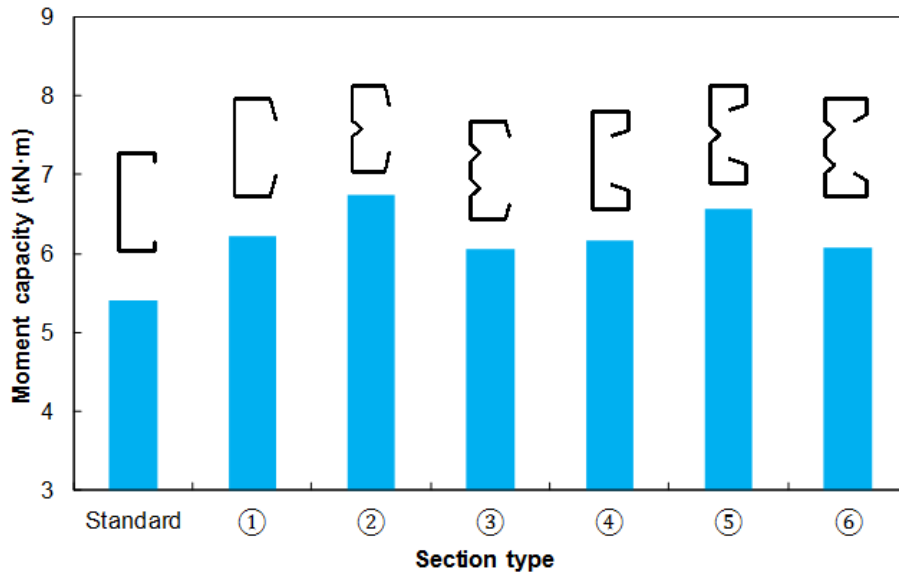
Prototype	$h$ (mm)	$b$ (mm)	$c$ (mm)	$d$ (mm)	$\theta_1$ (°)	$\theta_2$ (°)	$s$ (mm)	$R$
①	227	32	20	-	90	-	-	-
②	214	33	20	-	90	45	10	0.85
③	215	33	20	-	90	90	10	0.1
④	215	37	17	5	90	-	-	-
⑤	204	37	12	5	135	67	10	0.9
⑥	193	39	17	6	135	90	10	0.1

Prototype	①	②	③	④	⑤	⑥	
Optimised sections							

\*The bold lines indicate effective parts of the cross-section.

**Figure 4.4. Optimal cross-sections for laterally restrained beams using different prototypes**

Table 4.2 shows the dimensions of the optimised sections for prototypes ① to ⑥. The effective cross sections of the optimum solutions are also illustrated in Figure 4.4. The flexural strengths of the optimised cross-sections, as well as the standard cross-section taken as a starting point, are compared in Figure 4.5. The results indicate that the optimised shapes offer a significantly higher moment capacity (up to 25% higher) compared to the original section.



**Figure 4.5. Comparison of the flexural strength of standard and optimised cross-sections for laterally braced beams**

The results in Figure 4.5 also indicate that the most efficient prototype is a lipped channel section with one stiffener placed in the web. While adding one stiffener increased the capacity of the optimised section by 25%, adding two stiffeners in a symmetric arrangement (prototype ③) actually reduced the flexural capacity of the channel by 12.4% compared to prototype ①. This is due to the fact that, when the total developed length of the cross-section is kept constant, the height of the cross-section is reduced by adding the additional web stiffener, while, in a symmetric arrangement; the stiffener is ineffective in the tension zone. It is also noted that none of the imposed practical constraints, listed in the rightmost column of Table 4.1 turned out to be critical.

#### 4.4.2 Laterally unbraced beams

Laterally unbraced beams with low lateral and/or torsional stiffness may buckle in combined bending about the minor axis and twisting. For a simply supported channel beam subjected to equal but opposite end moments about the major axis, the critical lateral-torsional buckling load  $M_{cr}$  can be calculated in terms of the span length and the section properties of the gross section as follows:

$$M_{cr} = \frac{\pi}{L} \sqrt{EI_y \left( GJ + \frac{\pi^2 EI_w}{L^2} \right)} \quad (4.7)$$

where  $EI_y$  is the flexural rigidity about the minor axis,  $EI_w$  is the warping rigidity,  $GJ$  is the torsional rigidity and  $L$  indicates the span length. The EC3 reduction factor  $\chi_{LT}$ , accounting

for lateral-distortional buckling, can then be obtained using the slenderness  $\lambda_{LT}$  in Eq (5). The design moment resistance of a laterally unrestrained beam is calculated as:

$$f(x) = \chi_{LT} \cdot W_{eff} \cdot f_y / \gamma_{M_0} \quad (4.8)$$

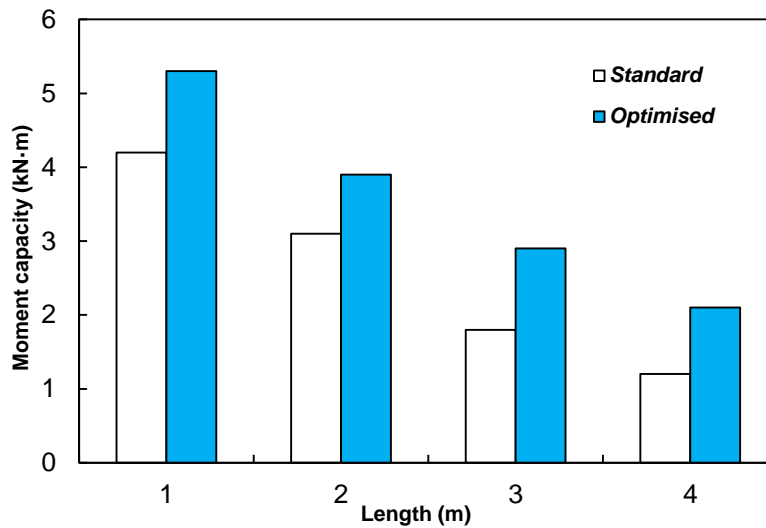
$$\text{with } \chi_{LT} = \frac{1}{\Phi_{LT} + \sqrt{\Phi_{LT}^2 - \lambda_{LT}^2}} \leq 1.0 \quad (4.9)$$

$$\text{and } \Phi_{LT} = 0.5 \left[ 1 + 0.34 (\bar{\lambda}_{LT} - 0.2) + \lambda_{LT}^2 \right] \quad (4.10)$$

The optimisation was carried out for the first prototype (lipped channel), while considering four different lengths: 1, 2, 3 and 4 m. The optimised cross-sections and their corresponding flexural strengths are summarised in Figure 4.6 and Figure 4.7, respectively.

Length	L=1m	L=2m	L=3m	L=4m
Optimum sectional dimensions				

Figure 4.6. Optimised results for member capacity of lipped channel beams



**Figure 4.7. Comparison of the flexural strength of the optimised and standard cross-sections for laterally unbraced beams**

A comparison between the optimised results in Figure 4.6 indicates that the flange width becomes larger with increasing unbraced length, and consequently, the total height of the section is diminished to keep the total coil width constant. This is due to the fact that longer beams are more susceptible to lateral-torsional buckling, and thus the dimensions of the flanges increase while the lips turn outwards to enhance the torsional stiffness and the minor axis bending stiffness. In contrast, beams with shorter spans are predominantly affected by the interaction of local/distortional buckling and lateral-torsional buckling, rather than failing purely in the global mode. It is noted that serviceability criteria (deflections) were not considered in this study and that the optimisation is solely carried out with respect to the ultimate capacity.

Figure 4.7 compares the flexural capacity of the optimised and the initial lipped channel sections for all four lengths. It is shown that a considerable increase in flexural capacity can be achieved by using the proposed optimisation method. While, for the same amount of material, the flexural capacity of a 1m long optimised beam is 26% higher than that of the standard section, the improvement is 75% for the 4m long beam. Once again, none of the practical constraints in the rightmost column of Table 4.1 turned out to be critical.

It is worth mentioning that the optimisation was carried out assuming a uniform bending moment in the beam and assuming the previously defined boundary conditions. When the laterally unbraced beams are exposed to a different applied loading (reflected in a different elastic lateral-torsional buckling moment) or different boundary conditions, the optimal sections will change. Besides, for longer beam elements, serviceability limits (in particular: maximum deflections) may govern the design. While serviceability criteria were not considered in the current scope, the proposed optimisation framework using PSO algorithm can easily be adapted to incorporate serviceability limits.

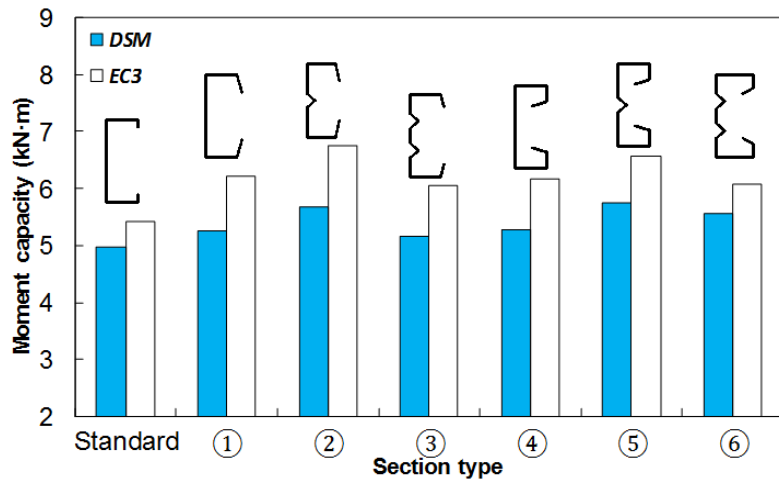


Figure 4.8. Comparison of the flexural strength of the optimised and standard cross-sections for laterally braced beams obtained using the DSM and EC3

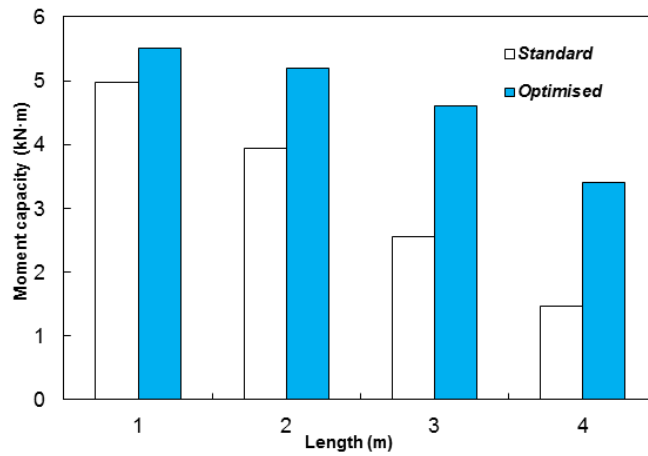


Figure 4.9. Comparison of the flexural strength of the optimised and standard cross-sections for laterally unbraced beams obtained using the DSM

Table 4.3. Local and distortional ultimate strengths for laterally braced beams obtained using the DSM

Section	Local Buckling (kN·m)	Distortional Buckling (kN·m)
Standard	5.52	4.98
①	5.25	5.47
②	7.34	5.68
③	5.71	5.16
④	5.27	5.27
⑤	5.94	5.74
⑥	6.07	5.56

**Table 4.4. Local, distortional, and global ultimate strengths for laterally unbraced beams obtained using the DSM**

Length (m)	Section	Local Buckling Strength (kN·m)	Distortional Buckling Strength (kN·m)	Global Buckling Strength (kN·m)
1	Standard	5.53	4.98	6.59
	Optimised	5.48	5.66	5.5
2	Standard	5.53	4.98	3.94
	Optimised	5.54	5.28	5.2
3	Standard	5.53	4.98	2.56
	Optimised	4.98	4.61	4.6
4	Standard	5.53	4.98	1.47
	Optimised	4.22	4.15	3.4

In this study the flexural strengths of the optimised as well as the original sections were determined based on the DSM (see Section 2.2), for both laterally braced and laterally unbraced conditions, for the purpose of comparison with the Eurocode. The results are shown in Figure 4.8 and Figure 4.9. For the laterally braced beams, the flexural strength was determined as the minimum of the local and distortional strengths (Table 4.3). However, for laterally unbraced beams, the ultimate strength was determined based on the minimum of the local, distortional and lateral-torsional strengths (Table 4.4). The strength in local buckling thereby accounts for the possibility of local-global mode interaction.

For both laterally braced and unbraced conditions, the results obtained from the DSM confirm that the flexural strengths of the optimised shapes have been considerably improved compared to the original cross-sections. Comparison between the results predicted by the DSM and EC3 indicates that both methods show a very similar trend across the range of prototypes.

However, it should be mentioned that only prototypes ① (lipped channel) and ② (lipped channel with one intermediate stiffener in the web) are ‘pre-qualified’ cross-sections according to Appendix 1 of AISI (AISI 2007). This means that, in principle, the DSM should not be applied to prototypes ③-⑥.

#### 4.5 Nonlinear FE analysis considering initial geometric imperfections

The flexural capacity of the optimised cross-sections in this study was also determined using detailed nonlinear FE analyses performed with ABAQUS (2007). The results were used to assess the adequacy and performance of the proposed optimisation procedure. In this section, a

detailed description of the modelling approach is first presented, followed by its verification against experimental data available in the literature.

#### 4.5.1 FE modelling

The FE models of the CFS sections were developed using a 4-node quadrilateral shell element with reduced integration (S4R). By performing sensitivity analyses, a mesh size of  $10 \times 10 \text{ mm}$  was found to be optimal (as shown in Figure 4.13), so that further refinement did not result in any noticeable improvement in accuracy. However, smaller elements were used to model the rounded corner zones. The stress-strain behaviour of the CFS plates was simulated using the constitutive model proposed by Haidarali and Nethercot (Haidarali and Nethercot 2011), which is illustrated in Section 3.5.

The solution was obtained using the displacement control method which has previously been shown capable of adequately modelling large deformations in the post-buckling range (ABAQUS 2011).

#### 4.5.2 Experimental verification of the FE model

##### 4.5.2.1 Laterally braced beams

For the purpose of verifying the FE modelling approach with respect to CFS members failing by local/distortional buckling, the four-point bending distortional buckling tests performed by Yu and Schafer (Yu and Schafer 2006, Yu and Schafer 2007) were selected. Figure 4.10 presents a schematic illustration of the test set-up and also shows the cross-section of the test specimens. This test set-up was designed to prevent global buckling and, therefore, the test specimens acted as laterally braced beams.

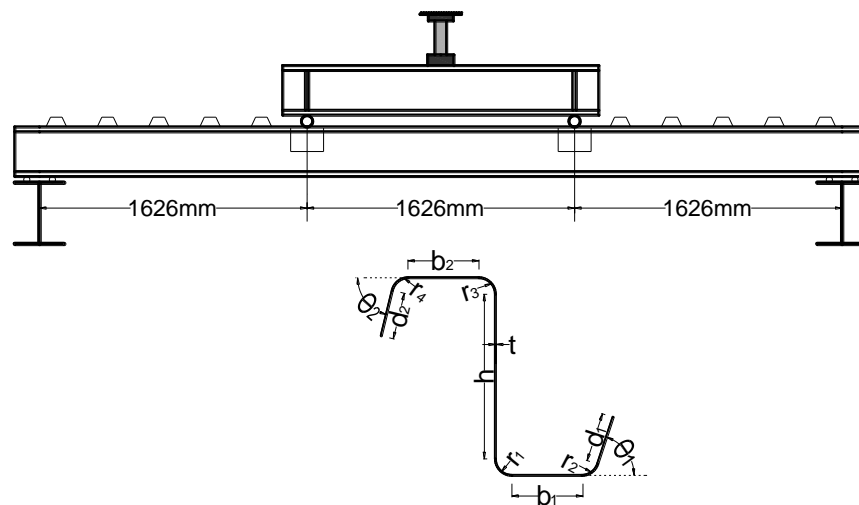


Figure 4.10. Schematic illustration of Yu and Schafer's (Yu and Schafer 2006, Yu and Schafer 2007) distortional buckling test set-up and cross-sectional geometry

Table 4.5. Cross-sectional dimensions

Specimen	$h$ (mm)	$b_2$ (mm)	$d_2$ (mm)	$\theta_2$ (deg)	$b_1$ (mm)	$d_1$ (mm)	$\theta_1$ (deg)	$r_3$ (mm)	$r_4$ (mm)	$r_2$ (mm)	$r_1$ (mm)	$t$ (mm)	$f_y$ (MPa)
D8.5Z120-4	196	53.4	19.4	54.2	49.8	20.8	50.2	7.5	7.5	7.5	7.5	3	423
D8.5Z115-1	197	56.9	17	48.3	48.5	17.5	48.3	7.5	7.5	8.5	8.5	2.96	453
D8.5Z092-3	198	55.6	20.6	51.9	49.1	20.1	51.6	5.9	5.9	6.9	6.9	2.27	397
D8.5Z082-4	200	53.8	20.8	48.5	49.2	21.2	51.3	6	6	7	7	2.06	408
D8.5Z065-7	199	51.3	17.3	50	49.9	16.9	49.3	7.2	7.2	8.2	8.2	1.63	430
D8.5Z065-4	198	49.5	17.5	47.3	46.6	12.6	51.2	7.2	7.2	6.2	6.2	1.57	401
D11.5Z092-3	270	75.3	19.3	49.3	76.3	18.3	49.5	6.9	6.9	6.9	6.9	2.26	483
D11.5Z082-4	274	75.4	18.4	48.4	74.3	18.3	49.9	7	7	7	7	2.06	507

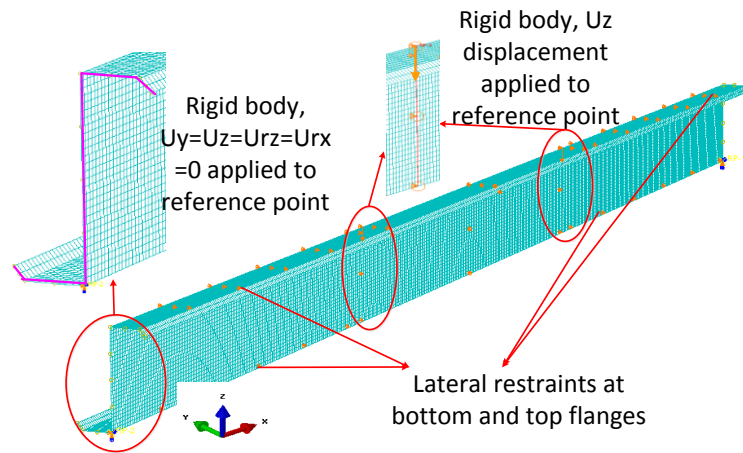
The total length of the test specimens was 4878 mm, and the top and bottom flanges of the beams were unrestrained in the middle 1626mm long span to allow distortional buckling to occur. The dimensions of the cross-section and their material properties are summarised in Table 4.5.

The beams were modelled using hinged boundary conditions about the horizontal axis, while the rotations about the vertical axis were prevented, as shown in Figure 4.11. The end sections were also fixed against warping (Figure 4.11) to prevent lateral-torsional buckling in the FE model. At both ends of the beam, the displacements of the end section nodes were coupled to those of the bottom corner using a single point constraint (SPC). The cross-sections underneath the application points of the load were defined as rigid bodies in order to prevent localised failure. Vertical downward displacements were then imposed on the reference points of these rigidized cross-sections at the top corners of the web. These boundary conditions are similar to the ones previously adopted by Haidarali and Nethercot (Haidarali and Nethercot 2011).

Residual stresses were not included in the model. It has previously been demonstrated that the effects of membrane residual stresses can safely be neglected in open sections (Schafer et al. 2010, Schafer and Pekoz 1998), while the (longitudinal) bending residual stresses are implicitly accounted for in the coupon test results, provided that the coupons are cut from the fabricated cross-section rather than from the virgin plate. Indeed, cutting a coupon releases the bending residual stresses, causing the coupon to curl (Jandera et al. 2008). However, these stresses are re-introduced when the coupon is straightened under tensile loading in the initial stages of the coupon test. Apart from introducing residual stresses, the cold-rolling process has the effect of increasing the material yield stress through work-hardening. This effect is most pronounced in the corner regions of the cross-sections. Schafer and Moen (Schafer et al. 2010) have in this respect proposed that, when residual stresses are not modelled, the increased properties of the corner regions should also not be modelled. Their rationale is that, while both effects have a

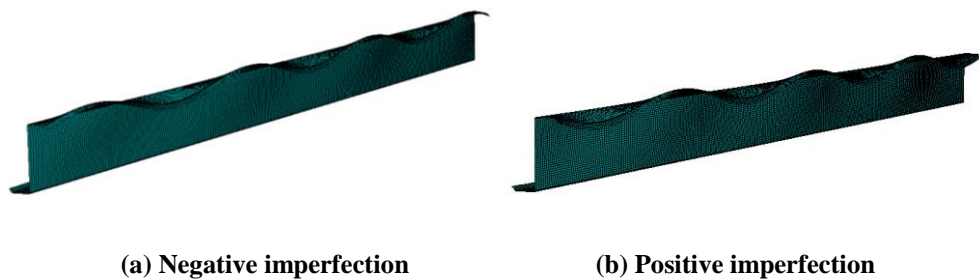


relatively minor influence on the ultimate capacity, the detrimental effect of the residual stresses will largely be offset by the gain in capacity resulting from the work-hardened corners. Their recommendation was followed in this chapter.



**Figure 4.11. FE model and boundary conditions**

The FE analysis included the effects of geometric imperfections. The local, distortional and global buckling modes were generated using the CUFSM finite strip software (Schafer 2006). The same cross-sectional discretization as in the FE mesh was employed in CUFSM. Sinusoidal functions with a wavelength equal to the critical local/distortional wavelength obtained from CUFSM were then used to propagate the cross-sectional local/distortional imperfection along the beams by adjusting the nodal coordinates of the FE mesh. It was thereby necessary to slightly adjust the wavelength in order to obtain an integer number of half-waves.



**(a) Negative imperfection**

**(b) Positive imperfection**

**Figure 4.12. Distortional imperfections in the FE model**

**Table 4.6. Comparison of the bending resistances obtained from FE analysis and experiment with different imperfection values in negative direction**

Specimen	Flexural Strength (kN·m)				FE to experimental flexural strength		
	$M_{test}$	$M_{25\%}$	$M_{50\%}$	$M_{75\%}$	$M_{25\%}/M_{test}$	$M_{50\%}/M_{test}$	$M_{75\%}/M_{test}$
D8.5Z120-4	28.7	27.92	28.32	27.88	0.97	0.99	0.97
D8.5Z115-1	26.8	28.47	27.8	26.66	1.06	1.04	0.99
D8.5Z092-3	17.3	18.45	18.22	17.45	1.07	1.05	1.01
D8.5Z082-4	14.3	15.98	15.31	15.12	1.12	1.07	1.06
D8.5Z065-7	10.5	11.64	11.37	11.18	1.11	1.08	1.06
D8.5Z065-4	9	10.93	10.56	10.21	1.21	1.17	1.13
D11.5Z092-3	29.6	30.84	30.56	29.6	1.05	1.04	1.00
D11.5Z082-4	26.4	27.4	26.32	25.48	1.04	1.00	0.97
Average					1.08	1.06	1.02
St. Dev.					0.07	0.06	0.06

**Table 4.7. Comparison of the bending resistances obtained from FE analysis and experiment with different imperfection values in positive direction**

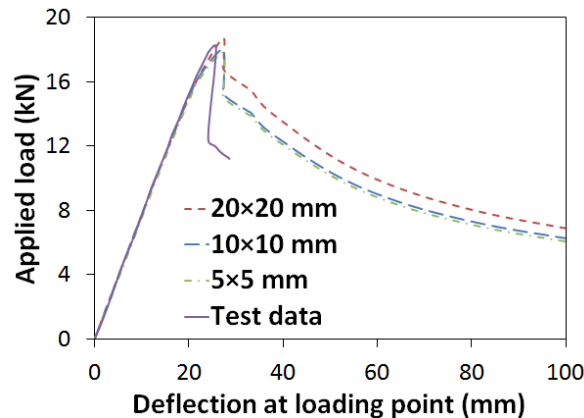
Specimen	Flexural Strength (kN·m)				FE to experimental flexural strength		
	$M_{test}$	$M_{25\%}$	$M_{50\%}$	$M_{75\%}$	$M_{25\%}/M_{test}$	$M_{50\%}/M_{test}$	$M_{75\%}/M_{test}$
D8.5Z120-4	28.7	28.66	28.12	27.49	1.00	0.98	0.96
D8.5Z115-1	26.8	29.46	28.52	28.03	1.10	1.06	1.05
D8.5Z092-3	17.3	18.1	17.46	16.93	1.05	1.01	0.98
D8.5Z082-4	14.3	16.81	15.92	14.36	1.18	1.11	1.00
D8.5Z065-7	10.5	12.21	11.36	10.94	1.16	1.08	1.04
D8.5Z065-4	9	10.85	10.12	9.56	1.21	1.12	1.06
D11.5Z092-3	29.6	32.98	30.83	30.69	1.11	1.04	1.03
D11.5Z082-4	26.4	27.56	27.13	26.96	1.04	1.03	1.02
Average					1.11	1.06	1.02
St. Dev.					0.07	0.05	0.04

The local and distortional imperfections were multiplied with a scale factor and superimposed. The magnitudes of the local and distortional imperfections were based on the cumulative distribution function (CDF) values proposed by Schafer and Peköz (Schafer and Pekoz 1998). Three different CFD values (i.e. 25%, 50%, and 75%) were considered, in both a positive and a negative direction, according to the convention shown in Figure 4.12, in order to study their effect on the load carrying capacity.

A comparison of the experimental moment capacities with those obtained from FE analysis for the three different CDF values is provided in Table 4.6 and Table 4.7, for negative and positive imperfections, respectively. It is seen that, in general, good agreement was obtained between the models and the experimental results. The error was, on average, less than 7% for both positive and negative imperfections. The magnitude of the imperfection, in this particular case, did not

seem to have a major impact on the load-carrying capacity. In the remainder of this study, CDF values of 50% were used. This magnitude represents the ‘most probable’ imperfection and has also been suggested by other researchers (e.g. (Haidarali and Nethercot 2011)).

The experimental load–deflection response of specimen D11.5Z092-3 (Table 4.7) is compared to the FE predictions in Figure 4.13. The results confirm the accuracy of the FE model in predicting the buckling and post-buckling behaviour of the CFS member, including its stiffness, ultimate strength and deflection at the peak load.



**Figure 4.13. Comparison between experimental results (Yu and Schafer 2006, Yu and Schafer 2007) and results of FE analyses for laterally braced specimen D11.5Z092-3 for 3 mesh sizes (mesh sensitivity analysis)**

#### 4.5.2.2 Laterally unbraced beams

The FE models of the laterally unbraced beams were verified against tests conducted by Put et al. (Put et al. 1999). Table 4.8 shows the dimensions of the eight test specimens. In the experiment a special frame was attached to the cross-section at mid-span in order to apply the load through the shear centre by means of incremental weights. The beams were simply supported at their ends. The local/distortional imperfections of the test specimens were not measured and, in an identical approach to the one reported in Section 4.6.2.1, local and distortional imperfections with a CDF value of 50% were used in the FE model. An overall imperfection in the shape of the lateral-torsional mode with amplitude of  $L/1000$  was also added (Kankanamge and Mahendran 2012). It was thereby found that, generally, adding a negative imperfection (with the cross-section rotated as shown in Figure 4.14) resulted in a lower ultimate moment capacity in the unbraced channels and was therefore more critical. Similar observations were reported by Kankanamge and Mahendran (Kankanamge and Mahendran 2012). Therefore, only negative imperfections were considered in the FE studies covered in this chapter. Figure 4.15 illustrates the FE model and the boundary conditions. A reference point was defined at the shear centre of the cross-section at mid-span and all the nodes of the web at

the mid-span section were coupled to the reference point using rigid beams. A downward displacement was then imposed on the reference node without restricting its lateral displacement.

The typical failure mode of the unbraced beams in the FE model was interaction of local buckling and lateral-torsional buckling, as illustrated in Figure 4.16. This is consistent with the experimental results reported by Put et al. (Put et al. 1999). Table 4.8 compares the ultimate capacities of the laterally unbraced beams obtained from the FE analyses to the experimental values. It shows that, on average, the FE models predict the ultimate strength of the laterally unbraced beams with less than 6% error. The load vs. lateral displacement curves from both the experiment and the FE analysis are shown in Figure 4.17 for specimen 10L17e0. The graph shows very good agreement between the FE model and the test results.

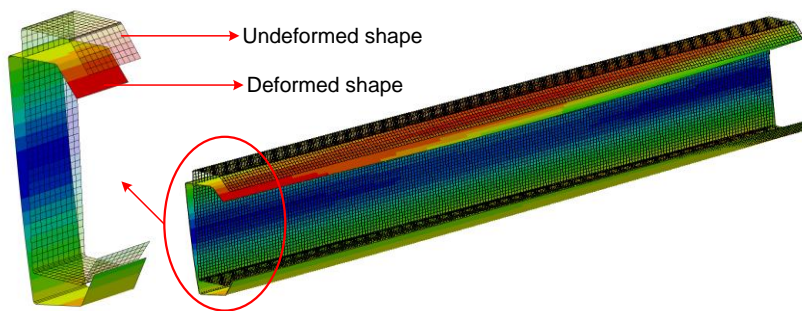


Figure 4.14. CFS beam with negative lateral-torsional imperfection

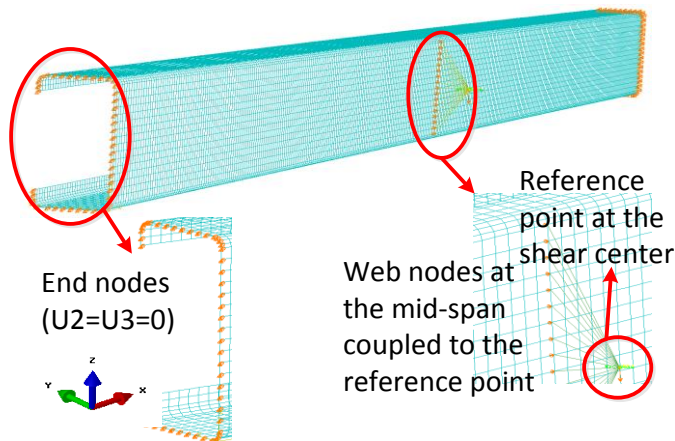


Figure 4.15. FE model and boundary conditions for laterally unbraced beams

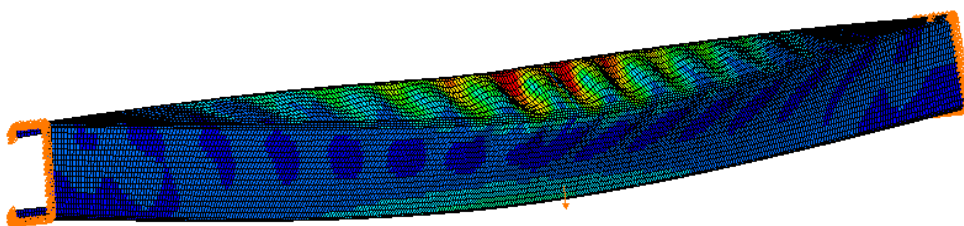
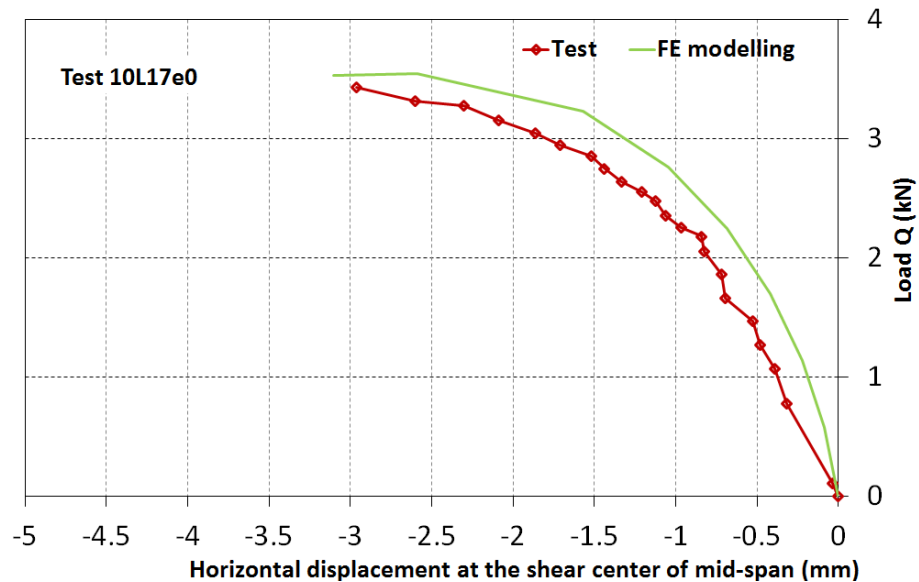


Figure 4.16. Typical failure mode of laterally unbraced beams (specimen 10L17e0 at ultimate load)

**Table 4.8. Comparison of ultimate capacities obtained from FE analysis and experiment for laterally unbraced braced beams (lipped channels)**

Specimen	$h$ (mm)	$b$ (mm)	$t$ (mm)	$r$ (mm)	$d$ (mm)	Length $h$ (m)	$Q$ (kN)	$Q_{test}$ (kN)	$Q_{test}/Q$ -
19L17e0	102	51	1.9	5	14.5	1.7	13.24	15.38	1.16
19L19e0	102	51	1.9	5	14.5	1.9	12.11	12.68	1.05
19L23e0	102	51	1.9	5	14.5	2.3	9.54	9.94	1.04
19L25e0	102	51	1.9	5	14.5	2.5	7.79	8.65	1.11
10L17e0	102	51	1	5	12.5	1.7	3.72	3.51	0.94
10L19e0	102	51	1	5	12.5	1.9	3.18	3.46	1.09
10L23e0	102	51	1	5	12.5	2.3	2.78	2.43	0.87
10L25e0	102	51	1	5	12.5	2.5	2.3	2.8	1.22
Average									1.06
St.Dev.									0.11

**Figure 4.17. Comparison between experimental results and FE analysis for laterally unbraced specimen 10L17e0 (Put et al. 1999)**

## 4.6 FE simulations of the optimised channel sections

The experimentally validated FE models were subsequently used to evaluate the efficiency of the optimised channel sections obtained in Section 4.4 and make a comparison with their standard counterpart.

### 4.6.1 Laterally braced beams

In the FE model, the laterally restrained beams were observed to fail by local and/or distortional buckling. As suggested by Shifferaw and Schafer (Shifferaw and Schafer 2012), the length of the FE models of both the optimised and the standard sections was taken as three times the

distortional buckling half-wave length calculated using the CUFSM (Schafer 2006) software. This was generally short enough to avoid lateral-torsional buckling. With respect to the boundary conditions, the member was pin-ended about the major axis and prevented from rotating about the minor axis, while the end sections were prevented from warping. Equal but opposite rotations were applied at both ends. Figure 4.18 illustrates the boundary conditions and loading of the FE models. Local/distortional imperfections with amplitude corresponding to the 50% value of the CDF were used. Table 4.9 summarises the local and distortional critical moments and the associated buckle half-wave lengths of the standard and optimised cross-sections of different prototypes obtained from CUFSM. The flexural strength of the optimised and the standard cross-sections obtained from FE analyses are compared in Figure 4.19. The results confirm that a considerable increase in the flexural capacity can be observed in the optimised shapes compared to the standard sections possessing the same amount of material (i.e. the same total coil width and thickness).

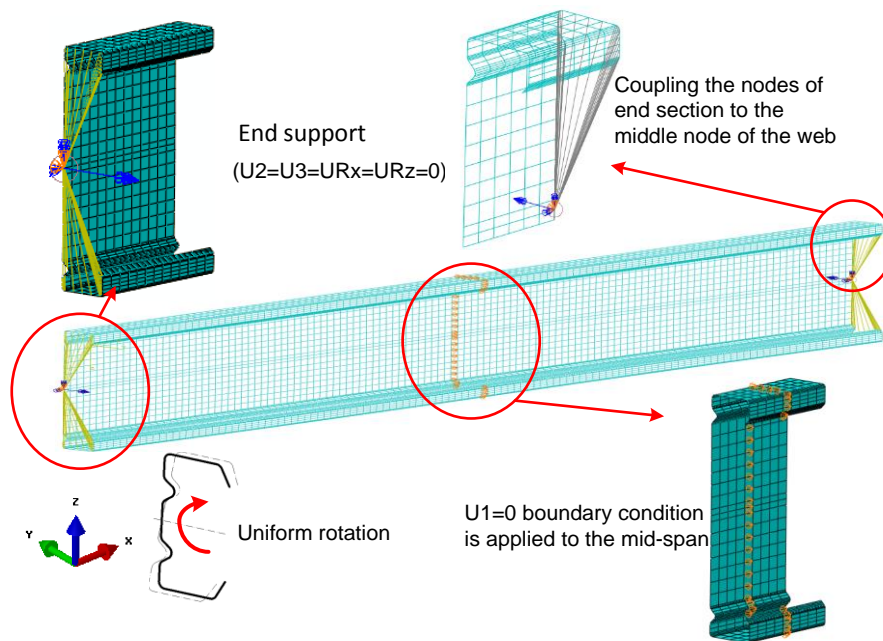


Figure 4.18. Boundary conditions in the FE models of channel sections

Table 4.9. The critical buckling modes and the buckling half-wave length for laterally restrained beams

Section	Buckling half-wave length (mm)		Buckling moment (kN·m)	
	Local	Distortional	Local	Distortional
Standard	100	400	4.79	4.81
Opt ①	120	600	4.12	6.09
Opt ②	80	600	16.99	7.18
Opt ③	100	500	7.14	6.08
Opt ④	100	500	4.31	5.69
Opt ⑤	100	600	7.43	8.57
Opt ⑥	120	600	8.80	8.60

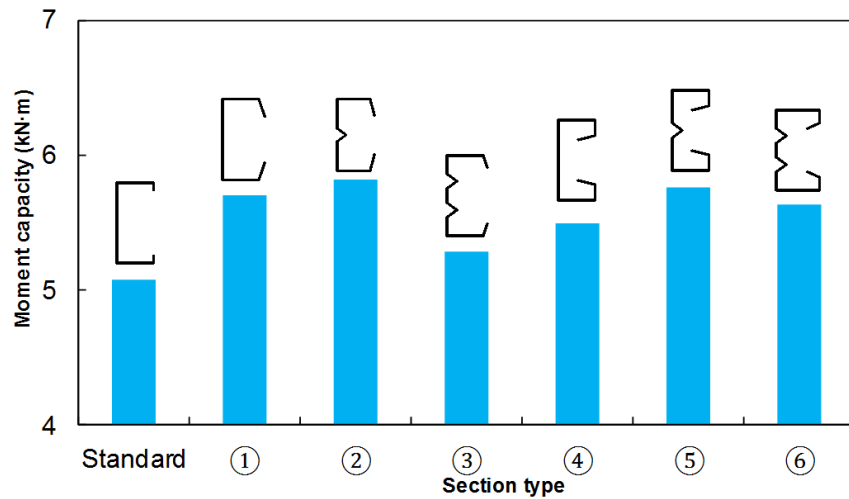


Figure 4.19. Comparison of FE predicted strengths of optimised and standard cross-sections for laterally braced beams

#### 4.6.2 Laterally unbraced beams

The laterally unbraced beams were assumed to be simply supported at the ends (with respect to both in-plane and out-of-plane rotations) with no lateral restraints in between. Warping of the end sections was free to occur and the load was applied by imposing an end rotation about the major axis, as shown in Figure 4.20. Four different lengths (i.e. 1m, 2m, 3m, and 4m) were considered, both for the standard and the optimised CFS cross-sections. Local/distortional imperfections were modelled and combined with an overall imperfection of  $L/1000$  in the shape of the lateral-torsional buckling mode.

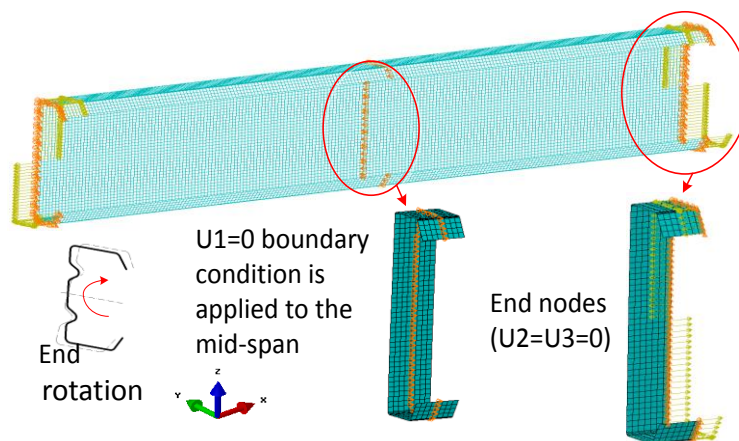


Figure 4.20. FE model for laterally unbraced standard and optimised beams



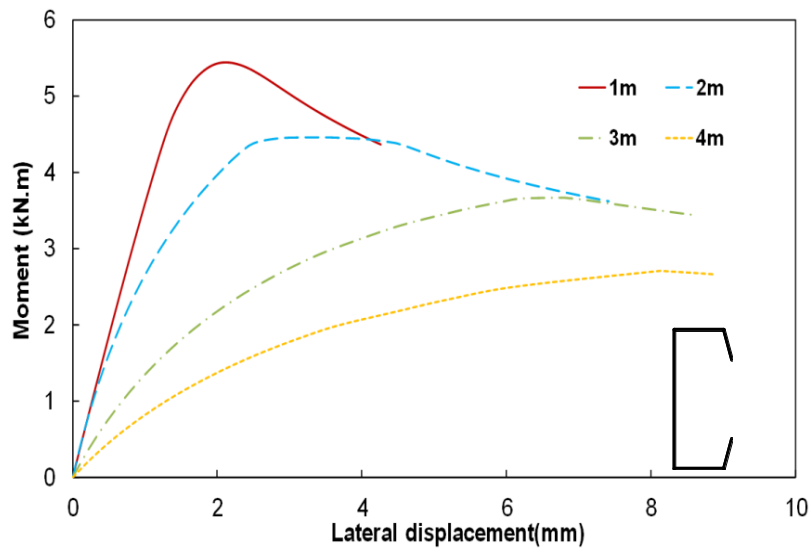


Figure 4.21. Moment-lateral deflection curves at mid-span of the optimised unbraced beams

The (uniform) bending moments obtained from the FE analysis are plotted in Figure 4.21 against the lateral displacement (at mid-span) of the optimised beams with four different lengths. The moment-lateral displacement curves illustrate the obvious fact that increasing the length of the CFS beams results in a decrease of the bending capacity due to lateral torsional buckling.

The flexural strengths of the optimised and the standard cross-sections with different lengths obtained using FE analyses are compared in Figure 4.22. Confirming the results obtained from the effective width method in EC3, Figure 4.22 shows that the optimised shapes offer a much higher flexural capacity (up to 108% higher) compared to the standard sections with the same amount of material, particularly in longer beams where global buckling is the dominant mode.

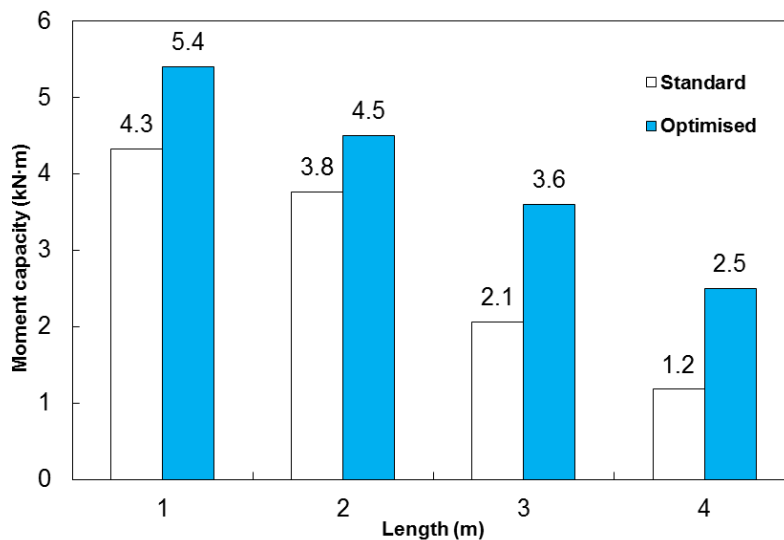


Figure 4.22. Comparison of FE predicted flexural strengths of optimised and standard cross-sections for laterally unbraced beams



## 4.7 Evaluation of the EC3 based approach

The results obtained from the experimentally validated FE models were treated as a benchmark to evaluate the accuracy of the DSM and the effective width method implemented in EC3. The EC3 and DSM predicted flexural strengths of the standard lipped channel and the optimised cross-sections obtained for all six prototypes (see Table 4.1) are compared in Table 4.10 for the laterally braced elements. For comparison purposes, the strength values are normalised with respect to the flexural strength obtained from FE analysis.

The results obtained from EC3 and from the DSM are both in good agreement with their FE counterparts. However, for the laterally braced beams, the DSM provided slightly more accurate and slightly more conservative estimates of the strengths than EC3. EC3 overestimated the flexural capacity of the laterally braced sections by 11% on average.

**Table 4.10. Comparison of predicted strengths with FE results for laterally braced beams**

Strength ratio	Section							Average	St. Dev.
	Standard	①	②	③	④	⑤	⑥		
EC3/FEM	1.07	1.09	1.16	1.15	1.12	1.14	1.08	1.11	0.036
DSM/FEM	0.98	0.92	0.98	0.98	0.96	1	0.99	0.97	0.028

**Table 4.11. Comparison of predicted strengths with FE results for laterally unbraced beams**

Length (m)	Standard section		Optimised section	
	EC3/FEM	DSM/FEM	EC3/FEM	DSM/FEM
1	0.97	1.15	0.98	1.02
2	0.82	1.05	0.87	1.16
3	0.87	1.24	0.81	1.28
4	1.02	1.25	0.84	1.36
Average	0.92	1.17	0.88	1.21
St. Dev.	0.091	0.093	0.074	0.148

For the unbraced beams, however, the findings are reversed. It is shown in Table 4.11 that the strengths calculated based on EC3 are conservative for the unbraced beams, while the DSM overestimated the flexural capacity of both the standard and the optimised sections by up to 36% and by 21% on average. Table 4.11 also indicates that the accuracy of the DSM decreased with increasing span length.

The FE simulations carried out in this study generally confirmed the accuracy of the EC3 design rules and therefore its suitability to be used as a tool for optimisation. It is thereby noted that using EC3 as a basis for optimisation leads to a significant simplification of the process compared to the effort it would take to use detailed non-linear FE analyses as part of the optimisation process.

As a final summary, Figure 4.23(a) and Figure 4.23(b) compare the ultimate capacities obtained using EC3, the DSM and the FE models, made dimensionless with respect to the capacity of the standard section obtained using the same method, for all braced and unbraced channel beams. It is shown that, while the EC3 predicts gains which are consistently about 10% higher than the FE/DSM predictions for the braced beams, a very good match is obtained for the unbraced beams. Most importantly, however, the trends of increasing/decreasing capacity over the range of prototypes (for the braced beams) and over the range of lengths (for the unbraced beams) are very well predicted by EC3 when the FE simulations are taken as a benchmark. In particular, the EC3 predicted conclusion that prototype ② is the most efficient prototype for unbraced beams, is confirmed by the FE models. In general, the results indicate that the proposed optimisation method is accurate and reliable and provides a practical tool for manufacturers and structural engineers to optimise the capacity of CFS elements.

By optimising each CFS beam in a given structure for a particular length and boundary conditions, a structure with minimum weight and optimal material efficiency could be obtained. However, in reality it would not be economical to custom roll each individual member, since a definite cost is incurred when reconfiguring the rolling process. Moreover, smaller roll-forming companies might not have this capability in the first place. Considering the range of optimum sections over lengths from 1m to 4m (Figure 4.6), a question of a very practical nature could be which section to commercialize and mass-produce as a ‘general purpose section’. In the authors’ design experience, the effective lengths of roof purlins, after taking into account the rotational restraint of the cladding (and given the reality in the UK that the market for roof cladding is almost monopolized by a single type of roofing panel), usually range from 1.5m to 2.5m. Therefore, the optimum section proposed for a 2m length would be a good candidate for a commercial roof purlin.

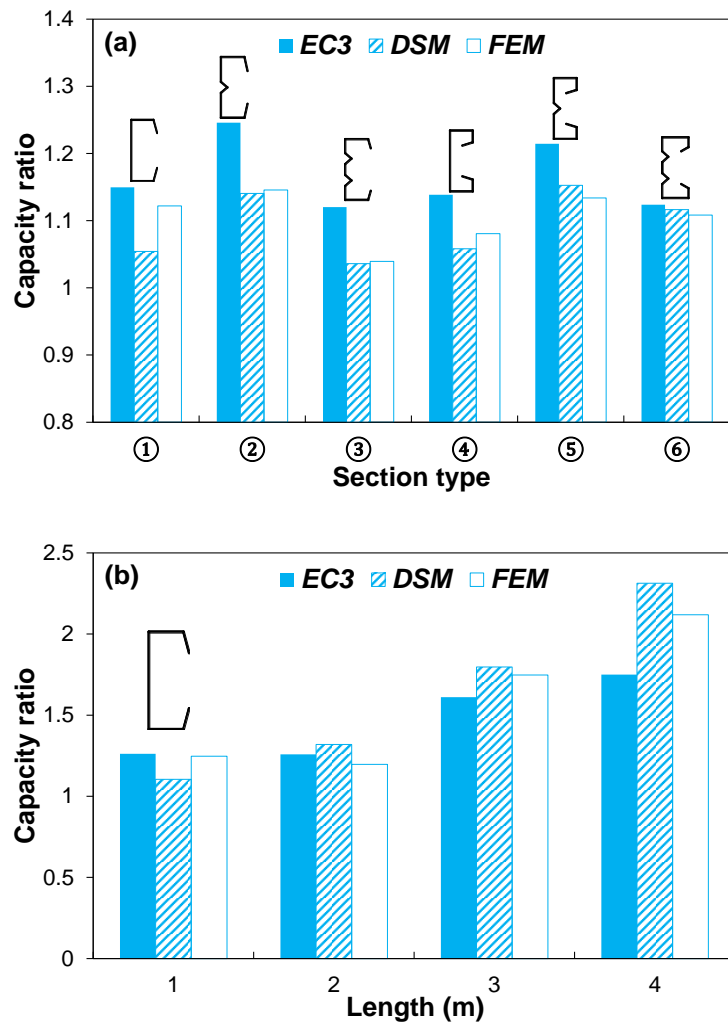


Figure 4.23. Flexural strength ratio of the optimised sections to the standard section for (a) laterally braced beams and (b) for laterally unbraced beams using the same amount of material

## 4.8 Summary and conclusions

This chapter presents a practical method to obtain more economical CFS channel sections for use as laterally braced or unbraced beams by optimising the dimensions of the cross-section and allowing for the addition of double-fold (return) lips, inclined lips and triangular web stiffeners. The optimisation process is thereby based on the Particle Swarm Optimisation (PSO) Algorithm, while the flexural strength of the sections is determined using the Effective Width Method as implemented in EC3. Six different prototypes were considered based on practical considerations. Based on the results of this study, the following conclusions could be drawn:

(1) By applying the proposed optimisation method to laterally braced beams, significant gains in cross-sectional bending capacity can be achieved: in the example, the bending capacity of a CFS cross-section was increased by up to 25% compared to the commercially available section taken as a starting point. The most effective cross-sectional prototype in this case was the lipped channel section with one stiffener located in the web. Using two stiffeners in a symmetrical

arrangement, while keeping the developed length constant, would again reduce the efficiency of the solution.

(2) The flexural capacity of the optimised 1m, 2m, 3m and 4m long unbraced beams was increased by 26%, 25.8%, 61% and 75%, respectively, compared to a commercially available section with the same amount of material. Comparison between the optimised results indicated that, when increasing the unbraced length, the flange width of the optimum solution increased, and consequently the total height of the section was reduced.

(3) The adequacy of the optimised sections was verified using detailed nonlinear FE analyses validated against experimental data, while also taking into account the effects of initial imperfections. The FE results, on average, showed less than a 6% error compared with the experimental data. The FE results of the commercially available and the optimised sections for both laterally braced and unbraced conditions generally showed good agreement with the flexural strengths estimated by EC3. The FE simulations also closely followed the increasing or decreasing trends in flexural capacity predicted by EC3 across the different prototypes. This demonstrates the reliability of the proposed optimisation method using the EC3 design rules.

(4) The flexural strengths of the optimised and the commercially available sections were also determined based on the DSM. Overall, the strengths calculated using EC3 and the DSM displayed a similar trend. Compared to the FE results, EC3 overestimated the flexural strength of the laterally braced beams by up to 16%, but underestimated the strength of the laterally unbraced beams by up to 19%. While the DSM, in general, provided accurate estimates of the capacities of the laterally braced beams, the accuracy of the method was seen to decrease with an increase of unbraced span length. It was shown that the DSM may overestimate the flexural capacity of long span laterally unbraced beams by up to 36%.

## **CHAPTER 5. Development of a more efficient CFS channel section in bending**

---

In the last chapter, optimisation on conventional CFS beams was conducted. This chapter aims to develop a more efficient CFS beam section with maximum flexural strength for practical applications. The optimised sections are designed to comply with the Eurocode 3 (EC3) geometrical requirements as well as with a number of manufacturing and practical constraints. The flexural strengths of the sections are determined based on the effective width method adopted in EC3, while the optimisation process is performed using the Particle Swarm Optimisation (PSO) method. To allow for the development of a new ‘folded-flange’ cross-section, the effective width method in EC3 is extended to deal with the presence of multiple distortional buckling modes. In total, ten different CFS channel cross-section prototypes are considered in the optimisation process. The flexural strengths of the optimised sections are verified using detailed nonlinear finite element (FE) analyses. The results indicate that the optimised folded-flange section possesses up to 57% higher bending capacity compared to other

optimum standard shapes with the same amount of material. The methodology presented in this chapter can be applicable to other innovative cross-sections.

## 5.1 Introduction

It has been pointed out that a folded flange cross-section (Figure 1.3(b)) can be better in terms of manufacturing and constructional aspects than a curved flange cross-section, as shown in (Figure 1.3(a)). However, the EC3 guidelines (CEN 2005, CEN 2005a, CEN 2005b) do not provide a direct procedure for the design of such cross-sections. In particular, there is a need to develop a design procedure that can account for the multiple distortional buckling modes which may occur in the folded-flange section.

This study aims to develop such a design methodology in order to subsequently use it to optimise the CFS folded-flange section. The efficiency of the folded-flange beam section is investigated alongside nine more conventional channel prototypes which are aimed at investigating the effects of intermediate web stiffeners, return lips and inclined lips. All sections are optimised by maximising the cross-sectional flexural capacity for a given thickness and coil width (equal to the total developed length of the cross-section). A brief overview of the effective width method adopted in EC3 (CEN 2005b) is first given in Section 5.2. This method is then extended to deal with the presence of multiple distortional buckling modes in the folded-flange cross-section. The particle swarm optimisation (PSO) method, used to solve the optimisation problem, is described in Section 5.3 and the optimum solutions are presented in Section 5.4. The accuracy of the proposed design model and the efficiency of the optimisation procedure are investigated through detailed nonlinear FE modelling in Section 5.5. A comprehensive comparison of the optimised results is provided in Section 6.

## 5.2 Design of CFS members based on EC3

The CFS sections to be optimised are evaluated according to the cross-sectional strength and stability provisions in EC3 (CEN 2005b) accounting for both local and distortional buckling modes. The “notional flat widths of the plate assemblies are used to determine the cross-sectional properties, which are then reduced by a factor ( $\delta$ ) to account for the influence of the rounded corners. A brief description of the EC3 provisions for the design of CFS members is provided in the following subsections.

### 5.2.1 Local buckling

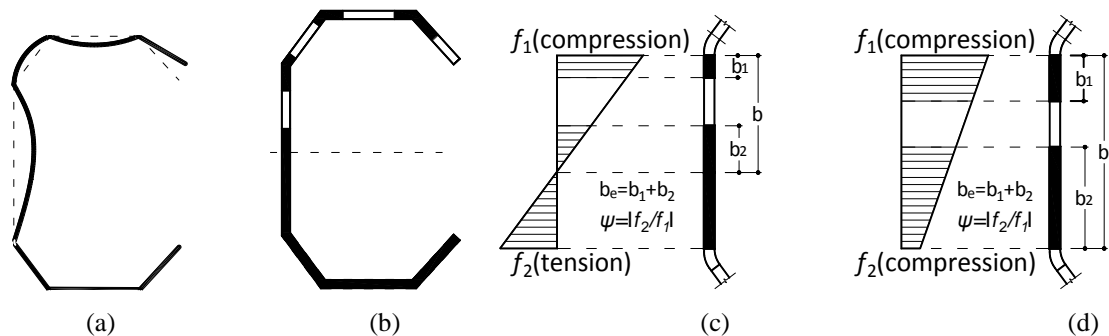
In EC3, the effect of local buckling is considered through the effective width concept. It recognizes the fact that local buckling of the plates constituting the cross-section has the effect of shifting the load-bearing stresses towards the corner zones, in the process reducing the effectiveness of the central parts in carrying compressive stresses. The cross-section is

consequently idealized as an “effective cross-section”, shown in solid black line in Figure 5.1(b). This effective area is assumed to resist the full bending action applied to the section. According to Eurocode 3, Part 1-5 (CEN 2005a), the effective width of a (doubly supported) plate is given by:

$$\frac{b_e}{b} = \frac{1}{\lambda_l} \left( 1 - \frac{0.055(3+\psi)}{\lambda_l} \right) \quad (5.1)$$

$$\text{with } \lambda_l = \sqrt{\frac{f_y}{\sigma_{cr}}} \quad (5.2)$$

where  $b$  and  $b_e$  are the total and the effective width of the plate, respectively.  $\psi = f_2/f_1$  is the stress ratio of the plate, as shown in Figure 5.1(c) and (d). An equation similar to Equation (5.1) is also provided for outstand elements. The slenderness ratio for local buckling,  $\lambda_l$ , relates the material yield stress,  $f_y$ , to the elastic local buckling stress of the plate,  $\sigma_{cr}$ . It is worth mentioning that Eurocode 3, Part 1-3 (CEN 2005b) always calculates the effective cross-section,  $W_{eff}$ , based on the yield stress,  $f_y$ , while some other design standards (e.g. the AISI (AISI 2007) and AS/NZS (AS/NZS 1996) specifications) use the stresses at global buckling.



**Figure 5.1. Local buckling mode of a folded-flange cross-section: (a) buckled shape, (b) effective area of the cross-section for local buckling, (c, d) web under stress gradient**

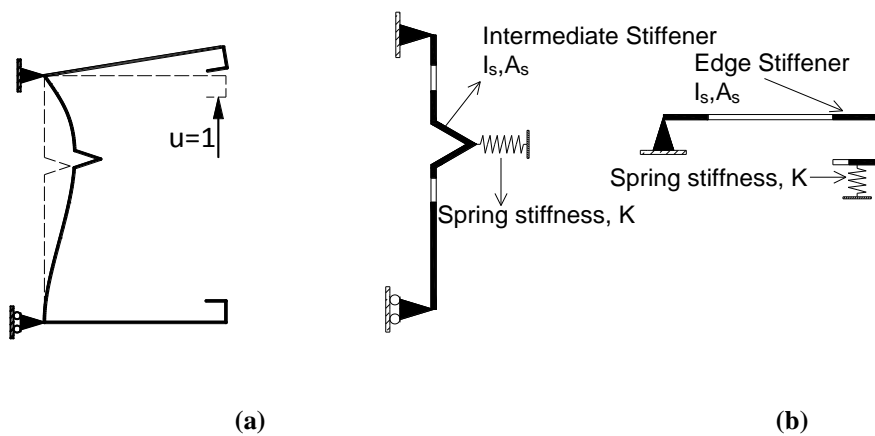
### 5.2.2 Distortional buckling

Distortional buckling of CFS members is linked to any buckling mode causing a distortion of the shape of the cross-section, but excludes those deformations related to local buckling (Figure 5.2(a)). As a result, distortional buckling is always associated with the displacement of one or more of the fold-lines of the section out of their original positions. Distortional buckling can also be interpreted as global (flexural or flexural-torsional) buckling of plate subassemblies within the cross-section. In line with this latter view, EC3 (CEN 2005b) bases the design for distortional buckling on the assumption that the plate subassembly at risk of buckling (which could be a stiffened web or a compressed flange-lip assembly) behaves as a strut continuously supported by elastic springs of stiffness  $K$  along its centroid axis. These springs replace the restraint experienced by the plate assembly from the omitted parts of the cross-section and

therefore depend on the flexural stiffness of the adjacent plates. The buckling behaviour can then be studied by considering an equivalent strut on an elastic foundation, as shown in Figure 5.2(b). The elastic critical buckling stress of the strut  $\sigma_{cr,s}$  is:

$$\sigma_{cr,s} = \frac{2\sqrt{KEI_s}}{A_s} \quad (5.3)$$

where  $E$  is the modulus of elasticity,  $I_s$  is the second moment of the area of the stiffener about the axis through its centroid parallel to the plate element being stiffened,  $K$  is the spring stiffness per unit length, and  $A_s$  is the effective cross-sectional area of the edge stiffener. The stiffness  $K$  is determined by applying a unit load  $u=1$  (per unit length) at the centroid of the effective part of the edge stiffener assembly, as shown in Figure 5.4 for the case of a double-fold stiffener. The stiffness of the equivalent springs thus depends on the flexural stiffness of the adjacent plane elements.



**Figure 5.2. Distortional buckling mode of a channel section with intermediate and edge stiffeners**  
**(a) distortionally buckled shape and (b) equivalent struts**

This procedure cannot directly be applied to the design of the folded-flange cross-section shown in Figure 1.3(b), because of the possibility of not one, but two distinctively different distortional buckling modes occurring, depending on the length of the flange segments. As illustrated in Figure 5.3, when the length of flange segment 2 is relatively large compared to segment 1, distortional buckling type 1 is dominant (i.e. buckling of the assembly consisting of flange segment 2 and the lip). However, for sections where flange segment 1 is much longer than segment 2, distortional buckling of type 2 (illustrated in Figure 5.4) is critical (i.e. buckling of the assembly consisting of flange segments 1 and 2 and the lip). Considering the two structural systems shown in Figure 5.3 and Figure 5.4 (and ignoring any second order effects), the deflections  $\delta_1$  and  $\delta_2$  produced by concentrated forces  $u_1$  and  $u_2$ , respectively, can be determined to be:



$$\delta_1 = \frac{u_1}{3D} \left[ e^3 + e^2b + b(e - b \cos \theta_1)(2e - b \cos \theta_1) + \frac{3}{2}h(e - b \cos \theta_1)^2 \right] \quad (5.4)$$

$$\delta_2 = \frac{u_2}{3D} \left[ e^3 + \frac{3}{2}he^2 \right] \quad (5.5)$$

where the bending rigidity of the plate,  $D$ , is determined by:

$$D = Et^3 / 12(1 - \nu^2) \quad (5.6)$$

In the above equations,  $e$  is the distance between the centroid of the edge stiffener (shown in Figure 5.3(b) and Figure 5.4(b)) and the pivot point (which is the web-to-flange junction for type 2 buckling and the junction between flange segments 1 and 2 for type 1 buckling),  $h$  is the height of the web,  $b$  is the length of flange segment 1 and  $\theta_1$  is the angle between flange segment 1 and segment 2 (see Figure 5.3(a) and Figure 5.4(a)). Furthermore,  $t$  is the plate thickness and  $E$  and  $\nu$  are the modulus of elasticity and the Poisson's ratio, respectively.

Distortional buckling is taken into account in EC3 (CEN 2005b) using a reduction factor  $X_d$  on the thickness of the stiffeners. This method can be extended to deal with folded-flange cross-sections by determining the elastic distortional buckling stress  $\sigma_{cr,s}$ , with Equation (5.3), using a stiffness  $K$  obtained from Equations (5.4-5.5). The effective cross-section needs to be calculated separately for each of the two distortional modes, yielding two effective cross-section moduli. For a particular cross-section, the effective section modulus is then taken as the minimum value of the two.

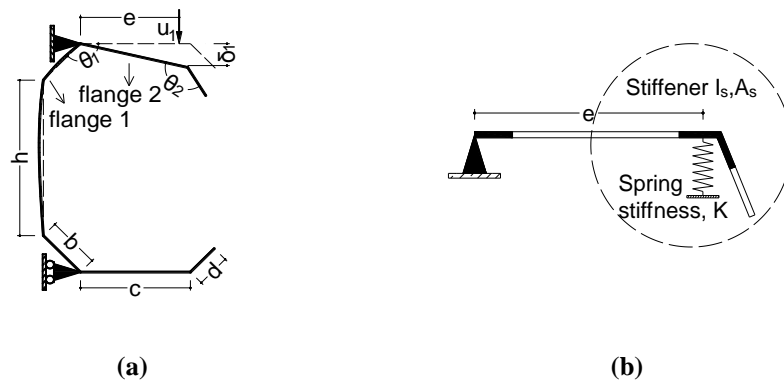


Figure 5.3. (a) Actual system, and (b) simplified model to analyse distortional buckling of type 1

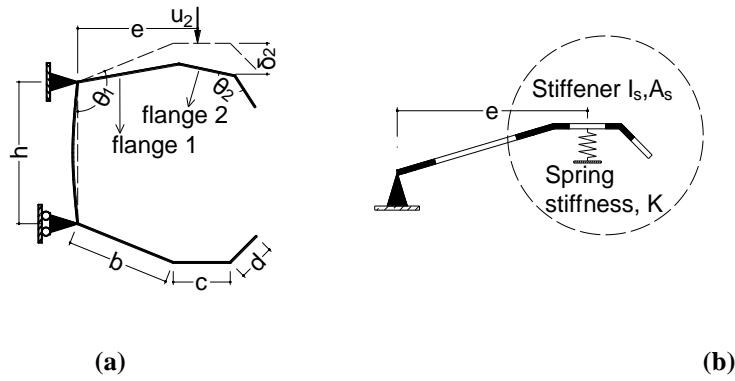


Figure 5.4. (a) Actual system, and (b) simplified model to analyse distortional buckling of type 2

The design model developed for the folded-flange section is further used during the optimisation process in Sections 5.3 and 5.4.

### 5.3 Optimisation procedure

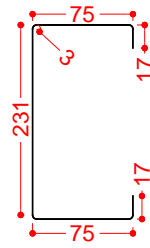
#### 5.3.1 Problem definition

The optimisation procedure in this study aimed to maximize the CFS cross-sections with respect to their bending capacity. The optimisation problem can be formulated as:

$$\max (M_{c,Rd} = W_{eff}(x) \cdot f_y) \quad d_{\min} \leq x_i \leq d_{\max} \quad \text{for } i = 1, \dots, N \quad (5.7)$$

where  $M_{c,Rd}$  is the moment resistance of a cross-section about its major axis and  $W_{eff}(x)$  is the effective section modulus. For each design variable,  $x_i$ , lower and upper bounds,  $d_{\min}$  and  $d_{\max}$ , were determined based on a combination of the constraints imposed by EC3 (CEN 2005b) and certain manufacturing limitations and practical considerations, which will be explained further in this section. Throughout the optimisation process, the thickness of the cross-sections was kept constant at 1.5 mm and the total developed length of the cross-section (the coil width) was also maintained at 415 mm. These values were taken from a commercially available channel section, shown in Figure 5.5, which was used as a benchmark and to which the performance of the optimised sections will be compared in section 4.2.

The values of the radius of the rounded corners (measured along the heart-line), the elastic modulus and the Poisson's ratio were taken as 3 mm, 210 GPa and 0.3, respectively. The yield stress of the CFS material was assumed to be  $f_y = 450 \text{ MPa}$ . It is again noted that the optimisation was carried out with respect to the cross-sectional capacity, excluding lateral-torsional buckling. This situation is representative, for instance, of purlins connected to a steel deck with concrete topping, where the compression flange is continuously supported, or even of roof purlins where the lateral and rotational stiffness of the roof diaphragm and/or the presence of sufficient bridging prevent any out-of-plane effects.



**Figure 5.5. Selected commercial CFS beam cross-section**

To ensure the practicality of the optimised sections, the following additional constraints were imposed:

(1) The basic overall shape of all the cross-sections was restricted to a channel. Channel sections are currently the most widely used CFS beams in practical applications. The fact that they are composed of flat plate elements both allows for a straightforward manufacturing process and facilitates the connections to trapezoidal steel decking or roof/wall systems, as well as bridging, cleat plates, etc... Ten different prototypes were optimised, which are shown in Table 5.1. They include nine relatively conventional sections and the newly proposed folded-flange channel section. All prototypes are based on a channel shape, but they allow the addition of a single web stiffener, double web stiffeners, inclined lips and double-fold (return) lips. These features are commonly encountered within commercially available sections and do not impose any excessive demands on the fabrication process. Each prototype was individually optimised, after which the overall optimum among the ten optimised prototypes was identified.

(2) In practice, additional constraints of a very concrete nature typically come into play. These constraints may be quite case-dependent and may, for instance, be related to the ability to connect the beam to other elements, or be imposed by the manufacturing process itself. In this particular case, the following constraints were imposed:

- a) The width of the flanges was required to be at least 50 mm in order to connect trapezoidal decking or plywood boards to the beam by means of screws. This width was determined after consultation with the industrial partner on the project. In the case of the folded flange section, it was the flat width of the central horizontal segment which was restricted to a minimum of 50 mm.
- b) The lip needs to be of a sufficient length. A lip of, for instance, 1 mm length cannot be rolled or brake-pressed. The industrial partner on the project suggested a minimum length of 5-15 mm. Therefore, as indicated in Table 5.1,  $c \geq 15$  mm was imposed for a single lip and combined with  $d \geq 5$  mm for a return lip.

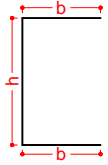
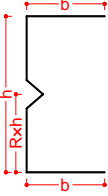
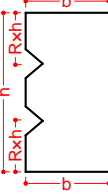
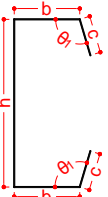
- c) The height of the web was specified to be at least 100 mm in order to allow a connection to be made (e.g. to a cleat plate) with at least two bolts and/or for bridging to be installed. An upper bound of 350 mm was also imposed limit the total floor depth.
- d) The ratio R (see Table 5.1) was restricted so that the intermediate web stiffener would be physically positioned within the web.

One of the major advantages of the PSO algorithm is that these constraints can easily be accommodated and others added. The constraints merely result in a restriction of the search space of the particle swarm.

In addition to the practical constraints mentioned above, the EC3 design rules (CEN 2005b) also impose certain limits on the plate width-to-thickness ratios, the relative dimensions of the cross-section and the angle of the edge stiffeners. These constraints were also taken into account in the optimisation procedure and are listed in Table 5.1 under the heading ‘Constraints based on EC3’.

Finally, the opening angle and the leg length of the intermediate stiffeners were limited to  $\pi/6$  and 15 mm, respectively.

**Table 5.1. Selected prototypes, design variables and constraints**

Prototype	Prototype section	Design variables	Constraints based on EC3	$u_{\min}$	$u_{\max}$	Manufacturing & practical limitations
①		$x = b/L$	$b/t \leq 50$ $b/t \leq 500$	0.1205	0.1807	$b \geq 50$ $100 \leq b \leq 350$
②		$x_1 = b/L$ $x_2 = R$	$b/t \leq 50$ $b/t \leq 500$	0.1205 0.1000	0.1807 0.9000	$b \geq 50$ $100 \leq b \leq 350$ $0.1 \leq R \leq 0.9$
③		$x_1 = b/L$ $x_2 = R$	$b/t \leq 50$ $b/t \leq 500$	0.1205 0.1000	0.1807 0.4000	$b \geq 50$ $100 \leq b \leq 350$ $0.1 \leq R \leq 0.4$
④		$x_1 = c/b$ $x_2 = b/L$ $x_3 = \theta_1$	$0.2 \leq c/b \leq 0.6$ $b/t \leq 60, c/t \leq 50$ $b/t \leq 500$ $\pi/4 \leq \theta_1 \leq 3/4\pi$	0.3000 0.1205 $\pi/4$	0.6000 0.2169 $3/4\pi$	$b \geq 50$ $100 \leq b \leq 350$ $c \geq 15$

Prototype	Prototype section	Design variables	Constraints based on EC3	$u_{\min}$	$u_{\max}$	Manufacturing & practical limitations
⑤		$x_1 = c/b$ $x_2 = b/L$ $x_3 = R$ $x_4 = \theta_1$	$0.2 \leq c/b \leq 0.6$ $b/t \leq 60, c/t \leq 50$ $b/t \leq 500$ $\pi/4 \leq \theta_1 \leq 3/4\pi$	0.3000 0.1205 0.1000 $\pi/4$	0.6000 0.2169 0.9000 $3/4\pi$	$b \geq 50$ $100 \leq b \leq 350$ $c \geq 15$ $0.1 \leq R \leq 0.9$
⑥		$x_1 = c/b$ $x_2 = b/L$ $x_3 = R$ $x_4 = \theta_1$	$0.2 \leq c/b \leq 0.6$ $b/t \leq 60, c/t \leq 50$ $b/t \leq 500$ $\pi/4 \leq \theta_1 \leq 3/4\pi$	0.3000 0.1205 0.1000 $\pi/4$	0.6000 0.2169 0.4000 $3/4\pi$	$b \geq 50$ $100 \leq b \leq 350$ $c \geq 15$ $0.1 \leq R \leq 0.4$
⑦		$x_1 = c/b$ $x_2 = d/b$ $x_3 = b/L$ $x_4 = \theta_1$	$0.2 \leq c/b \leq 0.6,$ $0.1 \leq d/b \leq 0.3$ $b/t \leq 90, c/t \leq 60$ $d/t \leq 50, b/t \leq 500$ $\pi/4 \leq \theta_1 \leq 3/4\pi$	0.3000 0.1000 0.1205 $\pi/4$	0.6000 0.3000 0.2169 $3/4\pi$	$b \geq 50$ $100 \leq b \leq 350$ $c \geq 15$ $d \geq 5$
⑧		$x_1 = c/b$ $x_2 = d/b$ $x_3 = b/L$ $x_4 = R$ $x_5 = \theta_1$	$0.2 \leq c/b \leq 0.6$ $0.1 \leq d/b \leq 0.3$ $b/t \leq 90, c/t \leq 60$ $d/t \leq 50$ $b/t \leq 500$ $\pi/4 \leq \theta_1 \leq 3/4\pi$	0.3000 0.1000 0.1205 0.1000 $\pi/4$	0.6000 0.3000 0.2169 0.9000 $3/4\pi$	$b \geq 50$ $100 \leq b \leq 350$ $c \geq 15, d \geq 5$ $0.1 \leq R \leq 0.9$
⑨		$x_1 = c/b$ $x_2 = d/b$ $x_3 = b/L$ $x_4 = R$ $x_5 = \theta_1$	$0.2 \leq c/b \leq 0.6$ $0.1 \leq d/b \leq 0.3$ $b/t \leq 90, c/t \leq 60$ $d/t \leq 50,$ $b/t \leq 500$ $\pi/4 \leq \theta_1 \leq 3/4\pi$	0.3000 0.1000 0.1205 0.1000 $\pi/4$	0.6000 0.3000 0.2169 0.4000 $3/4\pi$	$b \geq 50$ $100 \leq b \leq 350$ $c \geq 15, d \geq 5$ $0.1 \leq R \leq 0.4$
⑩		$x_1 = \theta_1$ $x_2 = \theta_2$ $x_3 = b$ $x_4 = c$ $x_5 = d$	$b/t \leq 500,$ $7/12\pi \leq \theta_1 \leq 5/6\pi$ $\pi/4 \leq \theta_2 \leq 3/4\pi,$ $30 \leq b \leq 48;$ $50 \leq c \leq 60;$ $15 \leq d \leq 60$	$7/12\pi$ $\pi/4$ 30 50 15	$5/6\pi$ $3/4\pi$ 48 60 60	$100 \leq b \leq 350$

### 5.3.2 Optimisation solutions

To facilitate the optimisation process, both the design procedure and the optimisation algorithm were implemented in Matlab (Mathworks 2011). The population of the particle swam  $N$  was taken as 100, and 100 iterations  $k_{\max}$  were used to obtain the optimum results. The maximum and minimum inertial weight factors  $w_{\max}$  and  $w_{\min}$  were taken as 0.95 and 0.4, respectively (Shi and Eberhart 1998). Each of the prototypes was optimised 3 times using a different set of

random initial particles and the result with the maximum bending capacity was retained as the optimum section. As an example, Figure 5.6 shows the iteration history of the bending capacity of prototype ⑩, where the convergence was practically achieved after about 50 steps.

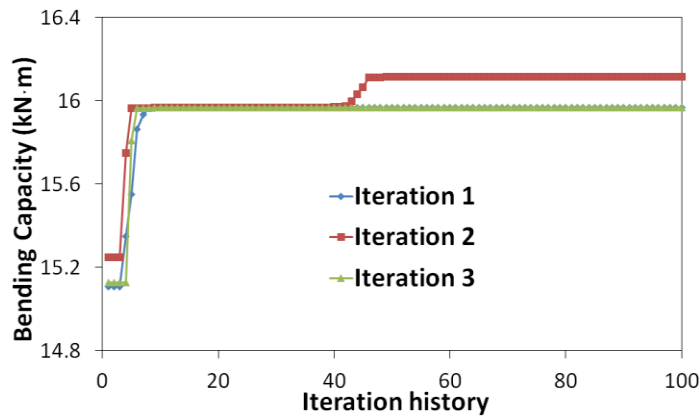


Figure 5.6. Iteration history of the maximum bending capacity of prototype ⑩

Table 5.2 summarises the dimensions and the bending capacity of the optimised cross-sections corresponding to each of the prototypes presented in Table 5.1. Table 5.3 illustrates the effective cross-section of the optimised prototypes, maintaining the same scale for all cross-sections. A thick black line represents a fully effective part of the cross-section, while a line with intermediate thickness indicates that the thickness has been reduced to account for distortional buckling.

Table 5.2. Geometrical details and bending capacities of the optimised sections

Section	h (mm)	b (mm)	c (mm)	d (mm)	$\theta_1$ (deg)	$\theta_2$ (deg)	R	Bending capacity (kN·m)
①	315	50	-	-	-	-	-	9.84
②	305	50	-	-	-	-	0.856	11.08
③	295	50	-	-	-	-	0.186	9.92
Standard (Figure 5.7)	231	75	17	-	90	-	-	10.30
④	270	50	23	-	91	-	-	13.38
⑤	263	50	21	-	92	-	0.79	13.66
⑥	234	50	20	-	90	-	0.223	12.69
⑦	242	50	29	7.5	90	-	-	15.11
⑧	240	50	25	7	135	-	0.9	14.62
⑨	232	50	25	6.5	135	-	0.1	13.41
⑩	185	48	50	17	105	95	-	16.12

It is clear from Table 5.3 that, in general, the optimised cross-sections tend to adopt the minimum specified flange width of 50 mm and, hence, have a large height-to-width ratio. However, prototypes ① to ③, which have the largest height, still show the lowest bending

capacity (one which is even lower than the standard non-optimised section taken as a starting point). This is due to the fact that the flanges without edge stiffeners are highly susceptible to local buckling and, therefore, the strength can only be marginally enhanced by adding intermediate stiffeners to the web in prototype ③. However, the optimised lipped channel section ④ shows that adding an edge stiffener can improve the bending capacity by more than 25%.

Adding an intermediate stiffener in prototype ⑤ increased the bending capacity of the optimum section by only 2%, compared to prototype ④. However, using two intermediate stiffeners in the web (prototype ⑥) actually reduced the flexural capacity of the optimum CFS section by 5.2% compared to the optimum lipped channel with no stiffener (prototype ④). This is due to the fact that folding the intermediate stiffeners into the section (while keeping the total developed length constant) causes a reduction in total height, which impacts negatively on the effective modulus of the section. Moreover, in this symmetric arrangement the web stiffener in the tension zone is completely ineffective. It can be concluded in general terms that for CFS beam sections, edge stiffeners are much more efficient in increasing the section capacity than intermediate web stiffeners.

The results also indicate that, using the same amount of material, the newly developed folded-flange section (prototype ⑩) provides the maximum flexural strength compared to the other prototypes. Moreover, this cross-section can easily be manufactured and satisfies all the practical constraints which were imposed.

It is also noted that the practical constraints imposed on the floor depth  $h$  of the sections (listed in the rightmost column of Table 5.1) never turned out to be critical. However, other practical restraints, in particular the minimum flange width and the restrictions on the ratio  $R$  and the angle  $\theta_1$ , were often found to govern the cross-sectional shape.

**Table 5.3. Effective cross-sections of the optimised beams, presented at the same scale**

Prototypes	①	②	③	④	⑤
Effective sections					
Prototypes	⑥	⑦	⑧	⑨	⑩
Effective sections					

## 5.4 FE analysis

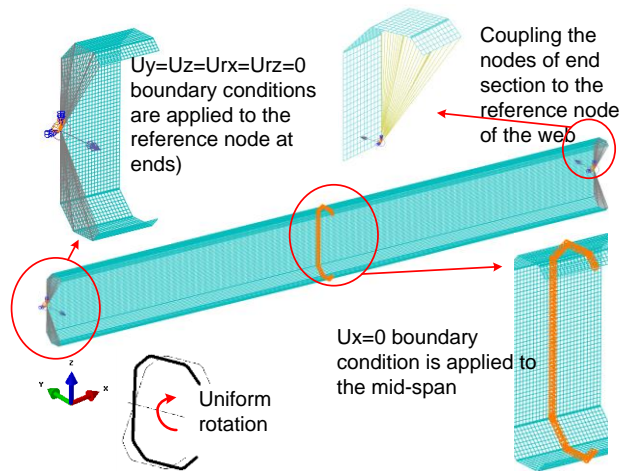
Detailed geometric and material non-linear FE analyses were performed using ABAQUS (ABAQUS 2011) to evaluate the flexural behaviour and capacity of the optimised cross-sections for the ten considered prototypes (see Table 5.2) as well as the standard lipped channel taken as a starting point (Figure 5.5). The main purposes of the FE analyses were: (a) to examine the accuracy of the method proposed in Section 5.2 for the flexural design of folded-flange cross-sections; and (b) to investigate the overall effectiveness of the developed optimisation framework in obtaining sections with increased capacity.

### 5.4.1 FE modelling and parameters

The FE models were developed in ABAQUS (ABAQUS 2011) using the general-purpose S4R element (Figure 5.7). This element is a 4-node quadrilateral shell element with reduced integration. Through a sensitivity analysis, a mesh size of  $5\text{mm} \times 5\text{mm}$  for the flat plate sections,



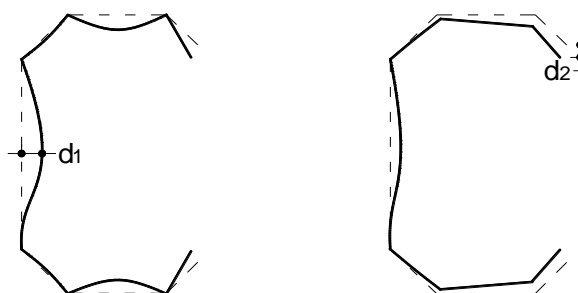
with smaller elements used in the rounded corner sections was found to be appropriate. No significant change on the ultimate capacity was observed by reducing the mesh size.



**Figure 5.7. FE model of the folded-flange beam subjected to local/distortional buckling**

The stress-strain behaviour of the CFS plate material was simulated using the constitutive model suggested by Haidarali and Nethercot (Haidarali and Nethercot 2011), as shown in Section 3.5.

In the FE analysis, the effects of the geometric imperfections were included in the FE analysis by scaling the local and distortional modes to specific amplitudes and superposing them onto the initial perfect geometry. The critical buckling modes were obtained using CUFSM, a finite strip based software (Schafer 2006). The magnitudes of the local/distortional geometric imperfections were obtained from the cumulative distribution function (CDF) values presented by Schafer and Peköz (Schafer and Pekoz 1998). In particular, the local and distortional imperfections with a CDF value of 50% were considered, corresponding to values of  $d_1/t$  and  $d_2/t$  equal to 34% and 94%, respectively, with  $d_1$  and  $d_2$  illustrated in Figure 5.8.



**Figure 5.8. Geometric imperfections: (a) local buckling, and (b) distortional buckling**

To simulate pin-ended boundary conditions with warping prevented, the nodes of each end section of the CFS member were coupled to the central point of the web (acting as the master node) (Shifferaw and Schafer 2012). The external load was then applied in the form of uniform rotations of the end sections about the major axis using the Riks solver in ABAQUS . The

boundary conditions and the applied loading are illustrated in Figure 5.7. Large deformation effects were considered in the element formulation in order to be able to accurately track the post-buckling behaviour of the CFS beams. It is worth mentioning that the modelling techniques utilized in this study, including the type of elements, the material behaviour, the meshing and the imperfection modelling borrow heavily from the work by Haidarali and Nethercot (Haidarali and Nethercot 2011) and Shifferaw and Schafer (Shifferaw and Schafer 2012). These techniques have been extensively verified against experimental results (Yu and Schafer 2006, Yu and Schafer 2003), demonstrating excellent predictive capability with an average error typically less than 4%.

#### **5.4.2 FE analysis of folded-flange sections with varying dimensions**

This section presents the results of FE analyses used to evaluate the accuracy of the design approach proposed in Section 5.2 to calculate the flexural strength of folded-flange CFS cross-sections. To achieve this, six folded-flange sections with a range of different dimensions were investigated. Table 5.4 provides the geometric details of all selected sections. The ratio  $b/c$  of the flange segments lengths (Table 5.1) and the angles of the inclined lips were varied. The sections failed by local buckling and/or distortional buckling of the two possible types described in Section 5.2. Since the CFS beams in the current study were laterally restrained, however, lateral-torsional buckling did not occur.

As used by Galambos (Galambos 1998), the lengths of the FE models were taken as three times the distortional buckling half-wave length.

The flexural strengths of the selected sections obtained from detailed FE analyses are compared to those calculated using the proposed design method (Section 5.2) in Table 5.4. The results indicate that the proposed design methodology predicts the flexural capacity of the folded-flange sections with reliable accuracy. The average and the standard deviation of the ratio of FE to EC3 results are 1.02 and 8%, respectively, as shown in Table 5.4.

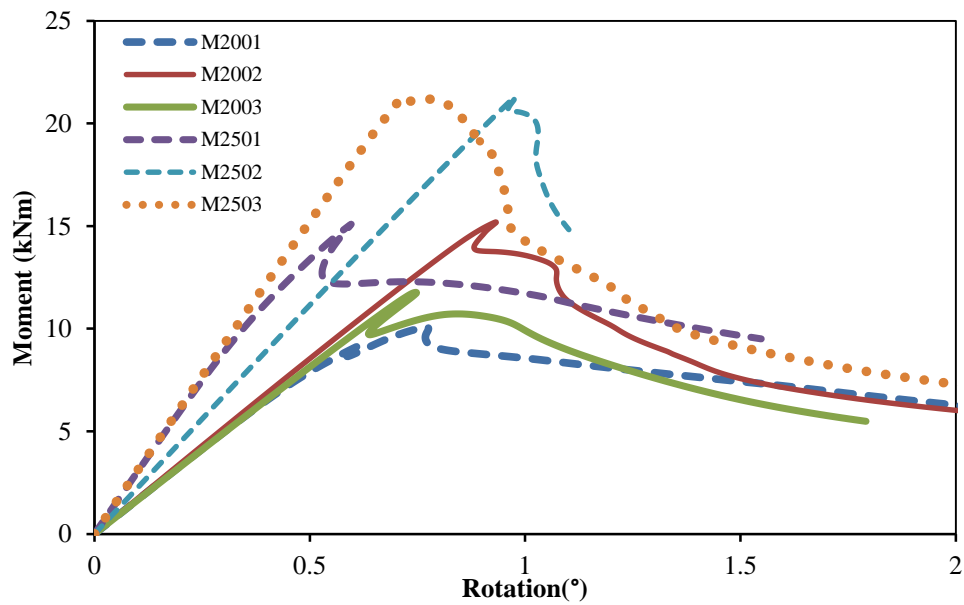
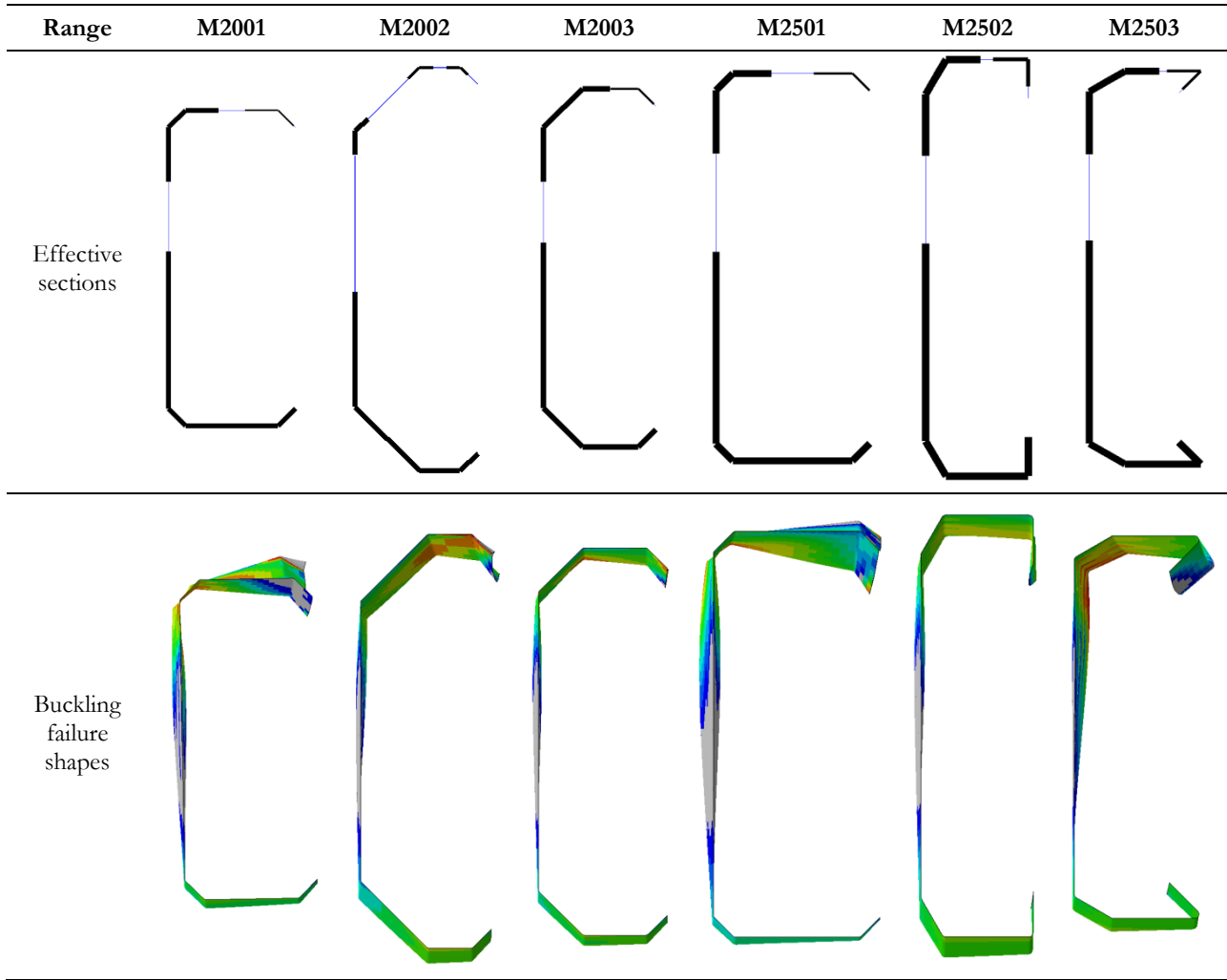
For illustrative purposes, the effective cross-sections calculated according to EC3, as well as the failed shapes at the ultimate load obtained from the FE analyses are presented in Table 5.5. With respect to the effective cross-sections it should be noted that the reduction in thickness of the black lines indicates distortional buckling of the section. These results show that the type 2 distortional buckling mode (see Figure 5.4) is dominant for the folded-flange cross-section M2002, where the length of flange segment-1 is around 2 times of the segment-2. For all other folded-flange sections in Table 5.4, distortional buckling of type 1 (see Figure 5.3) is critical. This result was predicted by the design methodology and confirmed by the FE analysis results.

**Table 5.4. Dimensions of the folded-flange cross-sections and bending capacity obtained from EC3 and FEM**

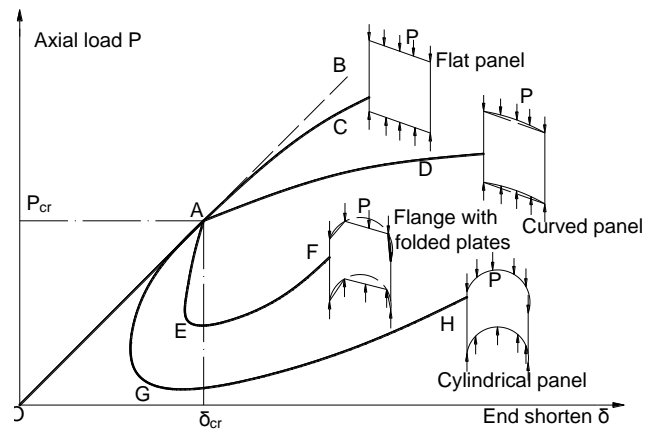
Sections (Also see Table 5.5)	Thickness (mm)	Depth (mm)	$\theta_1$ (°)	$\theta_2$ (°)	Flange1 b(mm)	Flange2 c(mm)	Lip d(mm)	Corner radius (mm)	Capacity (kN·m)		FEM/ EC3
									EC3	FEM	
M2001	1.4	200	135	135	18	66	18	2.8	10.14	10.06	0.99
M2002	1.4	200	135	135	66	30	18	2.8	13.74	15.20	1.11
M2003	1.4	200	135	135	40	40	18	2.8	12.71	11.77	0.93
M2501	1.6	250	135	135	18	85	18	3.2	16.50	15.09	0.91
M2502	1.6	250	120	90	30	61	30	3.2	19.76	21.30	1.08
M2503	1.6	250	150	45	30	61	30	3.2	19.43	21.11	1.09
Average Standard deviation											1.02 0.08

The moment-rotation responses of the folded-flange sections obtained from FE analysis are plotted in Figure 5.9. It is seen that, with the exception of section M2503, all sections display, to a varying degree, some sort of “snap-back” behaviour past the peak load. This is a phenomenon which is not commonly observed in regular lipped channel sections and is more reminiscent of the post-peak behaviour of, for instance, cylindrical shells or strongly curved plates under compression (Figure 5.10). It appears that replacing the semi-circular flange shape in Figure 1.3(a) by a segmental approximation for practical reasons causes the folded-flange section to ‘inherit’ some of the typical snap-back behaviour of the former.

**Table 5.5. Effective cross-sections and buckled shapes of the folded-flange beams (presented at a consistent scale)**



**Figure 5.9. Moment-rotation curve of the folded-flange sections**



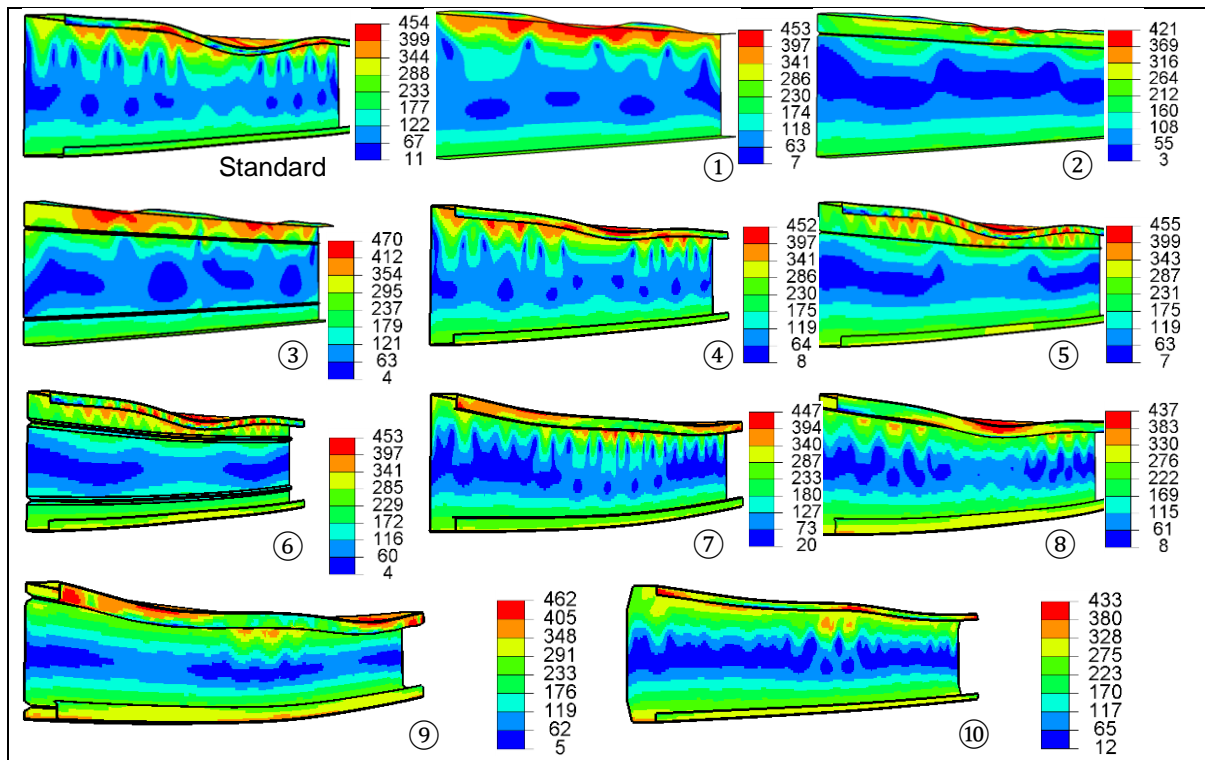
**Figure 5.10. Schematic view of the behaviour of axially compressed panels (adapted from (Jones 2006))**

### 5.4.3 FE results of optimised cross-sections

The bending moment capacities of the standard channel (Figure 5.5) and the optimised prototypes (Table 5.2) were determined using FE analysis. The adopted boundary conditions were identical to the models of the folded-flange sections previously described, and the load was again applied as uniform rotations at both ends. The lengths of the modelled beams (Table 5.6) were selected as three times the distortional buckling half-wave length. For prototypes without edge stiffeners (prototypes ①, ②, ③) only the local buckling imperfection was incorporated, since local buckling was the dominant mode. Table 5.6 shows the bending capacities of the optimised and standard cross-sections obtained from the FE analyses and compares them to those determined based on the EC3 effective width method. Even though the results obtained from EC3 are slightly unconservative compared to the FE predicted capacities, this study shows that the effective width method is generally reliable and provides a reasonable prediction for the bending moment capacities of the selected CFS prototypes. The average ratio of the capacity determined using FEM to the capacity calculated using EC3 was 0.95 with a standard deviation of 5%. The failed shapes at ultimate capacity, obtained from FE analysis, are also illustrated in Figure 5.11.

**Table 5.6. Comparison of the bending moment capacities of the optimised and standard sections obtained from EC3 and FE analysis**

Section	Buckling half-wave lengths		Modelling length (mm)	Bending moment capacity (kN·m)		EC3/FEM
	Local (mm)	Distortional (mm)		EC3	FEM	
Standard Channel	100	600	1800	10.30	10.40	0.99
①	200	-	600	9.84	9.11	1.08
②	200	-	600	11.08	11.22	0.99
③	200	-	600	9.92	9.41	1.05
④	140	600	1800	13.38	12.73	1.05
⑤	50	600	1800	13.66	12.08	1.13
⑥	50	600	1800	12.69	11.15	1.14
⑦	120	800	2400	15.11	14.09	1.07
⑧	100	800	2400	14.62	12.99	1.13
⑨	100	800	2400	13.41	12.33	1.09
⑩	100	800	2400	16.12	15.52	1.04
Average						0.95
Standard deviation						0.05



**Figure 5.11. Buckling shapes at peak load of the optimised and standard sections (Stress: MPa)**

## 5.5 Comparison of the results and discussion

Figure 5.12 compares the EC3 predicted capacities of the optimised sections to the results obtained from detailed FE analysis. As a general conclusion, the FE results follow the trends predicted by the EC3 very well and confirm the reliability of the proposed optimisation method. The results also indicate that, for the same amount of material, the optimisation procedure can significantly increase the bending moment capacity of the CFS cross-sections.

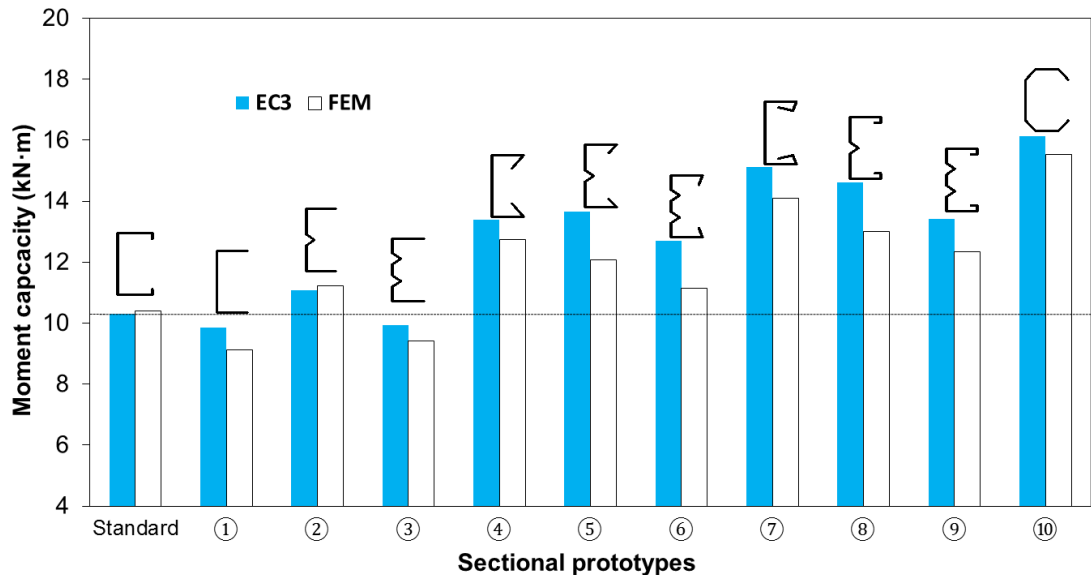


Figure 5.12. Comparison of the moment capacities of different prototypes

It is shown specifically in Figure 5.12 that by only optimising the relative dimensions of the plates and the angles of the inclined lips (i.e. prototype ④), the bending capacity of the commercially available channel section taken as a starting point can be increased by more than 30%. A comparison between the optimum results of prototypes ①, ④ and ⑦ indicates that the bending capacity of CFS channel sections can be significantly increased (by up to 55% in this case) by adding edge stiffeners which suppress the distortional mode. On the other hand, comparing the bending capacity of the prototypes ④ and ⑤, and also ⑦ and ⑧, it can be seen that adding intermediate stiffeners in the web does not necessarily increase the optimal bending capacity of the sections. This is also illustrated by the sections with two web stiffeners (prototypes ⑥ and ⑨), where the flexural capacity of the section with stiffeners was up to 13% less than the optimum channel section without web stiffener (prototype ④). The main reason for this behaviour is that, when placing the stiffener at the centre of the web or in a symmetric arrangement with one stiffener ending up in the tension zone of the beam, the stiffeners are not at their full effectiveness. At the same time, the total developed length of the cross-section is kept constant, so that folding the stiffeners into the section reduces the total height of the cross-section and, therefore, its bending capacity. For practical reasons, however, it is not recommended to place the stiffeners in an asymmetric configuration since errors during the installation of the beams would almost be inevitable. Figure 5.12 also highlights the increased

efficiency of the proposed folded-flange prototype compared to any other prototype considered. It is shown that, for the same amount of material, prototype ⑩ leads to a maximum flexural capacity which is around 57% higher than the standard commercially available channel section and 22 % higher than the optimum lipped channel section (prototype ④). Folded-flange sections are also easy to manufacture and connect to typical floor systems and, hence, are ideal candidates for practical CFS beam sections.

## 5.6 Summary and conclusions

In this chapter, a practical framework is proposed to optimise CFS beam cross-sections while considering code-based design constraints as well as manufacturing issues and practical limitations. Using the framework, a commercially available CFS lipped channel section was optimised based on ten different prototypes, including a folded-flange cross-section, while keeping the material use constant. A modification of the EC3 design methodology was first developed in order to account for the multiple distortional buckling modes which may occur in the folded-flange cross-section. The cross-sectional buckling behaviour was taken into account by considering an equivalent strut in compression on an elastic foundation, where the stiffness of the foundation depends on the relative dimensions of the flanges. The particle swarm optimisation algorithm was then used to obtain the solutions with the maximum flexural strength. The accuracy of the modified design model and the effectiveness of the proposed optimisation framework were also evaluated using detailed non-linear FE analysis. The following conclusions can be drawn:

- The FE simulations of the folded-flange sections confirm that the proposed additions to the effective width based design method in EC3 to account for the multiple distortional buckling modes in the folded-flange section lead to accurate predictions of the ultimate bending capacity.
- By applying the proposed optimisation framework to laterally braced beams, the bending capacity of a commercially available CFS beam was increased by 30% by only optimising the relative dimensions of the flat plates and the inclination of the lips. The results also indicate that flanges with double fold lips have the potential to considerably increase the flexural capacity of CFS beams (by up to 50%), while using intermediate stiffeners in the web does not necessarily increase the capacity of the sections. As expected, plain CFS channel cross-sections provided the minimum flexural capacity, even when using intermediate web stiffeners.
- Folded-flange sections, which can be easily designed and manufactured due to their simple sequence of straight plate segments with a relatively small number of folds, are shown to be viable and even superior alternatives to typical lipped channel sections. For



the same amount of material (i.e. the same total coil width and plate thickness), the folded-flange section possesses a flexural capacity which is 57% and 22% higher than the selected commercial section and the optimum lipped channel section, respectively.

This page is intentionally left in blank

## **CHAPTER 6. Development of optimum CFS sections for maximum energy dissipation in seismic applications**

---

While conventional building structures exceed their elastic limits in severe earthquakes, previous optimisation studies concentrated mainly on the optimum elastic buckling strength of CFS elements. This chapter aims to, for the first time, improve the seismic performance of CFS elements by optimising their post-buckling behaviour in the nonlinear inelastic range. A novel non-linear shape optimisation method is presented for the optimum design of CFS beam sections in moment-resisting frames. The relative dimensions of the cross-section, the location and number of intermediate stiffeners and the inclined lip angle are considered as main design variables. All plate slenderness limit values and limits on the relative dimensions of the cross-sectional components, set by the Eurocode 3, are taken into account as constraints on the optimisation problem. An additional constraint is considered where maximum equivalent plastic strain is restricted to ensure a sufficient level of ductility. Global optimal solutions are obtained through the Particle Swarm Optimisation (PSO) algorithm. The developed PSO algorithm is

linked to the ABAQUS (ABAQUS 2011) finite element programme for inelastic post-buckling analysis and optimisation.

## 6.1 Introduction

Cold-formed steel (CFS) elements are produced by bending relatively thin metal sheets into a variety of cross-sectional shapes by either cold-rolling or press braking. Structural systems composed of CFS members provide a wide range of advantages. They typically offer a high strength-to-weight ratio, are lightweight, and are easy to handle, transport and install. However, typically large width-to-thickness ratios of CFS cross-sectional plate assemblies, resulting from practical limitations on the sheet thicknesses which can be processed at room temperature, leaves CFS members susceptible to several instabilities including local, distortional and global buckling modes. The large width-to-thickness ratios of CFS members are also typically outside the limits prescribed by seismic design codes (AISC 341-05 2005, CEN 2008).

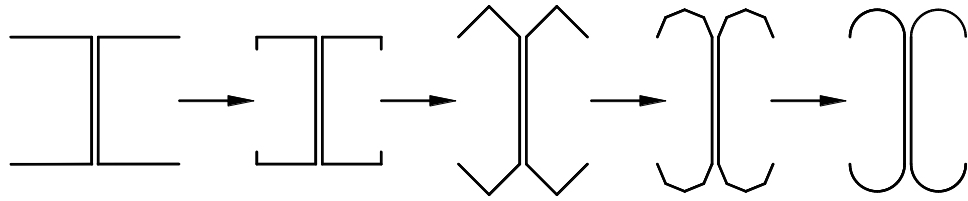
Whilst some research has previously been carried out on the seismic behaviour of CFS stud walls (Nithyadharan and Kalyanaraman 2012, Wang et al. 2015), research into the plastic behaviour and the energy dissipation capacity of CFS primary load-bearing elements is still very limited.

Calderoni et al. (Calderoni et al. 2009) conducted monotonic and cyclic tests to study the seismic behaviour of CFS channel beams. The results of their study showed substantial ductility and energy dissipation capacity in the CFS beam sections despite their full plastic moment capacity being reduced by local buckling. The axial cyclic behaviour of typical wall stud elements used as CFS framing members was investigated by Adilla-Llano et al. (Padilla-Llano et al. 2014). Their experimental tests showed a damage accumulation within the tested specimens. The results of their study indicated that the amount of dissipated energy in the stud elements varies with the dimensions and the shape of the profiles, typically decreasing with increasing cross-sectional slenderness ratio.

Another research project on the development of elements and bolted connections for CFS moment-resisting frames has shown that their ductility and energy dissipation can significantly be improved by gradually adding intermediate folds into the flat plate sections to eventually form curved profiles (Sabbagh et al. 2012a), as shown in Figure 6.1. However, curved profiles are difficult to manufacture and connect to other elements and, therefore, more practical shapes could be developed by taking into account manufacturing and construction constraints.

While typical CFS cross-sections are generally unable to prevent the local buckling in practical seismic design, the previous research has indicated that local buckling can be postponed by

optimising the shapes of CFS profiles to allow for development of ductility and energy dissipation (Sabbagh et al. 2012a).



**Figure 6.1. Development of CFS sections towards curved flanges to increase cross-sectional ductility (Sabbagh et al. 2012a)**

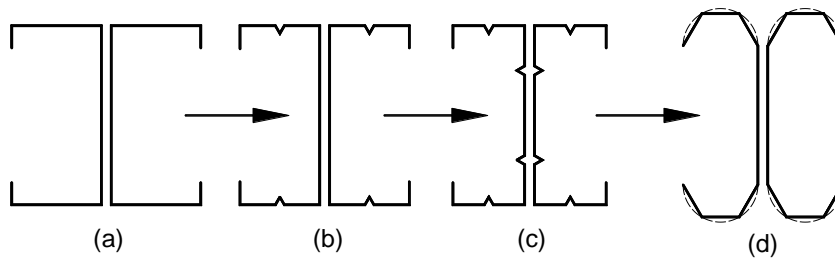
Pan et al. (Pan et al. 2007) developed an optimisation method to obtain H-beams with optimal flange shapes to increase the energy dissipation capacity of the elements under monotonic and cyclic loads. To achieve this, they combined Simulated Annealing optimisation algorithm with detailed nonlinear Finite Element Analysis. In a similar research project, Deng et al. (Deng et al. 2015) optimised the length and shape of the straight part of U-shaped dampers, working as passive control devices in hot-rolled eccentrically braced frames, to maximise their energy dissipation capacity.

The flexibility of CFS members with respect to the manufacturing and construction processes offers potential to develop cross-sections with high ductility and energy dissipation capacity. However, no research has previously been carried out on the optimisation of CFS members based on their post-buckling behaviour, ductility and energy dissipation. In this chapter, a new framework is proposed to optimise cold formed steel sections with respect to their maximum dissipated energy capacity. The relative dimensions of the cross-sections, the location and number of intermediate stiffeners and the angle of the inclined lips are considered as the main design variables. The commercially available FE program ABAQUS (ABAQUS 2011) is combined with a Particle Swarm Optimisation (PSO) algorithm to conduct the optimisation. During the optimisation process, the efficiency of the design solutions is investigated by using non-linear detailed FE models including the effects of imperfections.

## 6.2 Development of optimum CFS sections for seismic applications

In seismic design of hot-rolled steel members, the width-to-thickness ratios of the compressive plate assemblies of the cross-sections are often restricted in code of practice (AISC 341-05 2005 and CEN 2008) to avoid local buckling before yielding, therefore allows for the development of plastic deformations. It is, however, almost impossible for typical CFS cross-sections to satisfy the width-to-thickness ratios stipulated in the seismic design code. Nevertheless, due to the flexibility in their manufacturing process, intermediate stiffeners and lips as well as additional

folds can be easily rolled into CFS cross-sections. As a result, the flat width-to-thickness ratios of the plate assemblies of the CFS cross-sections can be significantly reduced.



**Figure 6.2. Reduction of the width-to-thickness ratio by using intermediate stiffeners and folding the flanges**

Figure 6.2 illustrates a number of typical CFS sections that are generally easy to be manufactured and connected to other members and/or floor systems. It also indicates a process in which the flat width-to-thickness ratios of a conventional back-to-back CFS channel beam plate assemblies (Figure 6.2(a)) are reduced by gradually including intermediate stiffeners and bends in the cross-sections. Since the normal stress is maximum in the flange of CFS beam elements under bending, the intermediate stiffeners were introduced first in the flanges as shown in Figure 6.2(b). The web typically has high width-to-thickness ratio under the stress gradient and therefore intermediate stiffeners can be also added to the web to delay local buckling (see Figure 6.2(c)). The folded-flange cross-section shown in Figure 6.2(d) provide reduced width-to-thickness ratios and therefore can be used as a good replacement for the curved sections.

An analytical design model was developed in Chapter 5 for the flexural design of the folded-flange cross-section, where the effective width method in EC3 was extended to deal with the possible occurrence of multiple distortional buckling modes. To show the efficiency of the folded-flange cross-sections, an optimisation method was conducted to maximise the flexural strength of CFS C sections with different shapes using the Particle Swarm Optimisation (PSO) algorithm.

It is shown in Figure 5.12 that for the same amount of material, the optimised folded-flange section can provide a bending capacity which is up to 57% higher than other standard optimised shapes. More information about the adopted optimisation process can be found in Chapter 5. In the current study, the efficiency of the folded-flange sections in terms of energy dissipation capacity is investigated.

### 6.3 FE analyses of CFS beam sections

As discussed before, CFS sections are susceptible to local, distortional and global buckling failure modes under serviceability loads due to the large width-to-thickness ratios of the plate assemblies. Previous numerical and experimental research studies have shown that detailed

Finite Element (FE) models can accurately predict the ultimate load carrying capacity and collapse behaviour of CFS sections if appropriate element type, material parameters and imperfection profiles are selected (Haidarali and Nethercot 2011, Yu and Schafer 2007). In this study the ABAQUS FE package (ABAQUS 2011) is used to (1) determine the flexural capacity of CFS beams and to track the load-deflection behaviour of the beam sections, and (2) search for the optimum cross-sectional shape to maximise the energy dissipation capacity of the beams. Two types of analyses have been performed in ABAQUS (ABAQUS 2011):

-Elastic Eigenvalue Buckling analysis using the linear perturbation procedure BUCKLE to capture the fundamental modal buckling shape to apply the initial imperfection.

-Nonlinear inelastic analysis using the Static General step with displacement control method, which takes into account the stiffness degradation due to buckling and material softening.

### **6.3.1 FE models**

The FE models of the CFS members were developed using an 8-node quadrilateral shell element with reduced integration (S8R). The stress-strain behaviour of CFS plates was simulated using the constitutive model presented in Section 3.4.

The effect of geometrical imperfections has been included in the FE analysis. The first buckling mode shape is used as the initial geometrical imperfection distribution (Young and Yan 2002). To this end, an elastic eigenvalue buckling analysis is first conducted on cantilever beam under end point displacement. The mode shape is then scaled and superimposed to the initial model. The amplitude of the imperfection in this study are selected according to the values recommended in (Schafer and Pekoz 1998). The magnitudes for local and distortional buckling modes are  $0.34t$  and  $0.94t$ , respectively, where  $t$  is the thickness of the profile.

The external loads were applied as imposed displacements at the end of the beam elements (see Figure 6.4). The effect of large deformations was taken into account in the FE models to simulate the post-buckling behaviour of the CFS beams.

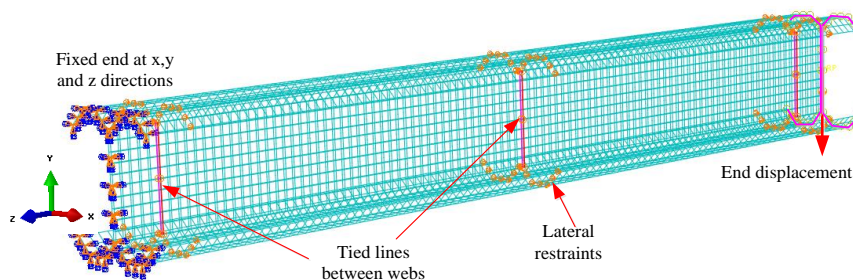
### **6.3.2 Flexural strength and post-buckling behaviour of sections**

In this section, as a procedure towards shape optimisation of the CFS beam sections, the behaviour of six different CFS beams with cross-sectional dimensions shown in Figure 6.2 was first simulated by using the nonlinear FE model described in Section 6.3.1. The selected sections include: two conventionally back-to-back lipped channel sections, two back-to-back lipped channel sections strengthened with intermediate stiffeners, one curved flange and one folded flange section. The single channels are assembled and connected by using “Tie” in the webs.

## Chapter 6. Development of optimum cold-formed steel sections for maximum energy dissipation in seismic applications

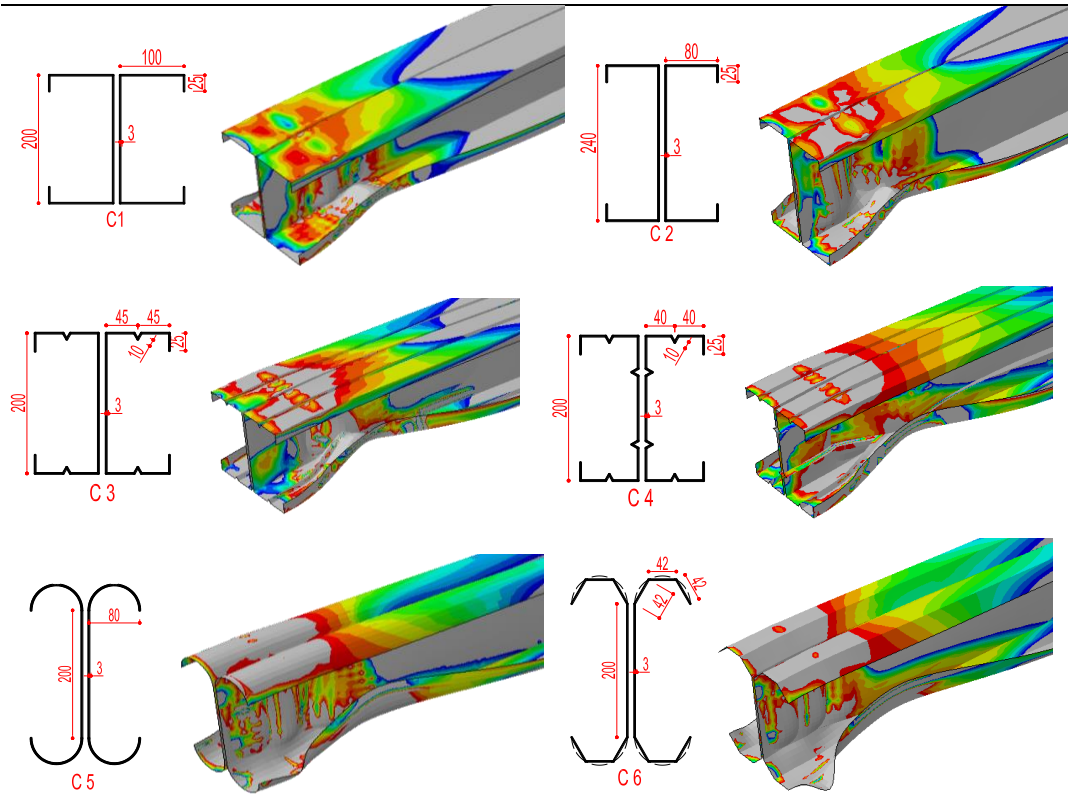
A two meter long cantilever beam was selected as representative of a four meter span beam in a laterally loaded moment-resisting frame (i.e. up to inflection point). The material model in Equation (3.4) was adopted by assuming 0.2% proof stress  $\sigma_{0.2\%} = 275 \text{ Mpa}$ . Details of the FE models including the boundary conditions, lateral restraints and the applied load are illustrated in Figure 6.4.

According to AISC Seismic Provisions (AISC 341-05 2005), Intermediate Moment Frames (IMF) and Special Moment Frames (SMF) should sustain at least 80% of their peak load carrying capacity at inter-storey drift angles of 0.02 and 0.04 rad, respectively. To check the eligibility of CFS beam sections for SMFs, a displacement of 150mm (equivalent to a drift angle of 0.075rad) was applied at the tip of the cantilever beam shown in Figure 6.3. For better comparisons, all the cross sections listed in Figure 6.4 had the same amount of material (i.e. identical coil width and thickness). Nonlinear inelastic post buckling analysis was conducted to track the load-displacement curve, by using displacement control scheme which considers stiffness degradation due to buckling. Figure 6.4 shows the failure shapes of six selected CFS beams obtained from detailed FE analysis. It is also shown that the buckling shape of curved flange and folded flange sections are very similar. The results also indicate that use of flange stiffeners could postpone the local buckling of the flange.



**Figure 6.3. Boundary conditions and loading points for the cantilever beam**





**Figure 6.4. Various cross-sectional shapes for back-to-back channel beams and their failure modes at a drift angle of 0.04rad (SMF limit)**

Figure 6.5 shows the moment rotation curves of selected beams up to a drift angle of 0.04rad. It is shown that there is a sudden loss of flexural capacity for the lipped channel C1, at a rotation less than 0.02 rad (i.e. IMF drift limit), due to the local buckling of the flanges. This is in agreement with the failure mode shown in Figure 6.5. By reducing the width of the flange and increasing the height of the section in C2, the flexural strength is improved by 19%, whereas there is no obvious benefit in the post buckling behaviour of the section. It is shown that the CFS section with intermediate stiffener in the flange (C3) has around 2% higher flexural capacity and less post-buckling strength degradation compared to the similar section without stiffener (C1). Comparison of C3 and C4 sections shows that use of the intermediate web stiffeners can improve the post buckling behaviour of the CFS section, while it has negligible effect on the flexural strength. The results shown in Figure 6.5 demonstrate again that, for the same amount of material, curved flange and folded flange sections provide the highest flexural strength compared to other sections.

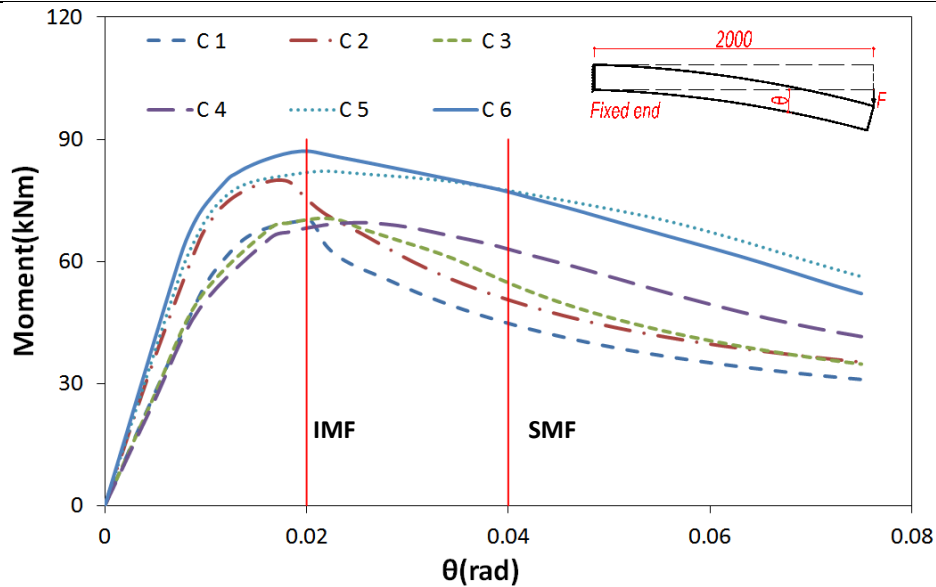
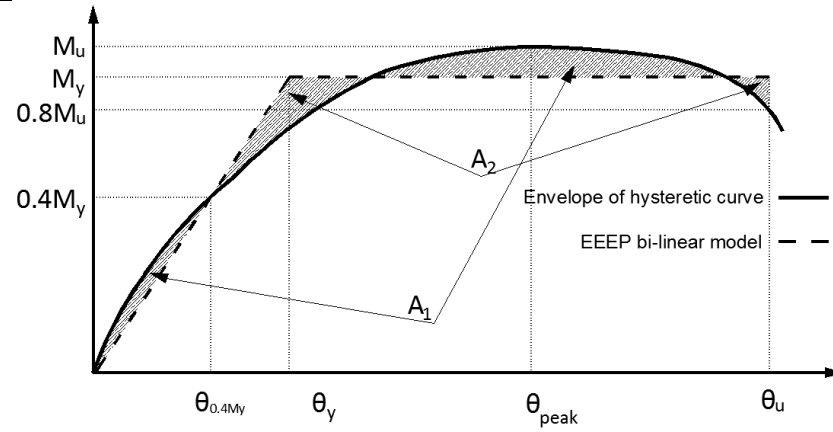


Figure 6.5. Moment-rotation curves of the beams with the dimensions in Figure 6.5

It is shown in Figure 6.5 that while C1 and C2 sections satisfy the drift requirement of IMF, they do not satisfy the SMF drift limits. Even by using intermediate stiffeners in the flange, C3 section still does not satisfy the SMF drift requirement due to buckling of the web. However, by using intermediate stiffeners in both flanges and webs (C4), the CFS section satisfies the SMF inter-storey drift angle requirement. Both curved flange (C5) and folded flange (C6) sections reach up to a rotation of 0.04 rad without significant drop of strength, which implies they both satisfy the SMF requirement.

### 6.3.3 Ductility capacity of sections

In accordance with ASTM E2126-09 (ASTM 2009), the ductility of the six selected sections was calculated using the equivalent energy elastic-plastic (EEEP) bi-linear models as shown in Figure 6.6. This model assumes an ideal elastic-perfectly plastic response of the system based on the moment-rotation response of the cross-sections. As shown in Figure 6.6, the idealized bi-linear curve includes two parts having the same areas above and below the curve ( $A_1 = A_2$ ). The elastic part of the EEEP curve is defined using initial secant stiffness ( $K_e$ ) associated with the moment equal to 40% of the idealised yield moment of the cross-section. The second segment line and the post-yield slope is then specified by a line passing through the point corresponds to 20% drop of the peak moment in the softening branch.

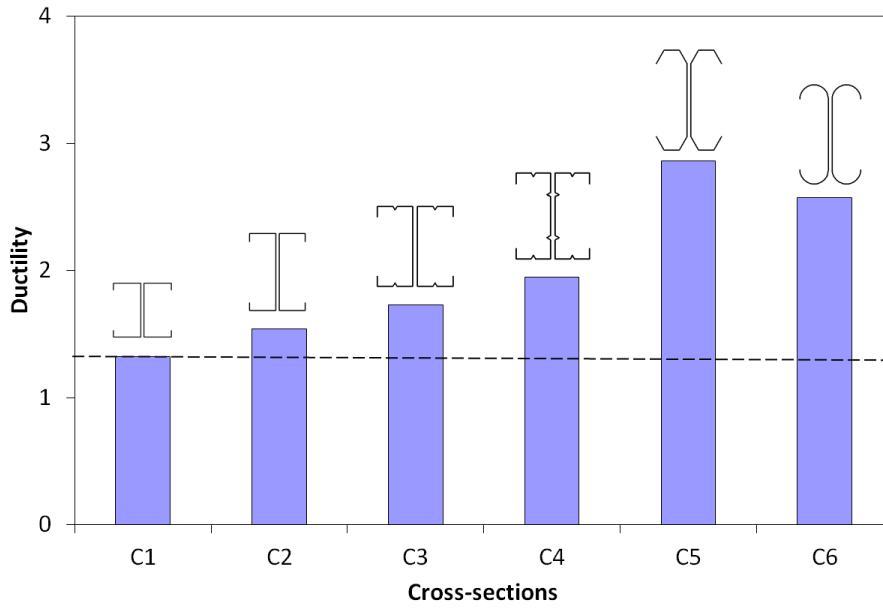


**Figure 6.6. Equivalent energy elastic-plastic (EEEEP) bi-linear models of the load-deformation curve (ASTM 2009)**

To investigate the effect of cross sectional shape on the ductility of the CFS beams, the moment rotation curves are used to calculate the ductility of the CFS sections based on the following equation:

$$\mu = \frac{\theta_u}{\theta_y} \quad (6.1)$$

where  $\theta_y$  is defined as the yield displacement based on the equivalent bi-linear curve and  $\theta_u$  is the rotation corresponding to the 80% of the peak bending moment in the post buckling range as shown in Figure 6.6. The ductility of the six selected beam sections (with the specification shown in Figure 6.4) is compared in Figure 6.7. The results indicate that, in general, using intermediate stiffeners in the flange can increase the ductility of the CFS beam sections by to 36% compare to the standard section. Additional intermediate stiffener in the web can further increase the ductility of the section by another 37%. It can also be seen that, for the same amount of material, curved flange and folded flange sections exhibit more than two times higher ductility compared to the standard channel sections.



**Figure 6.7. Ductility of the 6 selected CFS beams with the same amount of material**

It is worth mentioning that there is no significant difference between C5 and C6 in terms of strength and ductility even though there is a more complex manufacturing process for the curved flange cross-section C5, as stated in Section 6.2. This makes the folded flange sections as the best practical optimum solutions.

### 6.3.4 Energy dissipation capacity of sections

The failure of CFS beam elements under monotonic and cyclic loads usually starts by the flange local buckling in compression side followed by the web buckling and finally the fracture of the flanges (Calderoni et al. 2009, Padilla-Llano et al. 2014). Based on the previous research studies, the energy dissipation capacity of CFS beams is not negligible if sufficient ductility is provided (Calderoni et al. 2009). In general, the results of this study demonstrate that the energy dissipation capacity of CFS sections can be considerably improved by adding intermediate stiffeners and shape optimisation. Since the fracture of steel is mostly related to the equivalent plastic strain, in this study this parameter is used as the failure criterion for optimisation of CFS members towards maximum energy dissipation. The equivalent plastic strain  $\varepsilon_p(t)$  (EP) can be defined as following (Ohsaki and Nakajima 2012):

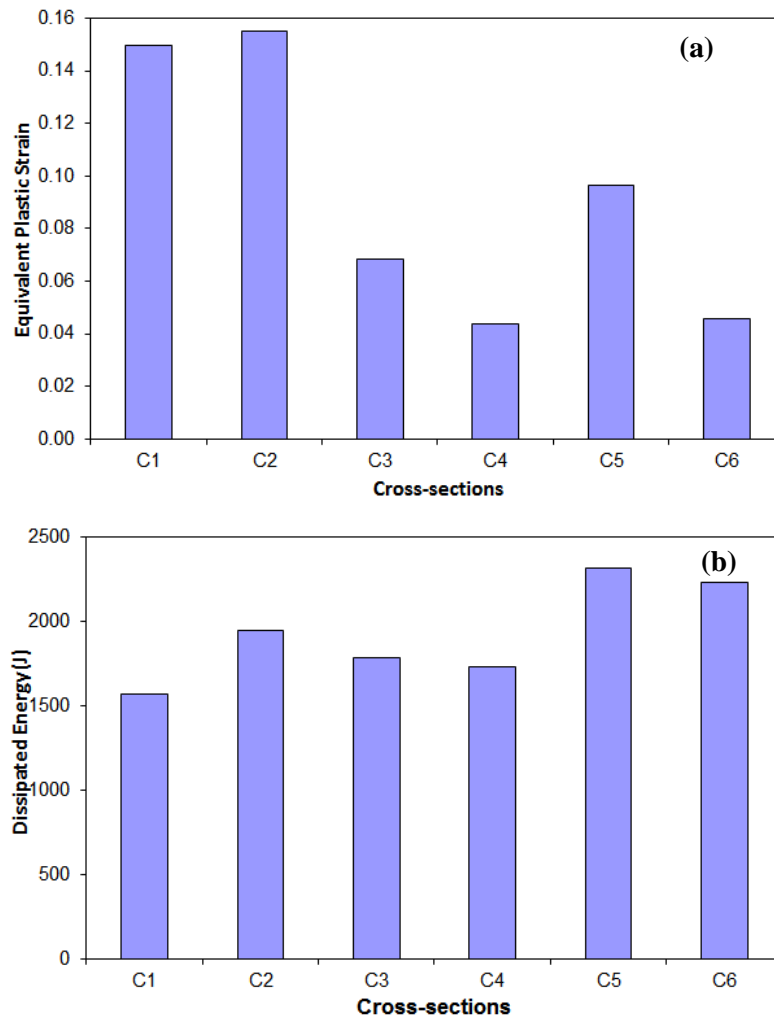
$$\varepsilon_p(t) = \int_0^t \sqrt{\frac{2}{3} \dot{\varepsilon}_{ij}^p(\tau) \dot{\varepsilon}_{ij}^p(\tau)} d\tau \quad (6.2)$$

where  $\varepsilon_{ij}^p(\tau)$  is the plastic strain tensor and  $(\dot{\cdot})$  is the derivative with respect to time. In this study, the Von Mises yield criterion is used as the yield surface. The magnitude of the equivalent plastic strain reflects the plastic rotational deformation capacity of the members and it is

evaluated at each integration point in FE analysis. The equivalent plastic strain can be used to evaluate the ultimate plastic rotation and the ductility of CFS members. Here the energy dissipation through plastic deformations is calculated in ABAQUS by using the following equation:

$$E = \int_V \int_0^t \sigma_{ij}(\tau) \dot{\epsilon}_{ij}^p(\tau) d\tau dV \quad (6.3)$$

where  $\sigma_{ij}$  is the plastic strain tensor. Figure 6.8 compares the equivalent plastic strains and energy dissipation capacity of the six selected CFS beam sections at the drift ratio of 4%. It is shown that, in general, the conventional lipped channels (C1 and C2) exhibited higher equivalent plastic strains compared to other sections.



**Figure 6.8. Comparison of (a): maximum equivalent plastic strain; (b): Energy dissipation capacity**

By adding the intermediate stiffeners in the flanges and webs (C3 and C4), the equivalent plastic strains were significantly reduced though the amount of energy dissipated was not considerably improved. The curved section (C5) dissipated the most amount of energy, while its

maximum plastic strain demand was considerably smaller than that of the conventional lipped channels. It is shown in Figure 6.8 that the folded flange cross-section (C6) has the potential to have a high energy dissipation capacity (almost similar to the curved section), while it exhibits minimum equivalent plastic strains. This is in agreement with the ductility results presented in the previous section.

In general the results presented in Figure 6.8 indicate that the post-buckling behaviour of CFS beam elements can be changed significantly by adjusting the dimensions and incorporating features such as intermediate stiffeners, inclined lips and bends.

## 6.4 Formulation of optimisation problem and optimisation method

This section aims to develop optimised cross-sectional shapes for CFS beams to have maximum energy dissipation capacity, which is especially important for seismic applications. A commercially available lipped channel section is taken as the starting point, whereas the optimisation process allows for the addition of inclined lips, rolled-in intermediate stiffeners in flange and web, and the folds of the plate to form more complex cross-sections. A folded flange cross-section is also considered in the optimisation process, since it was shown in Section 6.3 that, in general, the folded flange cross-section has the potential to dissipate higher energy levels with minimum plastic strain demands. The members are optimised with regard to their maximum energy dissipation capacity, determined according to the results from detailed FE modelling considering geometric and material nonlinearity. All plate slenderness limit values and all limits on the relative dimensions of the cross-sectional components, set by the Eurocode, are taken into account as constraints on the optimisation problem.

### 6.4.1 Problem formulation

A cantilever beam is considered which is fully fixed at one end and loaded at the other end, as shown in Figure 6.9. The length of the beam is  $l=1400\text{mm}$  that represents the distance between inflection points of a beam length of 2800 mm in a moment resisting frame. The optimal cross-sectional dimensions can be found for the beams subjected to a static loading defined by the end displacement at the tip as discussed before (see Figure 6.3).

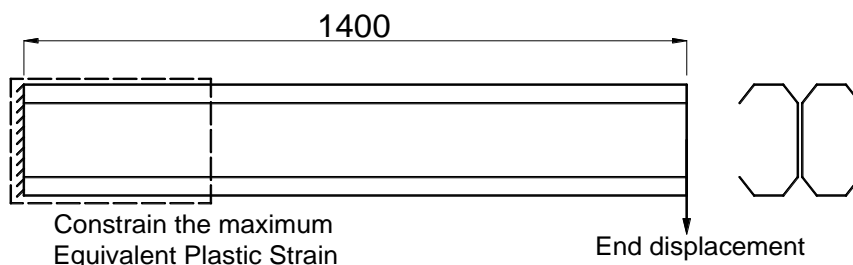


Figure 6.9. A cantilever beam model for optimisation process

In this study, the design variables were the dimensions and the angles of the plate assemblies as shown in Table 6.1. The same amount of material was used for all cross sections (i.e. same plate width). For practical applications, the selected cross sections were prequalified shapes according to EC3. The relative plate slenderness and limit values on the relative dimensions of the cross-sections were set as the design constraints during the optimisation process.

The optimisation procedure was aimed at optimising each CFS cross-section with regard to its energy dissipation capacity throughout the loading history until the drift ratio of 4% (i.e. SMF limit). Therefore, the optimisation problem was formulated to maximise the dissipated energy  $E(\mathbf{X})$  as follows:

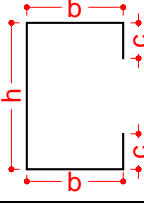
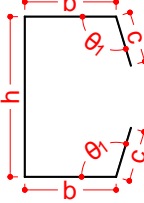
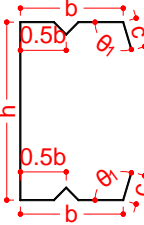
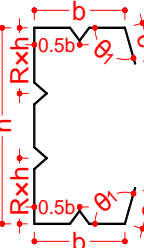
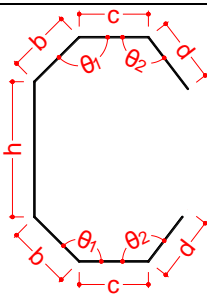
$$\max \quad E(\mathbf{X}) \quad (6.4)$$

$$s.t. \quad \varepsilon_p(\mathbf{X}) \leq \bar{\varepsilon}_p \quad (6.5)$$

$$x_i^L \leq x_i \leq x_i^U, \quad (i = 1, \dots, n) \quad (6.6)$$

where  $\mathbf{X}$  denotes the vector consisting the cross-sectional dimensions.  $\mathbf{X}^U$  and  $\mathbf{X}^L$  indicate the upper and lower bounds of the design variable vector, respectively. The components of vectors are indicated with subscript, such as  $\mathbf{X} = [x_1, \dots, x_n]$ , where  $n$  is the number of the design variables. The upper bound  $\bar{\varepsilon}_p$  in Equation (6.5) is the maximum allowable equivalent plastic strain  $\varepsilon_p$  of CFS steel material to prevent fracture under tensile loads.

**Table 6.1. Selected prototypes, design variables and constraints**

Prototype	Prototype section	Design variables	Constraints based on EC3	Comments
①		$x_1=c/b$ $x_2=b/L$	$0.2 \leq c/b \leq 0.6$ $b/t \leq 60$ $c/t \leq 50$ $b/t \leq 500$	EN1993-1-3 Clause 5.2
②		$x_1=c/b$ $x_2=b/L$ $x_3=\theta_1$	$0.2 \leq c/b \leq 0.6$ $b/t \leq 60$ $c/t \leq 50$ $b/t \leq 500$ $\pi/4 \leq \theta_1 \leq 3/4\pi$	EN1993-1-3 Clause 5.2
③		$x_1=c/b$ $x_2=b/L$ $x_3=\theta_1$	$0.2 \leq c/b \leq 0.6$ $b/t \leq 60$ $c/t \leq 50$ $b/t \leq 500$ $\pi/4 \leq \theta_1 \leq 3/4\pi$	EN1993-1-3 Clause 5.2
④		$x_1=c/b$ $x_2=b/L$ $x_3=R$ $x_4=\theta_1$	$0.2 \leq c/b \leq 0.6$ $b/t \leq 60$ $c/t \leq 50$ $b/t \leq 500$ $\pi/4 \leq \theta_1 \leq 3/4\pi$ $0.1 \leq R \leq 0.4$	EN1993-1-3 Clause 5.2
⑤		$x_1=\theta_1$ $x_2=\theta_2$ $x_3=b$ $x_4=c$ $x_5=d$	$b/t \leq 500$ $7/12\pi \leq \theta_1 \leq 5/6\pi$ $\pi/4 \leq \theta_2 \leq 3/4\pi$ $30 \leq b \leq 48$ ; $50 \leq c \leq 60$ ; $15 \leq d \leq 60$	--

In total, 5 different prototypes were considered in this study with the same thickness of  $t = 1.5\text{mm}$  and total coil width of  $L = 415\text{mm}$ , as shown in Table 6.1. The yielding stress  $f_y$ , elastic modulus  $E$  and Poisson's ratio  $\nu$  were  $450\text{MPa}$ ,  $210\text{GPa}$  and  $0.3$ , respectively. The start point of the optimisation was set to be the standard commercially available channel C1 (with lip=17mm, flange=75mm, depth=231mm and thickness=1.5 mm). The optimisation process allowed for the inclined lips, flange and web triangular intermediate stiffeners and folded flanges. The position of the triangular intermediate stiffeners in the webs was varied during the optimisation process to investigate their effects on the energy dissipation capacity of the sections. The intermediate stiffeners consisted of two 10 mm legs with an intersecting angle of  $60^\circ$ . To investigate the effect of plasticity development on the energy dissipation capacity of



the sections, four levels of plastic strain  $\bar{\varepsilon}^p = 0.2, 0.15, 0.1$  and  $0.07$  were used as the upper bound range in Equation (6.5). The upper bound of plastic strain is generally depended on different steel grades. These plastic strain values were based on the coupon tests reported in (Quach and Huang 2011). It should be noted that these plastic strain limits are based on monotonic coupon test without taking into account the cyclic effect.

#### 6.4.2 Optimisation technique

The purpose of the optimisation in this study was to demonstrate that the shape optimisation can be effectively applied to increase the energy dissipation capacity of CFS beams subjected to large deformations. The optimisation framework in this study was based on the result of detailed FE models by taking into account geometrical and material nonlinearities and imperfections, using a Particle Swarm Optimisation (PSO) method. The PSO method has been described in Section 3.3.

The optimisation constraints in Equation (6.5) was incorporated by using a penalty function. Assume a penalty factor  $\eta > 0$ , the objective function  $E(\mathbf{X})$  is then transformed to:

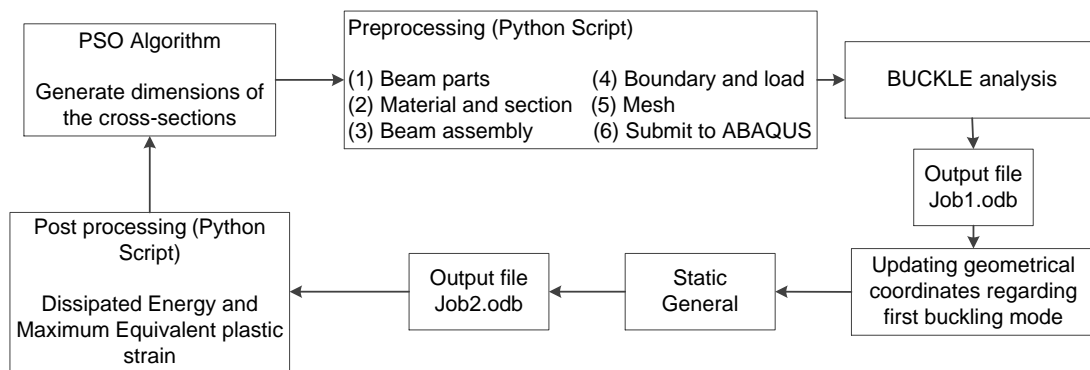
$$\tilde{E}(\mathbf{X}) = E(\mathbf{X}) - \eta \max\left[0, \varepsilon_p(\mathbf{X})/\bar{\varepsilon}_p - 1\right] \quad (6.7)$$

The flowchart of the proposed optimisation method to link the detailed FE models in ABAQUS (ABAQUS 2011) to the PSO algorithm in Matlab (Mathworks 2011) is Figure 6.10. For each generation, the PSO algorithm generates new input data for the CFS cross-sections (i.e. new design value vectors). This data is then transmitted to ABAQUS pre-processing module (ABAQUS 2011) for creation of the cantilever beam model shown in Figure 6.3. The entire FE analysis was programmed using Python script language by taking into account the non-linear inelastic behaviour of material and the effects of imperfections (ABAQUS 2011). The Python script (Appendix A.6) consisted of the following steps:

- (1) The FE model of the cantilever beam is developed according to the dimensions generated from PSO algorithm using the material properties calculated from Equation (6.1). The load and boundary conditions are then applied to the FE model.
- (2) An elastic linear BUCKLE analysis in ABAQUS is conducted. The normalized displacements of each node in the first buckling mode are extracted and used for the incorporation of the initial geometrical imperfection. The displacement field is then scaled and applied to the initial meshed geometry to form the initially imperfect model for Standard Static analysis. Since the first buckling mode is either local or distortional, which is unknown, an unfavourable imperfection (0.94 times of thickness) is used (Schafer and Pekoz 1998).

- (3) The Standard solver of ABAQUS is then used for the nonlinear FE analysis. The necessary data such as dissipated energy  $E(\mathbf{X})$  and maximum equivalent plastic strain  $\varepsilon^P(\mathbf{X})$  are extracted from the ABAQUS output files using the post processing module.
- (4) The extracted data from previous step are then returned to the PSO algorithm and new particle swarm is generated according to Equations (3.3) and (3.4). Subsequently, a new round of iteration is started from step 1.

The PSO algorithm was developed separately in Matlab (Mathworks 2011) and was adopted to perform the optimisation process. The number of iterations was taken as 100 for all prototype sections. To obtain good convergence, the population of the particle swarm was set to 10 for prototypes ① to ③, while this was 15 for prototypes ④ and ⑤ to accommodate more design variables. The maximum and minimum inertial weight factors were chosen as 0.95 and 0.4, respectively. Due to the high computational efforts required, the non-linear analyses were conducted on iceberg, the University of Sheffield High Performance Computing server.



**Figure 6.10. Flowchart of optimisation for maximum dissipated energy**

As an example, Figure 6.11 illustrates the iteration history of prototype ⑤ subjected to the restraint of equivalent plastic strains of  $\bar{\varepsilon}^P = 0.2, 0.15, 0.1$  and  $0.07$ . The results demonstrate the good convergence of the proposed optimisation method to obtain the best design solution in all cases. It is shown that there is no obvious increase to the objective value (i.e. energy dissipation capacity) after around 60 generations, which confirms the adequacy of the number of iterations used in this study.

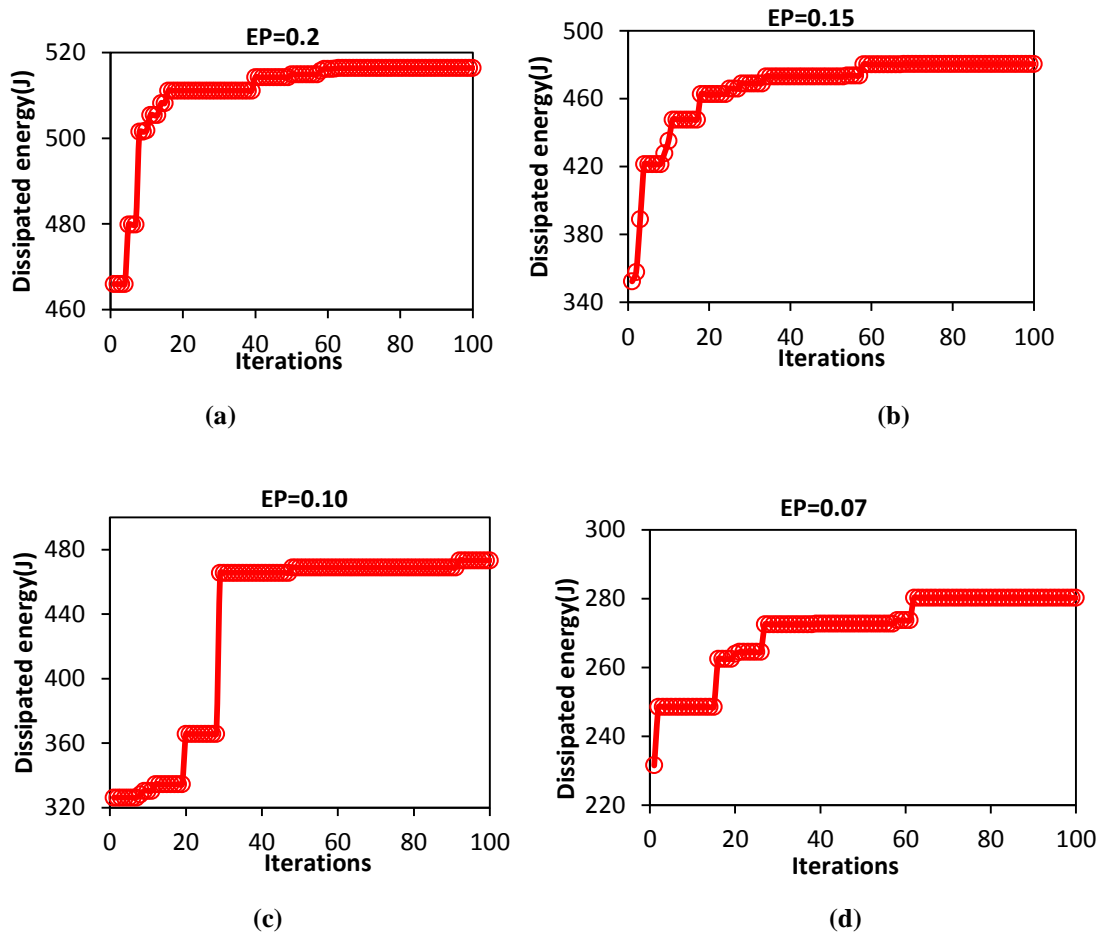


Figure 6.11. Iteration history of the objective of dissipated energy for folded flange channel section

## 6.5 Optimisation results and discussions

The selected prototypes in this study were aimed at investigating the effects of changing geometric dimensions of the cross-section and the positions of the edge and intermediate stiffeners (see Table 6.1). Optimal dimensions of the cross-sectional prototypes were found under monotonic loading condition and the optimum results were compared with those of the standard lipped channel section with the same amount of material. Optimal shapes corresponding to the constrained plastic strains of  $\bar{\epsilon}^P = 0.2, 0.15, 0.1$  and  $0.07$  are shown in Table 6.2.

**Table 6.2. Dimensions and energy dissipation capacity of optimum design CFS cross-sections using different prototypes**

Prototypes	$\bar{\varepsilon}^p$	$h(mm)$	$b(mm)$	$c(mm)$	$d(mm)$	$R$	$\theta_1$	$\theta_2$	$E(J)$
Standard	0.2	231	75	17	--	--	--	--	329
Type ①	0.2	256	50	30	--	--	--	--	404
	0.15	226	73	22	--	--	--	--	378
	0.1	187	78	36	--	--	--	--	323
	0.07	150	83	49	--	--	--	--	255
Type ②	0.2	228	59	35	--	--	79	--	405
	0.15	218	62	36	--	--	130	--	395
	0.1	212	66	36	--	--	59	--	376
	0.07	149	83	50	--	--	87	--	255
Type ③	0.2	207	61	28	--	--	96	--	503
	0.15	226	50	30	--	--	113	--	496
	0.1	216	58	27	--	--	89	--	496
	0.07	131	89	38	--	--	98	--	280
Type ④	0.2	205	50	25	--	0.23	92	--	528
	0.15	235	50	10	--	0.32	95	--	494
	0.1	196	50	30	--	0.22	91	--	493
	0.07	198	51	28	--	0.37	131	--	295
Type ⑤	0.2	176	48	50	21	--	135	57	516
	0.15	164	46	51	28	--	132	104	480
	0.1	155	39	53	39	--	116	101	473
	0.07	146	33	56	46	--	102	94	280

It is shown in Table 6.2 that the optimal shapes depend significantly on the selected plastic strain limit  $\bar{\varepsilon}_p$ . For better comparison, Figure 6.12 compares the energy dissipation capacity of the optimum sections as a function of maximum plastic strain limit. It is shown that, in general, increasing  $\bar{\varepsilon}_p$  leads to higher energy dissipation capacity levels especially for the lipped channel sections (Types ① and ②). The reason is that by using higher  $\bar{\varepsilon}_p$  limits, optimum sections can develop more plastic deformations in the post buckling range. It can be noted that increasing  $\bar{\varepsilon}_p$  beyond 0.15 does not considerably increase the energy dissipation capacity of the CFS sections. This is attributed to the fact that at the IMF drift ratio of 4%, the maximum equivalent plastic strains in most prototypes are close to the upper-bound limits, which makes this design constraint less critical.

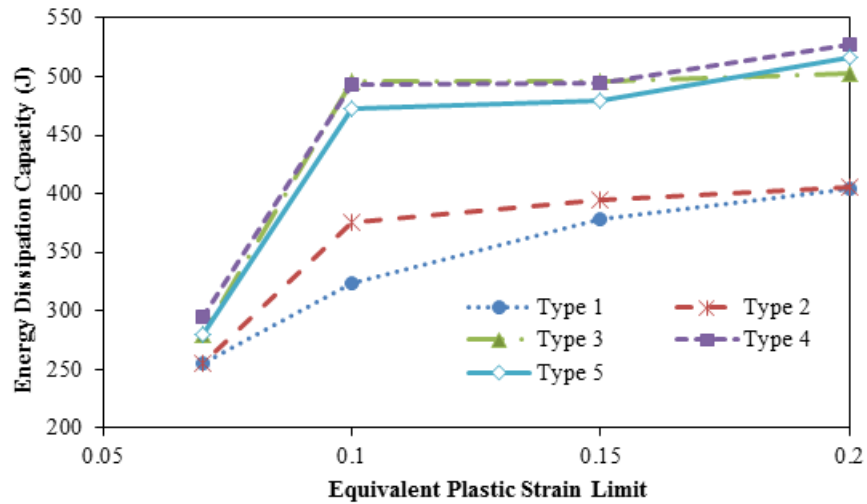


Figure 6.12. Energy dissipation capacity of optimum sections versus maximum plastic strain limit

Based on the results in Table 6.2, for typical lipped channels (prototype ① and ②), by increasing the equivalent plastic strain limits, the flange width of the optimal shape decreases while the height of the cross-sections increases. This can increase the energy dissipation capacity of the cross-sections in two ways: (a) By postponing the buckling of the flange due to using smaller width to thickness ratio ; and (b) Increases the extent of the plastic zone for a given drift ratio.

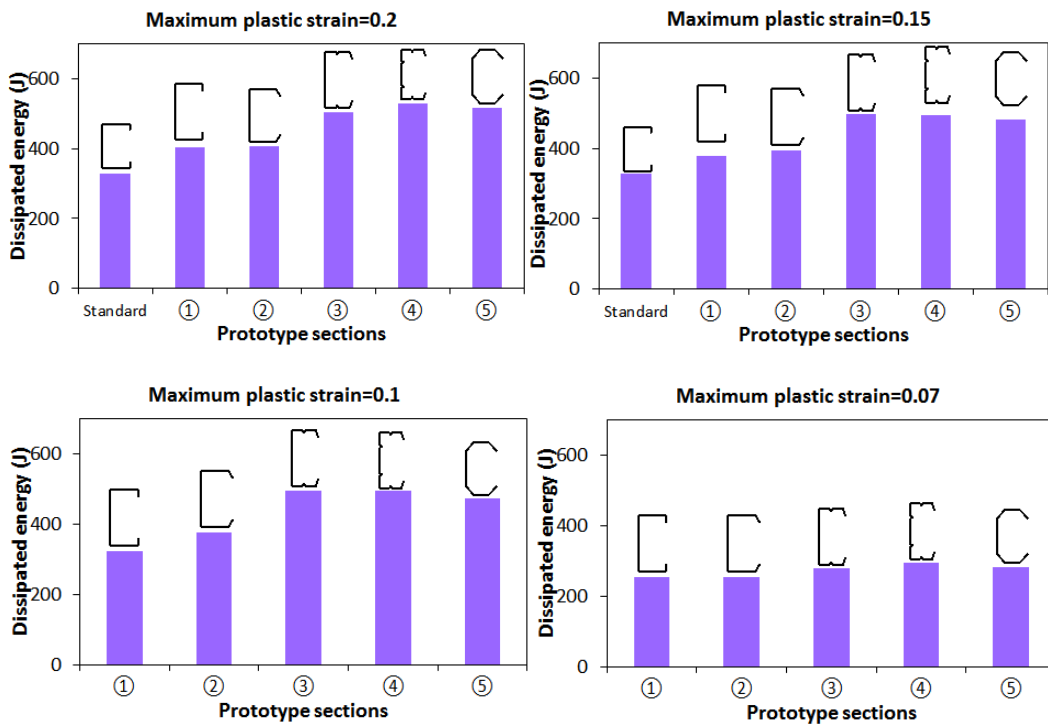


Figure 6.13. Maximum energy dissipated of prototypes subjected to various maximum plastic strain constraints at 4% drift ratio

To further demonstrate the efficiency of different prototypes, Figure 6.13 compares the energy dissipation capacity of the optimum sections, subjected to various maximum plastic strain limits,

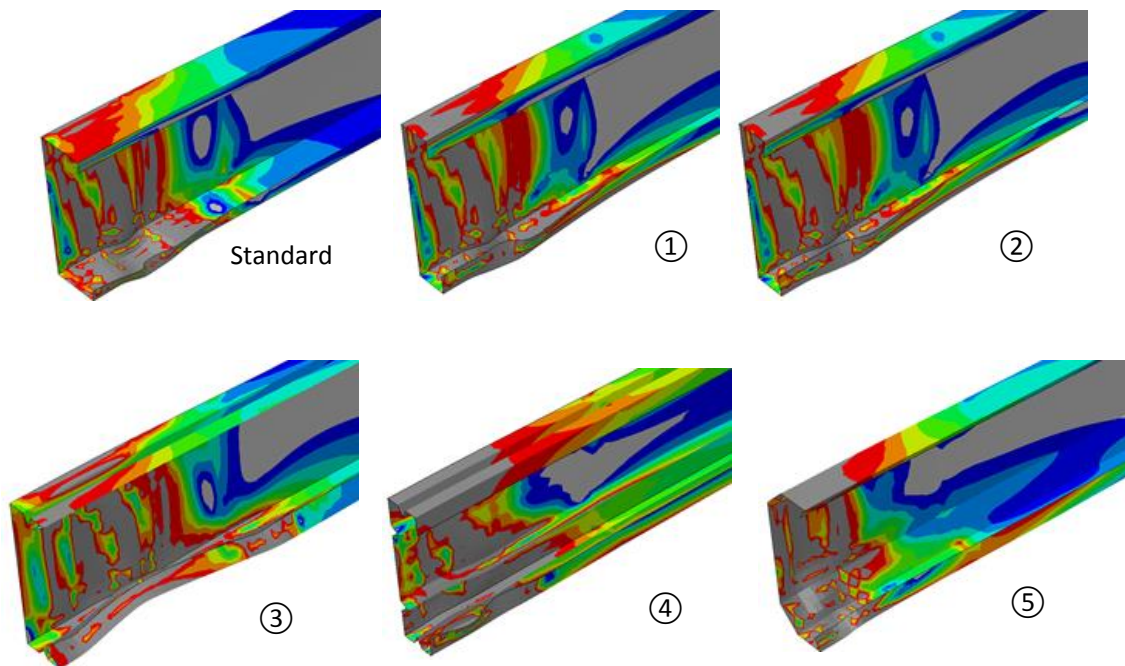
compared to a standard commercially available section shown in Table 6.2 (first row). It should be noted that the dissipated energy of the standard section is not shown for maximum plastic strain limits of 0.1 and 0.07, since this section does not satisfy the maximum strain limits at the drift ratio of 4%. The following general observations can be made from the optimum dissipated energy results in Figure 6.13:

- For low maximum plastic strain limits (i.e.  $\bar{\epsilon}_p = 0.07$ ), the effect of cross-sectional shape on the energy dissipation capacity of the sections is negligible. The main reason is that these sections cannot develop high plastic deformations due to the strictly restrained plastic strain limits.
- The results show around 23% improvement in the energy dissipation capacity of optimum lipped channel section (prototype ①) compared to the standard section. This implies that significant gains in the energy dissipation capacity of lipped channel sections can be achieved by adjusting the dimensions of the web, the flange and the lip. By relaxing the turned angle of lips in simple lipped channels, however, only an additional increase of 0.4% is achieved in the energy dissipation capacity of the optimum channel section (prototype ②).
- It is shown that using intermediate stiffeners in the flanges will increase the energy dissipation of the optimum lipped channel sections by 30% (prototype ③). By comparing the energy dissipated between prototypes ③ and ④, it is shown that there is no significant improvement by incorporating intermediate stiffeners in the web.
- The results indicate that the newly developed folded-flange section dissipated 28%, 27%, 16% and 10% more of energy than the optimal lipped channel section under plastic strain limitations of 0.2, 0.15, 0.1 and 0.07, respectively. Only a minor maximum reduction of 4% was observed by comparing the results of the folded-flange section (prototype ⑤) with prototypes ③ and ④. However, the number of bends to form prototype ⑤ is only 6, which is much smaller than 10 and 15 bends required for prototype ③ and ④, respectively. The folded-flange sections are also easy to connect to typical floor systems and, hence, are ideal candidates for practical CFS beam sections.

The optimal shapes and their distribution of von Mises stresses corresponding to  $\bar{\epsilon}_p \leq 0.2$  are shown in Figure 6.14, where the dark grey colour represents von Mises stress larger than 450 MPa. It is shown that by optimising the dimensions of the lipped channel section, the plastic area in prototype ① is considerably increased in the flange. This leads to a significant improvement of the energy dissipation capacity of the channel section as discussed before. However, when the lip-flange angle was considered as a design variable in the optimisation process, the plastic region did not considerably change in prototype ②. This conclusion is in

agreement with the energy dissipation results presented in Figure 6.13. By adding intermediate stiffeners in the flanges, it is shown that the plastic region is expanded in both flanges and web in prototype ③. The plastic region is further expanded by adding an intermediate stiffener in the web, as shown in the stress distribution pattern of optimal prototype ④. It is also clear from Figure 6.14 that the plastic region in prototype ⑤ was developed uniformly in both flanges and web, whereas was smaller than the plastic region in prototypes ③ and ④. This can explain the reason that the amount of energy dissipated by prototype ⑤ was slightly smaller than prototypes ③ and ④ as discussed in the previous section.

The results of this study, in general, indicate that the adopted optimisation method based on the post-buckling behaviour of CFS elements is robust and can considerably improve their ductility and energy dissipation capacity. These performance parameters are especially important for seismic design of CFS structural systems, where structures are expected to exceed their elastic limits in severe earthquakes.



**Figure 6.14. Distribution of von Mises stress of standard and optimal beams subjected to  $\bar{\epsilon}_p \leq 0.2$  at drift ratio of 4%**

## 6.6 Conclusions

A procedure is presented in this chapter to obtain optimised channel sections for maximum plastic dissipated energy for seismic applications. The EC3 design restraints were considered to reduce the design space. Five different prototypes were considered, including a standard lipped channel section, a channel section with inclined lips, a channel section with intermediate stiffeners in the flanges, a channel section with intermediate stiffeners in both web and flanges, and finally a folded-flange cross-section. A PSO algorithm was developed and linked to the

ABAQUS finite element programme for inelastic post-buckling analysis and optimisation. Optimal shapes were obtained for CFS beams using different prototypes. According to the results of this study, the following conclusions can be drawn:

- (1) Use of intermediate web stiffeners can improve the post buckling behaviour of CFS sections, while their effects are negligible on flexural strength. The results indicate that, for the same amount of material, curved flange and folded flange sections provide the highest flexural strength compared to other alternatives.
- (2) In general, using intermediate stiffeners in the flange can considerably (up to 36%) increase the ductility of the CFS beams. Additional intermediate stiffener in the web can increase the ductility of the section by around 70% compared to the standard one. For the same amount of material, curved flange and folded flange sections can provide more than two times more ductility compared to their standard counterparts.
- (3) The amount of dissipated energy in CFS beam elements is increased with increasing the equivalent plastic strain limit  $\bar{\varepsilon}_p$ , especially for the lipped channel sections. However, increasing  $\bar{\varepsilon}_p$  beyond 0.15 does not considerably affect the energy dissipation capacity of the sections.
- (4) Only by optimising the web, flanges and lip dimensions of a lipped channel section, the dissipated energy can be increased up to 23%. By relaxing the turned angle of lips, only a negligible gain of 0.4% will be achieved.
- (5) Placing a stiffener in the compressive flange of simple optimum lipped channel section can increase the energy dissipation capacity of the optimum solution by 30%. However, no obvious change was observed in the energy dissipation capacity of the optimum sections by placing an intermediate stiffener in the web. By optimising the shape of CFS beam sections, in general, the plastic area of the beams was significantly increased.
- (6) The folded-flange section, for the same amount of material, dissipates 28%, 27%, 16% and 10% more energy than the optimal lipped channel section under plastic strain limits of 0.2, 0.15, 0.1 and 0.07, respectively. This emerge the folded flange sections as the best optimum solutions for seismic applications.



## **CHAPTER 7. Experimental investigations on CFS channel columns considering interactive buckling**

---

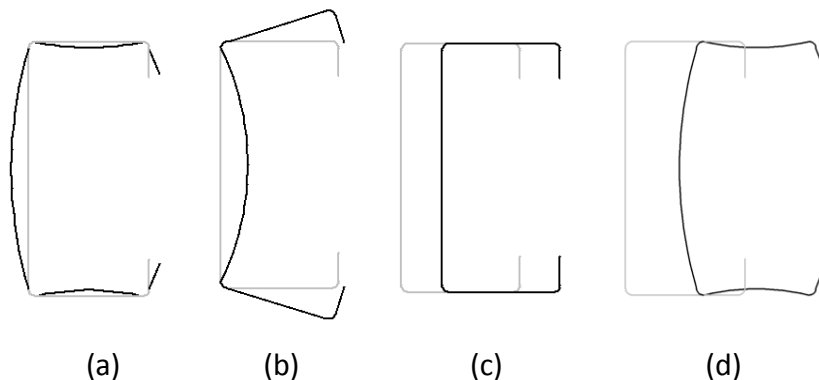
This chapter describes an experimental programme carried out at the University of Sheffield to investigate the design and optimisation, considering interaction of local/ overall buckling in cold-formed steel plain and lipped channels under axial compression. The design of the members to local/distortional and overall buckling was according to Eurocode 3, Part 1-3. Plain and lipped channel sections with a thickness of 1.5 mm and depths ranging from 125 to 200mm were tested under compression. The specimen imperfections were measured using a specially designed set-up with laser displacement transducers and the imperfections were statistically analysed. Material tests were also carried out to determine the tensile properties of the flat plate and of the cold-worked corners.

A total of 36 column tests with three lengths were completed with the aim of investigating the design allowing for local and overall buckling interaction. Four types of cross-sections were considered, these cross-sections were manufactured using the same coil width and thickness.

The specimens were tested under a concentrically applied load and with pin-ended boundary conditions.

## 7.1 Introduction

Cold-formed steel (CFS) cross-sections can be found in a wide range of applications in secondary load-carrying members, such as roof purlins and wall girts. In recent years, however, CFS cross-sections are also increasingly being employed as primary structural elements in low- to mid-rise multi-storey buildings (Fiorino et al. 2014) and CFS portal frames with short to intermediate spans (Lim and Nethercot 2004b, Lim and Nethercot 2003). Compared to hot-rolled members, CFS thin-walled members offer several advantages of economy and efficiency, including a high strength for a light weight, a relatively straightforward manufacturing process and an ease of transportation and erection. However, CFS framing components currently have the inevitable limitation of thin thickness, which make them susceptible to local, distortional, global buckling and their interaction, as shown in Figure 7.1. The steel sheet with thinner thickness requires more efforts to develop the design rules for more efficient design. This emphasizes the importance to investigate the complex failure modes and assess available mainstream design specifications in order to achieve optimal design of CFS elements.



**Figure 7.1. Buckling modes of a lipped channel: (a) local, (b) distortional, (c) global and (d) interactive modes.**

Experimental investigations of the ultimate strength of CFS columns have previously been conducted on plain and lipped channel columns with pin ended (Young and Rasmussen 1999, Young and Rasmussen 1998, Zhang et al. 2007b) and fixed ended boundary conditions (Young 2004, Young 2008a). More recently, CFS channel columns with intermediate web stiffeners and complex edge stiffeners have been tested with pin ended boundary conditions (Wang et al. 2016c).

The experimental work presented in this chapter is part of a wider study into the optimisation of CFS members (shown in Chapter 3-5), which is why all four cross-sections in the test programme were manufactured using the same coil width and thickness. However, the

experimental results are here presented independently of their wider context, as the results by themselves provide valuable data about the interactive buckling behaviour of CFS columns. A comparison with the relevant Eurocode 3 design guidelines (CEN 2005a, CEN 2005b, CEN 2005c) is also carried out.

In Chapter 3, Figures 3.6 and 3.7 shows that the simple prototype of lipped channel (prototype ④) possesses relatively high strength which is an excellent choice for application when the required length is not less than 2m. Apart from that, the simple lipped channel is more economical and efficient in terms of manufacturing process, which can be more acceptable for cold-rolling production. The purpose of the test is to: (a) provide verification on the optimisation framework proposed in Chapter 3; (b) calibrate a more reliable FE model for future application on more efficient CFS structural design and (c) verify the accuracy of design procedures adopted in EC3 which can be crucial in the optimisation process.

The experimental investigation included 36 tests on CFS channel columns, which were all performed at the Heavy Structures Laboratory at the University of Sheffield. All specimens failed by the interaction of local instability and flexural buckling about the minor axis. With respect to the boundary conditions, all columns were tested between hinged end plates which were allowed to rotate about the minor axis of the channel.

## 7.2 Specimen geometry

Four different cross-sections were considered in the test programme, of which the nominal dimensions are presented in Figure 7.2. The dimensions were measured between outer surfaces. All cross-sections had the same nominal thickness  $t = 1.5\text{mm}$  and the same total developed length (or coil width)  $l = 337\text{mm}$ .

The four types of cross-sections were labelled A-D, as shown in Figure 7.2. For each cross-section, three different lengths were considered:  $L_e = 1.0\text{m}, 1.5\text{m}$  and  $2.0\text{m}$ . Three columns were tested for each cross-section and length, in order to assess statistical variation and increase confidence in the results, amounting to a total of 36 specimens. Table 7.1-Table 7.4 list the measured dimensions of the test specimens, using the nomenclature illustrated in Figure 7.2. The reported dimensions are average values of multiple measurements. The symbol  $r$  is the radius of the rounded corner along the outer skin of the plate.  $L$  is the length of the column. Each specimen is labelled according to its cross-section (A, B, C or D), followed by the nominal length of the column in  $\text{mm}$  and 'a', 'b' or 'c', indicating the repeat tests.

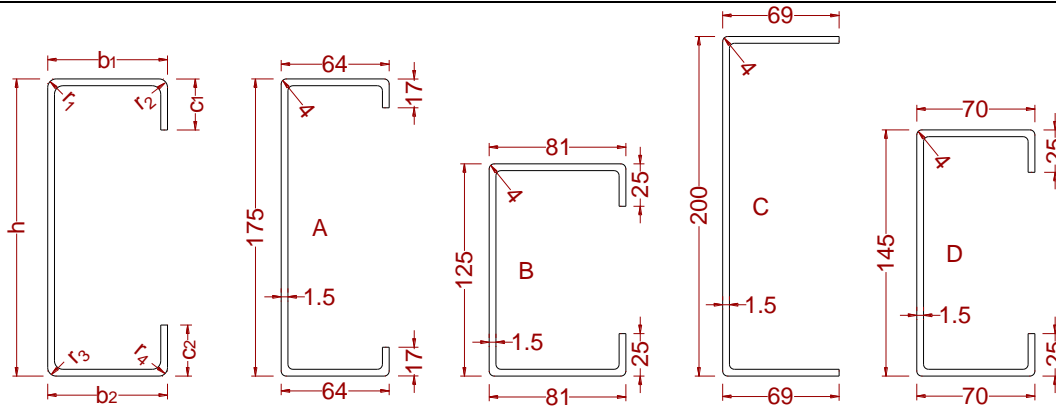


Figure 7.2. Symbol definitions and nominal cross-sectional dimensions

Table 7.1. Measured dimensions of specimens with cross-section A (mm)

Specimen	$L$	$r$	$t$	$h$	$b_1$	$c_1$	$b_2$	$c_2$
A1000-a	1000.1	4.2	1.51	174.94	64.45	17.72	64.09	18.21
A1000-b	1000.0	4.0	1.52	174.85	64.23	17.76	64.13	17.62
A1000-c	1000.0	4.1	1.50	174.89	64.27	17.82	64.12	17.51
A1500-a	1499.8	4.3	1.53	175.23	64.35	17.80	64.15	17.82
A1500-b	1500.0	4.1	1.50	174.97	63.84	18.50	63.68	17.03
A1500-c	1500.0	4.0	1.53	174.90	64.17	17.74	64.24	17.46
A2000-a	1999.8	4.1	1.52	175.62	63.86	18.86	64.09	18.11
A2000-b	2000.0	4.1	1.50	175.40	64.12	17.48	64.10	17.98
A2000-c	2000.1	4.0	1.51	175.33	64.74	18.57	64.23	16.77
Average		4.1	1.52	175.13	64.22	18.03	64.09	17.61
St. deviation		0.1	0.01	0.28	0.28	0.48	0.16	0.48

Table 7.2. Measured dimensions of specimens with cross-section B (mm)

Specimen	$L$	$r$	$t$	$h$	$b_1$	$c_1$	$b_2$	$c_2$
B1000-a	1000.2	4.2	1.52	125.07	81.15	25.91	81.15	25.60
B1000-b	1000.0	4.0	1.52	125.19	80.74	25.69	80.74	25.31
B1000-c	1000.1	4.3	1.48	125.27	81.13	25.70	80.74	25.41
B1500-a	1500.0	4.1	1.51	125.06	81.08	26.00	80.64	25.60
B1500-b	1500.4	4.3	1.52	125.11	81.09	26.55	80.60	25.46
B1500-c	1500.1	4.0	1.53	125.24	80.74	25.94	80.88	26.51
B2000-a	2000.1	4.3	1.49	125.26	80.75	25.65	80.94	26.44
B2000-b	2000.3	4.0	1.52	125.42	81.83	26.09	81.56	24.94
B2000-c	2000.1	4.2	1.52	125.31	81.68	26.16	81.06	25.73
Average		4.2	1.51	125.22	81.13	25.96	80.92	25.67
St. deviation		0.13	0.02	0.12	0.40	0.28	0.30	0.51

**Table 7.3. Measured dimensions of specimens with cross-section C (mm)**

Specimen	$L$	$r$	$t$	$h$	$b_1$	$b_2$
C1000-a	1000.1	4.2	1.53	199.84	69.23	69.47
C1000-b	1000.1	4.3	1.52	199.60	69.30	70.32
C1000-c	999.8	4.0	1.53	199.85	69.53	69.44
C1500-a	1500.0	4.1	1.53	199.87	69.48	70.44
C1500-b	1500.1	3.9	1.53	199.66	70.30	69.43
C1500-c	1500.2	3.8	1.52	199.90	69.83	69.53
C2000-a	2000.4	4.2	1.51	199.82	70.55	69.52
C2000-b	2000.3	4.1	1.52	199.83	70.50	69.52
C2000-c	2000.0	4.0	1.49	199.92	69.57	69.48
Average		4.1	1.50	199.80	69.80	69.70
St. deviation		0.16	0.01	0.11	0.51	0.40

**Table 7.4. Measured dimensions of specimens with cross-section D (mm)**

Specimen	$L$	$r$	$t$	$h$	$b_1$	$c_1$	$b_2$	$c_2$
D1000-a	1000.0	4.2	1.49	145.13	70.09	25.73	70.25	25.94
D1000-b	1000.2	4.1	1.51	144.90	70.43	24.60	70.47	26.82
D1000-c	1000.1	4.1	1.52	145.39	69.89	25.64	70.62	25.46
D1500-a	1500.2	4.0	1.51	145.28	69.97	25.29	70.72	25.76
D1500-b	1500.1	3.9	1.54	145.41	69.92	25.74	70.83	25.88
D1500-c	1500.0	4.2	1.52	145.34	69.92	26.01	70.62	25.87
D2000-a	2000.3	4.3	1.49	145.62	69.88	25.40	70.69	25.55
D2000-b	2000.0	4.1	1.52	145.30	69.84	25.50	70.31	26.55
D2000-c	2000.1	4.0	1.52	145.42	70.54	26.46	70.27	25.00
Average		4.1	1.5	145.30	70.10	25.6	70.50	25.90
St. deviation		0.12	0.02	0.20	0.26	0.51	0.21	0.55

**Table 7.5. Critical buckling stress and buckle half-wave length for nominal cross-sections A-D**

Sections	Buckle half-wave length (mm)		Buckling stress (MPa)		Tested buckling stress (MPa)
	Local	Distortional	Local	Distortional	
A	130	600	80.2	167.0	87.1
B	100	920	148.0	268.1	140.7
C	240	--	45.4	--	40.0
D	110	880	113.8	265.7	104.8

The software package CUFSM (Schafer 2006), which implements the finite strip method for elastic analysis, was used to determine the elastic buckling stresses of each cross-section type. The results are listed in Table 7.5. It is seen that the local buckling stress is critical for all cross-sections, while it is always smaller than the yield stress. The distortional buckling stress lies well above the local buckling stress for all cross-sections. Table 7.5 also compares the tested buckling stress to the values obtained through CUFSM (Schafer 2006), it is shown that the tested buckling stress has been well predicted by CUFSM (Schafer 2006).

### 7.3 Material properties

All specimens were manufactured using a conventional brake pressing process. Tensile coupons were cut from the flat portions of all four cross-section types in order to determine their material properties (Figure 7.3(a)). For each cross-section one coupon was taken along the centre line of web and another one along the centre line of the flange. In order to investigate the effect of the cold-working process on the material properties, coupons were also cut from the rounded corner zones. The corner coupons were tested in pairs in order to avoid eccentric loading (Figure 7.3(b)). All coupons were taken in the longitudinal direction from the end zones of the 1500 mm long columns after testing. The stresses during testing remained sufficiently low to justify this (Table 7.5). The coupons were tested in accordance with the specifications of the relevant European standard (ISO 2009). Table 6 lists the values of the Young's modulus ( $E$ ), the 0.2% stress ( $\sigma_{0.2\%}$ ) and the tensile strength ( $\sigma_u$ ) resulting from the tests.

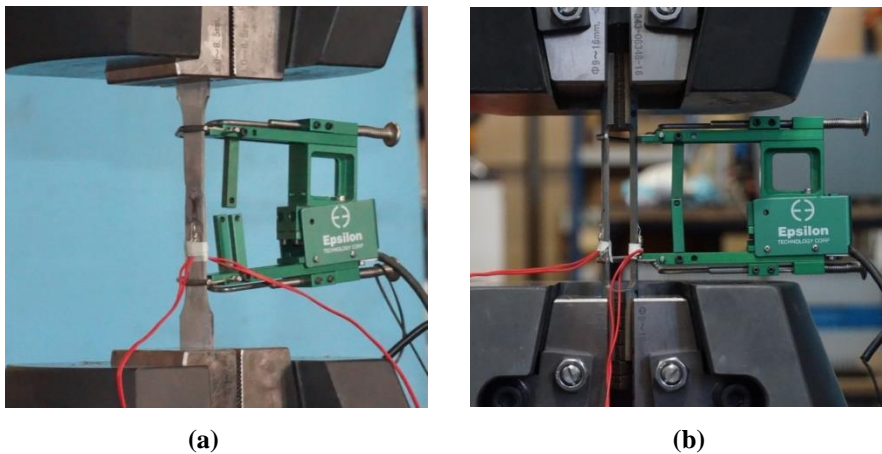


Figure 7.3. Tensile material tests for: (a) flat coupons (b) corner coupons

**Table 7.6. Tensile properties of the flat and corner regions**

Sections	Coupon	Type	$E$ (MPa)	$\sigma_{0.2\%}$ (MPa)	$\sigma_u$ (MPa)
A1500A	A01F	Flat	196057	447.0	599.6
	A02F	Flat	195355	448.5	599.1
	A03C	Corner	221076	525.8	614.2
	A04C				
B1500A	B01F	Flat	196194	440.3	606.9
	B02F	Flat	203486	441.2	594.9
	B03C	Corner	211164	529.6	613.3
	B04C				
C1500B	C01F	Flat	208443	453.1	609.6
	C02F	Flat	205302	459.0	621.5
	C03C	Corner	218921	530.7	592.4
	C04C				
D1500A	D01F	Flat	200226	453.9	611.8
	D02F	Flat	193743	448.5	603.2
	D03C	Corner	205742	525.6	600.0
	D04C				

## 7.4 Imperfection measurements

The stability of thin-walled CFS members may in some cases be significantly affected by the presence of imperfections, especially when coupled instabilities are involved. The magnitude and the shape of the imperfections of each specimen were therefore recorded before testing.

The set-up shown in Figure 7.4 was used to measure the imperfections. A laser was mounted on an aluminium cross beam, which was moved in the longitudinal direction of the frame at constant speed by an electrical motor. A second electrical motor allowed the laser to move in a perpendicular direction along the aluminium beam, thus enabling the laser to cover a rectangular surface area. The laser was able to measure the distance to the surface of the specimen with an accuracy of 0.0075 mm. The laser moved along high precision bars with minimal tolerances and its ability to maintain a level measuring plane was verified against measurements of the nominally flat table underneath in the absence of a test specimen. This flat table was guaranteed to be grade 3, providing a surface with a deviation from flatness of less than 0.06 mm (Standard 2008). During the measuring process, the translational speed of the laser was set at 5 mm/s while the sampling rate was 5 Hz, resulting in one reading every one millimeter.

The imperfections were measured along five lines for individual cross-section, as shown in Figure 7.5. The readings recorded along the lines of ①, ② and ③ indicated the imperfections relating to the overall flexural buckling and the local buckling of the web. The readings along lines ④ and ⑤ whereas provide data on the imperfections affecting the distortional buckling

Chapter 7. Experimental investigations on CFS channel columns considering interactive buckling mode. The maximum imperfections encountered in the webs of the channels were of the order of  $0.95\text{ mm}$ , while the flange tips of the plain channels displayed imperfections of up to  $1.60\text{ mm}$ .

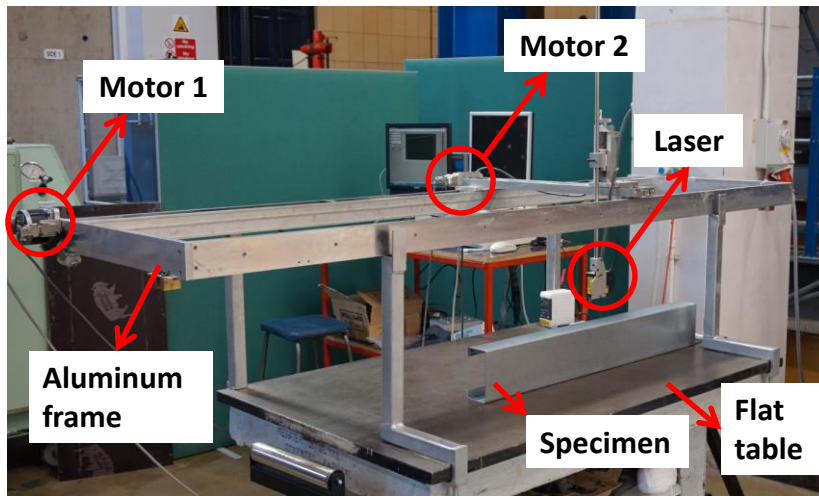


Figure 7.4. Imperfection measurement set-up

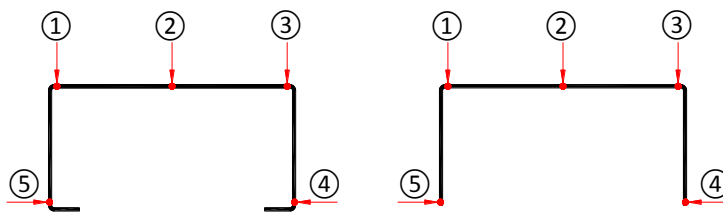


Figure 7.5. Location of the imperfection measurement



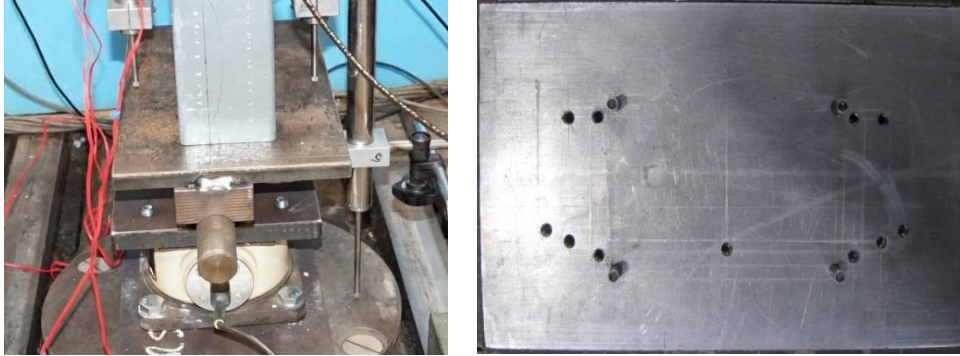
**Table 7.7. Maximum amplitudes of local, distortional and overall imperfections in tested columns**

Specimen	Local	Distortional	Overall
A1000-a	0.33	0.22	0.17
A1000-b	0.25	0.14	0.24
A1000-c	0.41	0.32	0.18
A1500-a	0.54	0.38	0.18
A1500-b	0.41	0.26	0.24
A1500-c	0.26	0.41	0.27
A2000-a	0.95	0.90	0.96
A2000-b	0.45	1.30	0.23
A2000-c	0.79	1.02	0.54
B1000-a	0.30	0.38	0.29
B1000-b	0.32	0.26	0.26
B1000-c	0.31	0.28	0.27
B1500-a	0.42	0.69	0.31
B1500-b	0.27	0.46	0.29
B1500-c	0.41	0.72	0.29
B2000-a	0.41	1.03	0.26
B2000-b	0.33	1.02	0.27
B2000-c	0.51	1.03	0.22
C1000-a	0.34	0.52	0.28
C1000-b	0.24	0.63	0.19
C1000-c	0.15	0.49	0.12
C1500-a	0.31	0.74	0.22
C1500-b	0.40	0.86	0.16
C1500-c	0.42	0.78	0.27
C2000-a	0.26	1.60	0.24
C2000-b	0.17	1.57	0.19
C2000-c	0.64	1.29	0.17
D1000-a	0.22	0.31	0.21
D1000-b	0.35	0.29	0.17
D1000-c	0.23	0.34	0.22
D1500-a	0.37	0.50	0.20
D1500-b	0.40	0.62	0.22
D1500-c	0.23	0.56	0.19
D2000-a	0.27	1.43	0.31
D2000-b	0.68	0.83	0.27
D2000-c	0.29	1.04	0.18

## 7.5 Column tests

All 36 columns were loaded concentrically and tested between pin ended boundary conditions. Figure 7.6 illustrates the hinge assemblies used to achieve this. The location of the minor centroidal axis was scribed onto the flanges of each specimen and the same axis was also indicated on the top plates of the hinge assemblies, facilitating exact alignment. Four steel dowels were bolted into the top plates as an additional measure in order to hold the corners of the channel in place and prevent possible slippage Figure 7.6 illustrates the holes to

accommodate the dowels for all four cross-section types. The distance between the horizontal axis of the hinge and the top surface of the plate was measured to be 44 mm. Thus, the effective length  $L_e$  of each column can be calculated by adding 88 mm to the measured specimen length  $L$ .



**Figure 7.6. Specimen boundary conditions**

The ultimate capacity and the behaviour of these columns are sensitive to the value of the initial load eccentricity (Becque and Rasmussen 2009a). While the specimens had been accurately positioned in the set-up with the assistance of scribed lines and the dowels on the end plate, a selected number of specimens were also instrumented with strain gauges at mid-height in order to allow an accurate verification of the initial loading eccentricity. Figure 7.7 and Figure 7.8 illustrate the locations of those strain gauges and also the LVDTs at the mid-height to determinate the load eccentricity. It is assumed that the material of the columns behaves in a linear way before local buckling and the plane sections remains plane after bending. The eccentricity of the mid-height section  $e_0$  can therefore be calculated based on the following equations (Becque 2008):

$$e_0 = \frac{I_x}{A} \frac{\varepsilon_1 - \varepsilon_2}{y_2 \varepsilon_1 + y_1 \varepsilon_2} - \frac{D_1 + D_2}{2} \quad (7.1)$$

where  $\varepsilon_1$  is the average reading from strain gauges SG1 and SG2,  $\varepsilon_2$  is the average reading from strain gauges SG3 and SG4,  $y_1$  and  $y_2$  are the distances from the centroid of the section to the extreme fibers in compression and tension, respectively.  $I_x$  and  $A$  are the second moment of inertia around  $x$  axis and cross-sectional area, and  $D_1$  and  $D_2$  are the displacement readings from LVDTs  $M_1$  and  $M_2$ , as shown in Figure 7.7. It is noted that  $e_0 > 0$  indicates an eccentricity towards the web.

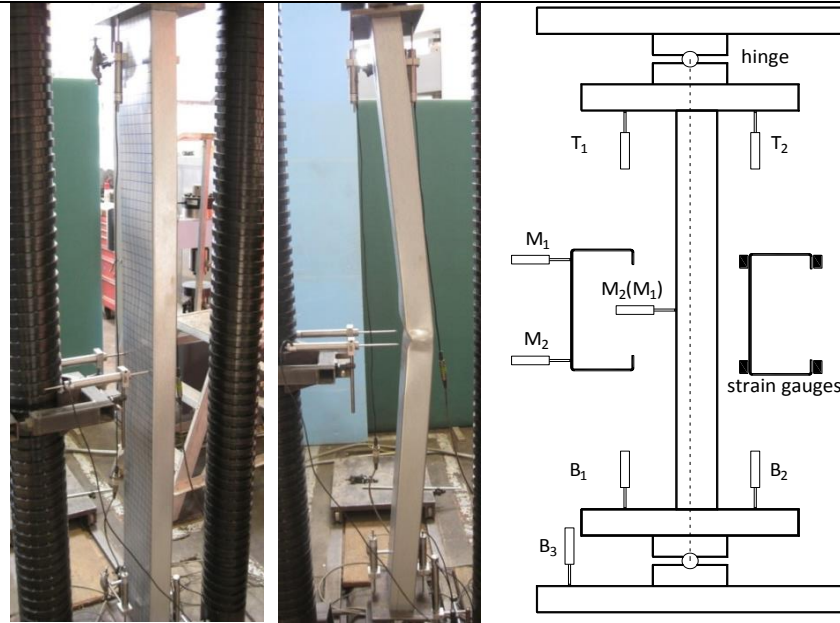


Figure 7.7. Test set-up

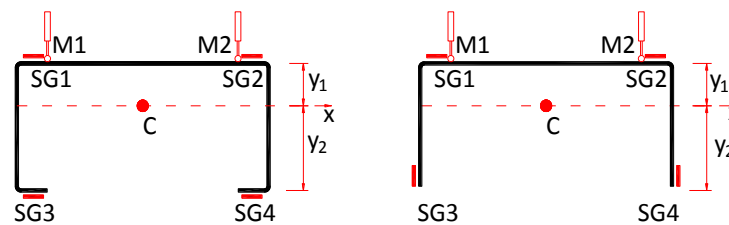


Figure 7.8. Positions of strain gauges and LVDTs at mid-height of columns

An Amsler universal testing machine with a 2000  $kN$  capacity was used to apply the compressive load, in combination with a load cell with a range of 150  $kN$ . The specimens were tested in a load control regime at a consistent rate of 5  $kN/min$ .

The experiment was terminated when the load reached less than 20% of the peak load in the descending path. The descending branch was thereby obtained through a controlled release of the hydraulic pressure.

## 7.6 Test results

All specimens were observed to exhibit local buckling first, followed by eventual failure by interaction of local and overall flexural buckling about the minor axis. No distortional buckling of any of the cross-sections was observed. Figure 7.9 and Figure 7.10 display the failed shapes of some of the specimens. In the final stage of the tests, a local plastic mechanism was seen to form with yield lines in both the web and the flanges.



Figure 7.9. Failure modes of 1000 mm long columns with section type B



Figure 7.10. Failure modes of 1000 mm long columns with section type C

Local buckling causes the effective centroid of a mono-symmetric section to shift in pin ended columns. In the tested lipped channel sections the web constituted the most slender plate element in the cross-section and, therefore, triggered local buckling, with the effective centroid consequently shifting away from the web. This was confirmed by the experimental observation that all the lipped channels bent out towards their flanges after buckling locally (Figure 7.9). In the plain channels on the other hand, the flanges were the more slender elements, leading to a shift of the effective centroid towards the web. Consequently, the plain channels consistently buckled towards the web in flexure, as shown in Figure 7.10. In this latter case, the yield line mechanism formed mainly in the flanges.

The ultimate capacities obtained for all specimens are listed in Tables 7.8-7.11 and the measured load-displacement curves of selected columns are presented in Figure 7.11. A good agreement was obtained within each set of repeat tests, with the ultimate capacities typically varying by less than 7% from the average. The dashed line shown in Figure 7.11 illustrates the buckling load levels and these values are used to calculate the tested buckling stress, which has been shown in Table 7.5.

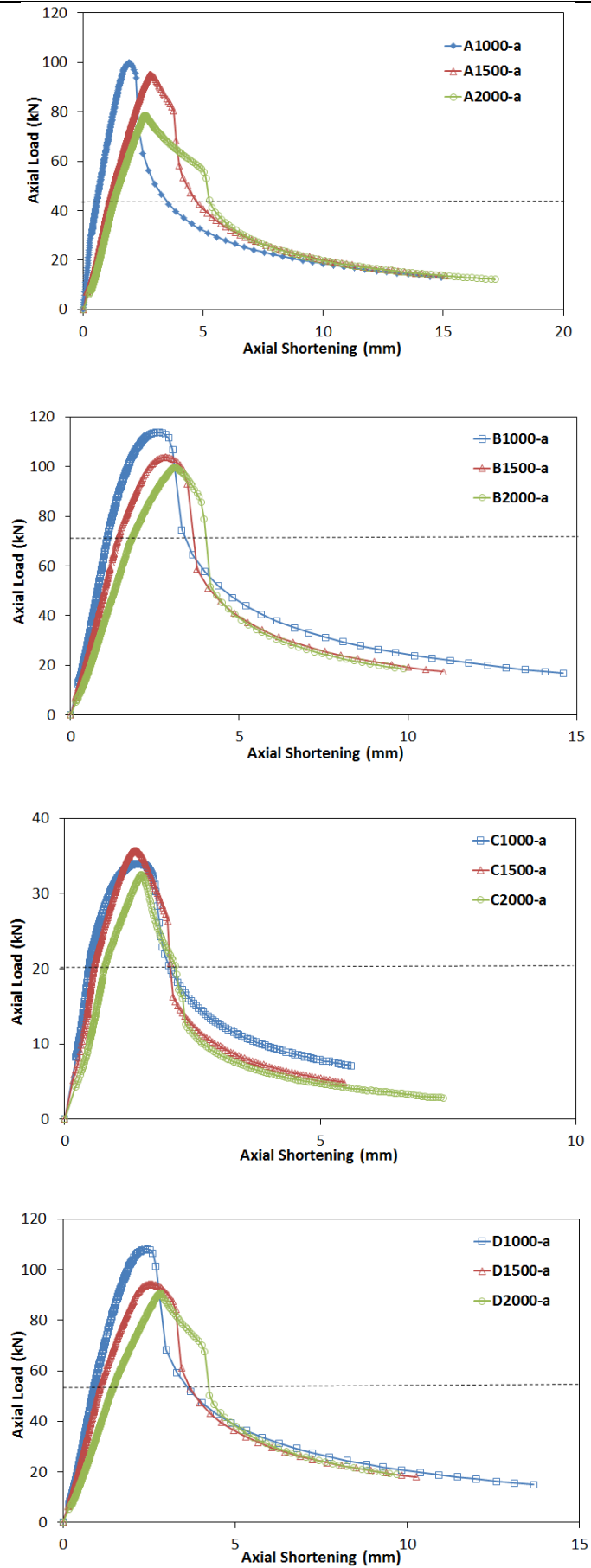


Figure 7.11. Axial load versus end shortening curves for tested specimens

**Table 7.8. Ultimate capacities of specimens with cross-section A**

Specimen	Eccentricity (mm)	Tested capacity $P_u$ (kN)	EC3 with iteration $P_{u1}$ (kN)	Shift of effective centroid $e_1$ (mm)	EC3 without iteration $P_{u2}$ (kN)	Shift of effective centroid $e_2$ (mm)	$P_{u1}/P_u$	$P_{u2}/P_u$
A1000-a	-1.742	99.8	81.6	5.3	84.2	1.1	0.82	0.84
A1000-b	X	98.3	82.5	5.3	84.6	1.3	0.84	0.86
A1000-c	X	98.7	80.6	5.3	83.2	1.07	0.82	0.84
A1500-a	-1.864	95.1	75.4	5.3	76.9	1.35	0.79	0.81
A1500-b	X	85.3	72.5	5.4	74.3	1.2	0.85	0.87
A1500-c	X	91.4	75.3	5.2	76.7	1.35	0.82	0.84
A2000-a	-1.634	78.4	64.1	5.5	65.6	1.3	0.82	0.84
A2000-b	X	75.8	62.7	5.3	64.2	1.1	0.83	0.85
A2000-c	X	88.8	63.7	5.4	65.3	1.1	0.72	0.74
Average							0.81	0.83
St. Dev.							0.04	0.04

**Table 7.9. Ultimate capacities of specimens with cross-section B**

Specimen	Eccentricity (mm)	Tested capacity (kN)	EC3 with iteration $P_{u1}$ (kN)	Shift of effective centroid $e_1$ (mm)	EC3 without iteration $P_{u2}$ (kN)	Shift of effective centroid $e_2$ (mm)	$P_{u1}/P_u$	$P_{u2}/P_u$
B1000-a	X	113.8	112.1	0.4	66.8	-6.6	0.99	0.59
B1000-b	-1.274	110.3	111.2	0.5	67.1	-6.4	1.01	0.61
B1000-c	X	107.7	107.3	0.3	62.8	-6.8	1.00	0.58
B1500-a	-1.343	103.8	99.8	0.4	61.6	-6.6	0.96	0.59
B1500-b	X	107.9	101.0	0.4	62.6	-6.5	0.94	0.58
B1500-c	X	106.2	102.0	0.4	63.6	-6.5	0.96	0.60
B2000-a	-1.436	99.6	88.2	0.3	54.6	-6.7	0.89	0.55
B2000-b	X	101.6	89.6	0.4	56.8	-6.6	0.88	0.56
B2000-c	X	105.3	90.1	0.3	56.9	-6.6	0.86	0.54
Average							0.94	0.58
St. Dev.							0.05	0.02

**Table 7.10. Ultimate capacities of specimens with cross-section C**

Specimen	Eccentricity (mm)	Tested capacity (kN)	EC3 with iteration $P_{u1}$ (kN)	Shift of effective centroid $e_1$ (mm)	EC3 without iteration $P_{u2}$ (kN)	Shift of effective centroid $e_2$ (mm)	$P_{u1}/P_u$	$P_{u2}/P_u$
C1000-a	X	33.6	24.5	-6.8	13.7	-7.4	0.73	0.41
C1000-b	+0.792	43.8	26.2	-6.7	13.8	-7.3	0.60	0.32
C1000-c	X	42.7	26.4	-6.8	13.5	-7.4	0.62	0.32
C1500-a	+0.683	36.3	21.3	-6.7	13.2	-7.3	0.59	0.36
C1500-b	X	35.2	21.1	-6.8	13.1	-7.4	0.60	0.37
C1500-c	X	37.1	22.0	-6.6	13.0	-7.4	0.59	0.35
C2000-a	+0.628	33.1	18.6	-6.8	12.3	-7.2	0.56	0.37
C2000-b	X	31.7	17.4	-6.8	12.3	-7.0	0.55	0.39
C2000-c	X	33.8	18.2	-6.8	12.2	-6.9	0.54	0.36
Average							0.60	0.36
St. Dev.							0.06	0.03

**Table 7.11. Ultimate capacities of specimens with cross-section D**

Specimen	Eccentricity (mm)	Tested capacity (kN)	EC3 with iteration $P_{u1}$ (kN)	Shift of effective centroid $e_1$ (mm)	EC3 without iteration $P_{u2}$ (kN)	Shift of effective centroid $e_2$ (mm)	$P_{u1}/P_u$	$P_{u2}/P_u$
D1000-a	X	109.0	93.5	3.1	80.4	-1.9	0.86	0.74
D1000-b	X	110.8	96.1	2.9	82	-2.0	0.87	0.74
D1000-c	-1.806	109.3	96.3	3.2	84.8	-1.7	0.88	0.78
D1500-a	-1.492	95.0	87.1	3.2	76.5	-1.9	0.92	0.81
D1500-b	X	98.2	89.9	3.3	81.8	-1.5	0.92	0.83
D1500-c	X	99.6	88.1	3.2	79.1	-1.6	0.88	0.79
D2000-a	X	90.8	74.8	3.1	66.1	-2.1	0.82	0.73
D2000-b	-1.634	97.8	77.1	3.2	71.1	-1.5	0.79	0.73
D2000-c	X	89.6	77.2	3.2	70.8	-1.75	0.86	0.79
Average							0.87	0.77
St. Dev.							0.04	0.04

Table 7.8-Table 7.11 also compare the test results with the Eurocode 3 predictions. It is noted that, when calculating the effective cross-sectional properties according to the Eurocode, full iterations were carried out (which are not strictly prescribed by the Eurocode). These iterations are necessary because the location of the neutral axis of the effective cross-section in bending is initially unknown and also because of the possible interaction between local and distortional buckling. The additional bending resulting from the shift of the effective centroid was accounted for by using the axial load-moment interaction equations in the Eurocode. The measured dimensions and the material properties obtained from the coupon tests were used in the process.

In general, Table 7.8-Table 7.11 illustrate that a reasonable agreement was achieved between the experimental and the calculated compressive capacities of the lipped channels, with the ratio of the Eurocode predicted values to the test results ranging from 0.81 to 0.94, depending on the cross-section type. Eurocode 3 is generally conservative in its predictions, especially so for the plain channel sections, for which the ratio of the predicted values to the test results was calculated to be 0.60.

As stated above, EC3 refines the effective section properties of a CFS section by updating the compressive stress in the cross-section. Table 7.8-Table 7.11 compare the results with and without considering the iteration process. All the compressive capacities were calculated by adopting the measured dimensions and material properties from the coupon tests. It is shown that, when iterations were not taken into account, the calculated compressive capacities of the tested specimens were generally more conservative than the ones with iterations. A comparison between the calculated shifts of effective centroid with and without considering the iteration process indicates that the centroid of the effective cross-section, without considering the iteration process, may shift towards the wrong direction. The fact that the centroid of effective cross-section shifts towards the wrong direction does not necessarily lead to ultimate loads on the safe side for thin-walled members.

## 7.7 Conclusions

A total of 36 channel column tests, including four different cross-section geometries and three different lengths, were carried out with the aim of investigating the interaction of local and overall flexural buckling. The specimens were tested under a concentrically applied load with pin ended boundary conditions. The specimen imperfections were measured and material tests of the flat and rounded corner regions of each cross-section type were carried out. The following conclusions can be drawn:

- (1) The tests were successful in achieving interaction between local buckling and flexural buckling about the minor axis. Good agreement was obtained within each set of three identical tests, with the ultimate loads differing by less than 7% from the average.
- (2) Additional overall bending of the specimens, resulting from a shift of the effective centroid, was observed after the appearance of a local buckling pattern. Bending thereby occurred towards the web in the plain channels and towards the flanges in the lipped channels, consistent with expectations.
- (3) A comparison between the Eurocode 3 predictions and the experimental results indicates that Eurocode 3 is generally conservative in predicting the strength of pin-ended axially compressed channel columns. The predictions are especially



conservative for plain channels, with an average ratio of the predicted to the measured capacity of 0.60.

- (4) The compressive capacities were calculated according to Eurocode 3 with and without considering the iteration process and were compared with tested results. It is found that ignoring the iteration process might lead to the effective centroid shift to the wrong direction.

This page is intentionally left in blank

## **CHAPTER 8. A numerical investigation of local-flexural interactive buckling of standard and optimised columns**

---

This chapter aims to develop a reliable numerical model to investigate the interaction of local and global buckling modes in pin-ended CFS columns. The model incorporates non-linear stress-strain behaviour and enhanced corner properties obtained from 12 coupon tests as well as initial imperfections measured by specially designed equipment. The developed FE model was verified against a program of 36 laboratory tests on CFS plain and lipped channel columns and produced excellent predictions of ultimate strength and deformation behaviour of the specimens. The validated FE model was then used to assess the adequacy of the effective width method in EC3 and Direct Strength Method (DSM) in estimating the design capacity of a wide range of conventional and optimum design CFS channel column sections.

## 8.1 Introduction

Due to their inherent weakness of thin-walled cross-section and complex buckling modes, the accurate prediction of the buckling and post-buckling behaviour of these elements becomes more difficult. Finite Element Analysis (FEA) has been widely and successfully used in the past to predict the non-linear behaviour of CFS elements. Young and Yan (Young and Yan 2002) developed a FE model to investigate the compressive strength of fixed ended CFS columns, using four node shell elements with five degrees of freedom per node. Reduced integration was used (SR4) in combination with linear perturbation analysis 'BUCKLE' to incorporate imperfection effects. Based on experimental results on CFS fixed-ended lipped channel columns, Young (Young 2004) used a nonlinear inelastic FE model to investigate the effect of inclined edge stiffeners on ultimate axial capacity. Similarly, Yan and Young (Yan and Young 2004, Young and Yan 2004) experimentally and numerically studied the ultimate capacity of fixed-ended CFS channel columns with complex stiffeners. SR4 element type in ABAQUS (ABAQUS 2011) was used by taking into account initial geometric imperfections and material non-linearity. Zhang et al. (Zhang et al. 2007b) conducted an experimental test programme on pin-ended CFS columns with perpendicular and inclined edge-stiffeners and developed FE models using four-node shell element type with six degrees of freedom at each node in ANSYS (ANSYS 2012). The rigid region at each end of the column elements was modelled with a reference point, where rotations around both strong and weak axis of the end sections were allowed. In a recent study, Wang et al. (Wang et al. 2016c) conducted a series of experimental tests on pin-ended columns with complex cross-sectional edge and intermediate stiffeners and the results were compared with the FE models similar to one proposed by Zhang et al. (Zhang et al. 2007b).

Compared with physical experiments, FEA is relatively inexpensive and time efficient, especially when a parametric study of cross-section geometry is involved. In addition, FEA is more suitable and convenient for investigations involving geometric imperfections and material nonlinearity of structural members, which could be difficult to investigate through physical tests. However, it is of crucial importance to obtain accurate and reliable FE models prior to any parametric study.

This chapter aims to investigate the local-flexural interactive buckling of CFS plain and lipped channel columns. Detailed FE models are developed in ABAQUS (ABAQUS 2011) to predict the compressive behaviour and load carrying capacity of plain and lipped channel column sections. The results of an experimental investigation including 36 tests on CFS channel columns, which failed by the interaction of local instability and flexural buckling about the minor axis, were used to validate the models. Compared to previous studies, the advantage of the developed models is to incorporate the non-linear stress-strain behaviour and enhanced

material properties based on coupon tests as well as measured initial imperfections. The models are then used to assess the adequacy of Eurocode 3 design guide lines (CEN 2005a, CEN 2005b, CEN 2005c) and Direct Strength Method (DSM) to design a wide range of conventional and optimum design CFS columns considering local/distortional and global buckling modes.

## 8.2 Direct strength method for CFS column design

Prior to the description of the numerical study, a brief induction is presented here to explain the Direct Strength Method (DSM). Eurocode 3 design guidelines to consider local, distortional and global buckling and their interaction in the compressive strength of CFS columns have been described in Chapter 3.

The Direct Strength Method (DSM) proposed in AISI (AISI 2007) is an alternative to the traditional effective width method to predict the load carrying capacity of CFS members. This method integrates a computational stability analysis into the design process. In a first step, the elastic local ( $P_{crl}$ ), distortional ( $P_{crd}$ ) and global ( $P_{cre}$ ) buckling loads are determined by using finite strip method. Using these elastic buckling loads and the load at first yield, the strength is then directly predicted based on a series of simple empirical equations. While calculation of the effective properties can be tedious for complex CFS cross-sections, only gross section properties are needed in the DSM. The elastic buckling loads of CFS members can be calculated using software such as CUFSM (Schafer 2006).

The equations for calculating the axial strength for global buckling in AISI (AISI 2007) are presented in terms of the compressive yield load  $P_y = A_g f_y$  and the non-dimensional slenderness ratio  $\lambda_c = \sqrt{P_y/P_{cre}}$ , where:

$$\begin{aligned} P_{ne} &= \left(0.658^{\lambda_c^2}\right) P_y \quad \text{for } \lambda_c \leq 1.5 \\ P_{ne} &= \left(\frac{0.877}{\lambda_c^2}\right) P_y \quad \text{for } \lambda_c > 1.5 \end{aligned} \quad (8.1)$$

The nominal axial strength of a column designed corresponding to local buckling and considering local–global interaction is related to the local–global slenderness ratio  $\lambda_l = \sqrt{P_{ne}/P_{crl}}$ , where:

$$\begin{aligned} P_{nl} &= P_{ne} \quad \text{for } \lambda_l \leq 0.776 \\ P_{nl} &= \left[1 - 0.15 \left(\frac{P_{crl}}{P_{ne}}\right)^{0.4}\right] \left(\frac{P_{crl}}{P_{ne}}\right)^{0.4} P_{ne} \quad \text{for } \lambda_l > 0.776 \end{aligned} \quad (8.2)$$

Finally, the nominal axial strength corresponding to distortional buckling is calculated as a function of slenderness ratio  $\lambda_d = \sqrt{P_y/P_{crd}}$ , where:

$$P_{nd} = P_y \text{ for } \lambda_d \leq 0.561$$

$$P_{nd} = \left[ 1 - 0.25 \left( \frac{P_{crd}}{P_y} \right)^{0.6} \right] \left( \frac{P_{crd}}{P_y} \right)^{0.6} P_y \text{ for } \lambda_d > 0.561 \quad (8.3)$$

The final axial strength of the column  $P_n$  is then determined by calculating the minimum value of axial strength values obtained from Equations (8.1) to (8.3) as follows:

$$P_n = \min\{P_{ne}, P_{nl}, P_{nd}\} \quad (8.4)$$

### 8.3 Optimisation of CFS beam-columns

An optimisation framework was proposed in order to offer practical solutions for more efficient CFS elements by the authors (Chapters 3-5). Their proposed optimisation process is capable of taking into account the interactive buckling by allowing for the effect of shift of the effective centroid induced by local buckling (see section 2). Using the same framework, in this study the following objective function is considered for optimum design of beam-column elements around weak axes:

$$\max N_{Ed} = \left( \frac{1}{(1/N_{b,Rd})^{0.8} + (e_N/M_{b,Rd})^{0.8}} \right)^{1.25} \quad (8.5)$$

subjected to:

$$b/t \leq 60, \quad c/t \leq 50, \quad h/t \leq 500 \quad (8.6)$$

$$0.2 \leq c/b \leq 0.6 \quad (8.7)$$

$$c \leq 25 \quad (8.8)$$

where  $h$  is the cross-sectional height, and  $b$  and  $c$  are the flange and lip width, respectively. Equations (8.6) and (8.7) represent the width-to-thickness ratio limits defined in EC3 (CEN 2005b). Equation (8.8) is to consider the manufacturing and construction constraints. No flexibility is offered for the lip angles in order to adapt to the typical cold-rolling machines for the stud production. The optimisation was thereby conducted for pin-ended columns with the total lengths of  $L_e = 1.0m, 1.5m$  and  $2.0m$ . Particle Swarm Optimisation (PSO) algorithm was adopted to solve the optimisation problem defined in Equations (8.5) to (8.8). More information on the PSO optimisation method can be found in Chapter 3.

The nominal dimensions of the cross-sections for the numerical study in this chapter are presented in Figure 8.1. All the dimensions in this figure are defined by the outer to outer surface. The cross-sections of the tested specimens have the same nominal thickness  $t = 1.5\text{mm}$  and coil width of steel sheet  $l = 337\text{mm}$ . The cross-section A is a standard commercially available cross-section. Sections B and C are the optimum solutions with highest axial capacity subjected to constraints in Equations (8.6) to (8.8) for lipped and plain channels, respectively. Cross-section D is a complementary section (with a flange width between the flange widths of sections A and B) used for comparison purposes. For the numerical study, these CFS column sections are considered with the lengths  $L_e = 1.0\text{m}, 1.5\text{m}$  and  $2.0\text{m}$ .

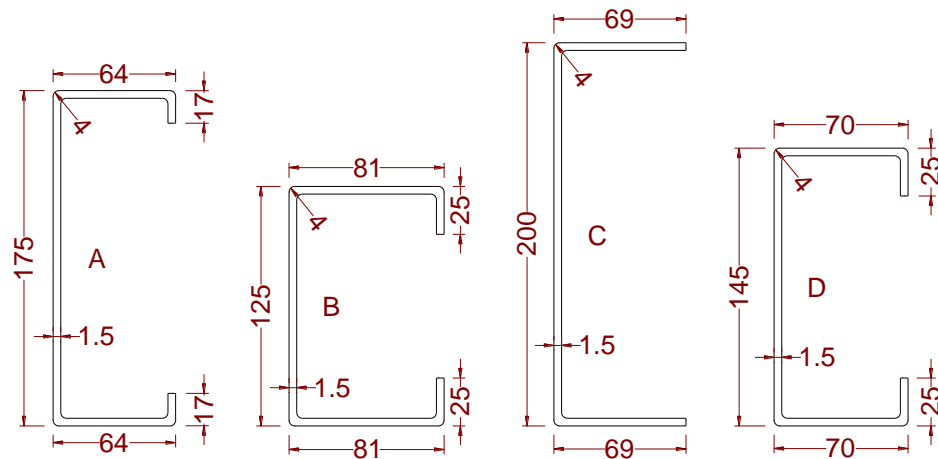


Figure 8.1. Symbol definitions and nominal cross-sectional dimensions

## 8.4 Numerical modelling

### 8.4.1 Material model

The inelastic properties of CFS material were found to have significant effects on the ultimate capacity and post-buckling behaviour of CFS elements. As a part of this study, 12 tensile coupons from the flat plates and round corner region in the cross-sections were tested in order to determine their material properties. For example, a comparison between the engineering and true stress-strain curves of a flat and a corner coupon is compared in Figure 8.2. The results indicate that the 0.2% proof stress of the corner coupon is around 24% higher than the flat coupon in the same section. A comparison between the dynamic and static stress-strain curves of the coupon specimens shows that the stress reduced by around 5–8% at yield strength and ultimate strength during the static drop, which is also called “stress relaxation” (Huang and Young 2014). The static stress-strain curves are calculated from the dynamic stress-strain curves by removing the dynamic effects of the tensile test machine. The material model was then included in the FEM by using the true stress vs true strain curve, which was calculated from the following equations:

$$\sigma_{true} = \sigma(1 + \varepsilon) \quad (8.9)$$

$$\varepsilon_{true} = \ln(1 + \varepsilon) \quad (8.10)$$

where  $\sigma$  and  $\varepsilon$  are the measured engineering stress and strain based on the original cross-section area of the coupon specimens. Tensile coupon tests were also performed in pair on smaller coupons taken from the round corner areas of the channels. The resulted stress-strain curves were incorporated into ABAQUS (ABAQUS 2011) and assigned to the rounded corner zones of the members.

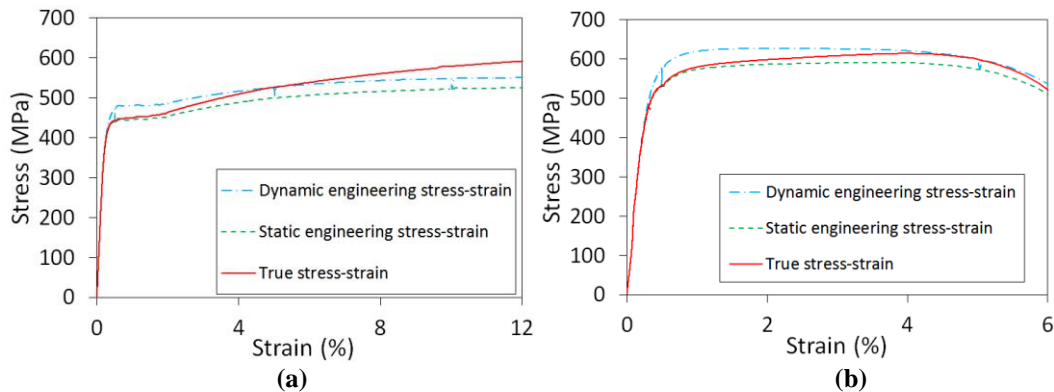


Figure 8.2. Stress–strain curves resulted from (a) flat and (b) corner coupon tests

#### 8.4.2 Boundary conditions

Four groups of cross-sectional shapes were considered including a commercially available standard lipped channel; two optimised lipped and plain channel sections and a complementary lipped channel (see Figure 8.1). The CFS elements were tested under compression with pinned end conditions, which were achieved by means of specially designed hinge assemblies shown in Figure 8.3. The distance between the centre of the roller and the hinge top plate was 44 mm. In the FE models, the hinge assemblies were modelled as 38 mm deep solid blocks with an arc-shaped groove, which were allowed to rotate about the longitudinal axis of the roller. The radius of the cylinder roller was measured 12mm. Figure 8.3 illustrates the developed FE model and the boundary conditions. The contact between the specimen and the end block was defined using a node-to-surface contact pair. The top surface of the block constituted the master surface while the edges of the channel were defined as a node-based slave surface. The contact normal to the surface was defined as “hard”, meaning that no penetration of the surfaces into each other was allowed. However, the slave nodes on the specimen were allowed to separate from the surface while no tensile stresses could be developed in the interface. The tangential properties were set to “rough”, indicating that friction restrained any tangential slip between the specimen and the hinge endplate. This reflects the actual test condition where the end sections were not allowed to expand laterally due to the Poisson effect as a result of friction. Contact pairs were also defined between the roller and the endplate using a surface-to-surface contact property.



Lubricating oil was used in order to reduce the friction effect that might produce restraints on the rotation of the endplate. Therefore, in the normal direction of the contact surface, “hard” property was used while in the tangent direction between the roller and the endplate, a friction factor was used. To obtain the most appropriate friction factor a sensitivity analysis was conducted by varying the friction properties between the roller and the endplate. Friction factors ranging from 0.1-0.4 were used and the corresponding relationships between axial load versus axial shortening were obtained as shown in Figure 8.4. The results indicate that the effect of friction factor on the rotational behaviour of the CFS column is not negligible. It is shown that the predicted compressive capacity decreases with the reduction of friction factor whereas no significant drop of the peak load is observed using friction factors smaller than 0.2. It will be shown in the following sections that a friction factor of 0.2 provides the best agreement between the predicted compressive strengths of CFS columns and the experimental results.

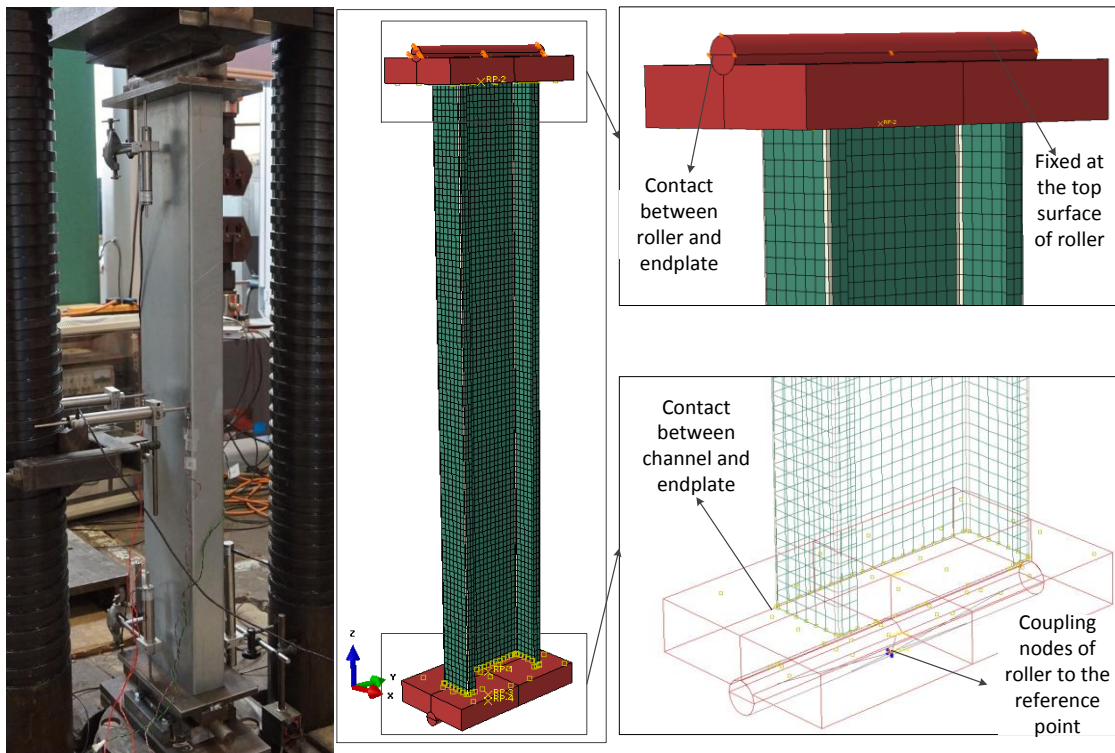


Figure 8.3. Boundary conditions of FE model against test

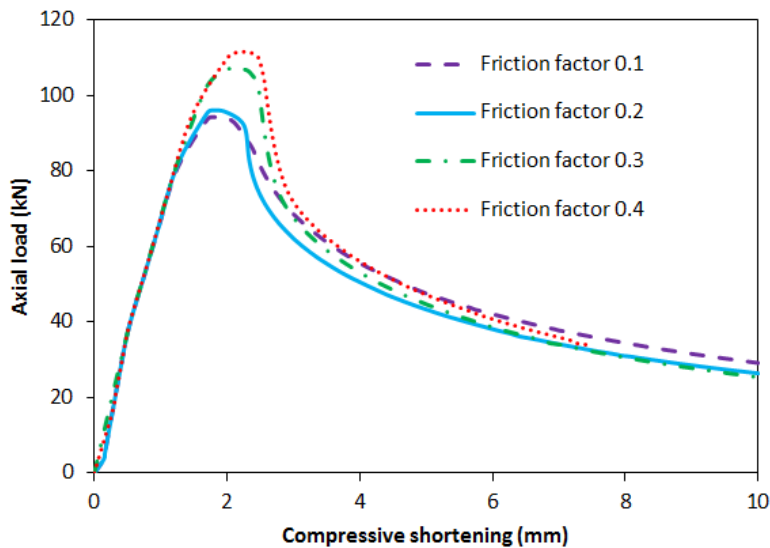


Figure 8.4. Axial load vs shortening of A1000-a specimen with various friction factors defined in the contact properties of FE analyses

### 8.4.3 Element type and mesh size

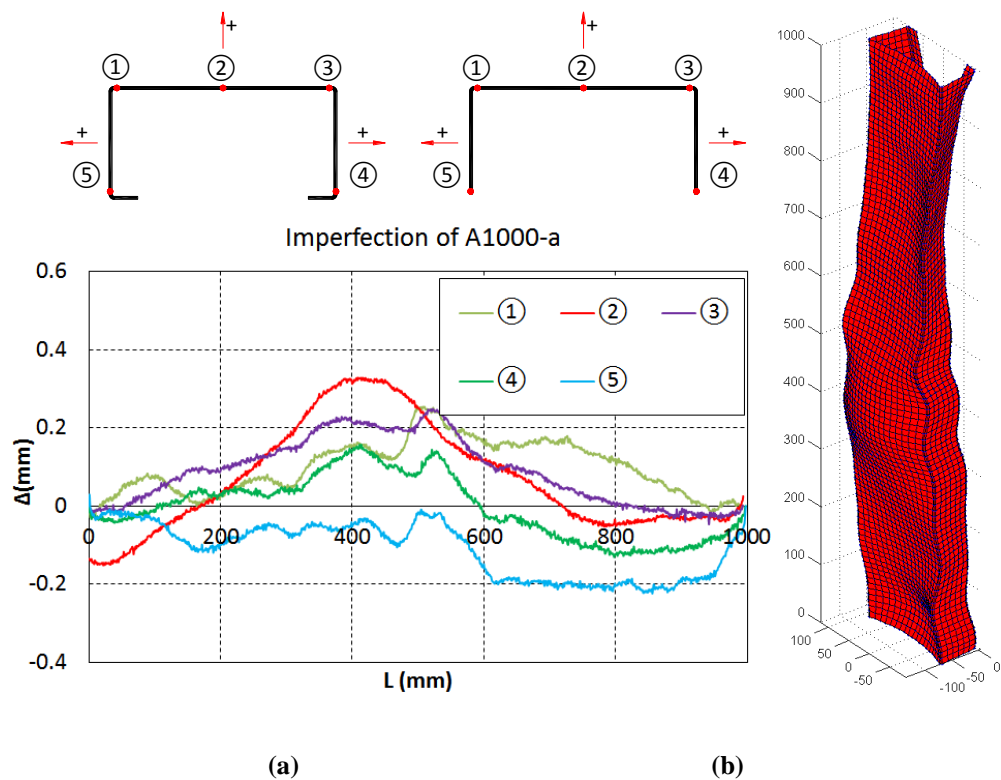
In the FE models, a four-node shell element with reduced integration (S4R) was selected from the available ABAQUS element library (ABAQUS 2011). This element uses three translational and three rotational degrees of freedom at each node. The element accounts for finite membrane strains and arbitrarily large rotations. Therefore, it is suitable for large-strain analyses and geometrically non-linear problems. Since the plate components constituting the cross-section are very slender, transverse shear deformations were not deemed to have a major effect on the solution. Nevertheless, they are accounted for in the S4R element formulation.

For the modelling of the endplate and the roller support, an 8-node linear brick element with reduced integration (C3D8R) and hourglass control was used. A sensitivity analysis was performed to choose an appropriate mesh size to model the CFS channel sections. The mesh size of the endplate and the roller support was found to have little effects on the peak capacity of the channel sections; however, it could affect the convergence of the FE analyses. It was found that using a 10x10mm element dimension for CFS channel and 5x5x5 mm for the linear brick element provides a balance between computational time and accuracy.

### 8.4.4 Imperfections

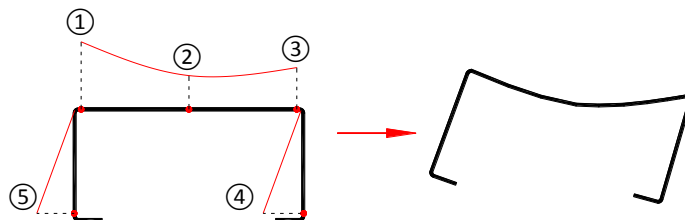
The stability of thin-walled CFS members may in some cases be significantly affected by the presence of imperfections, especially when interactive buckling of different modes is involved. Before conducting the experimental tests, the imperfections of the test specimens were measured along the five longitudinal lines indicated in Figure 8.5, by means of reflected laser beams. In a first step, the raw data were decomposed into their respective Fourier series (Becque and Rasmussen 2009a, Becque and Rasmussen 2009b). The Fourier series were then filtered by

cutting off the high frequency vibrations originating from the driving mechanisms of the moving motors. This has resulted in a smoother profile when the measured imperfections were included.



**Figure 8.5. (a) The measured imperfection profiles; (b) Incorporating measured imperfections into FE models**

It should be noted it is essential to use a significant number of Fourier terms to represent the shape of measured imperfection accurately. In this study, 10-50 Fourier terms were used by a trial and error process, depending on the specimen length. As an example, Figure 8.5 displays the measured imperfection profile along line 3 of specimen A1000-a, with the truncated Fourier representation shown as a solid black line. The program to incorporate the imperfections is presented in Appendix A.2.



**Figure 8.6. Imperfection inclusion**

To improve the accuracy of the predictions, the small eccentricities  $e_0$  of the applied loads were also measured and incorporated in the FE models by offsetting the specimen relative to the

centroid of the end blocks by a distance  $e_0$ . More information about the experimental tests can be found in Chapter 7.

#### 8.4.5 Numerical results

Table 8.1 compares the ultimate load carrying capacity  $P_u$  resulting from the FE models with the results obtained from the experiments on the CFS plain and lipped channels.  $P_{u1}$  is the predicted axial strength that takes into account the strain hardening effect of the material in the corner region but with a small horizontal 10N concentrated load in ABAQUS applied in the middle height of the column to incorporate the imperfection.  $P_{u2}$  indicates the predicted capacity through FE analysis where only the effect of the measured imperfection was taken into account. The predicted capacity  $P_{u3}$ , on the other hand, considers both the measured imperfection and the strain hardening effect of the material in the corner region. It is shown in Table 1 that, in general, an excellent agreement was obtained between the FE predictions and the experimental results when measured imperfections were taken into account. The average ratio of the FE predicted load capacity  $P_{u2}$  to the experimentally measured load carrying capacity  $P_u$  was 0.985, with a standard deviation of 0.066. In comparison, the average ratio of the FE predicted load capacity  $P_{u3}$  to the experimentally measured load carrying capacity  $P_u$  was 0.994, with a standard deviation of 0.067 while the average ratio of the FE predicted load capacity  $P_{u1}$  to the experimentally measured load carrying capacity  $P_u$  was 1.114, with a standard deviation of 0.191. This indicates that the strength variation caused by the strain hardening effect of the round corner material in the current test series was not significant (less than 3%). The main cause for the low contribution of the strain hardening can be the relative small area of the round corners compared to the total cross section area in this case. By comparing the predicted axial strength  $P_{u1}$  with  $P_{u3}$ , it is shown that the imperfection magnitude and distribution can have significant effects on the load carrying capacity, the variation is up to 20% for lipped channel columns and 40% for plain channel columns.

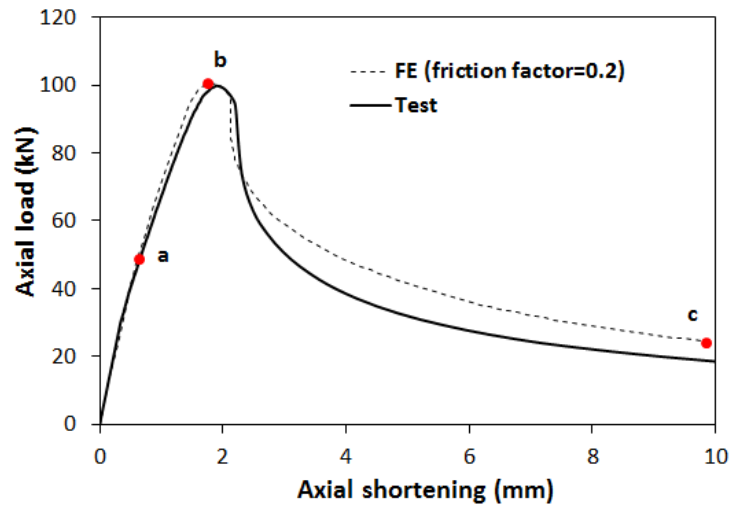


Figure 8.7. Axial load-axial shortening relationship resulting from FE against Test (A1000-a)

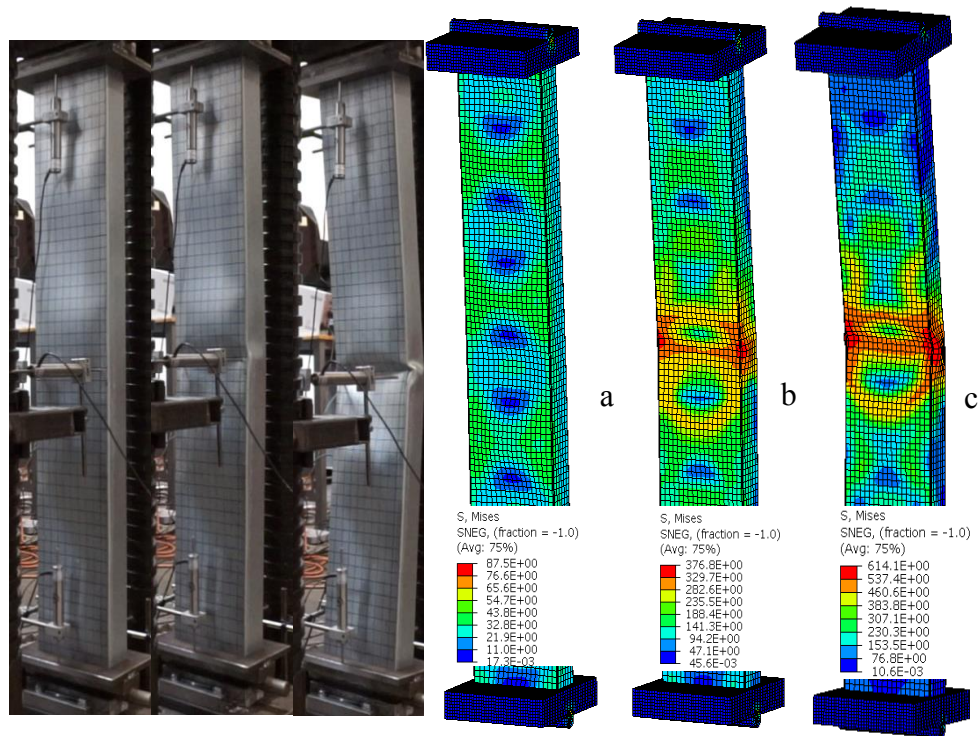


Figure 8.8. Deformation of FE model vs actual specimen (A1000-a) at points a, b and c (see Figure 8.7); stress (MPa)

Figure 8.7 illustrates the tested axial load-axial shortening relationship between the experiment tests and the predicted results from numerical study. It is shown that the proposed FE model was able to capture the peak load and stiffness of both CFS plain and lipped channel columns. The proposed FE model could also accurately predict the failed shape of the tested CFS columns and the post-buckling behaviour. All of the tested columns in this study exhibited a local buckling which was then followed by interactive local and flexural buckling failure modes. Figure 8.8 demonstrates the good agreement between the post-peak deformations of specimen A1000-a

observed in the experimental tests with the results of the corresponding FE model at different loading stages.

**Table 8.1. Comparison of FE results with tested compressive strength**

Specimen	Member length (mm)	$P_u$ (Test) (kN)	$P_{u1}$ (FE) (kN)	$P_{u2}$ (FE) (kN)	$P_{u3}$ (FE) (kN)	$P_{u1}/P_u$	$P_{u2}/P_u$	$P_{u3}/P_u$
A1000-a	1000.1	99.8	113.7	97.2	97.4	1.139	0.974	0.976
A1000-b	1000.0	98.3	117.5	97.0	97.8	1.195	0.987	0.995
A1000-c	1000.0	98.7	114.9	96.4	97.4	1.164	0.977	0.987
A1500-a	1499.8	95.1	89.8	91.9	92.7	0.944	0.966	0.975
A1500-b	1500.0	85.3	81.9	81	81.7	0.960	0.950	0.958
A1500-c	1500.0	91.4	94.06	87.6	88.1	1.029	0.958	0.964
A2000-a	1999.8	78.4	88.4	75.1	76.2	1.128	0.958	0.972
A2000-b	2000.0	75.8	68.0	72.2	73.4	0.897	0.953	0.968
A2000-c	2000.1	88.8	70.8	85.8	86.5	0.797	0.966	0.974
B1000-a	1000.2	113.8	109.8	114.2	114.7	0.965	1.004	1.008
B1000-b	1000.0	110.3	112.5	114.2	114.6	1.020	1.035	1.039
B1000-c	1000.1	107.7	110.1	108.3	109.2	1.022	1.006	1.014
B1500-a	1500.0	103.8	103.8	108.1	108.4	1.000	1.041	1.044
B1500-b	1500.4	107.9	108.3	109.6	110.0	1.004	1.016	1.019
B1500-c	1500.1	106.2	108.0	108.3	108.8	1.017	1.020	1.024
B2000-a	2000.1	99.6	95.6	102.2	103	0.960	1.026	1.034
B2000-b	2000.3	101.6	111.5	105.5	106.2	1.097	1.038	1.045
B2000-c	2000.1	105.3	113.3	108.3	109.1	1.076	1.028	1.036
(C1000-a)	1000.1	33.6	60.9	-- *	-- *	-- *	-- *	-- *
C1000-b	1000.1	43.8	61.6	42.2	42.5	1.406	0.963	0.970
C1000-c	999.8	42.7	60.2	44.1	44.6	1.410	1.033	1.044
C1500-a	1500.0	36.3	43.7	33.5	33.6	1.204	0.923	0.926
C1500-b	1500.1	35.2	51.1	32.8	32.9	1.452	0.932	0.935
C1500-c	1500.2	37.1	54.0	35.6	35.7	1.456	0.960	0.962
C2000-a	2000.4	33.1	34.9	29.5	29.9	1.054	0.891	0.903
C2000-b	2000.3	31.7	34.8	28.1	28.9	1.098	0.886	0.912
C2000-c	2000.0	33.8	36.1	29.9	30.6	1.068	0.885	0.905
D1000-a	1000.0	109.0	129.4	106.0	107.0	1.187	0.972	0.982
D1000-b	1000.2	110.8	125.4	109.1	112.2	1.132	0.985	1.013
D1000-c	1000.1	109.3	130.1	108.0	108.7	1.190	0.988	0.995
D1500-a	1500.2	95.0	100.3	94.2	94.6	1.056	0.992	0.996
D1500-b	1500.1	98.2	104.5	101.5	101.9	1.064	1.034	1.038
D1500-c	1500.0	99.6	101.9	98.1	99.7	1.023	0.985	1.001
D2000-a	2000.3	90.8	96.1	86.4	86.9	1.058	0.952	0.957
D2000-b	2000.0	97.8	94.2	93.3	94.2	0.963	0.954	0.963
D2000-c	2000.1	89.6	93.9	85.8	85.9	1.048	0.958	0.959
Average						1.114	0.985	0.994
St. deviation						0.191	0.066	0.067

\* C1000-a experienced an sudden impact from other machine in the lab during the test

### 8.5 Evaluation of EC3 and DSM design methods

The experimental results listed were compared with the predictions of the DSM and EC3 design equations presented in section 8.2 and 8.3. As shown in Table 8.2, in general, the DSM predictions for CFS lipped channel columns are found to be more accurate than the “effective width” based method in EC3. The ratio of the DSM predicted load capacity to the corresponding experimentally measured value was on average 0.945, with a standard deviation of 0.081. For the EC3 design method the average of the predicted load capacities to the experimental results was 0.804, with a standard deviation of 0.138. It is also evident that the EC3 design method generally leads to considerably more conservative predictions of the column axial load capacity.

While DSM is not qualified for the design of CFS plain channel columns, EC3 predictions on the plain channel column design were very conservative, where the ratio of EC3 prediction to the tested result was as small as 0.54 (i.e. up to 46% underestimation).

**Table 8.2. Evaluation of the EC3 and DSM design methods against experimental results**

Specimen	Member length (mm)	$P_u$ (Test) (kN)	EC3 (kN)	DSM (kN)	EC3/ $P_u$	DSM/ $P_u$
A1000-a	1000.1	99.8	81.6	92.34	0.818	0.925
A1000-b	1000.0	98.3	82.5	93.17	0.839	0.948
A1000-c	1000.0	98.7	80.6	91.45	0.817	0.927
A1500-a	1499.8	95.1	75.4	81.73	0.793	0.859
A1500-b	1500.0	85.3	72.5	78.6	0.850	0.921
A1500-c	1500.0	91.4	75.3	81.7	0.824	0.894
A2000-a	1999.8	78.4	64.1	65.36	0.818	0.834
A2000-b	2000.0	75.8	62.7	64.2	0.827	0.847
A2000-c	2000.1	88.8	63.7	65.43	0.717	0.737
B1000-a	1000.2	113.8	112.1	119.37	0.985	1.049
B1000-b	1000.0	110.3	111.2	118.88	1.008	1.078
B1000-c	1000.1	107.7	107.3	113.72	0.996	1.056
B1500-a	1500.0	103.8	99.8	108.66	0.961	1.047
B1500-b	1500.4	107.9	101.0	111.38	0.936	1.032
B1500-c	1500.1	106.2	102.0	110.88	0.960	1.044
B2000-a	2000.1	99.6	88.2	94.82	0.886	0.952
B2000-b	2000.3	101.6	89.6	98.60	0.882	0.970
B2000-c	2000.1	105.3	90.1	98.54	0.856	0.936
C1000-a	1000.1	33.6	24.5	NA	0.729	--#
C1000-b	1000.1	43.8	26.2	NA	0.598	--#
C1000-c	999.8	42.7	26.4	NA	0.618	--#
C1500-a	1500.0	36.3	21.3	NA	0.587	--#
C1500-b	1500.1	35.2	21.1	NA	0.599	--#
C1500-c	1500.2	37.1	22.0	NA	0.593	--#
C2000-a	2000.4	33.1	18.6	NA	0.562	--#
C2000-b	2000.3	31.7	17.4	NA	0.549	--#

Specimen	Member length (mm)	$P_u$ (Test) (kN)	EC3 (kN)	DSM (kN)	EC3/ $P_u$	DSM/ $P_u$
C2000-c	2000.0	33.8	18.2	NA	0.538	--#
D1000-a	1000.0	109.0	93.5	102.82	0.858	0.943
D1000-b	1000.2	110.8	96.1	105.39	0.867	0.951
D1000-c	1000.1	109.3	96.3	106.21	0.881	0.972
D1500-a	1500.2	95.0	87.1	94.48	0.917	0.995
D1500-b	1500.1	98.2	89.9	97.92	0.915	0.997
D1500-c	1500.0	99.6	88.1	95.67	0.885	0.961
D2000-a	2000.3	90.8	74.8	79.22	0.824	0.872
D2000-b	2000.0	97.8	77.1	82.16	0.788	0.840
D2000-c	2000.1	89.6	77.2	82.36	0.862	0.919
Average					0.804	0.945
St. deviation					0.138	0.081

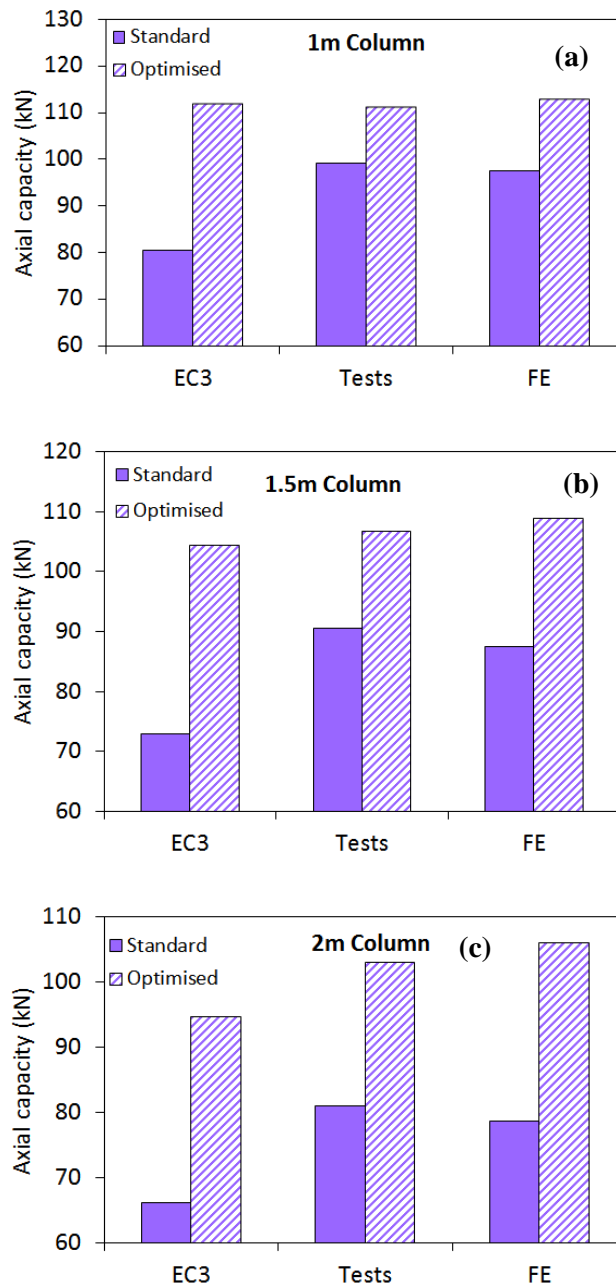
# Unpredefined sections for DSM

## 8.6 Evaluation of the optimisation process

In this section, the efficiency of the optimisation method explained in section 8.3 is further investigated. While section A is a standard commercially available cross-section, sections B is the optimum solution with highest axial capacity subjected to constraints in Equations (8.6)-(8.8) for lipped channels. The nominal cross-sectional dimensions of these sections are given in Figure 8.1.

Figure 8.9 compares the ultimate capacity of the standard and optimised sections for the 1m, 1.5m and 2m length columns obtained from the experimental results, detailed FE models and EC3 design method. Based on the experimental results, it is shown that the optimised shapes offer a much higher compressive capacity (up to 27% higher) compared to the standard lipped channel section with the same amount of material, particularly in longer columns where global buckling is the dominant mode. Similar results were obtained from FE models and EC3 design method, where the optimum design solutions showed, respectively, up to 35% and 43% higher compressive strength compared to the standard sections.





**Figure 8.9. Compressive strength of the standard section compared to the optimised sections using the same amount of material**

It is worth noting that the trends of increasing/decreasing capacity over the range of lengths for the columns are very well predicted by EC3 when the tested results are taken as a benchmark. This indicates that the proposed optimisation method is accurate and reliable and provides a practical tool for manufacturers and structural engineers to improve the capacity of CFS elements.

The results of this study in general demonstrate the accuracy and reliability of the developed FE models to predict the axial load bearing capacity of CFS columns with different cross sectional shapes and effective lengths. These validated models should prove useful in practical applications for more efficient design of CFS structural elements.

## 8.7 Conclusions

In this chapter, a finite element (FE) model was developed to study the interaction of local and global buckling in CFS lipped channel columns. The model takes into account the non-linear stress–strain behaviour of CFS material, the strength hardening effects at the round corners due to the cold-working process, and the experimentally measured initial imperfections. The FE models were validated against an experimental program on a total number of 36 plain and lipped channel columns with the total lengths of  $L_e = 1.0m, 1.5m \text{ and } 2.0m$ . The validated models were then used to assess the accuracy of EC3 and DSM design methods for standard and optimum design solutions. Based on the results presented in this chapter, the following conclusions can be drawn:

- (1) The ultimate capacity of the sections predicted by the FE models was on average less than 1% different from the experimental results. The proposed FE model was also successful in capturing the failure shapes and predicting the compressive strength of CFS columns subjected to local and global buckling modes.
- (2) It was shown that the geometric imperfections can change the FE predictions by around 20% and 40%, respectively, for lipped and plain channel columns, while the strength variation caused by the strain hardening effect at the round corners material in general has negligible effects (less than 3%).
- (3) The ratio of predicted to experimentally measured axial strength was on average 0.945 and 0.804 for DSM and EC3 design methods, respectively. The results show that EC3 design method generally leads to conservative predictions, especially for plain channel column sections where the EC3 predictions were up to 46% lower than the experimental results.
- (4) The axial capacity of the optimised CFS columns obtained from validated FE models and EC3 design methods were up to 35% and 43% higher, respectively, compared to their standard lipped channel counterparts with the same amount of material. This improvement was more evident for longer columns where global buckling was the dominant failure mode. This demonstrated the efficiency of the proposed optimisation method to improve the compressive capacity of CFS sections.
- (5) The results of this study in general demonstrate the accuracy and reliability of the developed FE models to predict the axial load bearing capacity of CFS columns with different cross sectional shapes and effective lengths. These validated models should prove useful in practical applications for more efficient design of CFS structural elements

## **CHAPTER 9. Experimental investigation of the bending capacity of CFS back-to-back standard and optimised beams**

---

This chapter describes an experimental programme carried out at the University of Sheffield to investigate the interaction between local and distortional buckling in cold-formed steel (CFS) back-to-back beams, assembled from standard and optimised lipped channel sections. The channels, with a nominal thickness of 1.5 mm and depths ranging from 180 mm to 270 mm, were assembled in a back-to-back configuration using 12 mm diameter bolts, tightened with a constant torque of 15 N·m. The geometric imperfections of the individual channels, as well as those of the back-to-back specimens, were recorded using a specially designed measurement rig. Tensile coupons were also extracted from the flat portions and the corner regions of the cross-sections in order to determine the material properties.

A total of six tests on back-to-back beams, including three different cross-sectional geometries, were completed. All cross-sections were manufactured using steel plate of the same coil width and thickness. The specimens were tested in a four-point bending configuration with simply supported boundary conditions, while being laterally braced at the loading points.

## 9.1 Introduction

The literature review (Chapter 2) has shown that available tests on CFS single sections were generally designed for the development of design guidelines on CFS specimens while no comparison between standard and optimised sections were presented. Therefore, newly proposed cross-sectional shapes and dimensions are not usually optimised on the basis of detailed experimental validation and calibration. This may lead to non-compliant shapes and plate width-to-thickness ratios against available design guidelines during the optimisation process.

The current experimental study on the behaviour of CFS back-to-back beam sections in this chapter is part of a wider study into the optimisation of CFS members (see Chapter 4 to Chapter 5), which is why all four cross-sections in the test programme were manufactured using the same coil width and thickness. The purpose of the test is to: (a) provide verification on the optimisation framework on CFS beams proposed in Chapter 4; (b) calibrate a more reliable FE model for future application on more efficient CFS beam design and (c) verify the accuracy of design procedures adopted in EC3 which can be crucial in the optimisation process. However, the experimental results are here presented independently of their wider context, as the results by themselves provide valuable data about the interactive buckling behaviour of CFS back-to-back beams. A comparison with the relevant Eurocode 3 design guidelines (CEN 2005a, CEN 2005b, CEN 2005c) is also carried out.

## 9.2 Section geometry and labelling

The back-to-back specimens were assembled using lipped channels with three different cross-sectional geometries. All channels were fabricated by brake pressing a pre-galvanized steel sheet with a width of 415 mm, a nominal thickness of 1.5 mm and a zinc coating of 0.04 mm thickness. The nominal yield stress of the sheet was 450 MPa. The back-to-back beams had a total length of 3300 mm and a distance between the end supports of 3100 mm. M12 zinc-plated bolts, tightened with a constant torque of 15 N·m, were used to connect the individual channel sections through the web, as illustrated in Figure 9.1, at the cross-sections under the loading points and over the end supports.

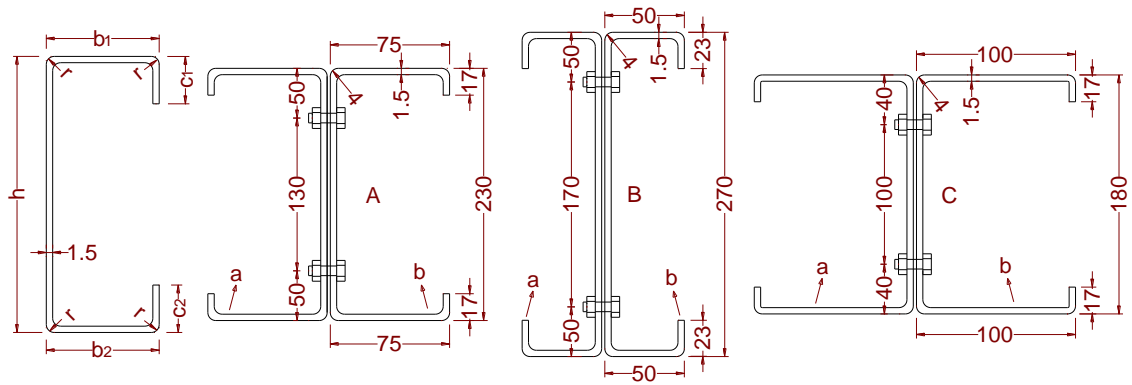


Figure 9.1. Symbol definitions and nominal cross-sectional dimensions

Table 9.1. Measured dimensions of specimens with cross-section A

Specimen	Channel	$r$ (mm)	$t$ (mm)	$h$ (mm)	$b_1$ (mm)	$c_1$ (mm)	$b_2$ (mm)	$c_2$ (mm)
A230-1	a	3.9	1.563	230.43	75.36	17.44	75.35	16.81
	b	4.3	1.551	230.35	75.33	17.44	75.33	16.86
A230-2	a	4.1	1.557	230.52	75.35	16.64	75.35	17.39
	b	3.7	1.564	230.48	74.90	16.09	74.90	17.25
Average		4.0	1.559	230.45	75.24	16.90	75.23	17.08
St. Dev.		0.15	0.01	0.07	0.22	0.66	0.22	0.29

Table 9.2. Measured dimensions of specimens with cross-section B

Specimen	Channel	$r$ (mm)	$t$ (mm)	$h$ (mm)	$b_1$ (mm)	$c_1$ (mm)	$b_2$ (mm)	$c_2$ (mm)
B270-1	a	4.1	1.561	269.49	150.19	24.70	50.10	23.79
	b	4.0	1.565	270.59	151.33	23.24	49.71	23.47
B270-2	a	4.2	1.555	270.43	150.95	23.01	49.91	23.50
	b	4.1	1.546	270.55	151.34	23.29	50.25	22.84
Average		4.1	1.557	270.30	151.00	23.60	50.00	23.40
St. Dev.		0.08	0.01	0.52	0.54	0.77	0.23	0.40

Table 9.3. Measured dimensions of specimens with cross-section C

Specimen	Channel	$r$ (mm)	$t$ (mm)	$h$ (mm)	$b_1$ (mm)	$c_1$ (mm)	$b_2$ (mm)	$c_2$ (mm)
C180-1	a	4.1	1.554	180.30	100.41	17.31	100.33	17.06
	b	3.9	1.567	180.20	100.38	17.53	100.14	16.80
C180-2	a	3.9	1.559	180.52	100.41	17.46	100.33	17.28
	b	4.2	1.554	180.41	100.43	17.34	100.32	16.75
Average		4.0	1.559	180.36	100.41	17.41	100.28	16.97
St. Dev.		0.15	0.01	0.14	0.02	0.10	0.09	0.25

Each back-to-back specimen was labelled according to its cross-section, using the letters A, B or C (Figure 9.1), followed by the height of the cross-section in mm. As each test was repeated, the numbers 1 and 2 were used to differentiate between the first and second twin specimen. For each back-to-back specimen, the letters ‘a’ and ‘b’ were used to refer to the individual channels

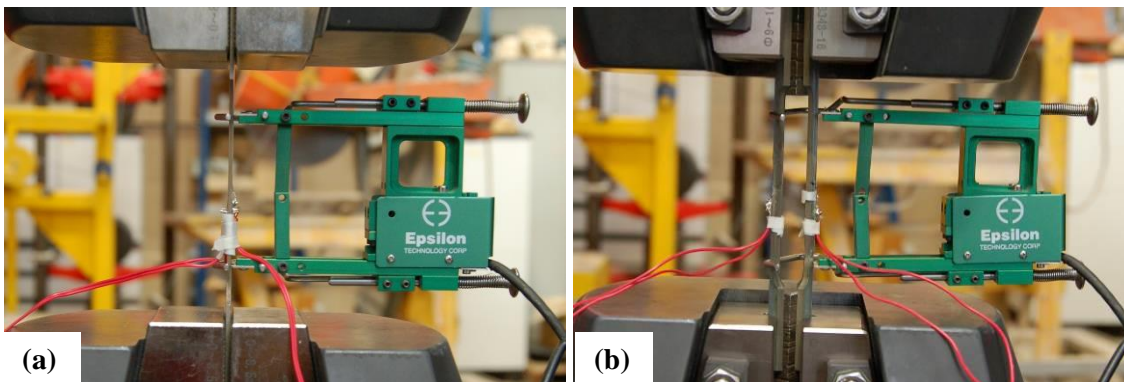
## Chapter 9. Experimental investigation of the bending capacity of CFS back-to-back beams

which formed the back-to-back cross-section. The cross-sectional dimensions of each channel were measured prior to their assemblage. Table 9.1-Table 9.3 list the measured dimensions of the test specimens, using the nomenclature illustrated in Figure 9.1. All the reported values correspond to outer dimensions and they are the averages of several measurements taken along the length of the channels.

### 9.3 Material properties

A series of tensile coupons were tested in order to determine the material properties of the test specimens. For each type of lipped channel used to construct the built-up specimens, one flat coupon was extracted from the center line of the web. Two corner coupons were also taken from the web-flange junctions in order to determine the effect of the cold-working process on the material properties. All coupons were taken from the end portions of test specimens after they were tested, since the beams were subject to strains in these regions which were low enough not to alter the material properties of the steel.

The flat coupons had a nominal width of 12.5 mm and each of them was instrumented with a 50 mm extensometer and two 5 mm strain gauges, one on each side of the coupon (Figure 9.2(a)). The corner coupons had a nominal width of 6 mm and were tested in pairs to avoid introducing unwanted bending moments due to their asymmetric cross-sectional shape. Each pair of corner coupons was instrumented with a 50 mm extensometer and a 5 mm strain gauge attached to the outside of each coupon, as shown in Figure 9.2(b).



**Figure 9.2. Tensile material tests for: (a) flat coupons (b) corner coupons**

All coupons were tested in accordance with the specifications of the relevant European standard. Table 9.4 lists the values of the material properties obtained for each flat coupon or set of corner coupons, where  $E$  is the Young's modulus,  $\sigma_{0.2\%}$  is the 0.2% proof stress,  $\sigma_u$  is the ultimate tensile strength and  $\varepsilon_f$  is the elongation after fracture, measured over a gauge length of 50 mm. For the pair of corner coupons belonging to section B270, the elongation after fracture reported in the table is lower than for the other corner coupons. This is due to the fact that the plastic

Chapter 9. Experimental investigation of the bending capacity of CFS back-to-back beams deformations localized slightly outside the gauge length. Therefore, this result should be disregarded.

**Table 9.4. Tensile properties of flat and corner coupons**

Section	Types	$E$ (GPa)	$\sigma_{0.2\%}$ (MPa)	$\sigma_u$ (MPa)	$\varepsilon_f$ (%)
A230	flat	196	416	511	18
	corner	218	516	575	6
B270	flat	199	424	517	17
	corner	208	508	560	(4)
C180	flat	200	427	521	18
	corner	209	514	576	7

#### 9.4 Imperfection measurements

Geometric imperfections may significantly affect the stability of thin-walled CFS members, especially when coupled instabilities are involved. For this reason, the magnitude and shape of the imperfections of each specimen were recorded before testing. As the beams were designed to fail by interaction of local and distortional buckling along the constant moment span (in between the loading points), only the out-of-plane imperfections along this region were of interest.

The out-of-plane imperfections were recorded using the set-up described in chapter 7, in which two electric motors were used to move a laser sensor along high precision bars. The laser sensor was used to take readings along different longitudinal lines on the web and flanges of the channels, as shown in Figure 9.3, and was able to measure the distance to the surface of the specimen with an accuracy of 0.0075 mm. The straightness of the high precision bars was verified against measurements of the nominally flat table underneath, in the absence of a test specimen, which provided a surface with a deviation from flatness of less than 0.06 mm. During the measuring process, the translational speed of the laser was set at 5 mm/s, while the sampling rate was 5 Hz, resulting in one reading every millimeter.

It was recognized that assembling the channels in a back-to-back configuration might alter the imperfection profile and, therefore, the imperfections were measured before and after the assemblage of the back-to-back specimens. Before the specimens were assembled, the maximum out-of-plane imperfections measured along the center line of the channel webs relative to the measurements taken along the corners were 0.66 mm, 0.53 mm and 0.32 mm for specimens B270, A230 and C180, respectively. Moreover, the flange tips of the channels exhibited maximum imperfections of 1.78 mm, 1.43 mm and 1.02 mm for specimens C180, B270 and A230, respectively. All of the measured imperfection magnitudes are show in Table 9.5 and Table 9.6.



**Figure 9.3. The set-up for imperfection measurement**

**Table 9.5. Maximum amplitudes of local, distortional imperfections in single channel before assembling**

Specimen	Local	Distortional
A230-1a	0.47	0.43
A230-1b	0.42	0.36
A230-2a	0.36	0.34
A230-2b	0.41	0.32
B270-1a	0.35	0.34
B270-1b	0.37	0.63
B270-2a	0.46	0.37
B270-2b	0.32	0.85
C180-1a	0.39	0.36
C180-1b	0.36	0.52
C180-2a	0.34	0.40
C180-2b	0.27	0.50

**Table 9.6. Maximum amplitudes of local, distortional imperfections in single channel after assembling**

Specimen	Local	Distortional
A230-1a	0.54	0.60
A230-1b	0.37	0.54
A230-2a	0.55	0.49
A230-2b	0.45	0.48
B270-1a	0.62	0.36
B270-1b	0.57	0.39
B270-2a	0.67	0.70
B270-2b	0.68	0.71
C180-1a	0.24	0.53
C180-1b	0.64	0.62
C180-2a	0.37	0.53
C180-2b	0.37	0.58



## 9.5 Test set-up

A total of six back-to-back beams were tested in a four-point bending configuration, as illustrated in Figure 9.4(a). The specimens were supported on rollers located 3100 mm apart. All specimens were bent about their major axis. The loading system consisted of an actuator with a maximum capacity of 160 kN which imposed the load, through a spreader beam, onto the test specimens at two discrete locations 1200 mm apart. The spreader beam was restrained against any out-of-plane movement by a specially designed guidance system, as shown in Figure 9.4(b). Nylon blocks were used as bearing pads between the spreader beam and the uprights in order to reduce vertical friction. A pin and a roller support were used to transfer the load from the spreader beam to the specimen. These supports were also designed to restrain any out-of-plane displacement of the top flange of the test specimen. Wooden blocks were packed tightly into the cross-section at the loading points and end supports to avoid localized bearing failure, as shown in Figure 9.5-Figure 9.7. Three potentiometers with a stroke of 25 mm were placed under the test specimen at mid-span and under the two loading points in order to record the vertical deflections of the beam.

A displacement control scheme with a rate of 1 mm/min was used for all test specimens. The tests were halted for 4 minutes slightly before the peak load was reached, in order to eliminate strain-rate dependent effects. The tests were then continued until well into the post-peak range.

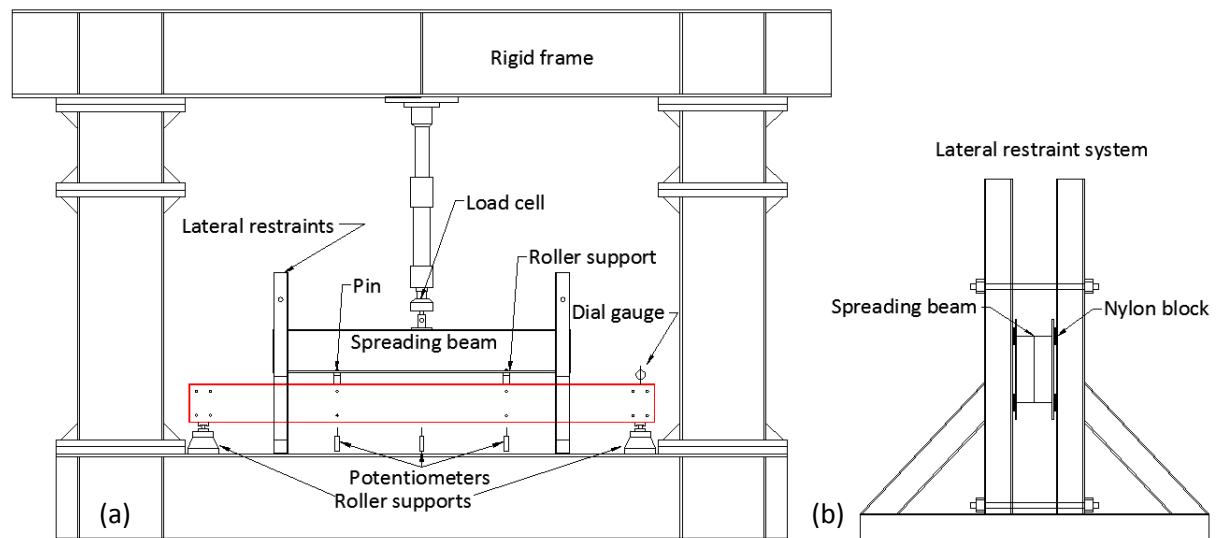


Figure 9.4. Schematic view of: (a) experimental set-up (b) lateral support system

## 9.6 Test results

### 9.6.1 Deformed shape

All test specimens failed within the constant moment span by interaction of local and distortional buckling. In specimens C180 pure local buckling was first observed in the top flanges. This was due to the high slenderness of the flanges, which had a width-to-thickness

## Chapter 9. Experimental investigation of the bending capacity of CFS back-to-back beams

ratio of 67, and the fact that they were subject to the highest compressive stress in the cross-section. As the bending moment increased, superimposed distortional buckling was recorded, as shown in Figure 9.5. Participation of the webs of the channels was also observed before the ultimate capacity of the specimens was reached.

Built-up specimens A230 also failed due to interaction between local and distortional buckling, as shown in Figure 9.6. However, in these specimens the webs constituted the most slender components of the cross-section and therefore triggered local buckling. As the load increased, the lips were unable to suppress the distortional mode.

Specimens B270 had the maximum web height, combined with relatively narrow flanges. Local buckling was again first detected in the webs of the channels, with distortional buckling participating at a higher load (Figure 9.7).

Past the peak load the buckling deformations localized in all specimens, forming an anti-symmetric yield line pattern in both flanges of the back-to-back channels. All test specimens showed an anti-symmetric distortionally buckled shape in which the top flange of one channel moved upward while the flange in the other channel moved downward. It is thereby noted that the webs of the channels were not connected by intermediate fasteners within the constant moment span and that the observed shape was a result of contact between the channel webs alone.

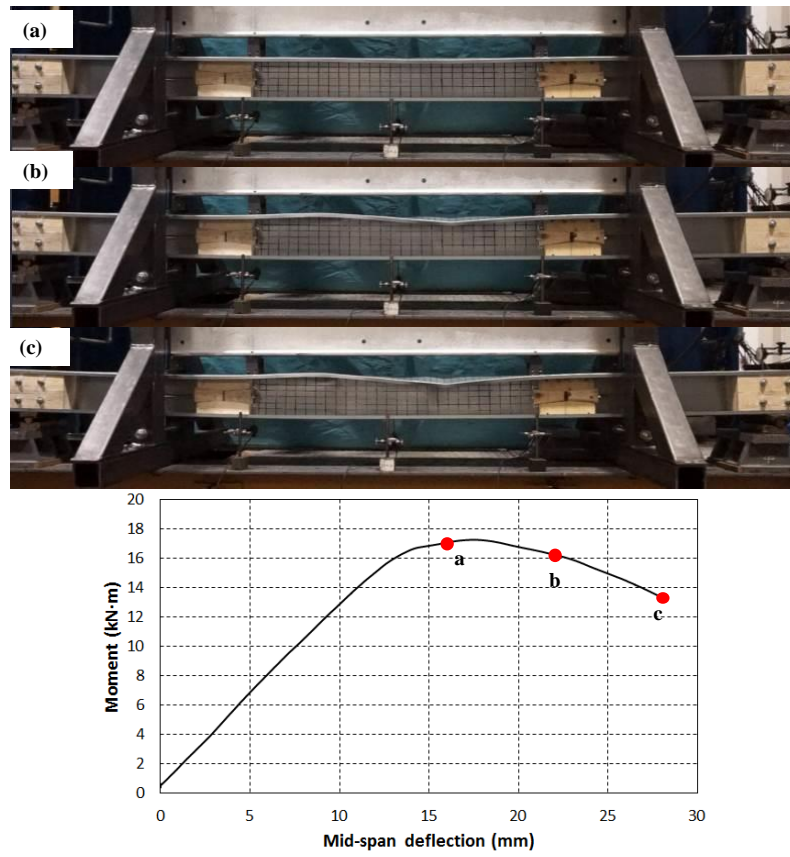


Figure 9.5. Failure progression and Moment vs Mid-span deflection in beam C180-2

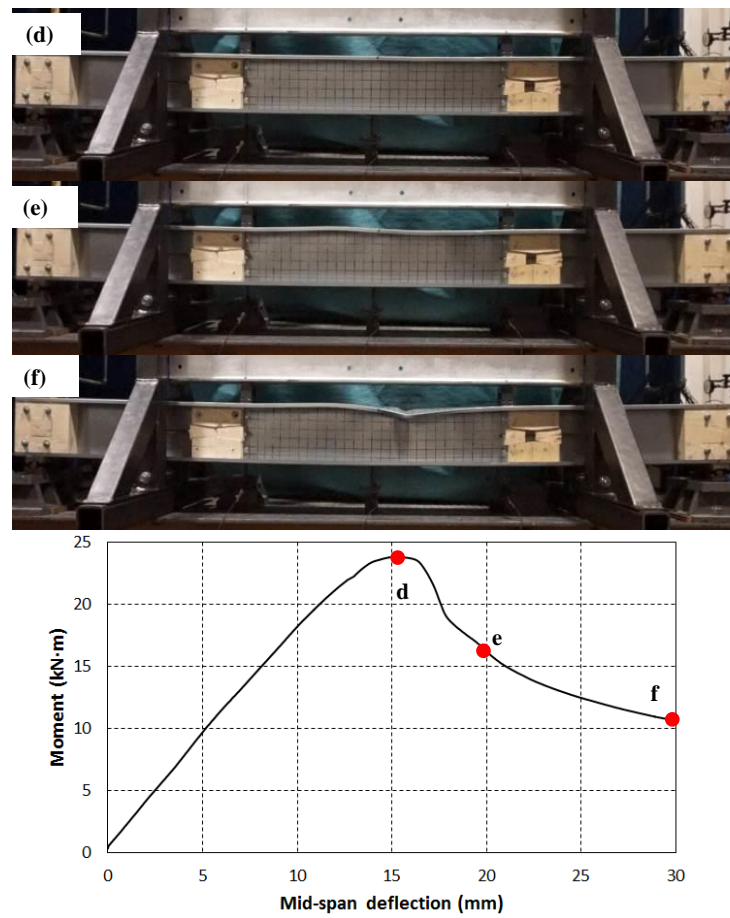


Figure 9.6. Failure progression and Moment vs Mid-span deflection in beam A230-2

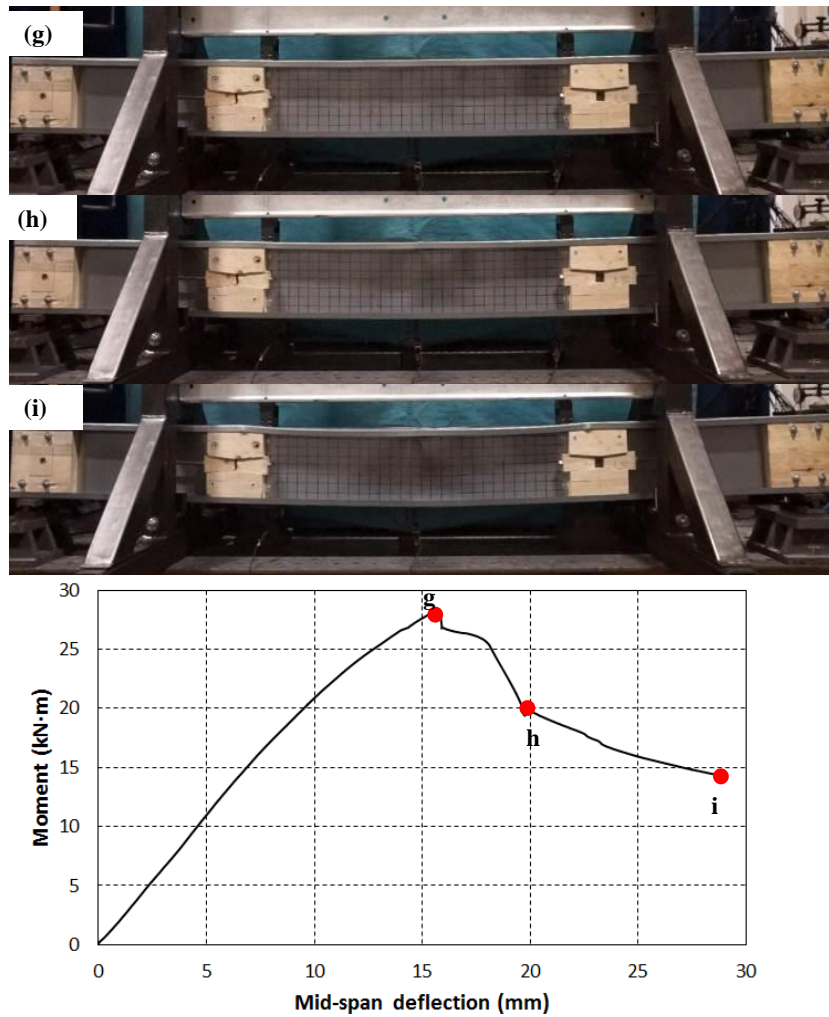


Figure 9.7. Failure progression and Moment vs Mid-span deflection in beam B270-2

### 9.6.2 Ultimate capacity

Figure 9.8 plots the bending moments against the mid-span deflections for all test specimens. The ultimate capacities of all test specimens are also listed in Table 9.7. In general, a good agreement was obtained within each set of twin specimens, with the ultimate capacities varying by less than 2% from each other. An exception to this occurred in specimens B270, where the ultimate capacity of specimen B270-1 was considerably lower than the one obtained for its counterpart. This was due to the fact that specimen B270-1 was tested without wooden blocks under the load application points. As a result, web crippling occurred under the loading points in combination with local buckling which extended all along the constant moment span. Therefore, the results of test B270-1 should be disregarded.

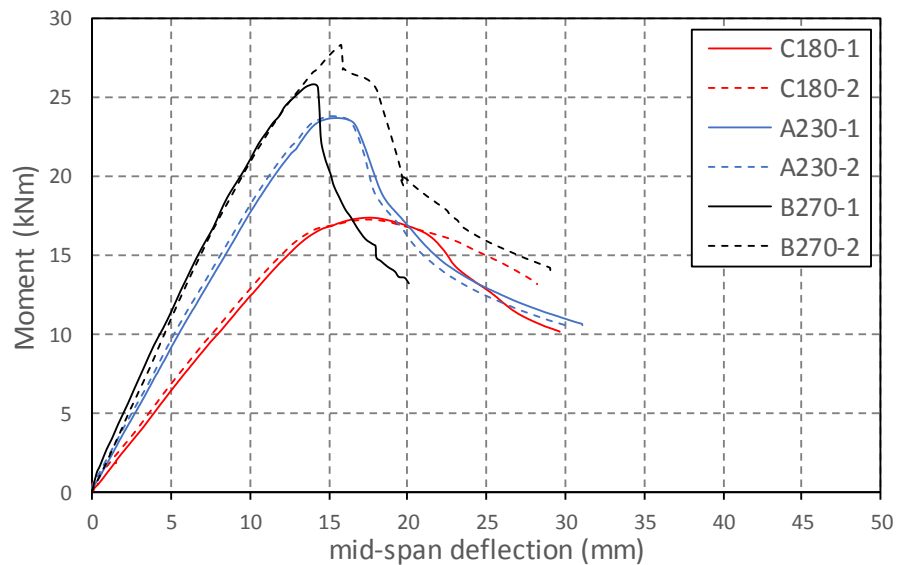


Figure 9.8. Moment vs mid-span deflection for all beams

Table 9.7. Ultimate capacities of the test specimens

Specimen	Experiment (kN·m)	Eurocode 3 (kN·m)	Eurocode 3 / Experiment
C180-1	17.43	18.59	1.067
C180-2	17.24	18.51	1.074
A230-1	23.72	22.56	0.951
A230-2	23.79	22.75	0.956
B270-1	(25.83)	26.74	-
B270-2	28.34	26.42	0.932
Average			0.996
St. Dev.			0.068

Table 9.7 also compares the ultimate capacities obtained from the experiments with the predictions given by Eurocode 3. It is thereby noted that, when calculating the effective cross-sectional properties according to the Eurocode, full iterations were carried out (which are not strictly prescribed by the Eurocode). These iterations are necessary because the location of the neutral axis of the effective cross-section is initially unknown and also because of the interaction between the local and distortional buckling modes. The measured dimensions and the material properties obtained from the coupon tests were used in the process. In general, Table 9.7 shows that a good agreement was achieved between the experimental and the calculated bending capacities of the back-to-back lipped channel beams, with the ratio of the Eurocode predicted values to the test results ranging from 0.932 to 1.074, depending on the cross-section type. The average ratio is 0.996 with a standard deviation of 0.07.

## 9.7 Conclusions

A total of six back-to-back beams, constructed from lipped channels with three different cross-sectional geometries, were tested, with the aim of investigating the interaction between local and distortional buckling. The specimens were tested in a four-point bending configuration with

## Chapter 9. Experimental investigation of the bending capacity of CFS back-to-back beams

simply supported boundary conditions, while being laterally braced at the loading points. The geometric imperfections were recorded before and after the back-to-back specimens were assembled. Coupons extracted from the flat portions and the corner regions of each cross-section type were also tested in order to determine the material properties.

All specimens failed due to interaction of local and distortional buckling, with local buckling being the primary buckling mode. In specimens C180, which displayed the widest flanges and the shallowest webs, local buckling originated in the top flanges, while in specimens A230 and B270, having a deeper cross-section and a smaller flange width, local buckling was triggered by the web.

A good agreement in the ultimate capacities was generally obtained within each set of twin beams, with the difference being less than 2 %. A comparison between the predictions given by Eurocode 3 and the experimental results indicated that Eurocode 3 is accurate in predicting the ultimate capacity of back-to-back lipped channel beams. The average ratio of the Eurocode predicted capacity to the experimental capacity was 0.996 with a standard deviation of 0.068.

## **CHAPTER 10. Local and distortional buckling of standard and optimised CFS Back-to-Back channels: a numerical study**

---

This chapter aims to develop a reliable numerical model to investigate the flexural strength and failure modes of CFS back-to-back channels beams. The model incorporates non-linear stress-strain behaviour and enhanced corner properties obtained from coupon tests as well as initial imperfections measured in the actual specimens. To simulate the behaviour of a bolt bearing against a steel plate, a connector model is used that takes into account both slippage and bearing deformations. The developed FE models are verified against six four point bending tests on CFS bac-to-back channel beams, where an excellent agreement between the experimental results and FE predictions are achieved. The validated FE models are then used to assess the adequacy of the effective width method in EC3 and Direct Strength Method (DSM) in estimating the design capacity of conventional and optimum design CFS channel beam sections. The results indicate that both EC3 and DSM provide accurate predictions for the bending capacity of lipped channel beam sections. A comparison between FE predictions and tested results show that, on average, the geometric imperfections can change the FE predictions by around 6%, while the strain-

Chapter 10. Local and distortional buckling of CFS Back-to-Back channels: a numerical study  
hardening of CFS material at the round corners has negligible effects. The proposed FE model will be hopefully used for future verification of optimisation on CFS elements.

## 10.1 Introduction

Although the accurate prediction of the behaviour of CFS elements can be a difficult task due to their complex failure modes, Finite Element Analysis (FEA) has been widely used in the past to predict the flexural behaviour of CFS beams. Compared to physical experiments, FEA is relatively inexpensive and time efficient, especially when a parametric study of cross-section geometry is involved. In addition, FEA can be efficiently used for investigations including geometric imperfections and material nonlinearity of structural members, while this could be difficult to achieve through physical tests.

Although FEA is a useful and powerful tool for the analysis of CFS structures, it is crucial to obtain accurate and reliable finite element models (FEM) prior to any analytical investigations. For example, Yu and Schafer (Yu and Schafer 2007) used nonlinear finite element models of CFS beams to develop the Direct Strength Method (DSM) design recommendations. They verified their FE models against four-point bending tests on local buckling (Yu and Schafer 2003) and distortional buckling (Yu and Schafer 2006) of CFS C or Z beams in pair, using steel corrugated panels and hot-rolled tubes as lateral restraints

Based on the experimental tests by Yu and Schafer (Yu and Schafer 2006, Yu and Schafer 2003), Haidarali and Nethercot (Haidarali and Nethercot 2011) developed a simplified numerical model that can significantly increase the computational efficiency of the non-linear analyses. In their study, the geometrical imperfection profiles were determined by using the constrained finite strip software CUFSM (Schafer 2006), while the imperfection amplitudes were based on the statistic results presented by Schafer and Peköz (Schafer and Pekoz 1998). Translational springs were employed to the lip/flange junction of the beams to allow for the modelling of the local and distortional buckling modes separately.

In another study, Kanganamge and Mahendran (Kankanamge and Mahendran 2012) investigated the behaviour of CFS beams subjected to lateral-torsional buckling. A detailed parametric study was conducted to simulate the lateral-torsional buckling behaviour and capacity of CFS beams under different boundary conditions using the four node shell element with five degrees of freedom per node and reduced integration (S4R) in ABAQUS (ABAQUS 2011). The results of their study were used to verify the design guidelines for the lateral-torsional buckling of CFS beams in different codes.



## Chapter 10. Local and distortional buckling of CFS Back-to-Back channels: a numerical study

Dubina et al. (Dubina et al. 2013) developed a FE model to investigate the behaviour of CFS beams with corrugated web and discrete web-to-flange fasteners. In their research, four node shell elements were used to model the CFS components while the connector element CONN3D2 with six degrees of freedom per node in ABAQUS (ABAQUS 2011) was employed to simulate the behaviour of self-drilling screws and bolts according to single-lap tests (Dubina et al. 2015). In a more recent study, Wang and Young (Wang and Young 2016a, Wang and Young 2016b) proposed a numerical model to investigate the flexural behaviour of CFS built-up sections with intermediate stiffeners subjected to bending. The S4R shell element in ABAQUS (ABAQUS 2011) was used to model the CFS sections while C3D8R solid element was used to model screws. The surfaces of the screws were tied to the hole edges of the beam specimens, while surface interactions between the overlapped elements of the built-up sections were defined using the contact pairs (ABAQUS 2011). The FE and the experimental results showed a good agreement in terms of ultimate bending strengths and failure modes.

This chapter aims to develop a numerical model to investigate the local/distortional buckling of CFS back-to-back channel beams. Detailed FE models are developed in ABAQUS (ABAQUS 2011) to predict the flexural behaviour and bending strength of CFS beam sections. An experimental investigation including six tests on CFS back-to-back channel beams, which were failed by the local/distortional buckling about the major axis, was used to verify the FE models. Compared to previous studies, the advantage of the developed models is to incorporate the non-linear stress-strain behaviour and enhanced material properties based on coupon tests, measured initial imperfections and a simplified/effective connector element to model the bolt behaviour. The models are then used to assess the adequacy of Eurocode 3 design guide lines (CEN 2005a, CEN 2005b, CEN 2005c) and Direct Strength Method (DSM) to design a range of conventional and optimum designed CFS beams considering local/distortional buckling modes.

### 10.2 Direct Strength Method (DSM)

Prior to the description of the numerical study on the CFS back-to-back beams, a brief induction is presented here to explain the Direct Strength Method (DSM). Eurocode 3 design guidelines to consider local, distortional and global buckling and their interaction in the flexural strength of CFS beams have been described in chapter 3.

The Direct Strength Method (DSM) is a finite strip based method that integrates stability analysis into the design process. First the elastic local ( $M_{cr1}$ ), distortional ( $M_{crd}$ ) and global ( $M_{cre}$ ) critical buckling moments of CFS members are calculated using software such as CUFSM (Schafer 2006). The ultimate strength of the section is then predicted based on a series of simple empirical equations using the calculated elastic buckling moments and the flexural yield moments. While calculation of the effective properties can be tedious for complex CFS

Chapter 10. Local and distortional buckling of CFS Back-to-Back channels: a numerical study  
cross-sections, only gross section properties are needed in the DSM. The equations for  
calculating the nominal flexural strength for global buckling are a function of the flexural yield  
moment  $M_y = W_y f_y$  and the critical elastic lateral-torsional buckling  $M_{cre}$  :

$$\begin{aligned}
& \text{for } M_{cre} < 0.56M_y \\
& M_{ne} = M_{cre} \\
& \text{for } 2.78M_y \geq M_{cre} \geq 0.56M_y \\
& M_{ne} = \frac{10}{9} M_y \left( 1 - \frac{10M_y}{36M_{cre}} \right) \\
& \text{for } M_{cre} \geq 2.78M_y \\
& M_{ne} = M_y
\end{aligned} \tag{10.1}$$

The nominal flexural strength of a CFS beam designed for local buckling and considering local–  
global interaction is related to the local–global slenderness  $\lambda_l = \sqrt{M_{ne}/M_{crl}}$  :

$$\begin{aligned}
& M_{nl} = M_{ne} \text{ for } \lambda_l \leq 0.776 \\
& M_{nl} = \left[ 1 - 0.15 \left( \frac{M_{crl}}{M_{ne}} \right)^{0.4} \right] \left( \frac{M_{crl}}{M_{ne}} \right)^{0.4} M_{ne} \text{ for } \lambda_l > 0.776
\end{aligned} \tag{10.2}$$

The nominal flexural strength for distortional buckling is calculated as a function of slenderness  
 $\lambda_d = \sqrt{M_y/M_{crd}}$  :

$$\begin{aligned}
& M_{nd} = M_y \text{ for } \lambda_d \leq 0.673 \\
& M_{nd} = \left[ 1 - 0.25 \left( \frac{M_{crd}}{M_y} \right)^{0.6} \right] \left( \frac{M_{crd}}{M_y} \right)^{0.6} M_y \text{ for } \lambda_d > 0.673
\end{aligned} \tag{10.3}$$

Finally the flexural strength of the CFS beam is determined based on the minimum value  
calculated from Equations (10.1)-(10.3):

$$M_n = \min \{ M_{ne}, M_{nl}, M_{nd} \} \tag{10.4}$$

### 10.3 Optimisation of CFS beams

In this section an optimisation framework proposed by the authors (Chapter 4 to Chapter 5) is  
adopted for optimum design of a back-to-back channel section by taking into account the  
interaction between local and distortional buckling modes. The objective function is to obtain a  
design solution with maximum bending capacity as follows:

$$\max M_{c,Rd} = W_{eff}(x) \cdot f_y \tag{10.5}$$

Chapter 10. Local and distortional buckling of CFS Back-to-Back channels: a numerical study  
subject to:

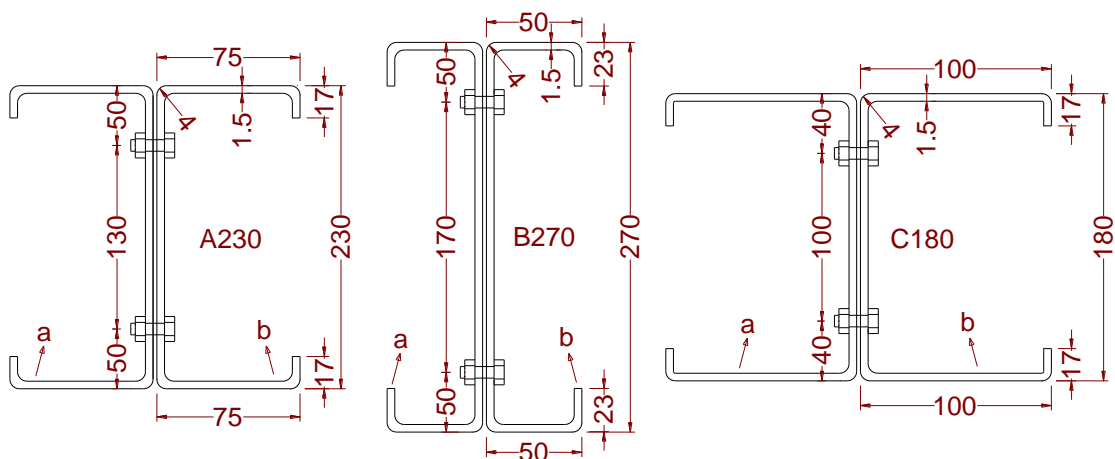
$$b/t \leq 60, c/t \leq 50, h/t \leq 500 \quad (10.6)$$

$$0.2 \leq c/b \leq 0.6 \quad (10.7)$$

$$b \geq 50, c \leq 25 \quad (10.8)$$

where  $h$  is the cross-sectional height, and  $b$  and  $c$  are the flange and lip width, respectively. Equations (10.6) and (10.7) represent the width-to-thickness ratio limits defined in EC3 (CEN 2005b). Equation (10.8) is used to take into account the manufacturing and construction constraints. No flexibility is offered for the lip angles in order to adapt to the typical cold-rolling machines for the CFS beam production. Particle Swarm Optimisation (PSO) algorithm was adopted to solve the above constraint optimisation problem defined. More information on the PSO optimisation method can be found in Chapter 4.

Figure 10.1 shows the nominal dimensions of the three different cross-sections used in this study. All the dimensions in this figure are defined by the outer to outer surface. The cross-section A230 is a standard commercially available cross-section, while sections B270 is the optimum solution with the highest flexural strength subjected to constraints in Equations (10.6) to (10.8). Cross-section C180 is a complementary section (with a flange width between the flange widths of sections A230 and B270) used for comparison purposes. All cross-sections have the same nominal thickness  $t = 1.5\text{mm}$  and coil width of steel sheet  $l = 415\text{mm}$  to use the same amount of material. The values for the radius of the round corner, the elastic modulus and the Poisson's ratio used were taken as  $3\text{mm}$ ,  $210\text{GPa}$  and  $0.3$ , respectively. The yield stress of the CFS plate was considered to be  $f_y = 450\text{MPa}$ .



**Figure 10.1. Symbol definitions and nominal cross-sectional dimensions**

The above mentioned sections were manufactured by press breaking process and were tested around their major axis using a four-point bending set-up as shown in Figure 10.3 to obtain their

Chapter 10. Local and distortional buckling of CFS Back-to-Back channels: a numerical study

flexural strength. For each cross-section, two similar specimens with the same cross-section were tested to ensure the consistency of the results. The non-linear stress-strain behaviour and enhanced corner properties of the material were obtained based on the results of six tensile coupons. The geometric imperfections of the back-to-back specimens were recorded using a specially designed measurement rig. Tensile coupons were also extracted from the flat portions and the corner regions of the cross-sections in order to determine the material properties. More information about the conducted experimental tests can be found in Chapter 9. In the next section, detailed FE models will be developed and validated against the experimental results of the three sections shown in Figure 10.1.

## 10.4 Numerical modelling

### 10.4.1 Material model

The inelastic properties of CFS material were found to have significant effects on the ultimate capacity and post-buckling behaviour of CFS beams. In this study, the results of the six tensile coupon test from the flat plates and round corner regions of the cross-sections were used to investigate the effects of forming process on the material properties. For example, a comparison between the engineering and true stress-strain curves of a flat and a corner coupon is compared in Figure 10.2 for the standard A230 section. The results indicate that the 0.2% proof stress of the corner coupon is around 24% higher than that of the flat coupon in the same section. Moreover, a comparison between the dynamic and static stress–strain curves of the coupon specimens shows that the stress reduced by around 5–8% at both yield and ultimate strengths during the static drop, which is also called “stress relaxation”(Huang and Young 2014). The static stress–strain curves are calculated from the dynamic stress–strain curves by removing the dynamic effects of the tensile test. The material model was then included in the FEM by using the true stress vs true strain curve, which was calculated from the following equations:

$$\sigma_{true} = \sigma(1 + \varepsilon) \quad (10.9)$$

$$\varepsilon_{true} = \ln(1 + \varepsilon) \quad (10.10)$$

where  $\sigma$  and  $\varepsilon$  are the measured engineering stress and strain based on the original cross-section area of the coupon specimens, respectively. The resulted stress-strain curves corresponding to the round corner areas were also incorporated into ABAQUS (ABAQUS 2011).

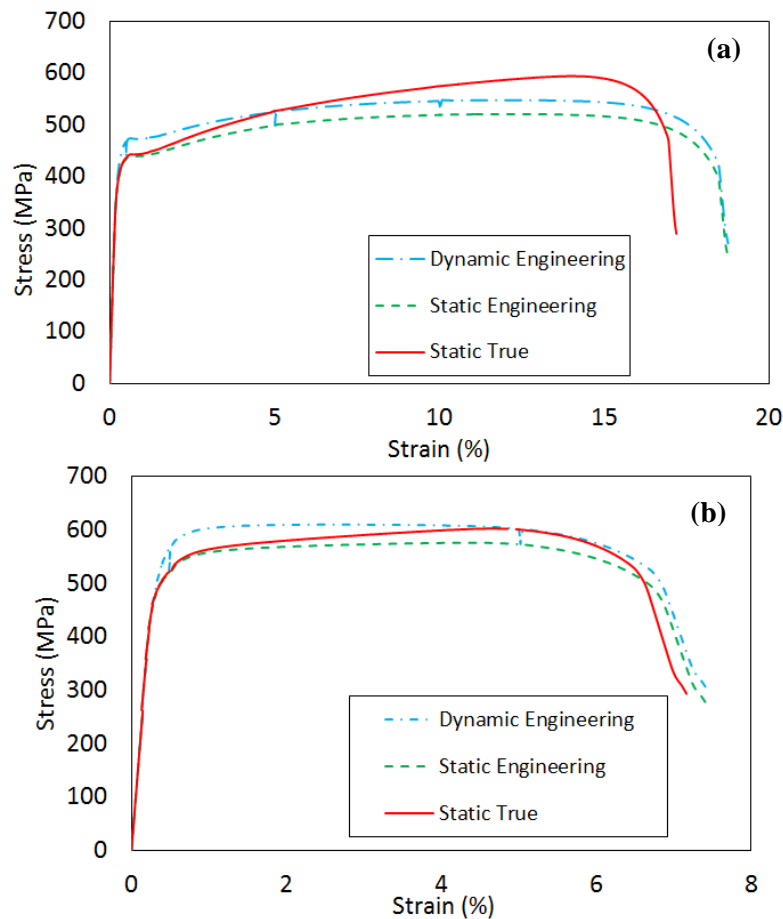


Figure 10.2. Stress–strain curves resulted from (a) flat and (b) corner coupon tests

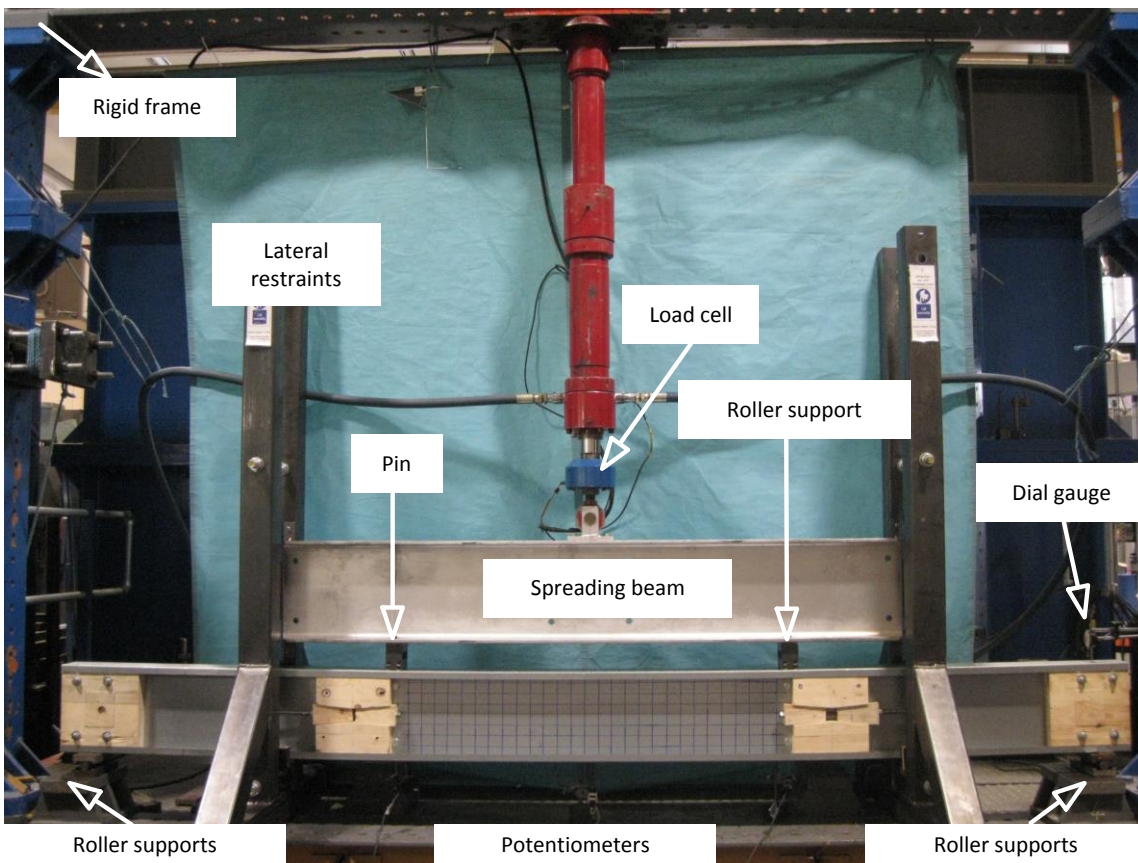
#### 10.4.2 Boundary conditions

To simulate the boundary conditions of the experimental program, a simply supported condition was used at both ends of the FE models as shown in Figure 10.4. Two reference points were established at the positions of the roller and pin supports at the middle of the gap between the top two flanges of the CFS back-to-back beams to apply the external loads,. The nodes under the region of the supports were coupled to the related reference point corresponding to the pin and roller supports as indicated in Figure 10.4.

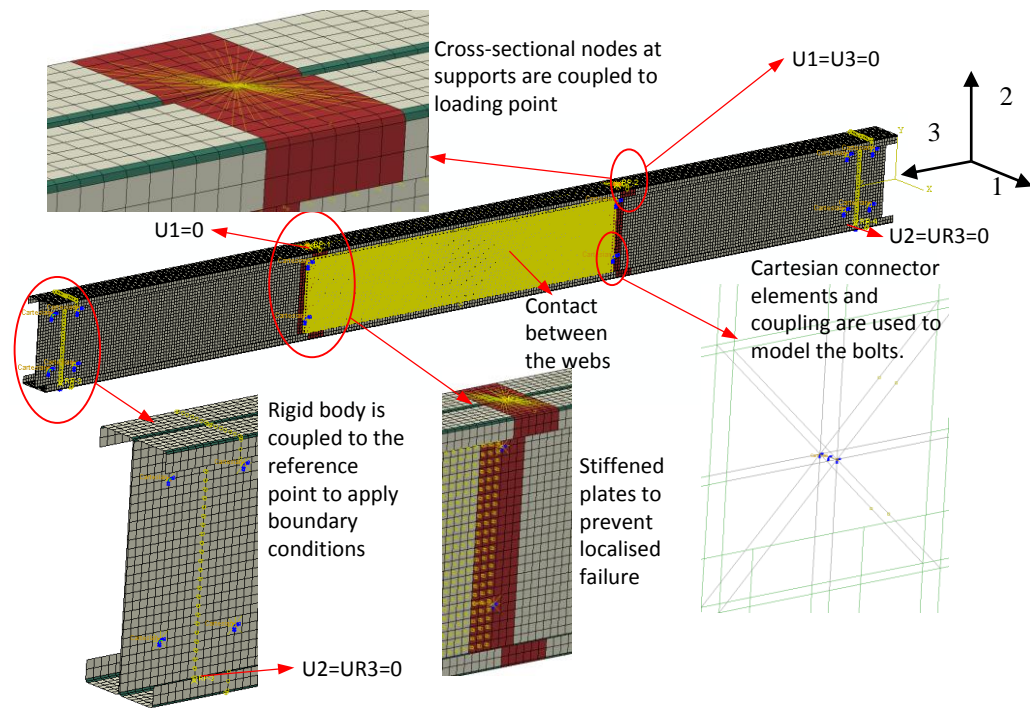
In order to avoid the localised bearing failure of the CFS sections during the experimental tests, wooden blocks were packed into the cross-section at the loading points and end supports (see Figure 10.3). Therefore, the elastic modulus  $10E$  was used for the steel plates in the areas with the wood blocks. A rigid body constraint, with a reference point at the middle of the gap between the two bottom flanges of the CFS back-to-back beams, was used at both ends of the CFS beam to prevent localised failure at the supports. To simulate the roller supports at the tow ends of the CFS beams, the degrees of freedoms at the reference points were set to be  $U2=UR3=0$  (see Figure 10.4). Regarding the reference points at the loading positions, the translations of  $U1$  and  $U3$  were fixed at the pin support while  $U1=0$  was used at the roller

Chapter 10. Local and distortional buckling of CFS Back-to-Back channels: a numerical study support. This was to prevent the lateral deformation and longitudinal displacement of the CFS beams.

The CFS back-to-back beams were assembled by using two single channels with bolts as shown in Figure 10.4. A connector element was used to model the bolt behaviour as will be explained in section 10.4.4. Contact pairs were also defined between the two webs of each CFS single channel section using a surface-to-surface contact property. In the normal direction of the contact pairs, “hard” surface was used while in the tangent direction between the two profiles, a “frictionless” property was defined.



**Figure 10.3. Typical experimental setup of four-point bending tests of back-to-back beam sections**



**Figure 10.4. Boundary conditions of FE model against test**

### 10.4.3 Element type and mesh

S4R was selected from the available ABAQUS element library for the modelling of the CFS beams. It is doubly curved, a four-node, quadrilateral and stress/strain shell element with induced integration and hourglass control. This shell element is chosen due to the fact that it is a general purpose element that takes account of transverse shear deformation. This element also uses three translational and three rotational degrees of freedom at each node. The element type has been successfully used in the modelling of CFS beam section behaviours (Haidarali and Nethercot 2011, Wang and Young 2016a, Yu and Schafer 2007).

The effects of mesh size in the FE model on the behaviour of the CFS beams were firstly investigated. It was found that using a 10x10mm element dimension for CFS channel was able to provide a balance between computational time and accuracy. Therefore, 10x10mm elements were used for all of the FE simulations. However, for the modelling of the corners of the CFS sections, it was found that two elements were suitable for the modelling of each round corner.

### 10.4.4 Bolt modelling

It was found from reference experimental tests that the position and behaviour of bolts can considerably influence the moment-rotation behaviour of CFS full-scale beams (Serror et al. 2016), both slippage and bolt bearing deformation were observed. Therefore, it is important to develop an accurate detailed model in ABAQUS in order to simulate the load-deformation behaviour of a single bolt bearing against a single steel sheet. Lim and Nethercot (Lim and

## Chapter 10. Local and distortional buckling of CFS Back-to-Back channels: a numerical study

Nethercot 2004a, Lim and Nethercot 2003) used a simplified bolt model which consisted of two perpendicular nonlinear springs to model the bearing behaviour of a single bolt by, In their study, good agreement was achieved between experimental test results and the modelled behaviour of CFS full-scale joint subjected to monotonic load. A more direct method to model bolt behaviour using FE analysis is to use solid brick element C3D8R and surface-to-surface contact interactions in ABAQUS(Gutierrez et al. 2015, Liu et al. 2015b, Öztürk and Pul 2015). The disadvantage of this model is that using solid elements makes the model more complex and, therefore, reduces the computational efficiency for cyclic modelling, especially in models with a large number of bolts. Besides, due to the presence of bolt rigid body movement and slippage, the convergence could be an issue (Liu et al. 2015b). A technique is therefore presented here to simulate the slippage and bearing behaviour of bolts in CFS back-to-back sections.

In assembling of CFS back-to-back channels, a fastener tension (or preloading force) is developed by using a torque wrench applied to the head of the bolt. The torque–preloading relationship is often simplified by using a constant  $K_0$ , known as torque coefficient, as shown in the following equation (Bickford 1997, Juvinall and Marshek 2006):

$$T = K_0 \cdot P_b \cdot d_0 \quad (10.11)$$

Where  $T$  ( $N \cdot mm$ ) is the input tightening torque applied to the fastener head or nut,  $P_b$  ( $N$ ) is the preloading force and  $d_0$  ( $mm$ ) is the nominal bolt diameter. An approximate value of 0.20 has been provided for the torque coefficient (Bickford 1997, Juvinall and Marshek 2006), therefore, an equivalent preloading force of  $P_b = 6.25kN$  is obtained, which is close to the tested results presented in Croccolo et al. (Croccolo et al. 2011). The slippage behaviour of the bolts depends mainly on the distribution of initial friction forces, which in return rely on the bolt pretension force  $P_b$  for a given applied torque and friction coefficient  $\mu$  of the contact surfaces. A formula which is used to calculate the bolt slip resistance  $F_{slip}$  can be expressed as (Wong and Chung 2002):

$$F_{slip} = \mu_0 \cdot P_b \cdot n_b \quad (10.12)$$

Where  $\mu_0$  is the mean frictional coefficient given as 0.19 for galvanised steel surfaces(Wong and Chung 2002), and  $n_b$  is the number of slip planes.

A bolt transfers the shear behaviour of CFS members through the bearing behaviour in addition to slippage described above. Once the slippage deformation overcomes the gap between bolt shank and the steel sheet, the bearing behaviour of the bolt against steel sheet will be activated. Fisher(Fisher 1964) proposed the following equation to calculate the bearing force and displacement, which reflects the bolt bearing force and the bearing deformation relationship:

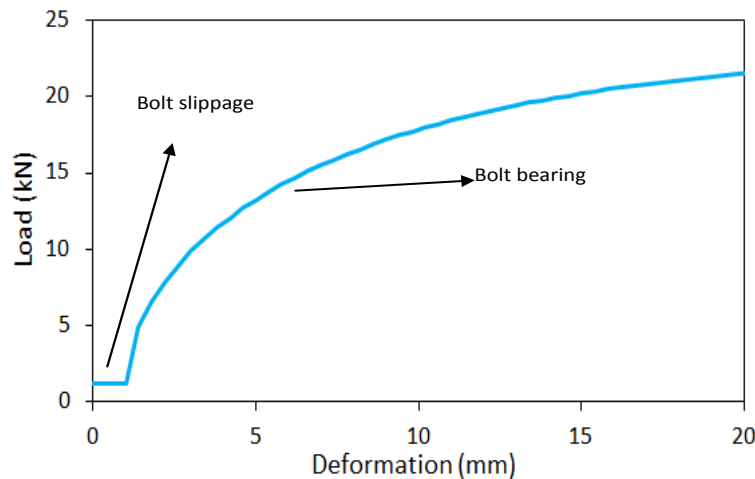


$$R_B = R_{ult} \left[ 1 - e^{-\mu_1 (\delta_{br}/25.4)} \right]^\lambda \quad (10.13)$$

$$R_{ult} = 2.1 d_0 t \sigma_u \quad (10.14)$$

where  $\delta_{br}$  is the bearing deformation (mm),  $R_B$  is the bearing force corresponding to the bearing deformation,  $R_{ult}$  is the ultimate bearing strength,  $t$  is the web thickness,  $d_0$  is the bolt diameter,  $\sigma_u$  is the tensile strength of the web plate material, which can be obtained from coupon tests.  $e = 2.718$  is the nature exponential while  $\mu_1 = 5$  and  $\lambda = 0.55$  are the regression coefficients presented by Uang et al. (Uang et al. 2010).

In the current tests presented in chapter 9, the bolt shank diameter was 12mm. The bolt slippage behaviour is generally defined for a limited range of slip movement within the bolt hole clearance (typically  $\pm 1$ mm for standard bolts by assuming that the bolt shanks are centrally positioned). According to Equations (10.11)-(10.14), a slip-bearing relationship can be defined in Figure 10.5.

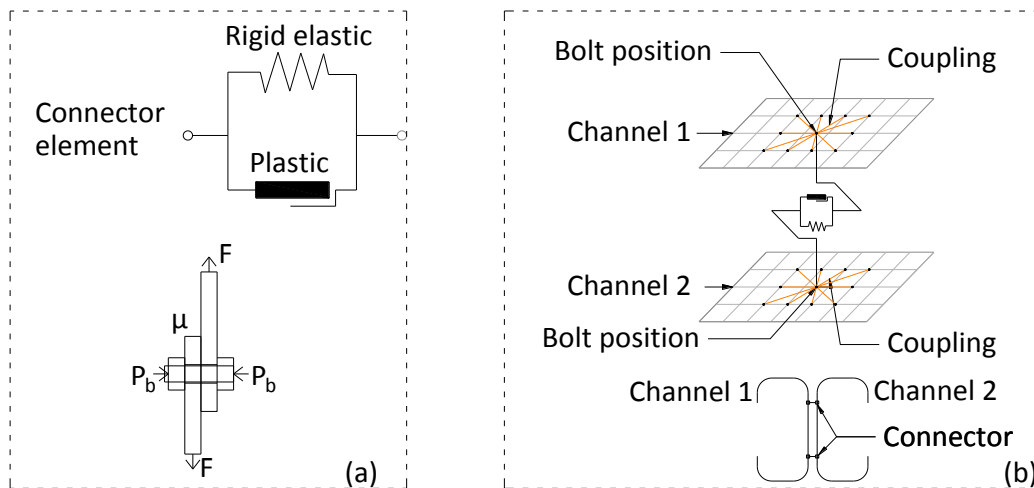


**Figure 10.5. Load-deformation relationship of a bolt slipping and bearing against a steel plate**

In order to model a group of bolts, the connector element in ABAQUS (ABAQUS 2011) was used, as shown in Figure 10.6. For each single bolt, a two-layer fastener configuration was used at the position of each individual bolt in the full-scale connection (see Figure 10.6(b)). The layer was connected by a node in one channel section and a point in its counterpart section using a connector element to define bolt property. The connector type of “Cartesian” with 3 translational degrees of freedom at each node was employed. This connector was characterised by a parallel combination of “Elasticity” and “Plasticity” behaviours, as defined in ABAQUS (ABAQUS 2011). In the “Elasticity” behaviour, the rigid material definition was used in the corresponding shear direction. For the definition of “Plasticity” behaviour, the load-deformation relationship shown in Figure 10.5 was employed to represent the behaviour of a bolt which is

Chapter 10. Local and distortional buckling of CFS Back-to-Back channels: a numerical study slipping and bearing against a steel plate. It should be noted that the “Elasticity” and “Plasticity” behaviours are defined in the directions of local coordinate system corresponding to the shear deformation of the bolts.

The bolt slippage and bearing behaviour, which are defined in Equations (10.11)-(10.14), are included in the connector element shown in Figure 10.6(a). Therefore, it is important to exclude the bearing deformation stemmed from the bearing of each node at the bolt position. To achieve this, the constraints “Coupling” in ABAQUS (Abaqus/CAE User's Manual, 2011) was employed, and its definition is shown in Figure 10.6(b). Each node at the position of the bolt was thereby connected to the nearby nodes in the CFS steel plates using the constraint that couples the displacement and rotation. These nodes should lie in a reasonably big region in the plates to reduce the bearing deformation to the maximum level.



**Figure 10.6. Single bolt modelling in ABAQUS: (a) components defined in a connector; (b) reducing the bearing behaviour by coupling the node at bolt position to a number of nodes around**

#### 10.4.5 Imperfections

The stability of thin-walled CFS members may in some cases be significantly affected by the presence of imperfections, especially when interactive buckling of different modes is involved. In the reference experimental programme, the magnitude and the shape of the imperfections of each specimen were therefore recorded before the testing.

The imperfections were measured along the five longitudinal lines indicated in Figure 10.7, by means of reflected laser beams. Since the span in pure bending (1200mm in length) is more critical, only the imperfection in this span was recorded. In a first step, the raw data were decomposed into their respective Fourier series. The Fourier series were removed after a finite number of terms to cut off the high frequency vibrations originating from the driving mechanisms of the moving motors. Using the approximation of Fourier series resulted in a more continuum node coordinates adjustment when the measured imperfections were included.

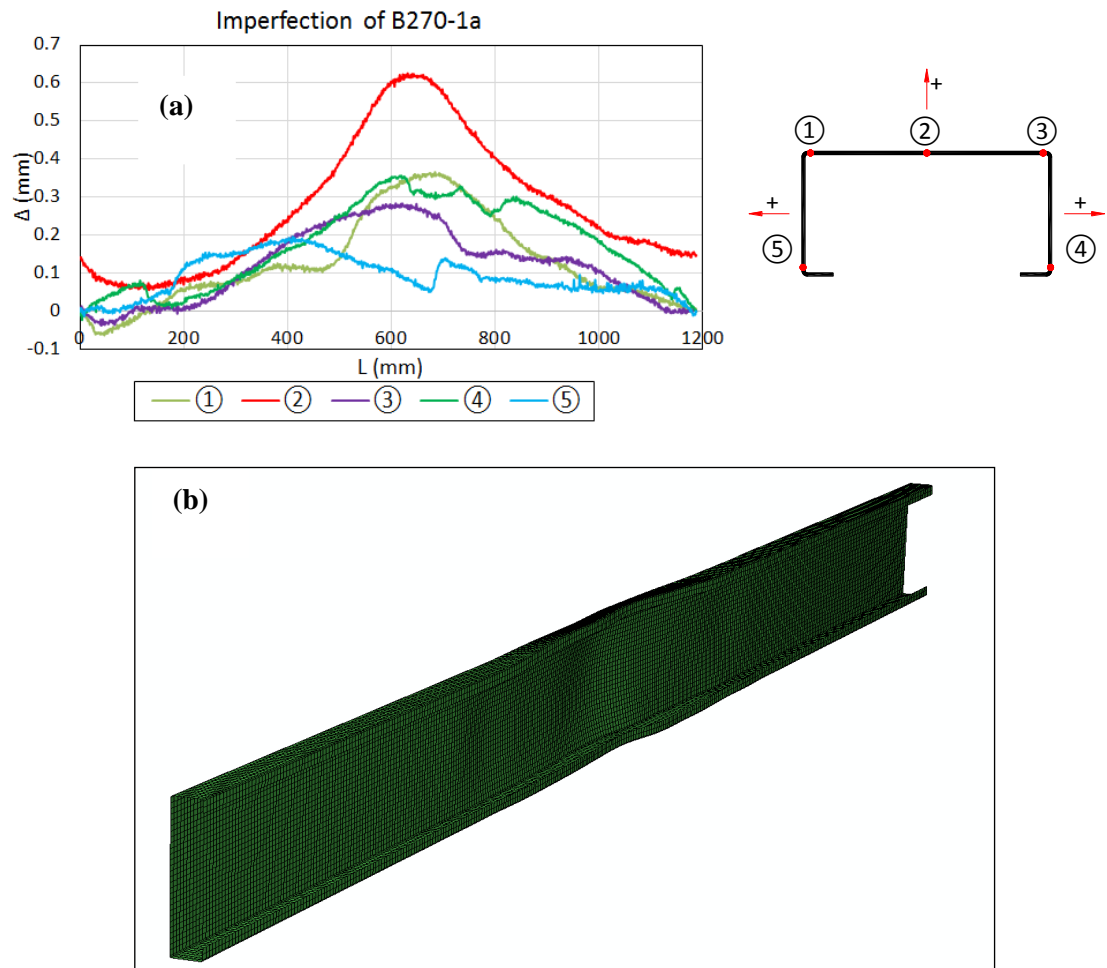


Figure 10.7. Measured imperfection in B270-1a (a) profile; (b) included in the FE model (magnified 50 times)

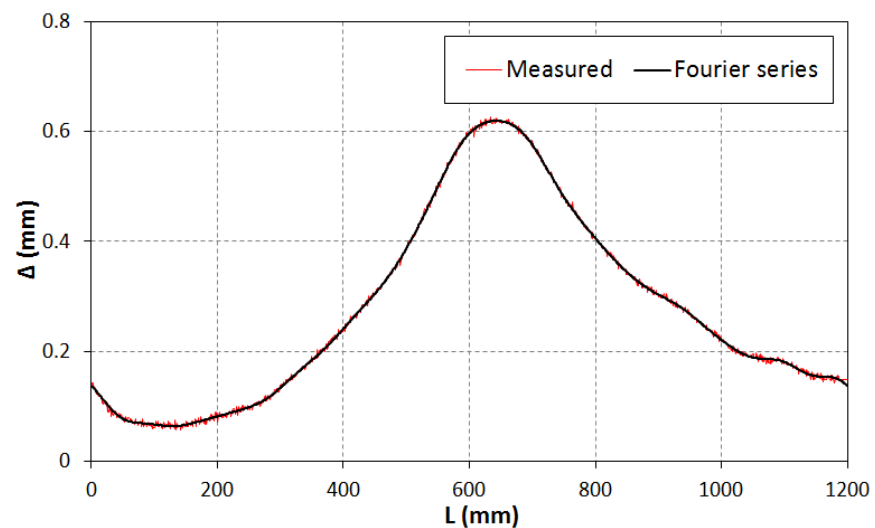
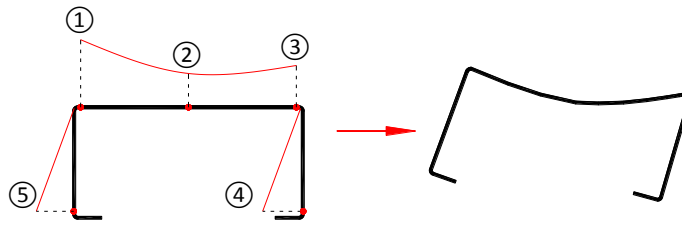


Figure 10.8. Measured imperfection profile and its Fourier representation



**Figure 10.9. Imperfection inclusion**

It should be noted that, in general, it is essential to use a significant number of Fourier terms to represent the shape of measured imperfections. In this study, by a trial and error process, it was found that using 20 Fourier terms typically leads to accurate results. As an example, Figure 10.8 compares the measured imperfection profile along line 3 of specimen B270-1a, with the truncated Fourier representation shown as a solid black line. Within a given cross-section the magnitude of the imperfection at the location of each node of the FE mesh was determined by interpolation of the measurements. Quadratic interpolation was used for the web imperfections, while linear interpolation was used at the flanges, as shown in Figure 10.9. The coordinates of each node were then adjusted to account for the imperfections. The program to incorporate the imperfections is presented in Appendix A.2.

#### 10.4.6 Numerical results

Table 10.1 compares the ultimate load carrying capacity  $M_u$  resulting from the FE model against those obtained from the experiments in chapter 9 on the CFS lipped channel beams with different cross-sections.  $M_{u1}$  is the predicted flexural strength that takes into account the strain hardening effect of the material in the corner region but without incorporating the imperfection.  $M_{u2}$  indicates the predicted moment capacity where only the effect of the measured initial imperfection was taken into account. The FE predicted capacity  $M_{u3}$ , on the other hand, considers both the measured initial imperfection and the strain hardening effect of the material in the corner region.

It is shown in Table 10.1 that an excellent agreement was obtained between experimental results and FE predictions. The average ratio of the FE predicted bending capacity  $M_{u2}$  to the experimentally measured flexural strength  $M_u$  was 0.960, with a standard deviation of 0.019. In comparison, the average ratio of the FE predicted bending capacity  $M_{u3}$  to the experimentally measured load carrying capacity  $M_u$  was 0.982, with a standard deviation of 0.013. This indicates that considering the strength variation caused by the strain hardening effect of the round corner material in the current test series could increase the accuracy of the bending capacity predictions by 2%, which is not significant. However, by comparing the predicted

flexural strength  $M_{u1}$  with  $M_{u3}$ , it is shown that the initial imperfection can have significant effects on the load carrying capacity. On average, the variation of flexural strength is 3% and 1% with and without taking into account the imperfection, respectively.

Figure 10.10 illustrates the tested moment versus mid-span deflection relationship between the experiment and the predicted results from numerical study. It is shown that the proposed FE model was able to capture the peak load and stiffness of CFS beam sections.

The proposed FE model was also able to accurately capture the failed shape of the tested CFS beams. Figure 10.11-Figure 10.13 compares the failure shape of the tested specimens with the predicted deformation of the corresponding FE models. It is shown that the proposed FE model could predict the failure mode of the CFS beams with a very good accuracy.

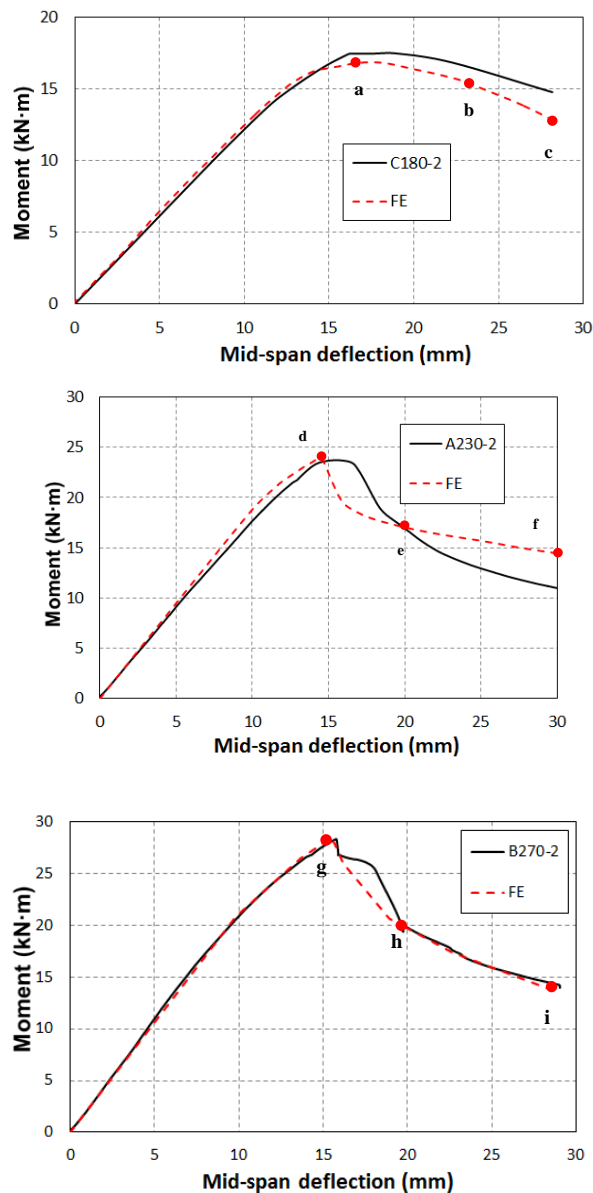


Figure 10.10. Moment versus mid-span deflection relationship resulting from FE against Test

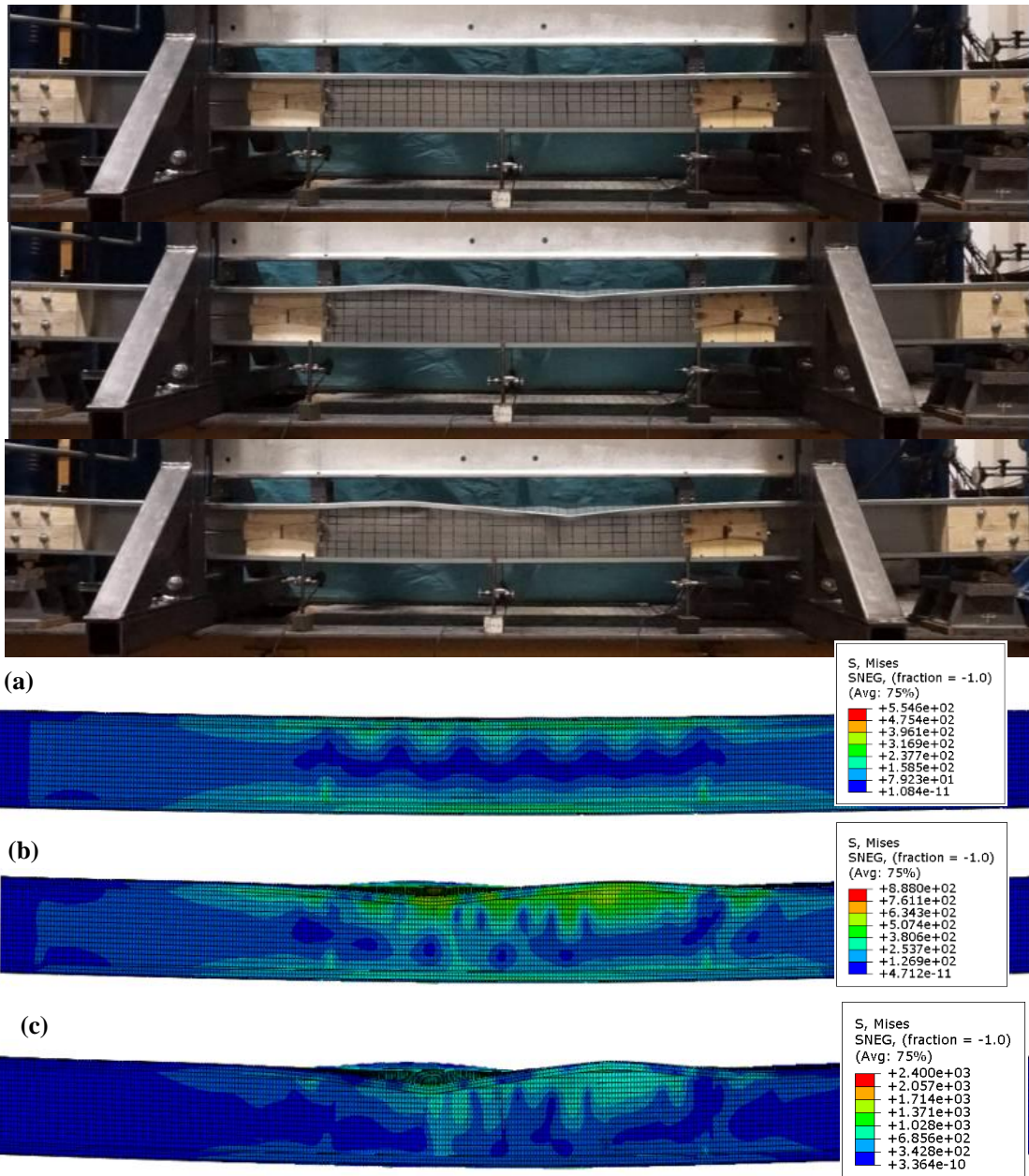


Figure 10.11. Deformed shapes from the test of beam C180-2 and stress distributions (MPa) from the FE analysis, recorded at three stages of loading (see Figure 10.10)



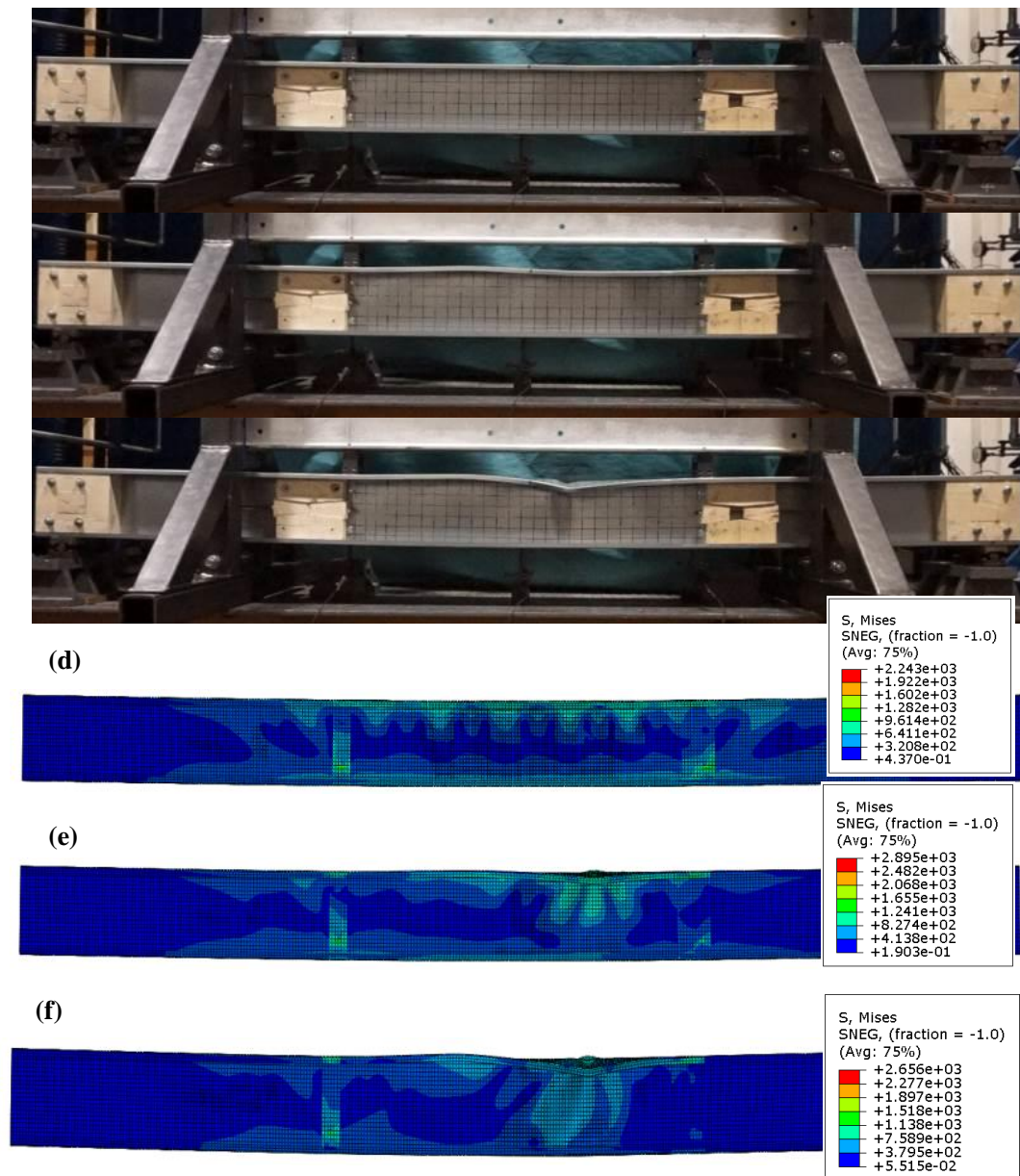


Figure 10.12. Deformed shapes from the test of beam A230-2 and stress distributions (MPa) from the FE analysis, recorded at three stages of loading (see Figure 10.10)

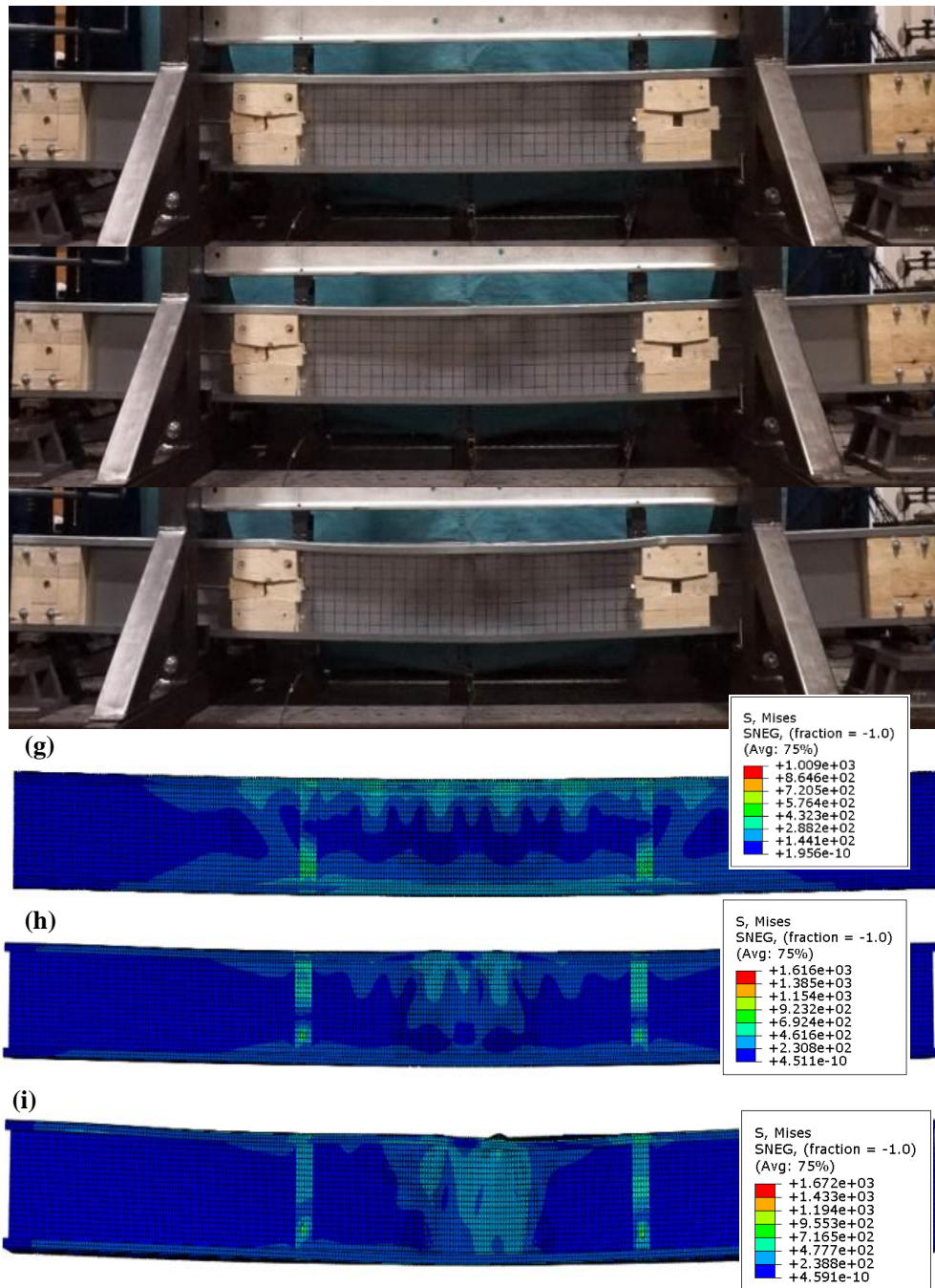


Figure 10.13. Deformed shapes from the test of beam B270-2 and stress distributions (MPa) from the FE analysis, recorded at three stages of loading (see Figure 10.10)



**Table 10.1. Comparison of FE results with tested flexural strength**

Specimen	$M_u$ (kN·m)	$M_{u1}$ (kN·m)	$M_{u2}$ (kN·m)	$M_{u3}$ (kN·m)	$M_{u1} / M_u$	$M_{u2} / M_u$	$M_{u3} / M_u$
A230-1	23.72	25.31	23.12	23.56	1.067	0.975	0.993
A230-2	23.79	25.58	22.39	23.01	1.075	0.941	0.967
B270-1	(25.83)	28.87	25.95	26.17	--	--	--
B270-2	28.34	28.25	27.82	28.11	0.997	0.982	0.992
C180-1	17.43	18.22	16.41	16.89	1.045	0.941	0.969
C180-2	17.24	17.89	16.53	17.01	1.038	0.959	0.987
Average					1.044	0.960	0.982
St. Dev.					0.031	0.019	0.013

### 10.5 Evaluation of current design methods of EC3 and DSM

In this section, the experimental results are compared to the predictions of the DSM and EC3 design equations presented in Section 10.2. As shown in Table 10.2, the DSM predictions on the design of CFS back-to-back beams are more accurate than the EC3 design method. The ratio of the DSM predicted load capacity to the experimentally measured load carrying capacity was 0.960, with a standard deviation of 0.046. It is also evident that the “effective width” based method comprised in EC3 generally leads to slightly unconservative predictions of the beam strengths with an average ratio 1.051 of EC3 prediction to test.

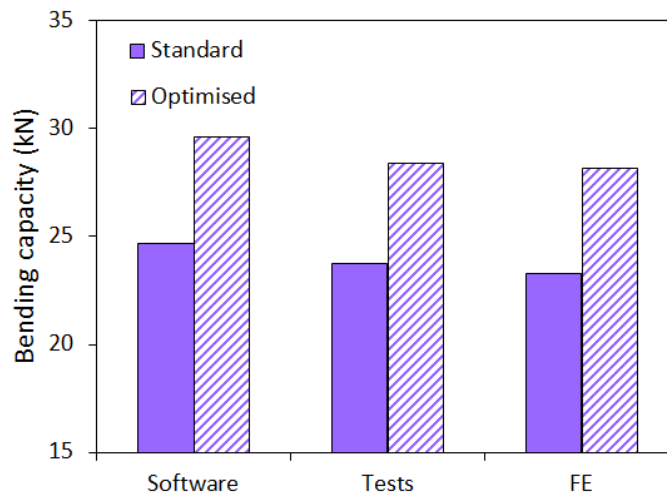
**Table 10.2. Evaluation of the design methods of DSM and EC3**

Specimen	Test (kN·m)	EC 3 (kN·m)	DSM (kN·m)	EC3 / Test	DSM/Test
A230-1	23.72	24.56	22.42	1.035	0.945
A230-2	23.79	24.75	22.61	1.040	0.950
B270-1	(25.83)	29.74	25.76	--	--
B270-2	28.34	29.42	25.38	1.038	0.896
C180-1	17.43	18.59	17.42	1.067	0.999
C180-2	17.24	18.51	17.40	1.074	1.009
Average				1.051	0.960
St. Dev.				0.018	0.046

### 10.6 Evaluation of the optimisation process

In this section, the efficiency of the optimisation method explained in Section 10.2 is further investigated. While section A230 is a standard commercially available cross-section, B270 is the optimum solution with highest flexural strength subjected to constraints in Equations (10.6)-(10.8) for lipped channel beam. The nominal cross-sectional dimensions of these sections are given in Figure 10.1.

Figure 10.14 compares the ultimate bending capacity of the standard and optimised sections for the CFS beams obtained from the experimental results, detailed FE models and EC3 design method. Based on the experimental results, it is shown that the optimised shapes offer a much higher flexural strength (up to 19% higher) compared to the standard lipped channel section with the same amount of material. Similar results were obtained from FE models and EC3 design method, where the optimum design solutions showed, around 20% higher flexural strength compared to the standard sections.



**Figure 10.14. Flexural strength of the optimised sections to the standard section using the same amount of material**

It is worth noting that the trends of increasing/decreasing capacity over the range of sections for the CFS beams are very well predicted by EC3 when the tested results are taken as a benchmark. This indicates that the proposed optimisation method is accurate and reliable and provides a practical tool for manufacturers and structural engineers to improve the capacity of CFS beams.

The results of this study in general demonstrate the accuracy and reliability of the developed FE models to predict the flexural strength of CFS beams with different cross sectional shapes. These validated models should prove useful in practical applications for more efficient design of CFS back-to-back beams.

## 10.7 Conclusions

In this chapter, a finite element (FE) model was developed to study the local/distortional buckling behaviour in CFS lipped back-to-back channel beams. The model takes into account the non-linear stress–strain behaviour of CFS material, the strength hardening effects at the round corners due to the cold-working process, and the experimentally measured initial imperfections. The FE model was validated against an experimental program on a total number of six lipped channel back-to-back beams. The validated models were then used to assess the

Chapter 10. Local and distortional buckling of CFS Back-to-Back channels: a numerical study accuracy of EC3 and DSM design methods for standard and optimum design solutions. Based on the results presented in this chapter, the following conclusions can be drawn:

- (1) The ultimate capacity of the sections predicted by the FE models was on average less than 2% in variation from the experimental results. The proposed FE model was also successful in capturing the failure shapes and predicting the compressive strength of CFS columns subjected to local and global buckling modes.
- (2) It was shown that, on average, the geometric imperfections can change the FE predictions by 6%, while the strength variation caused by the strain hardening effect at the round corners material in general has negligible effects (less than 2%).
- (3) The ratio of predicted to experimentally measured flexural strength was on average 0.960 and 1.051 for DSM and EC3 design methods, respectively. The results show that DSM generally leads to conservative predictions, while EC3 generally leads to slightly unconservative predictions of the beam flexural strengths.
- (4) The bending capacity of the optimised CFS beams obtained from validated FE models and EC3 design methods were up to 20% higher, than their standard lipped channel counterpart sections with the same amount of material. This demonstrated the efficiency of the proposed optimisation method to improve the compressive capacity of CFS sections.
- (5) The results of this study in general demonstrate the accuracy and reliability of the developed FE models to predict the flexural strength of CFS beams with different cross sectional shapes. These validated models should prove useful in practical applications for more efficient design of CFS beam elements.

This page is intentionally left in blank

## **CHAPTER 11. Behaviour of CFS bolted connections: a numerical parametric study**

---

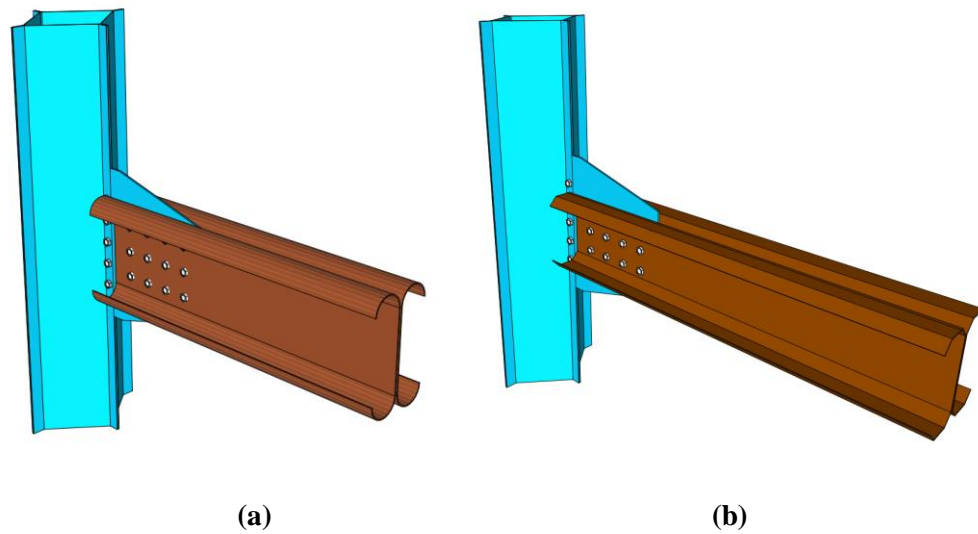
The ductility of cold-formed steel unbraced multi-story moment-resisting frame or portal frame mainly depends on the performance of beam-to-column connections and beam cross-sectional shapes. This trend emphasises the importance of investigating the behaviour of CFS bolted moment-resisting connections with complex sectional shapes for seismic application. This chapter aims at presenting an extensive parametric study on the structural behaviour of CFS bolted beam-to-column connections with gusset plate under cyclic loading. In order to simulate hysteretic moment–rotation behaviour and failure modes of CFS connection, an experimentally validated finite element model taking into account the material property and geometrical imperfection using ABAQUS (ABAQUS 2011) was developed. A simplified connector element was adopted to simulate the behaviour of full-scale CFS connection considering the slip-bearing action in a single bolt. The developed numerical model was then used to investigate the connection performance in terms of strength, ductility, energy dissipation capacity and damping coefficient. Furthermore, the effects of bolt distribution, cross-sectional shapes, gusset plate and cross-sectional thicknesses on the connection performance were examined. Section classification on the unconventional CFS cross-sectional shapes with characteristics such as intermediate stiffeners in the flange, folded flange and curved flange were also studied. It is shown that the proposed FE model is robust and computationally efficient to simulate the failure modes and moment-rotation responses of CFS bolted connections.

## 11.1 Introduction

Cold-formed steel (CFS) cross-sections have traditionally been employed as secondary load-carrying members in a wide range of applications, such as roof purlins and wall girts. In a more recent trend, CFS members are also increasingly being employed as primary structural elements in low- to mid-rise multi-storey buildings (Fiorino et al. 2014) and CFS portal frames with short to intermediate spans (Lim and Nethercot 2004a, Lim and Nethercot 2003). These have increased the demand for CFS elements in the application of architectural layout with large spans. Compared to hot-rolled members, CFS thin-walled members provide several advantages of economy and efficiency, including a high strength for a light weight, a relatively straightforward manufacturing process and an ease of transportation and erection. In addition, in the application of long span floors and roofs, the CFS built-up sections have been employed to improve strength and stiffness of structure. Therefore, research has been conducted on the CFS built-up sections (Lamín et al. 2013, Manikandan et al. 2014, Wang and Young 2016a, Wang and Young 2016b) in order to provide increased strength and stiffness. However, there is a need to develop robust and ductile connection types which are suitable for steel frames with CFS sections, especially for seismic areas.

The behaviour of beam-to-column CFS bolted moment resisting connections with gusset plate has been investigated experimentally and numerically under monotonic and cyclic loading conditions (Bučmys and Daniūnas 2015, Lim and Nethercot 2003, Sabbagh et al. 2012b, Serror et al. 2016, Uang et al. 2010, Wong and Chung 2002). It was found that CFS bolted moment resisting connections are able to provide high stiffness and ductility. The stiffness and ductility of CFS bolted connections were mainly determined by the bolt number and its bearing characteristics. An analytical research presented by Lim et al. (Lim et al. 2016) indicate that the bolt distributions in CFS connections have significant effect on the bending capacity of their connected sections. It was reported in (Calderoni et al. 2009, Padilla-Llano et al. 2016, Padilla-Llano et al. 2014) that cold-formed steel sections have shown not negligible ductility and energy dissipation capacity even subjected to local/distortional buckling. Recent experimental and analytical research on the CFS moment resisting frames (Sabbagh et al. 2012a) at the University of Sheffield showed that by increasing the number of flange bends in CFS channel sections, local buckling in the flanges can be delayed. Consequently, higher strength, stiffness, and ductility were observed in curved flange beams shown in Figure 11.1(a). Nevertheless, this type of cross-section is hard to manufacture and is difficult to be connected to typical floor systems. Considering the construction and manufacture restraints, a curved flange was substituted with a folded flange cross-section as an approximation (Figure 11.1(b)). A comparison among different beam shapes proved that the optimised folded flange section provides a bending capacity up to 57% higher than standard lipped channels (see Chapter 5). Therefore, It can be concluded that the ductility and amount of dissipated energy of CFS bolted connections are mainly related to

four factors: (a) material yielding and bearing around the bolt holes; (b) yielding lines resulted from the buckling of the CFS cross-sectional plates; (c) bolt distribution and (d) cross-sectional shapes of the CFS elements.



**Figure 11.1. Configuration of CFS moment resisting connections with (a) curved flange beam (Sabbagh et al. 2012a) and (b) folded flange beam (Ye et al. 2016b)**

This chapter therefore aims at presenting a numerical study on the structural behaviour of CFS bolted beam-to-column connections under cyclic loading, in order to achieve updated knowledge of such connection type and to promote the application of CFS connections. A nonlinear finite element model taking into account the geometrical imperfection and material nonlinearity was first developed. The FE model uncovers a simplified connector element to model the behaviour of a single bolt against CFS plate, which leads to improved calculation efficiency and convergence subjected to cyclic loading. The developed FE model was then verified against available experimental results of CFS bolted connections under cyclic loading and good agreement was achieved. Finally, an extensive parametric study was conducted in order to investigate the effects of various cross-sectional shapes, cross-sectional slenderness, bolt distributions and gusset plate thicknesses on the behaviour of such connections. The performance of bolted-moment connection with a curved flange section was compared with three practical cross-sectional shapes: a conventional lipped channel section (flat channel), a lipped channel with intermediate V-shape stiffener in the flange (stiffened flat channel) and a folded flange cross-section. Some aforementioned parameters show huge effect on the structural performance of the CFS bolted-moment connections in terms of maximum flexural moment capacity, ductility ratio, energy absorption and damping coefficient. Furthermore the performance of CFS bolted moment connections with and without slippage were briefly investigated.

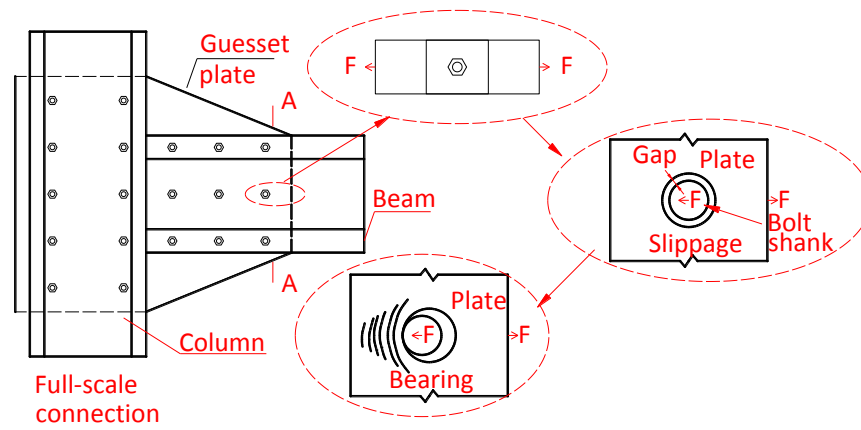
## 11.2 Finite element model

The numerical technique of Finite Element modelling has been previously applied to predict the behaviour of CFS bolted connections with gusset plate (Bučmys and Šaučiuvėnas 2013, Elkersh 2010, Lim and Nethercot 2004b, Lim and Nethercot 2003, Öztürk and Pul 2015, Sabbagh et al. 2013, Serror et al. 2016). Among these studies, two types of moment-rotation behaviours have been identified: (a) flexural deformation and local buckling in the beams and (b) slippage-bearing action. Good agreement has been achieved from numerical studies against experimental works under both monotonic (Lim and Nethercot 2004a, Öztürk and Pul 2015) and cyclic loading (Sabbagh et al. 2013). Detailed non-linear FE analyses were developed and calibrated in this chapter using ABAQUS (ABAQUS 2011) to simulate the two types of deformation behaviour of CFS bolted-moment connections, which were tested by Sabbagh et al. (Sabbagh et al. 2012b). The main purposes of the FE analysis in this section are: (a) to examine the accuracy of the proposed FE model for the moment-rotation behaviour of tested specimens (Sabbagh et al. 2012b); (b) to conduct a parametric study on the effect of beam cross-sectional shapes, bolt distribution and cross-sectional slenderness and so on; and (c) to uncover the detailed model for simulating single bolt behaviour in a connection assembly. The FE models include material nonlinearity, initial imperfections as well as bolt slippage that have been found affecting significantly the behaviour of CFS bolted connections (Sabbagh et al. 2013).

### 11.2.1 Bolt modelling

It was found that the position and movement of bolts had significant effect on the moment-rotation behaviour of CFS full-scale connections (Gilbert and Rasmussen 2010, Sabbagh et al. 2012b). Therefore, it is important to develop an acceptable detailed element in ABAQUS in order to simulate the load-deformation behaviour of a single bolt bearing against a single steel sheet. A simplified bolt model which consists of two perpendicular nonlinear springs has been used to model the slip-bearing behaviour of a single bolt by Lim and Nethercot (Lim and Nethercot 2004a, Lim and Nethercot 2003), good agreement was achieved for analysing the behaviour of CFS full-scale joint subjected to monotonic load. However, this element is not suitable for modelling the slip-bearing behaviour of a bolt under cyclic load since the unloading path is the same as the loading path. Sabbagh et al. (Sabbagh et al. 2013), therefore, used the connector element in ABAQUS (ABAQUS 2011) to model the behaviour of bolts under both monotonic and cyclic loading and good agreement against experiments has been achieved. A more direct method to model bolt behaviour using FE analysis is to use the solid element and surface-to-surface contact interactions in ABAQUS (Gutierrez et al. 2015, Liu et al. 2015b, Öztürk and Pul 2015). The disadvantage of using solid elements for the modelling of bolts is that it makes the model more complex and computational efficiency too low for cyclic modelling, especially in large models with large number of bolts. Besides, the convergence would be an issue in the presence of bolt rigid body movement and slippage (Liu et al. 2015b).





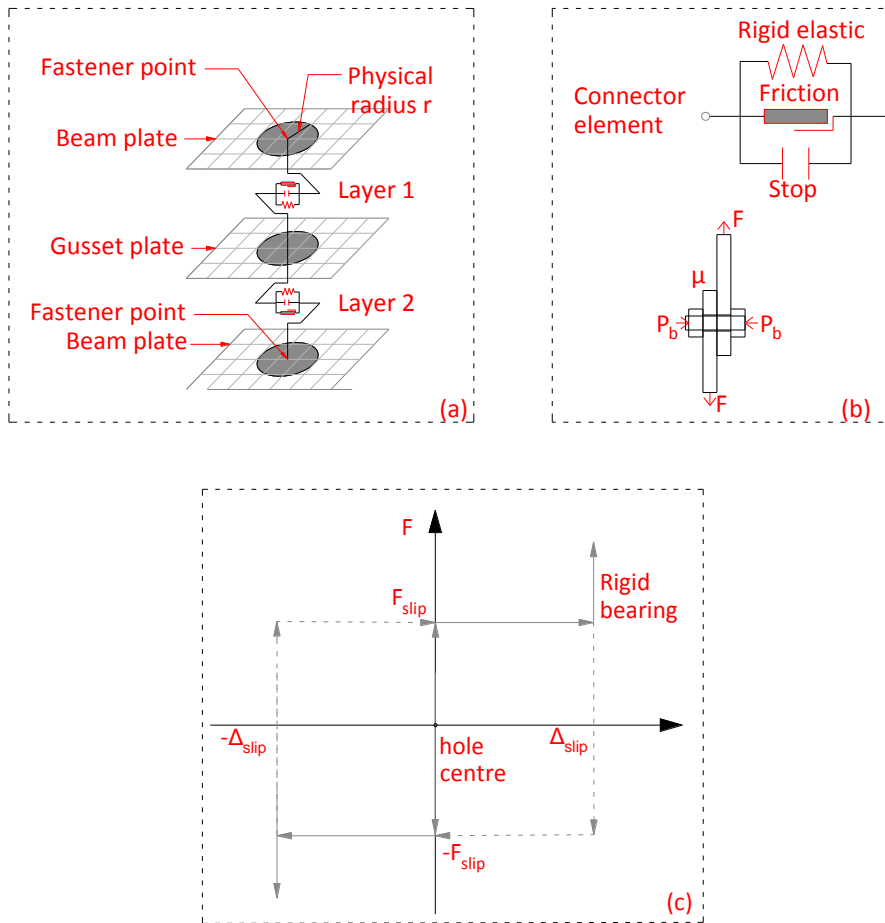
**Figure 11.2. Relationship between a single bolts bearing against steel plate to full CFS connection**

Therefore, a simplified connector element which is similar to the concept of “component method” (DIN 1993) is adopted herein to simulate the CFS full-scale connection behaviour. Substantially, characteristic load-deformation behaviour of a single bolt bearing against a single CFS plate includes slippage of bolt and the bearing deformation, is schematically presented in Figure 11.2. The slip behaviour of the bolted connections depends mainly on the distribution of initial friction forces, which in return rely on the bolt pretension force  $P_b$  for a given applied torque and friction coefficient  $\mu$  of the contact surfaces. A formula which is used to calculate the bolt slip resistance  $F_{slip}$  can be expressed as (Sato and Uang 2009):

$$F_{slip} = \mu \cdot P_b \cdot n_b \quad (11.1)$$

Where  $\mu$  is the mean frictional coefficient given as 0.19 for galvanised steel surfaces (Uang et al. 2010),  $n_b$  is the number of slip planes.

In order to model the bolt group, the point-based “Fastener” in ABAQUS (ABAQUS 2011) was employed, and its definition is shown in Figure 11.3. For each single bolt, a two-layer fastener configuration was used at the position of each individual bolt in the full-scale connection, as shown in Figure 11.3(a). Each layer was connected by a fastener point in beam section and a fastener point in the gusset plate, by the use of an element (connector element or MPC et al.) to define fastener interaction property. In the definition of fastener, a “physical radius”  $r$  which was half of the bolt shank diameter was employed. Each fastener point was thereby connected to the CFS steel plates using a constraint that couples the average displacement and rotation of the nearby nodes to each fastener point. These nodes lie in a circular region in the plates which takes their corresponding fastener point as the centre, as show in Figure 11.2(a).



**Figure 11.3. Single bolt modelling in ABAQUS: (a) definition of fastener; (b) components defined in a connector section and (c) slip-bearing relationship defined in a connector section**

In the definition of fastener section, the connector element in ABAQUS (ABAQUS 2011) was used, as shown in Figure 11.3(b). The connection type of “Cartesian” with 3 translational degrees of freedom was employed and this connector was characterised by a parallel combination of “Elasticity”, “Friction” and “Stop” behaviours, as shown in Figure 11.3(b). In the “Elasticity” behaviour, rigid behaviour was used in the corresponding shear direction. For the definition of “Friction” behaviour, the friction coefficient  $\mu$  and internal contact force  $P_b$  defined in Equation (11.1) were employed. The “Stop” behaviour was thereby defined for limiting the range of slip movement within the bolt hole clearance (typically  $\pm 1\text{mm}$  for standard bolts by assuming that the bolt shank are centrally positioned ). All of the behaviours should be defined in the directions of local coordinate system corresponding to the shear deformation of the bolts. The connector behaviour is then schematically presented in Figure 11.3(c) and its behaviour is concluded as following:

- (a) The connector is rigid up to the slip resistance  $F_{slip}$  before the slippage of bolts is activated. No slippage will be observed if the internal bolt force is smaller than the critical slip resistance.

(b) There is relative slip displacement between the two plates in each layer of the CFS connection (Figure 11.3(a)) subjected to the internal bolt shear force which is identical to the friction resistance  $F_{slip}$ . The slippage will stop when the bolt shank has contacted the hole perimeter.

(c) The bearing stiffness is infinite rigid when the relative displacement between two fastener points is larger than  $\Delta_{slip}$ .

It is worth noting that reduced slip resistance was observed after a number of cycles in the experiment (Sabbagh et al. 2012b). This was mainly because that the applied high torque during the assembling process would cause change of the contact surface between plates and this slippage will be stabilised after a number of loading cycles. This effect will not be taken into account since it is not reliable for design consideration.

### 11.2.2 Geometry, boundary conditions and element types

The general-purpose S8R element, which is an 8-noded quadrilateral shell element with reduced integration in ABAQUS element library (ABAQUS 2011), was selected. The length and width of the elements were 20mm in the mesh. It was observed that further refinement of the mesh did not result in any significant increase in accuracy. The boundary conditions have been applied according to the details of the test set-up presented in (Sabbagh et al. 2012b) and Figure 11.4 illustrates the details. The translational degrees of freedom  $U_x$  and  $U_y$  on top face of the back-to-back channel columns were restrained while all of the translations on the bottom of the column were fixed. Since the back-to-back beam was assembled using bolts and filler plates, the web lines were connected together in the  $U_x$ ,  $U_y$  and  $U_z$  directions using the “Tie” constraint in ABAQUS (ABAQUS 2011). At the positions where lateral frames were used (Sabbagh et al. 2012b), lateral bracing in the  $x$  direction was applied, as shown in Figure 11.4. All the stiffeners in the FE model were tied accordingly to the sections at the corresponding positions in beams and columns. To apply the load, the nodes at the end of the CFS section were coupled to its centroid using a coupling constraint. Fasteners with connector element were used to model the bolts in the CFS gusset plate connections, as shown in Figure 11.5, the detailed explanation of fastener definition has been explained Section 11.2.1.

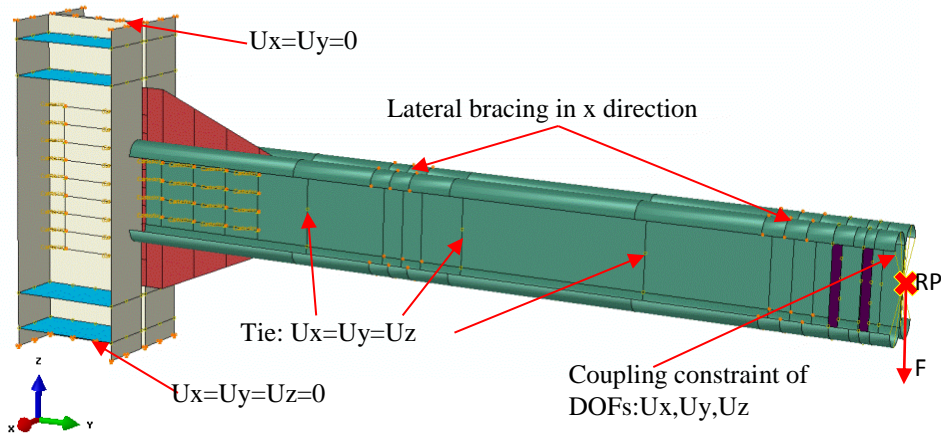


Figure 11.4. Boundary conditions of the FE model for beam-column connection

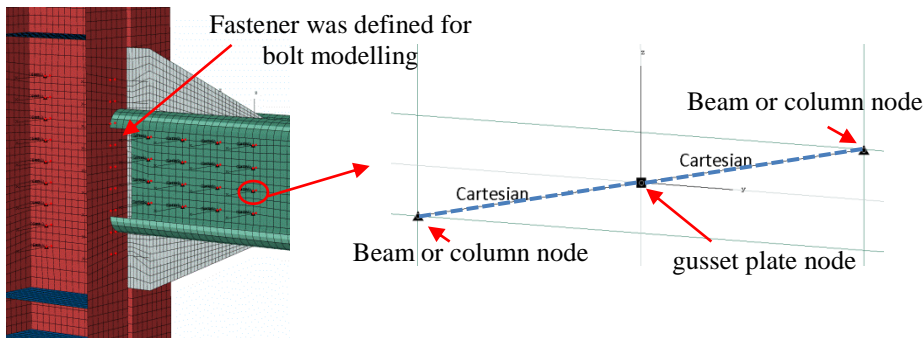


Figure 11.5. FE model of the beam-column connection with fastener definition

### 11.2.3 Material model

The inelastic properties of CFS material were found to have significant effects on the ultimate capacity and post-buckling behaviour of CFS elements. As a part of the experimental test by Sabbagh et al. (Sabbagh et al. 2012b), tensile coupons from the flat plates in the connections (Type A and Type B) and gusset plate were used in order to determine their material properties. The Kinematic hardening rule was applied to the von-Mises yielding surface during the cyclic loading. The material properties of the gusset plate and cross-sectional profiles are presented in Figure 11.6 and Table 11.1. Elastic modulus of  $E = 210 \text{ GPa}$  and Poisson's ratio of  $\nu = 0.33$  were used in the FE models

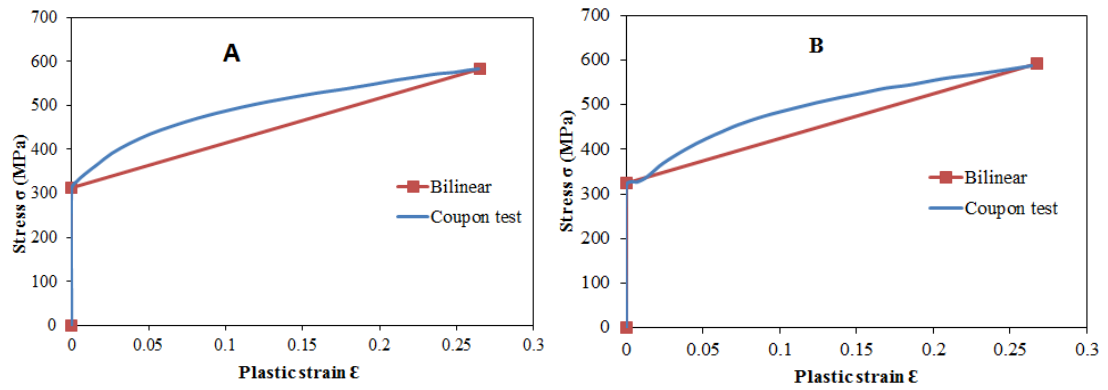


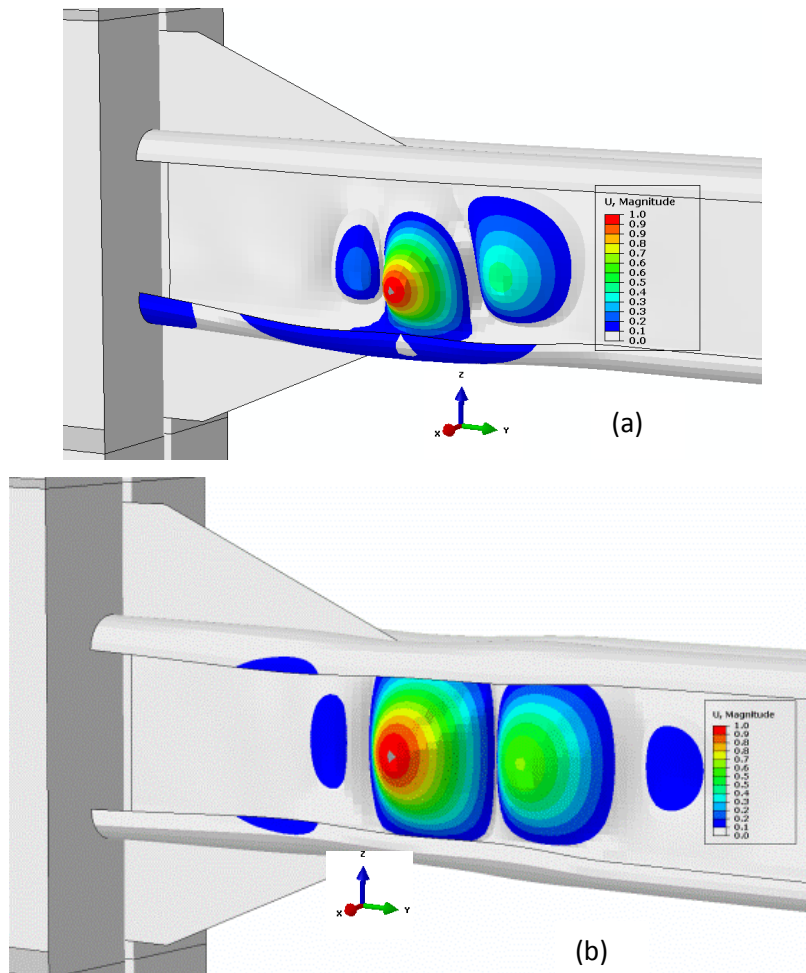
Figure 11.6. Stress-strain curve from the coupon test was used in the FE model(Sabbagh et al. 2012b).

Table 11.1. Basic properties of the gusset plates (Sabbagh et al. 2012b)

Specimen	Area	Yielding stress	Ultimate stress	Elongation on 50 mm
	mm <sup>2</sup>	N/mm <sup>2</sup>	N/mm <sup>2</sup>	%
A	100	353	516	31
B	124	308	474	36

### 11.2.4 Imperfections

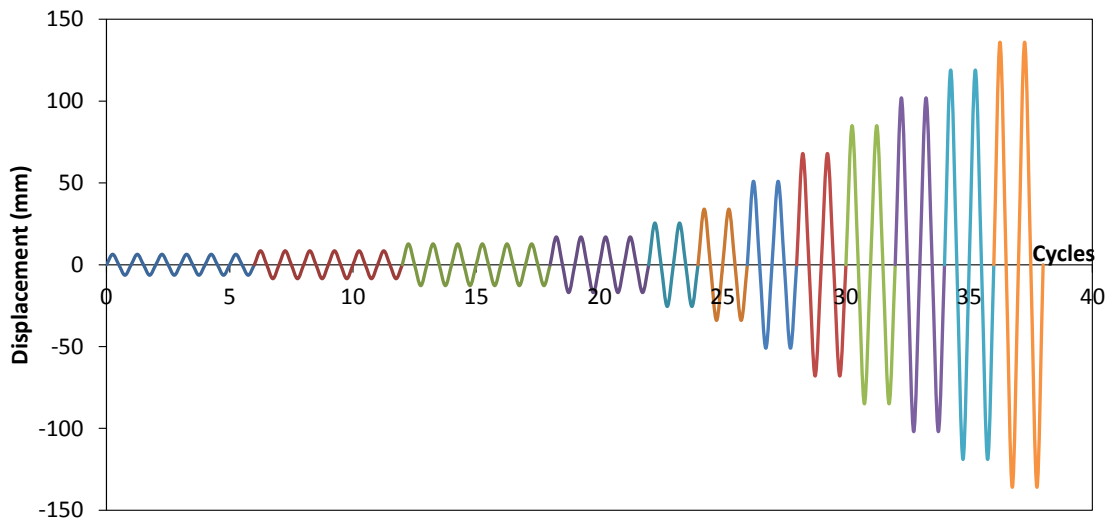
The lateral displacement has been restrained in the x direction in the experiment (Sabbagh et al. 2012b), no global buckling was observed. Therefore, either a local or a distortional imperfection was incorporated into the model, depending on which mode had the lower critical buckling resistance. The amplitude of this imperfection was determined based on the work by Schafer and Peköz (Schafer and Pekoz 1998), which is in a situation that the thickness of steel sheet is less than 3mm. The 50% value of the Cumulative Distribution Function of the imperfections was thereby adopted, amounting to values of 0.34 and 0.94 times the thickness for the local and distortional imperfection, respectively. The cross-sectional shape of the imperfection was generated by using an eigenvalue buckling analysis in ABAQUS. The coordinates of the resulted Eigen modes from the analysis were stored in a file with an extension of “fil”, this file was subsequently applied as input for the “\*IMPERFECTION” command in the ABAQUS “inp” file. In the case of monotonic load, a tip displacement in the -z direction was employed to conduct the eigenvalue buckling analysis, resulting in a unsymmetrical mode for including imperfection, as shown in Figure 11.7(a). However, in the case of cyclic loading, a tip displacement in the -y direction was used to generate a symmetrical imperfection pattern (Figure 11.7(b)). The imperfections corresponding to the local buckling or distortional buckling were therefore incorporated in the “Static, General” step.



**Figure 11.7. Deformation at first buckling mode shape: (a) in the case of monotonic load (b) in the case of cyclic load (Sabbagh et al. 2012b)**

### 11.2.5 Solution technique and load regime

A tip displacement was applied at a reference point at the end of the beam, as shown in Figure 11.4. A displacement corresponding to rotation of the connection was applied at the end of the beam. For the case of cyclic loading, a regime which is the same as the test (Sabbagh et al. 2012b) with varying magnitude of displacements at the beam end is applied in the FE analysis, as shown in Figure 11.8. The loading protocol was also in accordance with the AISC Seismic Provisions (AISC 341-05 2005) for the performance evaluation of beam-column moment connections. The displacement control was employed as a solution technique and the nonlinear FE analysis taking into account of geometric and material non-linearity was performed.



**Figure 11.8. Cyclic loading regime for the test (Sabbagh et al. 2012b) and numerical study**

### 11.2.6 Validation of FE modelling

The experimental study on the behaviour of CFS bolted connections under cyclic loading have been carried out at the University of Sheffield and the detailed configuration and test set-up can be found in Sabbagh et al. (Sabbagh et al. 2012b). The moment-rotation hysteresis behaviour of CFS connections with and without slippage was recorded during the test. The FE model modelling of the connection behaviour was thereby verified through the beam-to-column connection test conducted by Sabbagh et al. (Sabbagh et al. 2012b). In the test, connection A1 was designed to be controlled by bearing action in the bolts against steel plates while connection B2 was designed to activate the bolt slippage before the buckling of beam profile. The pretension force in the bolts was directly related to the torque applied, the torque was controlled by using a torque wrench in the test and the preloading-torque relationship was established by using a pretension measuring machine (Sabbagh et al. 2011). The applied pretension force was 67 kN for the beam-to-gusset plate and 53 kN for the gusset plate-to-column, respectively (Sabbagh et al. 2011). Therefore, this preloading was applied according to the definition, shown in Equation (11.1). The physical radius was defined in accordance with the bolt shank diameter, which was 18mm (Sabbagh et al. 2011). Further details can be found in (Sabbagh et al. 2011). Using the loading protocol discussed in Section 11.2.5, the tested models of connection A1 and B2 was modelled numerically. Material nonlinearity and geometrical imperfection were incorporated according to Section 11.2.3 and Section 11.2.4. It is worth noting that for modelling the bolts, the simplified model in Figure 11.3 was used in both cases. However, only the slippage in the connection B2 was activated while the deformation of connection A1 was dominated by the buckling of the profiles and bolt slippage was not activated. To partially account for the effect of bolt elongation of the plate holes (Sabbagh et al. 2012b), the range of slippage of the stop element in Figure 11.3 was increased from  $\pm 1\text{mm}$  to  $\pm 2\text{mm}$  in the first lines of the bolts. The experimental and FE responses subjected to both monotonic and cyclic



loading are compared in terms of the moment-rotation curves in Figure 11.9 and Figure 11.11 while the failure shapes are compared in Figure 11.10 and Figure 11.12, respectively. According to the results, the numerical simulation under cyclic load is generally in good agreement with the corresponding experimental results. However, the  $M-\Theta$  curve subjected to monotonic load shows less strength degradation than the response under cyclic load. This is due to the cyclic deterioration effects which will not happen in the case of monotonic loading. The numerical study has successfully captured the shape and position of local/distortional buckling in the beams.

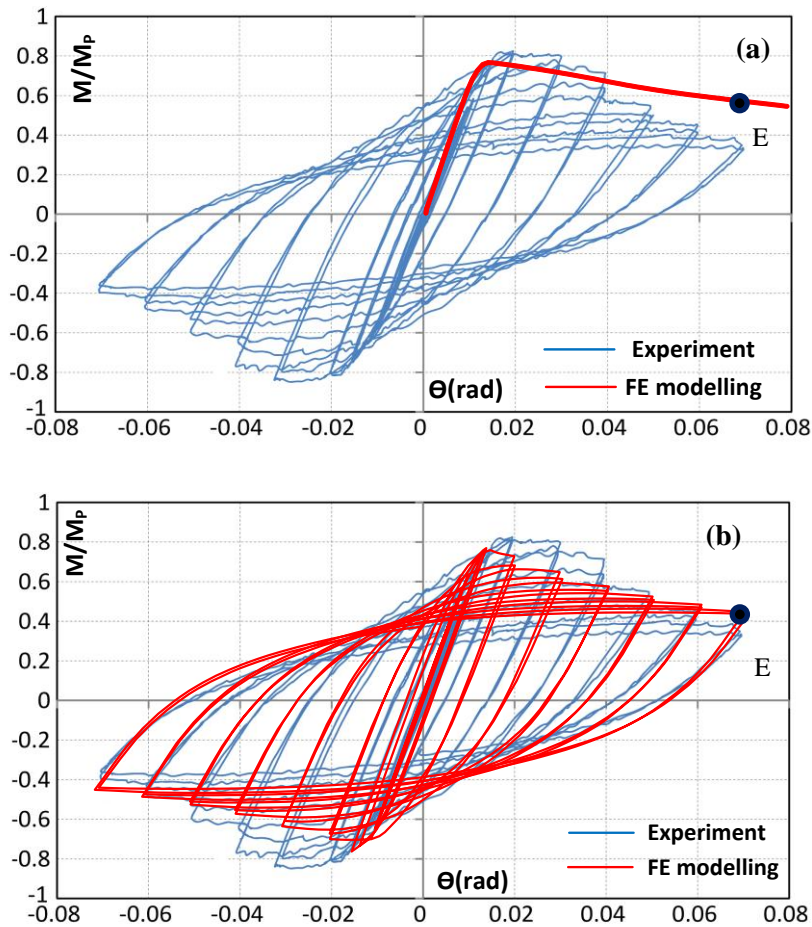
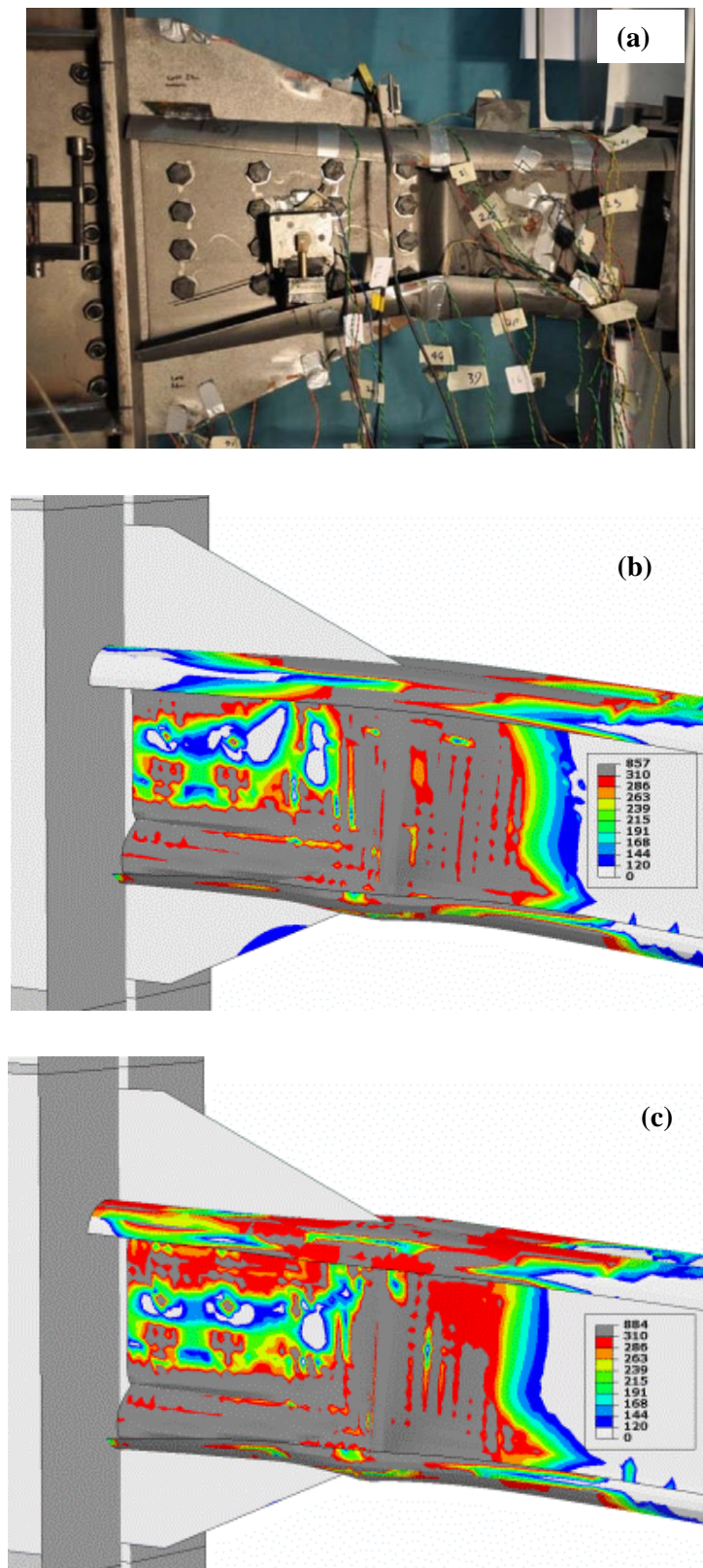
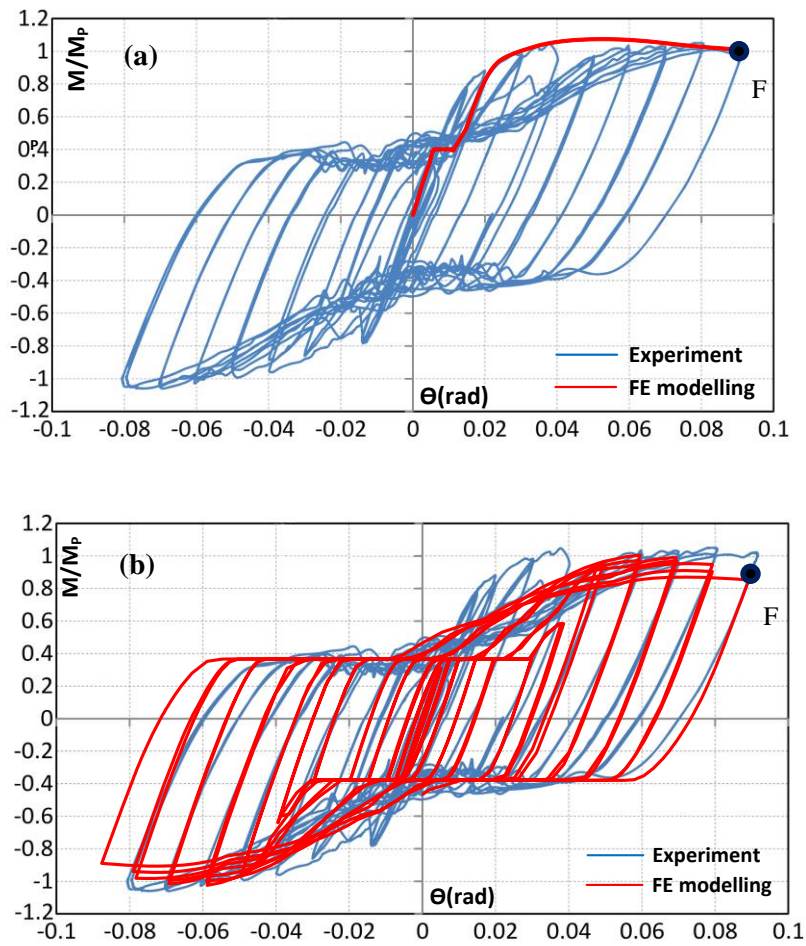


Figure 11.9. Comparison between tested (Sabbagh et al. 2011) and analysed moment-rotation curves of connection A1: (a) monotonic load and (b) cyclic load

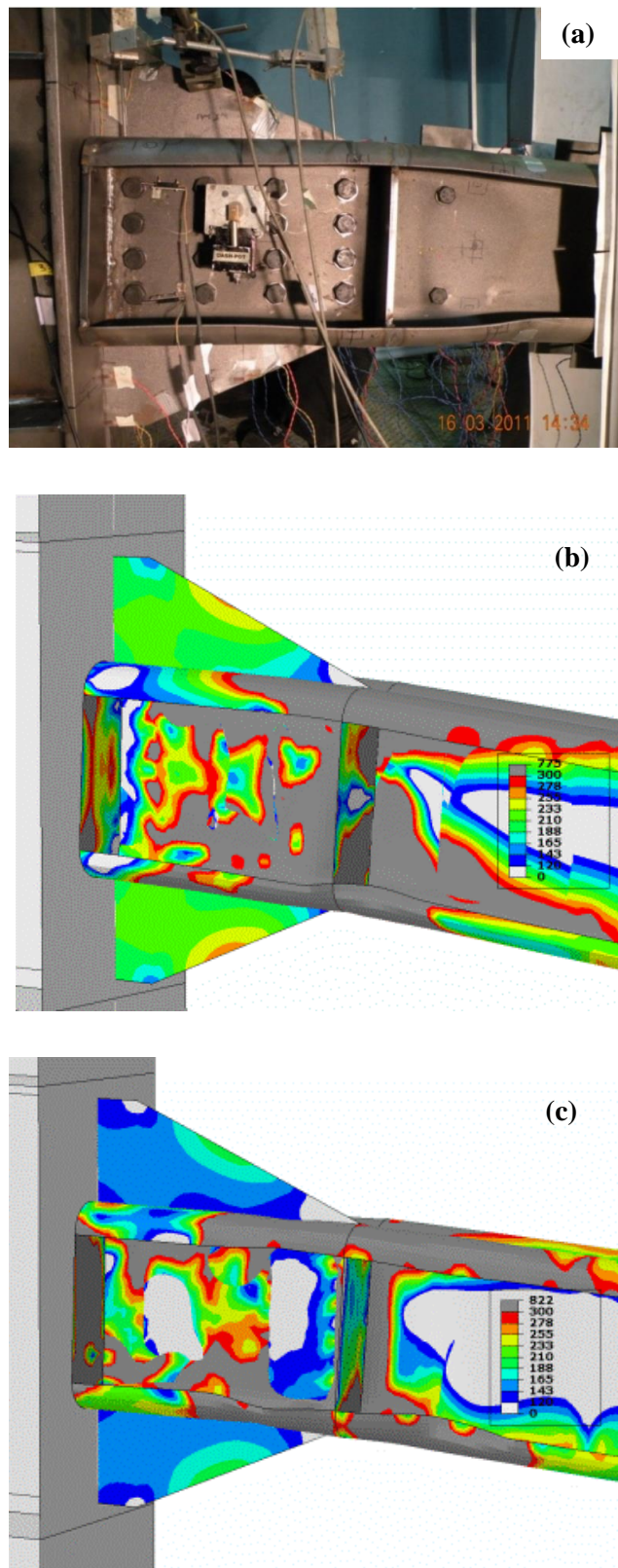




**Figure 11.10.** Comparison between tested and analysed buckled shape of the profiles of connection A1: (a) Failure shape from the test (Sabbagh et al. 2011); (b) monotonic load (MPa) and (c) cyclic load (MPa) at  $\theta=0.07$  rad (Point E in Figure 11.9)



**Figure 11.11. Comparison between tested (Sabbagh et al. 2011) and analysed moment-rotation curves of connection B2: (a) monotonic load and (b) cyclic load**



**Figure 11.12. Comparison between tested and analysed buckled shape of connection B2: (a) Failure shape from the test (Sabbagh et al. 2011); (b) monotonic load (MPa) and (c) cyclic load (MPa) at rotation of  $\theta=0.09$  rad (Point F in Figure 11.11)**

### 11.3 Connection configurations for parametric study

A wide range of parametric study using the verified nonlinear inelastic FE analysis and the simplified method of bolt modelling were then performed to examine the cyclic response of the CFS bolted moment connections. Variations in the parametric study include beam cross-sectional dimensions, beam thickness, bolt distribution and gusset plate thickness. Cold-formed steel plate assemblies are inherently with small width-to-thickness ratios, however, the flexible procedure to form cold-formed steel sections using cold-rolling or press-braking enables more complex shapes characterised by intermediate stiffeners or folded plates that typical hot rolled products do not possess. Therefore, as shown in Figure 11.13, the selected cross-sectional geometry consists of flat, stiffened flat, folded and curved shaped channel cross-sections. Different thicknesses of the channels (1, 2, 4, 6 mm) were used in the parametric study in terms of cross-sectional slenderness defined as:

$$\lambda = \sqrt{\frac{f_y}{\sigma_{cr}}} \quad (11.2)$$

where  $\sigma_{cr}$  is the critical buckling stress and  $f_y$  is corresponding to the yield stress.

Bolt distribution has non-negligible effects on the strength and stress field of CFS bolted moment connections (Lim et al. 2016). Three types of bolt distributions including circle, diamond and square shapes were therefore considered, as shown in Figure 11.14. Also FE analysis was employed in order to investigate the effects of gusset plate thickness on the cyclic behaviour of the CFS connections.

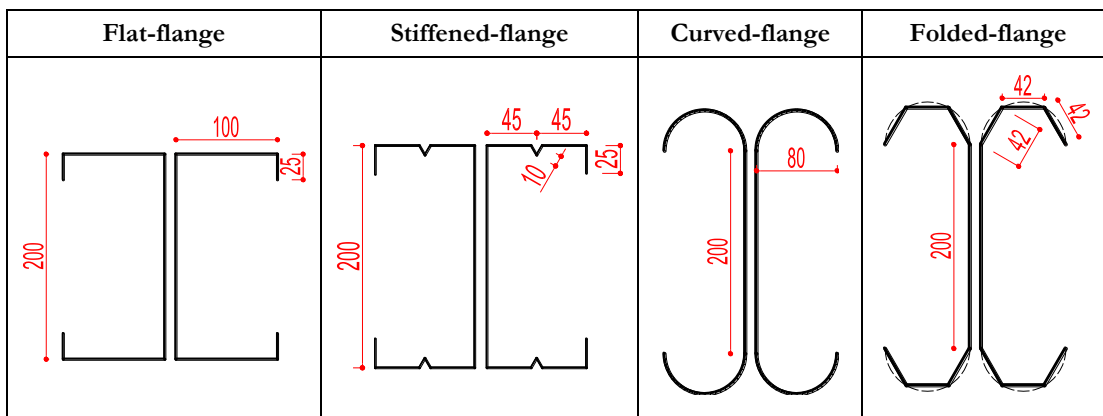


Figure 11.13. Details of the back-to-back beam sectional dimensions with L=2000 mm



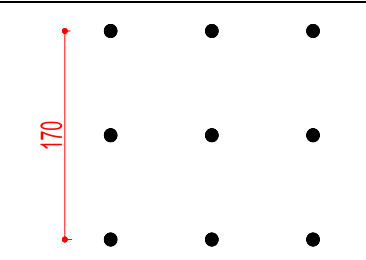
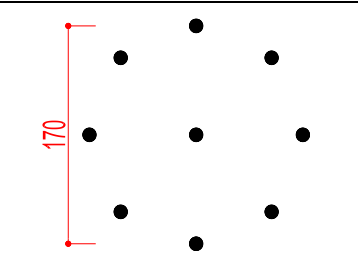
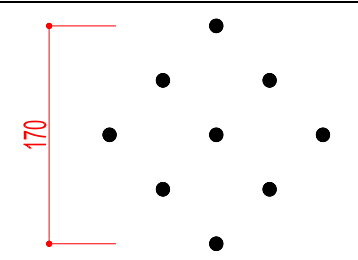
Bolt arrangement-1	Bolt arrangement-2	Bolt arrangement-3
Square	Circle	Diamond
		

Figure 11.14. Different bolt distribution patterns

## 11.4 Cross-sections classification

Before conducting cyclic analysis on the bolted moment connections, there is a need to recognize cross-section classification of the different cross-sectional shapes (Figure 11.13) with various thicknesses, since it is expected that the behaviour of connections will be related to the beam cross-section classifications. Based on the susceptibility of cross-sections to local buckling, EC3 (CEN 2005c) classifies cross-sections under four classes for steel members. EC3 (CEN 2005c) divides cross-sections into individual plates which are subject to the either compression, bending or combined bending and compression. Therefore the cross-sectional classification is determined based on their width to thickness ratio ( $c/t$ ), yield stress capacity, the edge boundary conditions, and the applied stress gradient of plate assembling. Regarding the edge boundary conditions, each plate is identified as an internal or outstand element, respectively (CEN 2005c). The overall classification of a cross-section is based on the highest (most unfavourable) class of its compression parts. According to this definition, the results of classification for each channel are listed in Table 11.2. As can be seen, classification for channel with flat, stiffened flat, and folded flanges are determined based on constituent internal or outstand element.

The limitation for width-to-thickness ratio ( $c/t$ ) in Eurocode 3 is defined just for channel with flat flanges and without lips, while there is no requirement for all of four channels which are used in this study. Hence, in order to obtain more reasonable classification of the cross-sections, Eurocode concepts (CEN 2005c) and Finite Strip Method (FSM) (Li and Schafer 2010a) were combined for section classification.

### 11.4.1 Eurocode concept

The concept of cross-sectional classification of EC3 is based on monotonic loading and used just for local buckling behaviour. Steel cross-sections are generally categorized into four classes as illustrated in Figure 11.15. Class 4 are those cross-sections in which local buckling happen before the attainment of the yield moment capacity ( $M_u < M_y$ ). Class 3 correspond to cross-

sections in which local buckling happen after reaching yield moment capacity but before reaching their plastic moment capacity ( $M_y < M_u < M_p$ ). Class 2 are the cross-sections which can reach their plastic moment capacity, but ultimate plastic rotation is limited by the occurrence of plastic buckling of compression part ( $M_p < M_u$ ). Finally, class 1 can reach their plastic moment capacity with adequate plastic rotation developed due to the effects of redistribution of moment ( $M_p < M_u$ ). Although it is not allowed to do plastic design in EN 1993-1-12 (CEN 2007), evaluation of class 1 and class 2 is specified in terms of R which is stipulated in EN 1993-1-1.  $R_0$  value which is the pure plastic rotation capacity based on moment-rotation response is defined as:

$$R_0 = \frac{\theta_u - \theta_p}{\theta_p} \quad (11.3)$$

where  $\theta_u$  is the ultimate rotation corresponding to the drop in moment-rotation curve up to plastic moment in the softening branch, and  $\theta_p$  is equal to rotation corresponding to plastic moment at the hardening branch.

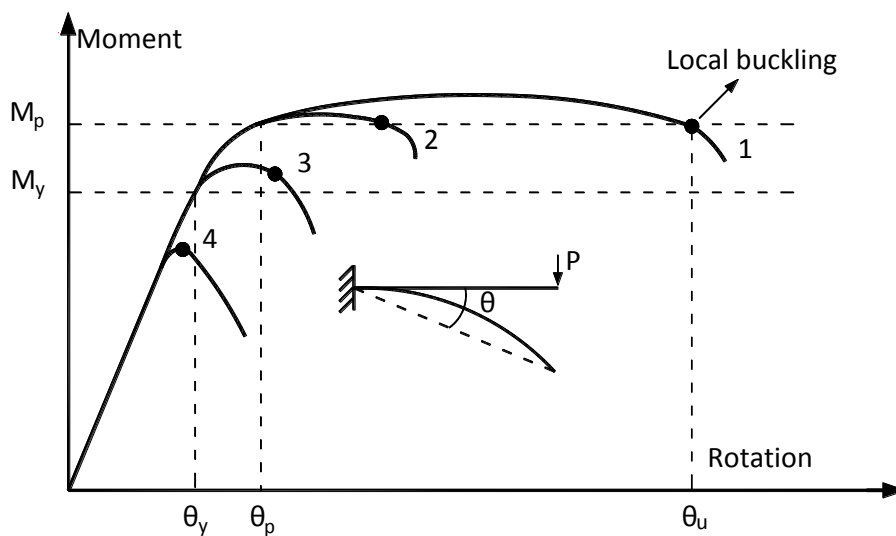
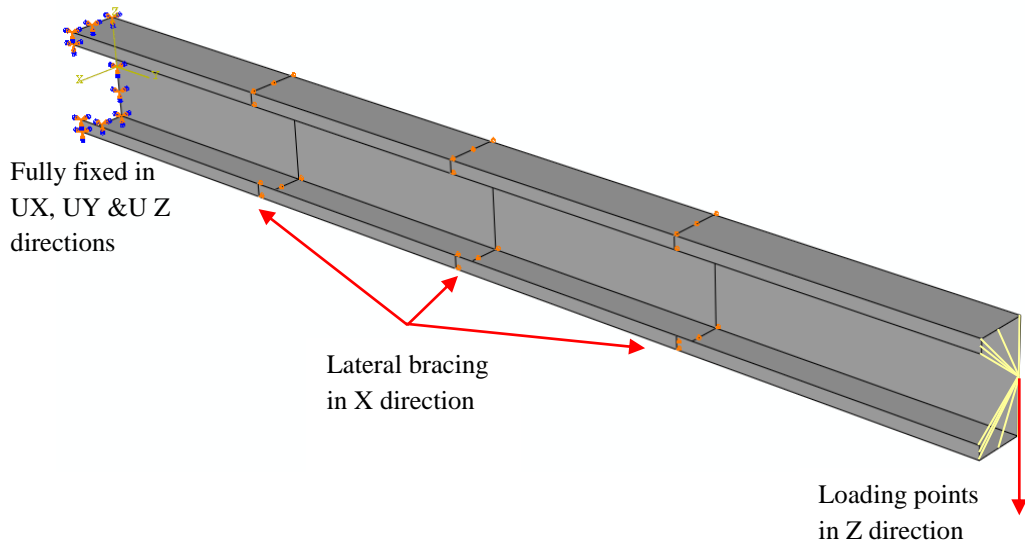


Figure 11.15. Cross-sectional classification based on moment-rotation curves

For the purpose of a better classification according to the EC3 concept, FE analysis was employed using ABAQUS to obtain flexural behaviour for each single channel cross-section. Therefore, the main purpose of the FE analyses was to examine the accuracy of the provisions in EC3 for the classification of the channels with different flange shapes. Non-linear inelastic post-buckling analysis were performed on the single channels with flat, stiffened flat, folded and curved flanges with cross-sectional dimensions shown in Figure 11.16 and Figure 11.17. The single channels with a length of  $L = 2$  m was fixed at one end while the load with displacement control was applied to the centroid of other end. The centroid was coupled to the end cross-section. The lateral supports were simulated by applying boundary conditions to prevent the

lateral movement of channel's flanges at an interval of 1/3 channel length, as shown in Figure 11.16. Other parameters of the FE models were defined as: shell element S8R in ABAQUS, mesh size 20 mm × 20 mm, and material behaviour and imperfections were applied the same as those defined in section 2 and 3.



**Figure 11.16. Typical boundary conditions, constrains and loading points of cantilever channels**

Cross-section classification can be achieved by comparing the maximum moment obtained from FE analysis with the yield moment ( $M_y$ ) and the plastic moment ( $M_p$ ). As shown in Table 11.2, all of the sections with 1, 2, 4, and 6 mm are identified as class 4, 3, 2 and 1, respectively. Comparison of the results between Eurocode classification and FE analysis shows that for the class 1 and 4 channels, Eurocode classification can be sufficient whereas this type of classification would not be accurate for the class 2 and 3 channels.

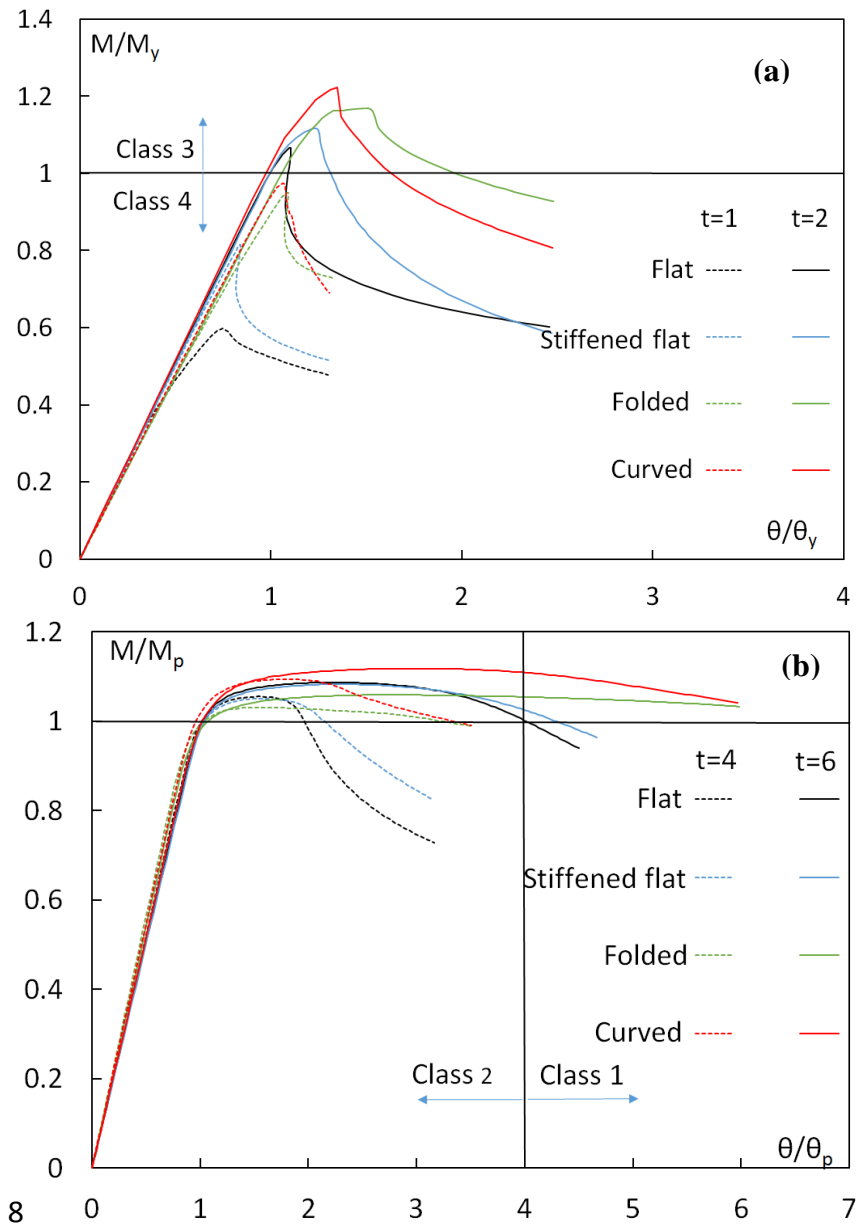


Figure 11.17. Normalised moment–rotation responses for cross-section classification: (a)  $t=1$  and 2 mm and (b)  $t=4$  and 6 mm



**Table 11.2. Cross-sectional classification of the CFS cross-sections**

Section	Thickness	EC3 classification					CUFSM	EC3 concept
		Flange		lip (outstand)	Web	Overall		
		Internal	Outstand					
Flat	1	4	-	4	4	4	$\frac{\sigma_l=0.2794 f_y}{\text{Local}}$	4
	2	4	-	3	3	4	$\frac{\sigma_D=1.0633 f_y}{\text{Distortional}}$	3
	4	1	-	1	1	1	$\frac{\sigma_d=2.3122 f_y}{\text{Distortional}}$	2
	6	1	-	1	1	1	$\frac{\sigma_d=3.7827 f_y}{\text{Distortional}}$	1
Stiffened Flat	1	4	-	4	4	4	$\frac{\sigma_l=0.5029 f_y}{\text{Local}}$	4
	2	1	-	3	3	3	$\frac{\sigma_d=1.1994 f_y}{\text{Distortional}}$	3
	4	1	-	1	1	1	$\frac{\sigma_d=2.6401 f_y}{\text{Distortional}}$	2
	6	1	-	1	1	1	$\frac{\sigma_d=3.1555 f_y}{\text{Distortional}}$	1
Folded	1	4	4	-	4	4	$\frac{\sigma_l=0.3995 f_y}{\text{Local}}$	4
	2	1	4	-	3	4	$\frac{\sigma_d=1.4895 f_y}{\text{Distortional}}$	3
	4	1	3	-	1	3	$\frac{\sigma_d=3.24 f_y}{\text{Distortional}}$	2
	6	1	1	-	1	1	$\frac{\sigma_d=5.2191 f_y}{\text{Distortional}}$	1
Curved	1	-	-	-	4	4	$\frac{\sigma_l=0.5808 f_y}{\text{Local}}$	4
	2	-	-	-	3	4	$\frac{\sigma_d=1.6887 f_y}{\text{Distortional}}$	3
	4	-	-	-	1	3	$\frac{\sigma_d=3.6603 f_y}{\text{Distortional}}$	2
	6	-	-	-	1	1	$\frac{\sigma_d=5.896 f_y}{\text{Distortional}}$	1

#### 11.4.2 Finite strip method

Elastic buckling FE analysis has been the most commonly used technique to calculate the elastic buckling load of CFS sections. However, CFS sections are susceptible to local, distortional, global buckling and their interaction. Therefore, numerical algorithms have been developed for mode decomposition and pure buckling modes are therefore can be distinguished (Ádány and Schafer 2006, Ádány and Schafer 2014). For example, the constrained finite strip software CUFSM (Li and Schafer 2010a) which implements the classical finite strip method is able to

## CHAPTER 11. Behaviour of CFS bolted connections: a numerical parametric study

examine and to calculate all elastic buckling modes and corresponding buckling capacity of thin-walled members. The members can be with arbitrary cross-section subjected to compression or/and bending. It was, therefore, used to determine the critical elastic buckling stress of the cross-sections in the parametric study. The critical buckling stress has been compared with the yield stress of the cross-sections to have a rough understanding of the cross-sectional classification. The resulted critical buckling stress of the cross-sections is presented in Table 11.2. In general, the critical buckling stress is around 2-3 times of the yield stress for class 2 sections while 1-1.5 times for the class 3 sections. For class 4 cross-sections, the critical buckling stress is generally smaller than the yield stress, however, for class 1 sections, the critical stress can be up to 3-6 times of the yield stress.

### 11.5 Parametric finite element analysis results

A parametric study was therefore conducted in this section. The parametric study consisted of 48 CFS bolted moment connections with different cross-sectional thicknesses (1, 2, 4, 6 mm), various beam channel shapes (flat, stiffened flat, folded, curved, as shown in Figure 11.13) and three bolt distribution configurations (circle, diamond, square, as shown in Figure 11.14). FE analysis using ABAQUS was employed to evaluate the cyclic behaviour of those connections. Column sectional dimensions, material properties, boundary conditions, loading protocol, and other FE parameters such as modelling of the bolts and mesh size are the same as those used in the experimental verification, which have been discussed in section 11.3. In order to trigger the dominant buckling modes in the beam of the connections, a thicker plate with 10 mm thickness was used for the gusset plate.

The flat flange channels with various thicknesses (1, 2, 4 and 6 mm) and circle distribution of the bolts was selected here to show the typical reversed cyclic response of the connections without slippage in the bolts (Figure 11.18). Also, backbone curves of the moment-rotation cyclic response was plotted in the same figures. For the hysteresis curve, backbone curves in both the positive and negative rotation were first specified by plotting locus of all the peak moment points at the first cycle of the same rotation amplitude cycles. Then the same parameters were determined from the backbone curves such as dissipated energy which was defined as the area under the back bone curve.

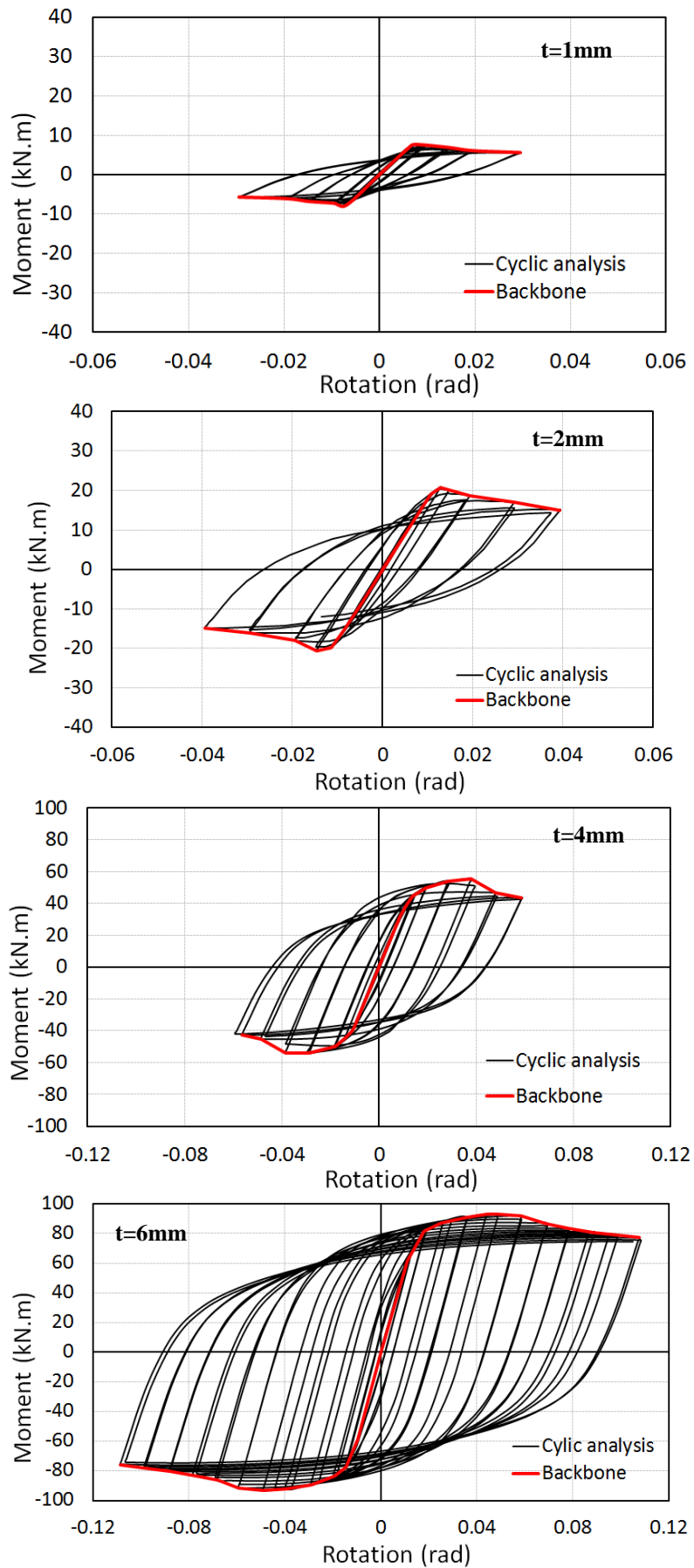


Figure 11.18. Moment-rotation cyclic relationship and backbone curve of the connections with flat flange beam section and circular bolt distribution configuration

CHAPTER 11. Behaviour of CFS bolted connections: a numerical parametric study

To provide a cyclic characterization of the bolted-moment connections performance, the EEEP models are presented. EEEP analysis which incorporates an energy balance approach was firstly introduced by Park (Park 1989), then modified by Foliente (Foliente 1996) , and was finally proposed in ASTM E2126 (Yu and Schafer 2006). In accordance with ASTM E2126-09, the equivalent energy elastic-plastic (EEEE) bi-linear model was used to extract the performance parameters of the connections. This model assumes an ideal elastic-perfectly plastic response of the system. Figure 6.7 indicates the general structural response of the connections obtained from cyclic analyses and was employed to idealize a moment–rotation curve based on EEEP model. The idealized bi-linear curve includes two parts. The line part utilizing an iterative graphical method that balances the size of the areas above and below of the curve ( $A_1=A_2$ ). The elastic section of the EEEP curve is defined using initial secant stiffness ( $K_e$ ) associated with the moment equal to 40% of the idealized yield moment of the connection. The second segment line and the post-yield slope should be specified by a line passing through the actual curve at the rotation corresponds to 20% drop of maximum moment in the softening branch. The characteristic parameter values of the EEEP model for all the cyclic modelling and the failure modes are presented in Table 11.3. For the class 4 flat channels, local buckling in the flanges is dominant, but for flat channel with other classes and also stiffened flat channel local buckling happen at both web and flanges.

**Table 11.3. Characteristic parameters of the EEEP model for all the cyclic modelling**

Bolt configuration	Beam thickness	Beam type	Yield moment My (kN.m)	Rotation at My (rad)	Buckling mode	AISC	FEMA
Circle	1	Flat	5.8	0.006	LF	×	×
		Stiffened flat	6	0.006	LF-LW	×	×
		Folded	6.4	0.006	LW	×	×
		Curved	7	0.006	LW	×	×
	2	Flat	18.6	0.01	LF-LW	×	×
		Stiffened flat	19.5	0.01	LF-LW	✓	×
		Folded	20.5	0.01	LW	×	×
		Curved	21.6	0.009	LW	×	×
	4	Flat	50.3	0.014	LF-LW	✓	×
		Stiffened flat	51.3	0.014	LF-LW	✓	✓
		Folded	53.8	0.012	LW	✓	×
		Curved	58.6	0.012	LW	✓	×
	6	Flat	84.5	0.014	LF-LW	✓	✓
		Stiffened flat	85.5	0.014	LF-LW	✓	✓
		Folded	93.7	0.013	LW	✓	✓
		Curved	99.8	0.013	LW	✓	✓

Bolt configuration	Beam thickness	Beam type	Yield moment My (kN.m)	Rotation at My (rad)	Buckling mode	AISC	FEMA
Diamond	1	Flat	5.7	0.007	LF	×	×
		Stiffened flat	5.9	0.007	LF-LW	×	×
		Folded	6.2	0.007	LW	×	×
		Curved	7.4	0.007	LW	×	×
	2	Flat	18.3	0.011	LF-LW	×	×
		Stiffened flat	18.6	0.011	LF-LW	×	×
		Folded	19.9	0.01	LW	×	×
		Curved	22.2	0.01	LW	×	×
	4	Flat	47.6	0.014	LF-LW	✓	×
		Stiffened flat	48	0.014	LF-LW	✓	✓
		Folded	50.8	0.013	LW	✓	✓
		Curved	55	0.014	LW	✓	×
	6	Flat	78.9	0.014	LF-LW	✓	✓
		Stiffened flat	79.2	0.014	LF-LW	✓	✓
		Folded	85.6	0.013	LW	✓	✓
		Curved	93.6	0.014	LW	✓	✓
Square	1	Flat	6.8	0.006	LF	×	×
		Stiffened flat	6.6	0.006	LF-LW	×	×
		Folded	7.3	0.005	LW	×	×
		Curved	7.8	0.005	LW	×	×
	2	Flat	22	0.011	LF-LW	×	×
		Stiffened flat	21.7	0.01	LF-LW	✓	×
		Folded	23.3	0.009	LW	×	×
		Curved	24	0.009	LW	×	×
	4	Flat	56	0.013	LF-LW	✓	×
		Stiffened flat	55.5	0.014	LF-LW	✓	✓
		Folded	62	0.012	LW	✓	×
		Curved	63.2	0.012	LW	✓	×
	6	Flat	106.1	0.015	LF-LW	✓	✓
		Stiffened flat	106.4	0.016	LF-LW	✓	✓
		Folded	117.6	0.013	LW	✓	✓
		Curved	119.7	0.013	LW	✓	✓

### 11.5.1 AISC requirements for the connection

AISC(AISC 341-05 2005) impose requirements for beam-to-column connections in the seismic force resisting system. AISC(AISC 341-05 2005) stipulate that the bolted-moment connection in special moment frame (SMF) should be able to incorporate at least 0.04 rad rotation at the connection while 20% drop happen after the peak moment. FEMA (FEMA 2000) suggested that

in order to satisfy the ductility requirements for SMF, the value of the inter-story drift angle capacity at the stage of connection failure, shall not be less than 0.06 rad. It means that at the rotation equal to 0.06 rad connection damage is so severe that continued ability to remain stable under gravity loading is unreliable. It is shown in Table 11.3 that the majority of bolted-moment connections with class 1 and 2 beam sections can satisfy AISC requirements for SMF, while according to the FEMA only class 1 cross-sections are able to satisfy the inter-story drift angle requirement of SMF. It is evident that the most of the cross-sections in class 3 and 4 are not sufficient to be utilised as SMF.

### **11.5.2 Moment capacity of the connections**

It was shown that CFS channel sections with folded-flange and curved flange section can provide flexural moment capacity approximately 57% more than lipped channels (Sabbagh et al. 2012b, Ye et al. 2016b). Nevertheless, Figure 11.19 proves that using bent flange channels (folded and curved) as a beam in the connection can withstand maximum moment only 10% more than plain flange channels (flat and stiffened flat), furthermore, the differences between two bent channels and also plain channels in terms of maximum flexural capacities are negligible. This conflict is mainly due to three significant reasons: (i) the bolts array in the web will result in the reduction of moment-capacity of the channel-sections at the connections due to the presence of bimoment (Lim et al. 2016), (ii) using channels with deep web reduced the effects of the flange on the moment capacity since bending moment are not able to transfer directly from web to flanges. (iii) the cross-sectional dimensions used in this study are not necessarily the optimum ones.

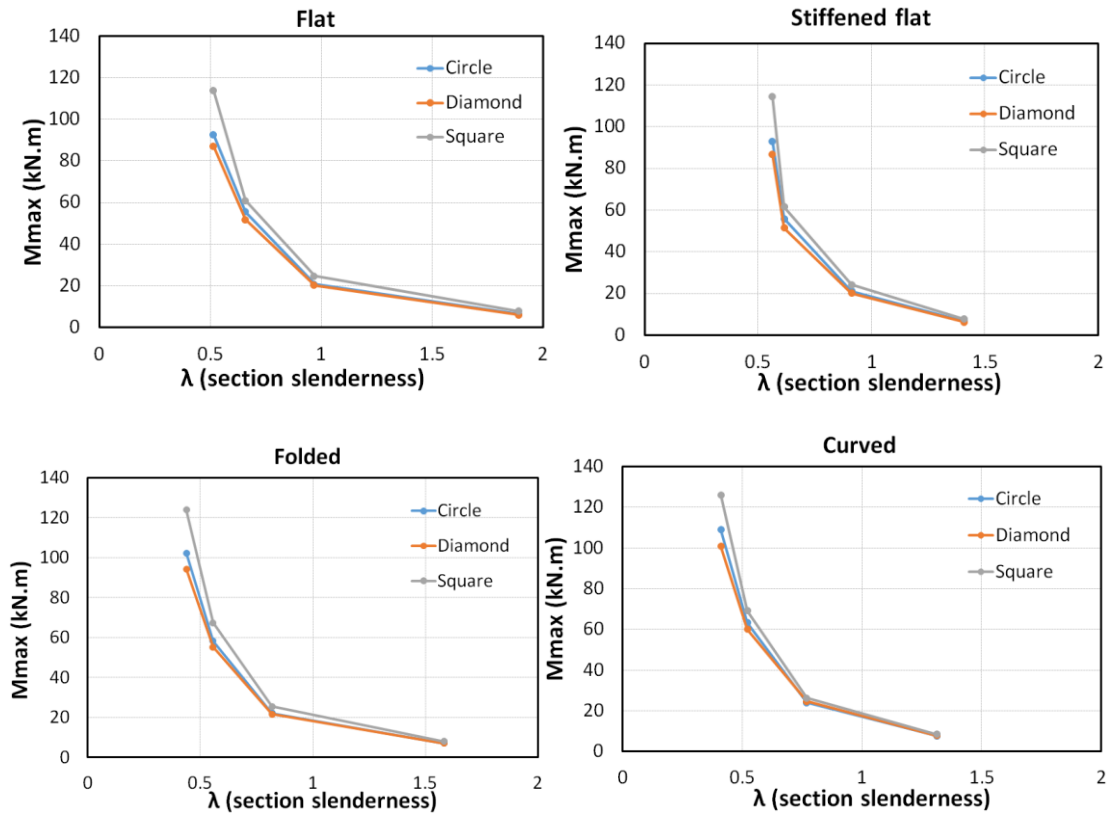


Figure 11.19. Strength to slenderness relationship of different sectional shapes

### 11.5.3 Ductility ratio

The fundamental definition of ductility ratio ( $\mu$ ) is defined as the ratio of ultimate rotation ( $\theta_u$ ) over the yield rotation ( $\theta_y$ ), as follows:

$$\mu = \theta_u / \theta_y > 1 \quad (11.4)$$

In the calculation of ductility ratio, the value of  $\mu$  is defined according to the rotation at 80% of post-ultimate moment (EEEE model). It can be observed from Figure 11.20 that the connection ductility ratio is highly related to the cross-sectional classification and shape of the beam as well as bolt distributions. Folded flange sections generally provide maximum ductility ratio which is especially evident for class 1 cross-sections (6mm thickness). Folded flange section provides higher ductility ratio up to 55%, 45% and 30 % compared with curved, flat and stiffened flat sections, respectively. In aspect of bolt configuration, it should be noted that the best configuration is related to cross-sectional classifications and shapes. For bent flange channels (folded and curved) which lie in class 1 and 2, diamond configuration has greatest ductility ratio while for class 3 and 4, circle configuration is considered as the best. In addition, for the specimens with plain flanges (flat and stiffened flat), circle configuration of the bolts provides higher ductility for all of the cross-section classifications. It is worth mentioning that the worst ductility ratio for all of the section shapes and classes belongs to conventional square configuration of the bolts. As an illustration, using circle and diamond bolt configuration leads

to up to 100% greater ductility ratio at the connection compared to conventional square configuration. Also, this trend will be more obvious when beam with smaller section slenderness (in higher class) would be employed.

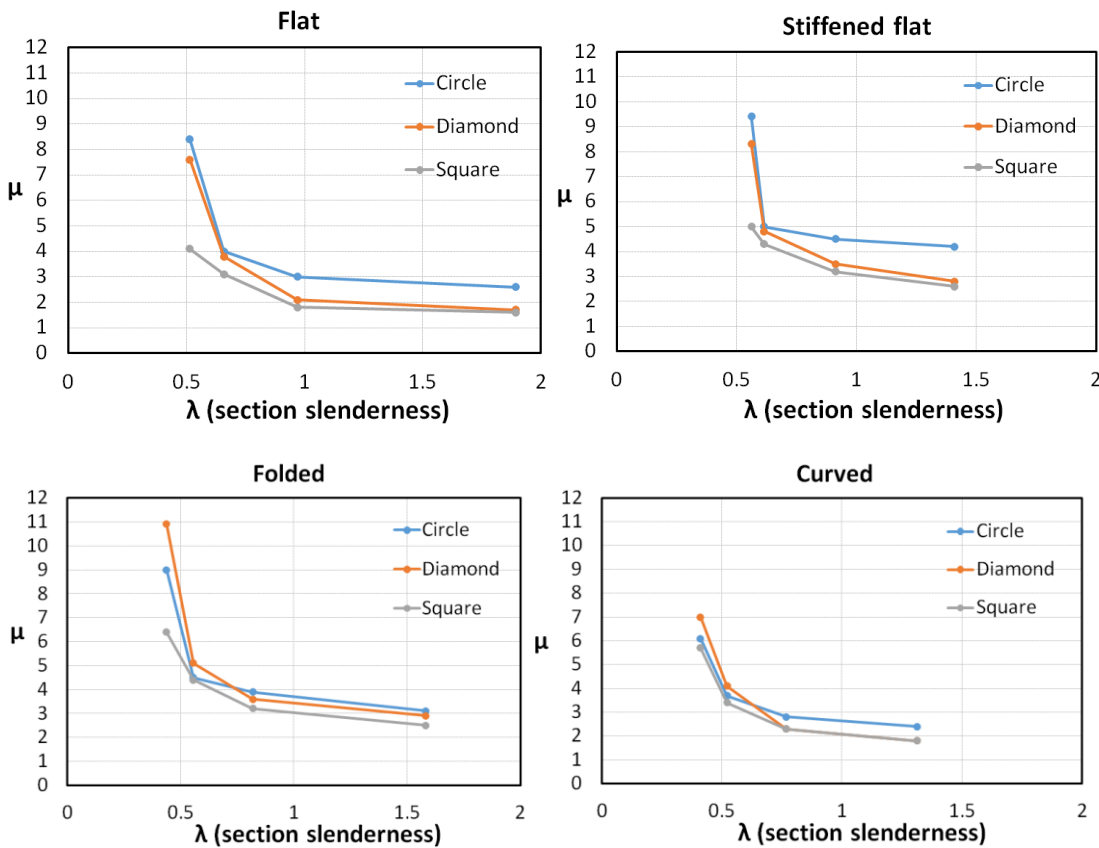


Figure 11.20. Ductility to slenderness relationship of different sectional shapes

### 11.5.4 Energy dissipation

The energy dissipation is the area under the moment-rotation curve. Therefore, bi-linear EEEP results for all the connections derived from the backbone curves of the hysteretic reversed cycles was used to obtain the energy dissipation capacity. The results are shown in Figure 11.21, it can be seen that the effect of cross-sectional shape and bolt configuration on energy dissipation capacity is only significant in the connections with class 1 and class 2 beam cross-sections, however, the effect on energy dissipation capacity is negligible for all connections with beam cross-sections in class 3 and 4 (1 and 2 mm thickness). Due to the cross-sectional buckling, class 3 and 4 sections did not reach their plastic moment capacity, therefore the beams in the connection possessed less ability to dissipate energy. On the contrary, as discussed in Section 11.4.1, class 1 cross-sections can rotate up to 3 times more in terms of plastic deformation; hence class 1 is expected to dissipate more energy.

Using the folded flange section as beam in the connections leads to up to 250%, 200% and 150% more energy dissipation capacity in connections compared to the flat, curved and stiffened flat sections, respectively. In general, diamond and circle distribution of the bolts can dissipate up to



250% more energy for beam with class 1 cross-section. Again similar to the ductility ratio, conventional square distribution of the bolts has the least ability in terms of energy dissipation capacity.

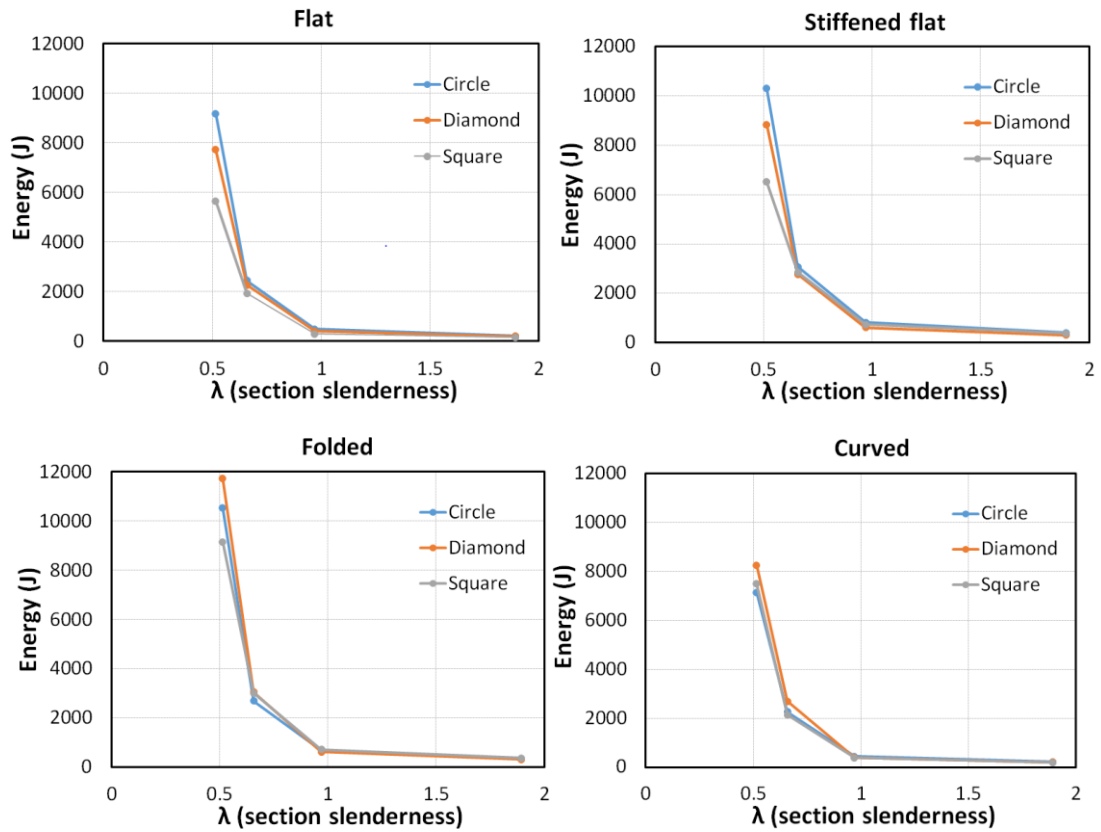


Figure 11.21. Energy dissipation to slenderness relationship of different sectional shapes

### 11.5.5 Damping coefficient

The equivalent viscous damping coefficient  $h_e$ , which is the measurement of the energy dissipation capability, can be derived by the plumpness of the hysteresis loop as shown in Figure 11.22, where the maximum plumpness happens after the limit bearing capacities (Points B and D). The equivalent viscous damping coefficient  $h_e$  is then calculated employing the method recommended in (Bolong 1989, JGJ101-96 1997):

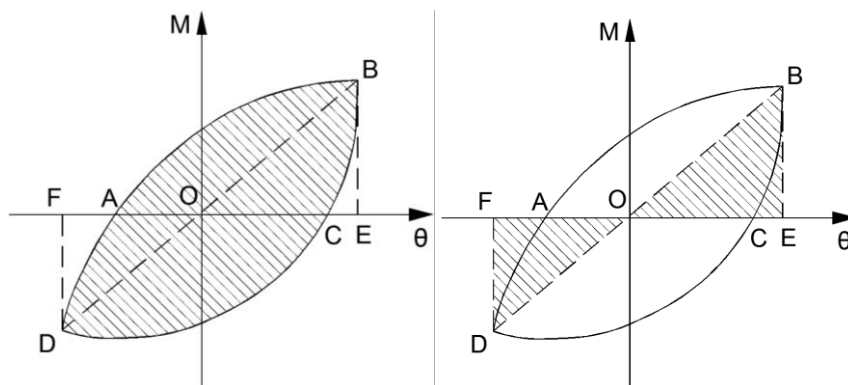
$$h_e = \frac{1}{2\pi} \frac{S_{ABC} + S_{CDA}}{S_{OBE} + S_{ODF}} \quad (11.5)$$

where the area of  $S_{\Delta ABC} + S_{\Delta CDA}$  is the amount of energy dissipated by the connection in one cycle at the expected rotation;  $S_{\Delta OBE} + S_{\Delta ODF}$  is the total strain energy of the connection at the expected rotation where the connection is assumed to behave in the elastic range.

For all the connections studied, the results are provided in Figure 11.23, with two equivalent viscous damping coefficients. One is for the maximum moment in which the hysteresis loop

reaches the peak flexural capacity while the other one is for the ultimate state which is assumed to be near the point when the hysteresis loop reaches 20% drop from peak moment in the softening stage. It should be noted that larger  $h_e$  indicates a better energy dissipation capability of the connection.

It is shown in Figure 11.24 that for all the connections studied, a relative high equivalent viscous damping coefficient was presented, which means that this kind of bolted moment connection in general has a high ability to damp energy. As it would be obvious there is significant improvement in the damping coefficient by using beams with larger thickness. However, cross-sectional shapes have a negligible effect on the damping coefficient. Damping coefficients at maximum moment loop show that using circle and diamond distribution of the bolts for the beam with class 1 and 2 cross-sections are more efficient, while conventional square distribution of the bolts leads to higher damping coefficient for class 3 and 4 cross-sections. However, the ultimate (near failure) damping coefficient has less change than the damping coefficient at maximum moment. A comparison of these two damping coefficients at both two stages illustrates that, unlike class 1 and 2 cross-sections, class 3 and 4 achieve most of the amount of energy dissipation through the softening branch of the moment-rotation curve.



**Figure 11.22. Definition of the damping coefficient**

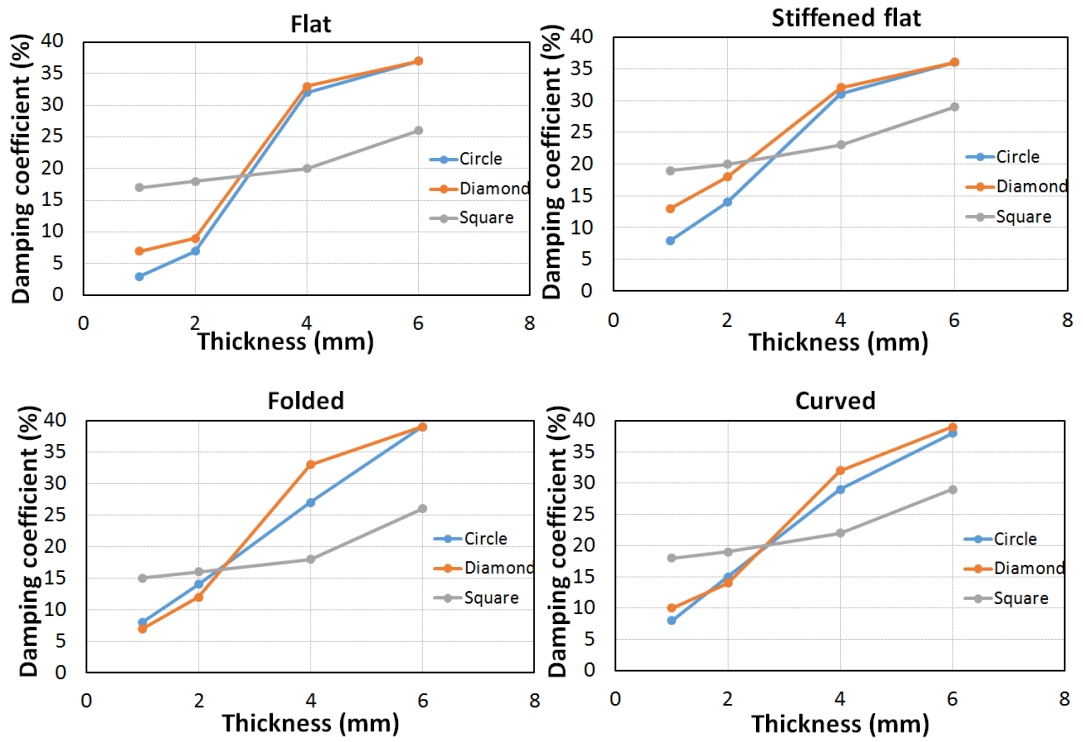


Figure 11.23. Damping coefficient at maximum moment

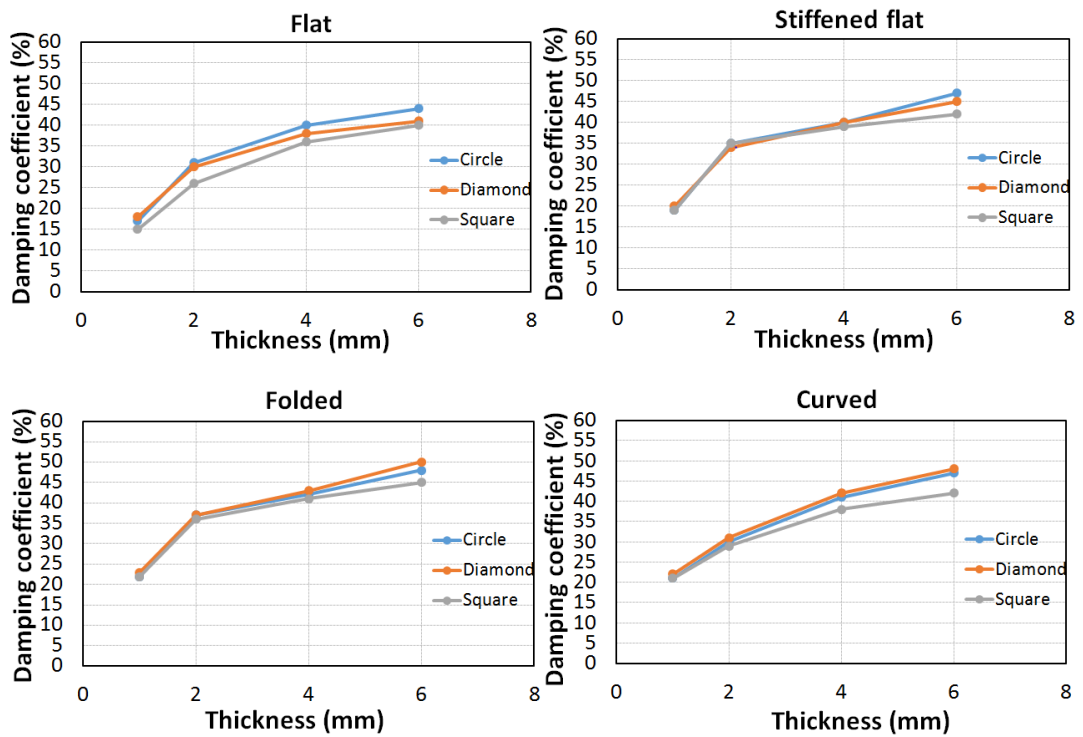


Figure 11.24. Damping coefficient at ultimate (near failure)

11.5.6 Effect of the thickness of gusset plate

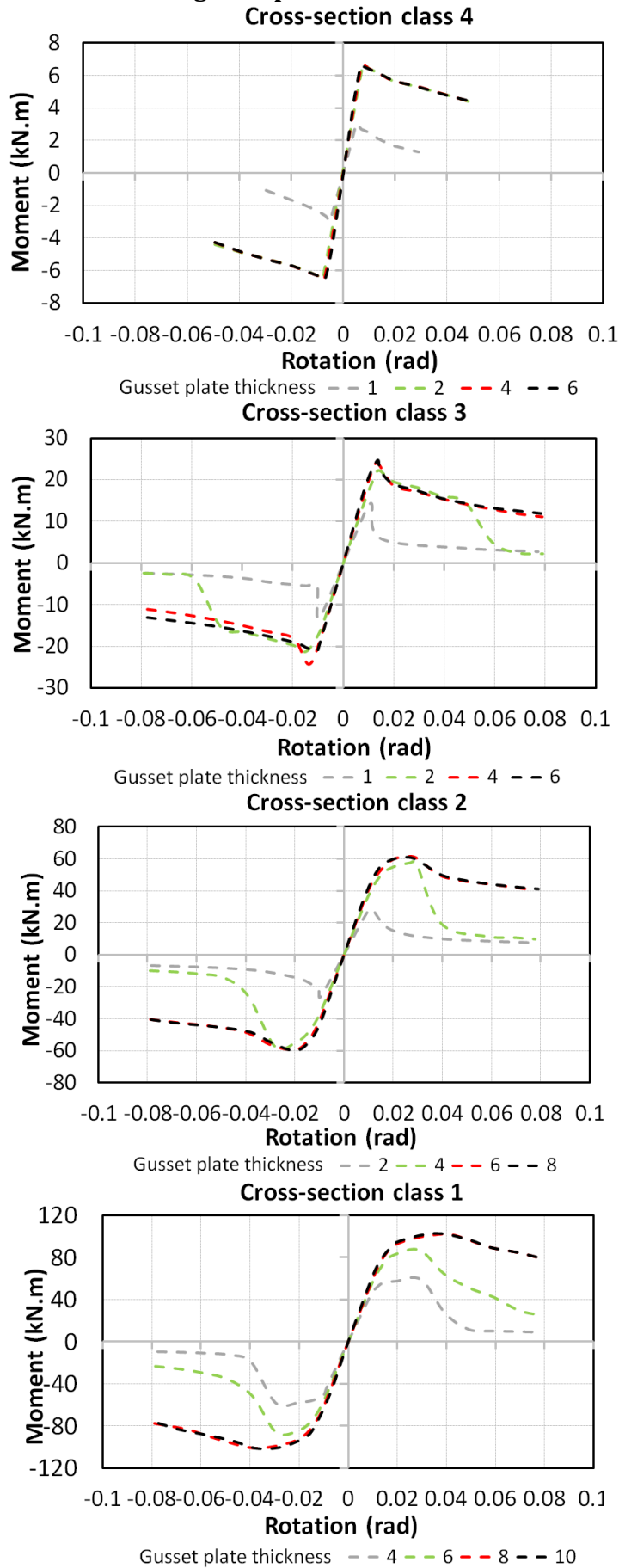


Figure 11.25. Effect of gusset plate thickness on the bending capacity of the connections

The effect of various gusset plate thicknesses on the cyclic behaviour of the bolted-moment connection was investigated using connection with flat flange channel as a beam and conventional square distribution of the bolts. For different flat channel classes (1, 2, 4, 6 mm thicknesses), various gusset plate thicknesses were selected. As can be seen from Figure 11.25, using the thickness which is the same as that of the beam causes premature local buckling at gusset plate and this local buckling shifted from beam to gusset plate. In addition, regarding the FE results when local buckling happens at beam, the effect of increasing gusset plate thickness on the global behaviour of the connections is negligible.

## 11.6 DSM design for cold-formed sections

The Direct Strength Method (DSM) is an alternative to the traditional effective width method to predict the load carrying capacity of CFS members. This method integrates a computational stability analysis into the design process. In a first step, the elastic local, distortional and global buckling loads are determined. Using these elastic buckling loads and the load that causes first yield, the strength is then directly predicted based on a series of simple empirical equations. While calculation of the effective properties can be tedious for complex CFS cross-sections, only gross section properties are needed in the DSM. Therefore, DSM is effective when dealing with innovative cross-sections with curved flange, stiffened flat and folded flange cross-sections. The elastic buckling loads of CFS members can be calculated using software such as CUFSM (Schafer 2006).

### 11.6.1 Local buckling strength

The nominal flexural strength for local buckling ( $M_{nl}$ ) is calculated from Section 1.2.2.2 of AISI S100-07 (AISI 2007) as follows:

$$\text{For } \lambda_{Sl} \leq 0.776: M_{nl} = M_y \quad (11.6)$$

$$\text{For } \lambda_{Sl} > 0.776: M_{nl} = \left[ 1 - 0.15 \left( \frac{M_{crl}}{M_y} \right)^{0.4} \right] \left( \frac{M_{crl}}{M_y} \right)^{0.4} M_y \quad (11.7)$$

where

$\lambda_{Sl}$ : cross-sectional slenderness ( $\lambda_{Sl} = \sqrt{M_y / M_{crl}}$ ;  $M_y = Z_f f_y$ );

$M_{crl}$ : elastic local buckling moment of back-to-back sections ( $M_{crl} = Z_f f_{crl}$ );

$Z_f$ : section modulus about horizontal axis of the back-to-back sections;

$f_{cr1}$ : elastic local buckling stress which was calculated by using finite strip method (Li and Schafer 2010a)

### 11.6.2 Distortional buckling strength

The nominal flexural strength for distortional buckling ( $M_{nd}$ ) is determined from Section 1.2.2.3 of AISI S100-07 (AISI 2007) s follows:

$$\text{For } \lambda_{sd} \leq 0.673: M_{nd} = M_y \quad (11.8)$$

$$\text{For } \lambda_{sd} > 0.673: M_{nd} = \left[ 1 - 0.22 \left( \frac{M_{crd}}{M_y} \right)^{0.5} \right] \left( \frac{M_{crd}}{M_y} \right)^{0.5} M_y \quad (11.9)$$

where

$\lambda_{sd}$ : cross-sectional slenderness ( $\lambda_{sd} = \sqrt{M_y / M_{crd}}$ ;  $M_y = Z_f f_y$ );

$M_{crd}$ : elastic local buckling moment of back-to-back sections ( $M_{crd} = Z_f f_{crd}$ );

$Z_f$ : section modulus about horizontal axis of the back-to-back sections;

$f_{crd}$ : elastic local buckling stress which was calculated by using finite strip method (Li and Schafer 2010a)

### 11.6.3 Comparison between FE results of CFS bolted-moment connections and DSM design rules for pure bending

The ratio of peak point of FE moment rotation hysteretic curves corresponding to the starting point of buckling over to yield moment capacity of different sections were specified in Figure 11.26. It is shown in Figure 11.26 that FE results of connection capacity proved that the capacity of connections is less than those which were predicted by DSM method for bending of beam section. This also indicates that using bolts to connect webs of back-to-back channels reduces the capacity of CFS channels. Hence, envelop of FE results is employed to propose an empirical design equation for design of CFS beam used in bolted-moment connections:

$$\text{For } \lambda_s \leq 0.378: M_{nd} = M_y \quad (11.10)$$

$$\text{For } \lambda_s > 0.378: M_{nd} = \left[ 1 - 0.6 \left( \frac{M_{crd}}{M_y} \right)^{0.1} \right] \left( \frac{M_{crd}}{M_y} \right)^{0.8} M_y \quad (11.11)$$

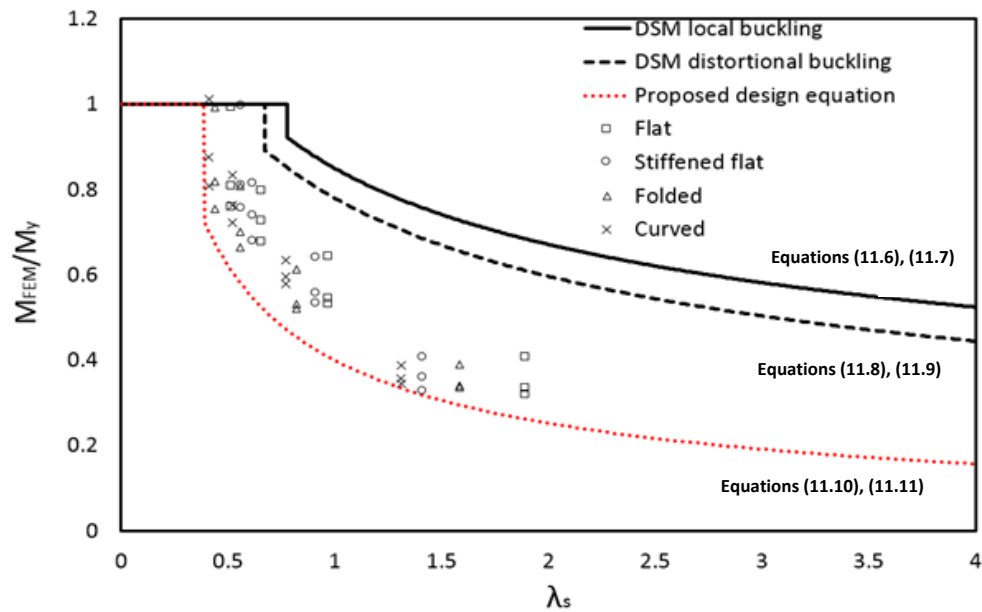


Figure 11.26. Comparison between FE cyclic results of bolted moment connections and DSM for design of CFS sections under pure bending

## 11.7 Connections with slippage

### 11.7.1 Effect of slip resistance

Generally, the simplified method of modelling slip action creates a horizontal shift in moment-rotation curve while the global behaviours of the connections are the same. In addition, adjusting the bolt pretension in the connections with all cross-section classes will just change the starting point of slippage while the performances of connection in elastic and inelastic stage are considered as the same. In order to evaluate the effect of various slip resistance of bolts on the global moment-rotation behaviour of the connections with class 1 beam cross section (6mm thickness), different bolt pretension forces were applied on the connections with flat flange channels. The slip resistances were selected to be at least equal to the allowable slip resistance determined according to ASTM A325 (ASTM 2004). Monotonic analyses were carried out on the connection with three different bolts pretensions and were compared with the behaviour of connections without slippage of the bolts. Bolt pretensions were assumed be:  $T_m=90\text{ kN}$  which is corresponding to activation of slip in elastic behaviour of connection,  $T_m=270\text{ kN}$  leads to slippage of the bolts in inelastic behaviour of connection, and pretension level leads to fully clamped where no slippage happens. The moment-rotation behaviours of connections with various clamping forces are the same except for the starting point of bolt slippage. In addition, as it is expected for class 1 cross-sections, fully clamped connection and connection with slippage show a slightly different behaviour in the inelastic stage and especially after the local buckling, which is due to bolt configurations. It is worth noting that accommodating slippage in the connections with different bolt configurations does not change the failure modes.

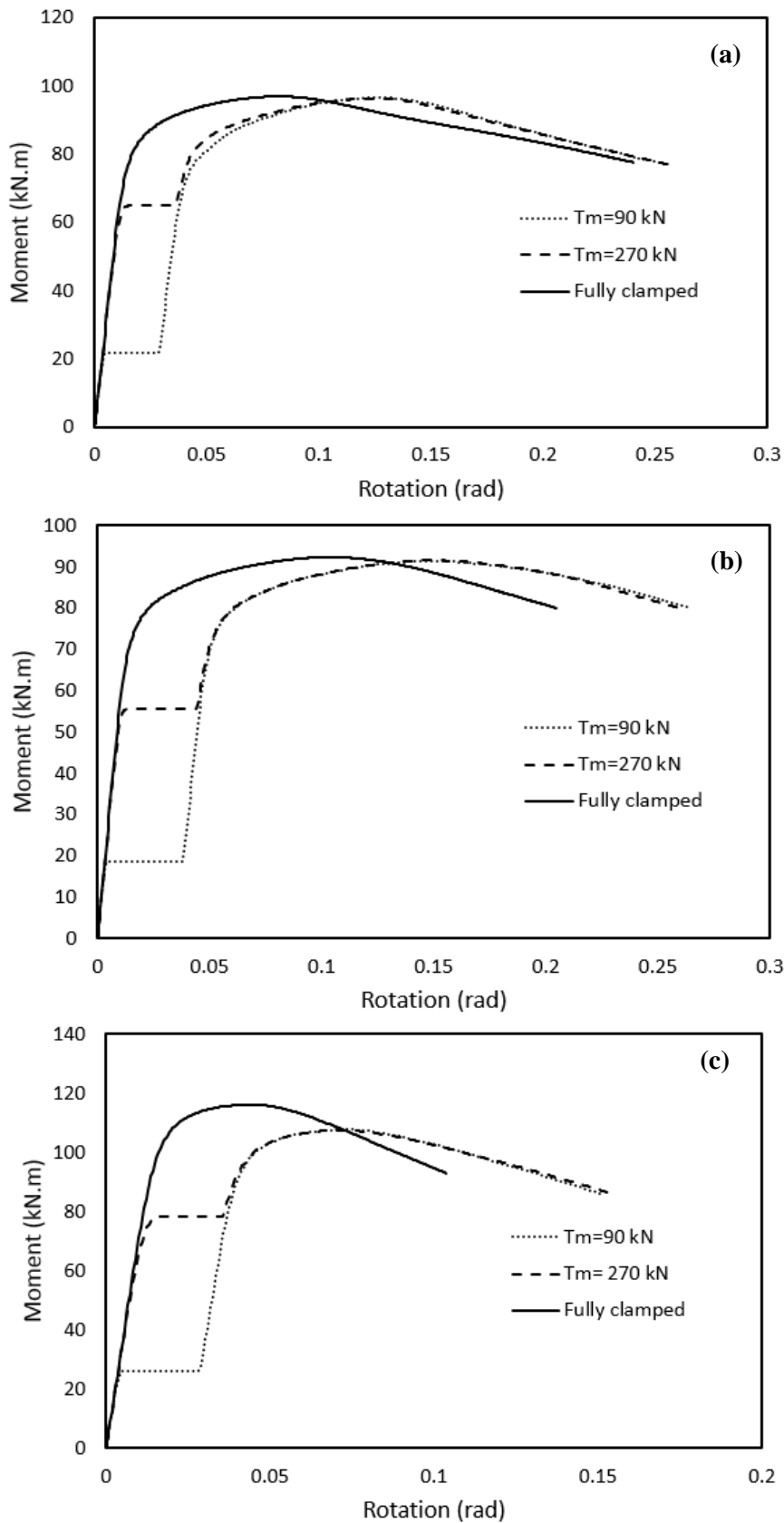


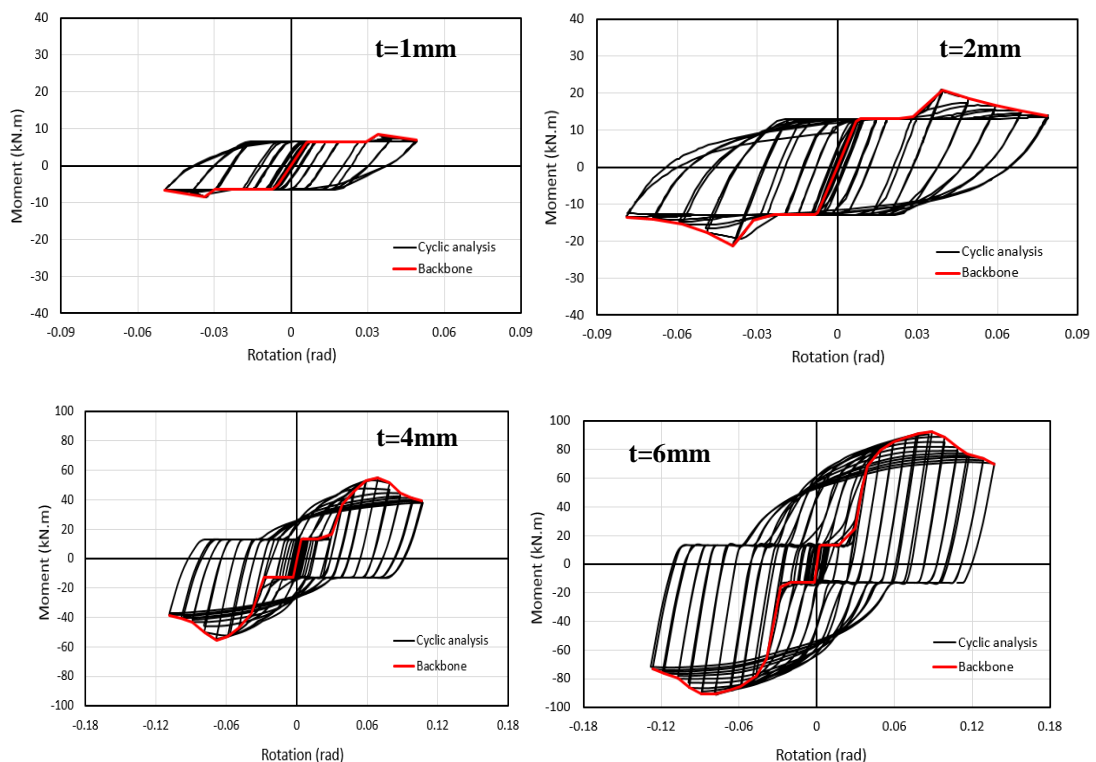
Figure 11.27. The behaviour of connection with cross section class 1 using different bolt pretensions and configurations: (a) Circle; (b) Diamond; (c) Square



### 11.7.2 Effect of bolt arrangement and channel thickness

This parametric study consisted of 48 CFS bolted moment connections with different section classification (1, 2, 4, 6 mm), various beam channel shapes (flat, Stiffened flat, folded, curved) and different bolts configurations (circle, diamond, square). FE analysis using ABAQUS (ABAQUS 2011) was employed to evaluate the cyclic behaviour of those connections. All of the column and beam dimensions, material properties, boundary conditions, loading protocol, and mesh size were the same as those used in the modelling of connection without slippage. A through plate with thickness of 10 mm was used in the FE analysis.

The flat flange channels with various thicknesses (1, 2, 4 and 6 mm) and circle distribution of the bolts was selected to show the typical reversed cyclic response of the connections with slippage of the bolts (Figure 11.28). Also, it is plotted along with the backbone curve of the connection. No significant differences were observed between the failure modes of connection with and without slippage of the bolts.



**Figure 11.28. Moment-rotation cyclic relationship and backbone curve of the connections with flat flange beam section and circular bolt distribution configuration (with slippage)**

### 11.7.3 Maximum moment capacity

Comparison of the values of maximum moment capacity between connections with and without slippage of the bolts indicates that generally the effect of bolt slippage is quite small on the flexural capacity of the connections for all cross-section classes. However, regarding beam cross section class 1 with square distribution of bolts, there is slight reduction in flexural moment

capacity when slip action is activated in the connection. Generally, according to (Uang et al. 2010), the centre of rotation in the bolted-moment connection tends to shift the centre of bolts due to the slipping deformation in the bolts. As discussed in Section 11.4.1, using class 1 cross-section in the connection can rotate more than 0.1 rad at maximum moment capacity, which increases the variation of position of the rotation centre. It should be noted that shift of centre of rotation is more critical when square distribution of bolts is used. For the same cross-sectional class and distribution of the bolts; cross-sectional shape has a little effect on shifting of rotation centre.

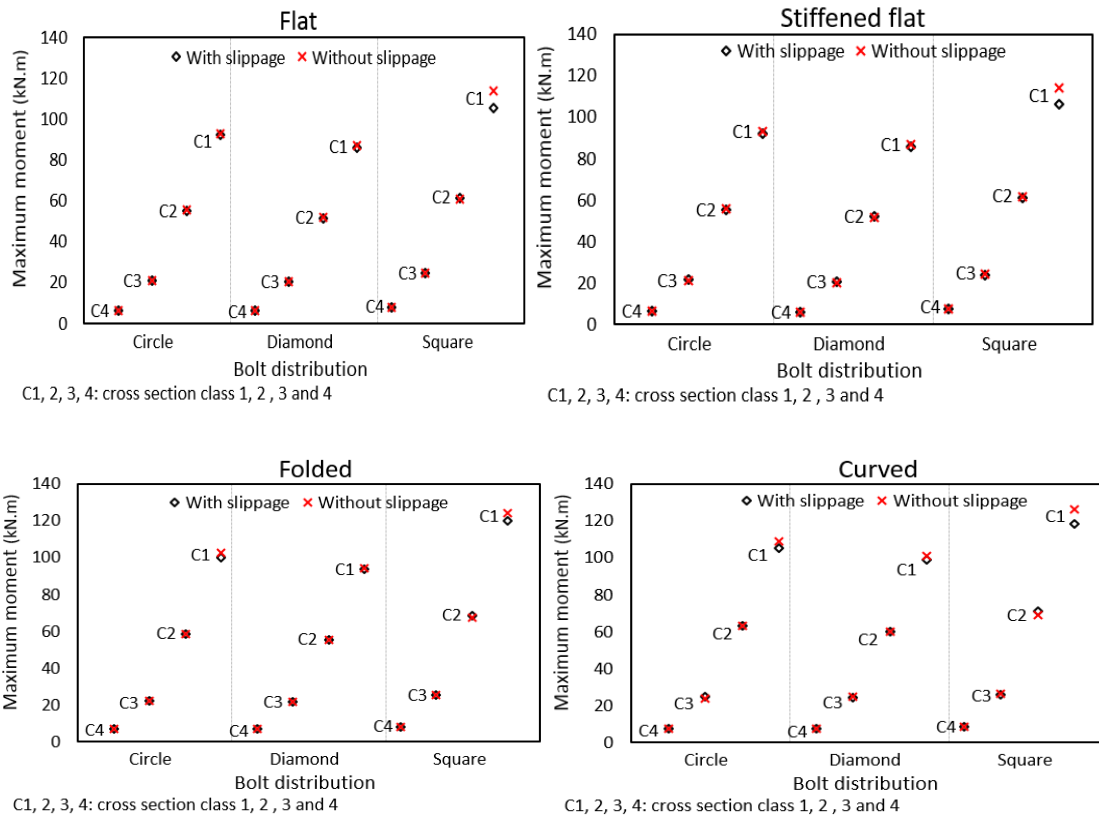


Figure 11.29. Comparison of moment capacities of connections with and without slippage

### 11.7.4 Energy dissipation

Generally, the capacity of energy dissipation reflects the ductility of the structures. Therefore, bi-linear EEEP results for all the connections derived from the backbone curves of the hysteretic reversed cycles was employed to obtain energy dissipation capacity. As shown in Figure 11.30, for both types of connections, the effects of cross-sectional shapes and bolt configurations on energy dissipation capacity are evident only when classes 1 and 2 beam cross-section are used, however, energy dissipation capacity is negligible for all connections with class 3 and 4 beam cross-sections (1 and 2 mm thickness). Due to the cross-sectional buckling, class 3 and 4 sections does not reach their plastic moment capacity therefore the beams in the connection possess less ability to dissipate energy. On the contrary, class 1 cross-sections can rotate up to 3 times more in terms of plastic deformation and are able to dissipate more energy. The effect of

CHAPTER 11. Behaviour of CFS bolted connections: a numerical parametric study

cross-sectional shape is the same for connections with and without slippage of the bolts, also, using the folded flange section as a beam in the connections leads to more energy dissipated. The effect of bolt distribution is only obvious when class 1 beam cross-section is used. In addition, the efficient configuration for connection with slippage of the bolts is diamond while it is correlated to cross-sectional classifications and shapes. It is also shown in Figure 11.30 that the connections with bolt slippage generally dissipated more energy than the ones without slippage.

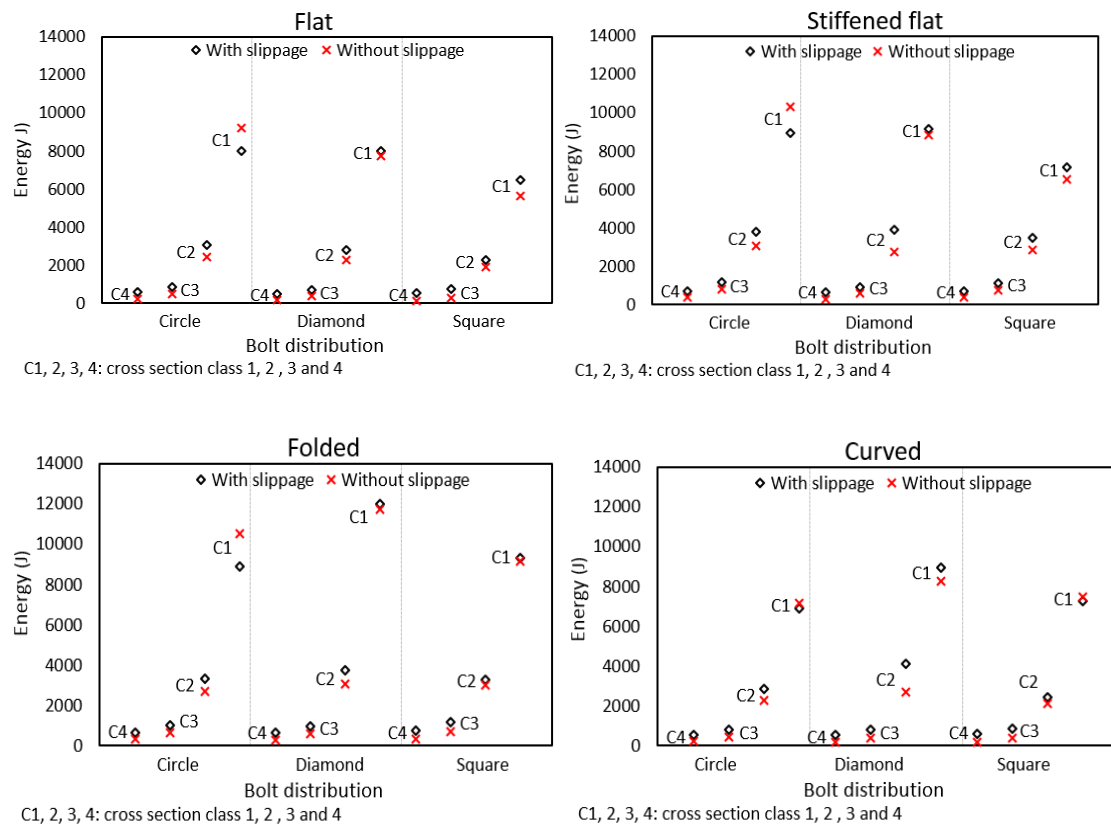


Figure 11.30. Comparison of energy dissipation capacities of connections with and without slippage

### 11.7.5 Damping coefficient

As shown in Figure 11.31, there is obvious difference between damping coefficients of slip critical connection and without slippage connection especially when class 3 and 4 cross-sections are used. As discussed in section 11.7.1, failure modes for class 4 cross-sections happen in elastic stage of moment-rotation behaviour, and also class 3 cross-sections cannot reach the plastic stage. As a result, most of the dissipated energy by hysteretic loop at maximum moment is due to the smaller plastic region development of the connection which leads to lower damping coefficient. Since slip action of the bolts was adjusted in a way which occurs in elastic range of the connections, slip action in the connection with class 3 and 4 beam cross-sections is able to damp energy up to 3 and 5 times more than connection without slippage. However, damping coefficient at the stage which is near failure is greater than that at the peak moment because of

CHAPTER 11. Behaviour of CFS bolted connections: a numerical parametric study

the development of plasticity around the bolt holes and in the connected sections. Hence, there is slightly increase in damping coefficient near failure when slip action is used. Consequently, using slip action of the bolts for the class 3 and 4 cross-sections increases damping coefficient regardless the value of slip resistance. However, it is noted that the changing the slip resistance and bolt hole clearance can make damping coefficient of the bolted-moment connections capable to be adjusted.

Nevertheless, the results for class 1 and 2 cross-sections indicate that including slippage action in bolted-moment connection leads to declined damping coefficient up to 50% and 30% at maximum moment, respectively (Figure 11.31). As class 1 and 2 cross-sections are able to develop plasticity, so the main reason to justify this different behaviour is more bearing deformation and plasticity in the connected members for the connection without slippage of the bolts. While using slippage of the bolts reduces the bearing deformation and plasticity around the bolt holes, again it should be noted that damping coefficient at the failure point slightly decreases when slip action is included into the connections with class 1 and 2 sections. In this case, slip action happen in the elastic stages of the connections. As a consequence, in order to obtain higher damping coefficient for the connection with class 1 and 2 cross-sections, adjusting the slip resistance which is activated in the inelastic range of the connection is suggested.

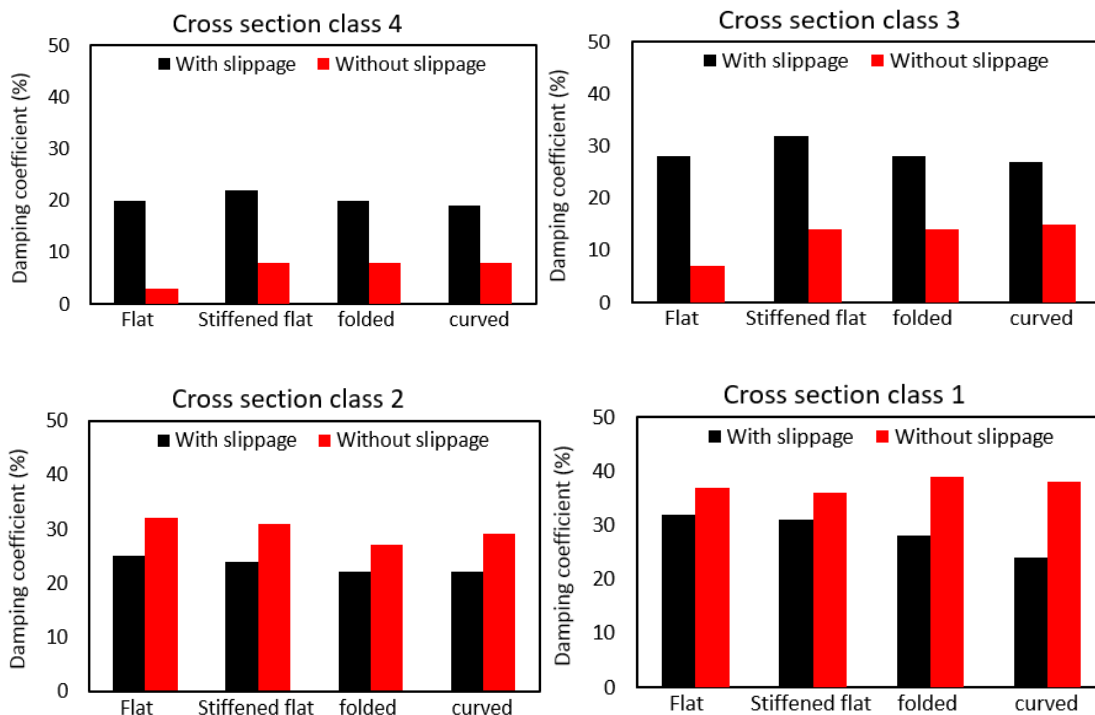


Figure 11.31. Damping coefficient up to maximum moment

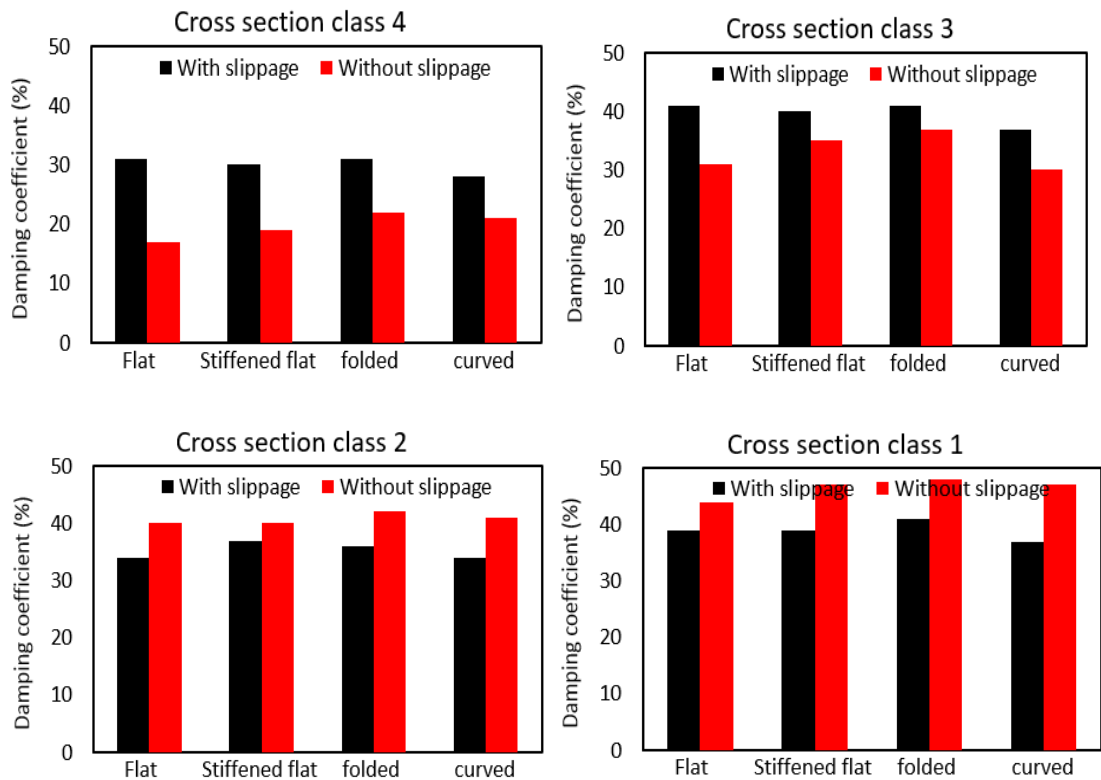


Figure 11.32. Damping coefficient at ultimate (near failure)

### 11.7.6 AISC requirements for the connection with slippage

As described in Section 11.5.1, the AISC (AISC 341-05 2005) impose requirements for beam-to-column, connections in the seismic force resisting system in order to satisfy ductility requirement of the connection using different seismic regions. Generally, as shown in Table 11.4, while some of the connections with class 3 and 4 beam cross-sections without slippage do not satisfy neither the SMF nor the IMF requirements, including the slippage of the bolts in bolted-moment connection improve ductility of the connections. Consequently, since most of the conventional cross-sections in CFS building industry lie in the class 3 and 4 ranges, the importance of mobilising slippage in CFS bolted-moment connection used in high seismic regions is recommended.

**Table 11.4. AISC requirements for the CFS bolted connection with slippage**

Bolt configuration	Beam thickness	Beam type	AISC	
			Without slippage	With slippage
Circle	1	Flat	×	IMF
		Stiffened flat	IMF	SMF
		Folded	IMF	SMF
		Curved	×	SMF
	2	Flat	IMF	SMF
		Stiffened flat	SMF	SMF
		Folded	IMF	SMF
		Curved	IMF	SMF
	4	Flat	SMF	SMF
		Stiffened flat	SMF	SMF
		Folded	SMF	SMF
		Curved	SMF	SMF
	6	Flat	SMF	SMF
		Stiffened flat	SMF	SMF
		Folded	SMF	SMF
		Curved	SMF	SMF
Diamond	1	Flat	×	IMF
		Stiffened flat	IMF	SMF
		Folded	IMF	SMF
		Curved	IMF	SMF
	2	Flat	IMF	SMF
		Stiffened flat	IMF	SMF
		Folded	IMF	SMF
		Curved	IMF	SMF
	4	Flat	SMF	SMF
		Stiffened flat	SMF	SMF
		Folded	SMF	SMF
		Curved	SMF	SMF
	6	Flat	SMF	SMF
		Stiffened flat	SMF	SMF
		Folded	SMF	SMF
		Curved	SMF	SMF
Square	1	Flat	×	IMF
		Stiffened flat	×	IMF
		Folded	×	SMF
		Curved	×	IMF
	2	Flat	×	SMF
		Stiffened flat	SMF	SMF
		Folded	IMF	SMF
		Curved	IMF	SMF

4	Flat	SMF	SMF
	Stiffened flat	SMF	SMF
	Folded	SMF	SMF
	Curved	SMF	SMF
6	Flat	SMF	SMF
	Stiffened flat	SMF	SMF
	Folded	SMF	SMF
	Curved	SMF	SMF

### 11.8 Development of a two node element to model the slip bearing behaviour of bolts

In the analysis of the CFS bolted connections, it was found that the slippage of the bolts was activated only in the first half cycle when using the predefined connector elements in ABAQUS (ABAQUS 2011), as shown in Figure 11.33. This is due to the fact that the load-deformation of the connector elements in ABAQUS (ABAQUS 2011) is based on relative motion and it is suitable only for monotonic loading, as shown in Section 10.4.4. In cyclic loading, when the bearing action happens in one cycle, the slip of the connection cannot be activated again in the subsequent cycles in the FE analysis. Therefore, the connector elements cannot be used for the modelling of CFS bolted connections subjected to cyclic loading. Moreover, the slip range of the bolts grows when the bearing action elongates in the bolt holes during the large rotation cycles in the test. This was also noticed by (Uang et al. 2010) through the cyclic testing of bolted moment frame connections in which the connection rotation was dominated by the slip-bearing action of the bolts. Proposed hysteresis rule of a bolt is shown in Figure 11.34.

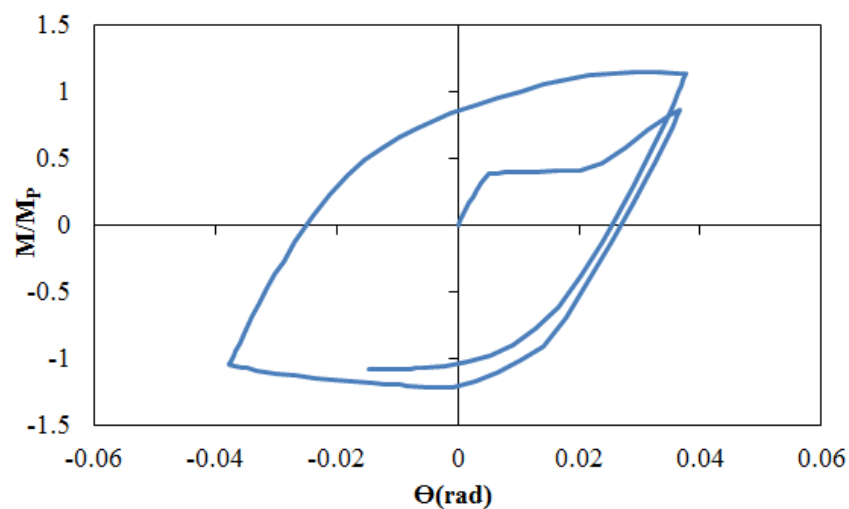
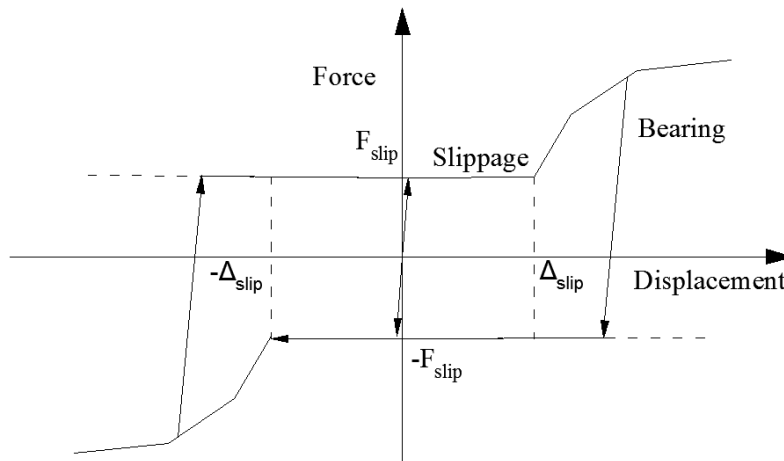


Figure 11.33. Moment-rotation curves of connection B2 with slippage-bearing action defined in ABAQUS (ABAQUS 2011)

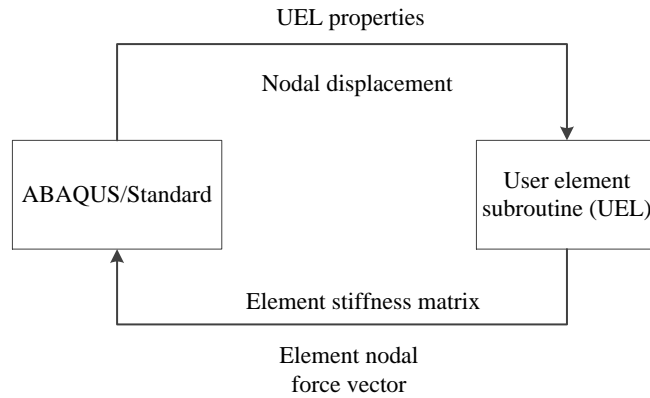


**Figure 11.34. Hysteresis rule for a bolt slipping and bearing against a steel sheet**

A user element subroutine (UEL) which is able to incorporate the hysteresis rule defined in Figure 11.34 is therefore developed to model the behaviour of bolts. ABAQUS has a library that contains a wide range of elements. However, there are still some types of elements which are not available in its element library, especially elements with a special purpose, for example to model the bolt behaviour. To overcome this limitation, ABAQUS allows users to define their own elements by programming a user element subroutine (UEL). A UEL is a FORTRAN based program written specifically for ABAQUS. Similar to other ABAQUS elements, user defined elements can be developed and assigned from an input file. However, no visualisation is provided for the user defined elements in ABAQUS (Ding 2015).

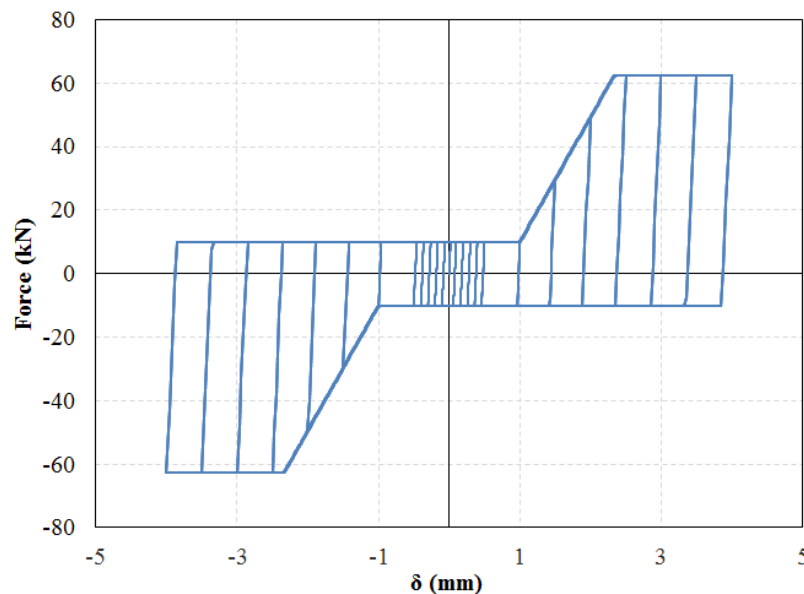
A user element subroutine (UEL) cannot be called separately and conduct finite element analysis. It needs to be linked between FORTRAN and ABAQUS. Once linked, UEL will be called every time when ABAQUS requires the input information from the UEL (Figure 11.35). In each call by ABAQUS, the UEL will be provided with element geometry information (coordinates, displacement and etc.), UEL properties, and solution-dependent variables from the last increment and analysis procedures. By using the information provided by ABAQUS, the UEL calculates and returns to ABAQUS a Jacobian matrix and residual forces contributed by the UEL and the updated solution-dependent variables. Solution dependent variables are carried in a vector where users can save data to be used in the next increment (Ding 2015).



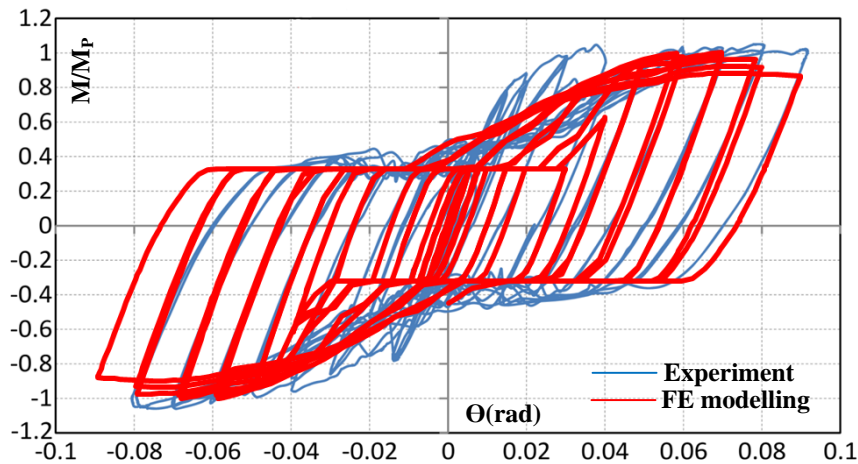


**Figure 11.35. Relationship between the UEL and ABAQUS**

A two node element is firstly defined and the force-displacement relationship of a bolt bearing against a steel sheet for connection B2, which is presented in Figure 11.36, the FORTRAN subroutine is attached in the Appendix 7. The subroutine is then incorporated in the full-scale CFS connection modelling for the tested connection B2. All the material properties, boundary conditions and loading scheme have been described in Section 11.2. The only difference is that a bolt hole clearance of  $\pm 1mm$  was defined and the bolt elongation is automatically taken into account in the UEL subroutine. Figure 11.37 illustrates the cyclic responses of the connection B2 subjected to cyclic loading. It is noted that the slippage defined in the analysis is 1mm, the two node element can take into account the bolt elongation by itself without defining an oversized hole prior to the analysis. The results also show that by using the proposed two node element, good agreement is achieved between experimental and numerical results. The proposed element should be proving useful for other forms of fastener modelling.



**Figure 11.36. Cyclic response of a single bolt during cyclic loading**



**Figure 11.37. Comparison between tested and analysed moment-rotation curves of connection B2 with 1mm slippage defined**

### 11.9 Summary and conclusions

In this chapter, nonlinear behaviour of CFS bolted connections under cyclic loading has been investigated by conducting extensive parametric geometric and material nonlinear analysis using the validated finite element model in ABAQUS. A simplified model that can be used to model the slip-bearing behaviour of a single bolt was developed. Cross-sections of different beam shapes that were connected in the connections have been classified according to Eurocode concept and nonlinear FE analysis. The factors of cross-sectional shapes, thicknesses of the beams and the bolt distribution configurations were analysed numerically, on the connection performance. The modes of failure and cyclic moment-rotation responses were compared to show the effects on the moment capacity, ductility, energy dissipation and damping coefficient. Based on the results of this study, the following conclusions could be drawn:

- (1) The bolted-moment connections with class 1 and 2 sections can satisfy AISC requirements for Special Moment Resisting Frame (SMF), while according to the FEMA only class 1 cross-sections are considered as SMF. It is shown that most of the class 3 cross-sections and 4 are not sufficient to utilize as SMF.
- (2) Using bent flange channels (folded and curved) as a beam in the connection can withstand maximum moment only 10% more than plain flange channels (flat and stiffened flat). Besides, the differences between two bent channels and the plain channels in terms of maximum flexural capacities are negligible. The bolts array in the web will result in the reduction of moment-capacity of the channel-sections which are connected to the connections. A direct strength design curve which can predict the lower bound of the strength of the connections is proposed.
- (3) The connection ductility ratio is highly related to the cross-section classification, shape of the beam and the bolt distribution. Connections with folded flange section provides higher

## CHAPTER 11. Behaviour of CFS bolted connections: a numerical parametric study

ductility ratio up to 55%, 45% and 30 % more than those with curved, flat and stiffened flat sections, respectively. In aspect of bolt configuration, it should be noted that the best configuration is related to cross-sectional classifications and shapes. For class 1 and 2 bent flange channels (folded and curved), diamond configuration has the largest ductility ratio while for class 3 and 4, circle configuration is considered as the best. For specimens with plain flanges (flat and stiffened flat), circle configuration of the bolts provides higher ductility for all of the cross-section classifications. It is worth mentioning that the worst ductility ratio for all of the section shapes and classes belongs to conventional square configuration of the bolts.

(4) Using the folded flange section as beam in the connections leads to up to 250%, 200% and 150% more energy dissipation capacity in connections compared to the flat, curved and stiffened flat sections, respectively. In general, diamond and circle distribution of the bolts can dissipate up to 250% energy for beam with class 1 cross-section. Conventional square distribution of the bolts has less capacity in terms of energy dissipation.

(5) For all the connections studied, a relative high equivalent viscous damping coefficient was presented, which means that the bolted moment connection studied here with gusset plate generally has a high energy damping capacity. As it would be evident there is significant improvement in the damping coefficient by using beams with larger thickness. However, cross-sectional shapes have a negligible effect on the damping coefficient.

(6) Using the thickness the same as that of the connected beam may lead to premature local buckling at gusset plate of the connections. In addition, regarding the FE results when local buckling happens at the beams, the effect of gusset plate thickness on the global behaviour of the connections is negligible.

(7) The effect of cross-sectional shapes is similar for connections with and without slippage of the bolts, also, using the folded flange section as a beam in the connections leads more energy dissipation capacity. However, the effect of bolt distribution is only obvious when class 1 beam cross-section is used for connections with slippage. In addition, the efficient configuration for connection with slippage of the bolts is diamond while it is related to cross-sectional classifications and shapes. It is also shown that the connections with bolt slippage generally dissipated more energy than the ones without slippage.

(8) When the slippage of the bolts is not considered, the connections with class 3 and 4 beam cross-sections cannot satisfy the SMF and the IMF requirements. However, including the slippage of the bolts in bolted-moment connection can significantly improves the ductility of CFS bolted moment connections.

## CHAPTER 11. Behaviour of CFS bolted connections: a numerical parametric study

(9) The proposed two node element, which is defined in a UEL subroutine can take into account the slippage, bearing deformation and the bolt hole elongation. By using the proposed element, good agreement has been achieved to model the moment-rotation response of the full-scale tested connection.

## **CHAPTER 12. Summary and conclusions, and recommendations for future work**

---

### **12.1 Summary and conclusions**

The main aim of this research is to understand, predict, and optimise CFS elements based on their buckling and post-buckling behaviour. The optimised elements can then be included in full-structure modelling to develop more efficient CFS structural sub-frames with high ductility and energy dissipation capacity, suitable for multi-story buildings in seismic regions. This was achieved through the development of optimisation frameworks for CFS elements based on their buckling and post-buckling behaviour and experimental works were used to verify the effectiveness of the proposed methods. This chapter gives a brief summary and reports on the main conclusions from each part of the work.

### 12.1.1 Optimisation of CFS columns

Ten channel cross-sections were selected and the geometrical dimensions of each individual prototype were optimised with respect to its axial capacity. The thickness and coil length of the prototypes were kept constant during the optimisation process. The selected prototypes were comprised of the plain channels, channels with single inclined lips, channels with double folded lips with one or two intermediate stiffeners incorporated into the web.

For comparison purposes, a commercially available standard cross-section with the same total coil width and thickness was selected and its axial capacity was compared with those of optimised cross-section in columns with 3 different lengths:  $1m$ ,  $2m$  and  $3m$ . The axial capacities of the optimised cross-sections determined based on EC3 were also verified against detailed nonlinear FE analysis considering the effect of geometrical imperfection. The compressive capacity has been found to be highly dependent on the shift of centroid and the effective cross-section of the prototypes.

It was concluded that the axial capacity of the standard cross-section can be enhanced up to 108.3%, 73.7% and 43.4% according to EC3 but 77.1%, 59.2% and 42.9% with regard to the FE modelling, in columns with  $1m$ ,  $2m$  and  $3m$  length, respectively. The largest axial capacity for columns with  $1m$  and  $2m$  in length was observed in channel with double-fold lips and one web intermediate stiffener while for  $3m$  long column, the channel with single lip and one intermediate web stiffener offered the highest axial capacity

### 12.1.2 Optimisation of CFS beams

A practical method to obtain more economical CFS channel sections for use as laterally braced or unbraced beams was developed by optimising the dimensions of the cross-section and allowing for the addition of double-fold (return) lips, inclined lips and triangular web stiffeners. Six different prototypes were considered based on practical considerations. Based on the results of the study, the following conclusions could be drawn:

(1) By applying the proposed optimisation method to laterally braced beams, significant gains in cross-sectional bending capacity can be achieved: in the example, the bending capacity of a CFS cross-section was increased by up to 25% compared to the commercially available section taken as a starting point. The most effective cross-sectional prototype in this case was the lipped channel section with one stiffener located in the web. Using two stiffeners in a symmetrical arrangement, while keeping the developed length constant, would again reduce the efficiency of the solution.

(2) The flexural capacity of the optimised  $1m$ ,  $2m$ ,  $3m$  and  $4m$  long unbraced beams was increased by 26%, 25.8%, 61% and 75%, respectively, compared to a commercially available

## Chapter 12. Summary and conclusions, and recommendations for future work

section with the same amount of material. Comparison between the optimised results indicated that, when increasing the unbraced length, the flange width of the optimum solution increased, and consequently the total height of the section was reduced.

(3) The adequacy of the optimised sections was verified using detailed nonlinear FE analyses validated against experimental data, while also taking into account the effects of initial imperfections. The FE results, on average, showed less than a 6% error compared with the experimental data. The FE results of the commercially available and the optimised sections for both laterally braced and unbraced conditions generally showed good agreement with the flexural strengths estimated by EC3. The FE simulations also closely followed the increasing or decreasing trends in flexural capacity predicted by EC3 across the different prototypes. This demonstrates the reliability of the proposed optimisation method using the EC3 design rules.

(4) The flexural strengths of the optimised and the commercially available sections were also determined based on the DSM. Overall, the strengths calculated using EC3 and the DSM displayed a similar trend. Compared to the FE results, EC3 overestimated the flexural strength of the laterally braced beams by up to 16%, but underestimated the strength of the laterally unbraced beams by up to 19%. While the DSM, in general, provided accurate estimates of the capacities of the laterally braced beams, the accuracy of the method was seen to decrease with an increase of unbraced span length. It was shown that the DSM may overestimate the flexural capacity of long span laterally unbraced beams by up to 36%.

### 12.1.3 Development of more efficient CFS beam sections

A practical framework was proposed to develop more efficient CFS beam cross-sections while considering code-based design constraints as well as manufacturing issues and practical limitations. Using the framework, a commercially available CFS lipped channel section was optimised based on ten different prototypes, including a folded-flange cross-section, while keeping the material use constant. A slight modification of the EC3 design methodology was first developed in order to account for the multiple distortional buckling modes which may occur in the folded-flange cross-section. The particle swarm optimisation algorithm was then used to obtain the solutions with the maximum flexural strength. The accuracy of the modified design model and the effectiveness of the proposed optimisation framework were also evaluated using detailed non-linear FE analysis. The following conclusions can be drawn:

(1) The FE simulations of the folded-flange sections confirm that the proposed additions to the effective width based design method in EC3 to account for the multiple distortional buckling modes in the folded-flange section led to accurate predictions of the ultimate bending capacity.

(2) By applying the proposed optimisation framework to laterally braced beams, the bending capacity of a commercially available CFS beam was increased by 30% by only optimising the

## Chapter 12. Summary and conclusions, and recommendations for future work

relative dimensions of the flat plates and the inclination of the lips. The results also indicate that flanges with double fold lips had the potential to considerably increase the flexural capacity of CFS beams (by up to 50%), while using intermediate stiffeners in the web did not necessarily increase the capacity of the sections. As expected, plain CFS channel cross-sections provided the minimum flexural capacity, even when using intermediate web stiffeners.

(3) Folded-flange sections, which can be easily designed and manufactured due to their simple sequence of straight plate segments with a relatively small number of folds, were shown to be viable and even superior alternatives to typical lipped channel sections. For the same amount of material (i.e. the same total coil width and plate thickness), the folded-flange section possessed a flexural capacity which is 57% and 22% higher than the selected commercial section and the optimum lipped channel section, respectively.

### 12.1.4 Optimisation of CFS beams based on their post-buckling behaviour

A procedure was presented to obtain optimised channel sections for maximum plastic dissipated energy for seismic applications. The EC3 design restraints were considered to reduce the design space. Five different prototypes were considered, including a standard lipped channel section, a channel section with inclined lips, a channel section with intermediate stiffeners in the flanges, a channel section with intermediate stiffeners in both web and flanges, and finally a folded-flange cross-section. A PSO algorithm was developed and linked to the ABAQUS finite element programme for inelastic post-buckling analysis and optimisation. Optimal shapes were obtained for CFS beams using different prototypes. According to the results, the following conclusions can be drawn:

(1) Using intermediate web stiffeners could improve the post buckling behaviour of CFS sections, while their effects were negligible on flexural strength. The results indicate that, for the same amount of material, curved flange and folded flange sections provided the highest flexural strength compared to other alternatives.

(2) In general, using intermediate stiffeners in the flange could considerably (up to 36%) increase the ductility of the CFS beams. Additional intermediate stiffener in the web could increase the ductility of the section by around 70% compared to the standard one. For the same amount of material, curved flange and folded flange sections could provide more than two times more ductility compared to their standard counterparts.

(3) The amount of dissipated energy in CFS beam elements was increased with increasing the equivalent plastic strain limit  $\bar{\varepsilon}_p$ , especially for the lipped channel sections. However, increasing  $\bar{\varepsilon}_p$  beyond 0.15 did not considerably affect the energy dissipation capacity of the sections.



## Chapter 12. Summary and conclusions, and recommendations for future work

(4) Only by optimising the web, flanges and lip dimensions of a lipped channel section, the dissipated energy could be increased up to 23%. By relaxing the turned angle of lips, only a negligible gain of 0.4% was achieved.

(5) Placing a stiffer in the compressive flange of simple optimum lipped channel section could increase the energy dissipation capacity of the optimum solution by 30%. However, no obvious change was observed in the energy dissipation capacity of the optimum sections by placing an intermediate stiffener in the web. By optimising the shape of CFS beam sections, in general, the plastic area of the beams was significantly increased.

(6) The folded-flange section, for the same amount of material, dissipates 28%, 27%, 16% and 10% more energy than the optimal lipped channel section under plastic strain limits of 0.2, 0.15, 0.1 and 0.07, respectively. This emerged the folded flange sections as the best optimum solutions for seismic applications.

### **12.1.5 Experimental work on standard and optimised CFS columns**

A total of 36 channel column tests, including four different cross-section geometries and three different lengths, were carried out with the aim of investigating the interaction of local and overall flexural buckling. The specimens were tested under a concentrically applied load with pin ended boundary conditions. The specimen imperfections were measured and material tests of the flat and rounded corner regions of each cross-section type were carried out. The following conclusions can be drawn:

(1) The tests were successful in achieving interaction between local buckling and flexural buckling about the minor axis. Good agreement was obtained within each set of three identical tests, with the ultimate loads differing by less than 7% from the average.

(2) Additional overall bending of the specimens, resulting from a shift of the effective centroid, was observed after the appearance of a local buckling pattern. Bending thereby occurred towards the web in the plain channels and towards the flanges in the lipped channels, consistent with expectations.

(3) A comparison between the Eurocode 3 predictions and the experimental results indicates that Eurocode 3 is generally conservative in predicting the strength of pin-ended axially compressed channel columns. The predictions are especially conservative for plain channels, with an average ratio of the predicted to the measured capacity of 0.60.

### **12.1.6 Experimental work on standard and optimised CFS beams**

A total of six back-to-back beams, constructed from lipped channels with three different cross-sectional geometries, were tested, with the aim of investigating the interaction between local

## Chapter 12. Summary and conclusions, and recommendations for future work

and distortional buckling of standard and optimised sections. The specimens were tested in a four-point bending configuration with simply supported boundary conditions, while being laterally braced at the loading points. The geometric imperfections were recorded before and after the back-to-back specimens were assembled. Coupons extracted from the flat portions and the corner regions of each cross-section type were also tested in order to determine the material properties. Based on the tested and analytical results, the following conclusions can be drawn:

(1) All specimens failed due to interaction of local and distortional buckling, with local buckling being the primary buckling mode. In specimens C180, which displayed the widest flanges and the shallowest webs, local buckling originated in the top flanges, while in specimens A230 and B270, having a deeper cross-section and a smaller flange width, local buckling was triggered by the web.

(2) A good agreement in the ultimate capacities was generally obtained within each set of twin beams, with the difference being less than 2%. A comparison between the predictions given by Eurocode 3 and the experimental results indicated that Eurocode 3 is accurate in predicting the ultimate capacity of back-to-back lipped channel beams. The average ratio of the Eurocode predicted capacity to the experimental capacity was 0.996 with a standard deviation of 0.068.

### 12.1.7 Numerical study on optimised CFS columns

A finite element (FE) model was developed to study the interaction of local and global buckling in CFS standard and optimised lipped channel columns. The model took into account the non-linear stress–strain behaviour of CFS material, the strength hardening effects at the round corners due to the cold-working process, and the experimentally measured initial imperfections. The FE models were validated against an experimental program on a total number of 36 plain and lipped channel columns with the total lengths of  $L_e = 1.0m, 1.5m \text{ and } 2.0m$ . The validated models were then used to assess the accuracy of EC3 and DSM design methods for standard and optimum design solutions. Based on the results, the following conclusions can be drawn:

(1) The ultimate capacity of the sections predicted by the FE models was on average less than 1% different from the experimental results. The proposed FE model was also successful in capturing the failure shapes and predicting the compressive strength of CFS columns subjected to local and global buckling modes.

(2) It was shown that the geometric imperfections can change the FE predictions by around 20% and 40%, respectively, for lipped and plain channel columns, while the strength variation caused by the strain hardening effect at the round corners material in general has negligible effects (less than 3%).

## Chapter 12. Summary and conclusions, and recommendations for future work

(3) The ratio of predicted to experimentally measured axial strength was on average 0.945 and 0.804 for DSM and EC3 design methods, respectively. The results show that EC3 design method generally leads to conservative predictions, especially for plain channel column sections where the EC3 predictions were up to 46% lower than the experimental results.

(4) The axial capacity of the optimised CFS columns obtained from validated FE models and EC3 design methods were up to 35% and 43% higher, respectively, compared to their standard lipped channel counterparts with the same amount of material. This improvement was more evident for longer columns where global buckling was the dominant failure mode. This demonstrated the efficiency of the proposed optimisation method to improve the compressive capacity of CFS sections.

(5) The results of this study in general demonstrate the accuracy and reliability of the developed FE models to predict the axial load bearing capacity of CFS columns with different cross sectional shapes and effective lengths. These validated models should prove useful in practical applications for more efficient design of CFS structural elements.

### **12.1.8 Numerical study on optimised CFS beams**

A finite element (FE) model was developed to study the local/distortional buckling in CFS lipped back-to-back channel beams. The model took into account the non-linear stress-strain behaviour of CFS material, the strength hardening effects at the round corners due to the cold-working process, and the experimentally measured initial imperfections. The FE model was validated against an experimental program on a total number of 6 lipped channel back-to-back beams. The validated models were then used to assess the accuracy of EC3 and DSM design methods for standard and optimum design solutions. Based on the results, the following conclusions can be drawn:

(1) The ultimate capacity of the sections predicted by the FE models was on average less than 2% in variation from the experimental results. The proposed FE model was also successful in capturing the failure shapes and predicting the compressive strength of CFS columns subjected to local and global buckling modes.

(2) It was shown that, on average, the geometric imperfections could change the FE predictions by 6%, while the strength variation caused by the strain hardening effect at the round corners material in general had negligible effects (less than 2%).

(3) The ratio of predicted to experimentally measured flexural strength was on average 0.960 and 1.051 for DSM and EC3 design methods, respectively. The results show that DSM generally led to conservative predictions, while EC3 generally led to slightly unconservative predictions of the beam flexural strengths.

## Chapter 12. Summary and conclusions, and recommendations for future work

(4) The bending capacity of the optimised CFS beams obtained from validated FE models and EC3 design methods were up to 20% higher, compared to their standard lipped channel counterparts with the same amount of material. This demonstrated the efficiency of the proposed optimisation method to improve the compressive capacity of CFS sections.

(5) The results of this study in general demonstrate the accuracy and reliability of the developed FE models to predict the flexural strength of CFS beams with different cross sectional shapes. These validated models should prove useful in practical applications for more efficient design of CFS beam elements.

### 12.1.9 Behaviour of CFS bolted connections

The nonlinear behaviour of CFS bolted connections under cyclic loading has been investigated by conducting extensive parametric geometric and material nonlinear analysis using the validated finite element model in ABAQUS. A simplified model that can be used to model the slip-bearing behaviour of a single bolt was developed. Cross-sections of different beam shapes that were connected in the connections have been classified according to Eurocode concept and nonlinear FE analysis. The factors of cross-sectional shapes, thicknesses of the beams and the bolt distribution configurations were analysed numerically, on the connection performance. The modes of failure and cyclic moment-rotation responses were compared to show the effects on the moment capacity, ductility, energy dissipation and damping coefficient. Based on the results, the following conclusions could be drawn:

(1) The bolted-moment connections with class 1 and 2 beam sections could satisfy AISC requirements for Special Moment Resisting Frame (SMF), while according to the FEMA only class 1 cross-sections were considered as SMF. It is shown that most of the class 3 cross-sections and 4 were not sufficient to utilize as SMF.

(2) Using bent flange channels (folded and curved) as a beam in the connection could withstand maximum moment only 10% more than plain flange channels (flat and stiffened flat). Besides, the differences between two bent channels and the plain channels in terms of maximum flexural capacities were negligible. The bolts array in the web would result in the reduction of moment-capacity of the channel-sections which were connected to the connections.

(3) The connection ductility ratio was highly related to the cross-section classification, shape of the beam and the bolt distribution. Connections with folded flange section provided higher ductility ratio up to 55%, 45% and 30 % more than those with curved, flat and stiffened flat sections, respectively. In aspect of bolt configuration, it should be noted that the best configuration was related to cross-sectional classifications and shapes. For class 1 and 2 bent flange channels (folded and curved), diamond configuration had the largest ductility ratio while for class 3 and 4, circle configuration was considered as the best. For specimens with plain

## Chapter 12. Summary and conclusions, and recommendations for future work

flanges (flat and stiffened flat), circle configuration of the bolts provided higher ductility for all of the cross-section classifications. It is worth mentioning that the worst ductility ratio for all of the section shapes and classes belonged to the conventional square configuration of the bolts.

(4) Using the folded flange section as beam in the connections led up to 250%, 200% and 150% more energy dissipation capacity in connections compared to the flat, curved and stiffened flat sections, respectively. In general, diamond and circle distribution of the bolts could dissipate up to 250% energy for beam with class 1 cross-section. Conventional square distribution of the bolts had less capacity in terms of energy dissipation.

(5) For all the connections studied, a relative high equivalent viscous damping coefficient was presented, which means that the bolted moment connection studied here with gusset plate generally has a high energy damping capacity. There was significant improvement in the damping coefficient by using beams with larger thickness. However, cross-sectional shapes had a negligible effect on the damping coefficient.

(6) Using the same thickness as that of the connected beam might lead to premature local buckling at gusset plate of the connections. In addition, when local buckling happened at the beams, the effect of gusset plate thickness on the global behaviour of the connections was negligible.

(7) The effect of cross-sectional shapes was similar for connections with and without bolt slippage, also, using the folded flange section as a beam in the connections led to better energy dissipation capacity. However, the effect of bolt distribution was only obvious when class 1 beam cross-section is used for connections with slippage. In addition, the efficient configuration for connection with slippage was diamond bolt distribution while it was highly related to cross-sectional classifications and shapes. It is also shown that the connections with bolt slippage generally dissipated more energy than the ones without slippage.

(8) When the slippage of the bolts was not considered, the connections with class 3 and 4 beam cross-sections could not satisfy the SMF and the IMF requirements. However, including the slippage of the bolts in bolted-moment connection could significantly improve the ductility of CFS bolted moment connections.

(9) The proposed two node element, which was defined in a UEL subroutine could take into account the slippage, bearing deformation and the bolt hole elongation. By using the proposed element, good agreement has been achieved to model the moment-rotation response of the full-scale tested connections.

## 12.2 Recommendations for future work

Based on the research results of current thesis, the following topics can be studied in the future research:

- (1) Experimental study should be conducted in order to investigate the CFS folded flange cross-section to understand their performance and validate the design equations proposed in this thesis.
- (2) Based on the proposed framework for elements optimisation, a procedure to optimise full-scale framing system should be developed in the future to take into account both ultimate limit state and serviceability limit state.
- (3) CFS elements can be optimised based on other objectives such as maximum ductility, minimum weight design by integrating detailed nonlinear FE models in Python of ABAQUS and optimisation algorithms.
- (4) Apart from the numerical study on CFS beam-to-column connections in this thesis, testing beam-column assemblies in different configurations with different CFS beam and column sections should be performed to investigate the deformation capacity and performance.
- (5) Single lap bolted connections should be tested with the specified bolt torque to verify the connection slip-bearing action behaviour to improve the accuracy of the connection design and FE analyses. FE models of single lap connections verified by test results can be performed for parametric study on the connection behaviour with different pretension forces, bolt sizes and frictional behaviour.
- (7) Developing analytical models for slip-bearing behaviour of the full-scale connections based on the concept of instantaneous centre of rotation for both monotonic and cyclic loading.
- (8) It has been found that the bolt distribution pattern has significant effect on the strength and ductility of CFS connections, the calibrated FE models on connections can be combined with Python in ABAQUS and optimisation algorithm to maximise the strength, energy dissipation or ductility.
- (9) A direct strength design curve for CFS bolted connection has been proposed in the case of bending, equations on the shear and combined shear and bending design can be proposed.
- (10) A program to generate imperfections in CFS elements has been developed, new seismic resistant structural systems such as braced frames and dual frames can be proposed and detailed nonlinear FE models taking into account of imperfections and material nonlinearity can be used to analyse the behaviour of such structural systems.

## Chapter 12. Summary and conclusions, and recommendations for future work

(11) Currently there is no generic optimisation framework for optimum design of load-bearing CFS systems at the structural level taking into account the post-buckling behaviour of CFS elements and connections. Due to high computational effort, most existing optimisation techniques are not suitable for optimising complex CFS structural systems with a large number of non-linear structural elements and connections, therefore, a performance-based optimisation framework (structural level) that can simplify the optimum design of complex CFS structures for multiple performance levels, should be developed in the future.

This page is intentionally left in blank



## **REFERENCES**

---

## References

- ABAQUS (2007). HiSbitt, Karlsson & Sorensen, Inc, Pawtucket, USA.
- Ádány, S. (2016). "Shell element for constrained finite element analysis of thin-walled structural members." *Thin-Walled Structures*, 105, 135-146.
- Ádány, S., and Schafer, B. (2006). "Buckling mode decomposition of single-branched open cross-section members via finite strip method: derivation." *Thin-Walled Structures*, 44(5), 563-584.
- Ádány, S., and Schafer, B. W. (2014). "Generalized constrained finite strip method for thin-walled members with arbitrary cross-section: secondary modes, orthogonality, examples." *Thin-Walled Structures*, 84, 123-133.
- Adany, S., and Schafer, B. W. (2006a). "Buckling mode decomposition of single-branched open cross-section members via finite strip method: Application and examples." *Thin-Walled Structures*, 44(5), 585-600.
- Adany, S., and Schafer, B. W. (2006b). "Buckling mode decomposition of single-branched open cross-section members via finite strip method: Derivation." *Thin-Walled Structures*, 44(5), 563-584.
- Adeli, H., and Karim, A. (1997). "Neural network model for optimization of cold-formed steel beams." *Journal of Structural Engineering-ASCE*, 123(11), 1535-1543.
- AISC 341-05 (2005). "Seismic provisions for structural steel buildings", Chicago (IL): American Institute of Steel Construction.
- AISI (2007). "North American specification for the design of cold-formed steel structural members, 2007 Edition." *AISI S100-07*, Washington, DC.
- Ajeesh, S., and Jayachandran, S. A. (2016). "Simplified semi-analytical model for elastic distortional buckling prediction of cold-formed steel flexural members." *Thin-Walled Structures*, 106, 420-427.
- Amouzegar, H., Schafer, B., and Tootkaboni, M. (2016). "An incremental numerical method for calculation of residual stresses and strains in cold-formed steel members." *Thin-Walled Structures*, 106, 61-74.
- Anapayan, T., Mahendran, M., and Mahaarachchi, D. (2011). "Lateral distortional buckling tests of a new hollow flange channel beam." *Thin-Walled Structures*, 49(1), 13-25.
- Anbarasu, M. (2016). "Local-distortional buckling interaction on cold-formed steel lipped channel beams." *Thin-Walled Structures*, 98, 351-359.
- AS/NZS (1996). "Cold-formed steel structures." Sydney: AS/NZS 4600, Joint Technical Committee BD-082.
- ASTM E2126 (2009). "Standard test methods for cyclic (reversed) load test for shear resistance of vertical elements of the lateral force resisting systems for buildings ". *West Conshohocken, PA: American Society for Testing and Materials*.
- RCSC Committee. (2004). "Specification for structural joints using ASTM A325 or A490 Bolts " *American Institute of Steel Construction. Chicago, Illinois*.
- Avery, P., Mahendran, M., and Nasir, A. (2000). "Flexural capacity of hollow flange beams." *Journal of Constructional Steel Research*, 53(2), 201-223.

## References

- Bagheri Sabbagh, A. (2011). "Cold-formed steel elements for earthquake resistant moment frame buildings." PhD thesis, University of Sheffield.
- Baldassino, N., and Bernuzzi, C. (2000). "Analysis and behaviour of steel storage pallet racks." *Thin-Walled Structures*, 37(4), 277-304.
- Batista, E. D. (2009). "Local-global buckling interaction procedures for the design of cold-formed columns: Effective width and direct method integrated approach." *Thin-Walled Structures*, 47(11), 1218-1231.
- Becque, J. (2008). "The interaction of local and overall buckling of cold-formed stainless steel columns."
- Becque, J. "A new approach to modal decomposition of buckled shapes." *Proc., Structures*, Elsevier, 2-12.
- Becque, J., and Rasmussen, K. J. (2009a). "Experimental investigation of local-overall interaction buckling of stainless steel lipped channel columns." *Journal of Constructional Steel Research*, 65(8), 1677-1684.
- Becque, J., and Rasmussen, K. J. (2009b). "Numerical investigation of the interaction of local and overall buckling of stainless steel I-columns." *Journal of Structural Engineering*, 135(11), 1349-1356.
- Beghi, A., Cecchinato, L., Cosi, G., and Rampazzo, M. (2012). "A PSO-based algorithm for optimal multiple chiller systems operation." *Applied Thermal Engineering*, 32(0), 31-40.
- Bernuzzi, C. (2015). "European and United States approaches for steel storage pallet rack design Part 1: Discussions and general comparisons." *Thin-Walled Structures*, 97, 308-320.
- Bernuzzi, C., and Castiglioni, C. A. (2001). "Experimental analysis on the cyclic behaviour of beam-to-column joints in steel storage pallet racks." *Thin-Walled Structures*, 39(10), 841-859.
- Bernuzzi, C., and Maxenti, F. (2015). "European alternatives to design perforated thin-walled cold-formed beam-columns for steel storage systems." *Journal of Constructional Steel Research*, 110, 121-136.
- Bernuzzi, C., and Simoncelli, M. (2015). "European design approaches for isolated cold-formed thin-walled beam-columns with mono-symmetric cross-section." *Engineering Structures*, 86, 225-241.
- Bickford, J. H. (1997). "An introduction to the design and analysis of bolted joints." Marcel Dekker, New York.
- Bolandim, E. A., Beck, A. T., and Malite, M. (2013). "Bolted Connections in Cold-Formed Steel: Reliability Analysis for Rupture in Net Section." *Journal of Structural Engineering-ASCE*, 139(5), 748-756.
- Bolong, Z. (1989). "Seismic test of structure." *Beijing : Earthquake Express [in chinese]*.
- Bryan, E. R. (1993). "The Design of Bolted Joints in Cold-Formed Steel Sections." *Thin-Walled Structures*, 16(1-4), 239-262.
- Bučmys, Ž., and Daniūnas, A. (2015). "Analytical and experimental investigation of cold-formed steel beam-to-column bolted gusset-plate joints." *Journal of Civil Engineering and Management*, 21(8), 1061-1069.

## References

- Bučmys, Ž., and Šaučiuvėnas, G. (2013). "The behavior of cold formed steel structure connections." *Engineering Structures and Technologies*, 5(3), 113-122.
- Calderoni, B., De Martino, A., Formisano, A., and Fiorino, L. (2009). "Cold formed steel beams under monotonic and cyclic loading: Experimental investigation." *Journal of Constructional Steel Research*, 65(1), 219-227.
- Camotim, D., and Basaglia, C. (2013). "Buckling analysis of thin-walled steel structures using generalized beam theory (GBT): state-of-the-art report." *Steel Construction*, 6(2), 117-131.
- Cava, D., Camotim, D., Dinis, P., and Madeo, A. (2016). "Numerical investigation and direct strength design of cold-formed steel lipped channel columns experiencing local–distortional–global interaction." *Thin-Walled Structures*, 105, 231-247.
- CEN (2005a). "Eurocode 3: Design of Steel Structures, part 1-5: Plated structural elements." Brussels: European Committee for Standardization.
- CEN (2005b). "Eurocode 3: design of steel structures, part 1.3: general rules—supplementary rules for cold formed members and sheeting." Brussels: European Committee for Standardization.
- CEN (2005c). "Eurocode 3: Design of Steel Structures. part 1-1: General Rules and Rules for Buildings." Brussels: European Committee for Standardization.
- CEN (2006). "Eurocode 3: Design of steel structures. part 1–12: additional rules for the extension of EN 1993 up to steel grades S700." European Committee for Standardization.
- CEN (2005d). "Eurocode 3: Design of steel structures—Part 1-8: Design of joints." Brussels: European Committee for Standardization.
- CEN. (2005). "Eurocode 8: Design of structures for earthquake resistance-Part 1: General rules, seismic actions and rules for buildings." Brussels: European Committee for Standardization.
- Chen, J., He, Y., and Jin, W.-L. (2010). "Stub column tests of thin-walled complex section with intermediate stiffeners." *Thin-Walled Structures*, 48(6), 423-429.
- Chen, Y., Chen, X., and Wang, C. (2015). "Experimental and finite element analysis research on cold-formed steel lipped channel beams under web crippling." *Thin-Walled Structures*, 87, 41-52.
- Chung, K. F., and Ip, K. H. (2001). "Finite element investigation on the structural behaviour of cold-formed steel bolted connections." *Engineering Structures*, 23(9), 1115-1125.
- Chung, K. F., and Ip, K. H. (2000). "Finite element modeling of bolted connections between cold-formed steel strips and hot rolled steel plates under static shear loading." *Engineering Structures*, 22(10), 1271-1284.
- Croccolo, D., De Agostinis, M., and Vincenzi, N. (2011). "Failure analysis of bolted joints: Effect of friction coefficients in torque–preloading relationship." *Engineering Failure Analysis*, 18(1), 364-373.
- Dao, T. N., and van de Lindt, J. W. (2014). "Numerical Seismic Performance of an Innovative CFS Midrise Building Designed Using DDD." *Journal of Performance of Constructed Facilities*, 28(5).
- Dao, T. N., and van de Lindt, J. W. (2013). "Seismic Performance of an Innovative Light-Frame Cold-Formed Steel Frame for Midrise Construction." *Journal of Structural Engineering-Asce*, 139(5), 837-848.

## References

- Davies, J. M. (2000). "Recent research advances in cold-formed steel structures." *Journal of Constructional Steel Research*, 55(1-3), 267-288.
- Degtyareva, N. V., and Degtyarev, V. V. (2016). "Experimental investigation of cold-formed steel channels with slotted webs in shear." *Thin-Walled Structures*, 102, 30-42.
- Deng, K. L., Pan, P., Su, Y. K., and Xue, Y. T. (2015). "Shape optimization of U-shaped damper for improving its bi-directional performance under cyclic loading." *Engineering Structures*, 93, 27-35.
- Ding, C. (2015). "Monotonic and Cyclic Simulation of Screw-Fastened Connections for Cold-Formed Steel Framing." Virginia Tech.
- Dinis, P. B., Batista, E. M., Camotim, D., and dos Santos, E. S. (2012). "Local-distortional-global interaction in lipped channel columns: Experimental results, numerical simulations and design considerations." *Thin-Walled Structures*, 61, 2-13.
- Dinis, P. B., and Camotim, D. (2015). "Cold-formed steel columns undergoing local-distortional coupling: Behaviour and direct strength prediction against interactive failure." *Computers & Structures*, 147, 181-208.
- Dubina, D., Landolfo, R., Ungureanu, V., and ECCS. (2012). *Design of Cold-formed Steel Structures: Eurocode 3 : Design of Steel Structures. Design of cold-formed steel structures. Part 1-3*, ECCS.
- Dubina, D., and Ungureanu, V. (2014). "Instability mode interaction: From Van Der Neut model to ECBL approach." *Thin-Walled Structures*, 81, 39-49.
- Dubina, D., Ungureanu, V., and Gîlia, L. (2013). "Cold-formed steel beams with corrugated web and discrete web-to-flange fasteners." *Steel Construction*, 6(2), 74-81.
- Dubina, D., Ungureanu, V., and Gîlia, L. (2015). "Experimental investigations of cold-formed steel beams of corrugated web and built-up section for flanges." *Thin-Walled Structures*, 90, 159-170.
- Dundu, M. (2011). "Design approach of cold-formed steel portal frames." *International Journal of Steel Structures*, 11(3), 259-273.
- Elkersh, I. (2010). "Experimental investigation of bolted cold formed steel frame apex connections under pure moment." *Ain Shams Engineering Journal*, 1(1), 11-20.
- FEMA-356, 2000, Prestandard and Commentary for the Seismic Rehabilitation of Buildings, American Society of Civil Engineers, Federal Emergency Management Agency, Washington, D.C
- Fiorino, L., Della Corte, G., and Landolfo, R. (2007). "Experimental tests on typical screw connections for cold-formed steel housing." *Engineering Structures*, 29(8), 1761-1773.
- Fiorino, L., Iuorio, O., and Landolfo, R. (2014). "Designing CFS structures: The new school bfs in naples." *Thin-Walled Structures*, 78, 37-47.
- Fisher, J. W. (1964). "On the Behavior of Fasteners and Plates with Holes." Fritz Engineering Laboratory, Department of Civil Engineering, Lehigh University.
- Foliente, G. C. "Issues in seismic performance testing and evaluation of timber structural systems." *Proc., Proceedings of the international wood engineering conference*, 29-36.

## References

- Fulop, L. A., and Dubina, D. (2004). "Performance of wall-stud cold-formed shear panels under monotonic and cyclic loading Part I: Experimental research." *Thin-Walled Structures*, 42(2), 321-338.
- Galambos, T. V. (1998). *Guide to stability design criteria for metal structures*, John Wiley & Sons.
- Gardner, L., and Ashraf, M. (2006). "Structural design for non-linear metallic materials." *Engineering Structures*, 28(6), 926-934.
- Gilbert, B. P., and Rasmussen, K. J. R. (2010). "Bolted moment connections in drive-in and drive-through steel storage racks." *Journal of Constructional Steel Research*, 66(6), 755-766.
- Gilbert, B. P., Savoyat, T. J. M., and Teh, L. H. (2012). "Self-shape optimisation application: Optimisation of cold-formed steel columns." *Thin-Walled Structures*, 60, 173-184.
- Goncalves, R., Ritto-Correa, M., and Camotim, D. (2010). "A new approach to the calculation of cross-section deformation modes in the framework of generalized beam theory." *Computational Mechanics*, 46(5), 759-781.
- Ansys.14.5 "Theory Guide." Canonsburg, PA, USA: ANSYS Inc (2012).
- Gutierrez, R., Loureiro, A., Lopez, M., and Moreno, A. (2011). "Analysis of cold-formed purlins with slotted sleeve connections." *Thin-Walled Structures*, 49(7), 833-841.
- Gutierrez, R., Loureiro, A., Reinosa, J. M., and Lopez, M. (2015). "Numerical study of purlin joints with sleeve connections." *Thin-Walled Structures*, 94, 214-224.
- Hadley Industries plc, P. O. B., Downing Street, Smethwick, West Midlands, B66 2PA, UK "http://www.hadleygroup.co.uk/ URL." <http://www.hadleygroup.co.uk/ URL>.
- Haidarali, M. R., and Nethercot, D. A. (2011). "Finite element modelling of cold-formed steel beams under local buckling or combined local/distortional buckling." *Thin-Walled Structures*, 49(12), 1554-1562.
- Hanaor, A. (2000). "Tests of composite beams with cold-formed sections." *Journal of Constructional Steel Research*, 54(2), 245-264.
- Hancock, G. J., and Pham, C. H. (2015). "Buckling analysis of thin-walled sections under localised loading using the semi-analytical finite strip method." *Thin-Walled Structures*, 86, 35-46.
- Hancock, G. J., and Pham, C. H. (2013). "Shear buckling of channel sections with simply supported ends using the Semi-Analytical Finite Strip Method." *Thin-Walled Structures*, 71, 72-80.
- Hassan, R., Cohanin, B., De Weck, O., and Venter, G. "A comparison of particle swarm optimization and the genetic algorithm." *Proc., Proceedings of the 1st AIAA multidisciplinary design optimization specialist conference*, 18-21.
- He, Z. Q., and Zhou, X. H. (2014). "Strength design curves and an effective width formula for cold-formed steel columns with distortional buckling." *Thin-Walled Structures*, 79, 62-70.
- Ho, H. C., and Chung, K. F. (2006). "Analytical prediction on deformation characteristics of lapped connections between cold-formed steel Z sections." *Thin-Walled Structures*, 44(1), 115-130.

## References

- Hsu, H.-L., and Chi, P.-S. (2003). "Flexural performance of symmetrical cold-formed thin-walled members under monotonic and cyclic loading." *Thin-Walled Structures*, 41(1), 47-67.
- Huang, Y. N., and Young, B. (2014). "The art of coupon tests." *Journal of Constructional Steel Research*, 96, 159-175.
- Hui, C., Gardner, L., and Nethercot, D. A. (2016). "Moment redistribution in cold-formed steel continuous beams." *Thin-Walled Structures*, 98, 465-477.
- ISO, E. (2009). "6892-1 Metallic materials Tensile testing Part 1: Method of test at room temperature." *CEN Brussels*.
- J. Ye, I. Hajirasouliha, J. Becque, and Eslami, A. (2015). "Optimum design of cold-formed steel beams using Particle Swarm Optimisation Method." *Journal of Constructional Steel Research*.
- Jandera, M., Gardner, L., and Machacek, J. (2008). "Residual stresses in cold-rolled stainless steel hollow sections." *Journal of Constructional Steel Research*, 64(11), 1255-1263.
- Jeong, S., Hasegawa, S., Shimoyama, K., and Obayashi, S. (2009). "Development and investigation of efficient GA/PSO-hybrid algorithm applicable to real-world design optimization." *Computational Intelligence Magazine, IEEE*, 4(3), 36-44.
- JGJ101-96 (1997 [in Chinese]). "Specification for test methods of seismic buildings." Peking: China Architecture Industrial Press.
- Johnston, R. P., Lim, J. B., Lau, H. H., Xu, Y., Sonebi, M., Armstrong, C. G., and Mei, C. C. (2015a). "Finite-element investigation of cold-formed steel portal frames in fire." *Proceedings of the Institution of Civil Engineers-Structures and Buildings*, 169(1), 3-19.
- Johnston, R. P., Sonebi, M., Lim, J. B., Armstrong, C. G., Wrzesien, A. M., Abdelal, G., and Hu, Y. (2015b). "The collapse behaviour of cold-formed steel portal frames at elevated temperatures." *Journal of Structural Fire Engineering*, 6(2), 77-102.
- Jones, R. M. (2006). *Buckling of bars, plates, and shells*, Bull Ridge Corporation.
- Juvinall, R. C., and Marshek, K. M. (2006). *Fundamentals of machine component design*, John Wiley & Sons New York.
- Kankanamge, N. D., and Mahendran, M. (2012). "Behaviour and design of cold-formed steel beams subject to lateral-torsional buckling." *Thin-Walled Structures*, 51, 25-38.
- Kim, T., Yoo, J., and Roeder, C. W. (2015). "Experimental investigation on strength and curling influence of bolted connections in thin-walled carbon steel." *Thin-Walled Structures*, 91, 1-12.
- Kim, T. S., Kuwamura, H., and Cho, T. J. (2008). "A parametric study on ultimate strength of single shear bolted connections with curling." *Thin-Walled Structures*, 46(1), 38-53.
- Kumar, J. V., and Jayachandran, S. A. (2016). "Experimental investigation and evaluation of Direct Strength Method on beam-column behavior of uprights." *Thin-Walled Structures*, 102, 165-179.
- Kumar, M. V. A., and Kalyanaraman, V. (2014). "Distortional Buckling of CFS Stiffened Lipped Channel Compression Members." *Journal of Structural Engineering*, 140(12).
- Kumar, N., and Sahoo, D. R. (2016). "Optimization of lip length and aspect ratio of thin channel sections under minor axes bending." *Thin-Walled Structures*, 100, 158-169.

## References

- Kwon, Y. B., Kim, B. S., and Hancock, G. J. (2009). "Compression tests of high strength cold-formed steel channels with buckling interaction." *Journal of Constructional Steel Research*, 65(2), 278-289.
- Kyvelou, P., Gardner, L., and Nethercot, D. A. (2015). "Composite Action Between Cold-Formed Steel Beams and Wood-Based Floorboards." *International Journal of Structural Stability and Dynamics*, 15(8).
- La ím, L., Rodrigues, J. P. C., and da Silva, L. S. (2013). "Experimental and numerical analysis on the structural behaviour of cold-formed steel beams." *Thin-Walled Structures*, 72, 1-13.
- Landesmann, A., and Camotim, D. (2013). "On the Direct Strength Method (DSM) design of cold-formed steel columns against distortional failure." *Thin-Walled Structures*, 67, 168-187.
- Landesmann, A., Camotim, D., and Garcia, R. (2016). "On the strength and DSM design of cold-formed steel web/flange-stiffened lipped channel columns buckling and failing in distortional modes." *Thin-Walled Structures*, 105, 248-265.
- Lawan, M., Tahir, M., Ngian, S., and Sulaiman, A. (2015). "Structural Performance of Cold-Formed Steel Section in Composite Structures: A Review." *Jurnal Teknologi*, 74(4).
- Lawson, R., Ogden, R., Pedreschi, R., Grubb, P., and Popo-Ola, S. (2005). "Developments in pre-fabricated systems in light steel and modular construction." *Structural Engineer*, 83(6), 28-35.
- Lee, J., Kim, S.-M., Park, H.-S., and Woo, B.-H. (2005a). "Optimum design of cold-formed steel channel beams using micro Genetic Algorithm." *Engineering Structures*, 27(1), 17-24.
- Lee, J., Kim, S.-M., and Seon Park, H. (2006a). "Optimum design of cold-formed steel columns by using micro genetic algorithms." *Thin-Walled Structures*, 44(9), 952-960.
- Lee, J., Kim, S. M., Park, H. S., and Woo, Y. H. (2005b). "Optimum design of cold-formed steel channel beams using micro Genetic Algorithm." *Engineering Structures*, 27(1), 17-24.
- Lee, J. H., Kim, S. M., and Park, H. S. (2006b). "Optimum design of cold-formed steel columns by using micro genetic algorithms." *Thin-Walled Structures*, 44(9), 952-960.
- Leng, J., Li, Z., Guest, J. K., and Schafer, B. W. (2014). "Shape optimization of cold-formed steel columns with fabrication and geometric end-use constraints." *Thin-Walled Structures*, 85(0), 271-290.
- Leng, J. Z., Guest, J. K., and Schafer, B. W. (2011). "Shape optimization of cold-formed steel columns." *Thin-Walled Structures*, 49(12), 1492-1503.
- Lennon, R., Pedreschi, R., and Sinha, B. P. (1999). "Comparative study of some mechanical connections in cold formed steel." *Construction and Building Materials*, 13(3), 109-116.
- Li, X., and Becque, J. "Modal decomposition of instabilities in thin-walled structural elements." *Proc., The Annual Postgraduate research Student Conference-2016*.
- Li, Y. S., Shan, W., Shen, H. Y., Zhang, Z. W., and Liu, J. Z. (2015). "Bending resistance of I-section bamboo-steel composite beams utilizing adhesive bonding." *Thin-Walled Structures*, 89, 17-24.
- Li, Y. S., Shen, H. Y., Shan, W., and Han, T. S. (2012). "Flexural behavior of lightweight bamboo-steel composite slabs." *Thin-Walled Structures*, 53, 83-90.



## References

- Li, Z., and Schafer, B. W. (2010a). "Buckling analysis of cold-formed steel members with general boundary conditions using CUFSM conventional and constrained finite strip methods."
- Li, Z., and Schafer, B. W. "Buckling analysis of cold-formed steel members with general boundary conditions using CUFSM: conventional and constrained finite strip methods." *Proc., Proceedings of the 20th Int.*
- Li, Z. J., Abreu, J. C. B., Leng, J. Z., Adany, S., and Schafer, B. W. (2014). "Review: Constrained finite strip method developments and applications in cold-formed steel design." *Thin-Walled Structures*, 81, 2-18.
- Lim, J. B., Hancock, G. J., Clifton, G. C., Pham, C. H., and Das, R. (2016). "DSM for ultimate strength of bolted moment-connections between cold-formed steel channel members." *Journal of Constructional Steel Research*, 117, 196-203.
- Lim, J. B. P., and Nethercot, D. A. (2004a). "Finite element idealization of a cold-formed steel portal frame." *Journal of Structural Engineering*, 130(1), 78-94.
- Lim, J. B. P., and Nethercot, D. A. (2004b). "Stiffness prediction for bolted moment-connections between cold-formed steel members." *Journal of Constructional Steel Research*, 60(1), 85-107.
- Lim, J. B. P., and Nethercot, D. A. (2003). "Ultimate strength of bolted moment-connections between cold-formed steel members." *Thin-Walled Structures*, 41(11), 1019-1039.
- Lin, S. H., Pan, C. L., and Hsu, W. T. (2014). "Monotonic and cyclic loading tests for cold-formed steel wall frames sheathed with calcium silicate board." *Thin-Walled Structures*, 74, 49-58.
- Liu, H., Igusa, T., and Schafer, B. W. (2004). "Knowledge-based global optimization of cold-formed steel columns." *Thin-Walled Structures*, 42(6), 785-801.
- Liu, J., Xu, L., and Fox, S. (2015a). "Lapped cold-formed steel Z-shaped purlin connections with vertical slotted holes." *Journal of Constructional Steel Research*, 107, 150-161.
- Liu, Q., Yang, J., and Wang, F. L. (2015b). "Numerical simulation of sleeve connections for cold formed steel sigma sections." *Engineering Structures*, 100, 686-695.
- Ma, W., Becque, J., Hajirasouliha, I., and Ye, J. (2015). "Cross-sectional optimisation of cold-formed steel channels to Eurocode 3." *Engineering Structures*, 101, 641-651.
- Madeira, J., Dias, J., and Silvestre, N. (2015). "Multiobjective optimisation of cold-formed steel columns." *Thin-Walled Structures*, 96, 29-38.
- Magnucka-Blandzi, E. (2011). "Effective shaping of cold-formed thin-walled channel beams with double-box flanges in pure bending." *Thin-Walled Structures*, 49(1), 121-128.
- Magnucka-Blandzi, E., and Magnucki, K. (2011). "Buckling and optimal design of cold-formed thin-walled beams: Review of selected problems." *Thin-Walled Structures*, 49(5), 554-561.
- Magnucki, K., Maćkiewicz, M., and Lewiński, J. (2006a). "Optimal design of a mono-symmetrical open cross section of a cold-formed beam with sinusoidally corrugated flanges." *Thin-Walled Structures*, 44(5), 554-562.
- Magnucki, K., and Paczos, P. (2009). "Theoretical shape optimisation of cold-formed thin-walled channel beams with drop flanges in pure bending." *Journal of Constructional Steel Research*, 65(8-9), 1731-1737.

## References

- Magnucki, K., Paczos, P., and Kasprzak, J. (2010). "Elastic buckling of cold-formed thin-walled channel beams with drop flanges." *Journal of Structural Engineering*, 136(7), 886-896.
- Magnucki, K., Rodak, M., and Lewiński, J. (2006b). "Optimisation of mono- and anti-symmetrical I-sections of cold-formed thin-walled beams." *Thin-Walled Structures*, 44(8), 832-836.
- Mahendran, M., and Keerthan, P. (2013). "Experimental studies of the shear behavior and strength of LiteSteel beams with stiffened web openings." *Engineering Structures*, 49, 840-854.
- Manikandan, P., and Arun, N. (2016). "Numerical Investigation on Cold-Formed Steel Lipped Channel Columns with Intermediate Web Stiffeners." *Journal of The Institution of Engineers (India): Series A*, 97(1), 1-7.
- Manikandan, P., Sukumar, S., and Balaji, T. (2014). "Effective Shaping of Cold-Formed Thin-Walled Built-up Beams in Pure Bending." *Arabian Journal for Science and Engineering*, 39(8), 6043-6054.
- Markazi, F. D., Beale, R. G., and Godley, M. H. R. (1997). "Experimental analysis of semi-rigid boltless connectors." *Thin-Walled Structures*, 28(1), 57-87.
- Martins, A. D., Dinis, P. B., and Camotim, D. (2016). "On the influence of local-distortional interaction in the behaviour and design of cold-formed steel web-stiffened lipped channel columns." *Thin-Walled Structures*, 101, 181-204.
- Mathieson, C., Clifton, G. C., and Lim, J. B. P. (2016). "Novel pin-jointed connection for cold-formed steel trusses." *Journal of Constructional Steel Research*, 116, 173-182.
- Mathworks (2011). "Matlab R2011a." Mathworks, Inc.
- Miller, T. H., and Pekoz, T. (1994). "Behavior of Gypsum-Sheathed Cold-Formed Steel Wall Studs." *Journal of Structural Engineering-ASCE*, 120(5), 1644-1650.
- Moharrami, M., Louhghalam, A., and Tootkaboni, M. (2014). "Optimal folding of cold formed steel cross sections under compression." *Thin-Walled Structures*, 76, 145-156.
- Mohebbi, S., Mirghaderi, R., Farahbod, F., and Sabbagh, A. B. (2015). "Experimental work on single and double-sided steel sheathed cold-formed steel shear walls for seismic actions." *Thin-Walled Structures*, 91, 50-62.
- Mohebbi, S., Mirghaderi, S. R., Farahbod, F., Sabbagh, A. B., and Torabian, S. (2016). "Experiments on seismic behaviour of steel sheathed cold-formed steel shear walls clad by gypsum and fiber cement boards." *Thin-Walled Structures*, 104, 238-247.
- Mohebkhah, A., and Azandariani, M. G. (2015). "Lateral-torsional buckling of Delta hollow flange beams under moment gradient." *Thin-Walled Structures*, 86, 167-173.
- Naderian, H. R., and Ronagh, H. R. (2015). "Buckling analysis of thin-walled cold-formed steel structural members using complex finite strip method." *Thin-Walled Structures*, 90, 74-83.
- Nakata, N., Schafer, B., and Madsen, R. "Seismic design of multi-story cold-formed steel buildings: the CFS-NEES archetype building." *Proc., Structures Congress 2012*, ASCE, 1507-1517.
- Nandini, P., and Kalyanaraman, V. (2010). "Strength of cold-formed lipped channel beams under interaction of local, distortional and lateral torsional buckling." *Thin-Walled Structures*, 48(10-11), 872-877.

## References

- Narayanan, S., and Mahendran, M. (2003). "Ultimate capacity of innovative cold-formed steel columns." *Journal of Constructional Steel Research*, 59(4), 489-508.
- Nedelcu, M. (2014). "Buckling mode identification of perforated thin-walled members by using GBT and shell FEA." *Thin-Walled Structures*, 82, 67-81.
- Nedelcu, M. (2012). "GBT-based buckling mode decomposition from finite element analysis of thin-walled members." *Thin-Walled Structures*, 54, 156-163.
- Nithyadharan, M., and Kalyanaraman, V. (2012). "Behaviour of cold-formed steel shear wall panels under monotonic and reversed cyclic loading." *Thin-Walled Structures*, 60, 12-23.
- Ohsaki, M., and Nakajima, T. (2012). "Optimisation of link member of eccentrically braced frames for maximum energy dissipation." *Journal of Constructional Steel Research*, 75, 38-44.
- Öztürk, F., and Pul, S. (2015). "Experimental and numerical study on a full scale apex connection of cold-formed steel portal frames." *Thin-Walled Structures*, 94, 79-88.
- Padilla-Llano, D. A., Eatherton, M. R., and Moen, C. D. (2016). "Cyclic flexural response and energy dissipation of cold-formed steel framing members." *Thin-Walled Structures*, 98, 518-532.
- Padilla-Llano, D. A., Moen, C. D., and Eatherton, M. R. (2014). "Cyclic axial response and energy dissipation of cold-formed steel framing members." *Thin-Walled Structures*, 78, 95-107.
- Pan, C. L., and Shan, M. Y. (2011). "Monotonic shear tests of cold-formed steel wall frames with sheathing." *Thin-Walled Structures*, 49(2), 363-370.
- Pan, P., Ohsaki, M., and Tagawa, H. (2007). "Shape optimisation of H-beam flange for maximum plastic energy dissipation." *Journal of Structural Engineering-ASCE*, 133(8), 1176-1179.
- Park, R. (1989). "Evaluation of ductility of structures and structural assemblages from laboratory testing." *Bull NZ Natl Soc Earthq Eng*, 22, 155-166.
- Peterman, K. D., Nakata, N., and Schafer, B. W. (2014). "Hysteretic characterization of cold-formed steel stud-to-sheathing connections." *Journal of Constructional Steel Research*, 101, 254-264.
- Pham, C. H., Bruneau, L. A., and Hancock, G. J. (2015). "Experimental Study of Longitudinally Stiffened Web Channels Subjected to Combined Bending and Shear." *Journal of Structural Engineering-ASCE*, 141(11).
- Pham, C. H., Davis, A. F., and Emmett, B. R. (2014a). "Numerical investigation of cold-formed lapped Z purlins under combined bending and shear." *Journal of Constructional Steel Research*, 95, 116-125.
- Pham, C. H., and Hancock, G. J. (2013). "Experimental Investigation and Direct Strength Design of High-Strength, Complex C-Sections in Pure Bending." *Journal of Structural Engineering*, 139(11), 1842-1852.
- Pham, S. H., Pham, C. H., and Hancock, G. J. (2014b). "Direct strength method of design for shear including sections with longitudinal web stiffeners." *Thin-Walled Structures*, 81, 19-28.
- Phan, D., Lim, J., Ming, C., Tanyimboh, T., Issa, H., and Sha, W. (2011). "Optimisation of cold-formed steel portal frame topography using real-coded genetic algorithm." *Procedia Engineering*, 14, 724-733.

## References

- Phan, D. T., Lim, J. B. P., Sha, W., Siew, C. Y. M., Tanyimboh, T. T., Issa, H. K., and Mohammad, F. A. (2012). "Design optimisation of cold-formed steel portal frames taking into account the effect of building topology." *Engineering Optimization*, 45(4), 415-433.
- Phan, D. T., Lim, J. B. P., Tanyimboh, T. T., Wrzesien, A. M., Sha, W., and Lawson, R. M. (2015). "Optimal design of cold-formed steel portal frames for stressed-skin action using genetic algorithm." *Engineering Structures*, 93, 36-49.
- Piyawat, K., Ramseyer, C., and Kang, T. H.-K. (2012). "Development of an axial load capacity equation for doubly symmetric built-up cold-formed sections." *Journal of Structural Engineering-ASCE*, 139(12), 04013008.
- Put, B. M., Pi, Y. L., and Trahair, N. S. (1999). "Lateral buckling tests on cold-formed channel beams." *Journal of Structural Engineering-ASCE*, 125(5), 532-539.
- Quach, W., and Huang, J. (2011). "Stress-strain models for light gauge steels." *Procedia Engineering*, 14, 288-296.
- Rahmanishamsi, E., Soroushian, S., and Maragakis, M. (2016). "Cyclic shear behavior of gypsum board-to-steel stud screw connections in nonstructural walls." *Earthquake Spectra*, 32(1), 415-439.
- Rasmussen, K. J., Zhang, X., and Zhang, H. (2016). "Beam-element-based analysis of locally and/or distortionally buckled members: Theory." *Thin-Walled Structures*, 98, 285-292.
- Ren, C., Zhao, X. Z., and Chen, Y. Y. (2016). "Buckling behaviour of partially restrained cold-formed steel zed purlins subjected to transverse distributed uplift loading." *Engineering Structures*, 114, 14-24.
- Rogers, C. A., and Hancock, G. J. (1998). "Bolted connection tests of thin G550 and G300 sheet steels." *Journal of Structural Engineering-ASCE*, 124(7), 798-808.
- Sabbagh, A. B., Mirghaderi, R., Petkovski, M., and Pilakoutas, K. (2010). "An integrated thin-walled steel skeleton structure (two full scale tests)." *Journal of Constructional Steel Research*, 66(3), 470-479.
- Sabbagh, A. B., Petkovski, M., Pilakoutas, K., and Mirghaderi, R. (2013). "Cyclic behaviour of bolted cold-formed steel moment connections: FE modelling including slip." *Journal of Constructional Steel Research*, 80, 100-108.
- Sabbagh, A. B., Petkovski, M., Pilakoutas, K., and Mirghaderi, R. (2012a). "Development of cold-formed steel elements for earthquake resistant moment frame buildings." *Thin-Walled Structures*, 53, 99-108.
- Sabbagh, A. B., Petkovski, M., Pilakoutas, K., and Mirghaderi, R. (2011). "Ductile moment-resisting frames using cold-formed steel sections: An analytical investigation." *Journal of Constructional Steel Research*, 67(4), 634-646.
- Sabbagh, A. B., Petkovski, M., Pilakoutas, K., and Mirghaderi, R. (2012b). "Experimental work on cold-formed steel elements for earthquake resilient moment frame buildings." *Engineering Structures*, 42, 371-386.
- Sato, A., and Uang, C. M. (2013). "A FEMA P695 Study for the Proposed Seismic Performance Factors for Cold-Formed Steel Special Bolted Moment Frames." *Earthquake Spectra*, 29(1), 259-282.
- Sato, A., and Uang, C. M. (2009). "Seismic design procedure development for cold-formed steel-special bolted moment frames." *Journal of Constructional Steel Research*, 65(4), 860-868.

## References

- Sato, A., and Uang, C. M. (2010). "Seismic Performance Factors for Cold-Formed Steel Special Bolted Moment Frames." *Journal of Structural Engineering-Asce*, 136(8), 961-967.
- Schafer, B. (2006). "CUFSM Version 3.12." Department of Civil Engineering, Johns Hopkins University, <http://www.ce.jhu.edu/bschafer/cufsm/>.
- Schafer, B., Ayhan, D., Leng, J., Liu, P., Padilla-Llano, D., Peterman, K., Stehman, M., Buonopane, S., Eatherton, M., and Madsen, R. "Seismic Response and Engineering of Cold-formed Steel Framed Buildings." *Proc., Structures*, Elsevier.
- Schafer, B. W. (2008). "Review: The Direct Strength Method of cold-formed steel member design." *Journal of Constructional Steel Research*, 64(7-8), 766-778.
- Schafer, B. W., Li, Z., and Moen, C. D. (2010). "Computational modeling of cold-formed steel." *Thin-Walled Structures*, 48(10-11), 752-762.
- Schafer, B. W., and Pekoz, T. (1998). "Computational modeling of cold-formed steel: characterizing geometric imperfections and residual stresses." *Journal of Constructional Steel Research*, 47(3), 193-210.
- Seaburg, P. A., and Salmon, C. G. (1971). "Minimum weight design of light gage steel members." *Journal of the Structural Division*, 97(1), 203-222.
- Serrette, R. L., Encalada, J., Juadines, M., and Nguyen, H. (1997). "Static racking behavior of plywood, OSB, gypsum, and fiberbond walls with metal framing." *Journal of Structural Engineering-ASCE*, 123(8), 1079-1086.
- Serror, M. H., Hassan, E. M., and Mourad, S. A. (2016). "Experimental study on the rotation capacity of cold-formed steel beams." *Journal of Constructional Steel Research*, 121, 216-228.
- Shah, S., Sulong, N. R., Jumaat, M., and Shariati, M. (2016). "State-of-the-art review on the design and performance of steel pallet rack connections." *Engineering Failure Analysis*, 66, 240-258.
- Shamim, I., DaBreo, J., and Rogers, C. A. (2013). "Dynamic Testing of Single- and Double-Story Steel-Sheathed Cold-Formed Steel-Framed Shear Walls." *Journal of Structural Engineering-ASCE*, 139(5), 807-817.
- Shi, Y., and Eberhart, R. "A modified particle swarm optimizer." *Proc., Evolutionary Computation Proceedings, 1998. IEEE World Congress on Computational Intelligence., The 1998 IEEE International Conference on*, IEEE, 69-73.
- Shifferaw, Y., and Schafer, B. W. (2012). "Inelastic Bending Capacity of Cold-Formed Steel Members." *Journal of Structural Engineering-ASCE*, 138(4), 468-480.
- Silvestre, N. (2007). "Generalised beam theory to analyse the buckling behaviour of circular cylindrical shells and tubes." *Thin-Walled Structures*, 45(2), 185-198.
- Smith, F. H., and Moen, C. D. (2014). "Finite strip elastic buckling solutions for thin-walled metal columns with perforation patterns." *Thin-Walled Structures*, 79, 187-201.
- Standard, B. (2008). "Specification for surface plates BS817."
- Tashakori, A., and Adeli, H. (2002). "Optimum design of cold-formed steel space structures using neural dynamics model." *Journal of Constructional Steel Research*, 58(12), 1545-1566.
- Teh, L. H., and Gilbert, B. P. (2014). "Net Section Tension Capacity of Equal Angle Braces Bolted at Different Legs." *Journal of Structural Engineering*, 140(6).

## References

- Teh, L. H., and Yazici, V. (2013). "Shear lag and eccentricity effects of bolted connections in cold-formed steel sections." *Engineering Structures*, 52, 536-544.
- Tian, Y., and Lu, T. (2004). "Minimum weight of cold-formed steel sections under compression." *Thin-Walled Structures*, 42(4), 515-532.
- Tondini, N., and Morbioli, A. (2015). "Cross-sectional flexural capacity of cold-formed laterally-restrained steel rectangular hollow flange beams." *Thin-Walled Structures*, 95, 196-207.
- Torabian, S., Fratamico, D. C., and Schafer, B. W. (2016). "Experimental response of cold-formed steel Zee-section beam-columns." *Thin-Walled Structures*, 98, 496-517.
- Torabian, S., Zheng, B. F., and Schafer, B. W. (2015). "Experimental response of cold-formed steel lipped channel beam-columns." *Thin-Walled Structures*, 89, 152-168.
- Tran, T., and Li, L. Y. (2006). "Global optimisation of cold-formed steel channel sections." *Thin-Walled Structures*, 44(4), 399-406.
- Uang, C. M., Sato, A., Hong, J. K., and Wood, K. (2010). "Cyclic Testing and Modeling of Cold-Formed Steel Special Bolted Moment Frame Connections." *Journal of Structural Engineering-ASCE*, 136(8), 953-960.
- Ungermann, D., Brune, B., and Lübke, S. (2012). "Numerical and analytical investigations on plain channels in coupled instabilities." *Steel Construction*, 5(4), 205-211.
- Ungermann, D., Lubke, S., and Brune, B. (2014). "Tests and design approach for plain channels in local and coupled local-flexural buckling based on eurocode 3." *Thin-Walled Structures*, 81, 108-120.
- Uzzaman, A., Wrzesien, A. M., Lim, J. B., Hamilton, R., and Nash, D. "Design of top-hat purlins for cold-formed steel portal frames." *Proc., Structures*, Elsevier.
- Von Karman, T., Sechler, E. E., and Donnell, L. (1932). "The strength of thin plates in compression." *Trans. ASME*, 54(2), 53-57.
- Wang, B., Bosco, G. L., Gilbert, B. P., Guan, H., and Teh, L. H. (2016a). "Unconstrained shape optimisation of singly-symmetric and open cold-formed steel beams and beam-columns." *Thin-Walled Structures*, 104, 54-61.
- Wang, B., Gilbert, B. P., Molinier, A. M., Guan, H., and Teh, L. H. (2016b). "Shape optimisation of cold-formed steel columns with manufacturing constraints using the Hough transform." *Thin-Walled Structures*, 106, 75-92.
- Wang, C. A., Zhang, Z. N., Zhao, D. Q., and Liu, Q. Q. (2016c). "Compression tests and numerical analysis of web-stiffened channels with complex edge stiffeners." *Journal of Constructional Steel Research*, 116, 29-39.
- Wang, H. M., and Zhang, Y. C. (2009). "Experimental and numerical investigation on cold-formed steel C-section flexural members." *Journal of Constructional Steel Research*, 65(5), 1225-1235.
- Wang, L. P., and Young, B. (2016a). "Behavior of Cold-Formed Steel Built-Up Sections with Intermediate Stiffeners under Bending. I: Tests and Numerical Validation." *Journal of Structural Engineering-ASCE*, 142(3).

## References

- Wang, L. P., and Young, B. (2016b). "Behavior of Cold-Formed Steel Built-Up Sections with Intermediate Stiffeners under Bending. II: Parametric Study and Design." *Journal of Structural Engineering-ASCE*, 142(3).
- Wang, L. P., and Young, B. (2014). "Design of cold-formed steel channels with stiffened webs subjected to bending." *Thin-Walled Structures*, 85, 81-92.
- Wang, X., Astroza, R., Hutchinson, T. C., Conte, J. P., and Restrepo, J. I. (2015). "Dynamic characteristics and seismic behavior of prefabricated steel stairs in a full-scale five-story building shake table test program." *Earthquake Engineering & Structural Dynamics*, n/a-n/a.
- Wang, X. X., and Ye, J. H. (2016). "Cyclic testing of two- and three-story CFS shear-walls with reinforced end studs." *Journal of Constructional Steel Research*, 121, 13-28.
- Wong, M. F., and Chung, K. F. (2002). "Structural behaviour of bolted moment connections in cold-formed steel beam-column sub-frames." *Journal of Constructional Steel Research*, 58(2), 253-274.
- Wrzesien, A., Lim, J. B. P., and Nethercot, D. (2012). "Optimum joint detail for a general cold-formed steel portal frame." *Advances in Structural Engineering*, 15(9), 1623-1640.
- Wrzesien, A. M., Lim, J. B. P., Xu, Y., MacLeod, I. A., and Lawson, R. M. (2015). "Effect of stressed skin action on the behaviour of cold-formed steel portal frames." *Engineering Structures*, 105, 123-136.
- Yan, J., and Young, B. (2002). "Column tests of cold-formed steel channels with complex stiffeners." *Journal of Structural Engineering-ASCE*, 128(6), 737-745.
- Yan, J. T., and Young, B. (2004). "Numerical investigation of channel columns with complex stiffeners - part I: test verification." *Thin-Walled Structures*, 42(6), 883-893.
- Yang, J., and Liu, Q. (2012). "Sleeve connections of cold-formed steel sigma purlins." *Engineering Structures*, 43, 245-258.
- Ye, J., Hajirasouliha, I., Becque, J., and Eslami, A. (2016a). "Optimum design of cold-formed steel beams using Particle Swarm Optimisation method." *Journal of Constructional Steel Research*, 122, 80-93.
- Ye, J., Hajirasouliha, I., Becque, J., and Pilakoutas, K. (2016b). "Development of more efficient cold-formed steel channel sections in bending." *Thin-Walled Structures*, 101, 1-13.
- Ye, J. H., Wang, X. X., Jia, H. Y., and Zhao, M. Y. (2015). "Cyclic performance of cold-formed steel shear walls sheathed with double-layer wallboards on both sides." *Thin-Walled Structures*, 92, 146-159.
- Ye, J. H., Wang, X. X., and Zhao, M. Y. (2016c). "Experimental study on shear behavior of screw connections in CFS sheathing." *Journal of Constructional Steel Research*, 121, 1-12.
- Yin, L. F., Tang, G., Zhang, M., Wang, B. J., and Feng, B. (2016). "Monotonic and cyclic response of speed-lock connections with bolts in storage racks." *Engineering Structures*, 116, 40-55.
- Young, B. (2004). "Design of channel columns with inclined edge stiffeners." *Journal of Constructional Steel Research*, 60(2), 183-197.
- Young, B. (2008). "Research on cold-formed steel columns." *Thin-Walled Structures*, 46(7-9), 731-740.

## References

- Young, B., and J.R. Rasmussen, K. (1999). "Behaviour of cold-formed singly symmetric columns." *Thin-Walled Structures*, 33(2), 83-102.
- Young, B., and Rasmussen, K. J. R. (1998). "Design of lipped channel columns." *Journal of Structural Engineering-ASCE*, 124(2), 140-148.
- Young, B., and Yan, J. T. (2002). "Finite element analysis and design of fixed-ended plain channel columns." *Finite Elements in Analysis and Design*, 38(6), 549-566.
- Young, B., and Yan, J. T. (2004). "Numerical investigation of channel columns with complex stiffeners - part II: parametric study and design." *Thin-Walled Structures*, 42(6), 895-909.
- Yu, C., and Panyanouvong, M. X. (2013). "Bearing strength of cold-formed steel bolted connections with a gap." *Thin-Walled Structures*, 67, 110-115.
- Yu, C., and Schafer, B. W. (2006). "Distortional buckling tests on cold-formed steel beams." *Journal of Structural Engineering-Asce*, 132(4), 515-528.
- Yu, C., and Schafer, B. W. (2003). "Local buckling tests on cold-formed steel beams." *Journal of Structural Engineering-Asce*, 129(12), 1596-1606.
- Yu, C., and Schafer, B. W. (2007). "Simulation of cold-formed steel beams in local and distortional buckling with applications to the direct strength method." *Journal of Constructional Steel Research*, 63(5), 581-590.
- Yu, C., and Yan, W. M. (2011). "Effective Width Method for determining distortional buckling strength of cold-formed steel flexural C and Z sections." *Thin-Walled Structures*, 49(2), 233-238.
- Yu, W.-W., and LaBoube, R. A. (2010). *Cold-formed steel design*, John Wiley & Sons.
- Yu, W. K., Chung, K. F., and Wong, M. F. (2005). "Analysis of bolted moment connections in cold-formed steel beam-column sub-frames." *Journal of Constructional Steel Research*, 61(9), 1332-1352.
- Zaharia, R., and Dubina, D. (2006). "Stiffness of joints in bolted connected cold-formed steel trusses." *Journal of Constructional Steel Research*, 62(3), 240-249.
- Zhang, J. H., and Young, B. (2015). "Numerical investigation and design of cold-formed steel built-up open section columns with longitudinal stiffeners." *Thin-Walled Structures*, 89, 178-191.
- Zhang, L., and Tong, G. S. (2008). "Moment resistance and flexural rigidity of lapped connections in multi-span cold-formed Z purlin systems." *Thin-Walled Structures*, 46(5), 551-560.
- Zhang, X., Rasmussen, K. J., and Zhang, H. (2015). "Beam-element-based analysis of locally and/or distortional buckled members: Application." *Thin-Walled Structures*, 95, 127-137.
- Zhang, X., Rasmussen, K. J., and Zhang, H. (2016a). "Second-order effects in locally and/or distortional buckled frames and design based on beam element analysis." *Journal of Constructional Steel Research*, 122, 57-69.
- Zhang, X., Rasmussen, K. J. R., and Zhang, H. (2016b). "Experimental investigation of locally and distortional buckled portal frames." *Journal of Constructional Steel Research*, 122, 571-583.



## References

Zhang, Y., Wang, C., and Zhang, Z. (2007a). "Tests and finite element analysis of pin-ended channel columns with inclined simple edge stiffeners." *Journal of Constructional Steel Research*, 63(3), 383-395.

Zhang, Y. C., Wang, C. G., and Zhang, Z. N. (2007b). "Tests and finite element analysis of pin-ended channel columns with inclined simple edge stiffeners." *Journal of Constructional Steel Research*, 63(3), 383-395.

Zhao, C. X., Yang, J., Wang, F. L., and Chan, A. H. C. (2014). "Rotational stiffness of cold-formed steel roof purlin-sheeting connections." *Engineering Structures*, 59, 284-297.

# APPENDIX Computer Programmes

---

## A.1 Computer programme to design CFS lipped channel elements

```

function [pn]=opt1(x)
%%%%%%%%%%%%%%%%%%%%%%%%%%%%%%%%%%%%%%%%%%%%%%%%%%%%%%%%%%%%%%%%%%%%%%%%
%%%%%%%%%%%%%%%%%%%%%%%%%%%%%%%%%%%%%%%%%%%%%%%%%%%%%%%%%%%%%%%%%%%%%%%%
% Main program
% This program is used to design of CFS members subjected to bending
and compression
% This is the main program and it is used for optimisation and calling
% the sub-programs
%%%%%%%%%%%%%%%%%%%%%%%%%%%%%%%%%%%%%%%%%%%%%%%%%%%%%%%%%%%%%%%%%%%%%%%%
%%%%%%%%%%%%%%%%%%%%%%%%%%%%%%%%%%%%%%%%%%%%%%%%%%%%%%%%%%%%%%%%%%%%%%%%
p=200;      %total length of plate in mm
b1=x(2)*p;
c1=x(1)*b1;
b2=b1;
c2=c1;
theta1=x(3);
theta2=x(3);
theta3=pi/2;
theta4=pi/2;
h = p-2*b1-2*c1;
r=0.1;
tnom=0.95;   %nominal thick
t=tnom;      %core thick
fyb=350;
fu=600;
E=210000;
v=0.3;
G=E/(1+v)/2;
rm0=1.00;
rm1=1.00;
%%%%%%%%%%%%%%%%%%%%%%%%%%%%%%%%%%%%%%%%%%%%%%%%%%%%%%%%%%%%%%%%%%%%%%%%Apply loads%%%%%%%%%%%%%%%%%%%%%%%%%%%%%%%%%%%%%%%%%%%%%%%%%%%%%%%%%%%%%%%%%%%%%%%%
NEd=1000000;
L=2700;%the length of the column(mm)
%dimensions measured to the middle points of round corner--used for
the calculation of effective cross-section properties.
cp1=c1-t/2*tan((pi-theta1)/2)-(r+t/2)*(tan((pi-theta1)/2)-...
sin((pi-theta1)/2));
bp1=b1-t/2-(r+t/2)*(tan(theta3/2)-sin(theta3/2))-...
t/2*tan((pi-theta1)/2)-(r+t/2)*(tan((pi-theta1)/2)...
-sin((pi-theta1)/2));
hp=h-t/2-(r+t/2)*(tan(theta3/2)-sin(theta3/2))...
-t/2-(r+t/2)*(tan(theta4/2)-sin(theta4/2));
bp2=b2-t/2-(r+t/2)*(tan(theta4/2)-sin(theta4/2))...
-t/2*tan((pi-theta2)/2)-...
(r+t/2)*(tan((pi-theta2)/2)-sin((pi-theta2)/2));
cp2=c2-t/2*tan((pi-theta2)/2)-(r+t/2)*(tan((pi-theta2)/2)-...
sin((pi-theta2)/2));
delta=0.43*(r*(pi-theta1)/pi*2+r+r+...
r*(pi-theta2)/pi*2)/(hp+bp1+cp1+bp2+cp2);

%Section properties
numj=6;
nume=5;
coordinates=[bp1-cp1*cos(theta1) cp1*sin(theta1);
             bp1 0;
             0 0;
             0 hp;

```

## APPENDIX

```

        bp2 hp;
        bp2-cp2*cos(theta2) hp-cp2*sin(theta2)];];
elements=[ 1 2 t;
           2 3 t;
           3 4 t;
           4 5 t;
           5 6 t];];
%dimensions should be checked;
[F,iy,iz,i0,IXX,IYY,XP,YP,y0,z0,PSI,IY,IZ,IXXC,IYYC,IT,IWW,XY] =
section_properties(numj,nume,coordinates,elements,delta);
[A_eff,ratiomax,eNy,eNz] =
compression(h,b1,b2,c1,theta1,c2,theta2,t,r,fyb,fu,E,v);
%axial compression
[W_eff_c,W_eff_t] =
bending_y(h,b1,b2,c1,theta1,c2,theta2,t,r,fyb,E,v,rm0,tnom);
%bending in major axis
[W_eff_z_t1,W_eff_z_c1] =
bending_z_lip(h,b1,b2,c1,theta1,c2,theta2,t,r,tnom,fyb,E,v,rm0);
%bending in minor axis with lips compressive
[W_eff_z_c2,W_eff_z_t2] =
bending_z_web(h,b1,b2,c1,c2,theta1,theta2,t,r,tnom,fyb,E,v,rm0);
%bending in minor axis with webs compressive

%%%%%%%%%%%%%%%%%%%%%%%%%%%%%%%%%%%%%%%%%%%%%%%%%%%%%%%%%%%%%%%%%%%%%%%%%for global buckling%%%%%%%%%%%%%%%%%%%%%%%%%%%%%%%%%%%%%%%%%%%%%%%%%%%%%%%%%%%%%%%%%%%%%%%%%
miu = 1.0;%length coefficient
%%%%%%%%%%%%%%%%%%%%%%%%%%%%%%%%%%%%%%%%%%%%%%%%%%%%%%%%%%%%%%%%%%%%%%%%%flexural buckling%%%%%%%%%%%%%%%%%%%%%%%%%%%%%%%%%%%%%%%%%%%%%%%%%%%%%%%%%%%%%%%%%%%%%%%%%
%buckling about y-y axis
lamda1 = pi*sqrt(E/fyb);
Lcr_y = miu*L; %buckling length
Lcr_z = miu*L; %buckling length

%Buckling about y-y axis

lamda_y = Lcr_y/iy*(sqrt(A_eff/F)/lamda1);
alpha_y = 0.34; %for buckling curve b;
fi_y = 0.5*(1+alpha_y*(lamda_y-0.2)+lamda_y^2);
if lamda_y <= 0.2||NEd/(pi^2*E*IY/Lcr_y^2) <= 0.04
    X_y = 1;
else
    X_y = min(1/(fi_y+sqrt(fi_y^2-lamda_y^2)),1);
end

%Buckling about z-z axis

lamda_z = Lcr_z/iz*(sqrt(A_eff/F)/lamda1);
alpha_z = 0.34; %for buckling curve b;
fi_z = 0.5*(1+alpha_z*(lamda_z-0.2)+lamda_z^2);
if lamda_z<=0.2||NEd/(pi^2*E*IZ/Lcr_z^2)<=0.04
    X_z=1;
else
    X_z=min(1/(fi_z+sqrt(fi_z^2-lamda_z^2)),1);
end

%Torsional buckling

Lcr_T = 0.7*L;
Ncr_T = (G*IT+pi^2*E*IWW/Lcr_T^2)/i0^2;
lamda_T = sqrt(A_eff*fyb/Ncr_T);
alpha_T=0.34; %For buckling curve b;
fi_T=0.5*(1+alpha_T*(lamda_T-0.2)+lamda_T^2);
if lamda_T<=0.2||NEd/Ncr_T<=0.04

```

## APPENDIX

```

X_T=1;
else
    X_T=min(1/(fi_T+sqrt(fi_T^2-lamda_T^2)),1);
end

%Torsional-flexural buckling

Lcr_TF = 0.7*L;
Ncr_y = pi^2*E*IY/Lcr_y^2;
beta = 1-(y0/i0)^2;
Ncr_TF = Ncr_y/2/beta*(1+Ncr_T/Ncr_y-sqrt((1-
Ncr_T/Ncr_y)^2+4*(y0/i0)^2*Ncr_T/Ncr_y));
lamda_TF = sqrt(A_eff*fyb/Ncr_TF);
alpha_TF = 0.34; %For buckling curve b;
fi_TF = 0.5*(1+alpha_TF*(lamda_TF-0.2)+lamda_TF^2);
if lamda_TF <= 0.2 || NEd/Ncr_TF<=0.04
    X_TF=1;
else
    X_TF=min(1/(fi_TF+sqrt(fi_TF^2-lamda_TF^2)),1);
end

%lateral-torsion buckling
%%calculate the elastic lateral torsional buckling load
Mcry=pi/L*sqrt(E*IZ*(G*IT+pi^2*E*IWW/L^2));
lamda_lt=sqrt(W_eff_c*fyb/Mcry);
alpha_lt=0.34;
fi_lt=0.5*(1+alpha_lt*(lamda_lt-0.2)+lamda_lt^2);
if lamda_lt<=0.2
    X_lt=1; %Not need check
else
    X_lt=min(1/(fi_lt+sqrt(fi_lt^2-lamda_lt^2)),1);
end

%%%minimum reduction factor for relevant buckling
%%%%%%%%%%%%%%%%%%%%%%%%%%%%%%%%%%%%%%%%%%%%%%%%%%%%%%%%%%%%%%%%%%%%%%%%mode%%%%%%%%%%%%%%%%%%%%%%%%%%%%%%%%%%%%%%%%%%%%%%%%%%%%%%%%%%%%%%%%%%%%%%%%
X = min([X_y,X_z,X_T,X_TF]);
%X = min([X_y,X_z]);
% X_y
% X_z
% X_T
% X_TF
%N_Y = X_y*A_eff*fyb/rm1
%N_Z = X_z*A_eff*fyb/rm1
%N_T = X_T*A_eff*fyb/rm1
%N_TF = X_TF*A_eff*fyb/rm1
NbRd = X*A_eff*fyb/rm1;

%%%%%%%%%%%%%%%%%%%%%%%%%%%%%%%%%%%%%%%%%%%%%%%%%%%%%%%%%%%%%%%%%%%%%%%% for cross-section checks
%%%%%%%%%%%%%%%%%%%%%%%%%%%%%%%%%%%%%%%%%%%%%%%%%%%%%%%%%%%%%%%%%%%%%%%%
%Axial compression with dimension of "N"
NcRd = A_eff*fyb/rm0;
%bending in minor axis with lip compression, moment with dimension
"N*mm"
McZ_Rd_com1 = W_eff_z_c1*fyb/rm0;
McZ_Rd_t1 =W_eff_z_t1*fyb/rm0;
%bending in minor axis with web compression
McZ_Rd_com2 = W_eff_z_c2*fyb/rm0;
McZ_Rd_t2 = W_eff_z_t2*fyb/rm0;

%%%%%%%%%%%%%%%%%%%%%%%%%%%%%%%%%%%%%%%%%%%%%%%%%%%%%%%%%%%%%%%%%%%%%%%%

```

## APPENDIX

```

%Apply load and output
%%%%%%%%%%%%%%%%%%%%%%%%%%%%%%%%%%%%%%%%%%%%%%%%%%%%%%%%%%%%%%%%%%%%%%%%
%combined compression and bending considering shift of centroidal axes
%local
if eNz <= 0      %the lips compressive
    pn1=1/(1/NcRd+abs(eNz)/Mcz_Rd_com1);
else            %the web compressive
    pn1=1/(1/NcRd+abs(eNz)/Mcz_Rd_com2);
end
%global
if eNz<=0
    pn2=1/((1/NbRd)^0.8+(abs(eNz)/Mcz_Rd_com1)^0.8)^1.25;
else
    pn2=1/((1/NbRd)^0.8+(abs(eNz)/Mcz_Rd_com2)^0.8)^1.25;
end

%pn=min([NcRd NbRd]);          %without considering the shift
pn=min([NcRd NbRd pn1 pn2])   %with considering the shift
%pn=W_eff_c*fyb
%W_eff_c
%pn=min(W_eff_c*fyb,X_lt*W_eff_c*fyb) %Considering lateral-
torsionalbuckling

function
[W_eff_c,W_eff_t]=bending_y(h,b1,b2,c1,theta1,c2,theta2,t,r,fyb,E,v,rm
0,tnom)
%%%%%%%%%%%%%%%%%%%%%%%%%%%%%%%%%%%%%%%%%%%%%%%%%%%%%%%%%%%%%%%%%%%%%%%%
%%%%%%%%%%%%%%%%%%%%%%%%%%%%%%%%%%%%%%%%%%%%%%%%%%%%%%%%%%%%%%%%%%%%%%%%
% This function is used to calculate the effective properties of the
CFS
% section in bending
% The effective modulus of the section is around its major axis
%%%%%%%%%%%%%%%%%%%%%%%%%%%%%%%%%%%%%%%%%%%%%%%%%%%%%%%%%%%%%%%%%%%%%%%%
%%%%%%%%%%%%%%%%%%%%%%%%%%%%%%%%%%%%%%%%%%%%%%%%%%%%%%%%%%%%%%%%%%%%%%%%
%bending about y-y axis
% %the dimension of the section centre line
%dimensions measured to the points of intersection of their middle
%lines--used for the calculation of effective cross-section
properties.
theta3=pi/2;
theta4=theta3;
cp1=c1-t/2*tan((pi-theta1)/2)-(r+t/2)*(tan((pi-theta1)/2)- ...
sin((pi-theta1)/2));
bp1=b1-t/2-(r+t/2)*(tan(theta3/2)-sin(theta3/2))- ...
t/2*tan((pi-theta1)/2)-(r+t/2)*(tan((pi-theta1)/2)- ...
sin((pi-theta1)/2));
hp=h-t/2-(r+t/2)*(tan(theta3/2)-sin(theta3/2))- ...
t/2-(r+t/2)*(tan(theta4/2)-sin(theta4/2));
bp2=b2-t/2-(r+t/2)*(tan(theta4/2)-sin(theta4/2))- ...
t/2*tan((pi-theta2)/2)-(r+t/2)*(tan((pi-theta2)/2)- ...
sin((pi-theta2)/2));
cp2=c2-t/2*tan((pi-theta2)/2)-(r+t/2)*(tan((pi-theta2)/2)- ...
sin((pi-theta2)/2));
%Section properties
numj=6;
nume=5;
coordinates=[bp1-cp1*cos(theta1) cp1*sin(theta1);
             bp1 0;
             0 0;
             0 hp;
             bp2 hp;

```

## APPENDIX

```

        bp2-cp2*cos(theta2) hp-cp2*sin(theta2)];
elements=[ 1 2 t;
           2 3 t;
           3 4 t;
           4 5 t;
           5 6 t;];
[numj,nume,coordinates,elements,fya,hp,bp1,bp2,cp1,cp2]=idealise_section(h,b1,b2,c1,theta1,c2,theta2,t,r,fyb,fu);
[A,iy,iz,IY,IZ,XY,XC,YC]=normal_properties(numj,nume,coordinates,elements);
%%%%%%%%%%%%%%%%%%%%%%%%%%%%%%%%%%%%%%%%%%%%%%%%%%%%%%%%%%%%%%%%%%%%%%%%
xd1=2.0;
xd_upper=1.0;
while abs(xd_upper-xd1)>=0.001
    xd1=xd_upper;
    sigma=fyb*xd_upper;
%STEP 1
%calculation of the effective length of upper flange
stress_ratio_upper=XY(5,2)/XY(4,2);
[beff21,beff22]=effectivelength_inter(stress_ratio_upper,XY(5,1)-XY(4,1),t,sigma);

%calculation of the effective length of the edge fold
%single edge fold stiffener
%for upper edge fold;
[ceff2]=effectivelengthe_single_edgestiffener(cp2,bp2,sigma,t);

%STEP 2
[IY_upper b2
As_upper]=properties_edgestiffener(bp2,beff22,theta2,ceff2,t);
%for upper flange
As_bottom=0;
kf_upper=As_bottom/As_upper;
K1=E*t^3/(4*(1-v^2))/(b2^2*hp+b2^3+0.5*b1*b2*hp*kf_upper); %spring
stiffness
%calculation of the properties of stiffener
sigma_upper=2*(K1*E*IY_upper)^(1/2)/As_upper;
%Calculation of the reduction factor Xd for distortional buckling
according to 5.12
%for upper stiffener
[xd_upper,lamb_d_upper]=reduction_distortion(sigma_upper,fyb);
end

%Calculation of the effective properties of the web
%Section properties
numj=9;
nume=8;
coordinates=[bp1-cp1*cos(theta1) cp1*sin(theta1);
            bp1 0;
            0 0;
            0 hp;
            beff21 hp;
            bp2-beff22 hp;
            bp2 hp;
            bp2-ceff2*cos(theta2) hp-ceff2*sin(theta2);
            bp2-cp2*cos(theta2) hp-cp2*sin(theta2)];
elements=[ 1 2 t;
           2 3 t;
           3 4 t;
           4 5 t;
           5 6 0;
           6 7 t*xd_upper;
           7 8 t*xd_upper;

```

## APPENDIX

```

            8 9 0;];
[A, iy, iz, IY, IZ, XY, XC, YC]=normal_properties(numj, nume, coordinates, elements);

%calculation of the effective length of web
stress_ratio_web=XY(3,2)/XY(4,2);
[heff1,heff2]=effectivelength_inter(stress_ratio_web, ...
XY(4,2)-XY(3,2), t, fyb);
%%Calculation of the effective properties of the WHOLE section
numj=11;
nume=10;
coordinates=[bp1-cp1*cos(theta1) cp1*sin(theta1);
            bp1 0;
            0 0;
            0 YC+heff2;
            0 hp-heff1;
            0 hp;
            beff21 hp;
            bp2-beff22 hp;
            bp2 hp;
            bp2-ceff2*cos(theta2) hp-ceff2*sin(theta2);
            bp2-cp2*cos(theta2) hp-cp2*sin(theta2)];
elements=[ 1 2 t;
            2 3 t;
            3 4 t;
            4 5 0;
            5 6 t;
            6 7 t;
            7 8 0;
            8 9 t*xd_upper;
            9 10 t*xd_upper;
            10 11 0;];
[A_eff, iy_eff, iz_eff, IY_eff, IZ, XY_eff, XC_eff, YC_eff]=normal_properties
(numj, nume, coordinates, elements);
IY_eff
max(XY_eff(:,2))
%Calculation of the effective second moment of area and effective
section modulus
delta=0.43*(r*(pi-theta1)/pi*2+r+r*(pi-
theta2)/pi*2)/(hp+bp1+cp1+bp2+cp2);
W_eff_c=IY_eff/max(XY_eff(:,2))*(1-2*delta);
W_eff_t=IY_eff/abs(min(XY_eff(:,2)))*(1-2*delta);

function[W_eff_z_t,W_eff_z_c]=bending_z_lip(h,b1,b2,c1,theta1,c2,theta
2,t,r,tnom,fyb,E,v,rm0)
%%%%%%%%%%%%%%%%%%%%%%%%%%%%%%%%%%%%%%%%%%%%%%%%%%%%%%%%%%%%%%%%%%%%%%%%
%%%%%%%%%%%%%%%%%%%%%%%%%%%%%%%%%%%%%%%%%%%%%%%%%%%%%%%%%%%%%%%%%%%%%%%%
% This function is used to calculate the effective properties of the
CFS
% section in bending
% The bending is around its minor axis with lips in compression
%%%%%%%%%%%%%%%%%%%%%%%%%%%%%%%%%%%%%%%%%%%%%%%%%%%%%%%%%%%%%%%%%%%%%%%%
%%%%%%%%%%%%%%%%%%%%%%%%%%%%%%%%%%%%%%%%%%%%%%%%%%%%%%%%%%%%%%%%%%%%%%%%
% %the dimension of the section centre line
theta3=pi/2;
theta4=theta3;
cp1=c1-t/2*tan((pi-theta1)/2)-(r+t/2)*(tan((pi-theta1)/2)- ...
sin((pi-theta1)/2));
bp1=b1-t/2-(r+t/2)*(tan(theta3/2)-sin(theta3/2))- ...
t/2*tan((pi-theta1)/2)-(r+t/2)*(tan((pi-theta1)/2)- ...
sin((pi-theta1)/2));
hp=h-t/2-(r+t/2)*(tan(theta3/2)-sin(theta3/2))- ...

```

## APPENDIX

```

t/2-(r+t/2)*(tan(theta4/2)-sin(theta4/2));
bp2=b2-t/2-(r+t/2)*(tan(theta4/2)-sin(theta4/2))- ...
t/2*tan((pi-theta2)/2)-(r+t/2)*(tan((pi-theta2)/2)- ...
sin((pi-theta2)/2));
cp2=c2-t/2*tan((pi-theta2)/2)-(r+t/2)*(tan((pi-theta2)/2)- ...
sin((pi-theta2)/2));
%Section properties
numj=6;
nume=5;
coordinates=[bp1-cp1*cos(theta1) cp1*sin(theta1);
             bp1 0;
             0 0;
             0 hp;
             bp2 hp;
             bp2-cp2*cos(theta2) hp-cp2*sin(theta2)];
elements=[ 1 2 t;
           2 3 t;
           3 4 t;
           4 5 t;
           5 6 t];
%[numj,nume,coordinates,elements,fya,hp,bp1,bp2,cp1,cp2]=idealise_section(h,b1,b2,c1,theta1,c2,theta2,t,r,fyb,fu);
[A,iy,iz,IY,IZ,XY,XC,YC]=normal_properties(numj,nume,coordinates,elements);
%STEP 1
xd1=2.0;
xd_upper=1.0;
while abs(xd_upper-xd1)>=0.001
    xd1=xd_upper;
    sigma=fyb*xd_upper;
%calculation of the effective length of the edge fold
%single edge fold stiffener
%for bottom edge fold
[ceff1]=effectivelengthe_single_edgestiffener(cp1,bp1,sigma,t);
%for upper edge fold
[ceff2]=effectivelengthe_single_edgestiffener(cp2,bp2,sigma,t);

%%Calculation of the effective length of the webs
%Section properties to calculate the stress ratio
numj=8;
nume=7;
coordinates=[bp1-cp1*cos(theta1) cp1*sin(theta1);
             bp1-ceff1*cos(theta1) ceff1*sin(theta1);
             bp1 0;
             0 0;
             0 hp;
             bp2 hp;
             bp2-ceff2*cos(theta2) hp-ceff2*sin(theta2);
             bp2-cp2*cos(theta2) hp-cp2*sin(theta2)];
elements=[ 1 2 0;
           2 3 t;
           3 4 t;
           4 5 t;
           5 6 t;
           6 7 t;
           7 8 0];
[A,iy,iz,IY,IZ,XY,XC,YC]=normal_properties(numj,nume,coordinates,elements);
%effective length of upper web
stress_ratio_web2=XY(5,1)/XY(6,1);
[be22,be21]=effectivelength_inter(stress_ratio_web2,XY(6,1)-XY(5,1),t,sigma);
%effective length of bottom web
stress_ratio_web1=XY(4,1)/XY(3,1);

```



## APPENDIX

```

[be12,be11]=effectivelength_inter(stress_ratio_web1,XY(3,1)-
XY(4,1),t,sigma);
%STEP 2
[IY_upper b2
As_upper]=properties_edgestiffener(bp2,be22,theta2,ceff2,t);
[IY_bottom b1
As_bottom]=properties_edgestiffener(bp1,be12,theta1,ceff1,t);

%for upper flange
kf_upper=As_bottom/As_upper;
K1=E*t^3/(4*(1-v^2))/(b2^2*hp+b2^3+0.5*b1*b2*hp*kf_upper); %spring
stiffness
%calculation of the properties of stiffener
sigma_upper=2*(K1*E*IY_upper)^(1/2)/As_upper;
%for bottom flange
kf_bottom=As_upper/As_bottom;
K2=E*t^3/(4*(1-v^2))/(b1^2*hp+b1^3+0.5*b1*b2*hp*kf_bottom); %spring
stiffness
%calculation of the properties of stiffener
sigma_bottom=2*(K2*E*IY_bottom)^(1/2)/As_bottom;
%Calculation of the reduction factor Xd for distortional buckling
according
%to 5.12
%for upper stiffener
[xd_upper,lamb_d_upper]=reduction_distortion(sigma_upper,fyb);
%for bottom stiffener
[xd_bottom,lamb_d_bottom]=reduction_distortion(sigma_bottom,fyb);

end

% xd_bottom=1;xd_upper=1;
%%Calculation of the effective properties of the WHOLE section
numj=12;
nume=11;
coordinates=[bp1-cp1*cos(theta1) cp1*sin(theta1);
             bp1-ceff1*cos(theta1) ceff1*sin(theta1);
             bp1 0;
             bp1-be12 0;
             XC+be11 0;
             0 0;
             0 hp;
             XC+be21 hp;
             bp2-be22 hp;
             bp2 hp;
             bp2-ceff2*cos(theta2) hp-ceff2*sin(theta2);
             bp2-cp2*cos(theta2) hp-cp2*sin(theta2)];
elements=[ 1 2 0;
           2 3 t*xd_bottom;
           3 4 t*xd_bottom;
           4 5 0;
           5 6 t;
           6 7 t;
           7 8 t;
           8 9 0;
           9 10 t*xd_upper;
           10 11 t*xd_upper;
           11 12 0;];
[A_eff,iy_eff,iz_eff,IY_eff,IZ_eff,XY_eff,XC_eff,YC_eff]=normal_proper
ties(numj,nume,coordinates,elements);
%calculation of section module
delta=0.43*(r*(pi-theta1)/pi^2+r+r*(pi-
theta2)/pi^2)/(hp+bp1+cp1+bp2+cp2);
W_eff_z_c=IZ_eff/max(XY_eff(:,1))*(1-2*delta);

```

## APPENDIX

```
W_eff_z_t=IZ_eff/abs(min(XY_eff(:,1)))*(1-2*delta);
```

```
function
```

```
[W_eff_z_c,W_eff_z_t]=bending_z_web(h,b1,b2,c1,c2,theta1,theta2,t,r,tn
om,fyb,E,v,rm0)
%%%%%%%%%%%%%%%%%%%%%%%%%%%%%%%%%%%%%%%%%%%%%%%%%%%%%%%%%%%%%%%%%%%%%%%%
%%%%%%%%%%%%%%%%%%%%%%%%%%%%%%%%%%%%%%%%%%%%%%%%%%%%%%%%%%%%%%%%%%%%%%%%
% This function is used to calculate the effective properties of the
CFS
% section in bending
% The bending is around its minor axis with webs in compression
%%%%%%%%%%%%%%%%%%%%%%%%%%%%%%%%%%%%%%%%%%%%%%%%%%%%%%%%%%%%%%%%%%%%%%%%
%%%%%%%%%%%%%%%%%%%%%%%%%%%%%%%%%%%%%%%%%%%%%%%%%%%%%%%%%%%%%%%%%%%%%%%%
theta3=pi/2;
theta4=theta3;
cp1=c1-t/2*tan((pi-theta1)/2)-(r+t/2)*(tan((pi-theta1)/2)- ...
sin((pi-theta1)/2));
bp1=b1-t/2-(r+t/2)*(tan(theta3/2)-sin(theta3/2))- ...
t/2*tan((pi-theta1)/2)-(r+t/2)*(tan((pi-theta1)/2)- ...
sin((pi-theta1)/2));
hp=h-t/2-(r+t/2)*(tan(theta3/2)-sin(theta3/2))- ...
t/2-(r+t/2)*(tan(theta4/2)-sin(theta4/2));
bp2=b2-t/2-(r+t/2)*(tan(theta4/2)-sin(theta4/2))- ...
t/2*tan((pi-theta2)/2)-(r+t/2)*(tan((pi-theta2)/2)- ...
sin((pi-theta2)/2));
cp2=c2-t/2*tan((pi-theta2)/2)-(r+t/2)*(tan((pi-theta2)/2)- ...
sin((pi-theta2)/2));
%Section properties
numj=6;
nume=5;
coordinates=[bp1-cp1*cos(theta1) cp1*sin(theta1);
             bp1 0;
             0 0;
             0 hp;
             bp2 hp;
             bp2-cp2*cos(theta2) hp-cp2*sin(theta2)];
elements=[ 1 2 t;
           2 3 t;
           3 4 t;
           4 5 t;
           5 6 t;];
[numj,nume,coordinates,elements,fya,hp,bp1,bp2,cp1,cp2]=idealise_sect
ion(h,b1,b2,c1,theta1,c2,theta2,t,r,fyb,fu);
[A,iy,iz,IY,IZ,XY,XC,YC]=normal_properties(numj,nume,coordinates,elemen
ts);
%Calculation of the effective width of compressive plate
stress_ratio_web=1;
[heff1,heff2]=effectivelength_inter(stress_ratio_web,XY(4,2)-
XY(3,2),t,fyb);
%Calculation of the effective properties of the web
%Section properties
numj=8;
nume=7;
coordinates=[bp1-cp1*cos(theta1) cp1*sin(theta1);
             bp1 0;
             0 0;
             0 heff1;
             0 hp-heff2;
             0 hp;
             bp2 hp;
             bp2-cp2*cos(theta2) hp-cp2*sin(theta2)];
```

## APPENDIX

```

elements=[ 1 2 t;
           2 3 t;
           3 4 t;
           4 5 0;
           5 6 t;
           6 7 t;
           7 8 t;];
[A,iy,iz,IY,IZ,XY,XC,YC]=normal_properties(numj,nume,coordinates,elements);
%effective length of upper web
stress_ratio_web2=XY(7,1)/XY(6,1);
[be21,be22]=effectivelength_inter(stress_ratio_web2,XY(7,1)-XY(6,1),t,fyb);
%effective length of bottom web
stress_ratio_web1=XY(2,1)/XY(3,1);
[be11,be12]=effectivelength_inter(stress_ratio_web1,XY(2,1)-XY(3,1),t,fyb);
%%Calculation of the effective properties of the WHOLE section
numj=12;
nume=11;
coordinates_eff=[bp1-cp1*cos(theta1) cp1*sin(theta1);
                 bp1 0;
                 XC-be12 0;
                 be11 0;
                 0 0;
                 0 heff1;
                 0 hp-heff2;
                 0 hp;
                 be21 hp;
                 XC-be22 hp;
                 bp2 hp;
                 bp2-cp2*cos(theta2) hp-cp2*sin(theta2)];
elements_eff=[ 1 2 t;
               2 3 t;
               3 4 0;
               4 5 t;
               5 6 t;
               6 7 0;
               7 8 t;
               8 9 t;
               9 10 0;
               10 11 t;
               11 12 t;];
[A_eff,iy_eff,iz_eff,IY_eff,IZ_eff,XY_eff,XC_eff,YC_eff]=normal_properties(numj,nume,coordinates_eff,elements_eff);
delta=0.43*(r*(pi-theta1)/pi^2+r+r*(pi-theta2)/pi^2)/(hp+bp1+cp1+bp2+cp2);
W_eff_z_c=IZ_eff/abs(min(XY_eff(:,1)))*(1-2*delta);
W_eff_z_t=IZ_eff/max((XY_eff(:,1)))*(1-2*delta);

function
[A_eff,ratiomax,eNy,eNz]=compression(h,b1,b2,c1,theta1,c2,theta2,t,r,fyb,fu,E,v)
%%%%%%%%%%%%%%%%%%%%%%%%%%%%%%%%%%%%%%%%%%%%%%%%%%%%%%%%%%%%%%%%%%%%%%%%
%%%%%%%%%%%%%%%%%%%%%%%%%%%%%%%%%%%%%%%%%%%%%%%%%%%%%%%%%%%%%%%%%%%%%%%%
% This function is used to calculate the effective properties of the
CFS
% section in compression
%%%%%%%%%%%%%%%%%%%%%%%%%%%%%%%%%%%%%%%%%%%%%%%%%%%%%%%%%%%%%%%%%%%%%%%%
%%%%%%%%%%%%%%%%%%%%%%%%%%%%%%%%%%%%%%%%%%%%%%%%%%%%%%%%%%%%%%%%%%%%%%%%
% % the dimension of the section centre line
theta3=pi/2;
theta4=theta3;

```

## APPENDIX

```

cp1=c1-t/2*tan((pi-theta1)/2)-(r+t/2)*(tan((pi-theta1)/2)- ...
sin((pi-theta1)/2));
bp1=b1-t/2-(r+t/2)*(tan(theta3/2)-sin(theta3/2))-t/2*tan((pi-
theta1)/2)-(r+t/2)*(tan((pi-theta1)/2)-sin((pi-theta1)/2));
hp=h-t/2-(r+t/2)*(tan(theta3/2)-sin(theta3/2))-t/2-
(r+t/2)*(tan(theta4/2)-sin(theta4/2));
bp2=b2-t/2-(r+t/2)*(tan(theta4/2)-sin(theta4/2))-t/2*tan((pi-
theta2)/2)-(r+t/2)*(tan((pi-theta2)/2)-sin((pi-theta2)/2));
cp2=c2-t/2*tan((pi-theta2)/2)-(r+t/2)*(tan((pi-theta2)/2)-sin((pi-
theta2)/2));
%Section properties
numj=6;
nume=5;
coordinates=[bp1-cp1*cos(theta1) cp1*sin(theta1);
             bp1 0;
             0 0;
             0 hp;
             bp2 hp;
             bp2-cp2*cos(theta2) hp-cp2*sin(theta2)];
elements=[ 1 2 t;
           2 3 t;
           3 4 t;
           4 5 t;
           5 6 t];
[A, iy, iz, IY, IZ, XY, XC, YC]=normal_properties(numj, nume, coordinates, eleme
nts);

%%%%%%%%%%%%%%%%%%%%%%%%%%%%%%%%%%%%%%%%%%%%%%%%%%%%%%%%%%%%%%%%%%%%%%%%
%compression
%%%%%%%%%%%%%%%%%%%%%%%%%%%%%%%%%%%%%%%%%%%%%%%%%%%%%%%%%%%%%%%%%%%%%%%%
%Calculation of the stress ratio of web
stress_ratio_web=1;
[heff1,heff2]=effectivelength_inter(stress_ratio_web, hp, t, fyb);
%calculation of the effective length of web
kfi=4;
lamb_web=hp/t/(28.4*sqrt(235*kfi/fyb));
ratio_3=lamb_web/0.673;

%STEP 1
xd1=2.0;
xd_upper=1.0;
while abs(xd_upper-xd1)>=0.001
    xd1=xd_upper;
    sigma=fyb*xd_upper;
    %calculation of the effective length of bottom flange
    stress_ratio_bott=1;
    [beff11,beff12]=effectivelength_inter(stress_ratio_bott, bp1, t, sigma);
    %calculation of the effective length of upper flange
    stress_ratio_upper=1;
    [beff21,beff22]=effectivelength_inter(stress_ratio_upper, bp2, t, sigma);

    %calculation of the effective length of the edge fold
    %single edge fold stiffener
    %for upper edge fold
    [ceff2]=effectivelengthe_single_edgestiffener(cp2, bp2, sigma, t);
    %for bottom edge fold
    [ceff1]=effectivelengthe_single_edgestiffener(cp1, bp1, sigma, t);

%STEP 2
[IY_upper b2
As_upper]=properties_edgestiffener(bp2, beff22, theta2, ceff2, t);
[IY_bottom b1
As_bottom]=properties_edgestiffener(bp1, beff12, theta1, ceff1, t);

```

## APPENDIX

```

%for upper flange
kf_upper=As_bottom/As_upper;
K1=E*t^3/(4*(1-v^2))/(b2^2*hp+b2^3+0.5*b1*b2*hp*kf_upper); %spring
stiffness
%calculation of the properties of stiffener
sigma_upper=2*(K1*E*IY_upper)^(1/2)/As_upper;

%for bottom flange
kf_bottom=As_upper/As_bottom;
K2=E*t^3/(4*(1-v^2))/(b1^2*hp+b1^3+0.5*b1*b2*hp*kf_bottom); %spring
stiffness
%calculation of the properties of stiffener
sigma_bottom=2*(K2*E*IY_bottom)^(1/2)/As_bottom;

%Calculation of the reduction factor Xd for distortional buckling
according
%to 5.12
%for upper stiffener
[xd_upper,lamb_d_upper]=reduction_distortion(sigma_upper,sigma);
ratio_1=lamb_d_upper/0.65;
%for bottom stiffener
[xd_bottom,lamb_d_bottom]=reduction_distortion(sigma_bottom,sigma);
ratio_2=lamb_d_bottom/0.65;
%As_bottom_redu=As_stiff_bottom*xd_bottom*fyb/rm0/fyb;
%t_redu_bottom=t*xd_bottom;
%Calculation of the effective properties of the web
end

%%Calculation of the effective properties of the WHOLE section
new_numj=14;
new_nume=13;
new_coordinates=[bp1-cp1*cos(theta1) cp1*sin(theta1);
                bp1-ceff1*cos(theta1) ceff1*sin(theta1);
                bp1 0;
                bp1-beff12 0;
                beff11 0;
                0 0;
                0 heff1
                0 hp-heff2
                0 hp;
                beff21 hp;
                bp2-beff22 hp;
                bp2 hp;
                bp2-ceff2*cos(theta2) hp-ceff2*sin(theta2);
                bp2-cp2*cos(theta2) hp-cp2*sin(theta2)];
new_elements=[ 1 2 0;
              2 3 t*xd_bottom;
              3 4 t*xd_bottom;
              4 5 0;
              5 6 t;
              6 7 t;
              7 8 0;
              8 9 t;
              9 10 t;
              10 11 0;
              11 12 t*xd_upper;
              12 13 t*xd_upper;
              13 14 0;];
[A_eff,iy_eff,iz_eff,IY_eff,IZ_eff,XY_eff,XC_eff,YC_eff]=normal_proper
ties(new_numj,new_nume,new_coordinates,new_elements);
delta=0.43*(r*(pi-theta1)/pi^2+r+r*(pi-
theta2)/pi^2)/(hp+bp1+cp1+bp2+cp2);

```

## APPENDIX

```

A_eff=A_eff*(1-delta);
%Calculation of the shift of centroidal axis
eNz = XC_eff-XC; %shif of centroidal z-z axis
eNy = YC_eff-YC; %shif of centroidal y-y axis
ratiomax=max([ratio_1 ratio_2 ratio_3]);

function [bel,be2]=effectivelength_inter(stress_ratio,b,t,fyb)
%%%%%%%%%%%%%%%%%%%%%%%%%%%%%%%%%%%%%%%%%%%%%%%%%%%%%%%%%%%%%%%%%%%%%%%%
%%%%%%%%%%%%%%%%%%%%%%%%%%%%%%%%%%%%%%%%%%%%%%%%%%%%%%%%%%%%%%%%%%%%%%%%
% This function is used to calculate the effective properties of the
%CFS single/internal plate element in compression
% The plate is supported at two edges
%%%%%%%%%%%%%%%%%%%%%%%%%%%%%%%%%%%%%%%%%%%%%%%%%%%%%%%%%%%%%%%%%%%%%%%%
%%%%%%%%%%%%%%%%%%%%%%%%%%%%%%%%%%%%%%%%%%%%%%%%%%%%%%%%%%%%%%%%%%%%%%%%
if stress_ratio==1
    kfi=4;
elseif stress_ratio>=0&&stress_ratio<1
    kfi=8.2/(1.05+stress_ratio);
elseif stress_ratio>=-1&&stress_ratio<0
    kfi=7.81-6.29*stress_ratio+9.78*stress_ratio^2;
else
    kfi=5.98*(1-stress_ratio)^2;
end
lamdap=b/t/(28.4*sqrt(235*kfi/fyb)); %relative slenderness
if lamdap<=0.673
    ro=1;%width reduction factor for internal compression elements
else
    ro=min((lamdap-0.055*(3+stress_ratio))/lamdap^2,1);%width
reduction factor for internal compression elements
end
if stress_ratio==1
    beff=ro*b;
    bel=0.5*beff;
    be2=0.5*beff;
elseif stress_ratio>=0&&stress_ratio<1
    beff=ro*b;
    bel=2/(5-stress_ratio)*beff;
    be2=beff-bel;
else
    beff=ro*b/(1-stress_ratio);
    bel=0.4*beff;
    be2=beff-bel;
end

function [ceff]=effectivelengthe_single_edgestiffener(bpc,bp,fyb,t)
%%%%%%%%%%%%%%%%%%%%%%%%%%%%%%%%%%%%%%%%%%%%%%%%%%%%%%%%%%%%%%%%%%%%%%%%
%%%%%%%%%%%%%%%%%%%%%%%%%%%%%%%%%%%%%%%%%%%%%%%%%%%%%%%%%%%%%%%%%%%%%%%%
% This function is used to calculate the effective properties of the
CFS
% edge stiffener in compression
% The plate is supported at one edges
%%%%%%%%%%%%%%%%%%%%%%%%%%%%%%%%%%%%%%%%%%%%%%%%%%%%%%%%%%%%%%%%%%%%%%%%
%%%%%%%%%%%%%%%%%%%%%%%%%%%%%%%%%%%%%%%%%%%%%%%%%%%%%%%%%%%%%%%%%%%%%%%%
if bpc/bp<=0.35
    kfi=0.5;
elseif bpc/bp>0.35
    r4=min(bpc/bp,0.6);
    kfi=0.5+0.83*(r4-0.35)^(2/3);
end
lambda=bpc/t/(28.4*sqrt(235*kfi/fyb)); %relative slenderness
if lambda<=0.748

```

## APPENDIX

```

    ro=1;%width reduction factor for outstand compression elements
else
    ro=min((lambda-0.188)/lambda^2,1);%width reduction factor for
outstand compression elements
end
ceff=ro*bps;           %effective width of single edge fold

function
[F,iy,iz,IY,IZ,XY,XC,YC]=normal_properties(numj,nume,coordinates,elements)
%This program is to calculate the properties of arbitrary prismatic
cross section
%%%%%%%%%input data%%%%%%%%%
%numj is the number of joints of arbitrary section
%nume is the number of elements of arbitrary prismatic cross section
%numij is the number of internal joints
%array [a] is the coordinates with regard to arbitrary origin
%c=[xi yi ti] represents the start, end joint number and thickness of
each
%elements;
%%%%%%%%%output data%%%%%%%%%
% F is the total cross sectional area
% IXX,IYY,IXY are the moments of inertia about original X,Y axis and
product of
% inertia
% PSI is the angle in RAIDANS to principle axis
% IY,IZ are the moments of inertia about principle Y and Z axis.
% numj=10; %number of joints
% nume=9; %number of elements
%XC YC is the position of centroid

x=coordinates(:,1);% store the x-coordinates of the joints
y=coordinates(:,2);% store the y-coordinates of the joints
n1=elements(:,1);%first joint number of elements
n2=elements(:,2);%second joint number of elements
tt=elements(:,3);%store the thickness for every element

F=0;IXX=0;IYY=0;IXY=0;SX=0;SY=0;dd=zeros(1,nume);
for i=1:nume
    dd(i)=sqrt((x(n2(i))-x(n1(i)))^2+(y(n2(i))-y(n1(i)))^2);
    [ni,nj,y2,y1,x2,x1,d,t,s,c]=com(n1(i),n2(i),x(n2(i)),x(n1(i)), ...
y(n2(i)),y(n1(i)),dd(i),tt(i));
    F=F+d*t;
    IXX=IXX+((x2+x1)/2)^2*d*t+d*t^3/12*c^2+t*d^3*s^2/12;
    IYY=IYY+((y2+y1)/2)^2*d*t+d*t^3/12*s^2+t*d^3*c^2/12;
    IXY=IXY+(y1+y2)*(x1+x2)/4*d*t+(d*t^3/12-d^3*t/12)*s*c;
    SX=SX+x1*d*t-0.5*d^2*t*s;
    SY=SY+y1*d*t+0.5*d^2*t*c;
end
XC=SX/F;
YC=SY/F;
IXXC=IXX-XC^2*F;
IYYC=IYY-YC^2*F;
XN=zeros(1,numj);YN=zeros(1,numj);
for i=1:numj
    XIC=x(i)-XC;
    YIC=y(i)-YC;
    XN(i)=XIC;
    YN(i)=YIC;
end
IY=IYYC;
IZ=IXXC;
iy=sqrt(IY/F);

```

## APPENDIX

```
iz=sqrt (IZ/F);
XY=[XN', YN'];
```

```
function [NI, NJ, Y2, Y1, X2, X1, D, T, S, C]=com(N1, N2, XNJ, XNI, YNJ, YNI, DD, TT)
NI=N1;
NJ=N2;
X2=XNJ;
X1=XNI;
Y2=YNJ;
Y1=YNI;
D=max([DD, 0.00000000001]);
T=TT;
S=(X1-X2)/D;
C=(Y2-Y1)/D;
end
end
```

```
function [xd, lamb_d]=reduction_distortion(sigma, fyb)
%%%%%%%%%%%%%%%%%%%%%%%%%%%%%%%%%%%%%%%%%%%%%%%%%%%%%%%%%%%%%%%%%%%%%%%%
%This program is to calculate the reduction factor due to
%distortional buckling
lamb_d=(fyb/sigma)^(1/2);
if lamb_d<=0.65
    xd=1.0;
elseif lamb_d>0.65&&lamb_d<1.38
    xd=1.47-0.723*lamb_d;
else
    xd=0.66/lamb_d;
end
```

```
function [IY b F]=properties_edgestiffener(bp, beff, theta, ceff, tt, r)
%This function is to calculate the properties of an edge stiffener
assembly.
numj=3; %number of joints
nume=2; %number of elements
coordinates=[0 0;
             ceff*cos(theta) ceff*sin(theta);
             -beff+ceff*cos(theta) ceff*sin(theta)];
elements=[1 2 tt;
          2 3 tt;];
x=coordinates(:,1);% store the x-coordinates of the joints
y=coordinates(:,2);% store the y-coordinates of the joints
n1=elements(:,1);%first joint number of elements
n2=elements(:,2);%second joint number of elements
tt=elements(:,3);%store the thickness for every element

F=0; IXX=0; IYY=0; IXY=0; SX=0; SY=0; dd=zeros(1, nume);
for i=1:nume
    dd(i)=sqrt((x(n2(i))-x(n1(i)))^2+(y(n2(i))-y(n1(i)))^2);

[ni, nj, y2, y1, x2, x1, d, t, s, c]=com(n1(i), n2(i), x(n2(i)), x(n1(i)), y(n2(i)),
y(n1(i)), dd(i), tt(i));
    F=F+d*t;
    IXX=IXX+((x2+x1)/2)^2*d*t+d*t^3/12*c^2+t*d^3*s^2/12;
    IYY=IYY+((y2+y1)/2)^2*d*t+d*t^3/12*s^2+t*d^3*c^2/12;
    IXY=IXY+(y1+y2)*(x1+x2)/4*d*t+(d*t^3/12-d^3*t/12)*s*c;
    SX=SX+x1*d*t-0.5*d^2*t*s;
    SY=SY+y1*d*t+0.5*d^2*t*c;
end
XC=SX/F;
YC=SY/F;
IXXC=IXX-XC^2*F;
IYYC=IYY-YC^2*F;
```



## APPENDIX

```
XN=zeros(1,numj);YN=zeros(1,numj);
for i=1:numj
    XIC=x(i)-XC;
    YIC=y(i)-YC;
    XN(i)=XIC;
    YN(i)=YIC;
end
IY=IYYC;
IZ=IXXC;
XY=[XN',YN'];
b=bp-XY(2,1);
delta=0.43*(r*theta/pi*2)/(beff+ceff);
F=F*(1-delta);
IY=IY*(1-2*delta);
end
function [NI,NJ,Y2,Y1,X2,X1,D,T,S,C]=com(N1,N2,XNJ,XNI,YNJ,YNI,DD,TT)
NI=N1;
NJ=N2;
X2=XNJ;
X1=XNI;
Y2=YNJ;
Y1=YNI;
D=max([DD,0.00000000001]);;
T=TT;
S=(X1-X2)/D;
C=(Y2-Y1)/D;
end
```

## APPENDIX

### A.2 Computer programme to incorporate imperfections for CFS column

```
%%%%%%%%%%%%%%%%%%%%%%%%%%%%%%%%%%%%%%%%%%%%%%%%%%%%%%%%%%%%%%%%%%%%%%%%%
%This program is used to generate imperfection for tested column
%The imperfections were measured using a specially designed facility.
%%%%%%%%%%%%%%%%%%%%%%%%%%%%%%%%%%%%%%%%%%%%%%%%%%%%%%%%%%%%%%%%%%%%%%%%%
c1=17.72;
theta1=pi-pi/2;
b1=64.45;
theta2=pi/2;
h=174.94;
b2=64.09;
theta3=pi/2;
c2=18.21;
theta4=pi-pi/2;
r=3.2;
t=1.51;
%central line dimensions
c11=c1
b11=b1
h11=h
b22=b2
c22=c2
cp11=c1-t/2*tan(theta1/2);
bp11=b1-t/2*tan(theta1/2)-t/2*tan(theta2/2);
hp11=h-t/2*tan(theta2/2)-t/2*tan(theta3/2);
bp22=b2-t/2*tan(theta3/2)-t/2*tan(theta4/2);
cp22=c2-t/2*tan(theta4/2);

nplate=5; %number of plates
ncorner=nplate-1;%nuber of corners
r=[r, r, r, r];
beta=[theta1,theta2,theta3,theta4];
beta=[-pi+beta(1),beta(1),beta(2),beta(3),beta(4)];
NR=[2,2,2,2];%the number of elements for every round corner.
NP=[2,6,18,6,2];%the number of elements for every flat plate.
L=[c11,b11,h11,b22,c22];%the length of every plate
nodeco=zeros((sum(NR(:))+sum(NP)+1),2);%
%nodeco(1,:)= [0,0]
alpha=beta(1);
k=1;
for i=1:nplate-1
    for j=1:NP(i)
        nodeco(k+j,1:2)=[nodeco(k+j-
1,1)+L(i)/NP(i)*cos(alpha),nodeco(k+j-1,2)+L(i)/NP(i)*sin(alpha)];
        end
        k=k+NP(i);
        alpha=alpha-beta(i+1)/2/NR(i);
        LL=abs(2*r(i)*sin(beta(i+1)/2/NR(i)));
        k=k+1;
        nodeco(k,1:2)=[nodeco(k-1,1)+LL*cos(alpha),nodeco(k-
1,2)+LL*sin(alpha)];

        for j=1:(NR(i)-1)
            alpha=alpha-beta(i+1)/NR(i);
            nodeco(k+j,:)= [nodeco(k+j-1,1)+LL*cos(alpha), ...
nodeco(k+j-1,2)+LL*sin(alpha)];
        end
        k=k+NR(i)-1;
        alpha=alpha-beta(i+1)/2/NR(i);
end
for j=1:NP(nplate)
```

## APPENDIX

```

        nodeco(k+j,1:2)=[nodeco(k+j-
1,1)+L(i+1)/NP(length(NP))*cos(alpha),nodeco(k+j-
1,2)+L(i+1)/NP(length(NP))*sin(alpha)];
    end
%plot(nodeco(:,1),nodeco(:,2),'.');
for i=1:length(nodeco(:,1))
    nodeco(i,2)=nodeco(i,2)-(h11/2-c11);
end

nodeco2=nodeco;
%¶ÁÈÈimperfectionËÝ¼Ý
hei=1000;%length of the column
A = xlsread('imperfection.xlsx');
Alen=0:1:length(A(:,1))-1;
meshsize=10;%this is the size of mesh in the longitudinal direction
heiin=0:meshsize:1000;
nodeco3d=zeros((sum(NR(:))+sum(NP)+1)*length(heiin),3);

%Scaling facor
sf=200.0;
terms=10;
[a,b,yfit] = Fseries(Alen,A(:,1)',terms);
yi_spline1=-sf*Fseriesval(a,b,heiin);

[a,b,yfit] = Fseries(Alen,A(:,2)',terms);
yi_spline2=-sf*Fseriesval(a,b,heiin);

[a,b,yfit] = Fseries(Alen,A(:,3)',terms);
yi_spline3=-sf*Fseriesval(a,b,heiin);

[a,b,yfit] = Fseries(Alen,A(:,4)',terms);
yi_spline4=-sf*Fseriesval(a,b,heiin);

[a,b,yfit] = Fseries(Alen,A(:,5)',terms);
yi_spline5=-sf*Fseriesval(a,b,heiin);

[a,b,yfit] = Fseries(Alen,A(:,6)',terms);
yi_spline6=sf*Fseriesval(a,b,heiin);

[a,b,yfit] = Fseries(Alen,A(:,7)',terms);
yi_spline7=sf*Fseriesval(a,b,heiin);

for i=1:length(heiin)

nodeco=nodeco2;
%for the first lip
nodeco(1:NP(1),2)=nodeco(1:NP(1),2)+interp1([-b11-r(1) 0],[0
yi_spline1(i)],nodeco(1:NP(1),1),'spline');
%
nodeco(NP(1)+1:NP(1)+NR(1),2)=nodeco(NP(1)+1:NP(1)+NR(1),2)+ ...
interp1([-b11-r(1) 0],[0
yi_spline1(i)],nodeco(NP(1)+1:NP(1)+NR(1),1),'spline');

nodeco((NP(1)+NR(1)+1):(NP(1)+NR(1)+NP(2)),2)=nodeco((NP(1)+NR(1)+1):(
NP(1)+NR(1)+NP(2)),2) ...
+interp1([-b11-r(1) 0],[0
yi_spline1(i)],nodeco((NP(1)+NR(1)+1):(NP(1)+NR(1)+NP(2)),1),'spline'
)';

```

## APPENDIX

```

nodeco (length (nodeco (:,1)) - NP (5) - NR (4) - NP (4) : length (nodeco (:,1)) -
NP (5) - NR (4), 2) = nodeco (length (nodeco (:,1)) - NP (5) - NR (4) -
NP (4) : length (nodeco (:,1)) - NP (5) - NR (4), 2) ... ,
+interp1 ([-b22-r (4) 0], [0
yi_spline7 (i)], nodeco (length (nodeco (:,1)) - NP (5) - NR (4) -
NP (4) : length (nodeco (:,1)) - NP (5) - NR (4), 1), 'spline');

nodeco ( (NP (1) + NR (1) + NP (2) + NR (2) + 2) : (NP (1) + NR (1) + NP (2) + NR (2) + NP (3)), 1) =
nodeco ( (NP (1) + NR (1) + NP (2) + NR (2) + 2) : (NP (1) + NR (1) + NP (2) + NR (2) + NP (3)), 1)
... ,
+interp1 ([-h11/2 0 h11/2], [yi_spline3 (i) yi_spline4 (i)
yi_spline5 (i)], nodeco ( (NP (1) + NR (1) + NP (2) + NR (2) + 2) : (NP (1) + NR (1) + NP (2) + N
R (2) + NP (3)), 2), 'spline');

nodeco3d ( (sum (NR (:)) + sum (NP) + 1) * (i-
1) + 1 : (sum (NR (:)) + sum (NP) + 1) * i, 1:2) = nodeco;
nodeco3d ( (sum (NR (:)) + sum (NP) + 1) * (i-
1) + 1 : (sum (NR (:)) + sum (NP) + 1) * i, 3) = ones ( (sum (NR (:)) + sum (NP) + 1), 1) * (i-
1) * meshsize;

end

scatter3 (nodeco3d (:,1), nodeco3d (:,2), nodeco3d (:,3), 4, 'o');
axis equal;
for j = 1 : length (heiin)
for i = 1 : length (nodeco (:,1)) - 1
hold on;
plot3 (nodeco3d (i + (sum (NR (:)) + sum (NP) + 1) * (j-
1) : i + 1 + (sum (NR (:)) + sum (NP) + 1) * (j-
1), 1), nodeco3d (i + (sum (NR (:)) + sum (NP) + 1) * (j-
1) : i + 1 + (sum (NR (:)) + sum (NP) + 1) * (j-1), 2), ... ,
nodeco3d (i + (sum (NR (:)) + sum (NP) + 1) * (j-
1) : i + 1 + (sum (NR (:)) + sum (NP) + 1) * (j-1), 3), 'b', 'LineWidth', 1);
end
end
for j = 1 : length (heiin) - 1
for i = 1 : length (nodeco (:,1))
hold on;
plot3 (nodeco3d ([i + (sum (NR (:)) + sum (NP) + 1) * (j-1)
i + (sum (NR (:)) + sum (NP) + 1) * j], 1), nodeco3d ([i + (sum (NR (:)) + sum (NP) + 1) * (j-
1) + (sum (NR (:)) + sum (NP) + 1) * j], 2), ... ,
nodeco3d ([i + (sum (NR (:)) + sum (NP) + 1) * (j-1)
i + (sum (NR (:)) + sum (NP) + 1) * j], 3), 'b', 'LineWidth', 1);
end
end
elem = zeros ( (sum (NR (:)) + sum (NP)) * (length (heiin) - 1), 5);
for j = 1 : length (heiin) - 1
for i = 1 : length (nodeco (:,1)) - 1
% %axis off;
%axis ([min (nodeco (:,1)) - 4, max (nodeco (:,1)) + 4, min (nodeco (:,2)) -
4, max (nodeco (:,2)) + 4]);
%axis equal;
elem ( (sum (NR (:)) + sum (NP)) * (j-1) + i, 1:5) = [ (sum (NR (:)) + sum (NP)) * (j-
1) + i i + (sum (NR (:)) + sum (NP) + 1) * (j-1) i + (sum (NR (:)) + sum (NP) + 1) * j
i + 1 + (sum (NR (:)) + sum (NP) + 1) * j i + 1 + (sum (NR (:)) + sum (NP) + 1) * (j-1) ];
ax = nodeco3d ([i + (sum (NR (:)) + sum (NP) + 1) * (j-1)
i + (sum (NR (:)) + sum (NP) + 1) * j i + 1 + (sum (NR (:)) + sum (NP) + 1) * j
i + 1 + (sum (NR (:)) + sum (NP) + 1) * (j-1)], 1);
ay = nodeco3d ([i + (sum (NR (:)) + sum (NP) + 1) * (j-1)
i + (sum (NR (:)) + sum (NP) + 1) * j i + 1 + (sum (NR (:)) + sum (NP) + 1) * j
i + 1 + (sum (NR (:)) + sum (NP) + 1) * (j-1)], 2);

```

## APPENDIX

```
    az=nodeco3d([i+(sum(NR(:))+sum(NP)+1)*(j-1)
i+(sum(NR(:))+sum(NP)+1)*j i+1+(sum(NR(:))+sum(NP)+1)*j
i+1+(sum(NR(:))+sum(NP)+1)*(j-1)],3);
    fill3(ax,ay,az,'red')
    hold on;
end
end
```

## APPENDIX

### A.3 Computer programme to incorporate imperfections for CFS beam

```
%This program is used to generate imperfection for tested beam.
%The imperfections were measured using a specially designed facility.
c1=17.72;
thetal=pi-pi/2;
b1=64.45;
theta2=pi/2;
h=174.94;
b2=64.09;
theta3=pi/2;
c2=18.21;
theta4=pi-pi/2;
r=3.2;
t=1.51;
%central line dimensions
c11=c1;
b11=b1;
h11=h;
b22=b2;
c22=c2;
%dimensions measured to the points of intersection of their middle
%lines--used for the calculation of effective cross-section
properties.
cp11=c1-t/2*tan(theta1/2);
bp11=b1-t/2*tan(theta1/2)-t/2*tan(theta2/2);
hp11=h-t/2*tan(theta2/2)-t/2*tan(theta3/2);
bp22=b2-t/2*tan(theta3/2)-t/2*tan(theta4/2);
cp22=c2-t/2*tan(theta4/2);

nplate=5; %number of plates
ncorner=nplate-1;%nuber of corners
r=[r,r,r,r];
beta=[thetal,theta2,theta3,theta4];
beta=[-pi+beta(1),beta(1),beta(2),beta(3),beta(4)];
NR=[2,2,2,2];%the number of elements for every round corner.
NP=[2,6,18,6,2];%the number of elements for every flat plate.
L=[c11,b11,h11,b22,c22];%the length of every plate
nodeco=zeros((sum(NR(:))+sum(NP)+1),2);%
%nodeco(1,:)= [0,0]
alpha=beta(1);
k=1;
for i=1:nplate-1
    for j=1:NP(i)
        nodeco(k+j,1:2)=[nodeco(k+j-
1,1)+L(i)/NP(i)*cos(alpha),nodeco(k+j-1,2)+L(i)/NP(i)*sin(alpha)];
    end
    k=k+NP(i);
    alpha=alpha-beta(i+1)/2/NR(i);
    LL=abs(2*r(i)*sin(beta(i+1)/2/NR(i)));
    k=k+1;
    nodeco(k,1:2)=[nodeco(k-1,1)+LL*cos(alpha),nodeco(k-
1,2)+LL*sin(alpha)];

    for j=1:(NR(i)-1)
        alpha=alpha-beta(i+1)/NR(i);
        nodeco(k+j,:)=[nodeco(k+j-1,1)+LL*cos(alpha),nodeco(k+j-
1,2)+LL*sin(alpha)];
    end
    k=k+NR(i)-1;
    alpha=alpha-beta(i+1)/2/NR(i);
end
for j=1:NP(nplate)
```

## APPENDIX

```

        nodeco(k+j,1:2)=[nodeco(k+j-
1,1)+L(i+1)/NP(length(NP))*cos(alpha),nodeco(k+j-
1,2)+L(i+1)/NP(length(NP))*sin(alpha)];
    end
%plot(nodeco(:,1),nodeco(:,2),'.');
for i=1:length(nodeco(:,1))
    nodeco(i,2)=nodeco(i,2)-(h11/2-c11);
end

nodeco2=nodeco;
hei=3300;%length of the column
A = xlsread('imperfection.xlsx');
Alen=0:1:length(A(:,1))-1;
meshsize=10;%this is the size of mesh in the longitudinal direction
heiin=0:meshsize:hei;
nodeco3d=zeros((sum(NR(:))+sum(NP)+1)*length(heiin),3);
%Scaling facor
sf=200.0;
terms=10;
[a,b,yfit] = Fseries(Alen,A(:,1)',terms);
yi_spline1=-sf*Fseriesval(a,b,heiin);

[a,b,yfit] = Fseries(Alen,A(:,2)',terms);
yi_spline2=-sf*Fseriesval(a,b,heiin);

[a,b,yfit] = Fseries(Alen,A(:,3)',terms);
yi_spline3=-sf*Fseriesval(a,b,heiin);

[a,b,yfit] = Fseries(Alen,A(:,4)',terms);
yi_spline4=-sf*Fseriesval(a,b,heiin);

[a,b,yfit] = Fseries(Alen,A(:,5)',terms);
yi_spline5=-sf*Fseriesval(a,b,heiin);

[a,b,yfit] = Fseries(Alen,A(:,6)',terms);
yi_spline6=sf*Fseriesval(a,b,heiin);

[a,b,yfit] = Fseries(Alen,A(:,7)',terms);
yi_spline7=sf*Fseriesval(a,b,heiin);

for i=1:length(heiin)

nodeco=nodeco2;
%for the first lip
nodeco(1:NP(1),2)=nodeco(1:NP(1),2)+interp1([-b11-r(1) 0],[0
yi_spline1(i)],nodeco(1:NP(1),1),'spline');
%
%for the first round corner
nodeco(NP(1)+1:NP(1)+NR(1),2)=nodeco(NP(1)+1:NP(1)+NR(1),2)+interp1([-
b11-r(1) 0],[0
yi_spline1(i)],nodeco(NP(1)+1:NP(1)+NR(1),1),'spline');

%for the second flat plate
nodeco((NP(1)+NR(1)+1):(NP(1)+NR(1)+NP(2)),2)=nodeco((NP(1)+NR(1)+1):(
NP(1)+NR(1)+NP(2)),2) +interp1([-b11-r(1) 0],[0
yi_spline1(i)],nodeco((NP(1)+NR(1)+1):(NP(1)+NR(1)+NP(2)),1),'spline'
)';

```

## APPENDIX

```

%for the last lip and corner
nodeco(length(nodeco(:,1))-NP(5)-
NR(4)+1:length(nodeco(:,1)),2)=nodeco(length(nodeco(:,1))-NP(5)-
NR(4)+1:length(nodeco(:,1)),2) ...,
+interp1([-b22-r(4) 0],[0
yi_spline7(i)],nodeco(length(nodeco(:,1))-NP(5)-
NR(4)+1:length(nodeco(:,1)),1),'spline');

%for the third flat plate

nodeco((NP(1)+NR(1)+NP(2)+NR(2)+2):(NP(1)+NR(1)+NP(2)+NR(2)+NP(3)),1)=
nodeco((NP(1)+NR(1)+NP(2)+NR(2)+2):(NP(1)+NR(1)+NP(2)+NR(2)+NP(3)),1)
...,
+interp1([-h11/2 0 h11/2],[yi_spline3(i) yi_spline4(i)
yi_spline5(i)],nodeco((NP(1)+NR(1)+NP(2)+NR(2)+2):(NP(1)+NR(1)+NP(2)+N
R(2)+NP(3)),2),'spline');

nodeco3d((sum(NR(:))+sum(NP)+1)*(i-
1)+1:(sum(NR(:))+sum(NP)+1)*i,1:2)=nodeco;
nodeco3d((sum(NR(:))+sum(NP)+1)*(i-
1)+1:(sum(NR(:))+sum(NP)+1)*i,3)=ones((sum(NR(:))+sum(NP)+1),1)*(i-
1)*meshsize;
end

elem=zeros((sum(NR(:))+sum(NP))*(length(heiin)-1),5);
for j=1:length(heiin)-1
for i=1:length(nodeco(:,1))-1
% axis off;
axis([min(nodeco(:,1))-4, max(nodeco(:,1))+4, min(nodeco(:,2))-
4,max(nodeco(:,2))+4]);
axis equal;
elem((sum(NR(:))+sum(NP))*(j-1)+i,1:5)=[(sum(NR(:))+sum(NP))*(j-
1)+i i+(sum(NR(:))+sum(NP)+1)*(j-1) i+(sum(NR(:))+sum(NP)+1)*j
i+1+(sum(NR(:))+sum(NP)+1)*j i+1+(sum(NR(:))+sum(NP)+1)*(j-1)];
ax=nodeco3d([i+(sum(NR(:))+sum(NP)+1)*(j-1)
i+(sum(NR(:))+sum(NP)+1)*j i+1+(sum(NR(:))+sum(NP)+1)*j
i+1+(sum(NR(:))+sum(NP)+1)*(j-1)],1);
ay=nodeco3d([i+(sum(NR(:))+sum(NP)+1)*(j-1)
i+(sum(NR(:))+sum(NP)+1)*j i+1+(sum(NR(:))+sum(NP)+1)*j
i+1+(sum(NR(:))+sum(NP)+1)*(j-1)],2);
az=nodeco3d([i+(sum(NR(:))+sum(NP)+1)*(j-1)
i+(sum(NR(:))+sum(NP)+1)*j i+1+(sum(NR(:))+sum(NP)+1)*j
i+1+(sum(NR(:))+sum(NP)+1)*(j-1)],3);
fill3(ax,ay,az,'red')
hold on;
end
end

```



## APPENDIX

### A.4 Computer programme to mesh CFS cross-section

```
%This program is used to generate the centreline element model for
CUFSM analysis
c11=6;
theta1=pi-2.356;
c12=17;
theta2=2*pi/4;
b1=39;
theta3=pi/2;
h=197.3;
b2=39;
theta5=pi/2;
c21=6;
theta6=2*pi/4;
c22=17;
theta7=pi-2.356;
theta4=pi/2;           %Angle between the intermediate stiffener
r=2.5;
s=10;                 %Dimension of the intermediate stiffener
RL1=13; %Distance from the intermedate stiffener intersection to the
bottom flange, change the 0.5 coeffecient
RL2=143;
RL3=RL1;
t=1.2;
%central line dimensions
c11=c11-(r+t)*tan(theta1/2);
c12=c12-(r+t)*tan(theta1/2)-(r+t)*tan(theta2/2);
b11=b1-(r+t)*tan(theta2/2)-(r+t)*tan(theta3/2);
b22=b2-(r+t)*tan(theta7/2)-(r+t)*tan(theta6/2);
c21=c21-(r+t)*tan(theta7/2);
c22=c22-(r+t)*tan(theta6/2)-(r+t)*tan(theta7/2);
RL11=RL1-(r+t)*tan(theta3/2)-(r+t)*tan((pi-theta4)/4);
RL22=RL2-2*(r+t)*tan((pi-theta4)/4);
RL33=RL3-(r+t)*tan(theta4/2)-(r+t)*tan((pi-theta5)/4);
s=s-(r+t)*tan((pi-theta4)/2)-(r+t)*tan((pi-theta4)/4);
%dimensions measured to the points of intersection of their middle
%lines--used for the calculation of effective cross-section
properties.
cp11=c11-t/2*tan(theta1/2);
cp12=c12-t/2*tan(theta1/2)-t/2*tan(theta2/2);
bp11=b1-t/2*tan(theta2/2)-t/2*tan(theta3/2);
bp22=b2-t/2*tan(theta7/2)-t/2*tan(theta6/2);
cp21=c21-t/2*tan(theta7/2);
cp22=c22-t/2*tan(theta6/2)-t/2*tan(theta7/2);
RLp11=RL1-t/2*tan(theta3/2)-t/2*tan((pi-theta4)/4);
RLp22=RL2-2*t/2*tan((pi-theta4)/4);
RLp33=RL3-t/2*tan(theta4/2)-t/2*tan((pi-theta5)/4);
sp=s-t/2*tan((pi-theta4)/2)-t/2*tan((pi-theta4)/4);

nplate=13; %number of plates
ncorner=nplate-1;%nuber of corners
r=[r,r,r,r,r,r,r,r,r,r,r,r,r];
beta=[theta1,theta2,theta3,(pi-theta4)/2,-(pi-theta4),(pi-
theta4)/2,(pi-theta4)/2,-(pi-theta4),(pi-
theta4)/2,theta5,theta6,theta7];
beta=[-pi/2+beta(1),beta(1:12)];
NR=[4,4,4,4,4,4,4,4,4,4,4,4,4];%the number of elements for every round
corner.
NP=[4,4,4,2,2,2,15,2,2,2,4,4,4];%the number of elements for every
plate.
L=[c11,c12,b11,RL11,s,s,RL22,s,s,RL33,b22,c22,c21];%the length of
every plate
```

## APPENDIX

```

nodeco=zeros((sum(NR(:))+sum(NP)+1),2);%
%nodeco(1,:)= [0,0]
alpha=beta(1);
k=1;
for i=1:nplate-1
    for j=1:NP(i)
        nodeco(k+j,1:2)=[nodeco(k+j-
1,1)+L(i)/NP(i)*cos(alpha),nodeco(k+j-1,2)+L(i)/NP(i)*sin(alpha)];
    end
    k=k+NP(i);
    alpha=alpha-(beta(i+1)/2/NR(i));
    LL=abs(2*r(i)*sin(beta(i+1)/2/NR(i)));
    k=k+1;
    nodeco(k,1:2)=[nodeco(k-1,1)+LL*cos(alpha),nodeco(k-
1,2)+LL*sin(alpha)];

    for j=1:(NR(i)-1)
        alpha=alpha-(beta(i+1)/NR(i));
        nodeco(k+j,:)=[nodeco(k+j-1,1)+LL*cos(alpha),nodeco(k+j-
1,2)+LL*sin(alpha)];
    end
    k=k+NR(i)-1;
    alpha=alpha-(beta(i+1)/2/NR(i));
end
for j=1:NP(nplate)
    nodeco(k+j,1:2)=[nodeco(k+j-
1,1)+L(i+1)/NP(length(NP))*cos(alpha),nodeco(k+j-
1,2)+L(i+1)/NP(length(NP))*sin(alpha)];
end
%plot(nodeco(:,1),nodeco(:,2),'.');
scatter(nodeco(:,1),nodeco(:,2),4,'o');
for i=1:length(nodeco(:,1))-1
%    %axis off;
    axis([min(nodeco(:,1))-4, max(nodeco(:,1))+4, min(nodeco(:,2))-
4,max(nodeco(:,2))+4]);
    hold on;
    plot(nodeco(i:i+1,1),nodeco(i:i+1,2),'g','LineWidth',1);
end

```

## APPENDIX

### A.5 Python script to generate ABAQUS model for CFS connection modelling (curved section with circular bolt distribution)

```
from part import *
from material import *
from section import *
from assembly import *
from step import *
from interaction import *
from load import *
from mesh import *
from job import *
from sketch import *
from visualization import *
from connectorBehavior import *
from abaqus import *
from abaqusConstants import *
myModel = mdb.Model(name='Connection')
#Dimentionions
#####Column channel#####
ch = 300; cb = 150; ##profile dimenstions:web height, flange
width, lip length
mc = 9; nc = 2; ##number of bolt rows and
columns
vc = 50; hc = 200; ##bolt hole distance
lc = 900; ##column height
tc=10;
ctheta=pi/2;
tg = 8
#####Beam channel#####
#import numpy as np
R = 40;
thetal = pi;
h = 200; ##profile dimenstions:web height, flange width, lip
length
hbolts=h-30;
lb = 2100; ##beam height
tb=3; ##thickness of beam
udisp=1; ##displacement applied
imperf=h/200.0; ##imperfection applied
#mb = 3; nb = 3; ##number of bolt rows and
columns
#vb = 85; hb = 85; ##bolt hole distance
mb=8;
rb=85;
xb = 135;
slipage=2;
distanceb=((tg/2.0+tb/2.0)**2+slipage**2)**(0.5);
distancec=((tg/2.0+tc/2.0)**2+slipage**2)**(0.5);
#####Gusset plate#####
vedge = 75;hedge=60; edgev=150; edgeh=50; ##vertical and
horizontal edge distance of bolts
bp1 = 320; ##left width of gusset plate, 10mm is the
redundant length.
bp2 = 400-100-30; ##right width of
gusset plate
```

## APPENDIX

```
hp1 = 550;                                ##left height of
gusset plate.
hp2 = 250;                                ##right width of gusset plate, 10mm is the
redundant length.
xp = xb+bp1;
tbstiff=10;
tcstiff=10;
#####Gusset plate profile#####

mySketchG = myModel.ConstrainedSketch(name='Gussetprofile',
sheetSize=bp1+bp2+50)
mySketchG.Line(point1=(-bp1/2.0, hp1/2.0), point2=(bp1/2.0+50,
hp1/2.0))
mySketchG.Line(point1=(bp1/2.0+50, hp1/2.0), point2=(bp1/2.0+bp2,
hp2/2.0))
mySketchG.Line(point1=(bp1/2.0+bp2, hp2/2.0),
point2=(bp1/2.0+bp2, -hp2/2.0))
mySketchG.Line(point1=(bp1/2.0+bp2, -hp2/2.0),
point2=(bp1/2.0+50, -hp1/2.0))
mySketchG.Line(point1=(bp1/2.0+50, -hp1/2.0), point2=(-bp1/2.0,
-hp1/2.0))
mySketchG.Line(point1=(-bp1/2.0, -hp1/2.0), point2=(-bp1/2.0,
hp1/2.0))

myPartgusset = myModel.Part(name='Gussetplate',
dimensionality=THREE_D,
type=DEFORMABLE_BODY)
myPartgusset.BaseShell(sketch=mySketchG)

#####Partition of
plate#####
t =
myPartgusset.MakeSketchTransform(sketchPlane=myPartgusset.faces.
findAt((0.0,0.0,0.0)), sketchPlaneSide=SIDE1, origin=(0.0,
0.0,0.0))
sketch1 = myModel.ConstrainedSketch(name='__profile__',
sheetSize=bp1+bp2, gridSpacing=50, transform=t)
myPartgusset.projectReferencesOntoSketch(sketch=sketch1,
filter=COPLANAR_EDGES)

##left
j=- (nc-1)/2.0
while (j<=(nc-1)/2.0):
    i=- (mc-1)/2.0
    while (i<=(mc-1)/2.0-1):
        sketch1.Line(point1=(j*hc,i*vc),
point2=(j*hc, (i+1)*vc))
        i=i+1
    j=j+1

i=- (mc-1)/2.0
while (i<=(mc-1)/2.0):
    j=- (nc-1)/2.0
    while (j<=(nc-1)/2.0-1):
        sketch1.Line(point1=(j*hc,i*vc),
point2=((j+1)*hc,i*vc))
```

## APPENDIX

```

        j=j+1
    i=i+1

##right
sketch1.CircleByCenterPerimeter(center=(0.0+xp-bp1/2.0, 0.0),
point1=(rb+xp-bp1/2.0, 0.0))

for i in range(0, mb):
    sketch1.Line(point1=(0.0+xp-bp1/2.0,0.0),
point2=(rb*cos(2*pi/mb*i)+xp-bp1/2.0, rb*sin(2*pi/mb*i)))

myPartgusset.PartitionFaceBySketch(faces=myPartgusset.faces.find
At((0, 0, 0)), sketch=sketch1)
sketch1.unsetPrimaryObject()
del myModel.sketches['__profile__']

#####Beam profile#####
mySketchB = myModel.ConstrainedSketch(name='Bprofile',
sheetSize=500.0)
xy1=[(R*(1-cos(theta1)) +tg/2.0+tb/2.0, -R*sin(theta1)-
h/2.0), (R+tg/2.0+tb/2.0 , -h/2.0) , (0 +tg/2.0+tb/2.0, -h/2.0) ,
(0 +tg/2.0+tb/2.0, 0), (0+tg/2.0+tb/2.0 ,
h/2.0), (R+tg/2.0+tb/2.0 , h/2.0) , (R*(1-
cos(theta1))+tg/2.0+tb/2.0 , R*sin(theta1)+h/2.0)]

mySketchB.ArcByCenterEnds(center=xy1[1], point1=xy1[0],
point2=xy1[2],
direction=CLOCKWISE)
mySketchB.Line(point1 = xy1[2], point2 = xy1[3])
mySketchB.Line(point1 = xy1[3], point2 = xy1[4])
mySketchB.ArcByCenterEnds(center=xy1[5], point1=xy1[6],
point2=xy1[4],
direction=COUNTERCLOCKWISE)

xy2=[(-R*(1-cos(theta1)) -tg/2.0-tb/2.0, -R*sin(theta1)-
h/2.0), (-R-tg/2.0-tb/2.0 , -h/2.0) , (0-tg/2.0-tb/2.0, -h/2.0) ,
(0-tg/2.0-tb/2.0, 0),
(0-tg/2.0-tb/2.0 , h/2.0), (-R-tg/2.0-tb/2.0 ,
h/2.0) , (-R*(1-cos(theta1))-tg/2.0-tb/2.0 , R*sin(theta1)+h/2.0)]

mySketchB.ArcByCenterEnds(center=xy2[1], point1=xy2[0],
point2=xy2[2],
direction=COUNTERCLOCKWISE)
mySketchB.Line(point1 = xy2[2], point2 = xy2[3])
mySketchB.Line(point1 = xy2[3], point2 = xy2[4])
mySketchB.ArcByCenterEnds(center=xy2[5], point1=xy2[6],
point2=xy2[4],
direction=CLOCKWISE)

#####Beam Part#####
myPartbeam = myModel.Part(name='Beam', dimensionality=THREE_D,
type=DEFORMABLE_BODY)
myPartbeam.BaseShellExtrude(sketch=mySketchB, depth=lb)
axis1=myPartbeam.DatumAxisByTwoPoint(point1=(0.0, 0.0,
0.0),point2=(0.0,0.0,lb))

```

## APPENDIX

```
datums=myPartbeam.datums

t =
myPartbeam.MakeSketchTransform(sketchPlane=myPartbeam.faces.find
At((0.0+tg/2.0+tb/2.0,0.0,lb/2.0)),
sketchUpEdge=myPartbeam.edges.findAt((0.0+tg/2.0+tb/2.0,0.0,0)),
    sketchPlaneSide=SIDE1, origin=(0.0+tg/2.0+tb/2.0, 0.0, 0.0))
sketch1 =
mdb.models['Connection'].ConstrainedSketch(name='__profile__',
    sheetSize=4219.01, gridSpacing=105.47, transform=t)
sketch1.setPrimaryObject(option=SUPERIMPOSE)
myPartbeam.projectReferencesOntoSketch(sketch=sketch1,
filter=COPLANAR_EDGES)

partitionplace=[500 , 1000, 1500];
for i in range(len(partitionplace)):
    sketch1.Line(point1=(-partitionplace[i],0.0-hbolts/2.0),
point2=(-partitionplace[i],0.0+hbolts/2.0))

sketch1.CircleByCenterPerimeter(center=(0.0-xb, 0.0), point1=(-
rb-xb, 0.0))

for i in range(0, mb):
    sketch1.Line(point1=(0.0-xb,0.0), point2=(-
rb*cos(2*pi/mb*i)-xb, rb*sin(2*pi/mb*i)))

myPartbeam.PartitionFaceBySketchThruAll(sketchPlane=myPartbeam.f
aces.findAt((0.0+tg/2.0+tb/2.0,0.0,lb/2.0)),
sketchUpEdge=myPartbeam.edges.findAt((0.0+tg/2.0+tb/2.0,0.0,0)),

faces=myPartbeam.faces.findAt(((0.0+tg/2.0+tb/2.0,0.0,lb/2.0),),
((0.0-tg/2.0-tb/2.0,0.0,lb/2.0),)),sketchPlaneSide=SIDE1,
sketch=sketch1)
sketch1.unsetPrimaryObject()
del myModel.sketches['__profile__']

#####partition for the web ties and lateral
restraints#####

#reference point for load
P1=myPartbeam.ReferencePoint(point=(0.0, 0.0, lb));
#refPoints=(R1[12], )
Q2 = myPartbeam.referencePoints;
refPoints1=(Q2[P1.id], );
myPartbeam.Set(referencePoints=refPoints1, name='endnode');

## For beam : end cross-sections and start cross-sections for
fix end
EE = []
FF = []
V1 = myPartbeam.edges.findAt((R*(1-
cos(theta1/2.0))+tg/2.0+tb/2.0 , -R*sin(theta1/2.0)-h/2.0 , 0),)
V2 = myPartbeam.edges.findAt((R*(1-cos(theta1/2.0))
+tg/2.0+tb/2.0 , -R*sin(theta1/2.0)-h/2.0 , lb),)
```

## APPENDIX

```

EE.append(V1)
FF.append(V2)
V1 = myPartbeam.edges.findAt((( -R*(1-cos(theta1/2.0))-tg/2.0-
tb/2.0 , -R*sin(theta1/2.0)-h/2.0 , 0),))
V2 = myPartbeam.edges.findAt((( -R*(1-cos(theta1/2.0))-tg/2.0-
tb/2.0 , -R*sin(theta1/2.0)-h/2.0 , lb),))
EE.append(V1)
FF.append(V2)
V1=
myPartbeam.edges.findAt((((xy1[2][0]+xy1[3][0])/2.0,(xy1[2][1]+x
y1[3][1])/2.0,0),))
V2=
myPartbeam.edges.findAt((((xy1[2][0]+xy1[3][0])/2.0,(xy1[2][1]+x
y1[3][1])/2.0,lb),))
EE.append(V1)
FF.append(V2)
V1=
myPartbeam.edges.findAt((((xy1[3][0]+xy1[4][0])/2.0,(xy1[3][1]+x
y1[4][1])/2.0,0),))
V2=
myPartbeam.edges.findAt((((xy1[3][0]+xy1[4][0])/2.0,(xy1[3][1]+x
y1[4][1])/2.0,lb),))
EE.append(V1)
FF.append(V2)
V1=
myPartbeam.edges.findAt((((xy2[2][0]+xy2[3][0])/2.0,(xy2[2][1]+x
y2[3][1])/2.0,0),))
V2=
myPartbeam.edges.findAt((((xy2[2][0]+xy2[3][0])/2.0,(xy2[2][1]+x
y2[3][1])/2.0,lb),))
EE.append(V1)
FF.append(V2)
V1=
myPartbeam.edges.findAt((((xy2[3][0]+xy2[4][0])/2.0,(xy2[3][1]+x
y2[4][1])/2.0,0),))
V2=
myPartbeam.edges.findAt((((xy2[3][0]+xy2[4][0])/2.0,(xy2[3][1]+x
y2[4][1])/2.0,lb),))
EE.append(V1)
FF.append(V2)
V1 = myPartbeam.edges.findAt(((R*(1-
cos(theta1/2.0))+tg/2.0+tb/2.0 , R*sin(theta1/2.0)+h/2.0 , 0),))
V2 = myPartbeam.edges.findAt(((R*(1-cos(theta1/2.0))
+tg/2.0+tb/2.0 , R*sin(theta1/2.0)+h/2.0 , lb),))
EE.append(V1)
FF.append(V2)
V1 = myPartbeam.edges.findAt((( -R*(1-cos(theta1/2.0))-tg/2.0-
tb/2.0 , R*sin(theta1/2.0)+h/2.0 , 0),))
V2 = myPartbeam.edges.findAt((( -R*(1-cos(theta1/2.0))-tg/2.0-
tb/2.0 , R*sin(theta1/2.0)+h/2.0 , lb),))
EE.append(V1)
FF.append(V2)

myPartbeam.Set(edges=EE,name='beamstart')
myPartbeam.Set(edges=FF,name='beamend')

## For beam : tie master lines
ETM=[]

```

## APPENDIX

```

for i in range(len(partitionplace)):
    V3 =
myPartbeam.vertices.findAt(((0.0+tg/2.0+tb/2.0,hbolts/2.0,partit
ionplace[i]),),((0.0+tg/2.0+tb/2.0,-
hbolts/2.0,partitionplace[i]),))
    ETM.append(V3)

myPartbeam.Set(vertices=ETM,name='mastertie')
## For beam : tie slave lines

ETS=[]
for i in range(len(partitionplace)):
    V4 = myPartbeam.vertices.findAt(((0.0-tg/2.0-
tb/2.0,hbolts/2.0,partitionplace[i]),),((0.0-tg/2.0-tb/2.0,-
hbolts/2.0,partitionplace[i]),))
    ETS.append(V4)

myPartbeam.Set(vertices=ETS,name='slavetie')

## For beam : lateral restraints
ltplace=[500,1000,1500];

for i in range(len(ltplace)):
    d = myPartbeam.DatumPointByCoordinate(coords =
(0.0,0.0,ltplace[i]))
    myfaces= myPartbeam.faces
    e=myPartbeam.DatumPlaneByPointNormal(point=datums[d.id],
normal=datums[axis1.id])
    myPartbeam.PartitionFaceByDatumPlane(datumPlane=datums[e.i
d], faces=myfaces)

LT=[]
for i in range(len(ltplace)):
    V1 = myPartbeam.edges.findAt(((R*(1-
cos(theta1/2.0))+tg/2.0+tb/2.0 , -R*sin(theta1/2.0)-h/2.0 ,
ltplace[i]),))
    LT.append(V1)
    V1 = myPartbeam.edges.findAt(((R*(1-
cos(theta1/2.0))+tg/2.0+tb/2.0 , R*sin(theta1/2.0)+h/2.0 ,
ltplace[i]),))
    LT.append(V1)
    V1 = myPartbeam.edges.findAt(((R*(1-cos(theta1/2.0))-
tg/2.0-tb/2.0 , -R*sin(theta1/2.0)-h/2.0 , ltplace[i]),))
    LT.append(V1)
    V1 = myPartbeam.edges.findAt(((R*(1-cos(theta1/2.0))-
tg/2.0-tb/2.0 , R*sin(theta1/2.0)+h/2.0 , ltplace[i]),))
    LT.append(V1)
    i=i+1;

myPartbeam.Set(edges=LT,name='beamlateral')

#####Column profile#####
mySketchC = myModel.ConstrainedSketch(name='Cprofile',
sheetSize=500.0)
xyc1=[(cb+tg/2.0+tc/2.0 , -ch/2.0),(0+tg/2.0+tc/2.0 , -
ch/2.0),(0+tg/2.0+tc/2.0 , 0),(0+tg/2.0+tc/2.0 ,
ch/2.0),(cb+tg/2.0+tc/2.0 , ch/2.0)];

```



## APPENDIX

```

for i in range(len(xyc1)-1):
    mySketchC.Line(point1 = xyc1[i], point2 = xyc1[i+1])

xyc2=[(-cb-tg/2.0-tc/2.0 , -ch/2.0),(0-tg/2.0-tc/2.0 , -
ch/2.0),(0-tg/2.0-tc/2.0 , 0),(0-tg/2.0-tc/2.0 , ch/2.0),(-cb-
tg/2.0-tc/2.0 , ch/2.0)];

for i in range(len(xyc2)-1):
    mySketchC.Line(point1 = xyc2[i], point2 = xyc2[i+1])

#####Column Part#####
myPartcolumn = myModel.Part(name='Column',
dimensionality=THREE_D,
type=DEFORMABLE_BODY)
myPartcolumn.BaseShellExtrude(sketch=mySketchC, depth=lc)
axis1=myPartcolumn.DatumAxisByTwoPoint(point1=(tg/2.0+tc/2.0,0.0
,lc/2.0),point2=(tg/2.0+tc/2.0,0.0,lc))
axis2=myPartcolumn.DatumAxisByTwoPoint(point1=(tg/2.0+tc/2.0,0.0
,lc/2.0),point2=(tg/2.0+tc/2.0,ch,lc/2.0))
datums=myPartcolumn.datums =
myPartcolumn.MakeSketchTransform(sketchPlane=myPartcolumn.faces.
findAt((0.0+tg/2.0+tc/2.0,0.0,lc/2.0)),
sketchUpEdge=myPartcolumn.edges.findAt((0.0+tg/2.0+tc/2.0,0.0,0)
),
sketchPlaneSide=SIDE1, origin=(0.0+tg/2.0+tc/2.0,0.0, 0.0))
sketch1 =
mdb.models['Connection'].ConstrainedSketch(name='__profile__',
sheetSize=4219.01, gridSpacing=105.47, transform=t)
sketch1.setPrimaryObject(option=SUPERIMPOSE)
myPartcolumn.projectReferencesOntoSketch(sketch=sketch1,
filter=COPLANAR_EDGES)

j=- (nc-1)/2.0
while (j<=(nc-1)/2.0):
    i=- (mc-1)/2.0
    while (i<=(mc-1)/2.0-1):
        sketch1.Line(point1=(-lc/2.0-i*vc,j*hc), point2=(-
lc/2.0-(i+1)*vc,j*hc))
        i=i+1
    j=j+1

i=- (mc-1)/2.0
while (i<=(mc-1)/2.0):
    j=- (nc-1)/2.0
    while (j<=(nc-1)/2.0-1):
        sketch1.Line(point1=(-lc/2.0-i*vc,j*hc), point2=(-
lc/2.0-i*vc,(j+1)*hc))
        j=j+1
    i=i+1

myPartcolumn.PartitionFaceBySketchThruAll(sketchPlane=myPartcolu
mn.faces.findAt((0.0+tg/2.0+tc/2.0,0.0,lc/2.0)),
sketchUpEdge=myPartcolumn.edges.findAt((0.0+tg/2.0+tc/2.0,0.0,0)
),
),
faces=myPartcolumn.faces.findAt(((0.0+tg/2.0+tc/2.0,0.0,lc/2.0),
),(0.0-tg/2.0-tc/2.0,0.0,lc/2.0)),sketchPlaneSide=SIDE1,
sketch=sketch1)

```

## APPENDIX

```
sketch1.unsetPrimaryObject()
del myModel.sketches['__profile__']

## For column : top and bottom cross-sections
EE = []
FF = []
for i in range(len(xyc1)-1):
    V1 =
myPartcolumn.edges.findAt(((xyc1[i][0]+xyc1[i+1][0])/2.0, (xyc1[
i][1]+xyc1[i+1][1])/2.0,0),))
    V2 =
myPartcolumn.edges.findAt(((xyc1[i][0]+xyc1[i+1][0])/2.0, (xyc1[
i][1]+xyc1[i+1][1])/2.0,lc),))
    EE.append(V1)
    FF.append(V2)
V1=
myPartcolumn.edges.findAt(((xyc2[i][0]+xyc2[i+1][0])/2.0, (xyc2[
i][1]+xyc2[i+1][1])/2.0,0),))
    V2=
myPartcolumn.edges.findAt(((xyc2[i][0]+xyc2[i+1][0])/2.0, (xyc2[
i][1]+xyc2[i+1][1])/2.0,lc),))
    EE.append(V1)
    FF.append(V2)

myPartcolumn.Set(edges=EE,name='columnbottom')
myPartcolumn.Set(edges=FF,name='columntop')

#####COLUMN stiffener
profile#####
mySketchSC = myModel.ConstrainedSketch(name='SCprofile',
sheetSize=500.0)
xySC1=[(cb+tg/2.0+tc/2.0 , -ch/2.0),(0+tg/2.0+tc/2.0 , -
ch/2.0),(0+tg/2.0+tc/2.0 , 0),(0+tg/2.0+tc/2.0 ,
ch/2.0),(cb+tg/2.0+tc/2.0 , ch/2.0)];

for i in range(len(xySC1)-1):
    mySketchSC.Line(point1 = xySC1[i], point2 = xySC1[i+1])

mySketchSC.Line(point1 = xySC1[i+1], point2 = xySC1[0])

xySC2=[(-cb-tg/2.0-tc/2.0 , -ch/2.0),(0-tg/2.0-tc/2.0 , -
ch/2.0),(0-tg/2.0-tc/2.0 , 0),(0-tg/2.0-tc/2.0, ch/2.0),(-cb-
tg/2.0-tc/2.0, ch/2.0)];

for i in range(len(xySC2)-1):
    mySketchSC.Line(point1 = xySC2[i], point2 = xySC2[i+1])

mySketchSC.Line(point1 = xySC2[i+1], point2 = xySC2[0])
#####COLUMN stiffener
part#####
myPartstiffC = myModel.Part(name='StiffenerC',
dimensionality=THREE_D,
type=DEFORMABLE_BODY)
myPartstiffC.BaseShell(sketch=mySketchSC)

CSTIFFSLAVE = []
```

## APPENDIX

```

for i in range(len(xySC1)-1):
    V1 =
myPartstiffC.edges.findAt((((xySC1[i][0]+xySC1[i+1][0])/2.0, (xyS
C1[i][1]+xySC1[i+1][1])/2.0,0.0),))
    CSTIFFSLAVE.append(V1)
    V1=
myPartstiffC.edges.findAt((((xySC2[i][0]+xySC2[i+1][0])/2.0, (xyS
C2[i][1]+xySC2[i+1][1])/2.0,0.0),))
    CSTIFFSLAVE.append(V1)

myPartstiffC.Set(edges=CSTIFFSLAVE,name='CSTIFFSLAVE')
#####Partition for the COLUMN
stiffeners#####
partitionplace=[50 , 150 , lc-150 , lc-50];
for i in range(len(partitionplace)):
    d = myPartcolumn.DatumPointByCoordinate(coords =
(0.0,0.0,partitionplace[i]))
    myfaces= myPartcolumn.faces
    e=myPartcolumn.DatumPlaneByPointNormal(point=datums[d.id],
normal=datums[axis1.id])
    myPartcolumn.PartitionFaceByDatumPlane(datumPlane=datums[e
.id], faces=myfaces)

CSTIFF1=[]
j=0;
for i in range(len(xyc1)-1):
    V1 =
myPartcolumn.edges.findAt((((xyc1[i][0]+xyc1[i+1][0])/2.0, (xyc1[
i][1]+xyc1[i+1][1])/2.0,partitionplace[j]),))
    CSTIFF1.append(V1)
    V1=
myPartcolumn.edges.findAt((((xyc2[i][0]+xyc2[i+1][0])/2.0, (xyc2[
i][1]+xyc2[i+1][1])/2.0,partitionplace[j]),))
    CSTIFF1.append(V1)

myPartcolumn.Set(edges=CSTIFF1,name='CSTIFF1')

CSTIFF2=[]
j=1;
for i in range(len(xyc1)-1):
    V1 =
myPartcolumn.edges.findAt((((xyc1[i][0]+xyc1[i+1][0])/2.0, (xyc1[
i][1]+xyc1[i+1][1])/2.0,partitionplace[j]),))
    CSTIFF2.append(V1)
    V1=
myPartcolumn.edges.findAt((((xyc2[i][0]+xyc2[i+1][0])/2.0, (xyc2[
i][1]+xyc2[i+1][1])/2.0,partitionplace[j]),))
    CSTIFF2.append(V1)

myPartcolumn.Set(edges=CSTIFF2,name='CSTIFF2')

CSTIFF3=[]
j=2;
for i in range(len(xyc1)-1):
    V1 =
myPartcolumn.edges.findAt((((xyc1[i][0]+xyc1[i+1][0])/2.0, (xyc1[
i][1]+xyc1[i+1][1])/2.0,partitionplace[j]),))
    CSTIFF3.append(V1)

```

## APPENDIX

```
V1=
myPartcolumn.edges.findAt(((xyc2[i][0]+xyc2[i+1][0])/2.0, (xyc2[
i][1]+xyc2[i+1][1])/2.0,partitionplace[j]),))
    CSTIFF3.append(V1)

myPartcolumn.Set(edges=CSTIFF3,name='CSTIFF3')

CSTIFF4=[]
j=3;
for i in range(len(xyc1)-1):
    V1 =
myPartcolumn.edges.findAt(((xyc1[i][0]+xyc1[i+1][0])/2.0, (xyc1[
i][1]+xyc1[i+1][1])/2.0,partitionplace[j]),))
    CSTIFF4.append(V1)
    V1=
myPartcolumn.edges.findAt(((xyc2[i][0]+xyc2[i+1][0])/2.0, (xyc2[
i][1]+xyc2[i+1][1])/2.0,partitionplace[j]),))
    CSTIFF4.append(V1)

myPartcolumn.Set(edges=CSTIFF4,name='CSTIFF4')

#-----into assembly module -----
#-----#
myModel.rootAssembly.DatumCsysByDefault(CARTESIAN)
myModel.rootAssembly.Instance(name='Column', part=myPartcolumn,
dependent=ON)
myModel.rootAssembly.Instance(name='Beam', part=myPartbeam,
dependent=ON)
myModel.rootAssembly.Instance(name='Gussetplate',
part=myPartgusset, dependent=ON)
myModel.rootAssembly.Instance(name='Stiffenerc1',
part=myPartstiffC, dependent=ON)
myModel.rootAssembly.Instance(name='Stiffenerc2',
part=myPartstiffC, dependent=ON)
myModel.rootAssembly.Instance(name='Stiffenerc3',
part=myPartstiffC, dependent=ON)
myModel.rootAssembly.Instance(name='Stiffenerc4',
part=myPartstiffC, dependent=ON)
session.viewports['Viewport:
1'].assemblyDisplay.geometryOptions.setValues(
    datumPoints=OFF, datumAxes=OFF, datumPlanes=OFF,
datumCoordSystems=OFF)
##Locate the gusset plate
a1 = myModel.rootAssembly
a1.rotate(instanceList=('Gussetplate', ), axisPoint=(0.0, 0.0,
0.0),
    axisDirection=(1, 0.0, 0.0), angle=90.0)
#: The instance Gussetplate was rotated by 90. degrees about the
axis defined by the point 0., 0., 0. and the vector 1., 0., 0.
a1 = mdb.models['Connection'].rootAssembly
a1.rotate(instanceList=('Gussetplate', ), axisPoint=(0.0, 0.0,
0.0),
    axisDirection=(0.0, 0.0, 1), angle=90.0)
#: The instance Gussetplate was rotated by 90. degrees about the
axis defined by the point 0., 0., 0. and the vector 0., 0., 1.
a1 = mdb.models['Connection'].rootAssembly
a1.translate(instanceList=('Gussetplate', ), vector=(0.0, 0.0,
1c/2.0))
```

## APPENDIX

```
#: The instance Gussetplate was translated by 0., 0., LC/2. with
respect to the assembly coordinate system

##Locate the beam
a1 = myModel.rootAssembly
a1.rotate(instanceList=('Beam', ), axisPoint=(0.0, 0.0, 0.0),
          axisDirection=(1, 0.0, 0.0), angle=-90.0)
#: The instance Beam was rotated by 90. degrees about the axis
defined by the point 0., 0., 0. and the vector 1., 0., 0.
a1 = mdb.models['Connection'].rootAssembly
a1.translate(instanceList=('Beam', ), vector=(0.0, xp-bp1/2.0-xb,
lc/2.0))
#: The instance Beam was translated by 0., 0., LC/2. with
respect to the assembly coordinate system

##Locate the Stiffener
a1 = myModel.rootAssembly
a1 = mdb.models['Connection'].rootAssembly
a1.translate(instanceList=('Stiffenerc1', ), vector=(0.0, 0.0,
partitionplace[0]))

##Locate the Stiffener
a1 = myModel.rootAssembly
a1 = mdb.models['Connection'].rootAssembly
a1.translate(instanceList=('Stiffenerc2', ), vector=(0.0, 0.0,
partitionplace[1]))

##Locate the Stiffener
a1 = myModel.rootAssembly
a1 = mdb.models['Connection'].rootAssembly
a1.translate(instanceList=('Stiffenerc3', ), vector=(0.0, 0.0,
partitionplace[2]))

##Locate the Stiffener
a1 = myModel.rootAssembly
a1 = mdb.models['Connection'].rootAssembly
a1.translate(instanceList=('Stiffenerc4', ), vector=(0.0, 0.0,
partitionplace[3]))
##-----Build a set for the attached
points-----##
## For beam : bolts
XX = []

for i in range(0, mb):
    V1 = myPartbeam.vertices.findAt(((0.0+tg/2.0+tb/2.0 ,
rb*cos(2*pi/mb*i) ,rb*sin(2*pi/mb*i)+xb),))
    V2 = myPartbeam.vertices.findAt(((0.0-tg/2.0-tb/2.0 ,
rb*cos(2*pi/mb*i) ,rb*sin(2*pi/mb*i)+xb),))
    XX.append(V1)
    XX.append(V2)

V1 = myPartbeam.vertices.findAt(((0.0+tg/2.0+tb/2.0 , 0.0 ,
xb ),))
V2 = myPartbeam.vertices.findAt(((0.0-tg/2.0-tb/2.0 , 0.0 ,
xb ),))
XX.append(V1)
XX.append(V2)
```

## APPENDIX

```
myPartbeam.Set(vertices=XX,name='beambolts')

## For column : bolts

YY = []
j = -(nc-1)/2.0
while (j <= (nc-1)/2.0):
    i = -(mc-1)/2.0
    while (i <= (mc-1)/2.0):
        V1 =
myPartcolumn.vertices.findAt(((tg/2.0+tc/2.0,j*hc,i*vc+lc/2.0),))
        V2 = myPartcolumn.vertices.findAt((-tg/2.0-
tc/2.0,j*hc,i*vc+lc/2.0),))
        YY.append(V1)
        YY.append(V2)
        i=i+1
    j=j+1

myPartcolumn.Set(vertices=YY,name='columnbolts')

## For gusset plate : bolts

ZZC = []
j = -(nc-1)/2.0
while (j <= (nc-1)/2.0):
    i = -(mc-1)/2.0
    while (i <= (mc-1)/2.0):
        V1 = myPartgusset.vertices.findAt(((j*hc,i*vc,0.0),))
        ZZC.append(V1)
        i=i+1
    j=j+1

myPartgusset.Set(vertices=ZZC,name='gussetcolumnbolts')

ZZB = []
for i in range(0, mb):
    V1=myPartgusset.vertices.findAt(((xp-
bp1/2.0+rb*cos(2*pi/mb*i),rb*sin(2*pi/mb*i),0.0),))
    ZZB.append(V1)

V1 = myPartgusset.vertices.findAt(((xp-bp1/2.0+0.0, 0.0,0.0),))
ZZB.append(V1)

myPartgusset.Set(vertices=ZZB,name='gussetbeambolts')

##-----Material properties-----
-----##

##1,material property builded as follow:-----
-----
p=myModel.Material(name='beamat')
p.Elastic(table=((210000.0, 0.33), ))
p.Plastic(table=((323.84831, 0.0), (591.06742, 0.26764)))
p.plastic.setValues(hardening=KINEMATIC)

p=myModel.Material(name='columnmat')
p.Elastic(table=((210000.0, 0.33), ))
```

## APPENDIX

```
p=myModel.Material(name='cstiffenermat')
p.Elastic(table=((210000.0, 0.33), ))

p=myModel.Material(name='gussetmat')
p.Elastic(table=((210000.0, 0.33), ))
p.Plastic(table=((308.0, 0.0), (474.0, 0.36)))
p.plastic.setValues(hardening=KINEMATIC)

myModel.HomogeneousShellSection(name='beamsec',
    preIntegrate=OFF, material='beammat', thicknessType=UNIFORM,
    thickness=tb,
    thicknessField='', idealization=NO_IDEALIZATION,
    poissonDefinition=DEFAULT,
    thicknessModulus=None, temperature=GRADIENT, useDensity=OFF,
    integrationRule=SIMPSON, numIntPts=5)

myModel.HomogeneousShellSection(name='columnsec',
    preIntegrate=OFF, material='columnmat',
    thicknessType=UNIFORM, thickness=tc,
    thicknessField='', idealization=NO_IDEALIZATION,
    poissonDefinition=DEFAULT,
    thicknessModulus=None, temperature=GRADIENT, useDensity=OFF,
    integrationRule=SIMPSON, numIntPts=5)

myModel.HomogeneousShellSection(name='cstiffnersec',
    preIntegrate=OFF, material='cstiffenermat',
    thicknessType=UNIFORM, thickness=tcstiff,
    thicknessField='', idealization=NO_IDEALIZATION,
    poissonDefinition=DEFAULT,
    thicknessModulus=None, temperature=GRADIENT, useDensity=OFF,
    integrationRule=SIMPSON, numIntPts=5)

myModel.HomogeneousShellSection(name='gussetsec',
    preIntegrate=OFF, material='gussetmat',
    thicknessType=UNIFORM, thickness=tg,
    thicknessField='', idealization=NO_IDEALIZATION,
    poissonDefinition=DEFAULT,
    thicknessModulus=None, temperature=GRADIENT, useDensity=OFF,
    integrationRule=SIMPSON, numIntPts=5)

import regionToolset

pickregion =
regionToolset.Region(faces=myModel.parts['Beam'].faces)
myPartbeam.SectionAssignment(region=pickregion,
    sectionName='beamsec', offset=0.0,
    offsetType=MIDDLE_SURFACE, offsetField='',
    thicknessAssignment=FROM_SECTION)

pickregion =
regionToolset.Region(faces=myModel.parts['Column'].faces)
myPartcolumn.SectionAssignment(region=pickregion,
    sectionName='columnsec', offset=0.0,
    offsetType=MIDDLE_SURFACE, offsetField='',
    thicknessAssignment=FROM_SECTION)
```

## APPENDIX

```
pickregion =
regionToolset.Region(faces=myModel.parts['StiffenerC'].faces)
myPartstiffC.SectionAssignment(region=pickregion,
sectionName='cstiffnersec', offset=0.0,
    offsetType=MIDDLE_SURFACE, offsetField='',
    thicknessAssignment=FROM_SECTION)

pickregion =
regionToolset.Region(faces=myModel.parts['Gussetplate'].faces)
myPartgusset.SectionAssignment(region=pickregion,
sectionName='gussetsec', offset=0.0,
    offsetType=MIDDLE_SURFACE, offsetField='',
    thicknessAssignment=FROM_SECTION)

#####-----step module-----
-----#####
myModel.StaticStep(name='Step-1', previous='Initial',
    initialInc=0.1, nlgeom=ON)

##-----interaction module-----
-----##

a = myModel.rootAssembly
region1=a.instances['Beam'].sets['mastertie']
region2=a.instances['Beam'].sets['slavetie']
myModel.Tie(name='webconnect', master=region1, slave=region2,
    positionToleranceMethod=SPECIFIED, positionTolerance=tg+tb,
    adjust=OFF, tieRotations=OFF,
    thickness=ON)

a = myModel.rootAssembly
region1=a.instances['Column'].sets['CSTIFF1']
region2=a.instances['Stiffenerc1'].sets['CSTIFFSLAVE']
myModel.Tie(name='stifftocolumn1', master=region1, slave=region2,
    positionToleranceMethod=COMPUTED, adjust=OFF,
    tieRotations=OFF,
    thickness=ON)

a = myModel.rootAssembly
region1=a.instances['Column'].sets['CSTIFF2']
region2=a.instances['Stiffenerc2'].sets['CSTIFFSLAVE']
myModel.Tie(name='stifftocolumn2', master=region1, slave=region2,
    positionToleranceMethod=COMPUTED, adjust=OFF,
    tieRotations=OFF,
    thickness=ON)

a = myModel.rootAssembly
region1=a.instances['Column'].sets['CSTIFF3']
region2=a.instances['Stiffenerc3'].sets['CSTIFFSLAVE']
myModel.Tie(name='stifftocolumn3', master=region1, slave=region2,
    positionToleranceMethod=COMPUTED, adjust=OFF,
    tieRotations=OFF,
    thickness=ON)

a = myModel.rootAssembly
```



## APPENDIX

```
region1=a.instances['Column'].sets['CSTIFF4']
region2=a.instances['Stiffenerc4'].sets['CSTIFFSLAVE']
myModel.Tie(name='stifftocolumn4', master=region1, slave=region2,
            positionToleranceMethod=COMPUTED, adjust=OFF,
            tieRotations=OFF,
            thickness=ON)
##-----Rigid body for
point load-----##

region1=myModel.rootAssembly.instances['Beam'].sets['endnode']
region2=myModel.rootAssembly.instances['Beam'].sets['beamend']
mdb.models['Connection'].Coupling(name='endcouple',
controlPoint=region1,
    surface=region2, influenceRadius=WHOLE_SURFACE,
couplingType=KINEMATIC,
    localCsys=None, u1=ON, u2=ON, u3=ON, ur1=OFF, ur2=OFF,
ur3=OFF)

##-----define connector-----
-----##
import connectorBehavior

#define for beam-to-gusset
mdb.models['Connection'].ConnectorSection(name='ConnSect-1',
    translationalType=CARTESIAN)
friction_0 =
connectorBehavior.ConnectorFriction(table=((54000.0, ), ),
    frictionModel=USER_CUSTOMIZED, slipStyle=COMPUTE)
friction_0.TangentialBehavior(table=((0.19, ), ))
cp0 = connectorBehavior.ConnectorPotential(componentNumber=2)
cp1 = connectorBehavior.ConnectorPotential(componentNumber=3)
friction_0.setValues(connectorPotentials=(cp0, cp1, ))
friction_0.ConnectorOptions()
stop_1 = connectorBehavior.ConnectorStop(components=(2, 3),
minMotion=-3.0,
    maxMotion=3.0)
mdb.models['Connection'].sections['ConnSect-
1'].setValues(behaviorOptions =(
    friction_0, stop_1, ) )

#define for column-to-gusset
mdb.models['Connection'].ConnectorSection(name='ConnSect-2',
    translationalType=CARTESIAN)
elastic_0 = connectorBehavior.ConnectorElasticity(components=(1,
2, 3),
    behavior=RIGID)
elastic_0.ConnectorOptions()
mdb.models['Connection'].sections['ConnSect-
2'].setValues(behaviorOptions =(
    elastic_0, ) )

##-----Fasteners
definition-----##

a = mdb.models['Connection'].rootAssembly
#v3 = a.instances['Column'].vertices
```

## APPENDIX

```

#Beam to gusset plate

for i in range(0, mb):
    V1 =
a.instances['Beam'].vertices.findAt(((0.0+tg/2.0+tb/2.0, rb*cos(2
*pi/mb*i)+xp-bp1/2.0, rb*sin(2*pi/mb*i)+lc/2.0),))
    V2 = a.instances['Beam'].vertices.findAt(((0.0-tg/2.0-
tb/2.0, rb*cos(2*pi/mb*i)+xp-bp1/2.0, rb*sin(2*pi/mb*i)+lc/2.0),))
    V3 = a.instances['Gussetplate'].vertices.findAt(((0.0,
xp-bp1/2.0+rb*cos(2*pi/mb*i), rb*sin(2*pi/mb*i)+lc/2.0),))
    wi1=a.WirePolyLine(points=((V3[0], V1[0]), ),
mergeType=IMPRINT, meshable=OFF)
    edge1 = a.edges.findAt( ((tg/4.0+tb/4.0, xp-
bp1/2.0+rb*cos(2*pi/mb*i), rb*sin(2*pi/mb*i)+lc/2.0), ) )
    region=regionToolset.Region(edges=edge1)
    csa = a.SectionAssignment(sectionName='ConnSect-1',
region=region)
    wi2=a.WirePolyLine(points=((V3[0], V2[0]), ),
mergeType=IMPRINT, meshable=OFF)
    edge2 = a.edges.findAt( ((-tg/4.0-tb/4.0, xp-
bp1/2.0+rb*cos(2*pi/mb*i), rb*sin(2*pi/mb*i)+lc/2.0), ) )
    region=regionToolset.Region(edges=edge2)
    csa = a.SectionAssignment(sectionName='ConnSect-1',
region=region)

V1 =
a.instances['Beam'].vertices.findAt(((0.0+tg/2.0+tb/2.0, xp-
bp1/2.0, lc/2.0),))
V2 = a.instances['Beam'].vertices.findAt(((0.0-tg/2.0-
tb/2.0, xp-bp1/2.0, lc/2.0),))
V3 = a.instances['Gussetplate'].vertices.findAt(((0.0, xp-
bp1/2.0, lc/2.0),))
wi1=a.WirePolyLine(points=((V3[0], V1[0]), ), mergeType=IMPRINT,
meshable=OFF)
edge1 = a.edges.findAt( ((tg/4.0+tb/4.0, xp-bp1/2.0, lc/2.0), ) )
region=regionToolset.Region(edges=edge1)
csa = a.SectionAssignment(sectionName='ConnSect-1',
region=region)
wi2=a.WirePolyLine(points=((V3[0], V2[0]), ), mergeType=IMPRINT,
meshable=OFF)
edge2 = a.edges.findAt( ((-tg/4.0-tb/4.0, xp-bp1/2.0 ,
lc/2.0), ) )
region=regionToolset.Region(edges=edge2)
csa = a.SectionAssignment(sectionName='ConnSect-1',
region=region)

#Column to gusset plate
j = -(nc-1)/2.0
while (j <=(nc-1)/2.0):
    i = -(mc-1)/2.0
    while (i <=(mc-1)/2.0):
        V1 =
a.instances['Column'].vertices.findAt(((tg/2.0+tc/2.0, j*hc, i*vc+
lc/2.0),))

```

## APPENDIX

```

        V2 = a.instances['Column'].vertices.findAt((( -
tg/2.0-tc/2.0,j*hc,i*vc+lc/2.0),))
        V3 =
a.instances['Gussetplate'].vertices.findAt(((0.0 , j*hc ,
i*vc+lc/2.0),))
        wil=a.WirePolyLine(points=((V3[0], V1[0]), ),
mergeType=IMPRINT, meshable=OFF)
        edge1 = a.edges.findAt( ((tg/4.0+tb/4.0 , j*hc ,
i*vc+lc/2.0), ) )
        region=regionToolset.Region(edges=edge1)
        csa = a.SectionAssignment(sectionName='ConnSect-2',
region=region)
        wi2=a.WirePolyLine(points=((V3[0], V2[0]), ),
mergeType=IMPRINT, meshable=OFF)
        edge2 = a.edges.findAt( ((-tg/4.0-tb/4.0 , j*hc ,
i*vc+lc/2.0), ) )
        region=regionToolset.Region(edges=edge2)
        csa = a.SectionAssignment(sectionName='ConnSect-2',
region=region)
        i=i+1
        j=j+1

##-----load module-----
##
## Apply the boundary conditions and load
a = mdb.models['Connection'].rootAssembly
region = a.instances['Column'].sets['columnntop']
mdb.models['Connection'].DisplacementBC(name='topcolu',
createStepName='Initial', region=region, u1=SET, u2=SET,
u3=UNSET,
url1=UNSET, ur2=UNSET, ur3=UNSET, amplitude=UNSET,
distributionType=UNIFORM,
fieldName='', localCsys=None)

a = mdb.models['Connection'].rootAssembly
region = a.instances['Column'].sets['columnbottom']
mdb.models['Connection'].DisplacementBC(name='bottomcolu',
createStepName='Initial', region=region, u1=SET, u2=SET,
u3=SET,
url1=UNSET, ur2=UNSET, ur3=UNSET, amplitude=UNSET,
distributionType=UNIFORM,
fieldName='', localCsys=None)

a = mdb.models['Connection'].rootAssembly
region = a.instances['Beam'].sets['beamlateral']
mdb.models['Connection'].DisplacementBC(name='lateralrest',
createStepName='Initial', region=region, u1=SET, u2=UNSET,
u3=UNSET,
url1=UNSET, ur2=UNSET, ur3=UNSET, amplitude=UNSET,
distributionType=UNIFORM,
fieldName='', localCsys=None)

a = mdb.models['Connection'].rootAssembly
region = a.instances['Beam'].sets['beambolts']
mdb.models['Connection'].DisplacementBC(name='boltbeam',
createStepName='Initial', region=region, u1=SET, u2=UNSET,
u3=UNSET,

```

## APPENDIX

```
    ur1=UNSET, ur2=SET, ur3=SET, amplitude=UNSET,
distributionType=UNIFORM,
    fieldName='', localCsys=None)
```

```
a = mdb.models['Connection'].rootAssembly
region = a.instances['Column'].sets['columnbolts']
mdb.models['Connection'].DisplacementBC(name='boltcolumn',
    createStepName='Initial', region=region, u1=SET, u2=UNSET,
u3=UNSET,
    ur1=UNSET, ur2=SET, ur3=SET, amplitude=UNSET,
distributionType=UNIFORM,
    fieldName='', localCsys=None)
```

```
a = mdb.models['Connection'].rootAssembly
region = a.instances['Gussetplate'].sets['gussetcolumnbolts']
mdb.models['Connection'].DisplacementBC(name='gussetcolumnbolt',
    createStepName='Initial', region=region, u1=SET, u2=UNSET,
u3=UNSET,
    ur1=UNSET, ur2=SET, ur3=SET, amplitude=UNSET,
distributionType=UNIFORM,
    fieldName='', localCsys=None)
```

```
a = mdb.models['Connection'].rootAssembly
region = a.instances['Gussetplate'].sets['gussetbeambolts']
mdb.models['Connection'].DisplacementBC(name='gussetbeambolt',
    createStepName='Initial', region=region, u1=SET, u2=UNSET,
u3=UNSET,
    ur1=UNSET, ur2=SET, ur3=SET, amplitude=UNSET,
distributionType=UNIFORM,
    fieldName='', localCsys=None)
```

```
a = mdb.models['Connection'].rootAssembly
region = a.instances['Beam'].sets['endnode']
mdb.models['Connection'].DisplacementBC(name='endbolt',
    createStepName='Initial', region=region, u1=SET, u2=UNSET,
u3=UNSET,
    ur1=UNSET, ur2=SET, ur3=UNSET, amplitude=UNSET,
distributionType=UNIFORM,
    fieldName='', localCsys=None)
```

```
mdb.models['Connection'].TabularAmplitude(name='protocol',
timeSpan=STEP,
    smooth=SOLVER_DEFAULT, data=((0.0, 0.0), (1.0, 6.79125),
(2.0, 0.0), (3.0,
-6.79125), (4.0, 0.0), (5.0, 6.79125), (6.0, 0.0), (7.0, -
6.79125), (8.0,
0.0), (9.0, 6.79125), (10.0, 0.0), (11.0, -6.79125), (12.0,
0.0), (13.0,
6.79125), (14.0, 0.0), (15.0, -6.79125), (16.0, 0.0), (17.0,
6.79125), (
18.0, 0.0), (19.0, -6.79125), (20.0, 0.0), (21.0, 6.79125),
(22.0, 0.0), (
23.0, -6.79125), (24.0, 0.0), (25.0, 9.055), (26.0, 0.0),
(27.0, -9.055), (
28.0, 0.0), (29.0, 9.055), (30.0, 0.0), (31.0, -9.055),
(32.0, 0.0), (33.0,
9.055), (34.0, 0.0), (35.0, -9.055), (36.0, 0.0), (37.0,
9.055), (38.0,
```

APPENDIX

```

    0.0), (39.0, -9.055), (40.0, 0.0), (41.0, 9.055), (42.0,
0.0), (43.0,
    -9.055), (44.0, 0.0), (45.0, 9.055), (46.0, 0.0), (47.0, -
9.055), (48.0,
    0.0), (49.0, 13.5825), (50.0, 0.0), (51.0, -13.5825), (52.0,
0.0), (53.0,
    13.5825), (54.0, 0.0), (55.0, -13.5825), (56.0, 0.0), (57.0,
13.5825), (
    58.0, 0.0), (59.0, -13.5825), (60.0, 0.0), (61.0, 13.5825),
(62.0, 0.0), (
    63.0, -13.5825), (64.0, 0.0), (65.0, 13.5825), (66.0, 0.0),
(67.0,
    -13.5825), (68.0, 0.0), (69.0, 13.5825), (70.0, 0.0), (71.0,
-13.5825), (
    72.0, 0.0), (73.0, 18.11), (74.0, 0.0), (75.0, -18.11),
(76.0, 0.0), (77.0,
    18.11), (78.0, 0.0), (79.0, -18.11), (80.0, 0.0), (81.0,
18.11), (82.0,
    0.0), (83.0, -18.11), (84.0, 0.0), (85.0, 18.11), (86.0,
0.0), (87.0,
    -18.11), (88.0, 0.0), (89.0, 27.165), (90.0, 0.0), (91.0, -
27.165), (92.0,
    0.0), (93.0, 27.165), (94.0, 0.0), (95.0, -27.165), (96.0,
0.0), (97.0,
    36.22), (98.0, 0.0), (99.0, -36.22), (100.0, 0.0), (101.0,
36.22), (102.0,
    0.0), (103.0, -36.22), (104.0, 0.0), (105.0, 54.33), (106.0,
0.0), (107.0,
    -54.33), (108.0, 0.0), (109.0, 54.33), (110.0, 0.0), (111.0,
-54.33), (
    112.0, 0.0), (113.0, 72.44), (114.0, 0.0), (115.0, -72.44),
(116.0, 0.0), (
    117.0, 72.44), (118.0, 0.0), (119.0, -72.44), (120.0, 0.0),
(121.0, 90.55),
    (122.0, 0.0), (123.0, -90.55), (124.0, 0.0), (125.0, 90.55),
(126.0, 0.0),
    (127.0, -90.55), (128.0, 0.0), (129.0, 108.66), (130.0, 0.0),
(131.0,
    -108.66), (132.0, 0.0), (133.0, 108.66), (134.0, 0.0),
(135.0, -108.66), (
    136.0, 0.0), (137.0, 126.77), (138.0, 0.0), (139.0, -126.77),
(140.0, 0.0),
    (141.0, 126.77), (142.0, 0.0), (143.0, -126.77), (144.0,
0.0), (145.0,
    144.88), (146.0, 0.0), (147.0, -144.88), (148.0, 0.0),
(149.0, 144.88), (
    150.0, 0.0), (151.0, -144.88), (152.0, 0.0)))

```

```

#a = mdb.models['Connection'].rootAssembly
#region = a.instances['Beam'].sets['endnode']
#mdb.models['Connection'].DisplacementBC(name='endload',
#    createStepName='Step-1', region=region, u1=UNSET, u2=UNSET,
u3=-150.0,
#    ur1=UNSET, ur2=UNSET, ur3=UNSET, amplitude=UNSET, fixed=OFF,
#    distributionType=UNIFORM, fieldName='', localCsys=None)

##-----Mesh module-----
##

```

## APPENDIX

```
import mesh
##Beam
elemType1 = mesh.ElemType(elemCode=S8R, elemLibrary=STANDARD)
p = myModel.parts['Beam']
f = p.faces
pickregion =
regionToolset.Region(faces=myModel.parts['Beam'].faces)
p.setElementType(regions=pickregion, elemTypes=(elemType1,))

p = myModel.parts['Beam']
p.seedPart(size=20.0, deviationFactor=0.1, minSizeFactor=0.1)
p.generateMesh()

##column
elemType1 = mesh.ElemType(elemCode=S8R, elemLibrary=STANDARD)
p = myModel.parts['Column']
f = p.faces
pickregion =
regionToolset.Region(faces=myModel.parts['Column'].faces)
p.setElementType(regions=pickregion, elemTypes=(elemType1,))

p = myModel.parts['Column']
p.seedPart(size=20.0, deviationFactor=0.1, minSizeFactor=0.1)
p.generateMesh()

##column stiffeners
elemType1 = mesh.ElemType(elemCode=S8R, elemLibrary=STANDARD)
p = myModel.parts['StiffenerC']
f = p.faces
pickregion =
regionToolset.Region(faces=myModel.parts['StiffenerC'].faces)
p.setElementType(regions=pickregion, elemTypes=(elemType1,))

p = myModel.parts['StiffenerC']
p.seedPart(size=20.0, deviationFactor=0.1, minSizeFactor=0.1)
p.generateMesh()

##Gusset plate
elemType1 = mesh.ElemType(elemCode=S8R, elemLibrary=STANDARD)
p = myModel.parts['Gussetplate']
f = p.faces
pickregion =
regionToolset.Region(faces=myModel.parts['Gussetplate'].faces)
p.setElementType(regions=pickregion, elemTypes=(elemType1,))

p = myModel.parts['Gussetplate']
p.seedPart(size=20.0, deviationFactor=0.1, minSizeFactor=0.1)
p.generateMesh()

##-----Job module-----
-----##
import job

mdb.Job(name='boltconnectioin', model='Connection',
description='connection performance')

mdb.jobs['boltconnectioin'].submit(consistencyChecking=OFF)
```

## APPENDIX

```
#: The job input file "beam-OPT.inp" has been submitted for  
analysis.  
mdb.jobs['boltconnectioin'].waitForCompletion()
```

## APPENDIX

### A.6 Python script for optimisation of CFS elements based on their post-buckling behaviour

```
from part import *
from material import *
from section import *
from assembly import *
from step import *
from interaction import *
from load import *
from mesh import *
from job import *
from sketch import *
from visualization import *
from connectorBehavior import *
from abaqus import *
from abaqusConstants import *
import os
os.chdir(r'D:\Python\connections\pythonopt')
myModel = mdb.Model(name='Channelbeam')
#Dimentions
#####Beam channel#####
import numpy as np
p=415;      #total length of plate in mm
a = area[0];
b = area[1];
c = area[2];
h = p-2*a-2*b-2*c; ##profile dimenstions:web height, flange
width, lip length
theta1 = area[3];
theta2 = area[4];
lb = 1400;      ##beam height
tb=1.5;      ##thickness of beam
disp=56;
#####Beam profile#####
mySketchB = myModel.ConstrainedSketch(name='Bprofile',
sheetSize=500.0)
xy1=[(a*sin(theta2)+b-c*cos(theta1) , -h/2.0 +
a*cos(theta2)+c*sin(theta1)) , (a*sin(theta2)+b , -h/2.0 +
a*cos(theta2)) , (a*sin(theta2), -h/2.0 + a*cos(theta2)) , (0.0,
-h/2.0), (0.0, 0) ,
(0.0 , h/2.0) , (a*sin(theta2), h/2.0 -
a*cos(theta2)) , (a*sin(theta2)+b, h/2.0 - a*cos(theta2)) ,
(a*sin(theta2)+b-c*cos(theta1), h/2.0 - a*cos(theta2)-
c*sin(theta1))]

for i in range(len(xy1)-1):
    mySketchB.Line(point1 = xy1[i], point2 = xy1[i+1])

#####Beam Part#####
myPartbeam = myModel.Part(name='Beam', dimensionality=THREE_D,
type=DEFORMABLE_BODY)
myPartbeam.BaseShellExtrude(sketch=mySketchB, depth=lb)
axis1=myPartbeam.DatumAxisByTwoPoint(point1=(0.0, 0.0,
0.0),point2=(0.0,0.0,lb))
datums=myPartbeam.datums
```



## APPENDIX

```

partitionplace=[300 , lb/2.0 , lb-300];
for i in range(len(partitionplace)):
    d = myPartbeam.DatumPointByCoordinate(coords =
(0.0,0.0,partitionplace[i]))
    myfaces= myPartbeam.faces
    e=myPartbeam.DatumPlaneByPointNormal (point=datums[d.id],
normal=datums[axis1.id])
    myPartbeam.PartitionFaceByDatumPlane (datumPlane=datums[e.i
d], faces=myfaces)

#reference point for load
P1=myPartbeam.ReferencePoint (point=(0.0, 0.0, 0));
#refPoints=(R1[12], )
Q2 = myPartbeam.referencePoints;
refPoints1=(Q2[P1.id], );
myPartbeam.Set (referencePoints=refPoints1, name='endnode');

## For beam : end cross-sections AND start cross-sections for
fix end
EE = []
FF = []
for i in range(len(xy1)-1):
    V1 =
myPartbeam.edges.findAt (((xy1[i][0]+xy1[i+1][0])/2.0, (xy1[i][1]
+xy1[i+1][1])/2.0,0),)
    V2 =
myPartbeam.edges.findAt (((xy1[i][0]+xy1[i+1][0])/2.0, (xy1[i][1]
+xy1[i+1][1])/2.0,lb),)
    EE.append (V1)
    FF.append (V2)

myPartbeam.Set (edges=EE, name='beamend')
myPartbeam.Set (edges=FF, name='beamstart')

## For beam : lateral restraints
LT=[]
for i in range(len(partitionplace)):
    V3 =
myPartbeam.edges.findAt (((xy1[3][0]+xy1[4][0])/2.0, (xy1[3][1]+x
y1[4][1])/2.0,partitionplace[i]), ((xy1[4][0]+xy1[5][0])/2.0, (xy1
[4][1]+xy1[5][1])/2.0,partitionplace[i]),)
    LT.append (V3)

for i in range(len(partitionplace)):
    V5 =
myPartbeam.edges.findAt (((xy1[6][0]+xy1[7][0])/2.0, (xy1[6][1]+x
y1[7][1])/2.0,partitionplace[i]),)
    LT.append (V5)
    V5 =
myPartbeam.edges.findAt (((xy1[1][0]+xy1[2][0])/2.0, (xy1[1][1]+x
y1[2][1])/2.0,partitionplace[i]),)
    LT.append (V5)

myPartbeam.Set (edges=LT, name='beamlateral')

#-----into assembly module -----
-----#

```

## APPENDIX

```
myModel.rootAssembly.DatumCsysByDefault (CARTESIAN)
myModel.rootAssembly.Instance(name='Beam', part=myPartbeam,
dependent=ON)

##-----Material properties-----
-----##

##1,material property builded as follow:-----
-----
p=myModel.Material(name='beamm1')
p.Elastic(table=((210000.0, 0.3), ))
p.Plastic(table=((350.0, 0.0), (400.0, 0.000310257), (450.0,
0.002474433), (480.0, 0.00961729), (
520.0, 0.019141099)))

myModel.HomogeneousShellSection(name='beamsec',
preIntegrate=OFF, material='beamm1', thicknessType=UNIFORM,
thickness=tb,
thicknessField='', idealization=NO_IDEALIZATION,
poissonDefinition=DEFAULT,
thicknessModulus=None, temperature=GRADIENT, useDensity=OFF,
integrationRule=SIMPSON, numIntPts=5)

import regionToolset

pickregion =
regionToolset.Region(faces=myModel.parts['Beam'].faces)
myPartbeam.SectionAssignment(region=pickregion,
sectionName='beamsec', offset=0.0,
offsetType=MIDDLE_SURFACE, offsetField='',
thicknessAssignment=FROM_SECTION)

#####-----step module-----
-----#####
myModel.StaticStep(name='Step-1', previous='Initial',
initialInc=0.1, nlgeom=ON)
mdb.models['Channelbeam'].steps['Step-1'].control.setValues(
allowPropagation=OFF, resetDefaultValues=OFF,
discontinuous=ON,
timeIncrementation=(8.0, 10.0, 9.0, 16.0, 10.0, 4.0, 12.0,
20.0, 6.0, 3.0, 50.0))
##-----Rigid body for
point load-----##
a = myModel.rootAssembly
region3=a.instances['Beam'].sets['beamend']
a = myModel.rootAssembly
r1 = a.instances['Beam'].referencePoints
refPoints1=(r1[P1.id], )
region1=regionToolset.Region(referencePoints=refPoints1)
myModel.RigidBody(name='endregid', refPointRegion=region1,
pinRegion=region3)

##-----load module-----
-----##
## Apply the boundary conditions and load

a = mdb.models['Channelbeam'].rootAssembly
```

## APPENDIX

```
region = a.instances['Beam'].sets['beamstart']
mdb.models['Channelbeam'].DisplacementBC(name='endfix',
    createStepName='Initial', region=region, u1=SET, u2=SET,
u3=SET, ur1=SET,
    ur2=SET, ur3=SET, amplitude=UNSET, distributionType=UNIFORM,
fieldName='',
    localCsys=None)

a = mdb.models['Channelbeam'].rootAssembly
region = a.instances['Beam'].sets['beamlateral']
mdb.models['Channelbeam'].DisplacementBC(name='lateralrest',
    createStepName='Initial', region=region, u1=SET, u2=UNSET,
u3=UNSET,
    ur1=UNSET, ur2=UNSET, ur3=UNSET, amplitude=UNSET,
distributionType=UNIFORM,
    fieldName='', localCsys=None)

a = myModel.rootAssembly
r1 = a.instances['Beam'].referencePoints
refPoints1=(r1[P1.id], )
region = regionToolset.Region(referencePoints=refPoints1)
myModel.DisplacementBC(name='endload',
    createStepName='Step-1', region=region, u1=UNSET, u2=-disp,
u3=UNSET,
    ur1=UNSET, ur2=UNSET, ur3=UNSET, amplitude=UNSET, fixed=OFF,
distributionType=UNIFORM, fieldName='', localCsys=None)

##-----Mesh module-----
-----##
import mesh
##Beam
elemType1 = mesh.ElemType(elemCode=S8R, elemLibrary=STANDARD)
p = mdb.models['Channelbeam'].parts['Beam']
f = p.faces
pickregion =
regionToolset.Region(faces=myModel.parts['Beam'].faces)
p.setElementType(regions=pickregion, elemTypes=(elemType1,))

p = myModel.parts['Beam']
p.seedPart(size=20.0, deviationFactor=0.1, minSizeFactor=0.1)
p.generateMesh()

##-----Job module-----
-----##
import job

mdb.Job(name='beam-OPT1', model='Channelbeam', description='Beam
optimization')

mdb.jobs['beam-OPT1'].submit(consistencyChecking=OFF)
#: The job input file "beam-OPT.inp" has been submitted for
analysis.
mdb.jobs['beam-OPT1'].waitForCompletion()

##-----visualization
module-----##
from visualization import *
from odbAccess import*
```

## APPENDIX

```
odb = openOdb(r'D:\Python\connections\pythonopt\beam-OPT1.odb')
myPart=odb.rootAssembly.instances['BEAM']
step1=odb.steps['Step-1']
##-----
displacement output-----
-----##
#lastFrame=step1.frames[-1]
#displacement=lastFrame.fieldOutputs['U']
#endr=odb.rootAssembly.instances['BEAM'].nodeSets['ENDNODE']
#u1=displacement.getSubset(region=endr)
#dispvalues=u1.values
#for v in dispvalues:
#    print v.nodeLabel,v.data
history = step1.historyRegions['Assembly ASSEMBLY']
energdata = history.historyOutputs['ALLPD'].data
#print energdata[-1][-1]
```

APPENDIX

**A.7 ABAQUS User Defined Element for modelling of a bolt**

```

C#####
#####
C USER DEFINED ELEMENT:2D 4NODES ISOPARAMETER LINEAR-ELASTIC
MATERIA
C THIS CODE IS PROGRAMMED IN ONE PURPOSED:
C To implement complement the combination of UEL and UMAT
C-----C

C#####
#####
SUBROUTINE UEL(RHS,AMATRX,SVARS,ENERGY,NDOFEL,NRHS,NSVARS,
1  PROPS,NPROPS,COORDS,MCRD,NNODE,U,DU,V,A,JTYPE,TIME,DTIME,
2  KSTEP,KINC,JELEM,PARAMS,NDLOAD,JDLTYP,ADLMAG,PREDEF,
3  NPREDF,LFLAGS,MLVARX,DDL MAG,MDLOAD,PNEWDT,JPROPS,NJPROP,
4  PERIOD)
C
c IMPLICIT DOUBLE PRECISION (A-H,O-Z)
INCLUDE 'ABA_PARAM.INC'
C
DIMENSION RHS(MLVARX,*),AMATRX(NDOFEL,NDOFEL),
1  SVARS(*),ENERGY(7),PROPS(9),COORDS(MCRD,NNODE),
2  U(NDOFEL),DU(MLVARX,*),V(NDOFEL),A(NDOFEL),TIME(2),
3  PARAMS(*),JDLTYP(MDLOAD,*),ADLMAG(MDLOAD,*),
4  DDL MAG(MDLOAD,*),PREDEF(2,NPREDF,NNODE),LFLAGS(4),
5  JPROPS(*)
C
C
C***** DEFINE PARAMETERS AND M

PARAMETER (HALF=0.5D0,ZERO= 0.D0,ONE = 1.D0,TWO=2.D0,THREE=3.0D0)
PARAMETER (TWELVE=12.D0)
DIMENSION B(NDOFEL,NDOFEL),D(NDOFEL,NDOFEL),S(NDOFEL,NDOFEL)
DIMENSION T(NDOFEL,NDOFEL),TT(NDOFEL,NDOFEL),DD(NDOFEL,NDOFEL)
DIMENSION SSTRAIN(NDOFEL),SSTRESS(NDOFEL),UUU(NDOFEL)
C
C LFLAGS(1)=1,2
C
c
NN=NDOFEL
DX=COORDS(1,2)-COORDS(1,1)
DY=COORDS(2,2)-COORDS(2,1)
DL2=DX**2+DY**2
DL=SQRT(DL2)
HDL=DL/TWO
ACOS=DX/DL
ASIN=DY/DL
K1=PROPS(2)
UU1=PROPS(1)
K2=PROPS(4)
UU2=PROPS(3)
K3=PROPS(6)
UU3=PROPS(5)
K4=SVARS(7)
KN=PROPS(8)
AM=PROPS(9)

```

APPENDIX

C

C-----

C-----

IF (KSTEP .EQ. ONE .AND. KINC .EQ. ONE) THEN

F=0

SVARS(1)=F

UMA=0

FMA=0

UMI=0

FMI=0

FLIMP=0

FLIMN=0

SVARS(2)=UMA

SVARS(3)=FMA

SVARS(4)=UMI

SVARS(5)=FMI

FLAG=0

DO I=1, NDOFEL

DO KRHS = 1, NRHS

RHS(I,KRHS) = ZERO

ENDDO

DO J = 1, NDOFEL

AMATRX(J,I) = ZERO

ENDDO

ENDDO

END IF

DO I=1,NN

DO J=1,NN

B(I,J)=ZERO

S(I,J)=ZERO

D(I,J)=ZERO

ENDDO

ENDDO

CC  
 CCCCCCCCCCCCCCCCC

C Make B Matrix in Natural Coordinate System C

CC  
 CCCCCCCCCCCCCCCCC

B(2,2)=-1.0D0\*ONE/DL

B(8,8)=ONE/DL

CC  
 CCCCCCCCCCCCCCCCC

C MAKE D-MATRIX

CC  
 CCCCCCCCCCCCCCCCC

C

F1=UU1\*K1

F2=F1+(UU2-UU1)\*K2

F3=F1+(UU3-UU2)\*K3

UU=U(8)-U(2)

DUU=DU(8,1)-DU(2,1)

F0=SVARS(1)

IF(F0 .GE. ZERO)THEN

50 UMA=SVARS(2)

FMA=SVARS(3)

APPENDIX

```

UMI=SVARS(4)
FMI=SVARS(5)
IF (DUU .GE. ZERO) THEN
  IF (UMA .LE. UU2) THEN
    IF(UU .LE. UU2)THEN
      KD=K1
      D(2,2)=KD
      D(8,8)=KD
      D(2,8)=-1.0D0*KD
      D(8,2)=-1.0D0*KD
      F=F0+KD*DUU
      IF(F .GT. F1) THEN
        F=F1
        KD=0
      END IF
    END IF
  END IF
  IF(UU .GT. UU2 .AND. UU .LE. UU3)THEN
    KD=K3
    D(2,2)=KD
    D(8,8)=KD
    D(2,8)=-1.0D0*KD
    D(8,2)=-1.0D0*KD
    F=F1+K3*(UU-UU2)
  END IF
  IF(UU .GT. UU3)THEN
    KD=K4
    D(2,2)=KD
    D(8,8)=KD
    D(2,8)=-1.0D0*KD
    D(8,2)=-1.0D0*KD
    F=F3+K4*(UU-UU3)
  END IF
  END IF
  IF (UMA .GT. UU2) THEN
    IF(UU .LE. UU2)THEN
      KD=K1
      D(2,2)=KD
      D(8,8)=KD
      D(2,8)=-1.0D0*KD
      D(8,2)=-1.0D0*KD
      F=F0+KD*DUU
      IF(F .GT. F1) THEN
        F=F1
        KD=0
      END IF
    END IF
  END IF
  IF(UU .GT. UU2 .AND. UU .LE. UU3)THEN
    KD=K1
    F=F0+KD*DUU
    FLIMP3=K3*(UU-UU3)+F3
    FLIMP4=K4*(UU-UU3)+F3
    IF(F .GT. FLIMP3 .AND. FLIMP3 .LT. F3) THEN
      F=FLIMP3
      KD=K3
    END IF
    IF(FLIMP3 .GE. F3) THEN
      F=FLIMP4
    
```

APPENDIX

```

KD=K4
  END IF
  D(2,2)=KD
  D(8,8)=KD
  D(2,8)=-1.0D0*KD
  D(8,2)=-1.0D0*KD
END IF
IF(UU .GT. UU3)THEN
  KD=K1
  F=F0+KD*DUU
  FLIMP3=K3*(UU-UU3)+F3
  FLIMP4=K4*(UU-UU3)+F3
  IF(F .GT. FLIMP4) THEN
    F=FLIMP4
    KD=K4
  END IF
  D(2,2)=KD
  D(8,8)=KD
  D(2,8)=-1.0D0*KD
  D(8,2)=-1.0D0*KD
END IF
END IF
IF(UU .GT. UMA)THEN
  UMA=UU
  FMA=F
END IF
IF(UU .LT. UMI)THEN
  UMI=UU
  FMI=F
END IF
SVARS(1)=F
SVARS(2)=UMA
SVARS(3)=FMA
SVARS(4)=UMI
SVARS(5)=FMI
END IF
IF (DUU .LT. ZERO) THEN
  KD=K1
  D(2,2)=KD
  D(8,8)=KD
  D(2,8)=-1.0D0*KD
  D(8,2)=-1.0D0*KD
  F=F0+KD*DUU
  IF(F .LT. ZERO) THEN
    F=F-KD*DUU
  GO TO 60
END IF
IF(UU .GT. UMA)THEN
  UMA=UU
  FMA=F
END IF
IF(UU .LT. UMI)THEN
  UMI=UU
  FMI=F
END IF
SVARS(1)=F
SVARS(2)=UMA

```



APPENDIX

```

        SVARS(3)=FMA
        SVARS(4)=UMI
        SVARS(5)=FMI
    END IF
    GO TO 70
END IF
IF(F0 .LT. ZERO)THEN
60     UMA=SVARS(2)
        FMA=SVARS(3)
        UMI=SVARS(4)
        FMI=SVARS(5)
        IF (DUU .LE. ZERO) THEN
        IF (UMI .GE. (-1.0D0*UU2)) THEN
        IF(UU .GE. (-1.0D0*UU2))THEN
            KD=K1
            D(2,2)=KD
            D(8,8)=KD
            D(2,8)=-1.0D0*KD
            D(8,2)=-1.0D0*KD
            F=F0+KD*DUU
            IF(F .LT. -1.0D0*F1) THEN
                F=-1.0D0*F1
                KD=0
            END IF
        END IF
        IF(UU .GE. -1.0D0*UU3 .AND. UU .LT. -1.0D0*UU2)THEN
            KD=K3
            D(2,2)=KD
            D(8,8)=KD
            D(2,8)=-1.0D0*KD
            D(8,2)=-1.0D0*KD
            F=K3*(UU+UU2)-F1
        END IF
        IF(UU .LT. -1.0D0*UU3)THEN
            KD=K4
            D(2,2)=KD
            D(8,8)=KD
            D(2,8)=-1.0D0*KD
            D(8,2)=-1.0D0*KD
            F=K4*(UU+UU3)-F3
        END IF
    END IF
    IF (UMI .LT. (-1.0D0*UU2)) THEN
        IF(UU .GE. (-1.0D0*UU2))THEN
            KD=K1
            D(2,2)=KD
            D(8,8)=KD
            D(2,8)=-1.0D0*KD
            D(8,2)=-1.0D0*KD
            F=F0+KD*DUU
            IF(F .LT. -1.0D0*F1) THEN
                F=-1.0D0*F1
                KD=0
            END IF
        END IF
        IF(UU .LT. (-1.0D0*UU2) .AND. UU .GE. (-1.0D0*UU3))THEN
            KD=K1

```

APPENDIX

```

    F=F0+KD*DUU
    FLIMP3=K3*(UU+UU3)-F3
    FLIMP4=K4*(UU+UU3)-F3
IF(F .LT. FLIMP3 .AND. FLIMP3 .GT. (-1.0D0*F3)) THEN
    F=FLIMP3
    KD=K3
    END IF
    IF(FLIMP3 .LE. (-1.0D0*F3)) THEN
    F=FLIMP4
    KD=K4
    END IF
    D(2,2)=KD
    D(8,8)=KD
    D(2,8)=-1.0D0*KD
    D(8,2)=-1.0D0*KD
END IF
IF(UU .LT. (-1.0D0*UU3))THEN
    KD=K1
    F=F0+KD*DUU
    FLIMP3=K3*(UU+UU3)-F3
    FLIMP4=K4*(UU+UU3)-F3
    IF(F .LT. FLIMP4) THEN
    F=FLIMP4
    KD=K4
    END IF
    D(2,2)=KD
    D(8,8)=KD
    D(2,8)=-1.0D0*KD
    D(8,2)=-1.0D0*KD
    END IF
END IF
IF(UU .GT. UMA)THEN
    UMA=UU
    FMA=F
    END IF
IF(UU .LT. UMI)THEN
    UMI=UU
    FMI=F
    END IF
SVARS(1)=F
SVARS(2)=UMA
SVARS(3)=FMA
SVARS(4)=UMI
SVARS(5)=FMI
END IF
IF (DUU .GT. ZERO) THEN
    KD=K1
    D(2,2)=KD
    D(8,8)=KD
    D(2,8)=-1.0D0*KD
    D(8,2)=-1.0D0*KD
    F=F0+KD*DUU
    IF(F .GT. ZERO) THEN
    F=F-KD*DUU
    GO TO 50
    END IF
IF(UU .GT. UMA)THEN

```

APPENDIX

```

        UMA=UU
        FMA=F
    END IF
    IF(UU .LT. UMI)THEN
        UMI=UU
        FMI=F
    END IF
    SVARS(1)=F
    SVARS(2)=UMA
    SVARS(3)=FMA
    SVARS(4)=UMI
    SVARS(5)=FMI
    END IF
    GO TO 70
    END IF
70    CONTINUE
    D(1,1)=KN
    D(7,7)=KN
    D(1,7)=-1.0D0*KN
    D(7,1)=-1.0D0*KN
CCCC
CCCCCCCCCCCCCCCCCCCCCCCCCCCCCCCCCCCCCCCCCCCCCCCCCCCCCCCCCCCC
CCCCCCCCCCCC
C          MAKE S-MATRIX          C
CCCCCCCCCCCCCCCCCCCCCCCCCCCCCCCCCCCCCCCCCCCCCCCCCCCCCCCCCCCC
CCCCCCCCCCCCCCCCCCCC
    DO I=1,NN
        DO K=1,NN
            DO J=1,NN
                S(I,K)=S(I,K)+D(I,J)*B(J,K)
            ENDDO
        ENDDO
    ENDDO
CCCCCCCCCCCCCCCCCCCCCCCCCCCCCCCCCCCCCCCCCCCCCCCCCCCCCCCCCCCC
CCCCCCCCCCCCCCCCCCCC
C          CALCULATE STRESSES AND STRAINS          C
CCCCCCCCCCCCCCCCCCCCCCCCCCCCCCCCCCCCCCCCCCCCCCCCCCCCCCCCCCCC
CCCCCCCCCCCCCCCCCCCC
    DO I=1,NN
        DO J=1,NN
            SSTRAIN(I)=SSTRAIN(I)+B(I,J)*UUU(J)
        ENDDO
    ENDDO
    DO I=1,NN
        DO J=1,NN
            SSTRESS(I)=SSTRESS(I)+D(I,J)*SSTRAIN(J)
        ENDDO
    ENDDO
    DO I=1,NN
        SVARS(I+5)=SSTRAIN(I)
        SVARS(I+5+NN)=SSTRESS(I)
    ENDDO
CCCCCCCCCCCCCCCCCCCCCCCCCCCCCCCCCCCCCCCCCCCCCCCCCCCCCCCCCCCC
CCCCCCCCCCCCCCCCCCCC
C ASSEMBLE RHS AND LHS          C
CCCCCCCCCCCCCCCCCCCCCCCCCCCCCCCCCCCCCCCCCCCCCCCCCCCCCCCCCCCC
CCCCCCCCCCCCCCCCCCCC

```

APPENDIX

C

```

DO I=1,NN
  DO J=1,NN
c    T(I,J)=ZERO
c    TT(I,J)=ZERO
    DD(I,J)=ZERO
    ENDDO
  ENDDO

```

C

```

c T(1,1)=ACOS
c T(1,2)=ASIN
c T(2,1)=-ASIN
c T(2,2)=ACOS
c T(7,7)=ACOS
c T(7,8)=ASIN
c T(8,7)=-ASIN
c T(8,8)=ACOS

```

C

```

c TT(1,1)=ACOS
c TT(1,2)=-ASIN
c TT(2,1)=ASIN
c TT(7,7)=ACOS
c TT(7,8)=-ASIN
c TT(8,7)=ASIN
c TT(8,8)=ACOS

```

C

```

C DO I=1,NN
C DO K=1,NN
C DO J=1,NN
C DD(I,K)=DD(I,K)+TT(I,J)*D(J,K)
C ENDDO

```

C

```

C ENDDO
C DO I=1,NN
C DO K=1,NN
C AMATRX(I,K)=AMATRX(I,K)+D(I,K)
C ENDDO

```

C

```

ENDDO
DFORCE = D(2,2)*(U(8)-U(2))
RHS(2,1) = RHS(2,1)+F
RHS(8,1) = RHS(8,1)-F

```

```

write(6,100)(F)
write(6,100)(FLAG)
write(6,100)(SVARS(I),I=1,(TWO*NN+5))
write(6,*) 'D:'
DO I=1,NN
  write(6,100)(D(I,J),J=1,NN)
END DO
write(6,*) 'RHS:'
write(6,100)(RHS(I,1),I=1,NN)
write(6,*) 'AMATRX:'
DO I=1,NN
  write(6,100)(AMATRX(I,J),J=1,NN)
END DO

```

```

100 format(12e12.5)

```

```

CCCCCCCCCCCCCCCCCCCCCCCCCCCCCCCCCCCCCCCCCCCCCCCCCCCCCCCCCCCC
CCCCCCCCCCCCCCCC

```

APPENDIX

RETURN

END

C#####  
#####